AD NUMBER
ADB037421
LIMITATION CHANGES
TO: **Approved for public release; distribution is unlimited.**
FROM: **Distribution authorized to U.S. Gov't. agencies only; Test and Evaluation; MAY 1979. Other requests shall be referred to Arnold Engineering Development Center, Arnold AFB, TN.**
AUTHORITY
AEDC ltr 15 Aug 1980

AEDC-TR-79-10

cy. 1 Vol. II

WIND TUNNEL RESULTS FROM A NOZZLE AFTERBODY TEST OF A 0.2-SCALE FIGHTER AIRCRAFT IN THE MACH NUMBER REGIME OF 0.6 TO 1.5

Volume II
MODEL CONFIGURATION AND ENVIRONMENT EFFECTS

Ernest J. Lucas
ARO, Inc., a Sverdrup Corporation Company

PROPULSION WIND TUNNEL FACILITY
ARNOLD ENGINEERING DEVELOPMENT CENTER
AIR FORCE SYSTEMS COMMAND
ARNOLD AIR FORCE STATION, TENNESSEE 37389

May 1979

Final Report for Period July 1977 — September 1978

Prepared for

AIR FORCE AERO-PROPULSION LABORATORY/TBA
WRIGHT-PATTERSON AIR FORCE BASE, OHIO 45433

and

ARNOLD ENGINEERING DEVELOPMENT CENTER/DOTA
ARNOLD AIR FORCE STATION, TENNESSEE 37389

NOTICES

APPROVAL STATEMENT

This report has been reviewed and approved.

Russell B. Sorrells III

RUSSELL B. SORRELLS, III
Project Manager, Analysis and Evaluation Division
Directorate of Test Engineering

Approved for publication:

FOR THE COMMANDER

Robert W. Crossley

ROBERT W. CROSSLEY, Lt Colonel, USAF
Acting Director of Test Engineering
Deputy for Operations

REPORT DOCUMENTATION PAGE

READ INSTRUCTIONS BEFORE COMPLETING FORM

1. REPORT NUMBER: AEDC-TR-79-10 Volume II	2. GOVT ACCESSION NO.
3. RECIPIENT'S CATALOG NUMBER	
4. TITLE (and Subtitle): WIND TUNNEL RESULTS FROM A NOZZLE AFTERBODY TEST OF A 0.2-SCALE FIGHTER AIRCRAFT IN THE MACH NUMBER REGIME OF 0.6 TO 1.5 - VOLUME II MODEL CONFIGURATION AND ENVIRONMENT EFFECTS	5. TYPE OF REPORT & PERIOD COVERED: Final Report - July 1977 - September 1978
	6. PERFORMING ORG. REPORT NUMBER
7. AUTHOR(s): Ernest J. Lucas, ARO, Inc., a Sverdrup Corporation Company	8. CONTRACT OR GRANT NUMBER(s)
9. PERFORMING ORGANIZATION NAME AND ADDRESS: Arnold Engineering Development Center/DOTA, Air Force Systems Command, Arnold Air Force Station, Tennessee 37389	10. PROGRAM ELEMENT, PROJECT, TASK AREA & WORK UNIT NUMBERS: Program Element 65807F and 62203F
11. CONTROLLING OFFICE NAME AND ADDRESS: Arnold Engineering Development Center/OIS, Arnold Air Force Station, Tennessee 37389	12. REPORT DATE: May 1979
	13. NUMBER OF PAGES: 346
14. MONITORING AGENCY NAME & ADDRESS (if different from Controlling Office)	15. SECURITY CLASS (of this report): UNCLASSIFIED
	15a. DECLASSIFICATION DOWNGRADING SCHEDULE: N/A

16. DISTRIBUTION STATEMENT (of this Report)

Distribution limited to U.S. Government agencies only; this report contains information on test and evaluation of military hardware; May 1979; other requests for this document must be referred to Arnold Engineering Development Center/OIS, Arnold Air Force Station, Tennessee 37389.

17. DISTRIBUTION STATEMENT (of the abstract entered in Block 20, if different from Report)

18. SUPPLEMENTARY NOTES

Available in DDC

19. KEY WORDS (Continue on reverse side if necessary and identify by block number)

wind tunnels	scale	Mach numbers
tests	models	Reynolds numbers
nozzle closures	fighter aircraft	
afterbodies	YF-17 aircraft	

20. ABSTRACT (Continue on reverse side if necessary and identify by block number)

An investigation was conducted in the Propulsion Wind Tunnel (16T) to document the effect of throttle-dependent parameters (nozzle closure and nozzle pressure ratio) on the aft end surface pressures of a 0.2-scale model of a twin-engine fighter prototype (YF-17). The data are part of a data base to be used in a future analysis effort to define the validity of current wind tunnel test techniques to provide data for full-scale flight performance

DD FORM 1 JAN 73 1473 EDITION OF 1 NOV 65 IS OBSOLETE

UNCLASSIFIED

20. ABSTRACT (Continued)

predictions. Surface pressure data were obtained on several model configurations, using a wingtip support system, to define the effects of nozzle closure and jet exhaust flow on the test article nacelle and nozzle surfaces. Two additional test entries were conducted on sting support systems to evaluate support system interference produced by the wingtip support system and to evaluate the annular-jet test technique. The wingtip support system interference was equivalent to approximately ten drag counts ($|\Delta CA| = 0.0010$) at Mach number 1.2 and tended to decrease at lower Mach numbers. The data indicate the annular-jet technique has the possibility of masking the sting support system interference while providing a jet plume simulation that produces good aft end drag correlation at the nozzle design pressure ratio. The effect of varying nozzle closure, nozzle pressure ratio, model angle of attack, and horizontal tail deflections are documented herein. All of these parameters produced significant local perturbations in the local surface pressure distribution. Some of these local effects, however, tend to be self-compensating in that the aft end pressure-integrated axial force coefficient data are relatively unaffected, which indicates that the overall model performance data may not provide sufficient information to demonstrate wind tunnel-to-flight correlation. Data were obtained at model characteristic Reynolds number, based on model length, which match that of the flight vehicle at high altitude. The results indicated that pressure data obtained at subsonic speeds at $Re_{\ell} = 30 \times 10^6$ are directly applicable to the high-altitude flight environment ($Re_{\ell} \sim 60 \times 10^6$).

AFSC
Arnold AFS Tenn

UNCLASSIFIED

PREFACE

The investigation reported herein was conducted by the Arnold Engineering Development Center (AEDC), Air Force Systems Command (AFSC), Arnold Air Force Station, Tennessee, by ARO, Inc., AEDC Division (a Sverdrup Corporation Company), operating contractor for the AEDC. The work was accomplished under sponsorship of the Air Force Aero-Propulsion Laboratory (AFAPL/TBA), Wright-Patterson Air Force Base, Ohio, and AEDC/DOT. The test programs were conducted in the Propulsion Wind Tunnel Facility (PWT), Propulsion Wind Tunnel (16T), under ARO Projects No. P41T-L8 and P41T-09. The supporting analysis was accomplished under ARO Project No. P43T-71. The Air Force project manager was R. B. Sorrels, III, AEDC/DOTA, and the manuscript was submitted for publication on January 2, 1979.

CONTENTS

ILLUSTRATIONS

INTRODUCTION

Supplemental data are presented in this volume (Vol. II) to document the effects of test variables — model attitude (α), nozzle closure (A8), nozzle pressure ratio (NPR or NPRE), horizontal tail deflections (δ_H), Reynolds number (Re_ℓ), and bay purge exhaust flow ($\dot{w}_{BP}$) on the afterbody pressure distributions. Volume I contains the test technique evaluation of the test conducted. Most of the data presented herein were obtained using the wingtip and small-sting support systems. Jet effect definition with the wingtip support system was obtained with full-flowing (conventional) nozzles, whereas the sting-supported model used the annular-jet technique (Ref. 1). The annular-jet data were obtained at the equivalent nozzle pressure ratio (NPRE) which duplicated the maximum plume diameter of a conventional jet.

1.0 NOZZLE CLOSURE

Variable nozzle aircraft, such as the YF-17, have provisions for positioning the internal nozzle contour for maximum jet efficiency (thrust) at a given throttle setting. Altering the internal contour, however, changes the external nozzle shape affecting the nozzle axial projected area and the local flow over the aft end of the vehicle.

The purpose of the tests was to provide results for a wind tunnel-to-flight correlation study. Thus, the emphasis on nozzle closure effects is to define the influence that a mismatch between wind tunnel and flight nozzle configuration would have on the aft end surface pressure coefficients. The effect of closure contour was investigated by testing four simulated nozzle closures (A8 = 200-, 230-, 300-, and 360-in.^{2}, full-scale nozzle throat area) at jet off and at a constant NPR or NPRE of 5.0. The pressure coefficient data obtained with the four nozzle closures are presented in Figs. 1 through 10 as a function of orifice location (ϕ and X/L). Opening the nozzle (reducing nozzle closure) produces a flatter surface contour to the local flow which causes a decrease in the expansion over that region of the nozzle ($0.97 < X/L \leq 1.0$) and is evident in all six rows of orifices shown. The effect of changing the nozzle closure is most evident on the nozzle surface at jet-off conditions (see Figs. 1, 4, and 7); however, the jet-on conditions are of primary interest. Operating the nozzles at NPR = 5.0 tends to reduce the closure effect on the nozzle surface pressure coefficients compared to the jet-off data for either full-flowing (Figs. 2 and 5) or annular (Figs. 3 and 6) jets at Mach numbers 0.6 and 0.9. Significant effects of closure are evident at Mach number 1.2 (Figs. 8 and 9) but are more restricted to the nozzle region of the model.

Using the intermediate nozzle (A8 = 300 in.^{2}) operating at NPRE = 5.0 as a reference, the effect of changing closure is illustrated by the differential pressure coefficient data shown in Fig. 11. These results were obtained by subtracting the reference pressure coefficient data from the data of other configurations on an individual pressure orifice basis. The influence of the nozzle contour is evident over the entire model afterbody, but the predominant effects are in the vicinity of the nozzle. It should be noted that the differences are both positive and negative for each nozzle such that these effects could be obscured in an integration to obtain the aft end axial loadings.

The pressure-integrated axial force coefficient data are presented in Fig. 12 for Mach numbers 0.6, 0.9, 1.2, and 1.5. The nozzle component of axial force indicates no significant effect of closure at subsonic speed, although large variations were evident in the surface pressure distributions shown in Fig. 11. Thus, the combination of compensating pressure changes with closure configuration and the changing axial projected area as the nozzle opening is varied tend to cancel the closure effect on the nozzle axial force. The larger surface pressure coefficient changes caused by nozzle closure variation at Mach numbers 1.2 and 1.5 are more evident in the nozzle axial force loads. A decrease in nozzle closure (opening the nozzle) produces a significant decrease in the total axial force coefficient at any given nozzle pressure ratio.

Nozzle closure is, thus, shown to be an important parameter requiring almost exact simulation for a proper interpretation of its effect. Since there is not an orderly variation of the data with nozzle closure, interpolation of the data for off-condition predictions is not considered valid for this parameter.

2.0 NOZZLE PRESSURE RATIO

High-pressure air at the tunnel total temperature (560°R) was supplied to the model through the support system to simulate jet exhaust flow. Thus, jet exhaust temperature effects are not considered in this investigation. The nozzle pressure ratio (NPR for conventional jet or NPRE for annular jet) was varied from jet off (NPR $\approx$ 1.0) to approximately twice the design value for a full-flowing jet for each of the four nozzle closures investigated.

The necessity of a proper simulation of the jet exhaust is illustrated in the axial force and pressure coefficient data presented in Figs. 12 and 13 through 27, respectively, for each nozzle closure at the anticipated operational flight Mach numbers. The data are presented for both the wingtip-supported conventional jet model and the sting-supported annular-jet model. Similar trends with nozzle pressure ratio occur for both jet flow simulations, but the actual values of the data do not agree because corrections for the support system interference have not yet been applied.

The axial force coefficient data shown in Fig. 12 indicate that the influence of the NPR or NPRE is limited to the nozzle portion of the model. The afterbody axial force coefficient is relatively invariant with nozzle pressure ratio for any given nozzle closure. The external nozzle pressure distribution. however, was significantly affected by the changing flow field produced as NPR was varied. The jet-off condition generally produces the highest axial load since the external flow expands over the nozzle exit and creates the lowest surface pressure condition. As the NPR is increased the base flow separation region is filled, then pumped by the jet as NPR is further increased producing the "bucket effect" ($1 < NPR < 2$). This phenomenon is common to all nozzles tested. Increasing the NPR beyond the design value increases the plume diameter and causes the external flow over the model to compress as it encounters the enlarging plume. The compression pressurizes the nozzle and afterbody region reducing the nozzle axial force coefficient. The total force component reflects the net change from the nozzle and afterbody.

At subsonic speeds the jet exhaust flow effect extends upstream on the model to $X/L \approx 0.92$ as shown in Figs. 13 through 22. The effect of the plume is confined more to the nozzle region at the supersonic test conditions (Figs. 23 through 26), since the local supersonic flow over the model isolates the plume effects to the region downstream of the expansion over the nozzle ($X/L > 0.97$).

Documentation of small changes above and below the design NPR (value which produces a full-flowing jet for the nozzle setting and test environment) indicates the area of influence and magnitude of off-design jet exhaust effects. Data from this investigation are presented in Fig. 27 as a differential pressure coefficient, obtained by subtracting the surface pressure coefficients, one-for-one, between the two NPR test points of interest. Small changes in the NPR from the design value produce effects which seem orderly and could probably be interpolated between matrix test points to profice off-design condition data.

3.0 MODEL ATTITUDE

The majority of the data were obtained at 4-deg angle of attack which approximates the flight vehicle trim attitude for a major portion of the flight test program. The effects of model attitude were documented, however, at several test conditions and these data are presented in Figs. 28 through 38 for each nozzle configuration (A8) at Mach numbers 0.6, 0.9, and 1.2. The data presented were obtained on both the wingtip and sting support systems and, in general, exhibit similar trends. As expected, the surface pressures increased on the windward side of the model with increasing pitch angle while the leeside surface pressures decreased. The sensitivity of the model surface pressure-to-attitude at

Mach numbers 0.6 and 1.2 was found to be essentially linear (see Figs. 28 and 29). The pressure increments at Mach number 1.2 (Figs. 34 through 36) are larger, however, than those at Mach number 0.6. The incremental changes in surface pressure coefficients with model attitude are presented in Fig. 37 for two nozzle configurations (A8 = 200 in.^{2} and 300 in.^{2}) and both support systems. The changes in the local surface pressures are both negative and positive such that the pressure-area integration is unchanged. Thus, the effect of model attitude on axial force does not necessarily reflect the local effects indicated by the pressure data. Basically, the nozzle axial force coefficient is insensitive to model attitude as shown in Fig. 38, whereas the pressure data indicate large local effects, especially at Mach number 1.2.

Local surface pressure changes as a function of model attitude could be important (local stresses on actuators or intake or exhaust port operations) and should be considered in the wind tunnel-to-flight correlation even though the axis loads are not significantly affected.

4.0 HORIZONTAL TAIL DEFLECTION

The horizontal tail extends from X/L = 0.86 to 0.97. As the tail is rotated leading edge down ($-\delta_H$) the pressures above the horizontal tail plane (ϕ = 0, 45-, and 315-deg rows of orifices) are increased (less negative pressure coefficient), whereas the pressures below the horizontal tail (ϕ = 135-, 180-, and 225-deg rows) are decreased (see Figs. 39 through 45).

The surface pressure coefficient changes are both positive and negative with any tail angle change and tend to be compensating in the integration to obtain aft end axial loads. Thus, the axial force coefficient data presented in Fig. 45 indicate that the variation in nozzle and afterbody loads are at most only three or four counts (ΔCA ~ 0.0004) at the test conditions investigated.

5.0 REYNOLDS NUMBER

A major problem area with any subscale test is the effect of not simulating the correct characteristic Reynolds number. The 0.2-scale model investigation was conducted to obtain data at flight characteristic Reynolds number of 60 x 10^6, based on vehicle length. Reynolds number variation data were obtained with both the wingtip and large-sting support systems. Results are shown only, however, from the large-sting support program since that model had the proper upstream wing planform without the wingtip support simulation. The axial force data presented in Fig. 46 are relatively insensitive to Reynolds number variations above the nominal test value of ~ 30 x 20^6 at the subsonic test conditions. At Mach number 1.2 the model axial loading is still varying with

Reynolds number at the upper limit of this investigation (Figs. 46e and f). The model nozzle region is the area affected, indicating the expansion and shock locations on the nozzle are still being influenced by Reynolds number changes. Data are shown at both 0- and 4-deg angle of attack and indicate the same trend at both attitudes.

The surface pressure coefficient data presented in Figs. 47 through 53 verify the integrated data and additionally indicate some local sensitivity to Reynolds number at the lower Reynolds numbers. Changes in surface pressures are more clearly defined by the incremental surface pressure coefficient data presented in Fig. 53. The major areas of Reynolds number influence are in the expansion over the nozzle connect station (X/L = 0.97) and the maximum pressure recovery region at the nozzle exit (X/L ~ 1.0).

6.0 BAY PURGE EXHAUST

A simulation of the engine bay purge exhaust flow was conducted by locating scaled exhaust exit ports on the top and bottom of each nacelle at X/L ~ 0.95. An inlet was also provided in the engine inlet fairing (see Fig. 1, Vol. 1) which was sized to simulate the scaled scavenged flow on the actual flight vehicle. Replacing the exhaust port plugs with the screens (to allow bottom to top flow-through at angle of attack) or opening the inlet port (to pressurize the bay purge cavity) did not significantly affect the trend or value of the axial force data (see Fig. 54). Small perturbations in the local surface pressure coefficient fore and aft of the bay purge exhaust port were evident on the leeside pressures (ϕ = 0) as illustrated in the differential pressure coefficient data presented in Fig. 55. At subsonic speeds the effects were small and only evident on the top and bottom nacelle centerline rows of pressure orifices (ϕ = 0 and 180 deg). At supersonic speeds the local effects are significant on the upper surface centerline (ϕ = 0) and extend into the trough region between the engine nacelle (ϕ = 45 deg).

7.0 SUMMARY REMARKS

Data presented in this volume document the effect model configuration parameter variations have on the data. Generalized conclusions concerning the effects of these variables are as follows:

1. The nozzle closure configuration is a major vehicle parameter requiring proper simulation in a test program. The nozzle shape affects the entire aft end surface pressure profile, and thus the true contour and flow simulation is necessary to properly define the throttle-dependent performance.

2. Nozzle pressure ratio effects were orderly with the model surface pressure increasing as NPR increased above the design value. The NPR influence extended farther upstream on the model for the larger (more open) nozzle configuration.

3. Varying the model angle of attack over the range of 0 to 8 deg resulted in essentially linear variations in the model surface pressures, the windward pressures increasing with increasing pitch attitude whereas the leeside pressure decreased. Effects on the overall pressure-integrated axial force coefficients were minimal, however, since the pressure changes with model attitude were self-compensating in the integrations.

4. Data were obtained at a characteristic Reynolds number equivalent to that of the flight vehicle (60×10^6). The data obtained at the nominal Reynolds number (30×10^6) and subsonic speeds are representative of the data at the flight conditions, and thus, applicable for a direct comparison with flight results. Reynolds number effects are still evident in the supersonic data however.

5. Horizontal tail deflections produced significant changes in the model local surface pressures by producing a more compressed flow above and less compressed flow below the tail plane as the leading edge was deflected downward ($-\delta_H$). These local effects tend to cancel in the pressure integration and are not as evident in the axial load data.

6. Effects of model angle of attack, nozzle pressure ratio, and horizontal tail angle on the pressure data are of such a systematic nature that interpolation between wind tunnel matrix test conditions could be made to provide values for any intermediate condition if the effects of the variables are assumed to be independent.

7. The bay purge exhaust produced small localized effects at subsonic Mach numbers. At supersonic speeds, however, bay purge exhaust effects were significant in the trough region between the two engines.

REFERENCES

1. Price, Earl A., Jr. "A Parametric Investigation of the Annular Jet Concept for Obtaining Afterbody Drag Data at Transonic Mach Numbers." AEDC-TR-77-104 (ADA050891), February 1978.

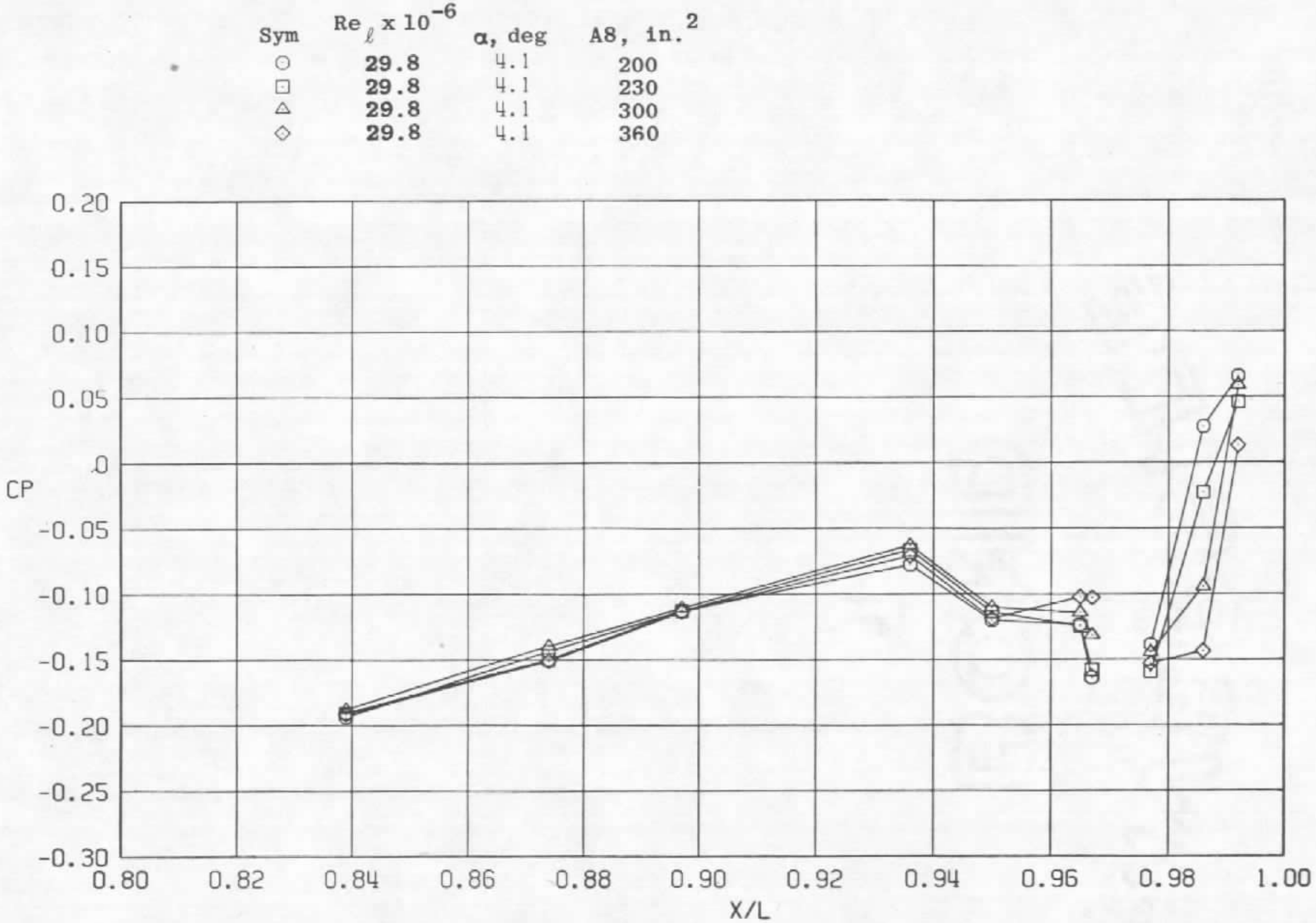

a. $\phi = 0$

Figure 1. Nozzle closure effects on surface pressure coefficients, NPR = 1.0, M = 0.6 (WT).

Sym	$Re_\ell \times 10^{-6}$	α, deg	A8, in.^{2}
○	29.8	4.1	200
□	29.8	4.1	230
△	29.8	4.1	300
◇	29.8	4.1	360

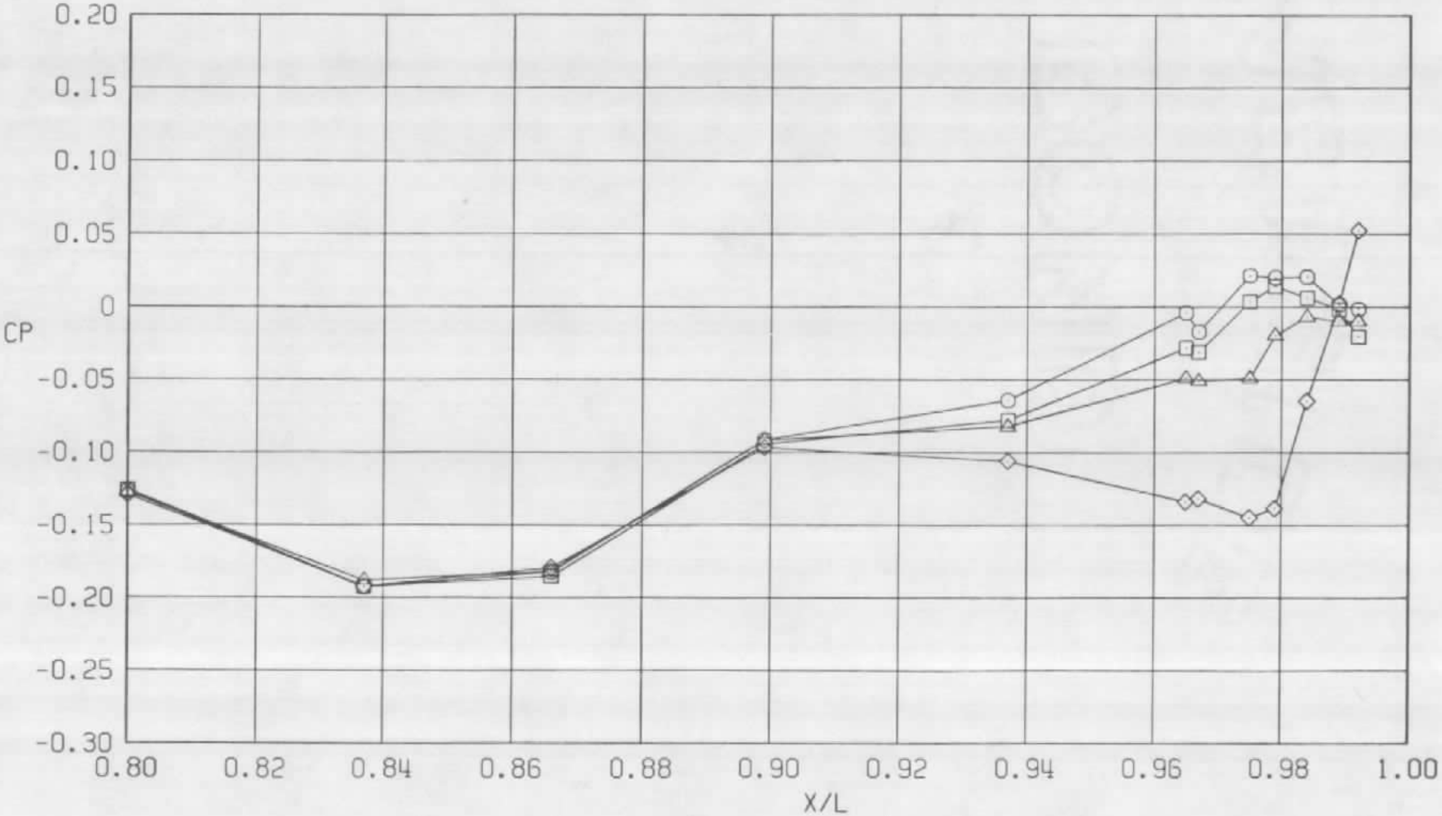

b. ϕ = 45 deg
Figure 1. Continued.

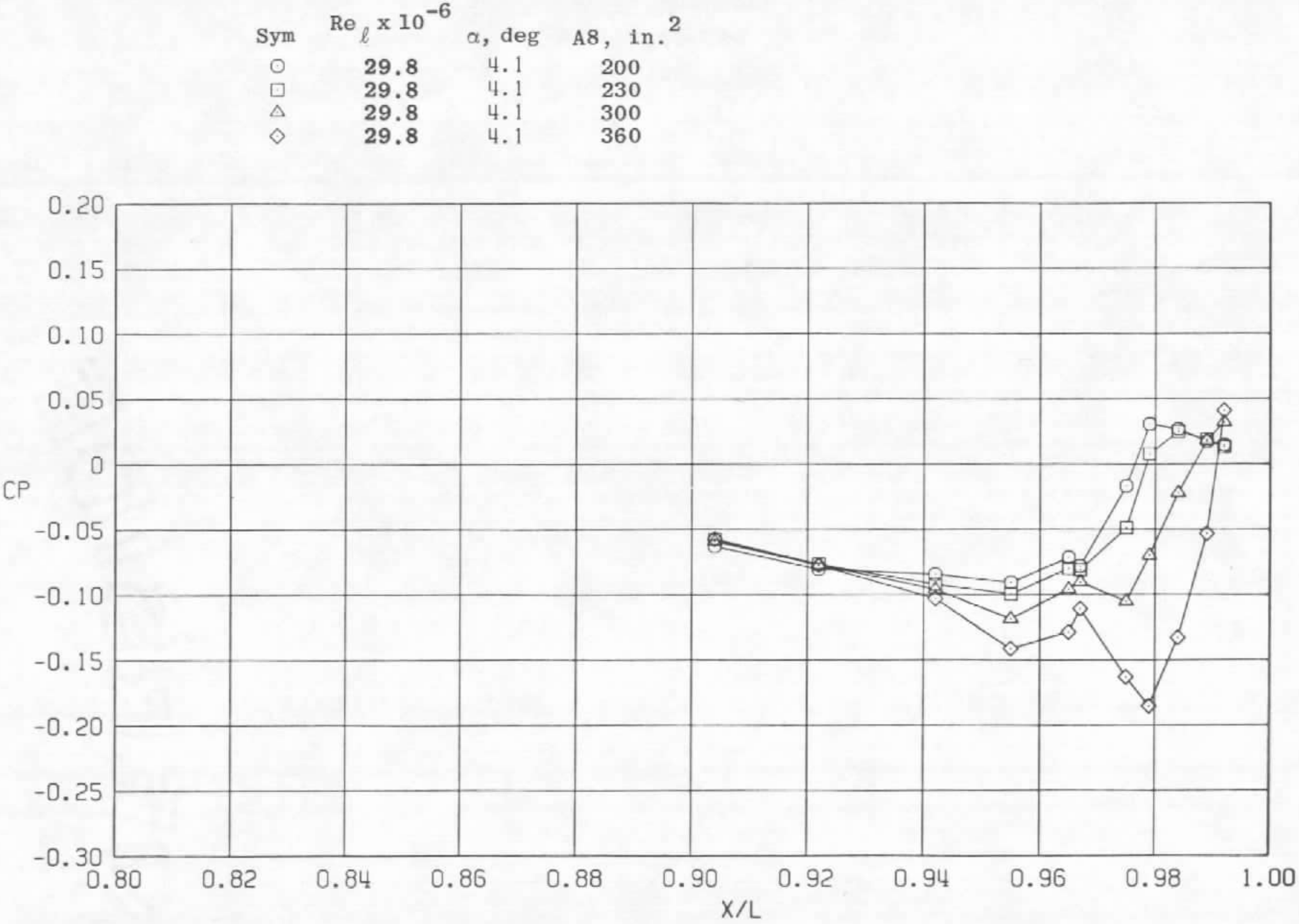

c. ϕ = 135 deg
Figure 1. Continued.

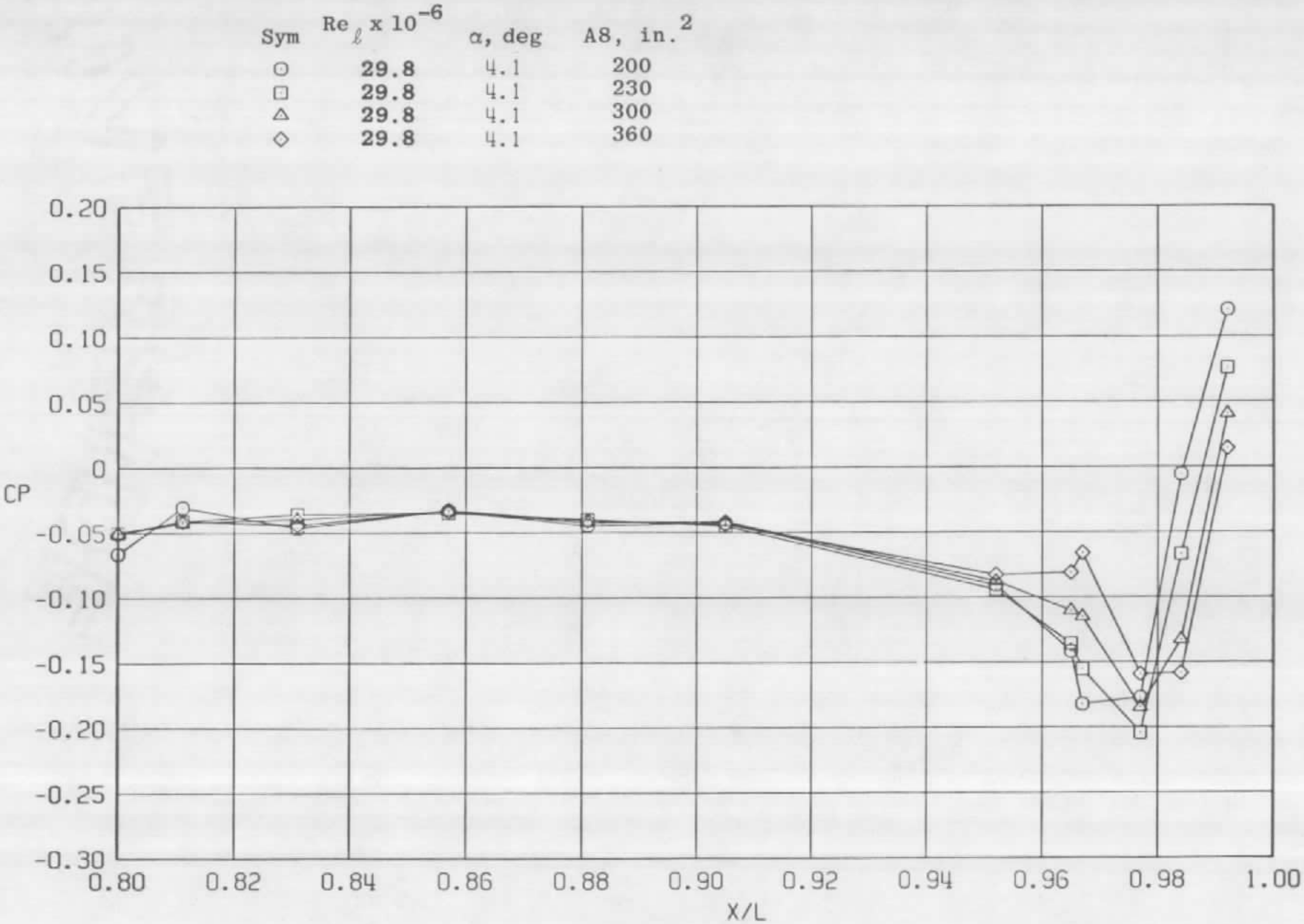

d. ϕ = 180 deg
Figure 1. Continued.

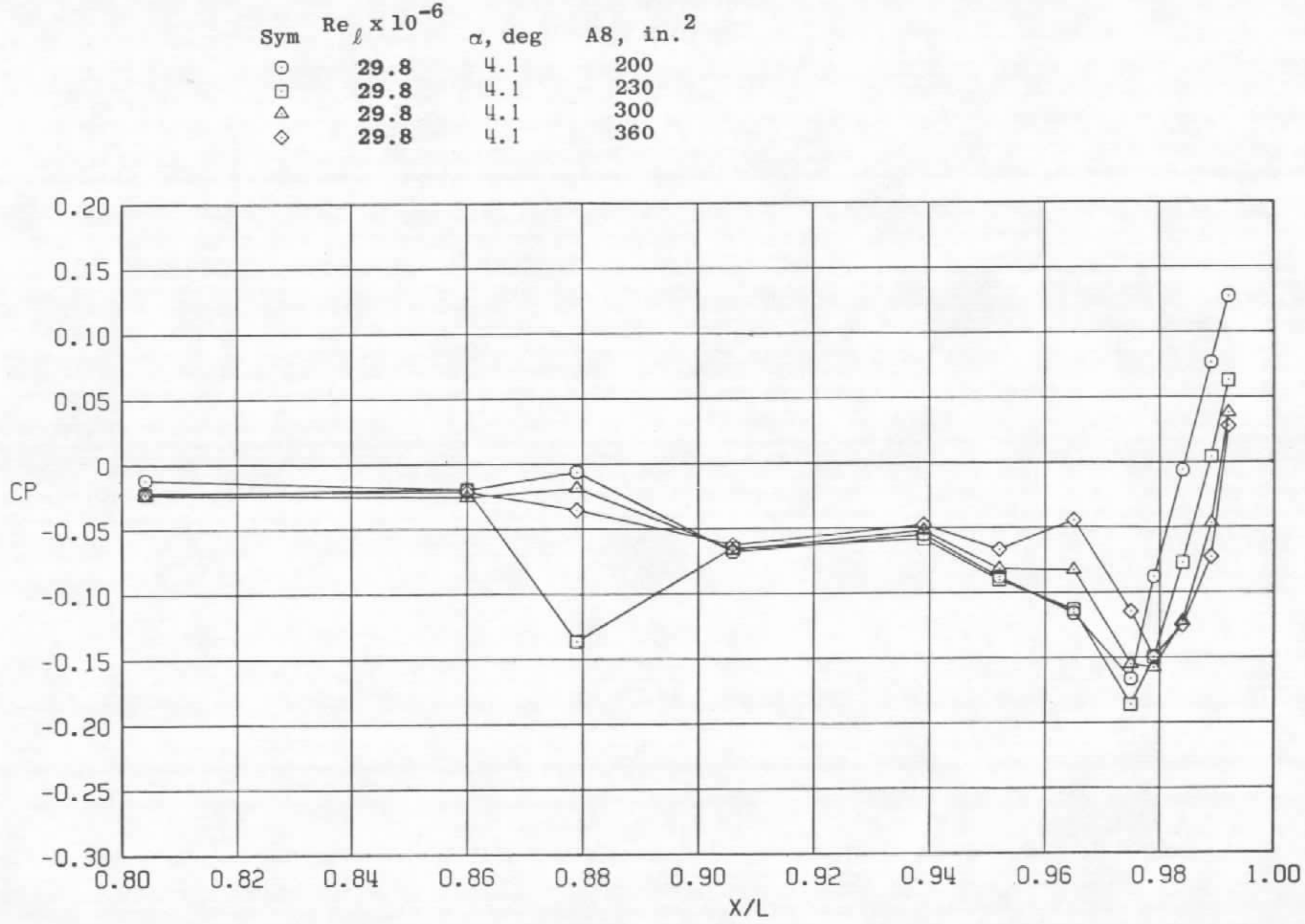

e. ϕ = 225 deg

Figure 1. Continued.

Sym	$Re_{\ell} \times 10^{-6}$	α, deg	A8, in.^{2}
○	29.8	4.1	200
□	29.8	4.1	230
△	29.8	4.1	300
◇	29.8	4.1	360

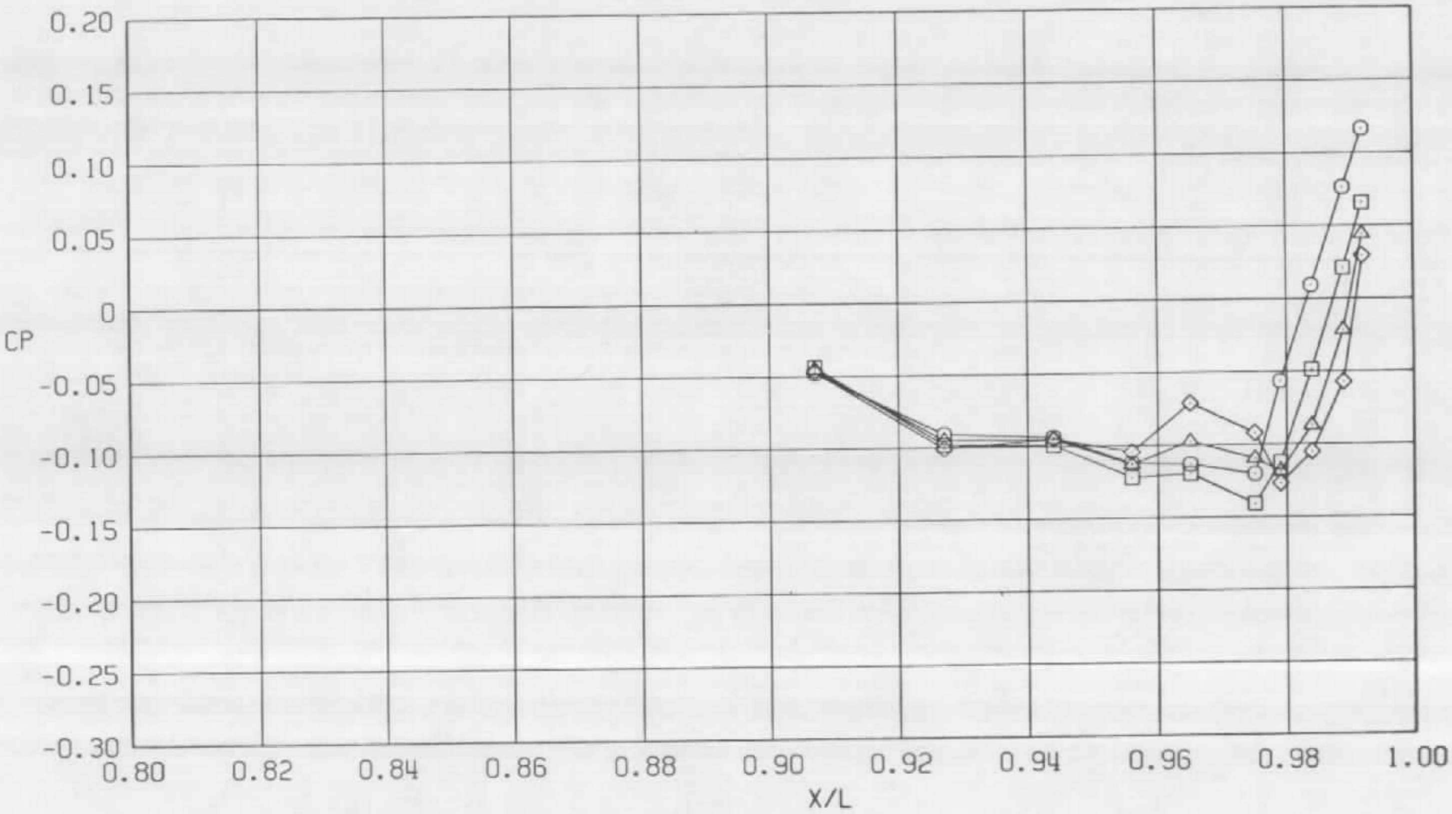

f. ϕ = 315 deg
Figure 1. Concluded.

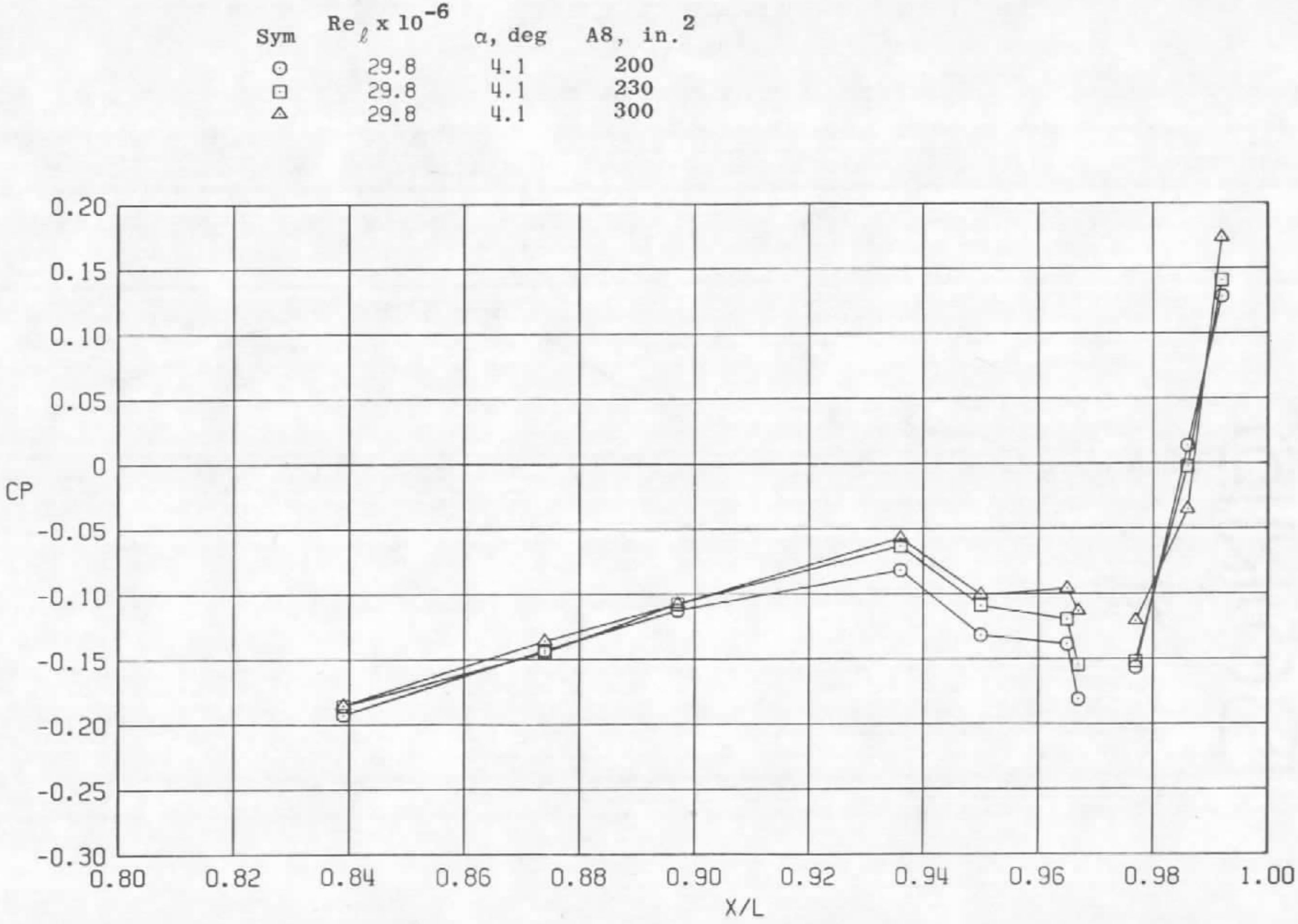

a. $\phi = 0$

Figure 2. Nozzle closure effects on surface pressure coefficients, NPR = 5.0, M = 0.6 (WT).

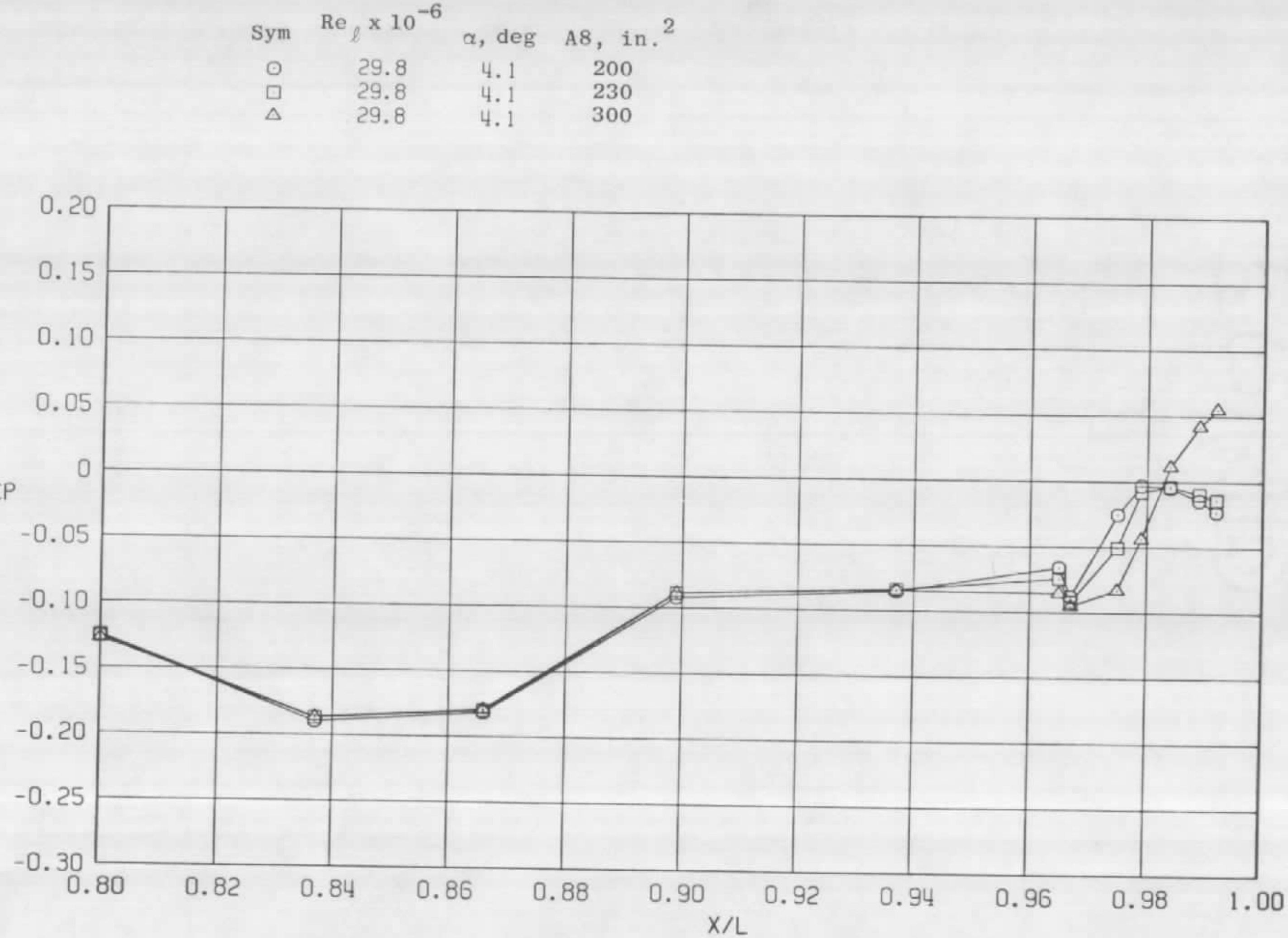

b. ϕ = 45 deg
Figure 2. Continued.

c. ϕ = 135 deg
Figure 2. Continued.

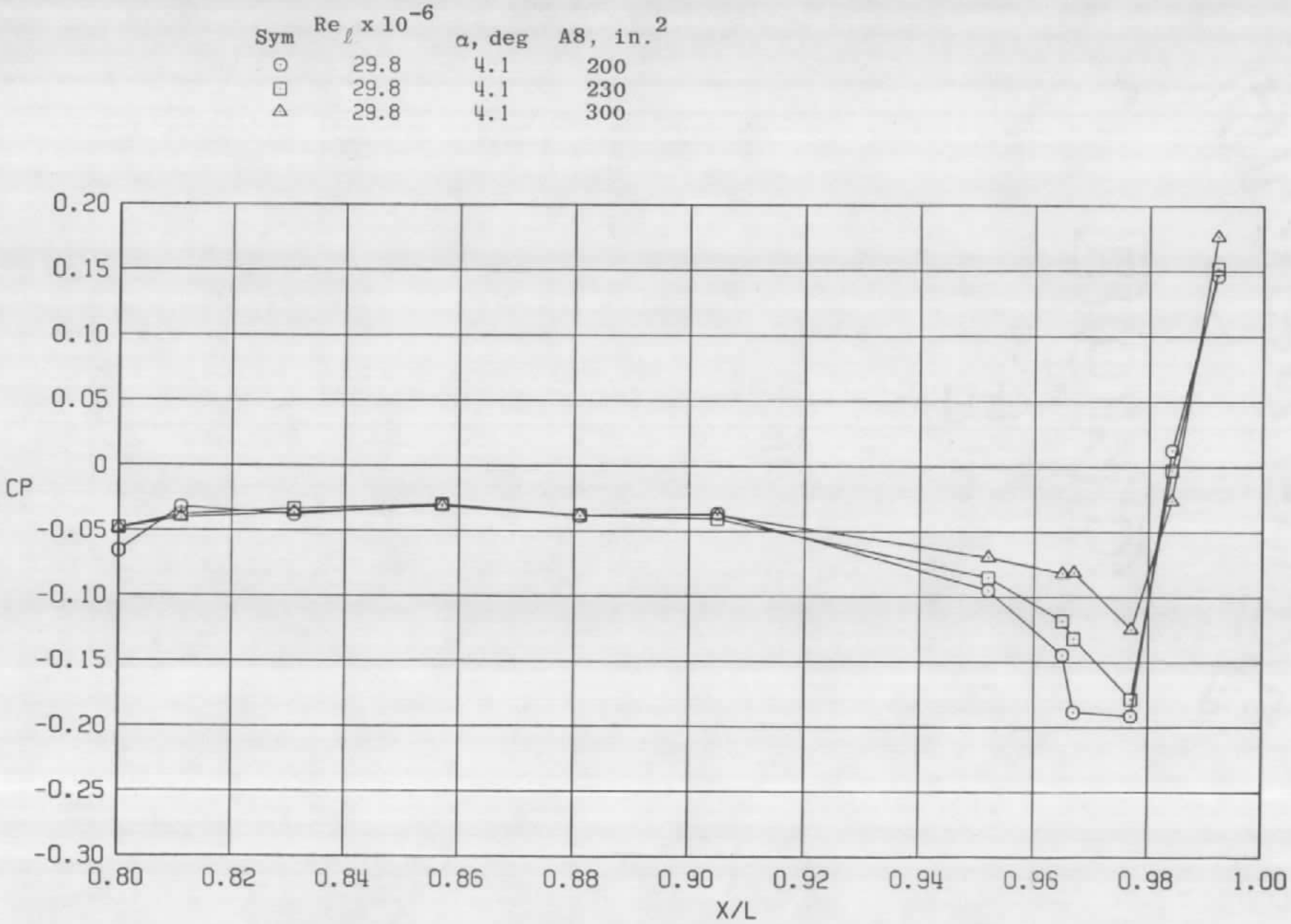

d. ϕ = 180 deg
Figure 2. Continued.

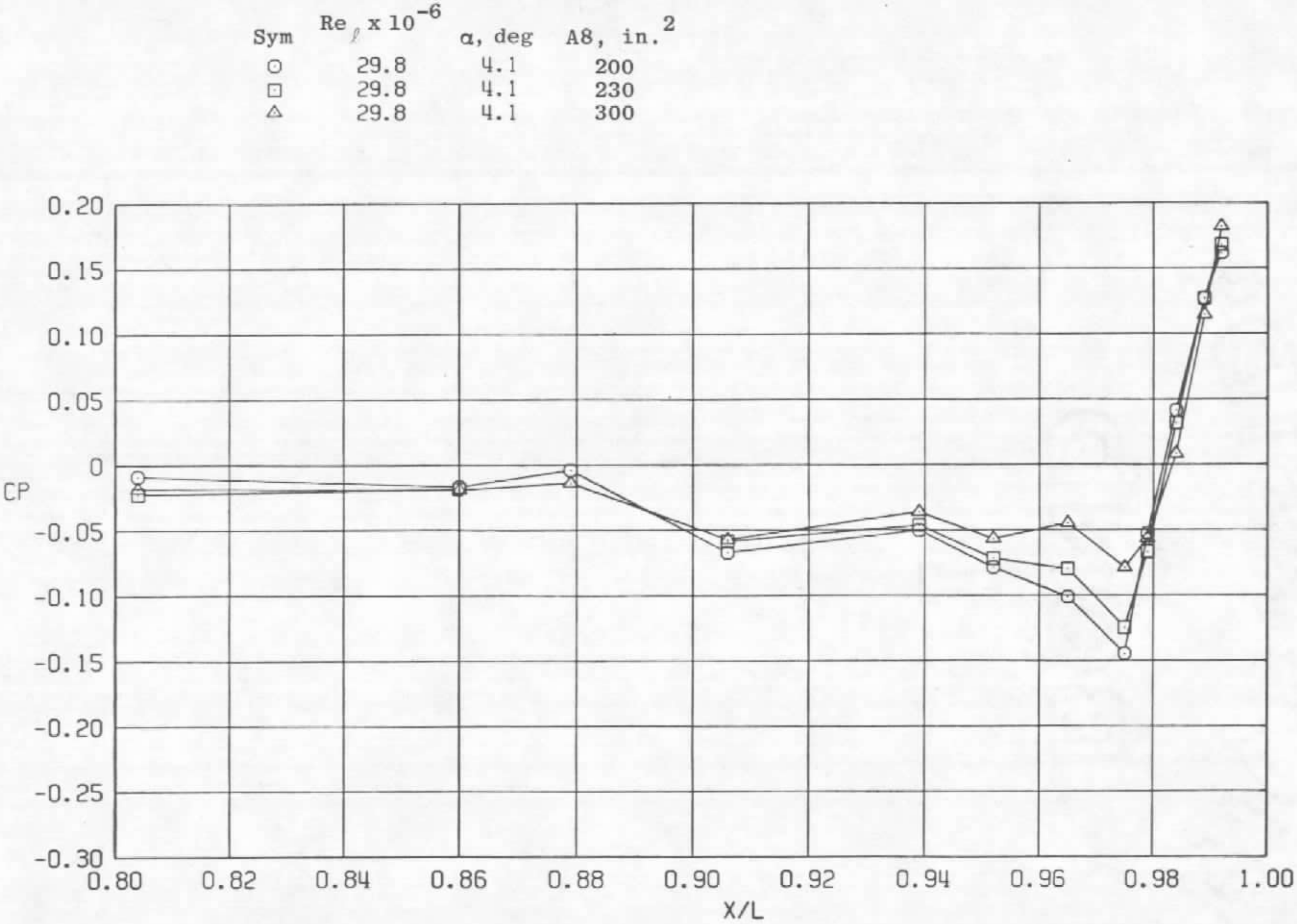

e. ϕ = 225 deg
Figure 2. Continued.

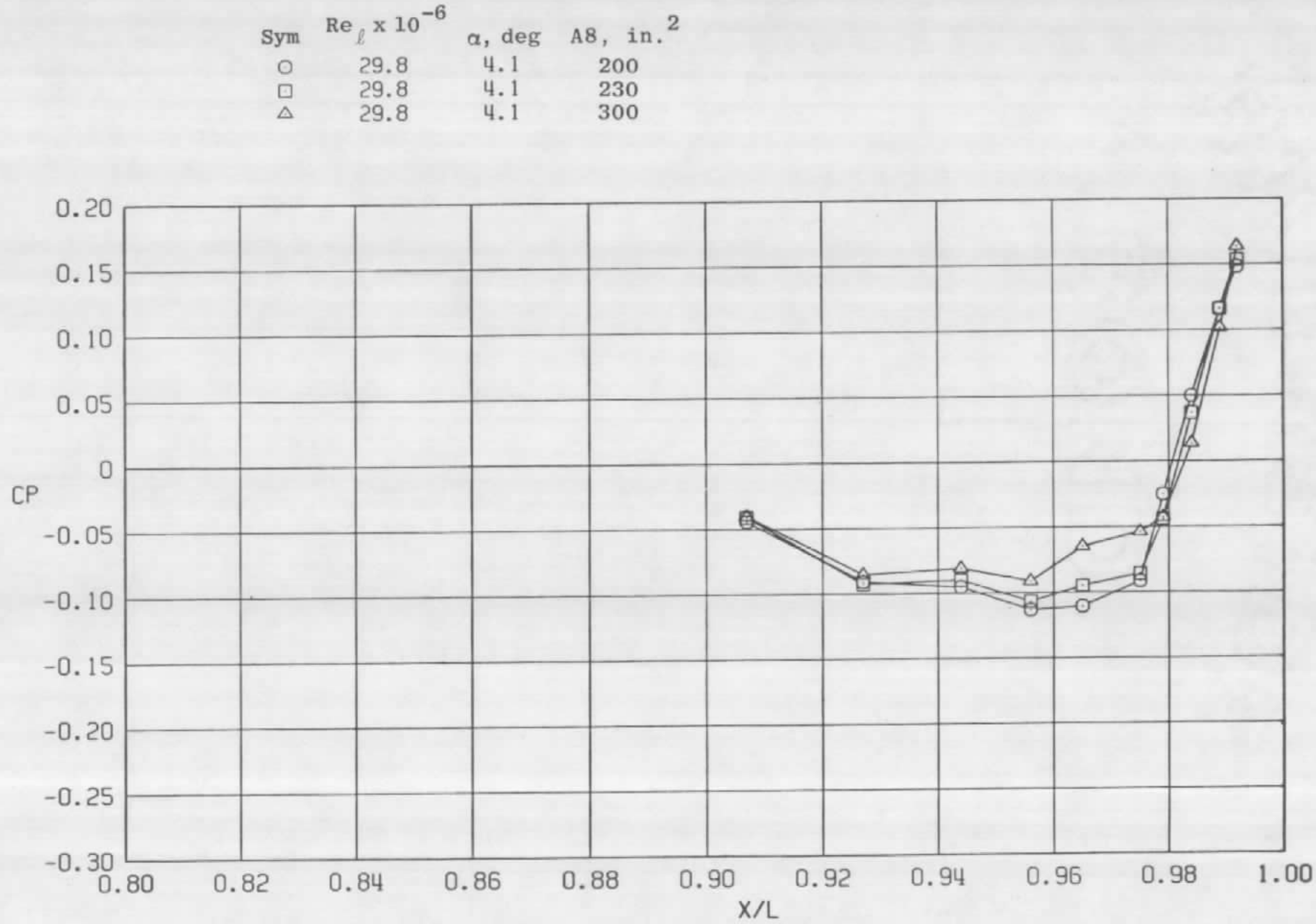

f. ϕ = 315 deg
Figure 2. Concluded.

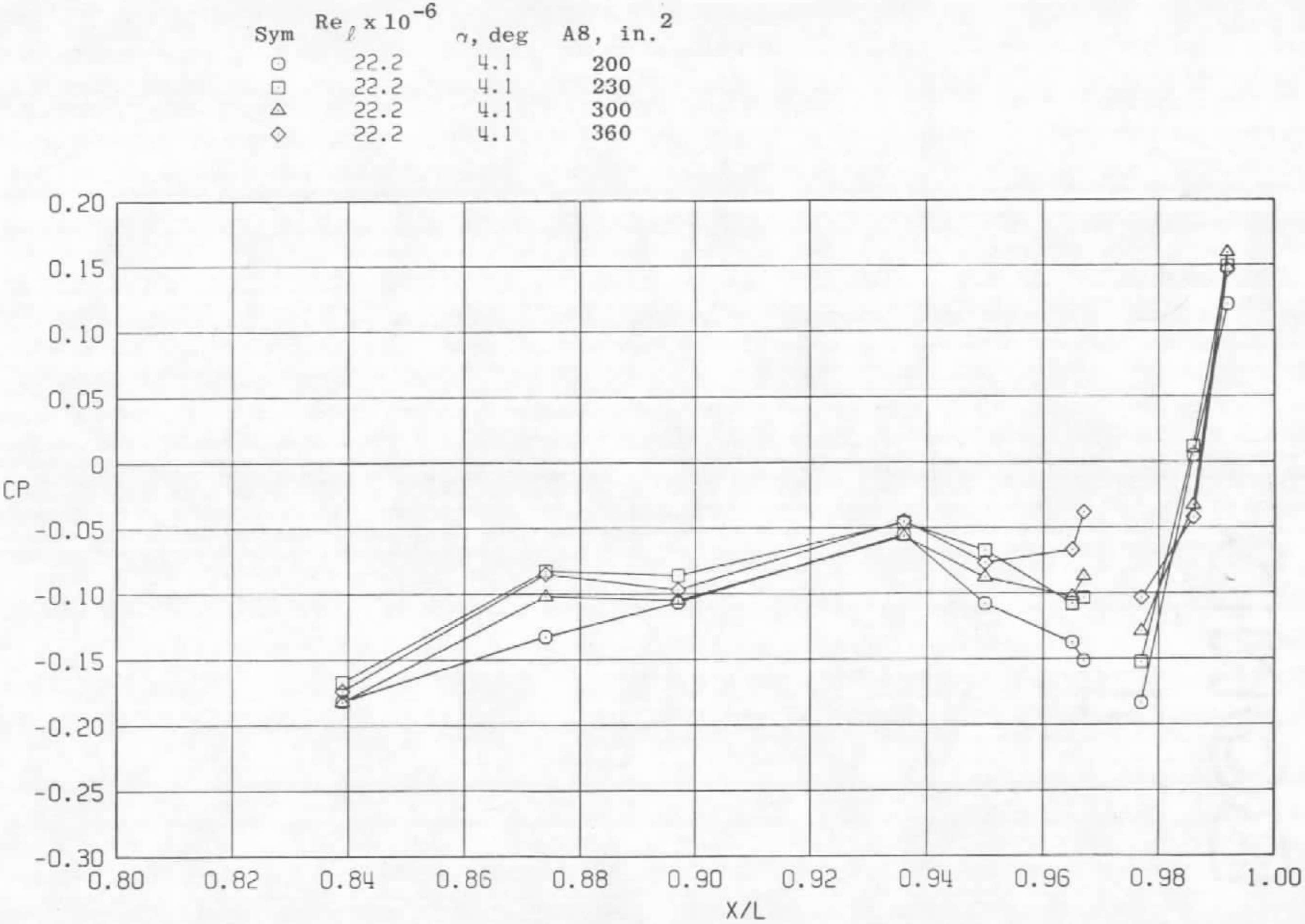

a. $\phi = 0$

Figure 3. Nozzle closure effects on surface pressure coefficients, M = 0.6, NPRE = 5.0 (SS).

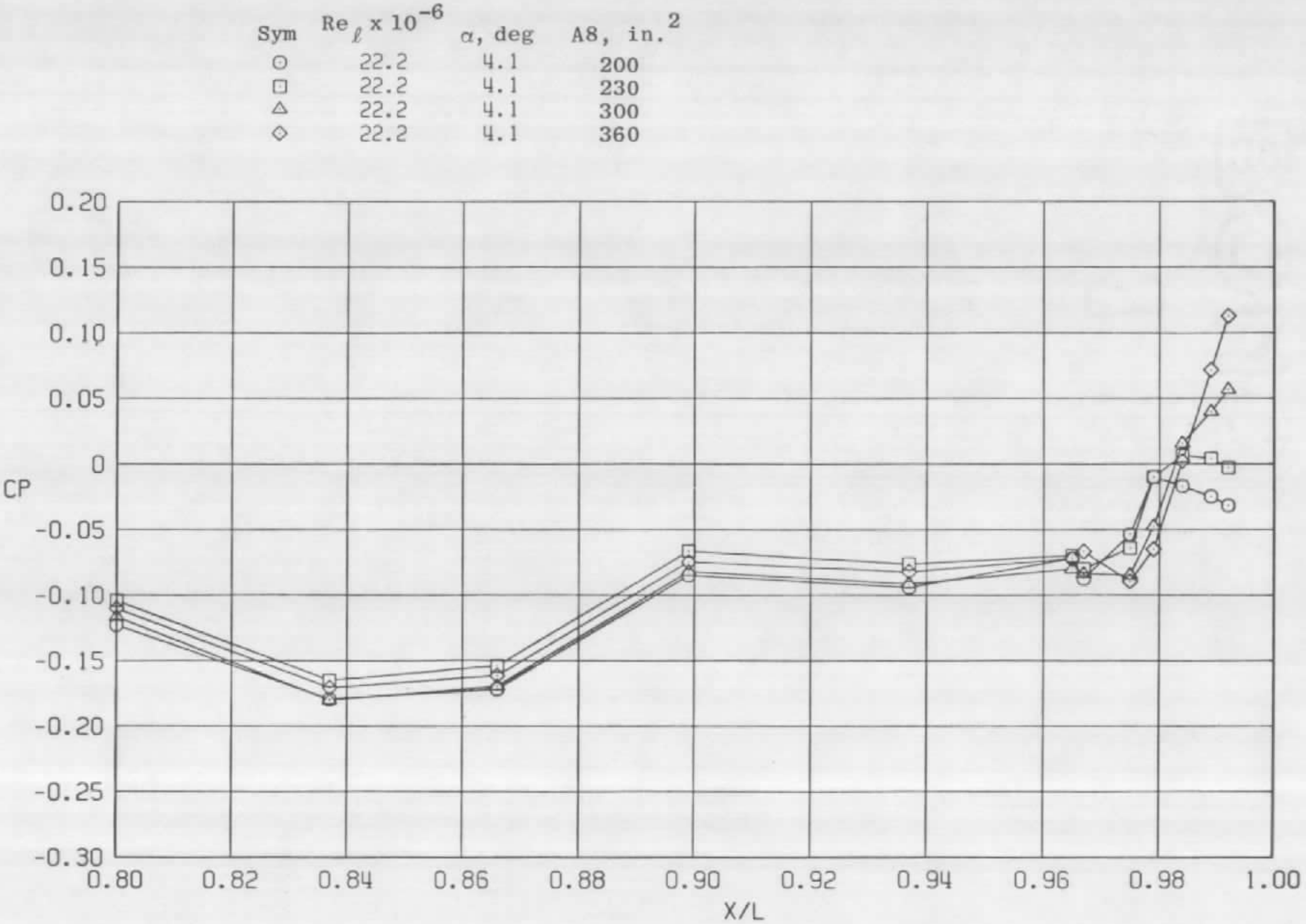

b. ϕ = 45 deg

Figure 3. Continued.

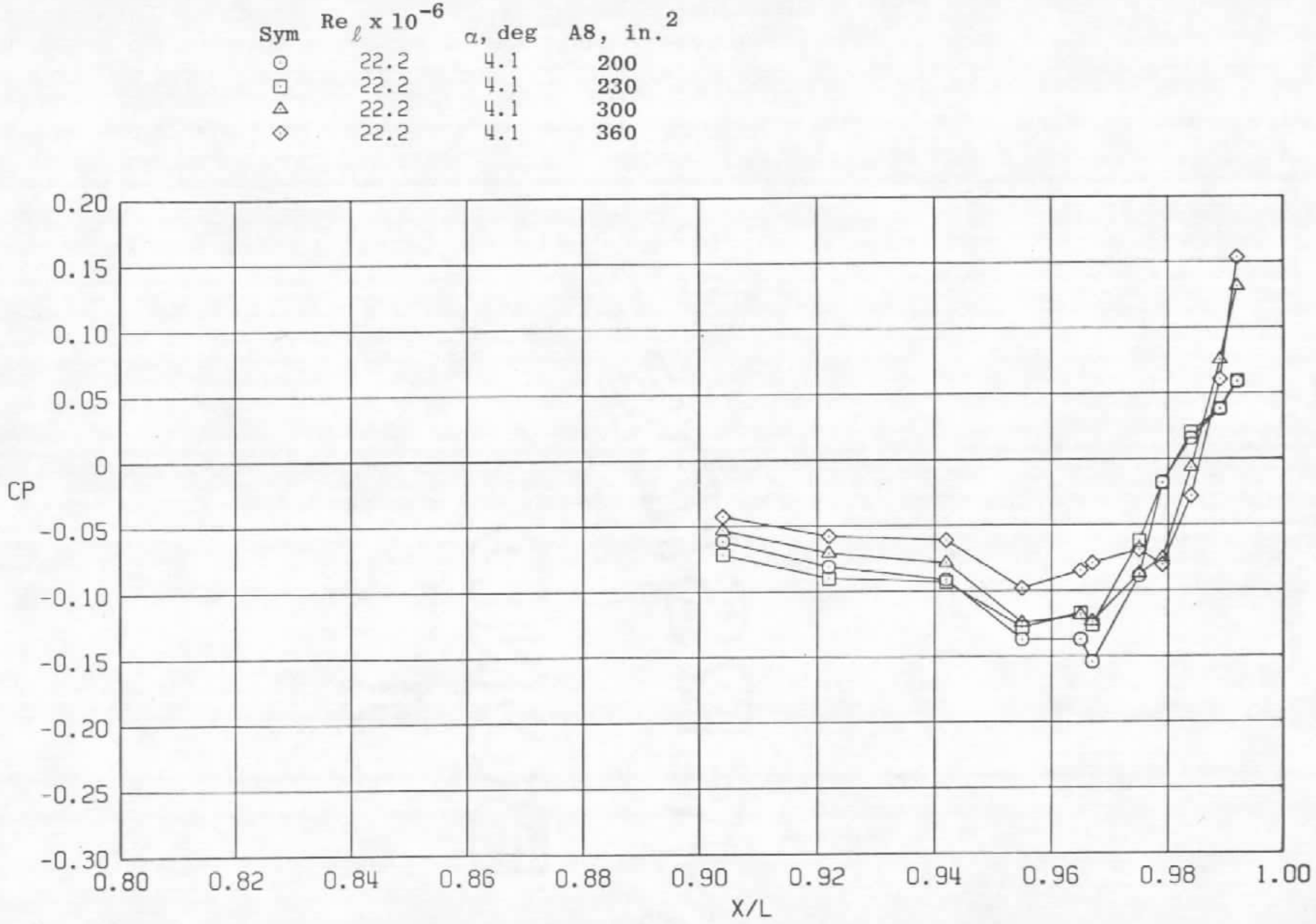

c. ϕ = 135 deg
Figure 3. Continued.

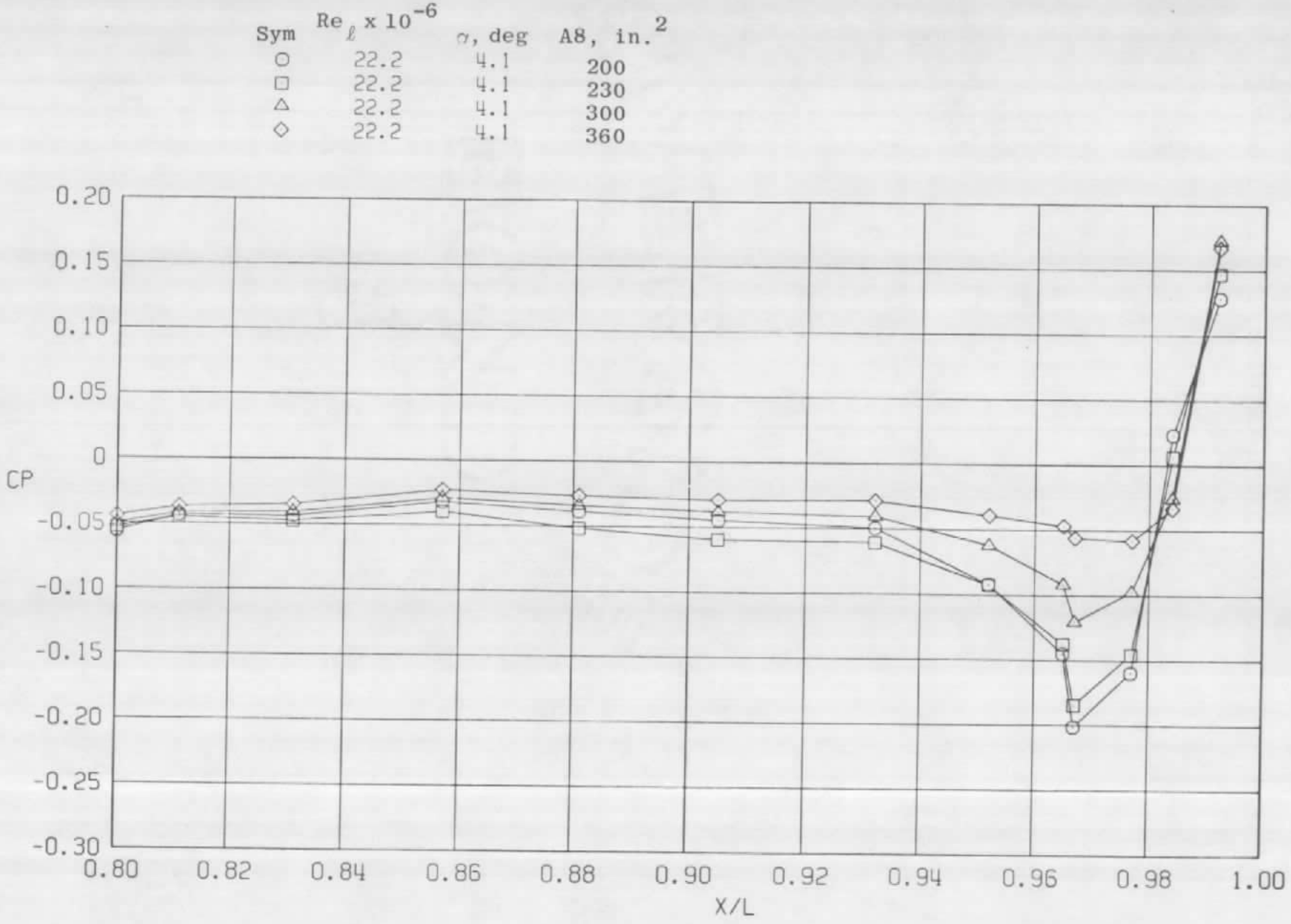

d. ϕ = 180 deg

Figure 3. Continued.

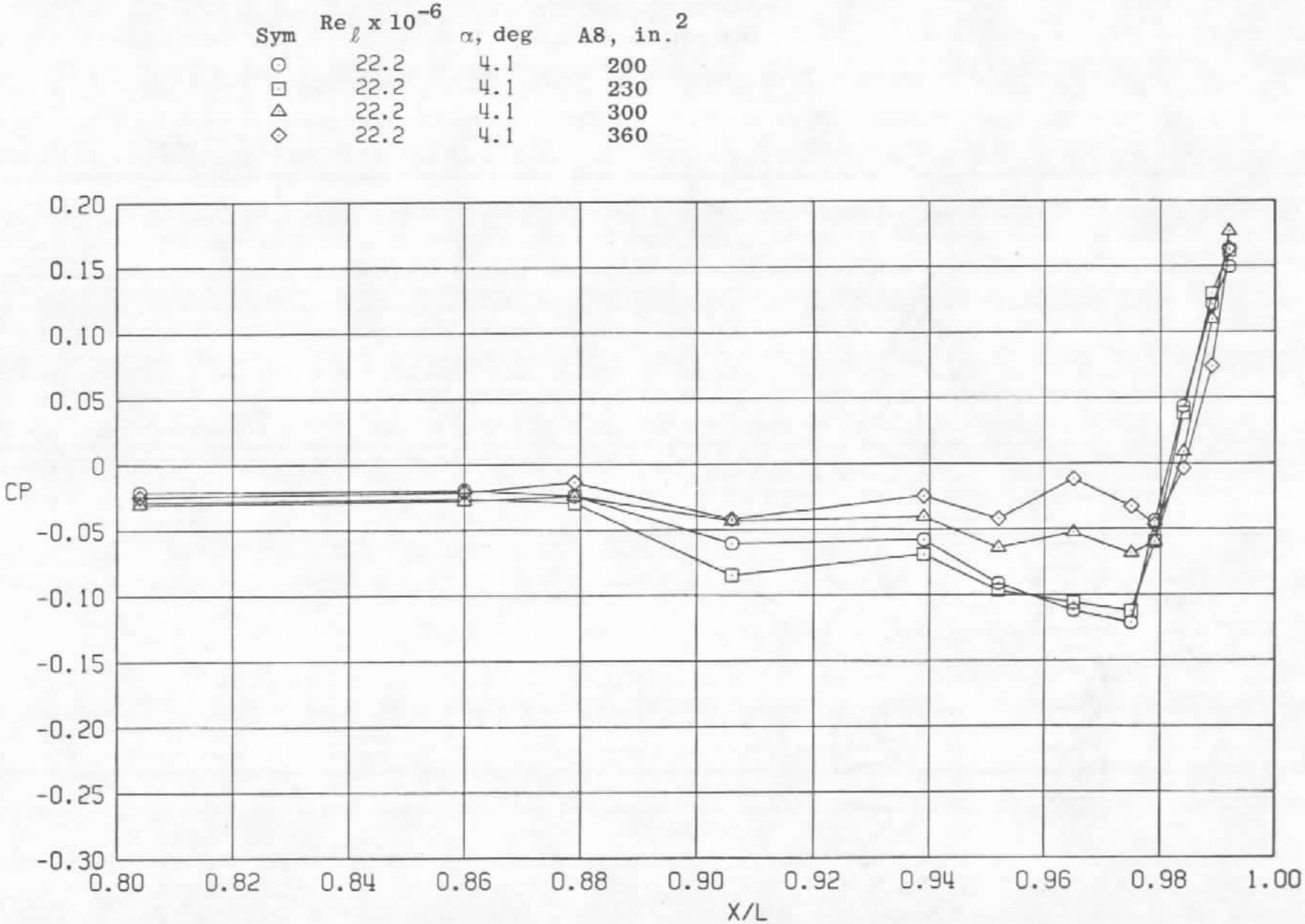

e. ϕ = 225 deg
Figure 3. Continued.

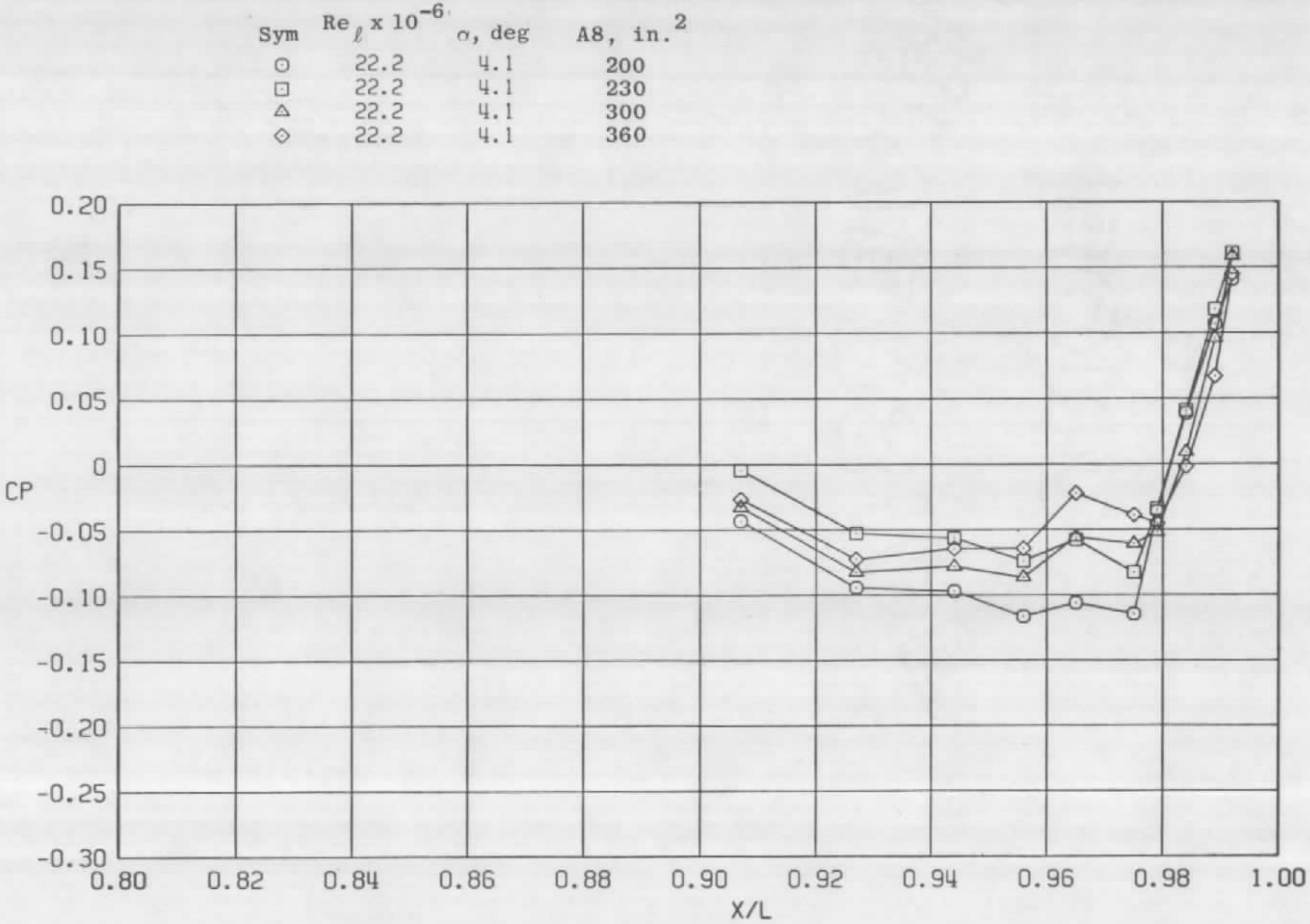

f. ϕ = 315 deg
Figure 3. Concluded.

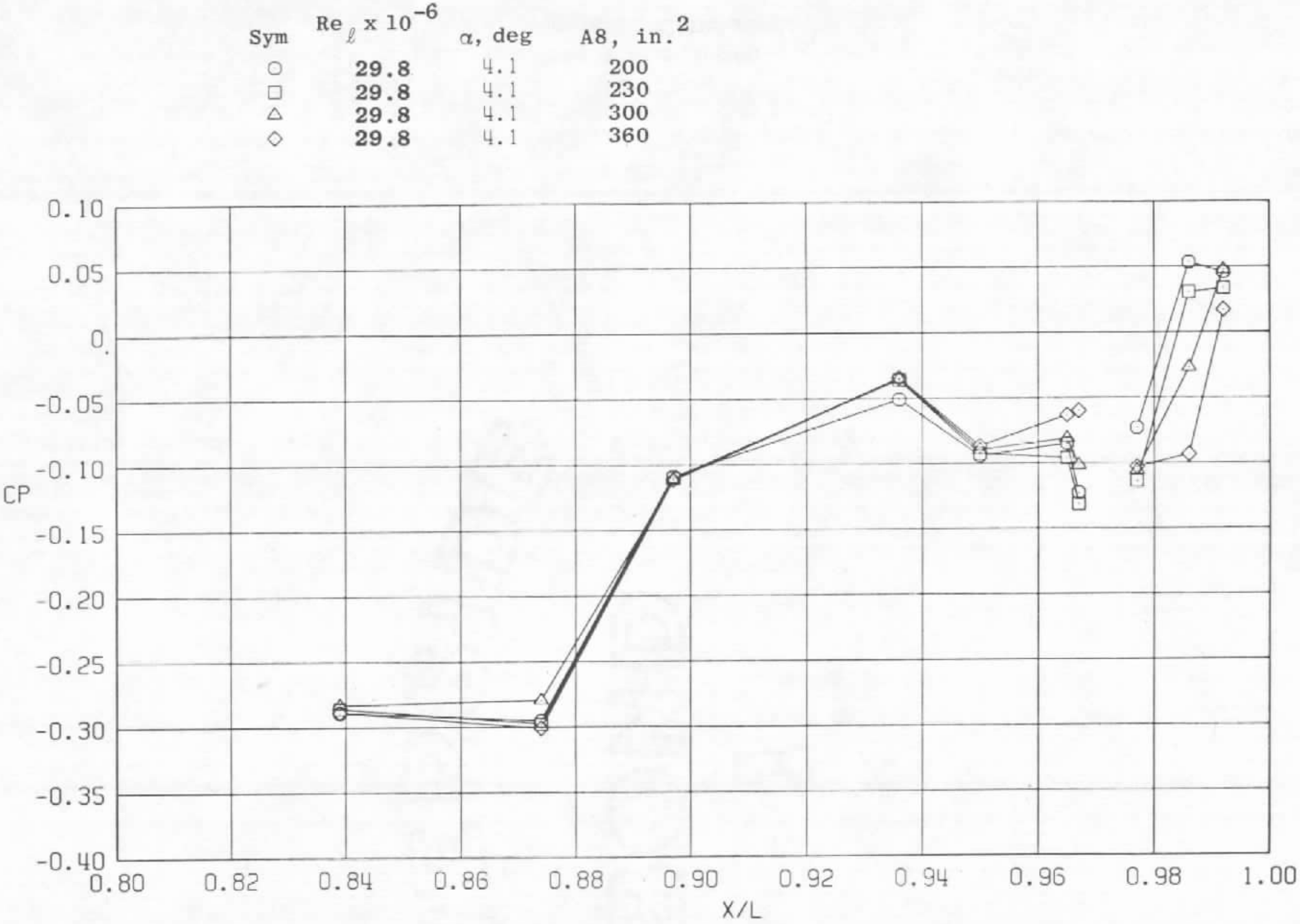

a. $\phi = 0$

Figure 4. Nozzle closure effects on surface pressure coefficients, NPR = 1.0, M = 0.9 (WT).

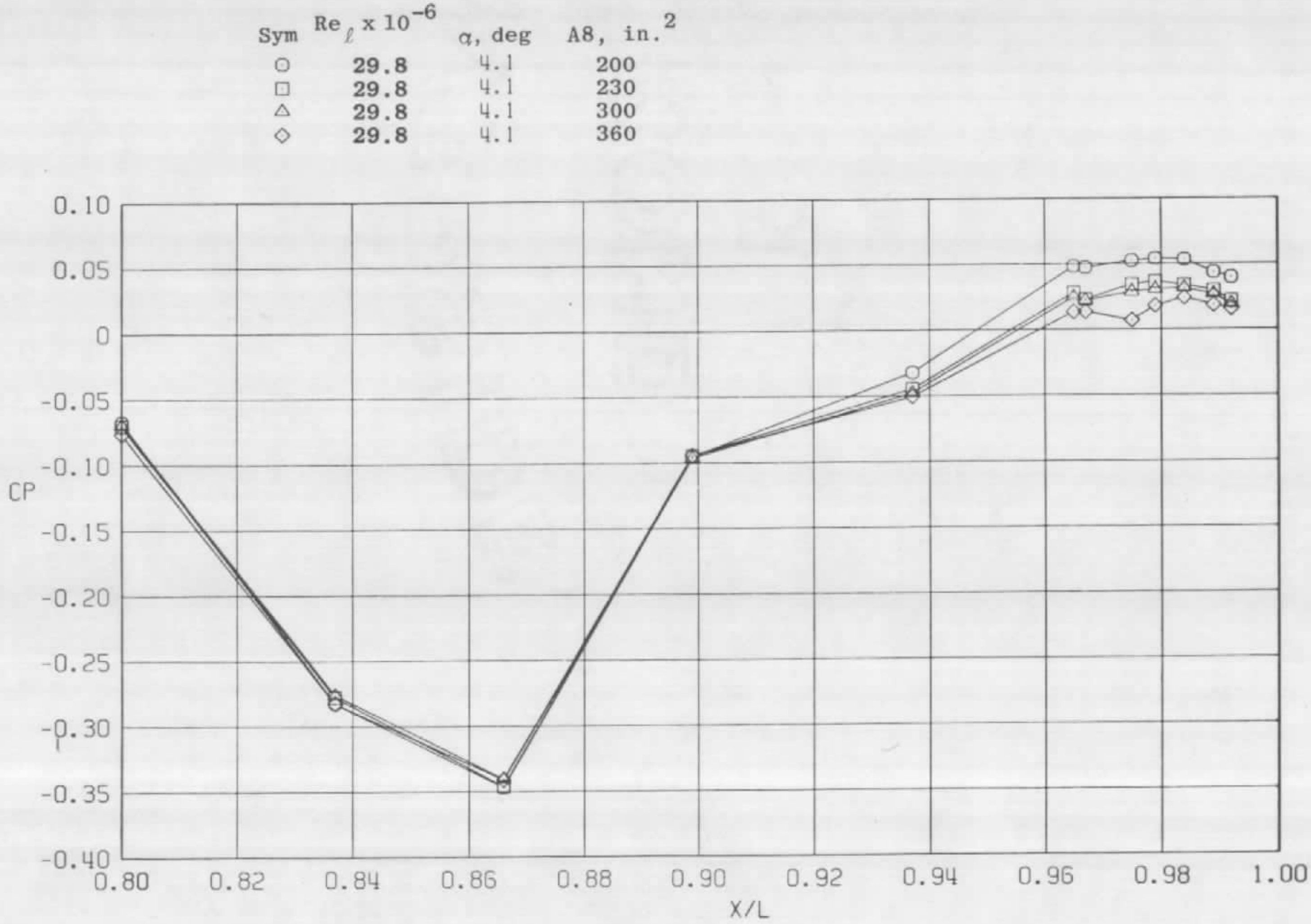

b. ϕ = 45 deg
Figure 4. Continued.

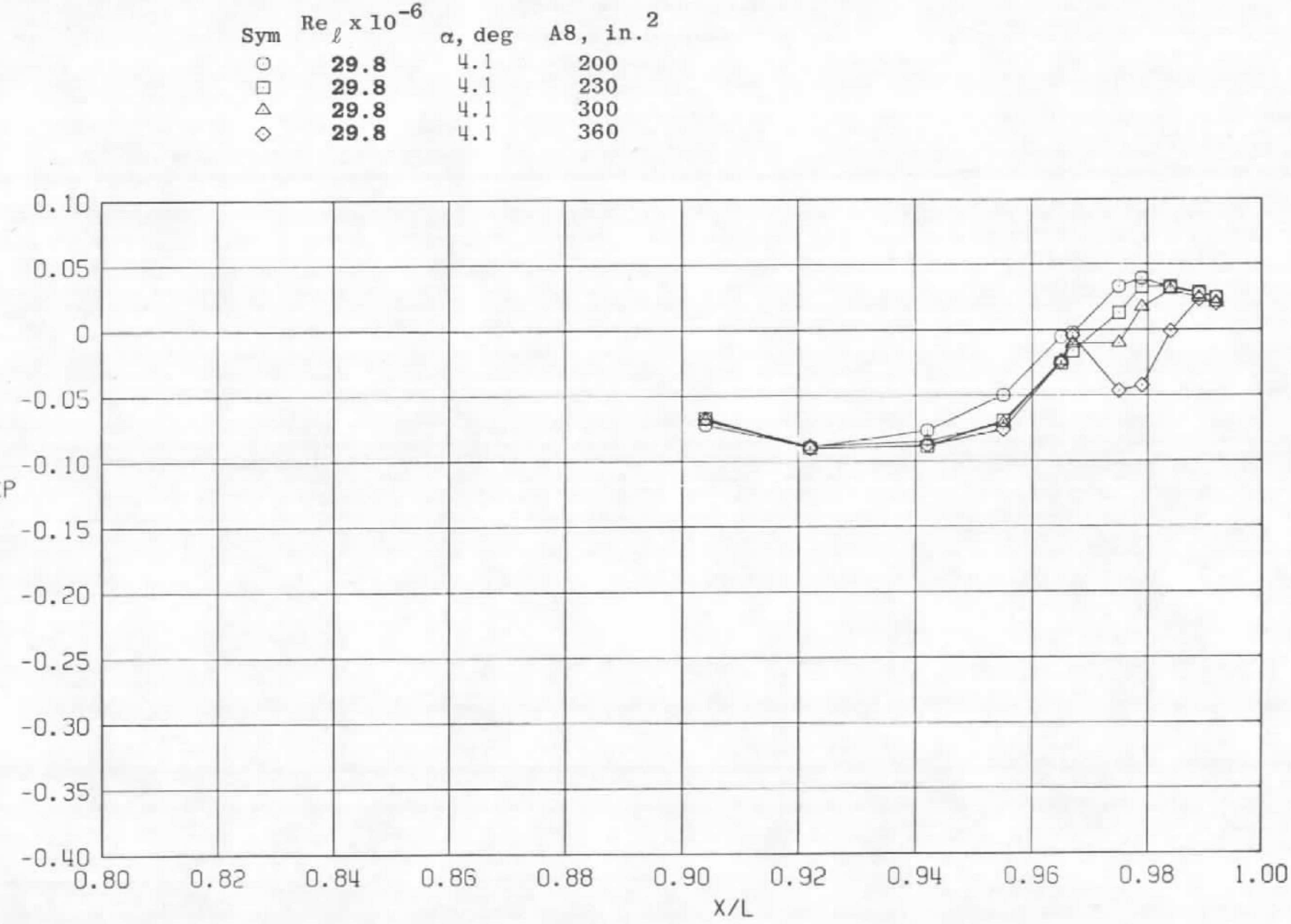

c. ϕ = 135 deg
Figure 4. Continued.

d. ϕ = 180 deg
Figure 4. Continued.

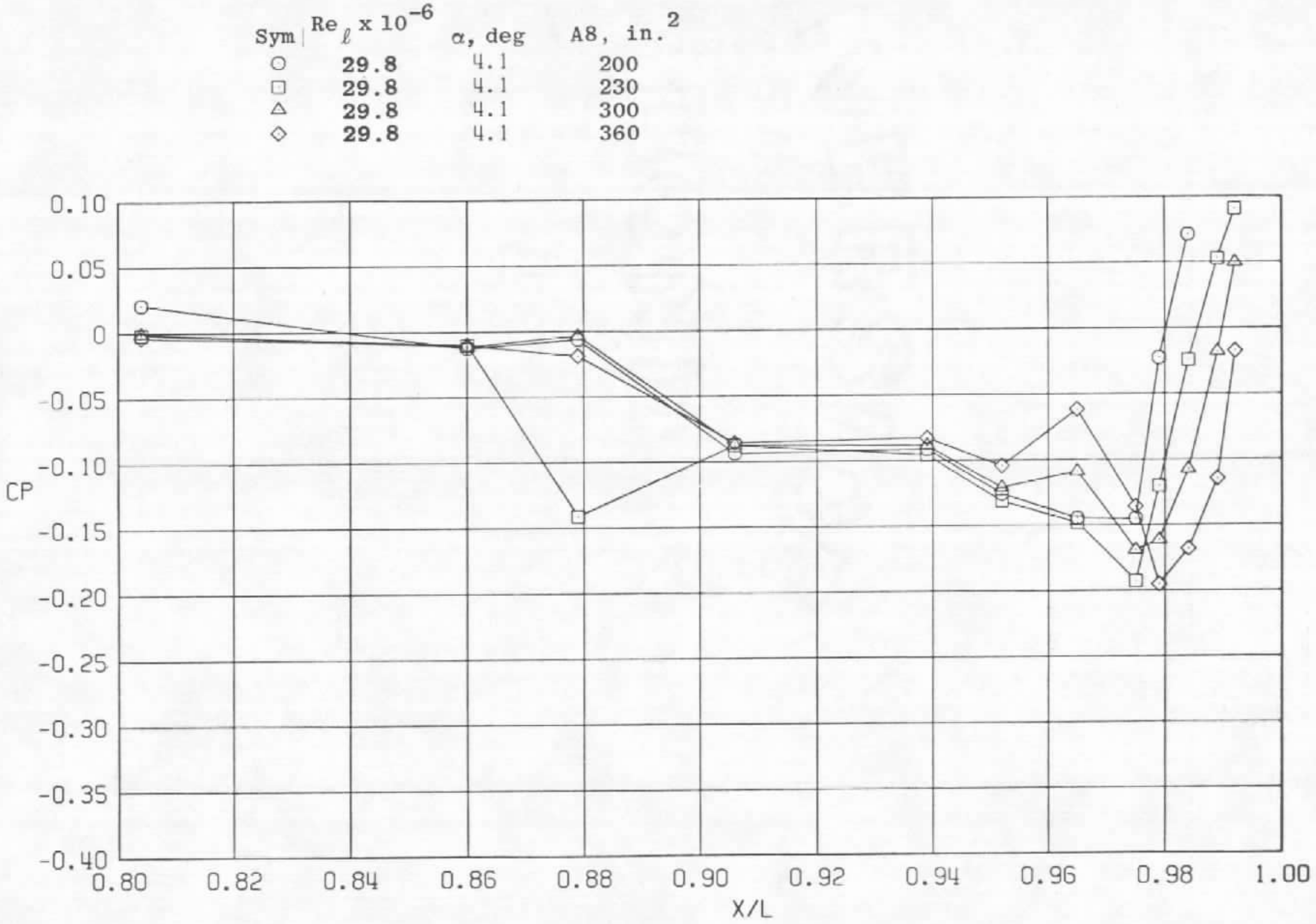

e. ϕ = 225 deg
Figure 4. Continued.

f. ϕ = 315 deg

Figure 4. Concluded.

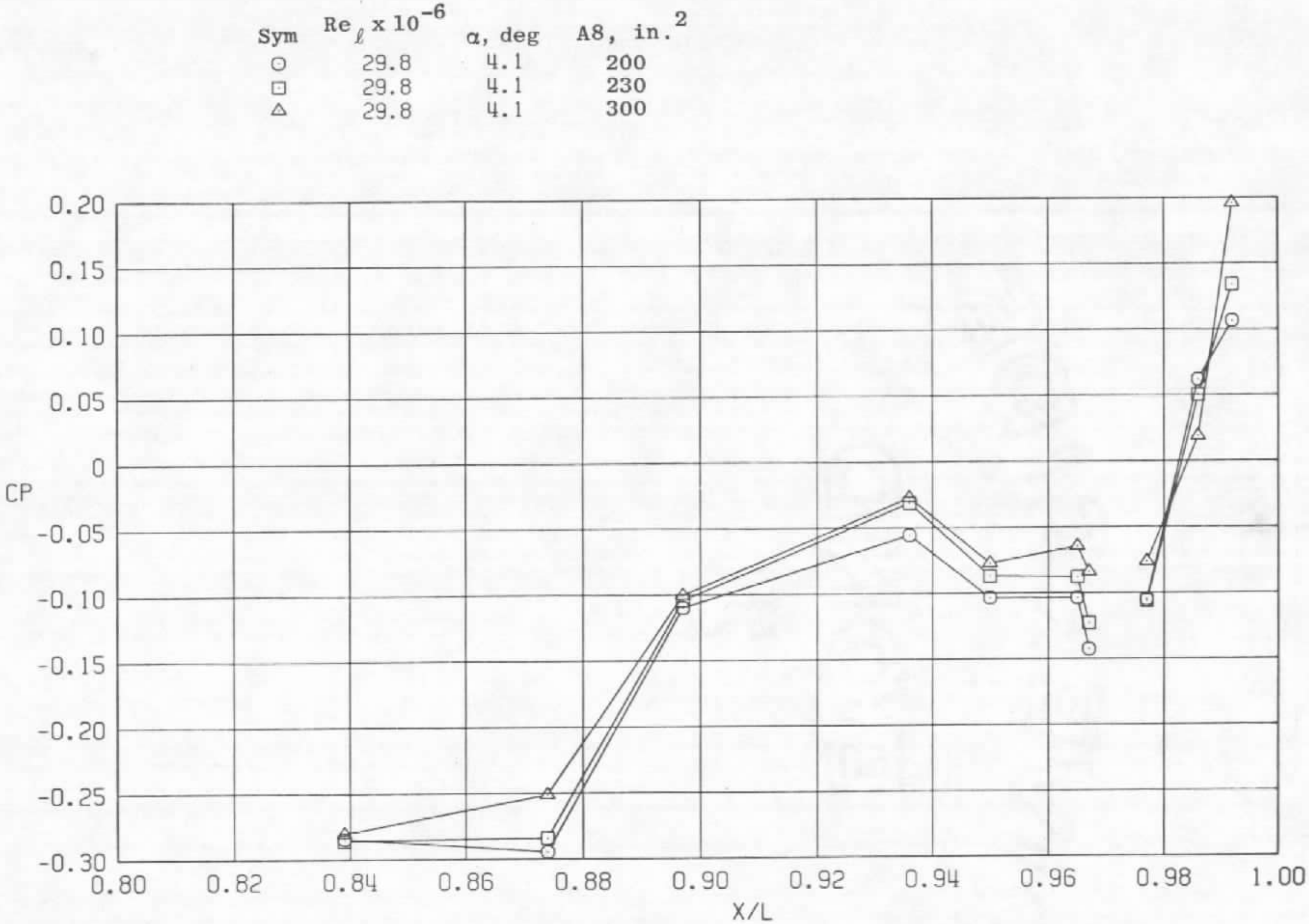

a. ϕ = 0

Figure 5. Nozzle closure effects on surface pressure coefficients, NPR = 5.0, M = 0.9 (WT).

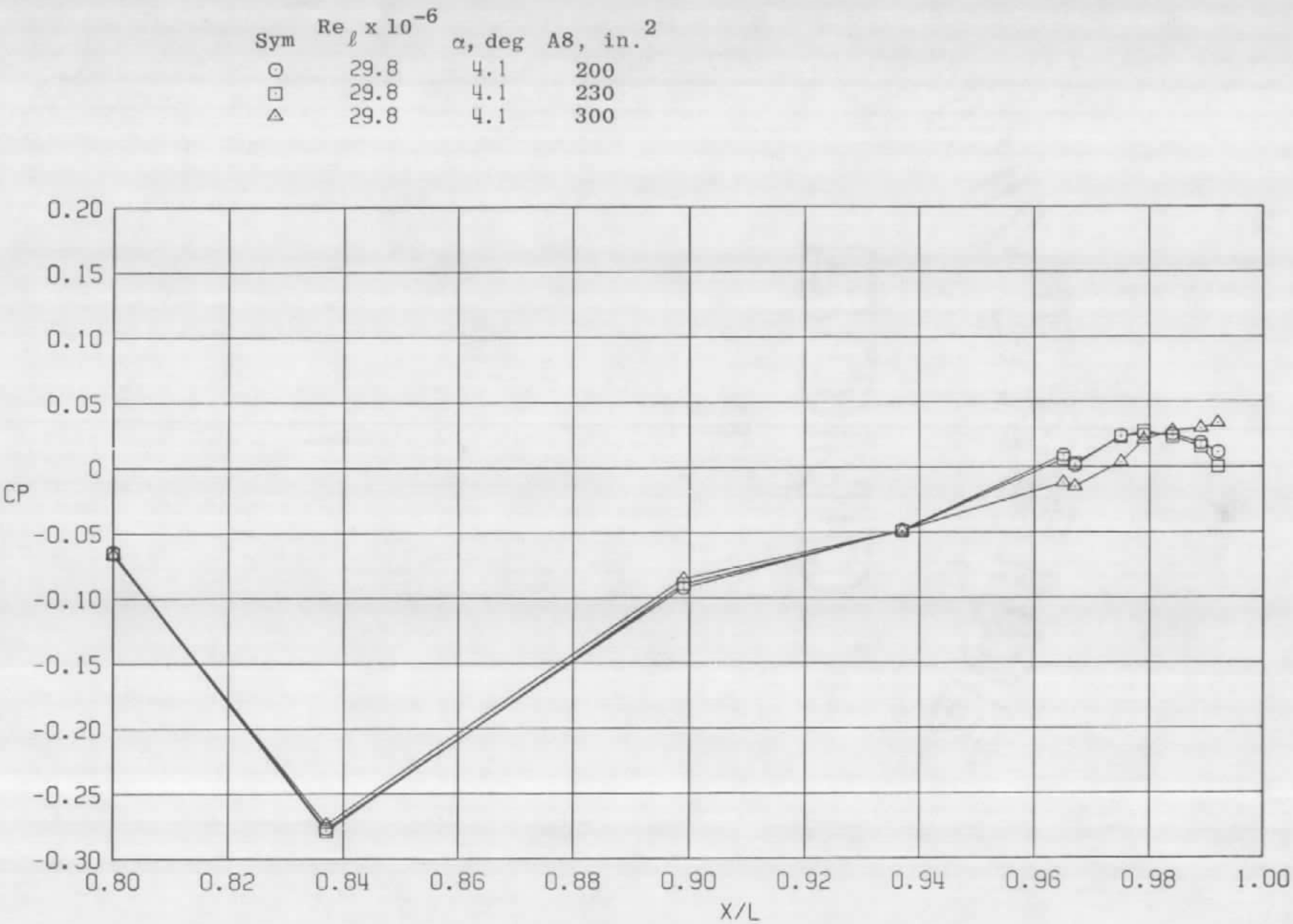

b. ϕ = 45 deg
Figure 5. Continued.

Sym	$Re_\ell \times 10^{-6}$	α, deg	A8, in.^{2}
○	29.8	4.1	200
□	29.8	4.1	230
△	29.8	4.1	300

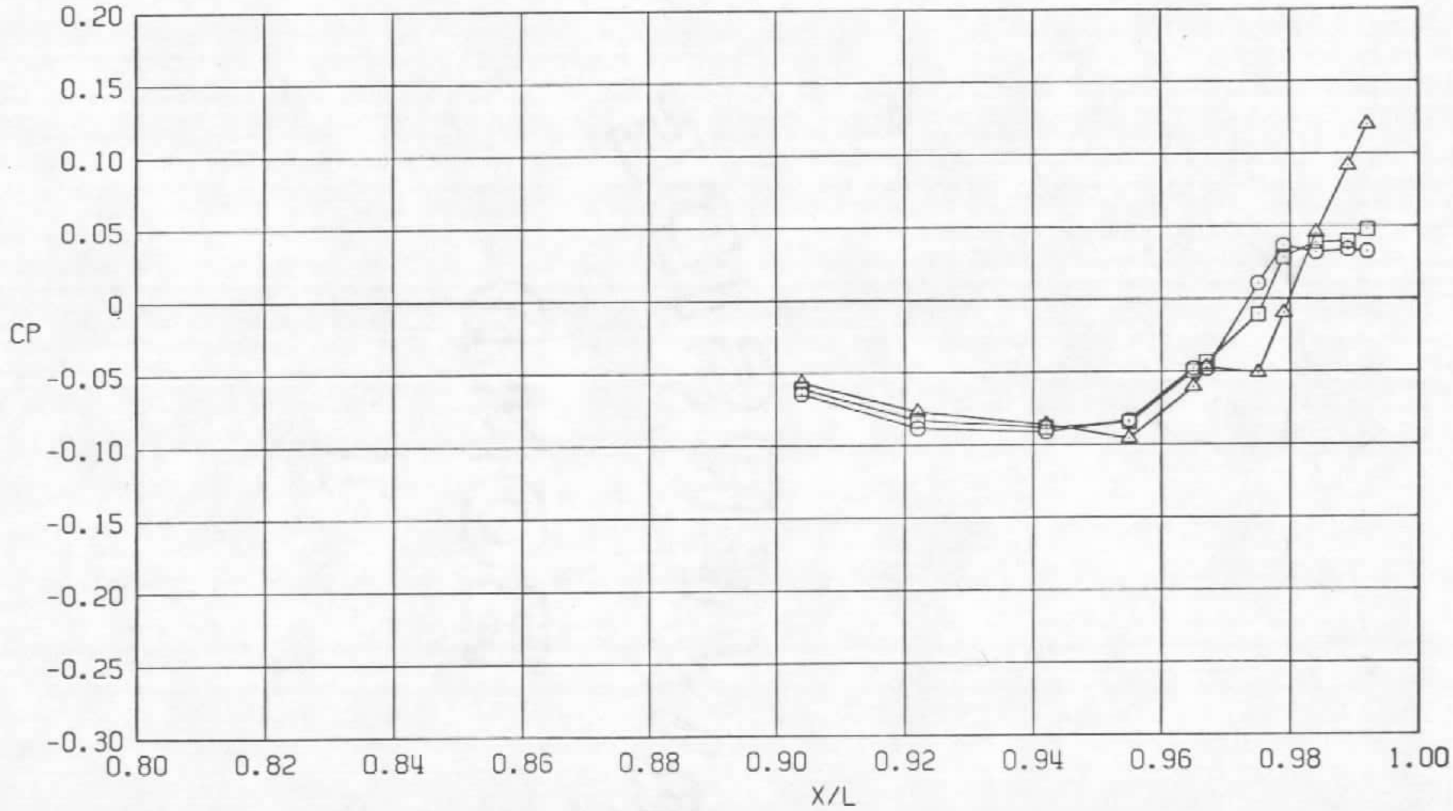

c. ϕ = 135 deg
Figure 5. Continued.

d. ϕ = 180 deg

Figure 5. Continued.

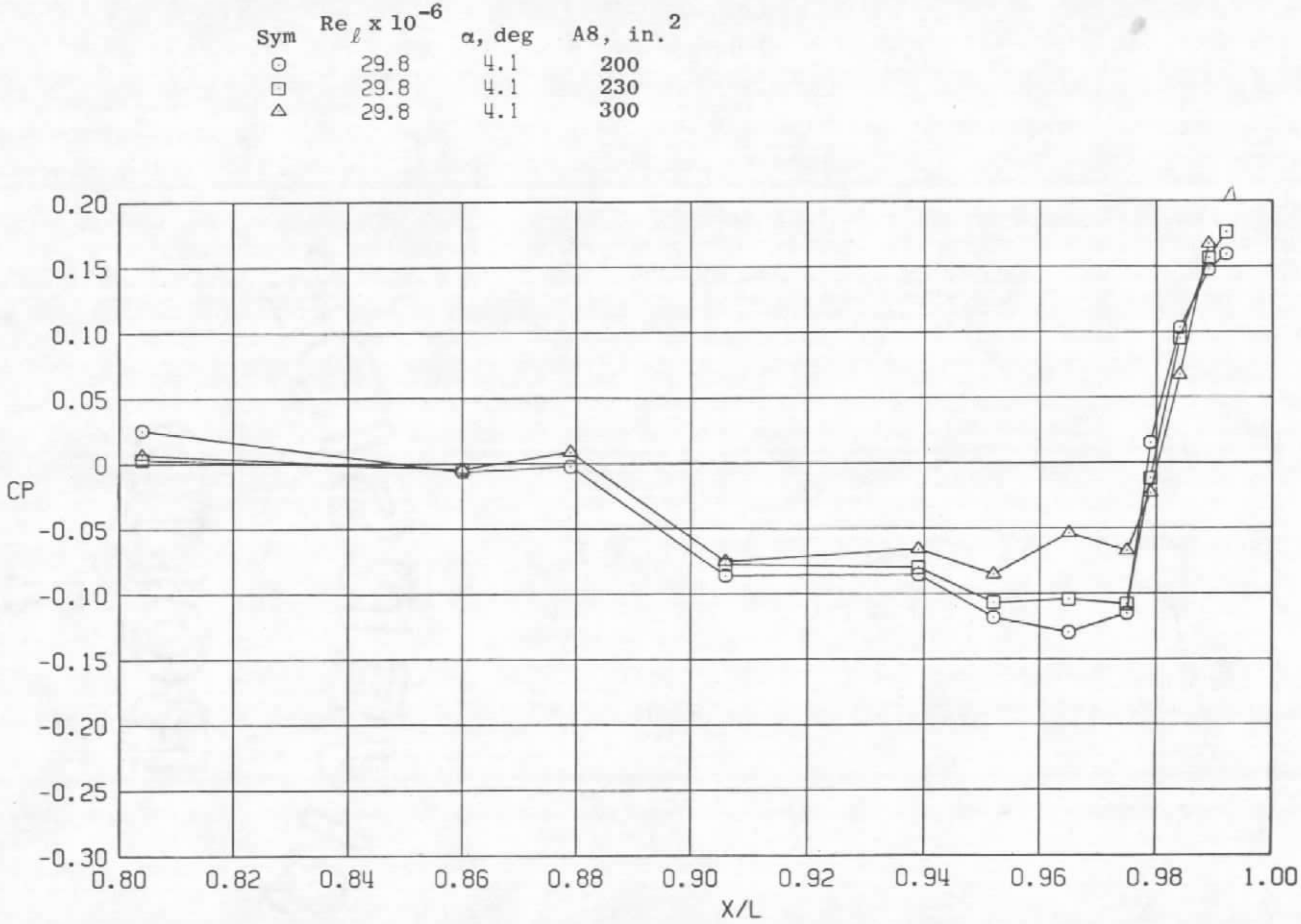

e. ϕ = 225 deg
Figure 5. Continued.

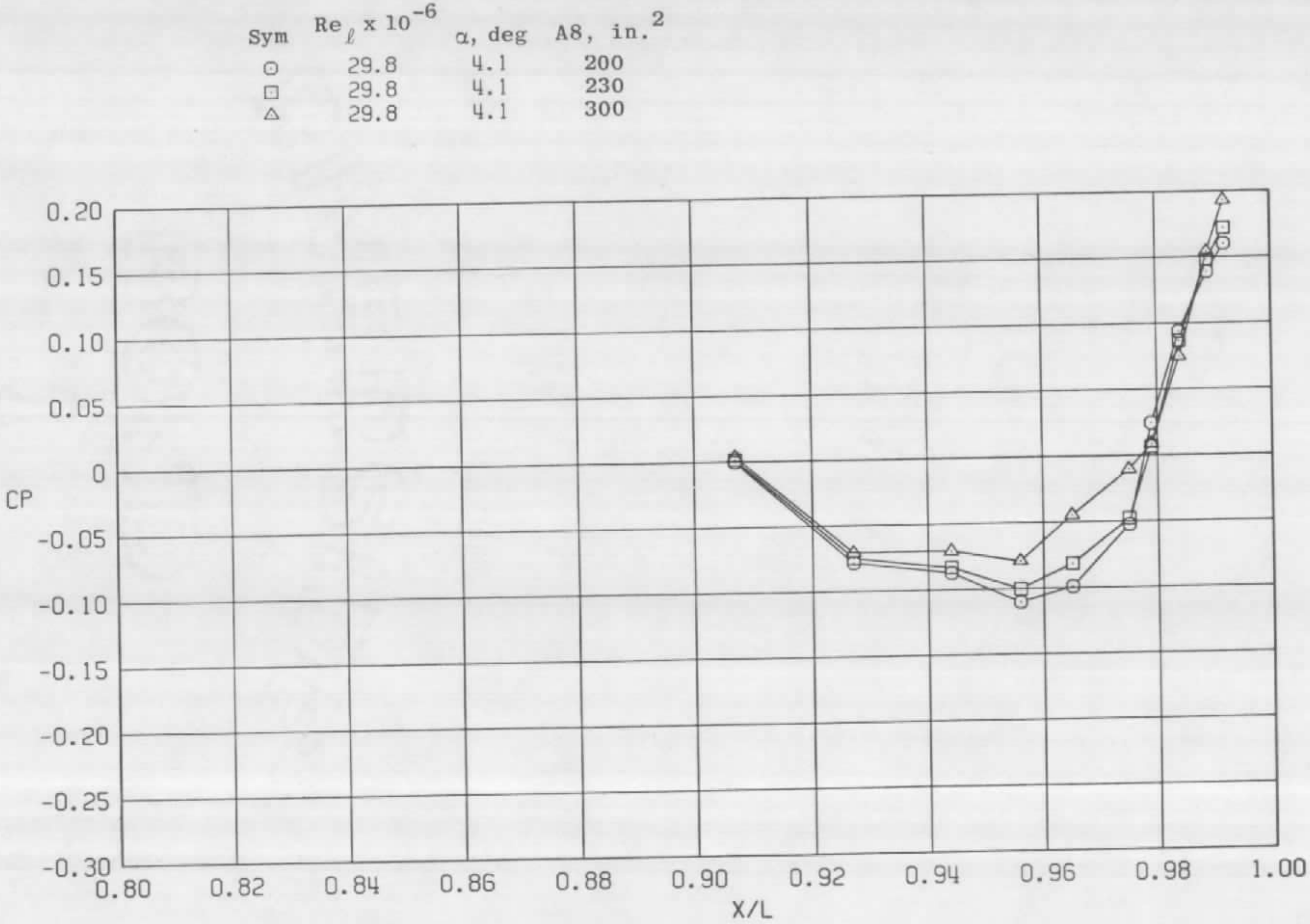

f. ϕ = 315 deg
Figure 5. Concluded.

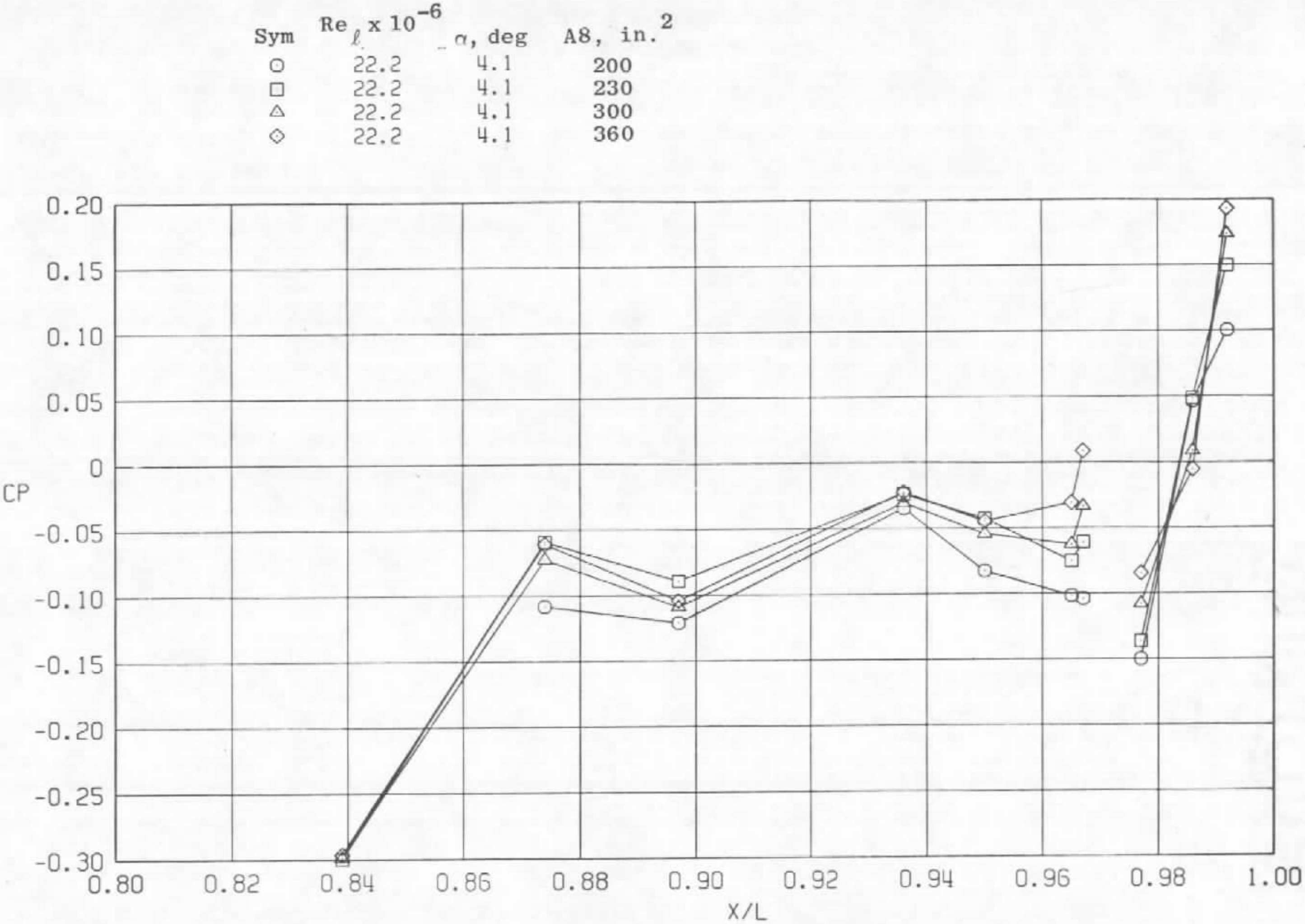

a. $\phi = 0$

Figure 6. Nozzle closure effects on surface pressure coefficients, M = 0.9, NPRE = 5.0 (SS).

Sym	$Re_{\ell} \times 10^{-6}$	α, deg	A8, in.^{2}
⊙	22.2	4.1	200
□	22.2	4.1	230
△	22.2	4.1	300
◇	22.2	4.1	360

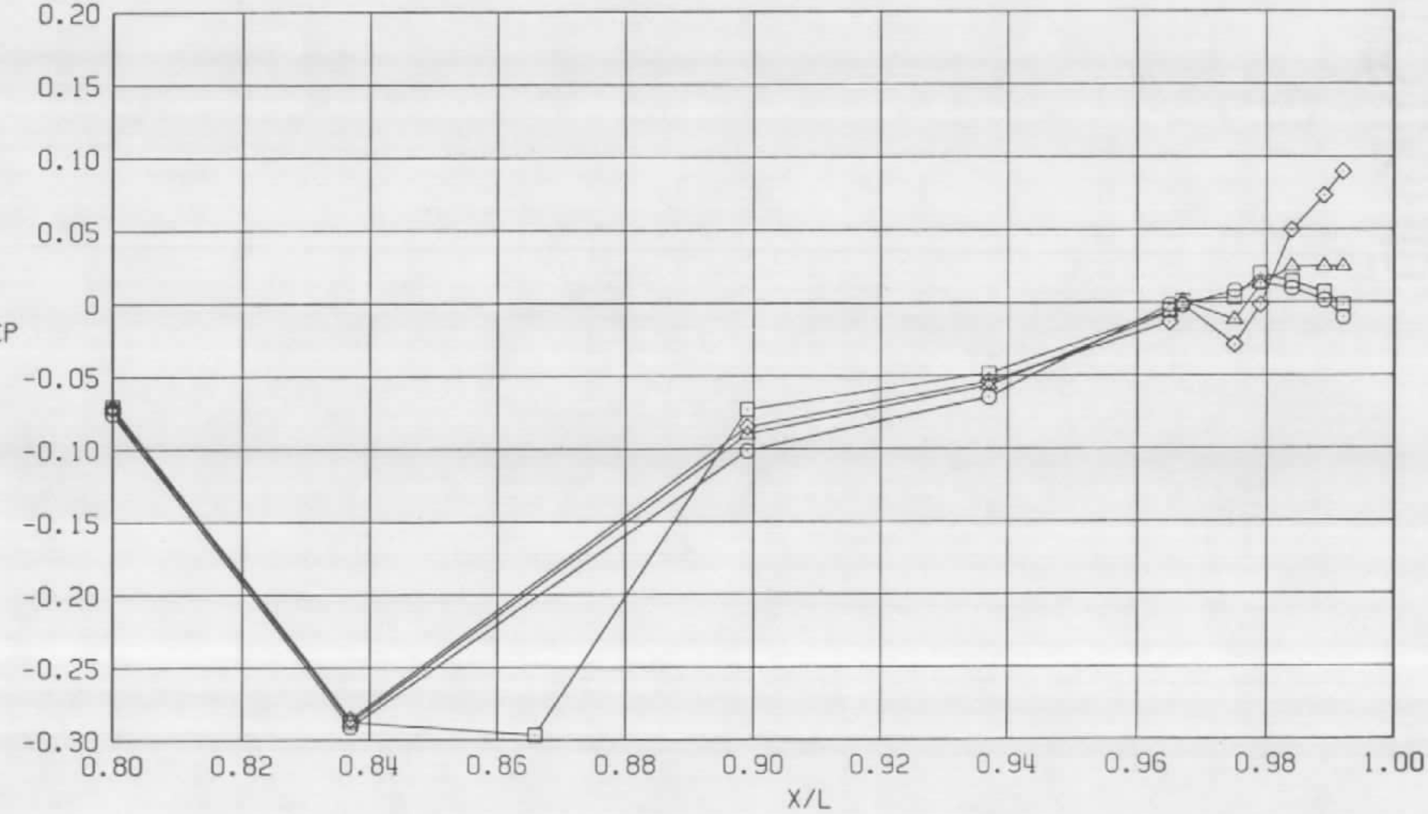

b. ϕ = 45 deg
Figure 6. Continued.

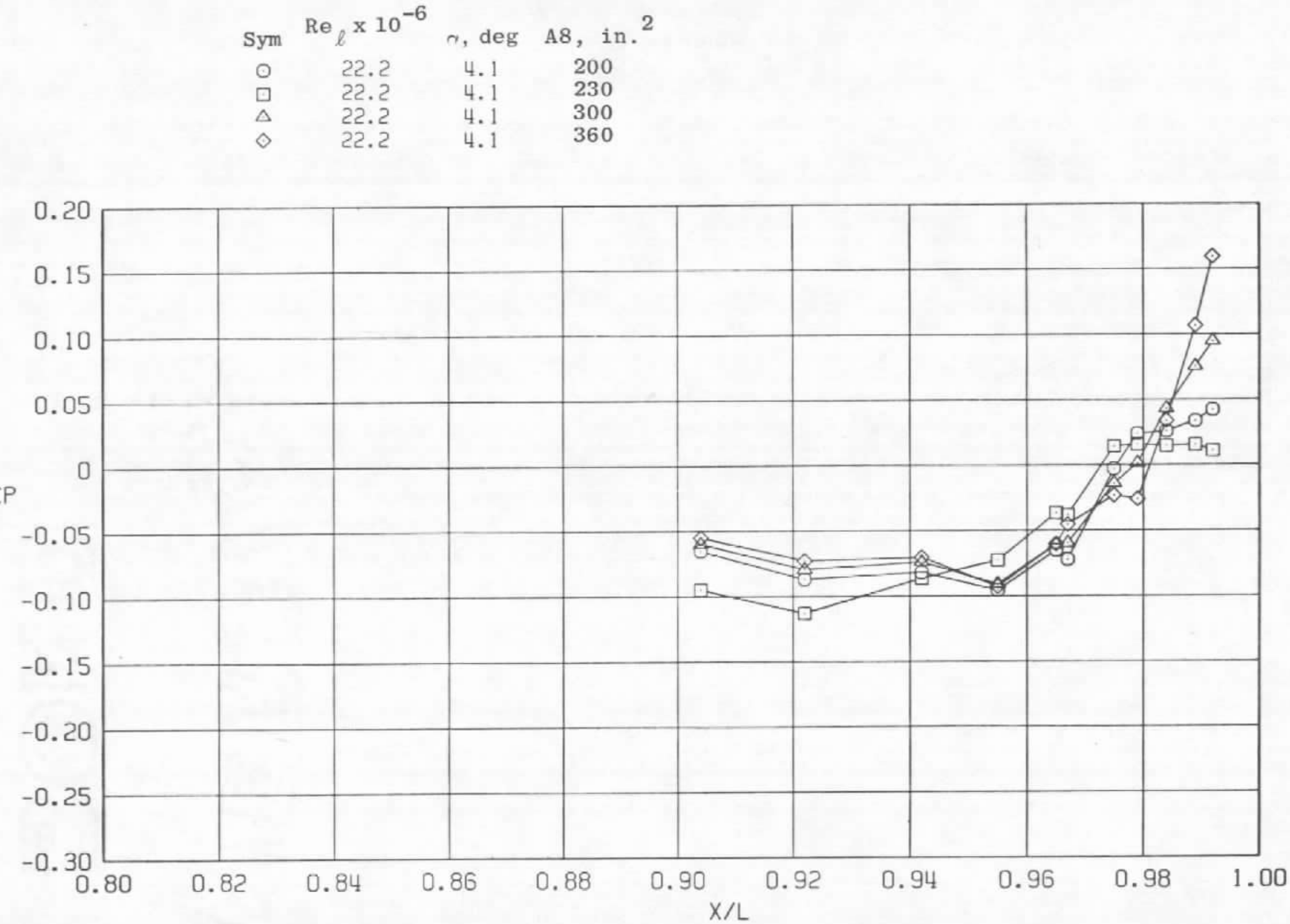

c. ϕ = 135 deg
Figure 6. Continued.

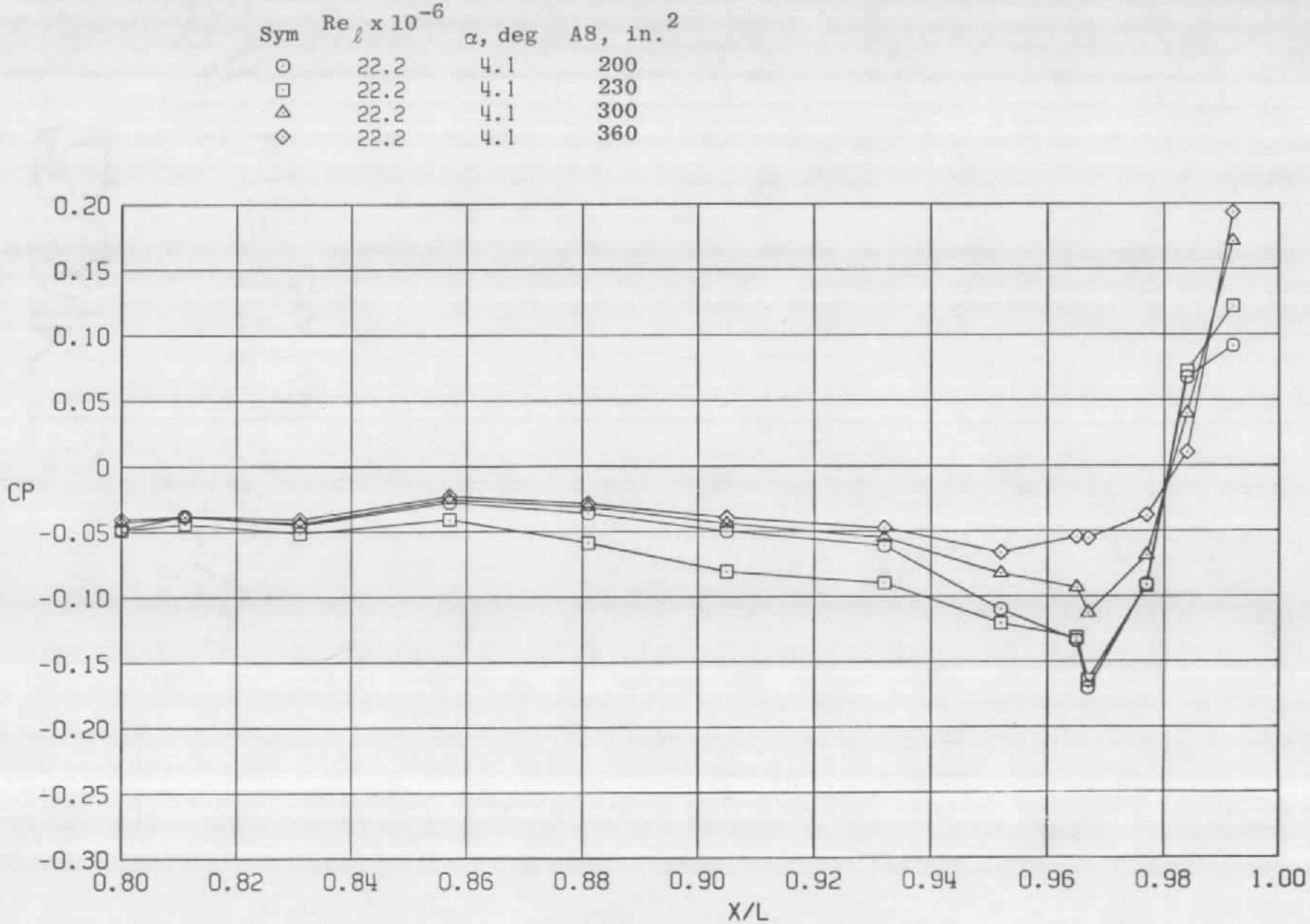

d. ϕ = 180 deg
Figure 6. Continued.

Sym	$Re_\ell \times 10^{-6}$	α, deg	A8, in.^{2}
⊙	22.2	4.1	200
⊡	22.2	4.1	230
△	22.2	4.1	300
◇	22.2	4.1	360

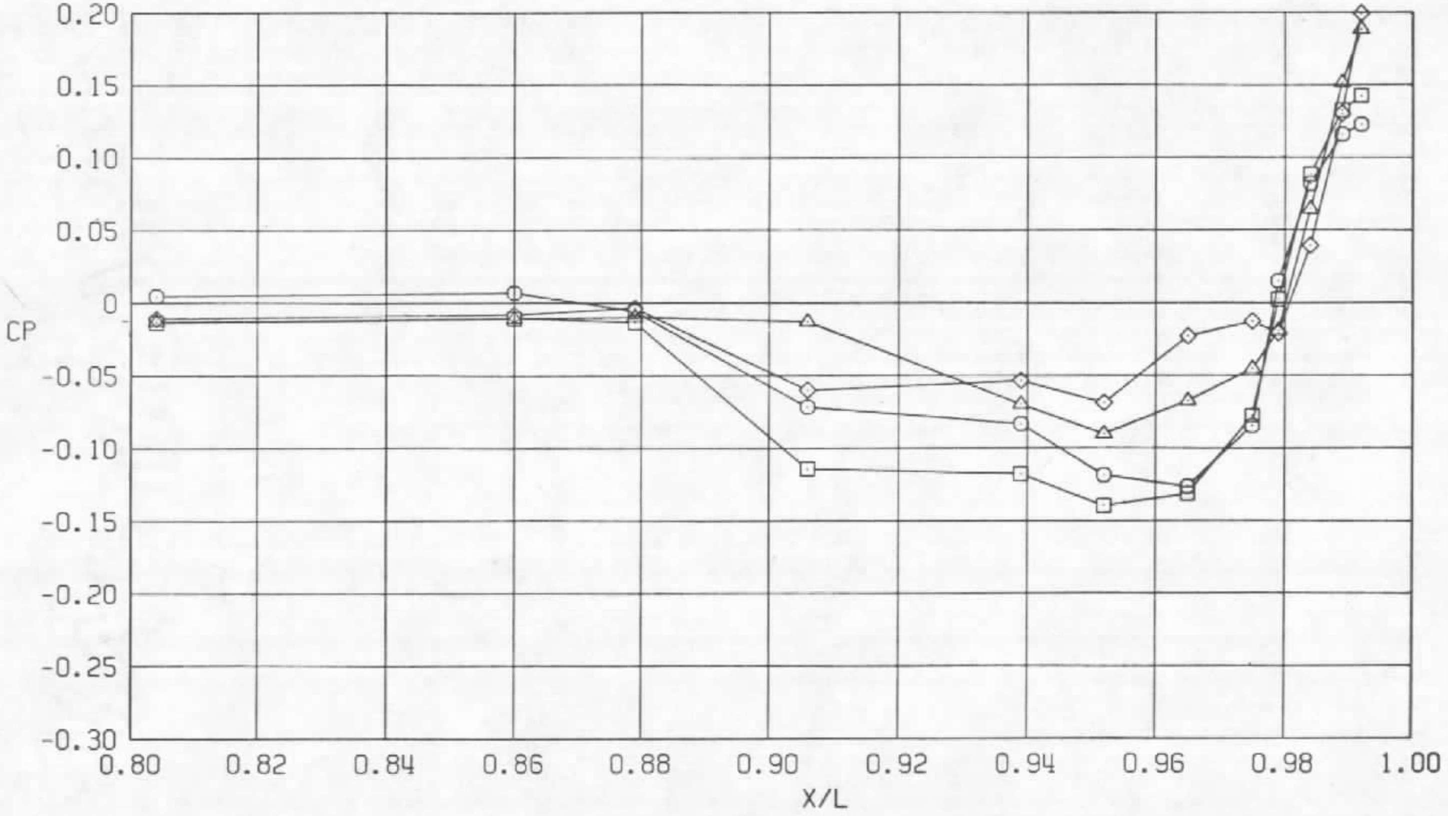

e. ϕ = 225 deg

Figure 6. Continued.

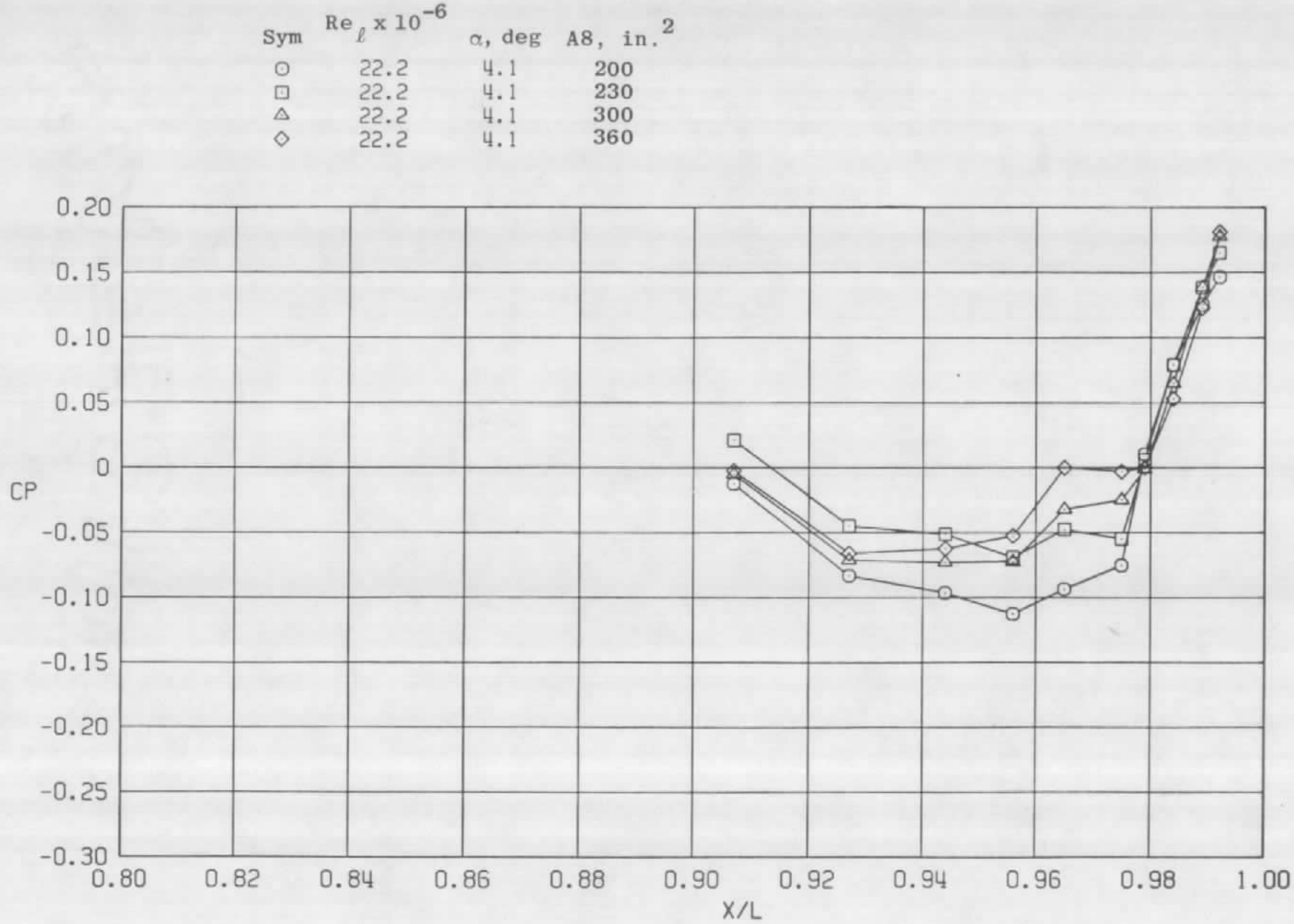

f. ϕ = 315 deg

Figure 6. Concluded.

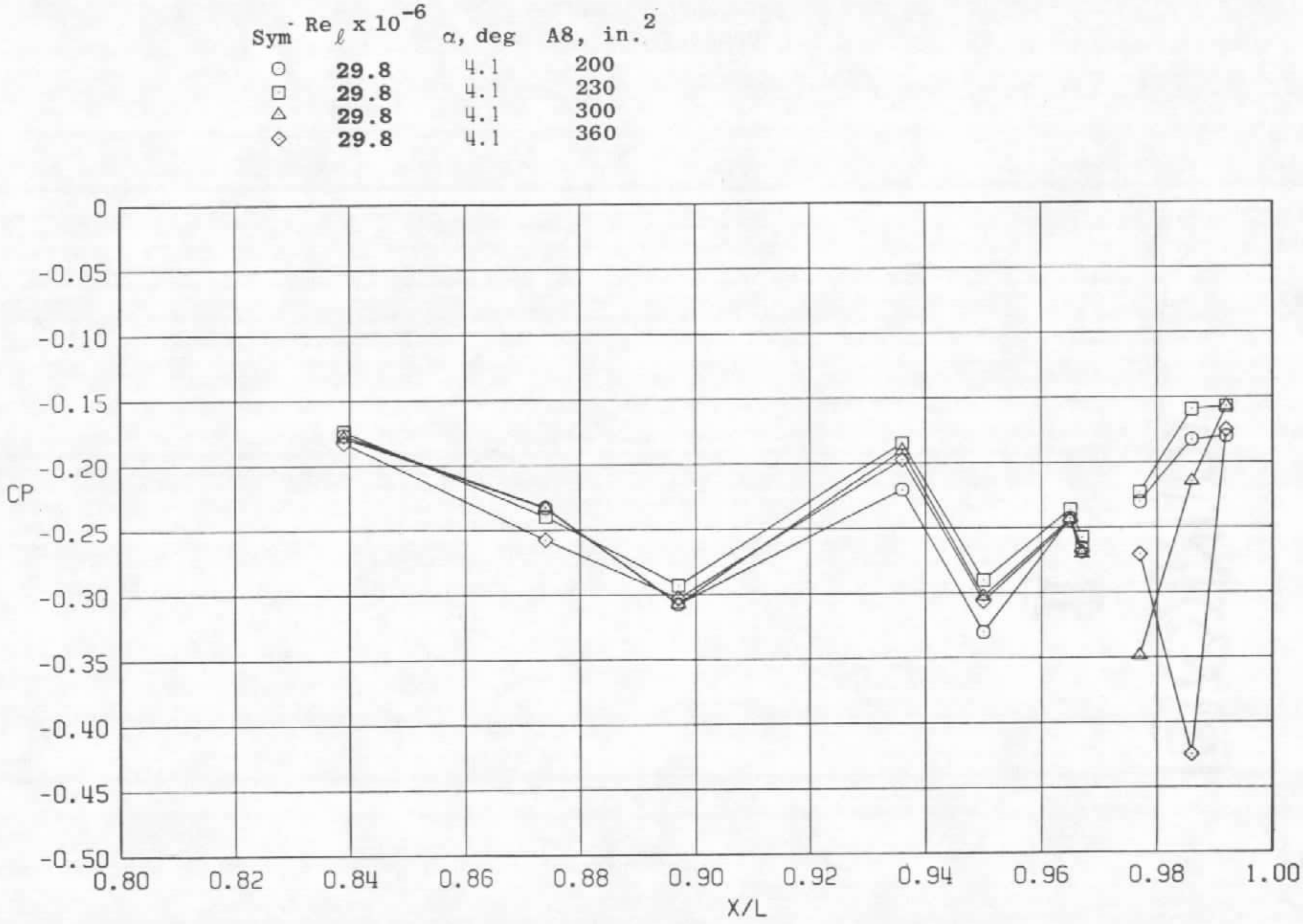

a. $\phi = 0$

Figure 7. Nozzle closure effects on surface pressure coefficients, NPR = 1.0, M = 1.2 (WT).

b. ϕ = 45 deg
Figure 7. Continued.

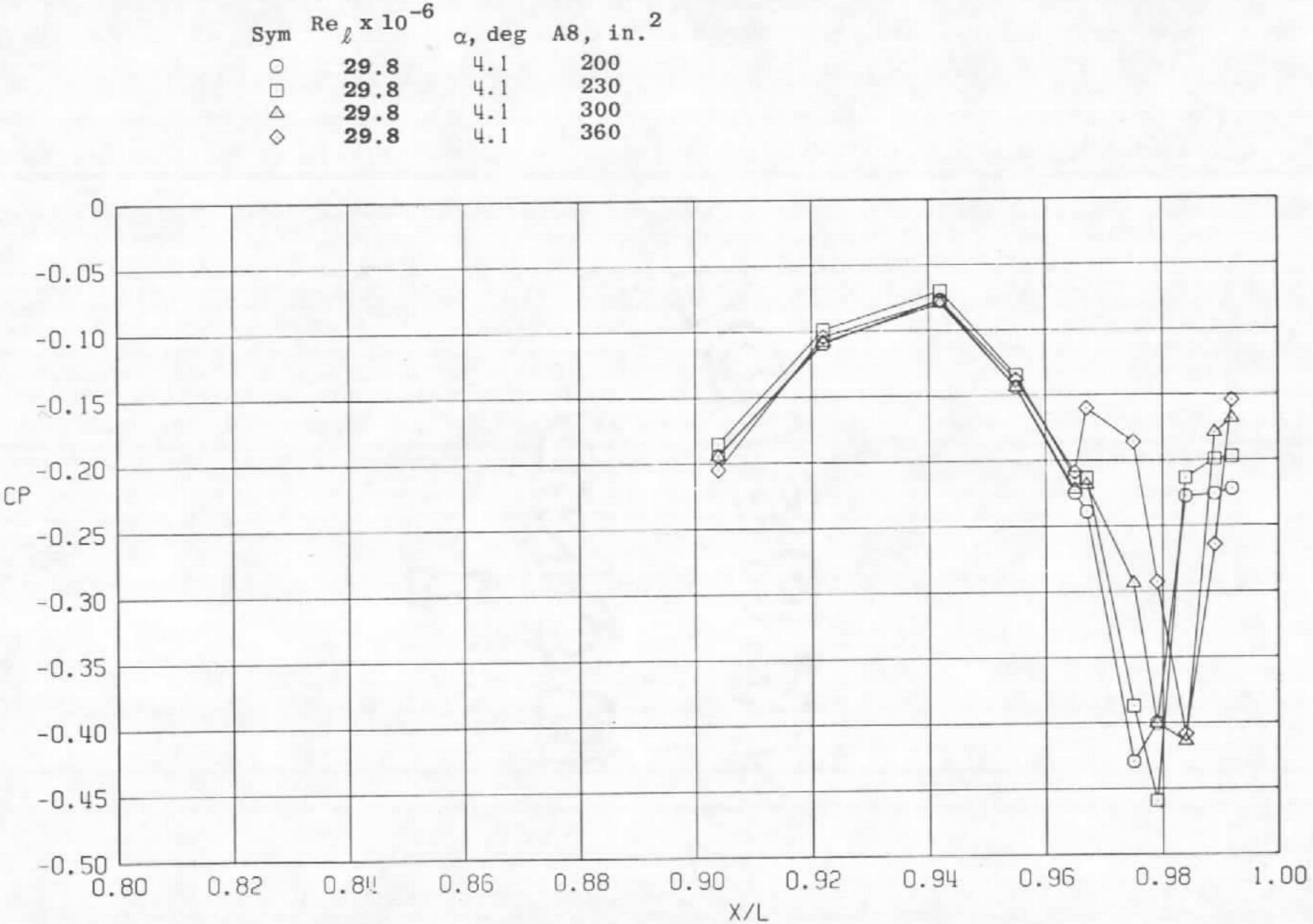

c. ϕ = 135 deg
Figure 7. Continued.

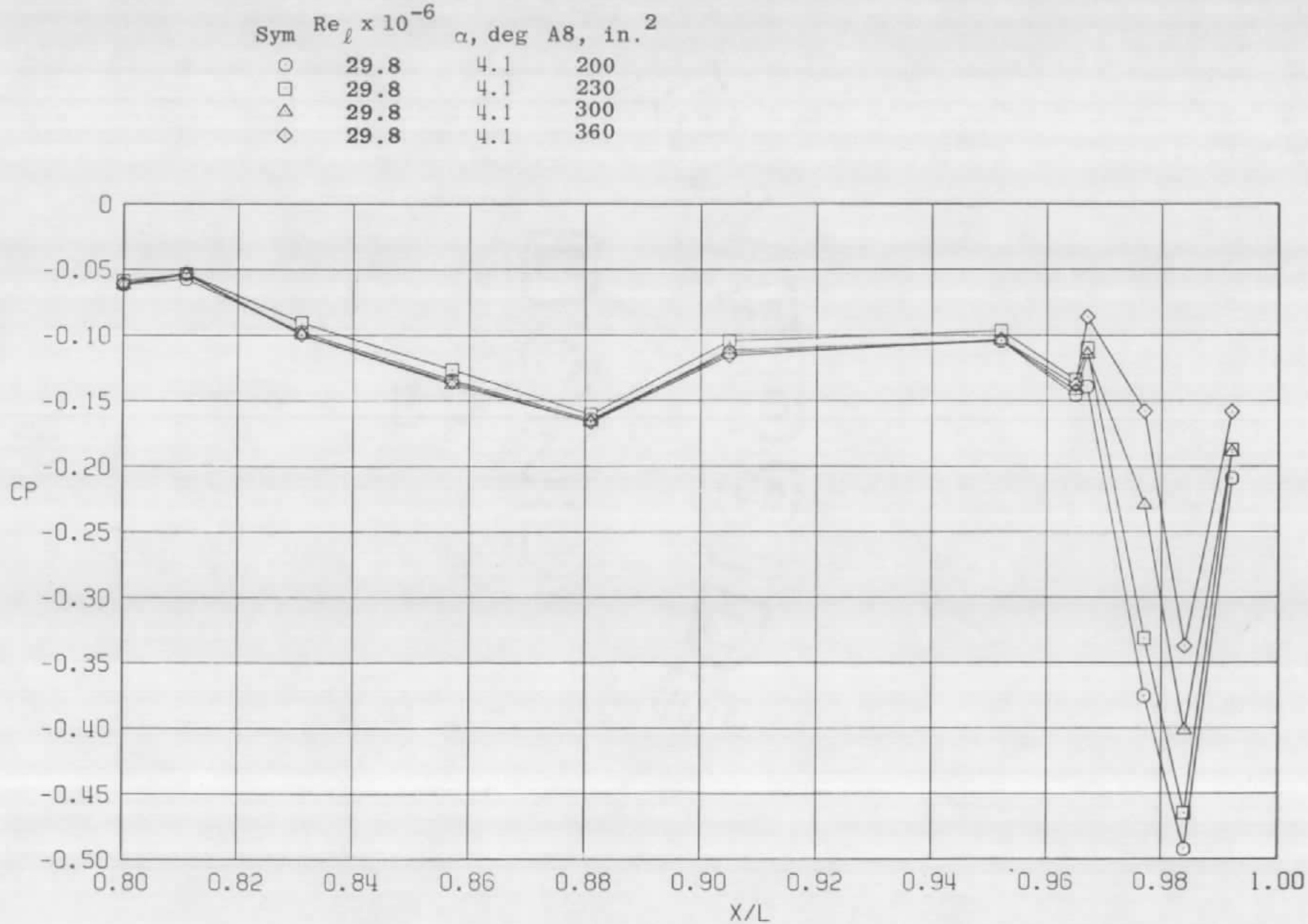

d. ϕ = 180 deg
Figure 7. Continued.

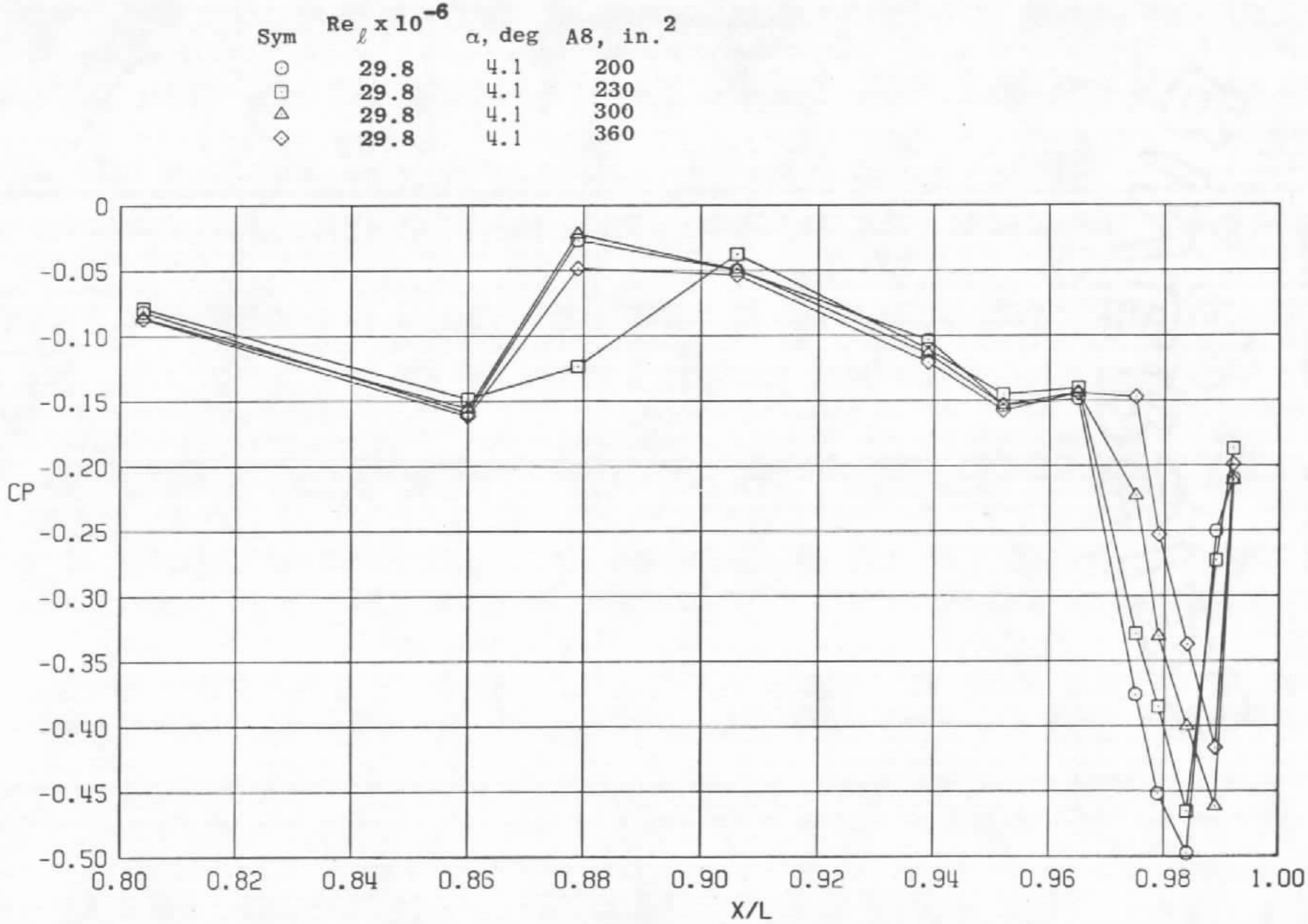

e. ϕ = 225 deg
Figure 7. Continued.

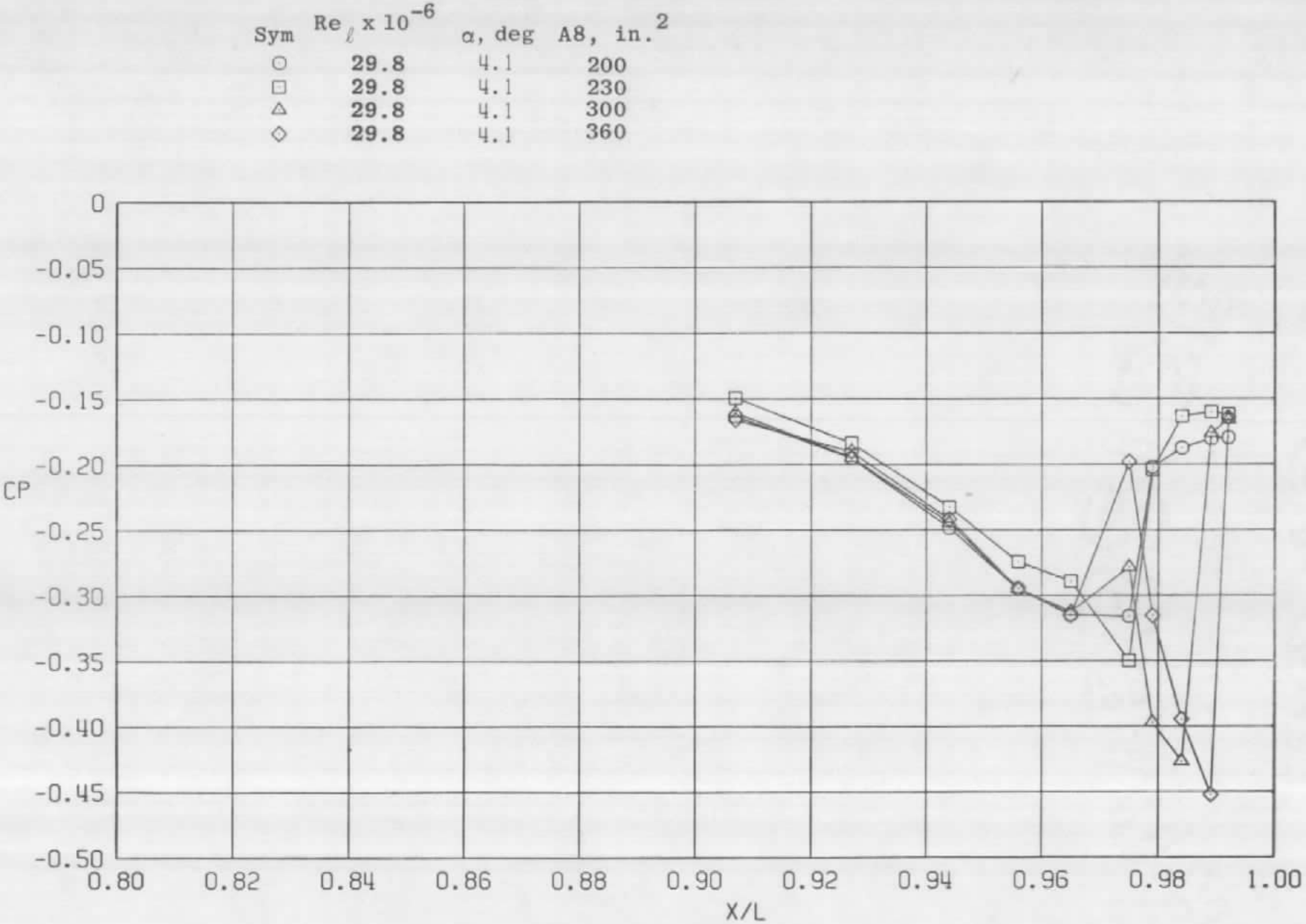

f. ϕ = 315 deg
Figure 7. Concluded.

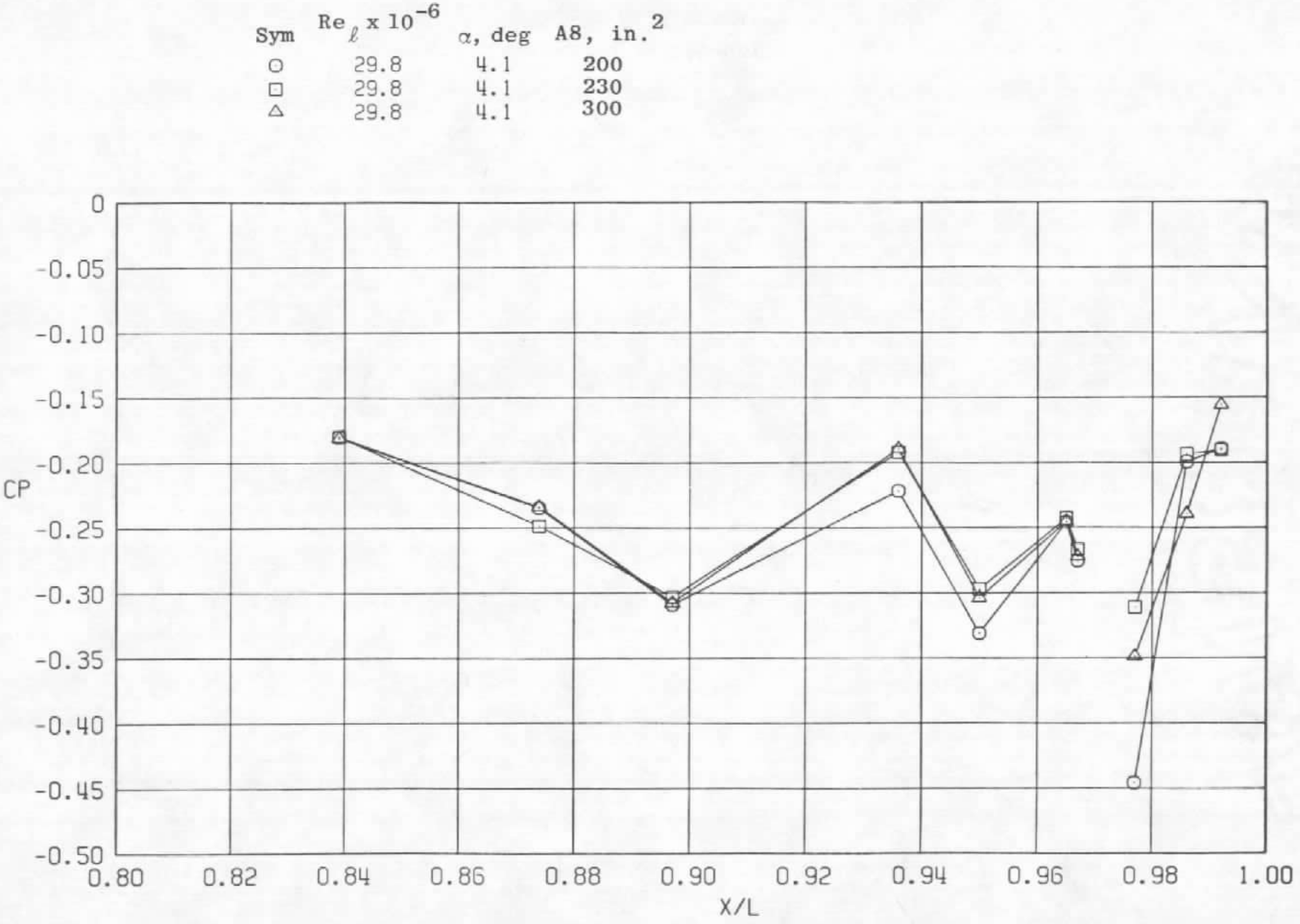

a. $\phi = 0$

Figure 8. Nozzle closure effects on surface pressure coefficients, NPR = 5.0, M = 1.2 (WT).

b. ϕ = 45 deg
Figure 8. Continued.

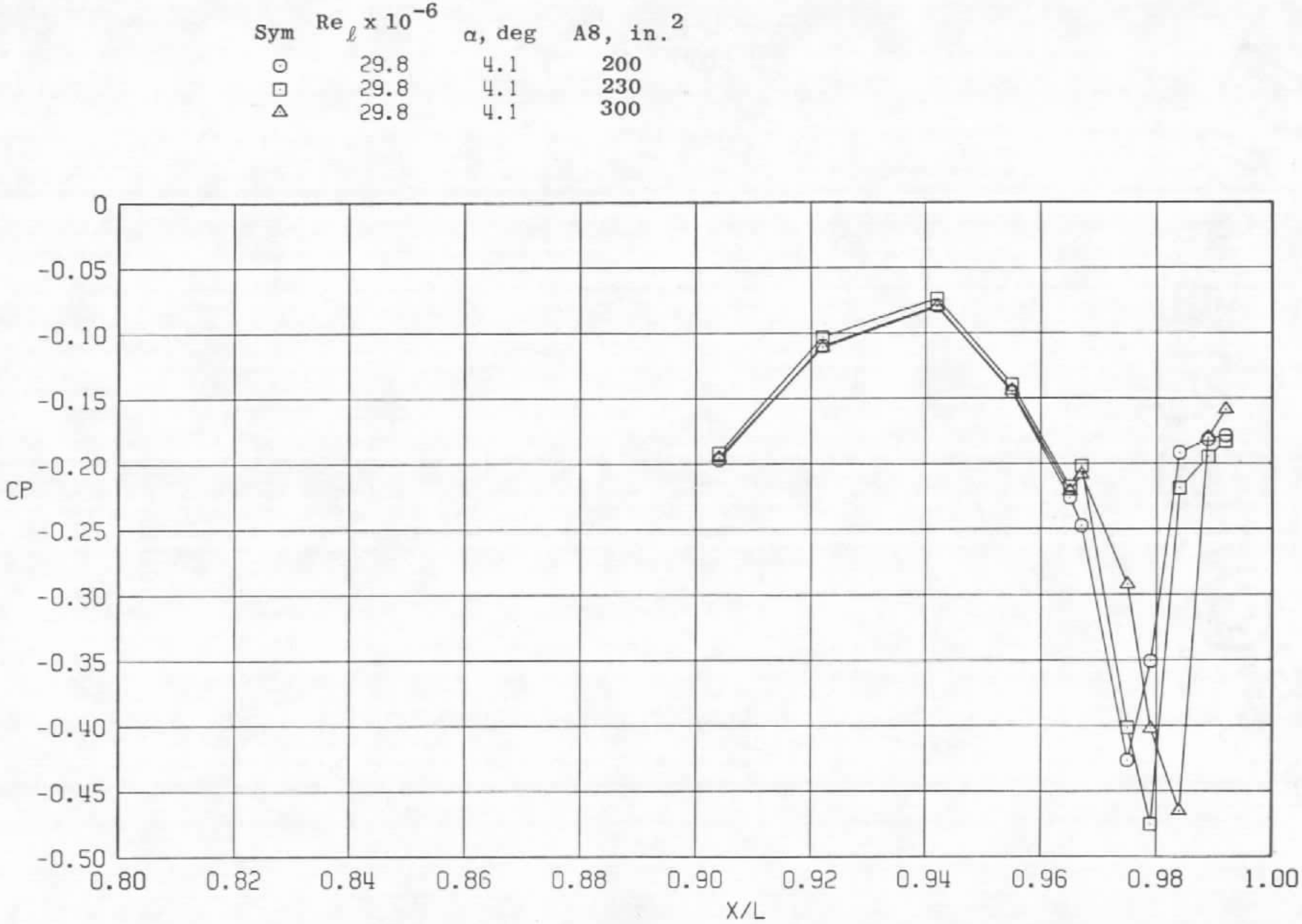

c. ϕ = 135 deg

Figure 8. Continued.

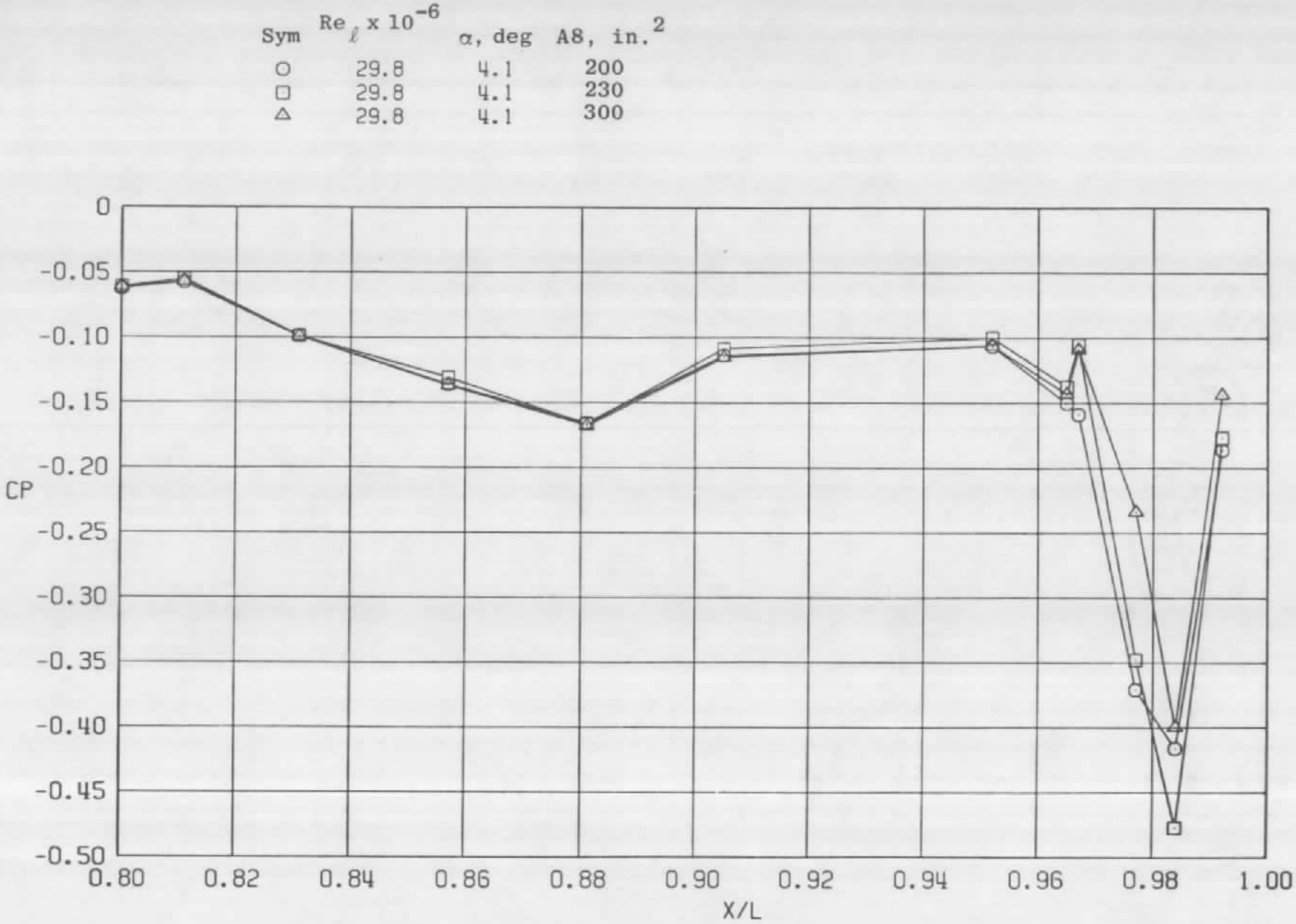

d. ϕ = 180 deg

Figure 8. Continued.

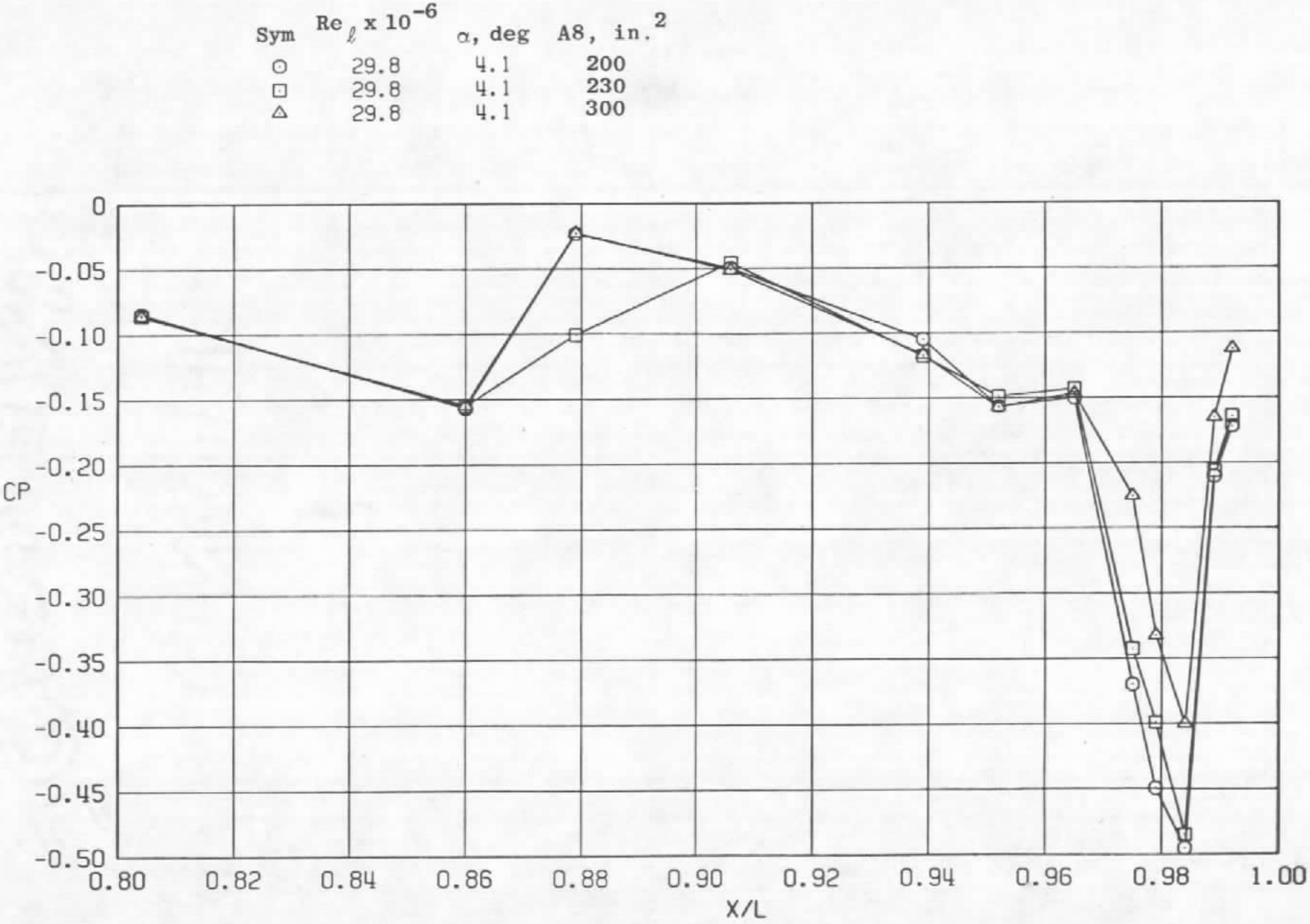

e. ϕ = 225 deg
Figure 8. Continued.

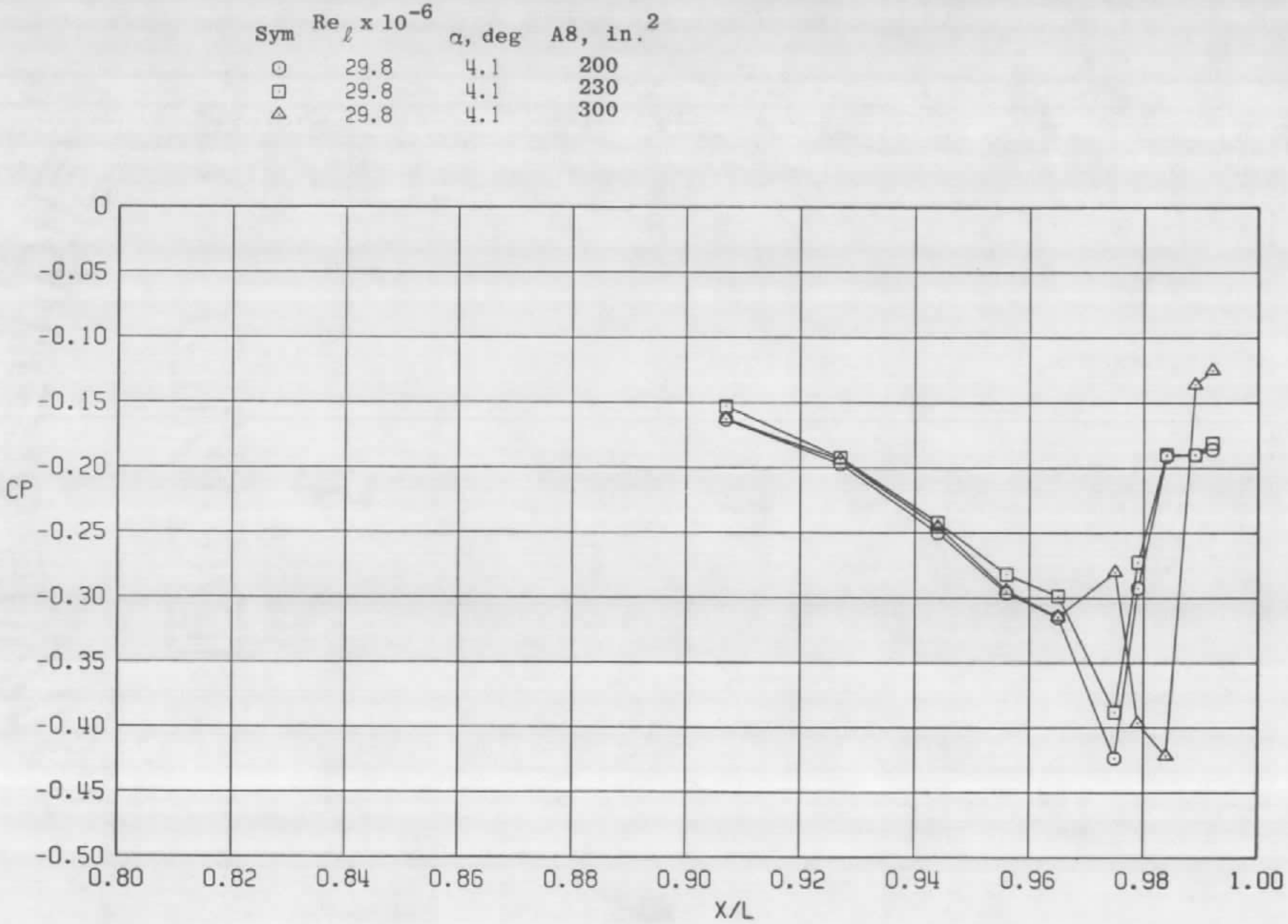

f. ϕ = 315 deg
Figure 8. Concluded.

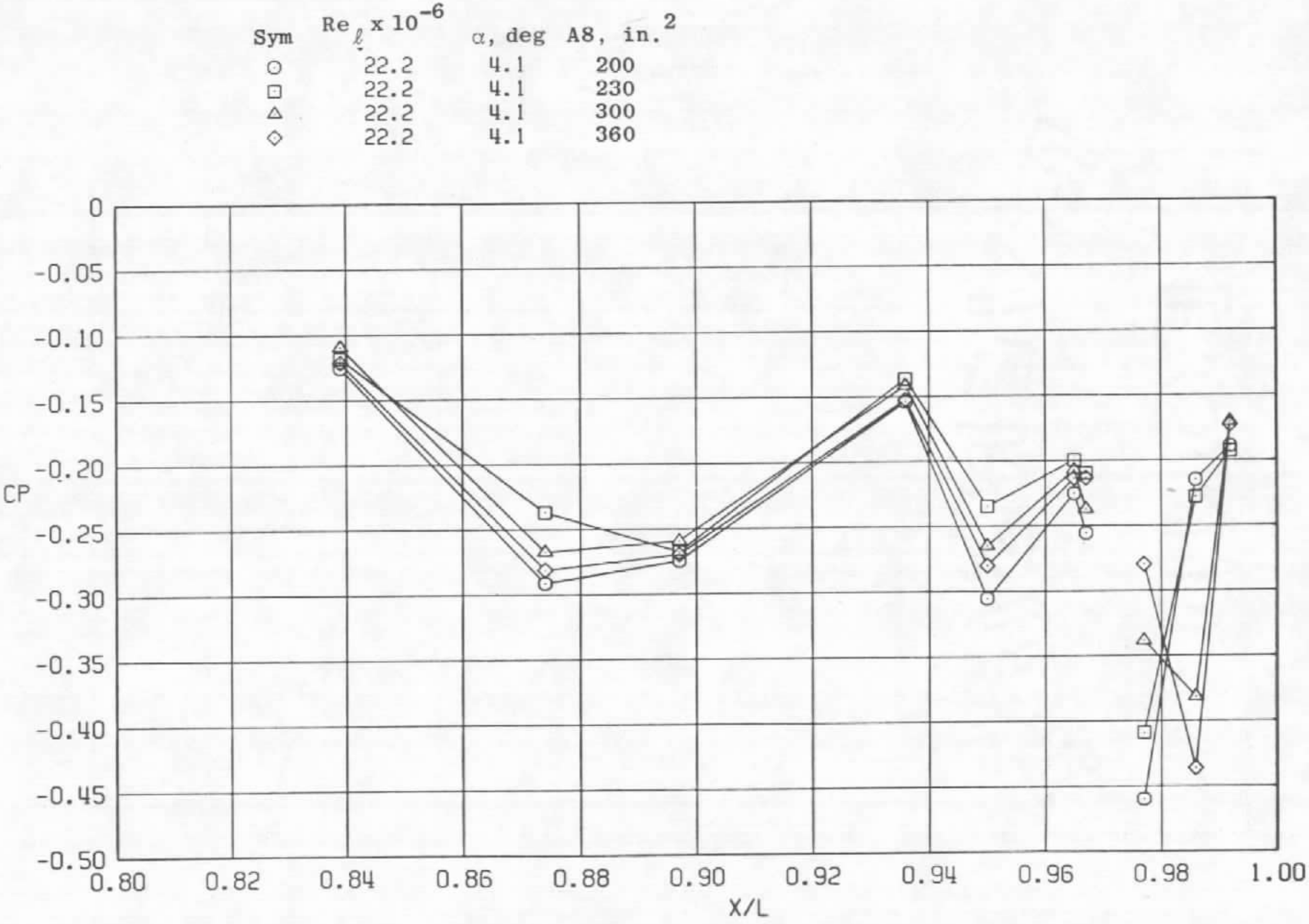

a. $\phi = 0$

Figure 9. Nozzle closure effects on surface pressure coefficients, M = 1.2, NPRE = 5.0 (SS).

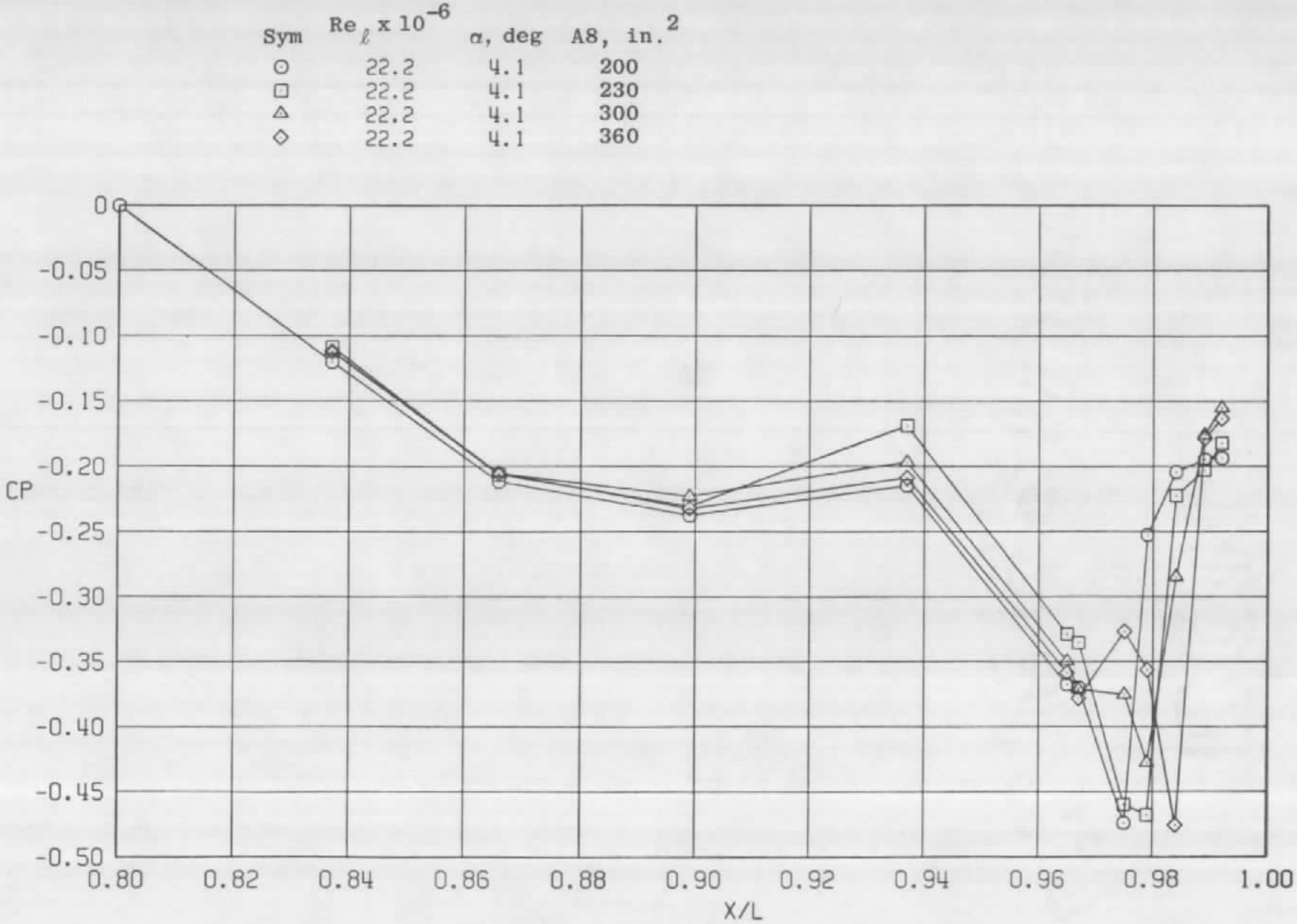

b. ϕ = 45 deg
Figure 9. Continued.

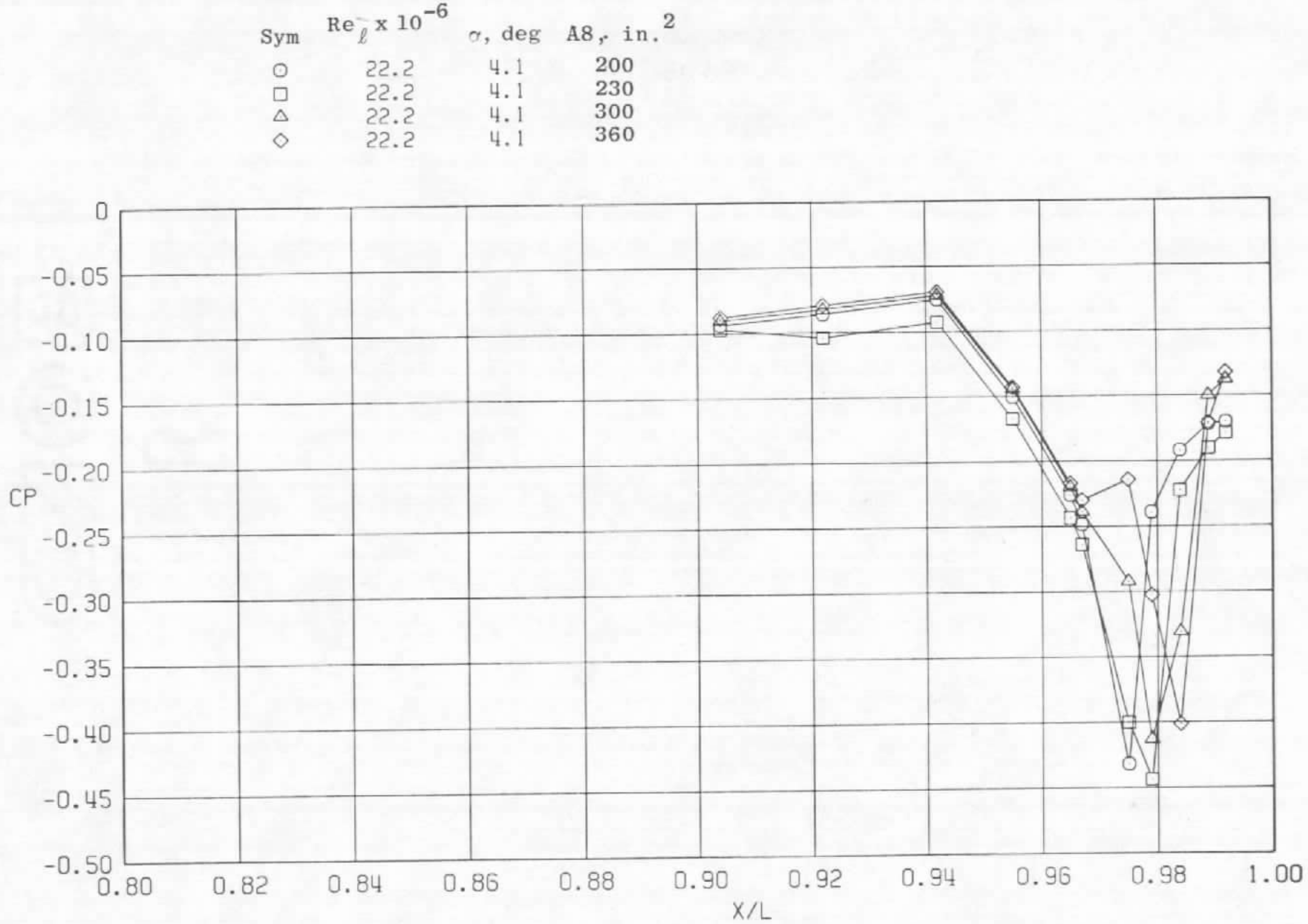

c. ϕ = 135 deg
Figure 9. Continued.

d. ϕ = 180 deg
Figure 9. Continued.

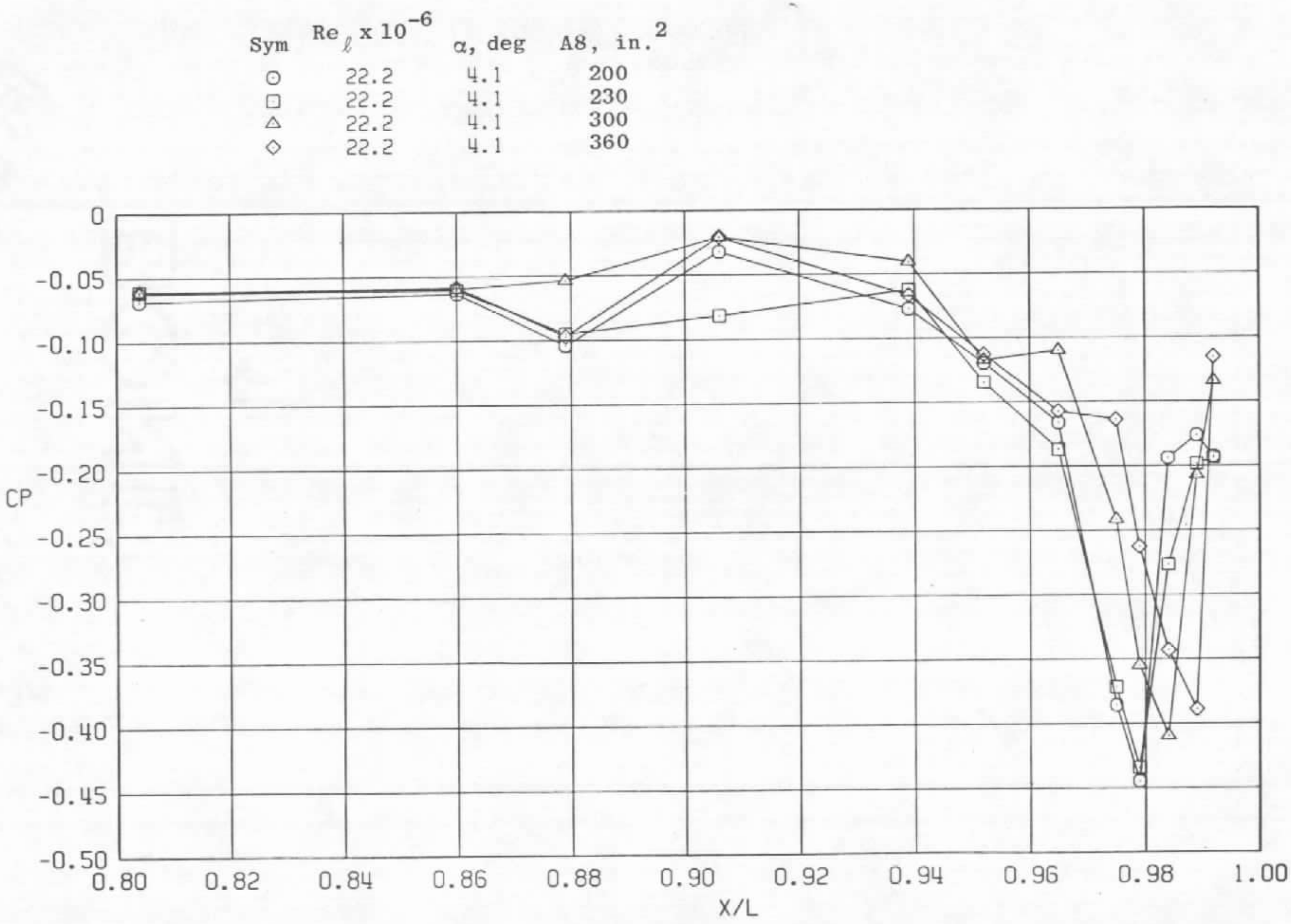

e. ϕ = 225 deg
Figure 9. Continued.

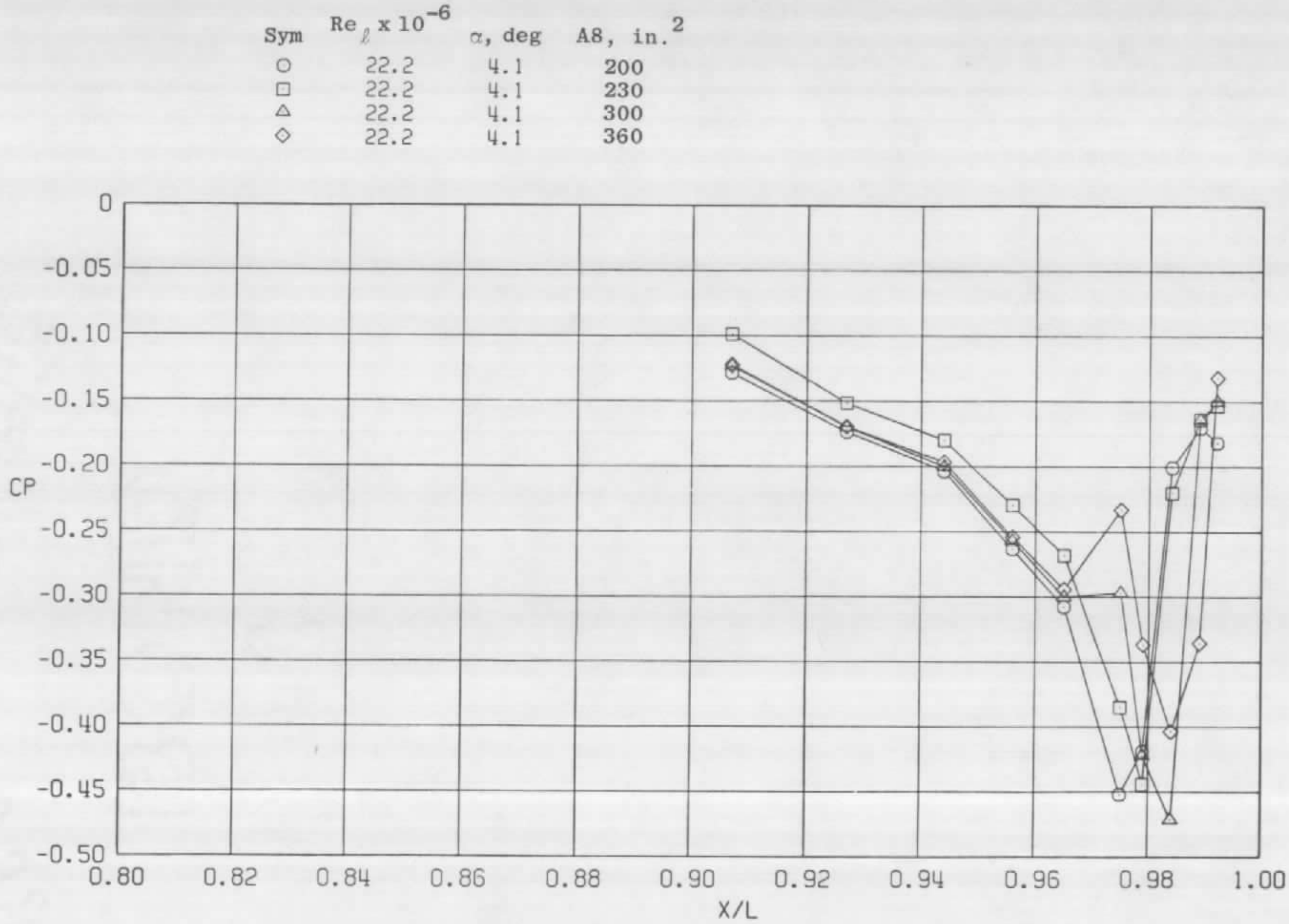

f. ϕ = 315 deg
Figure 9. Concluded.

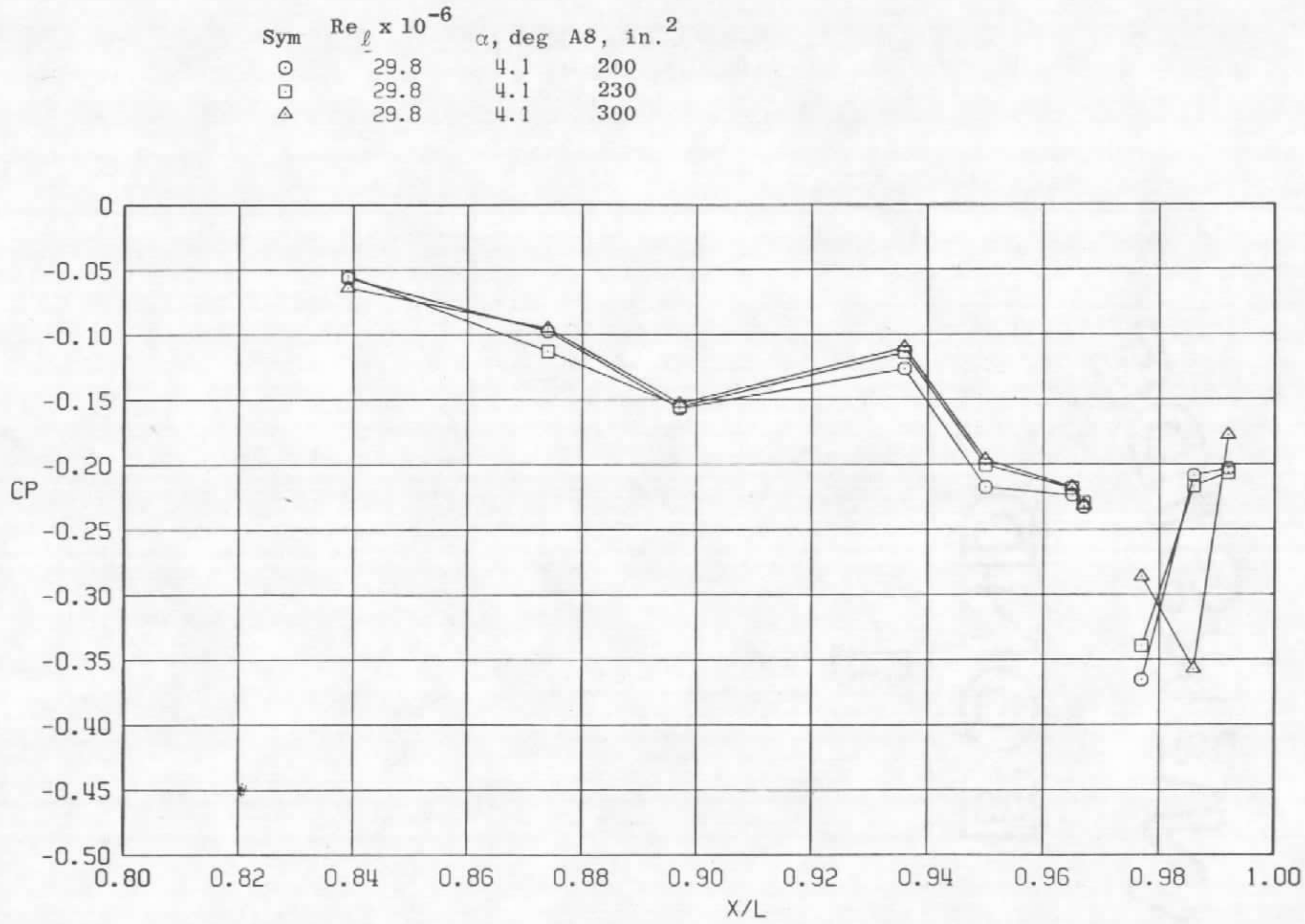

a. $\phi = 0$

Figure 10. Nozzle closure effects on surface pressure coefficients, NPR = 5.0, M = 1.5 (WT).

Sym	$Re_{\ell} \times 10^{-6}$	α, deg	A8, in.^{2}
⊙	29.8	4.1	200
⊡	29.8	4.1	230
△	29.8	4.1	300

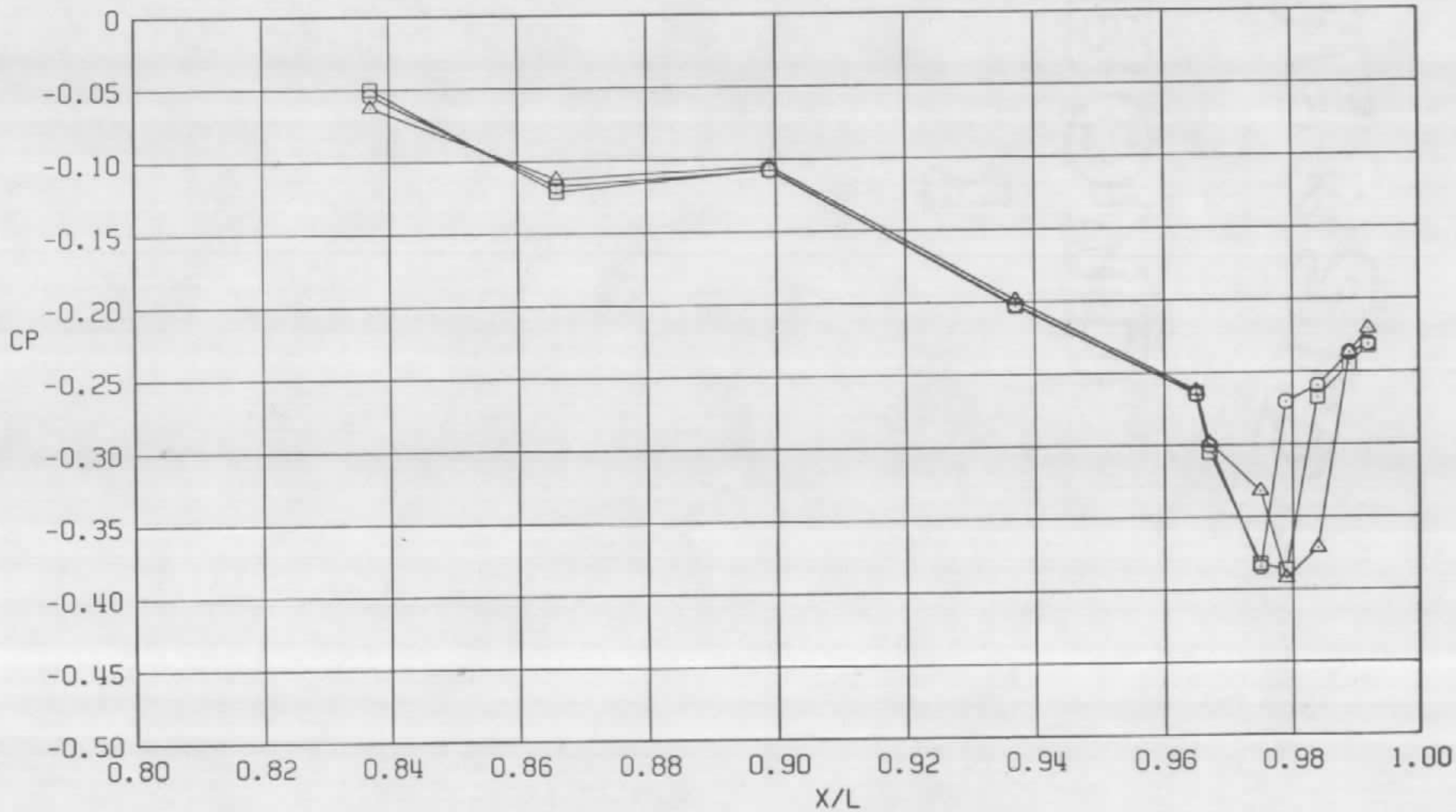

b. ϕ = 45 deg
Figure 10. Continued.

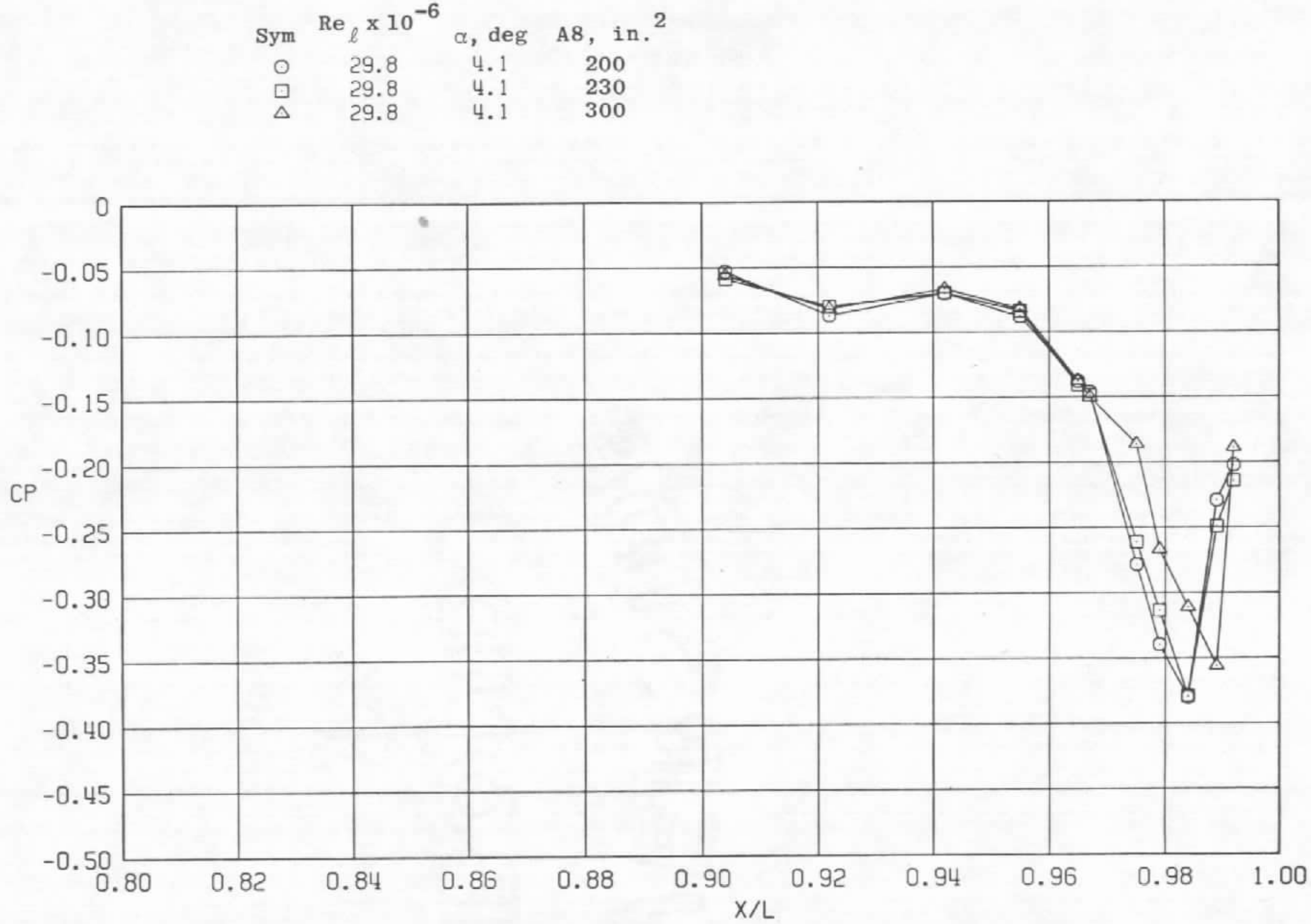

c. ϕ = 135 deg
Figure 10. Continued.

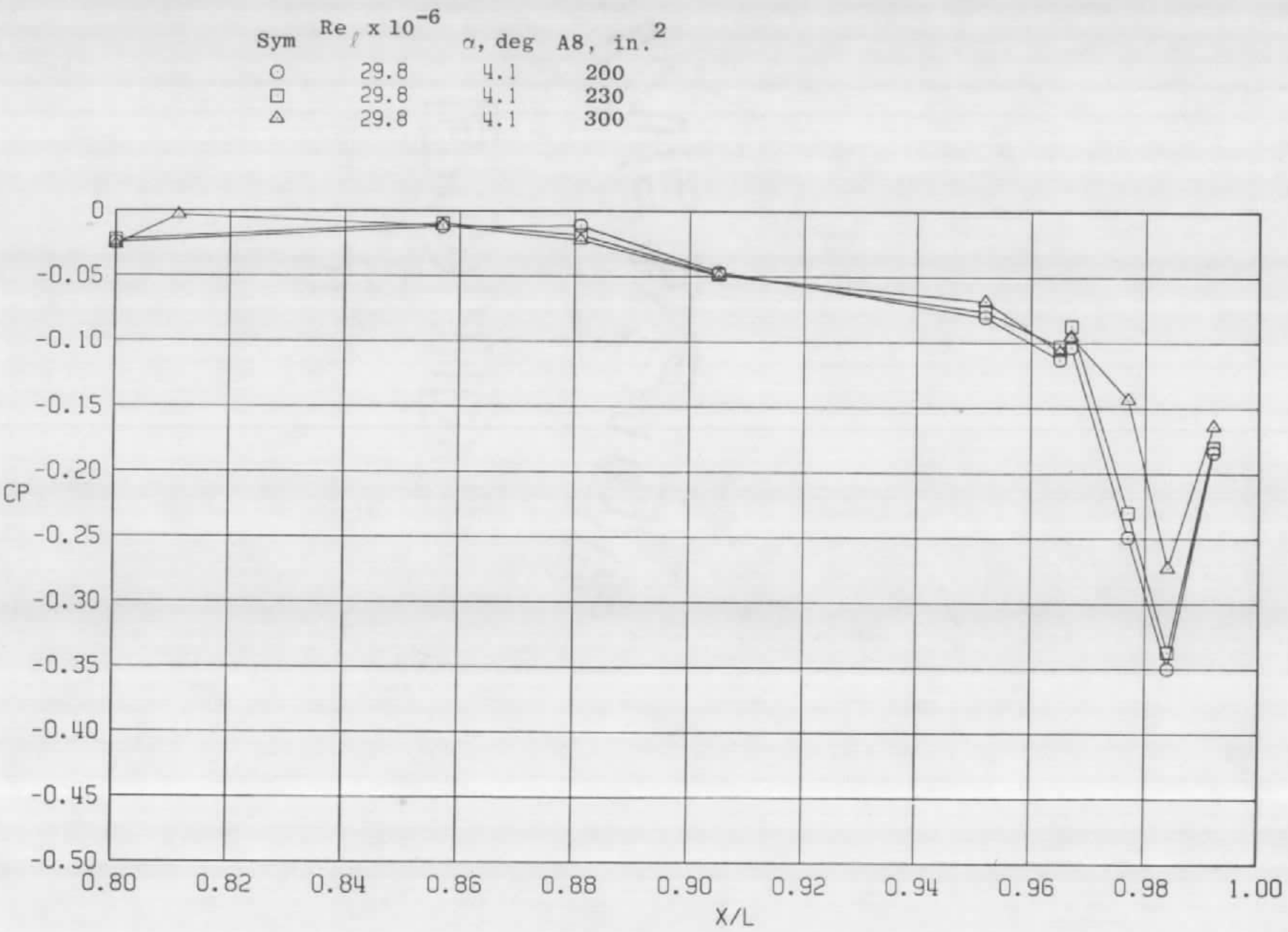

d. ϕ = 180 deg
Figure 10. Continued.

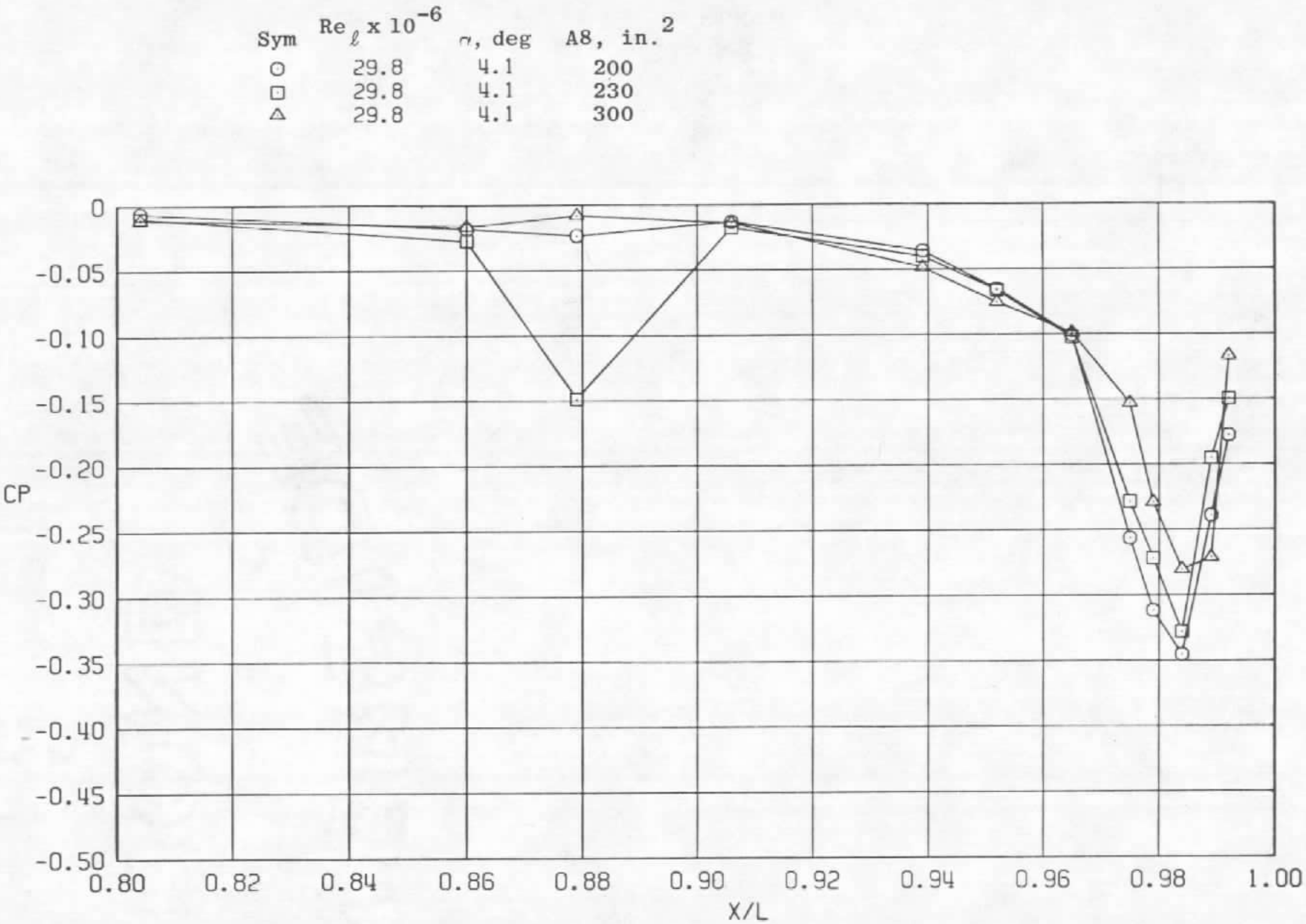

e. ϕ = 225 deg

Figure 10. Continued.

f. ϕ = 315 deg
Figure 10. Concluded.

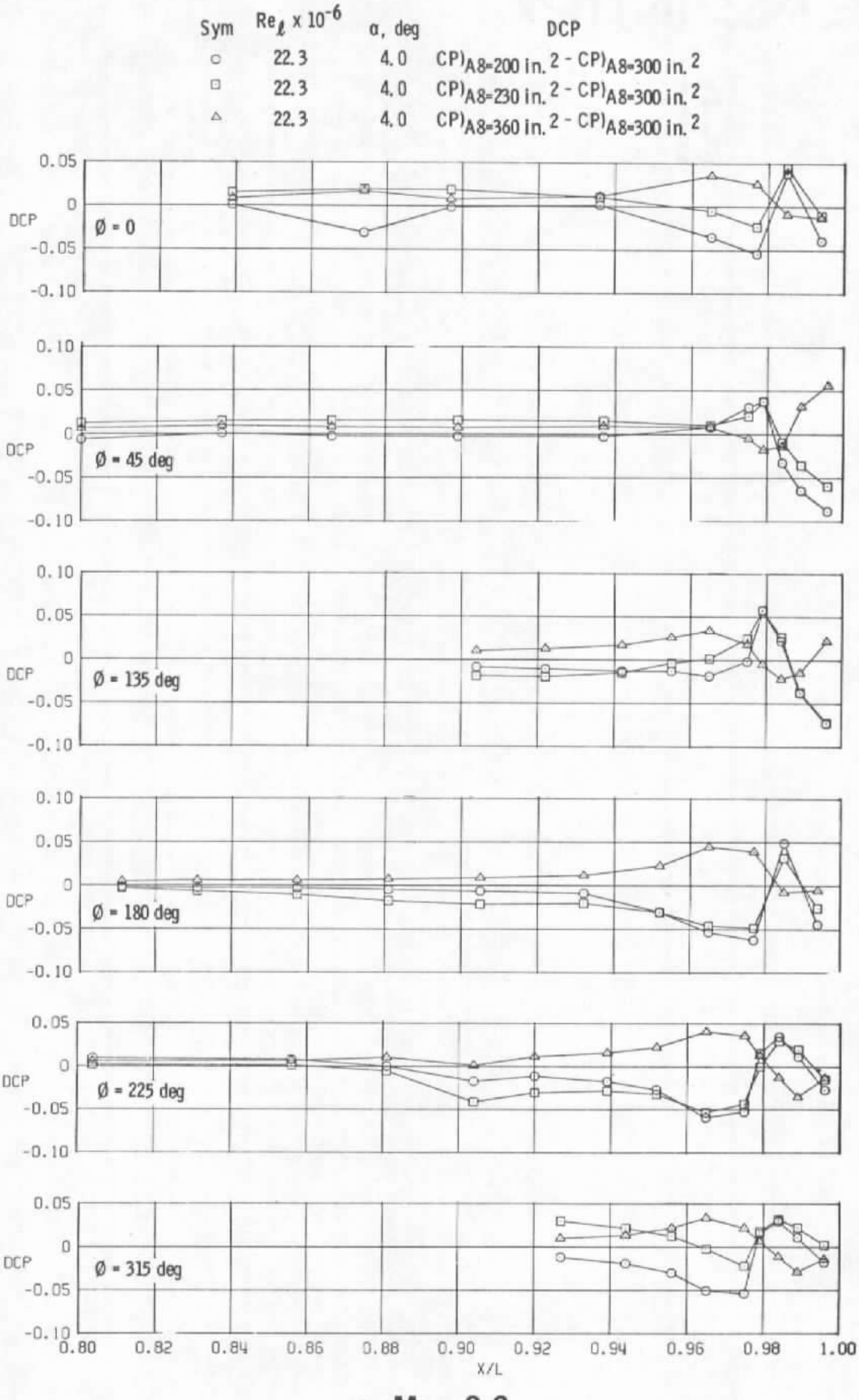

a. M = 0.6

Figure 11. Effects of incremental changes in nozzle closure on surface pressure coefficients, NPR = 5.0 (SS).

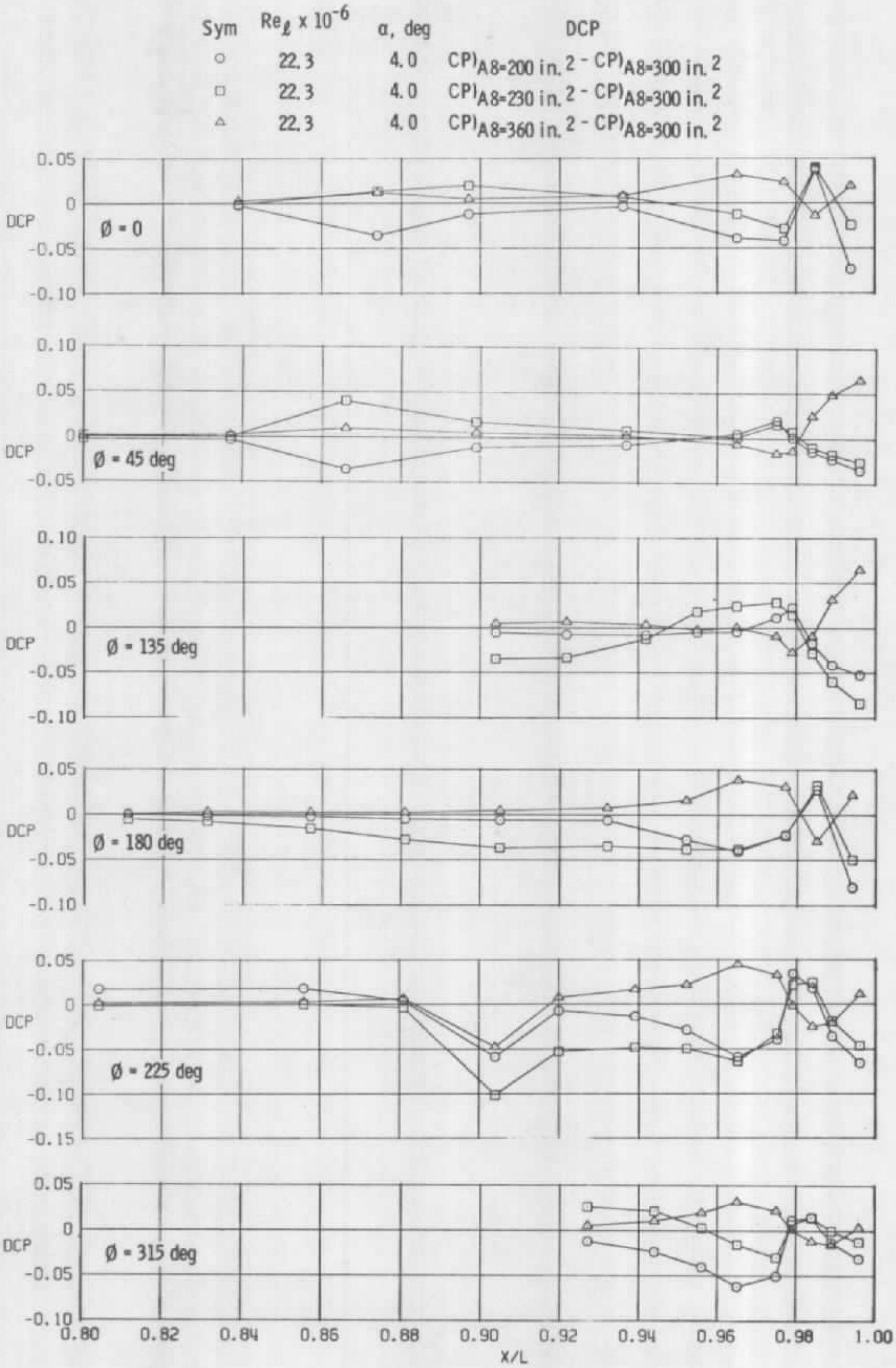

b. M = 0.9
Figure 11. Continued.

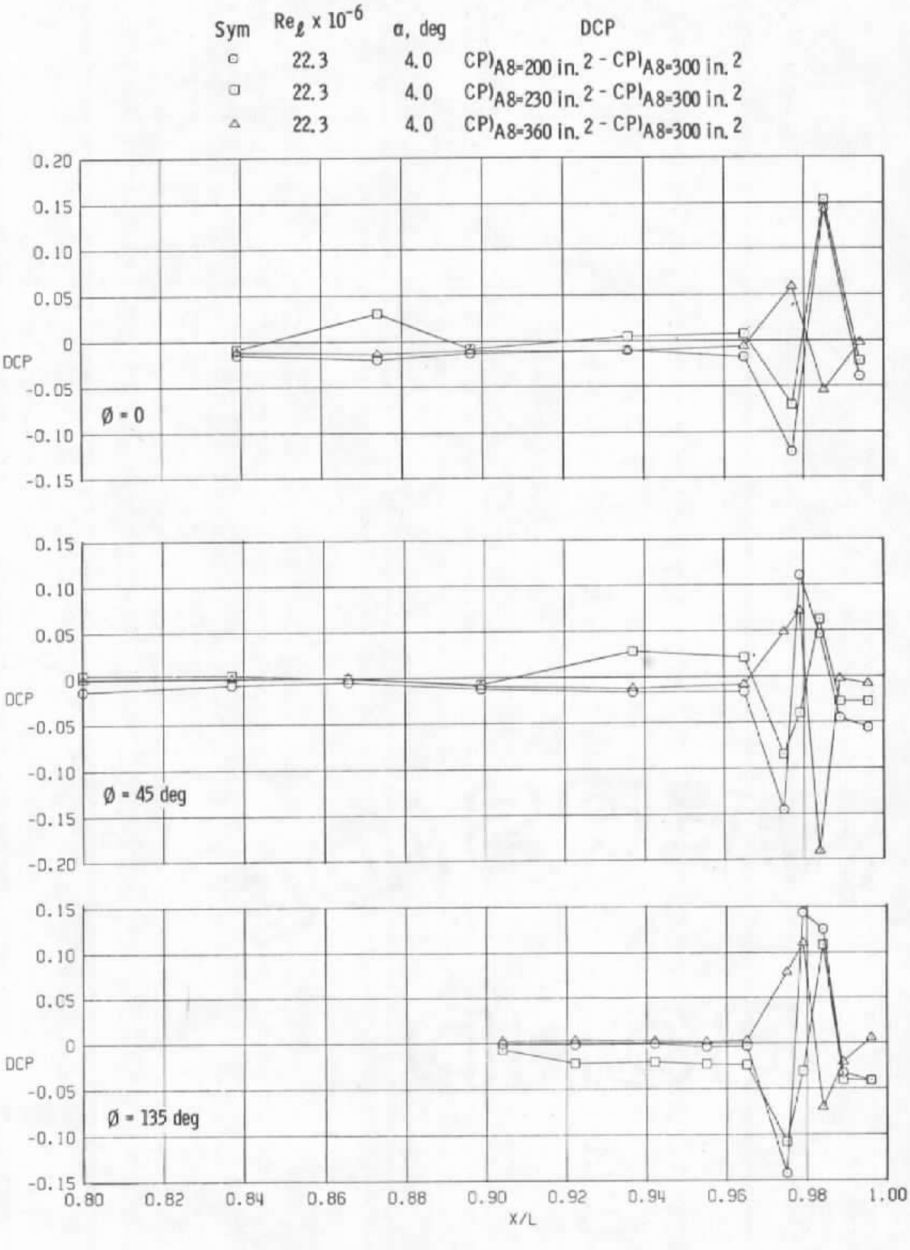

c. M = 1.2
Figure 11. Continued.

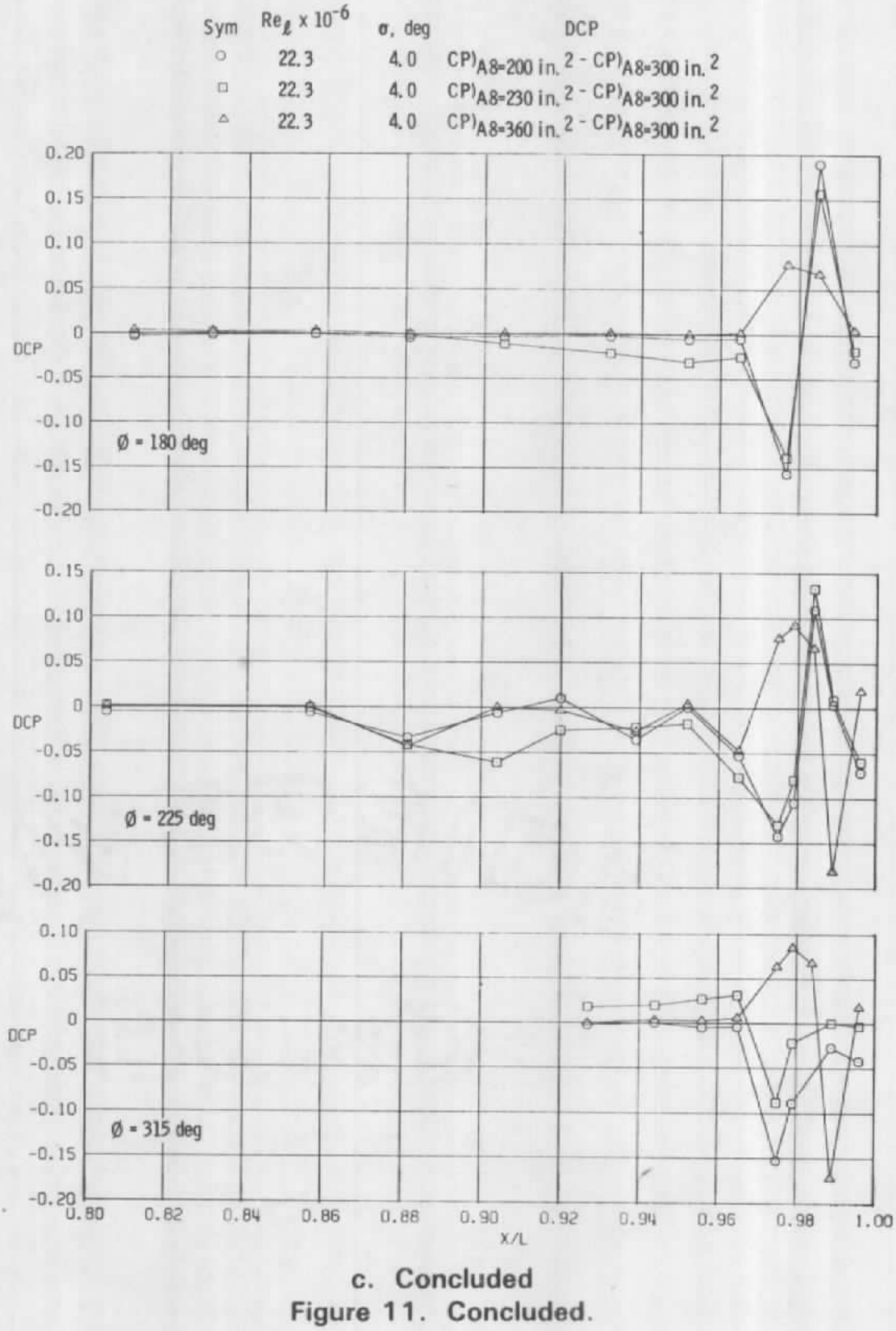

c. Concluded
Figure 11. Concluded.

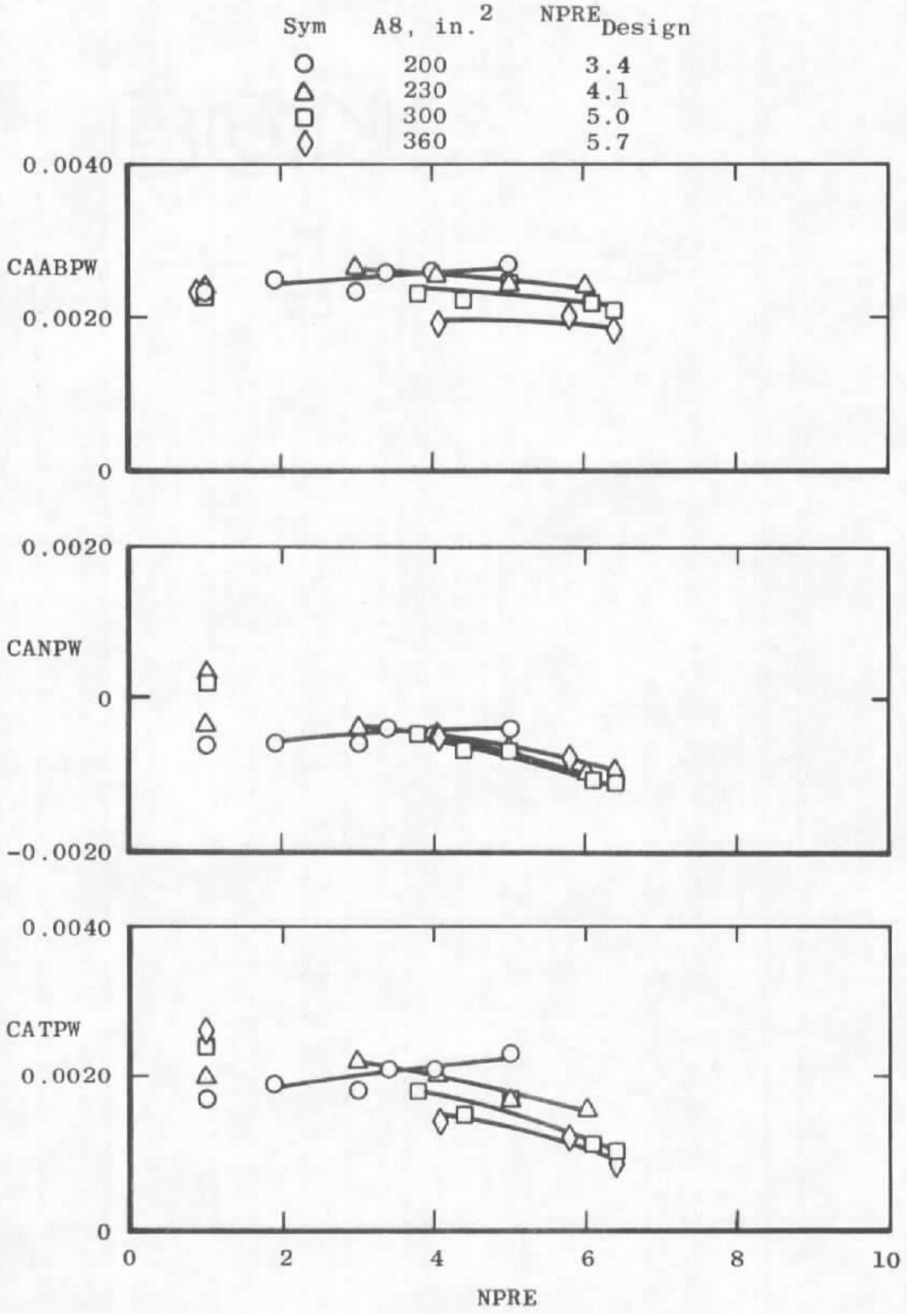

a. M = 0.6 (SS)

Figure 12. Nozzle pressure ratio effects on axial force coefficients, α = 4.1 deg.

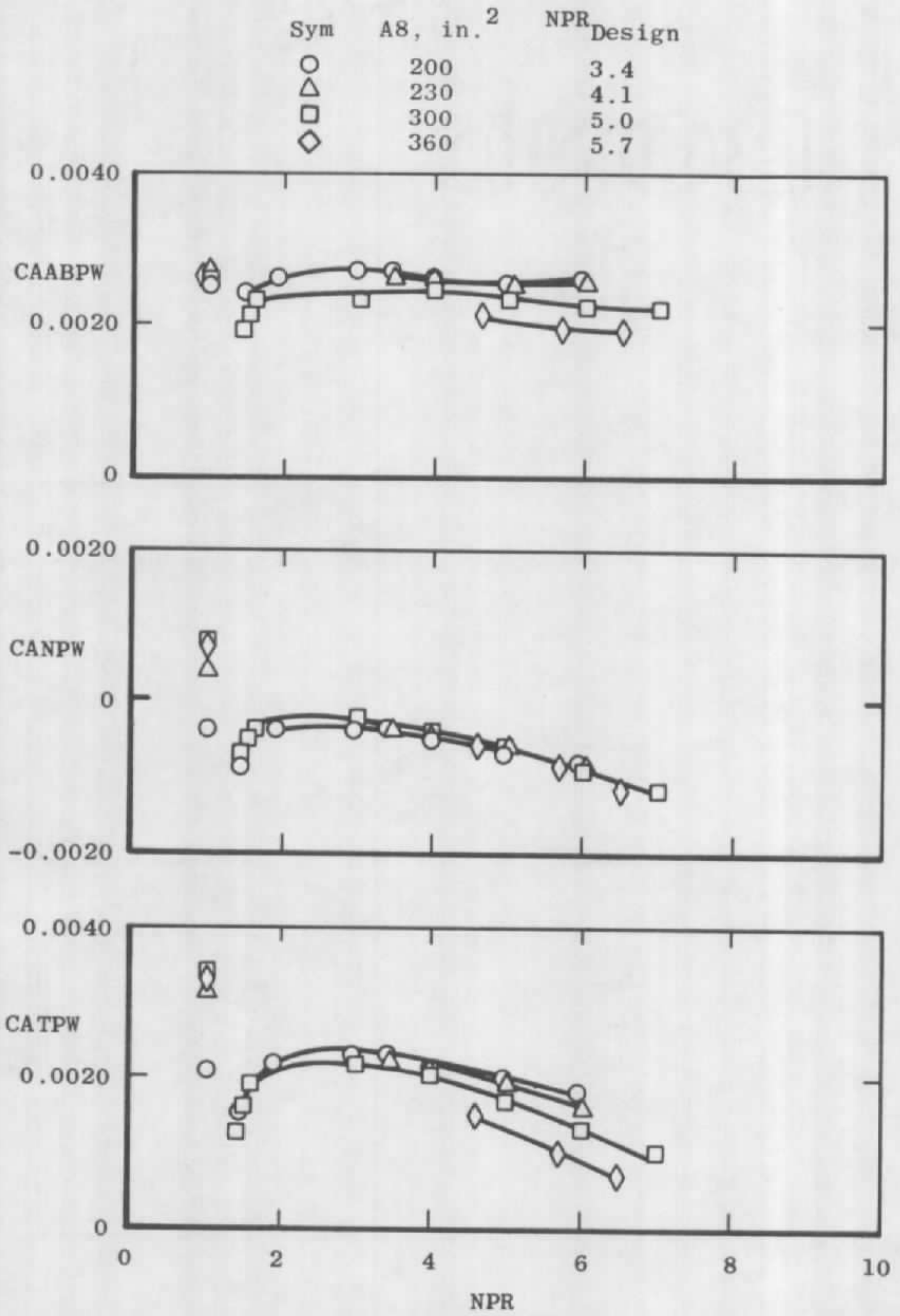

b. M = 0.6 (WT)

Figure 12. Continued.

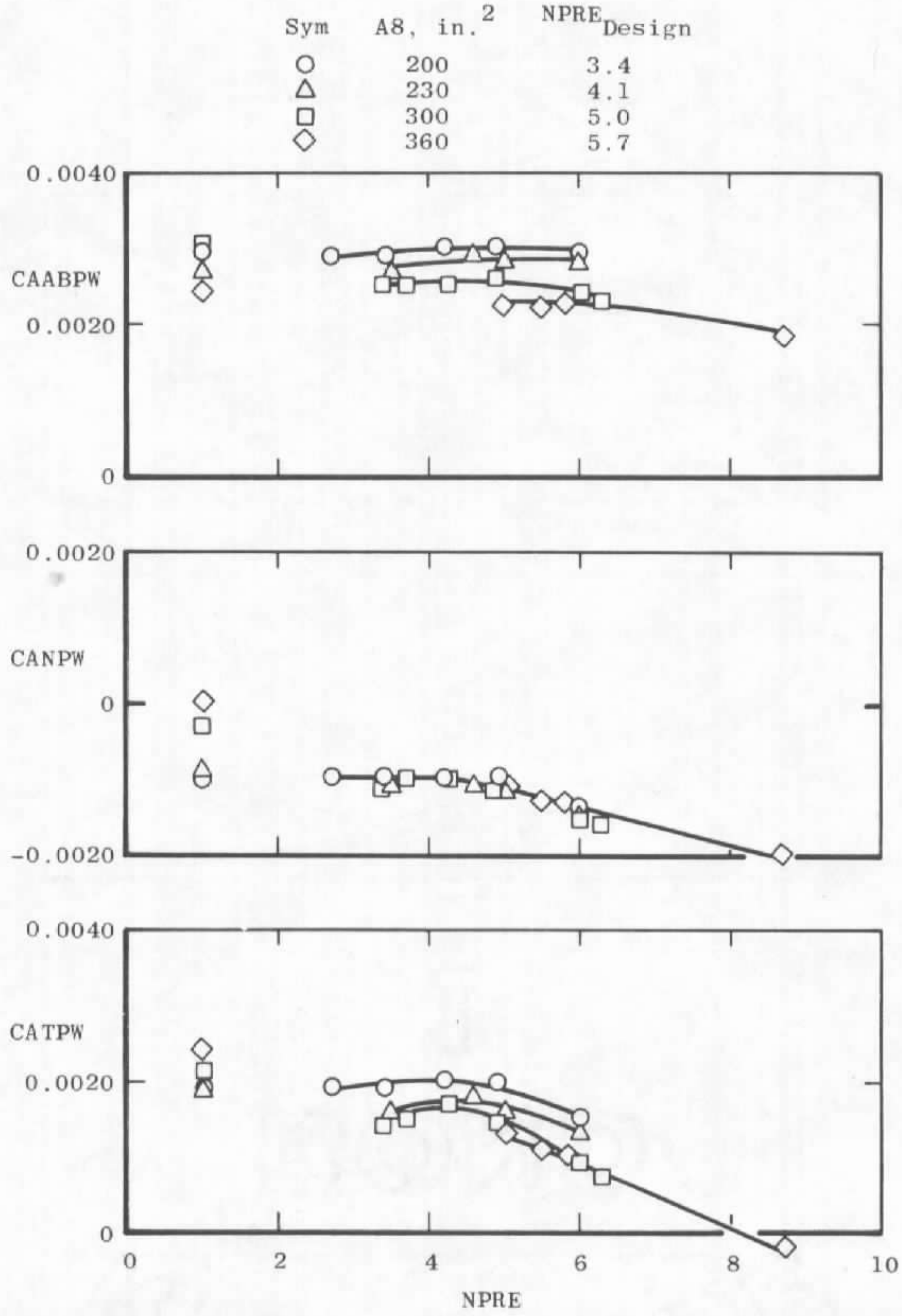

c. M = 0.9 (SS)
Figure 12. Continued.

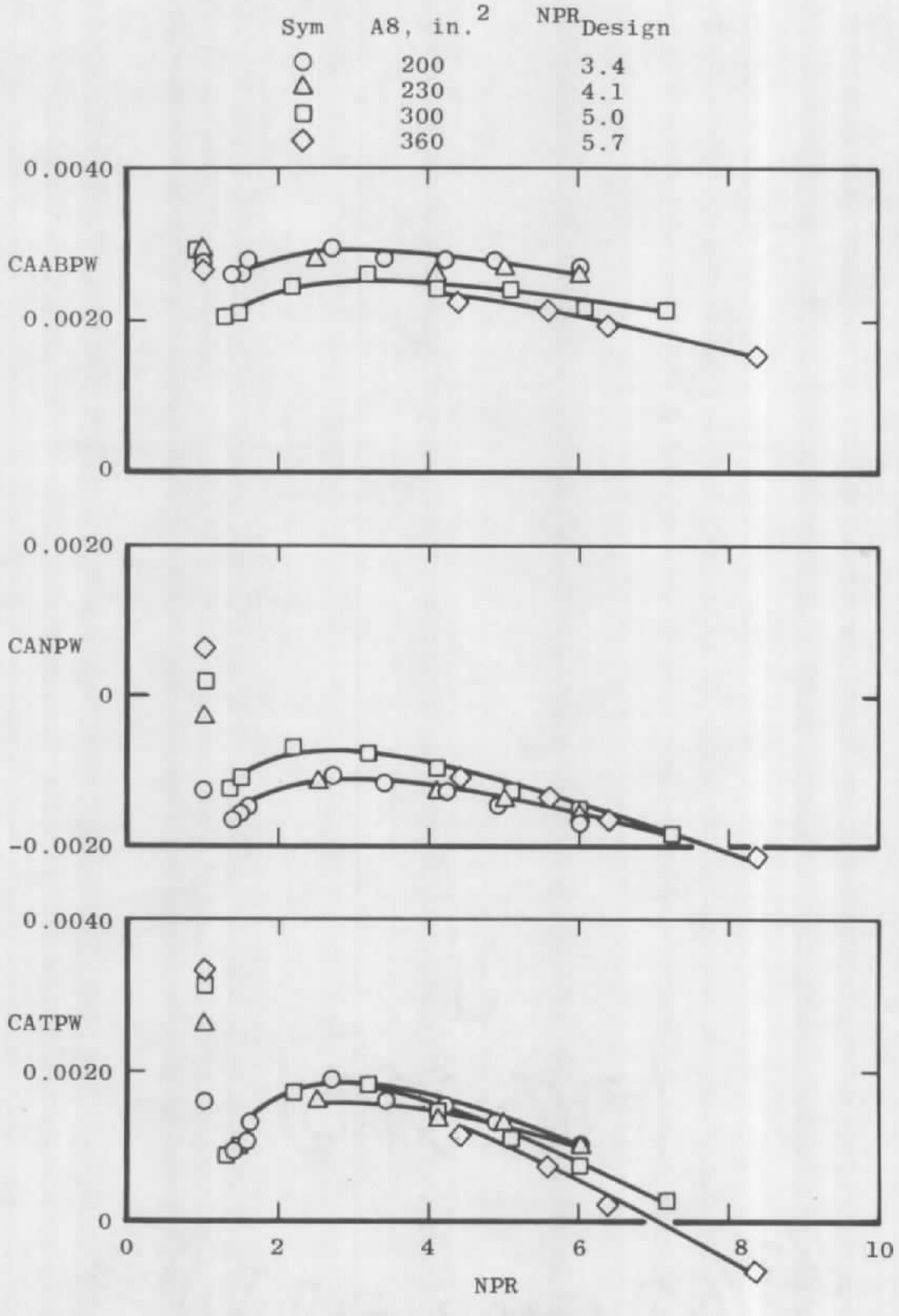

d. M = 0.9 (WT)
Figure 12. Continued.

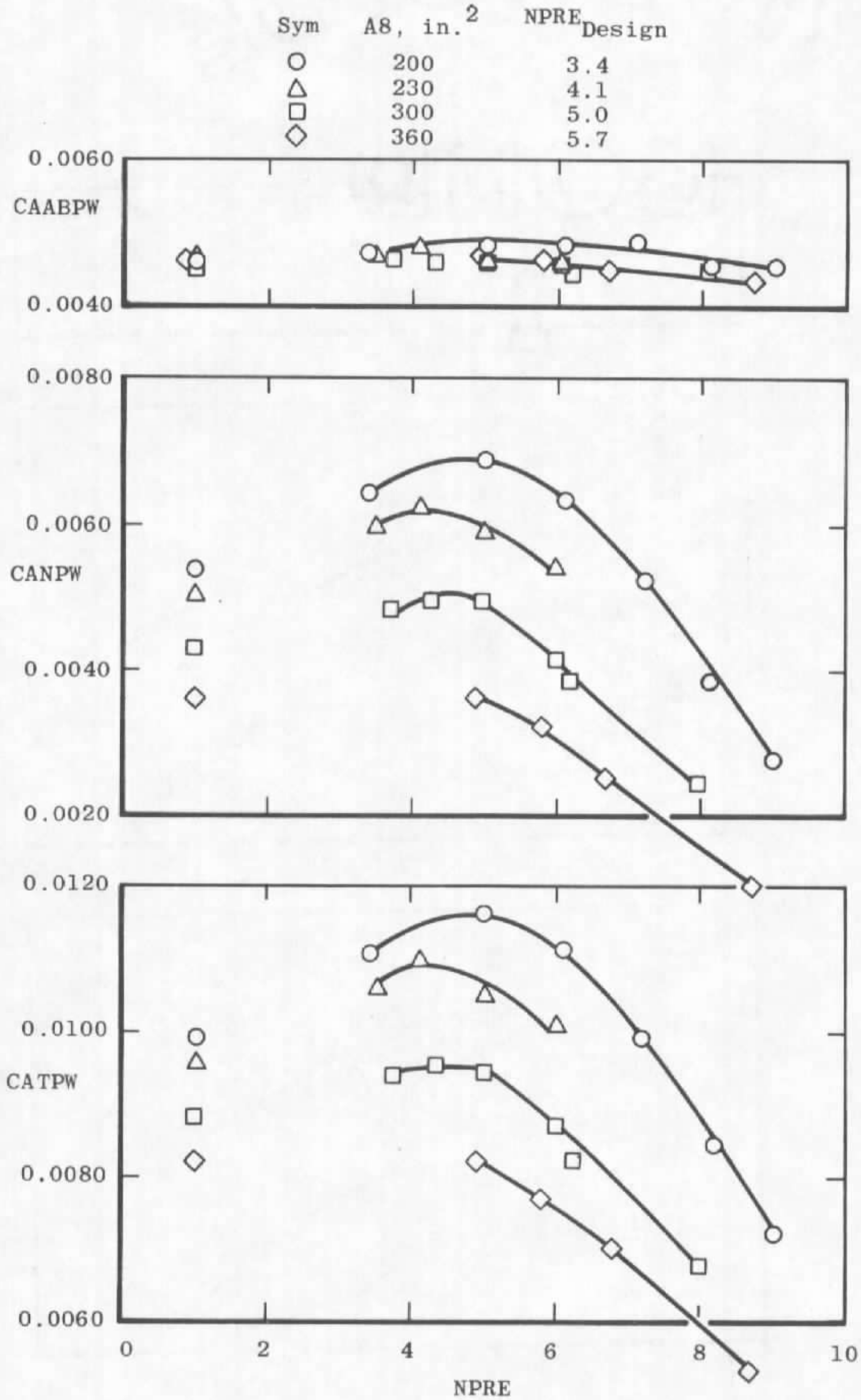

e. M = 1.2 (SS)
Figure 12. Continued.

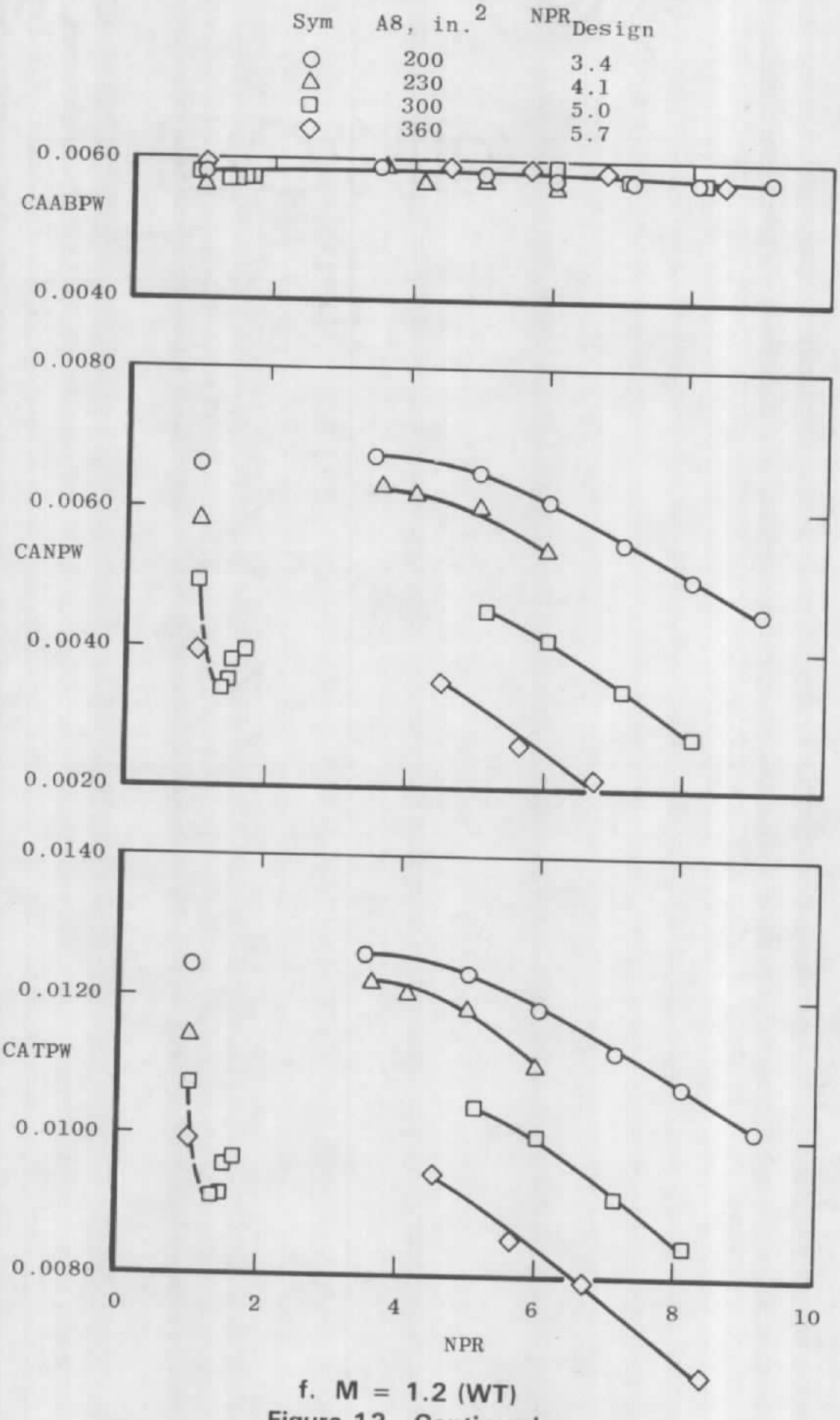

f. M = 1.2 (WT)
Figure 12. Continued.

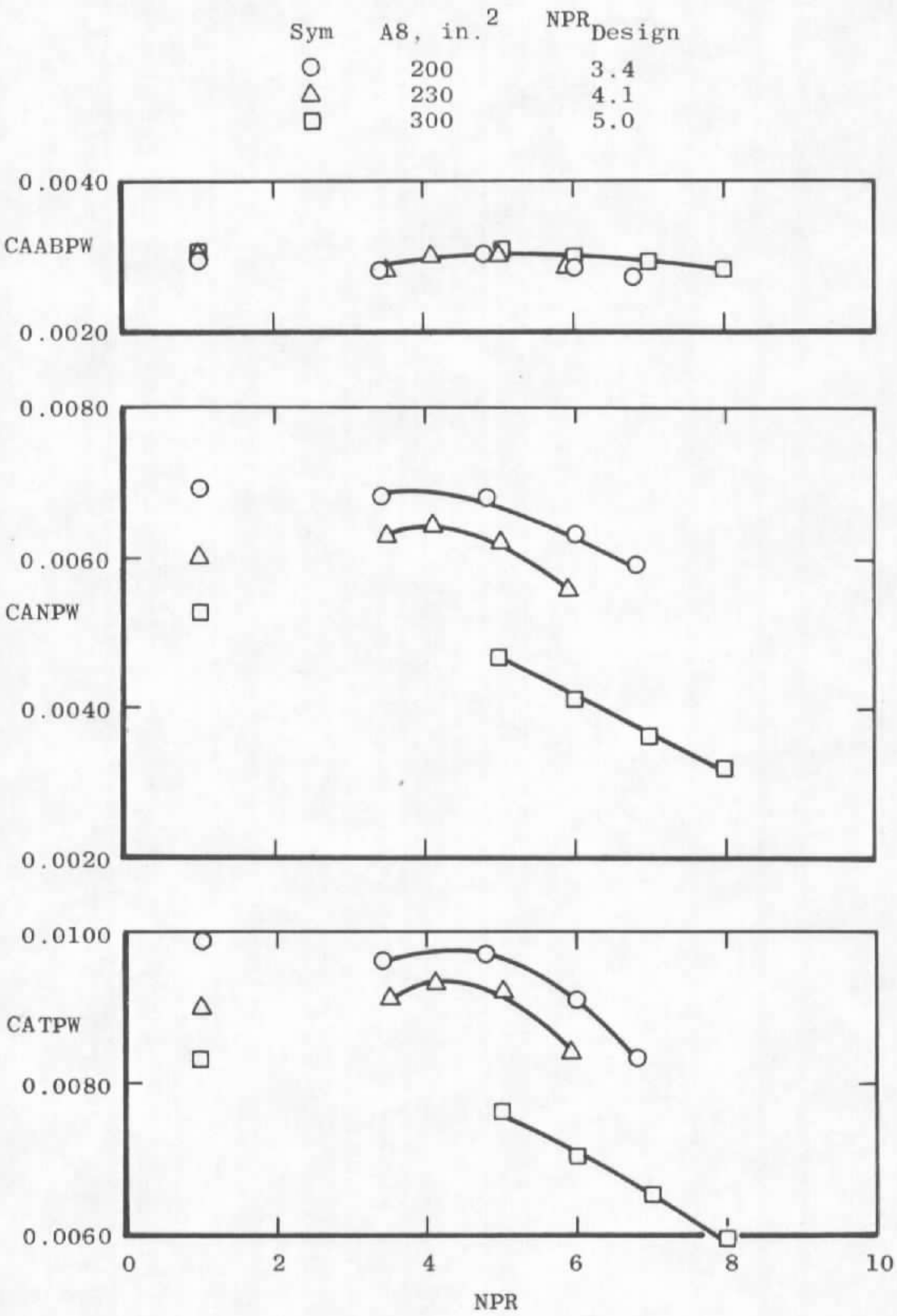

g. M = 1.5 (WT)
Figure 12. Concluded.

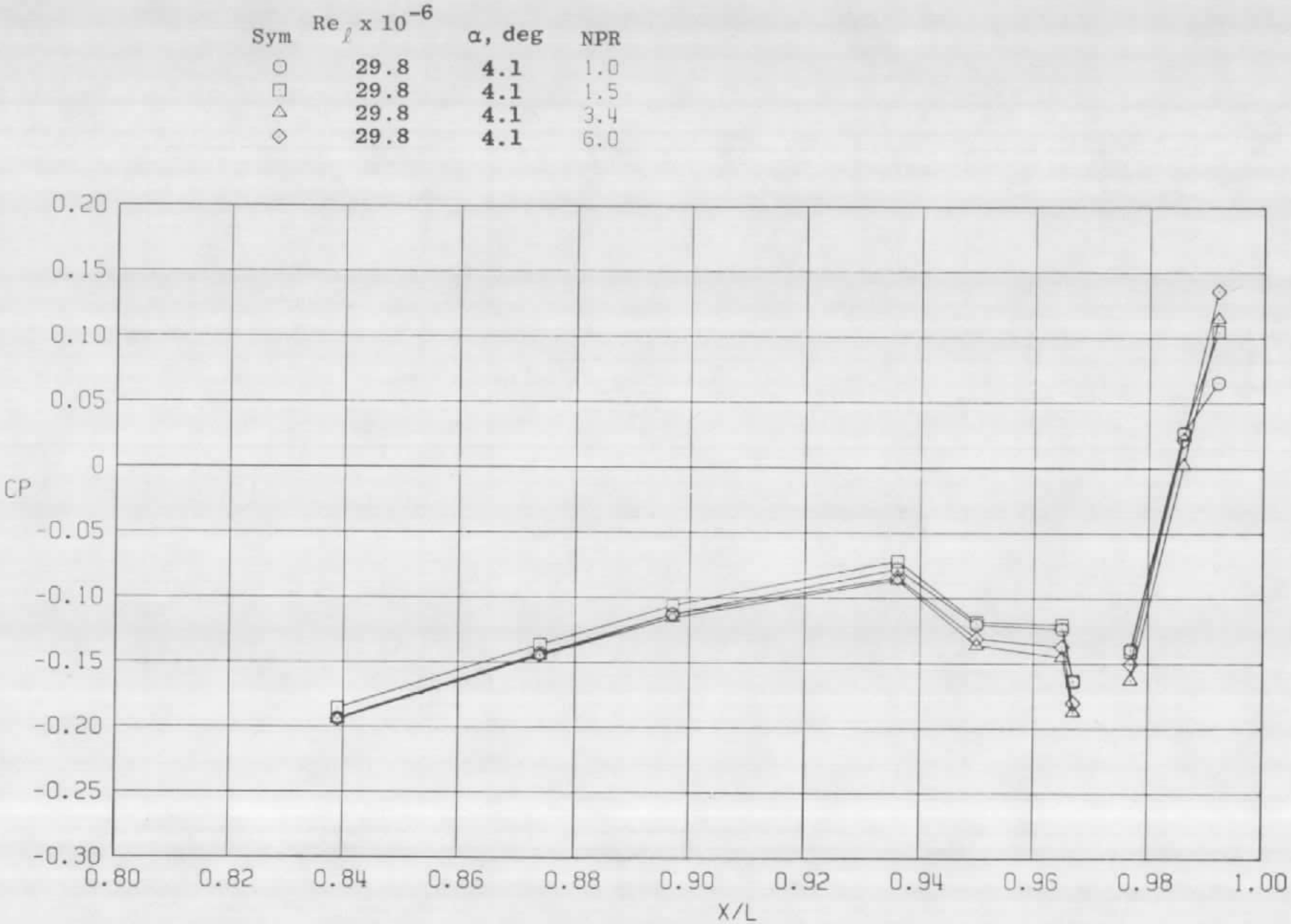

a. $\phi = 0$

Figure 13. Nozzle pressure ratio effects on surface pressure coefficients, A8 = 200 in.², M = 0.6 (WT).

Sym	$Re_{\ell} \times 10^{-6}$	α, deg	NPR
○	29.8	4.1	1.0
□	29.8	4.1	1.5
△	29.8	4.1	3.4
◇	29.8	4.1	6.0

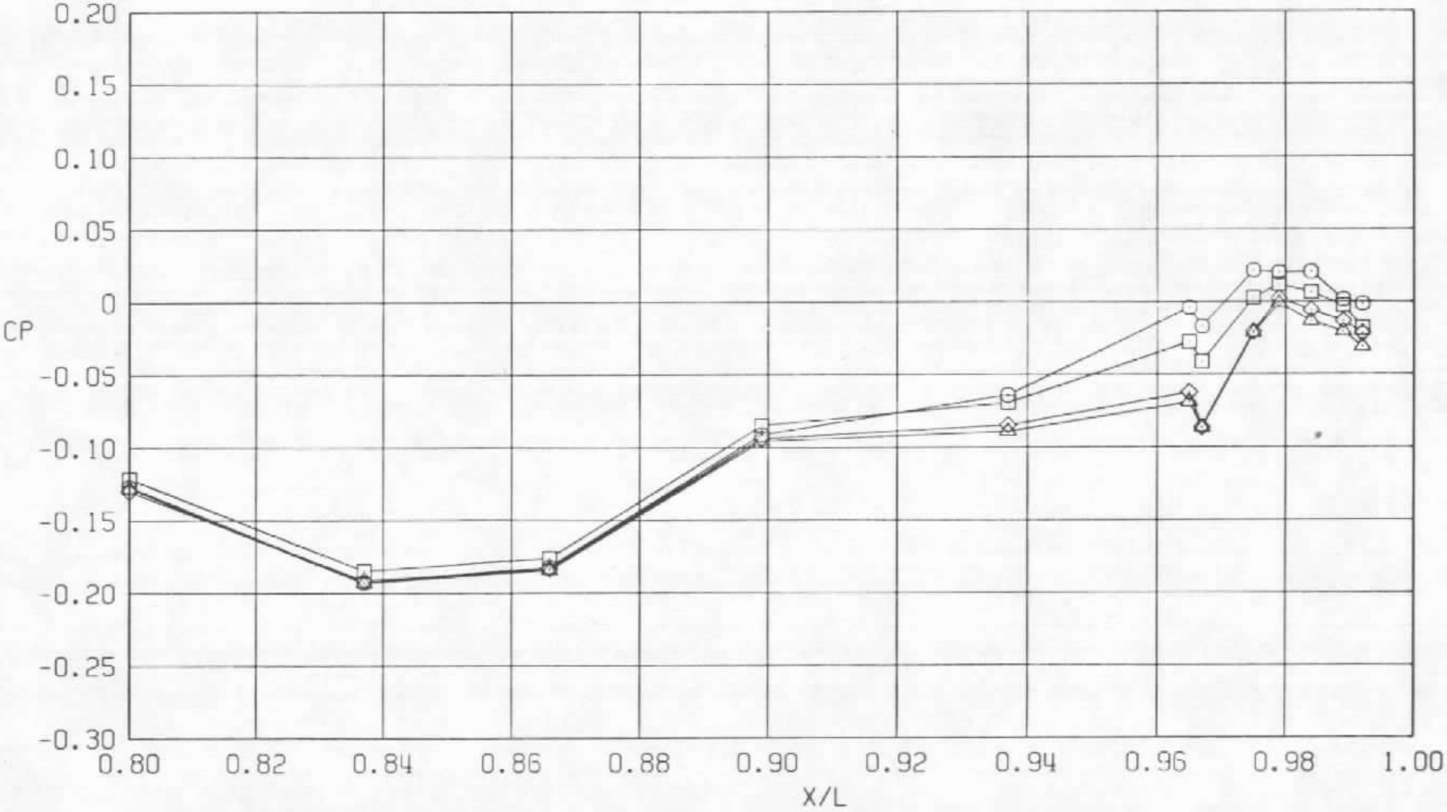

b. ϕ = 45 deg
Figure 13. Continued.

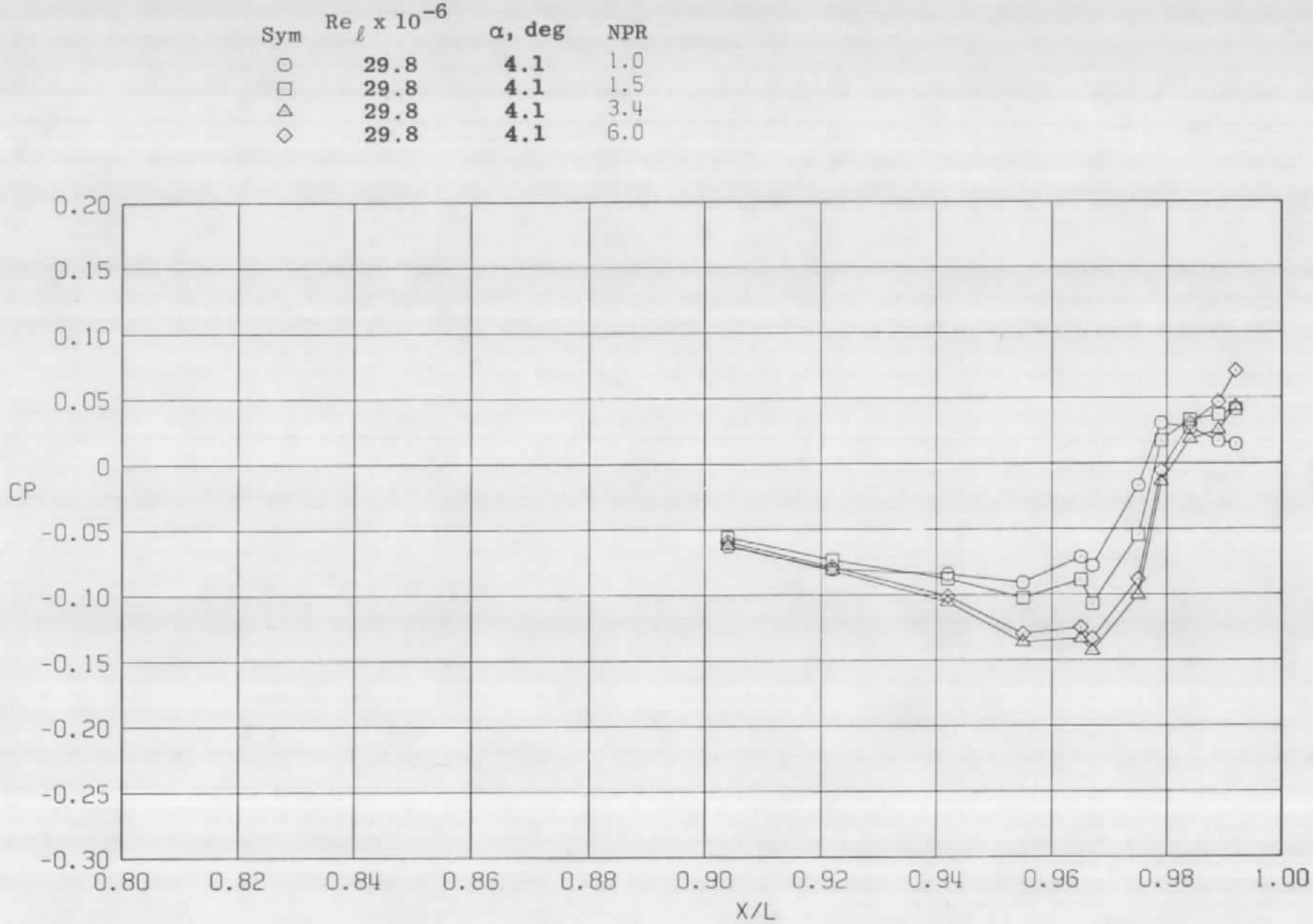

c. ϕ = 135 deg
Figure 13. Continued.

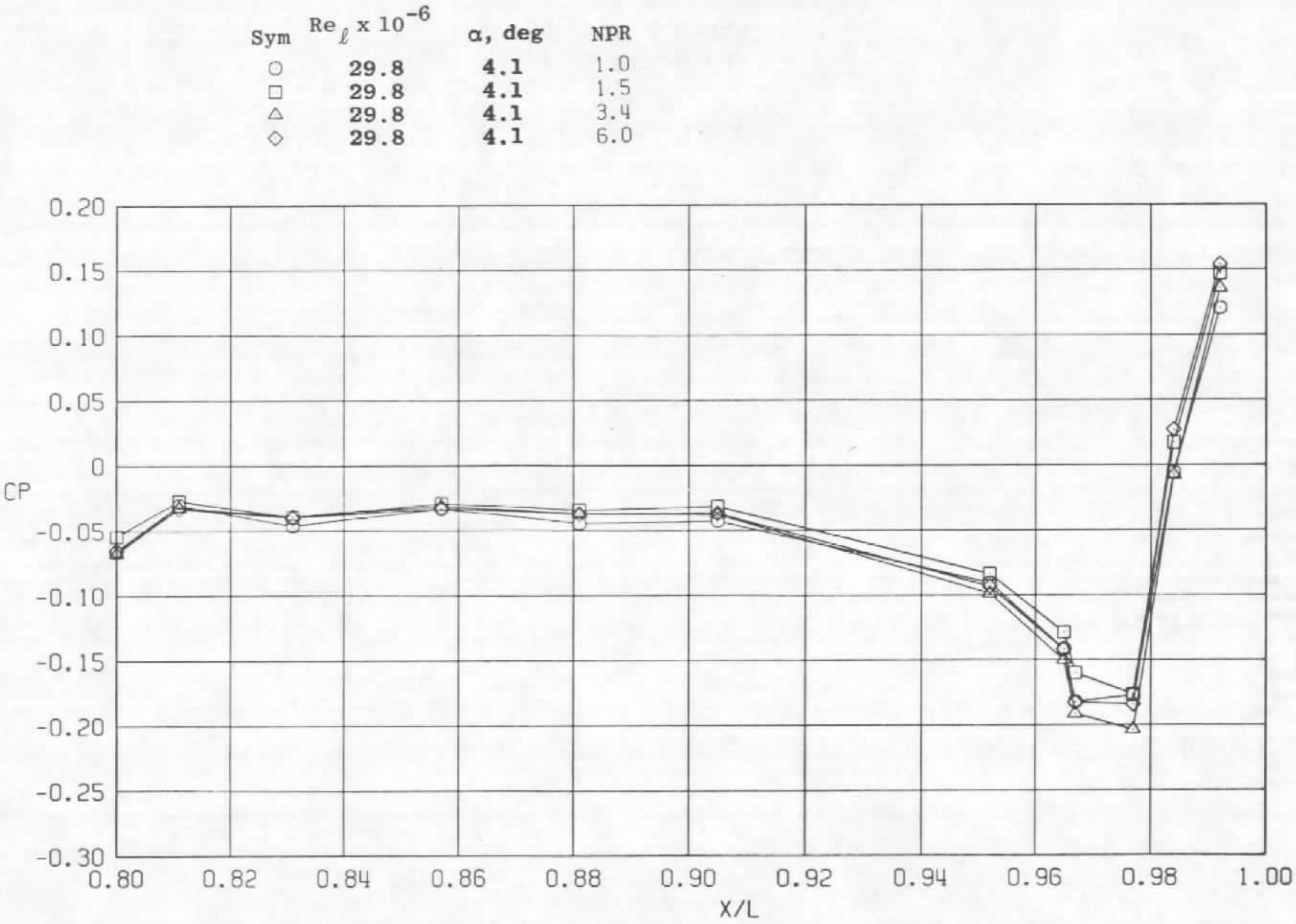

d. ϕ = 180 deg
Figure 13. Continued.

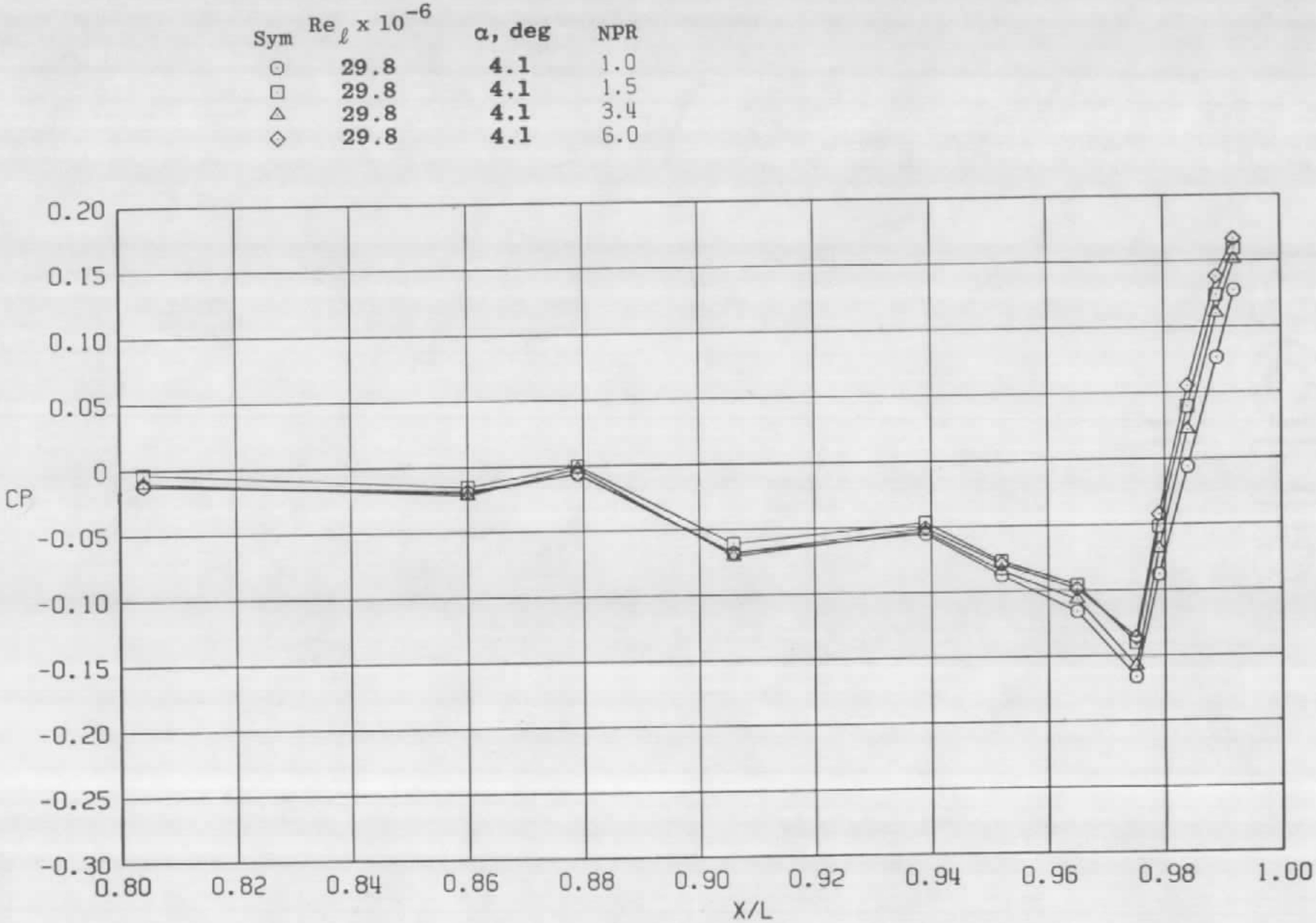

e. ϕ = 225 deg
Figure 13. Continued.

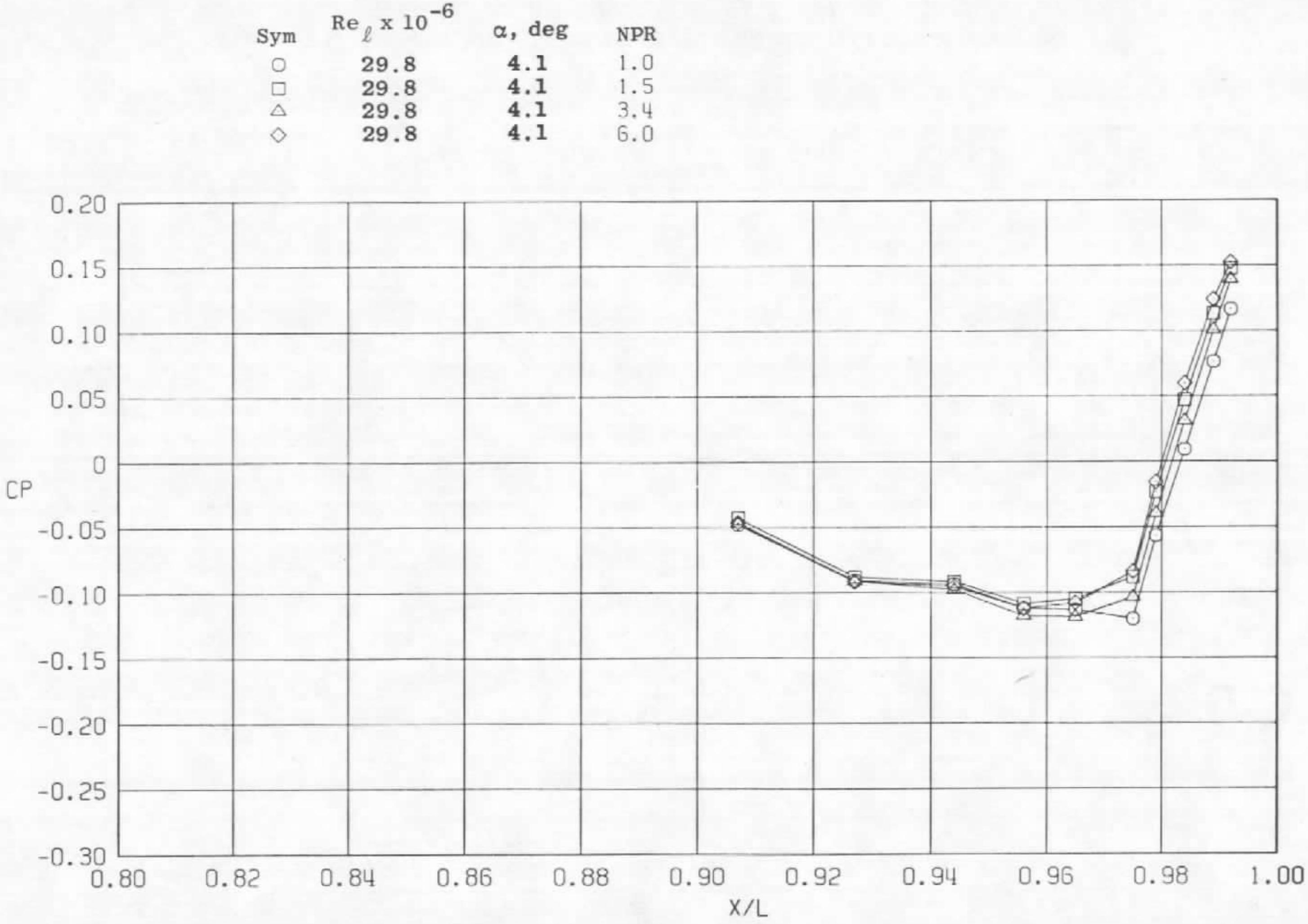

f. ϕ = 315 deg
Figure 13. Concluded.

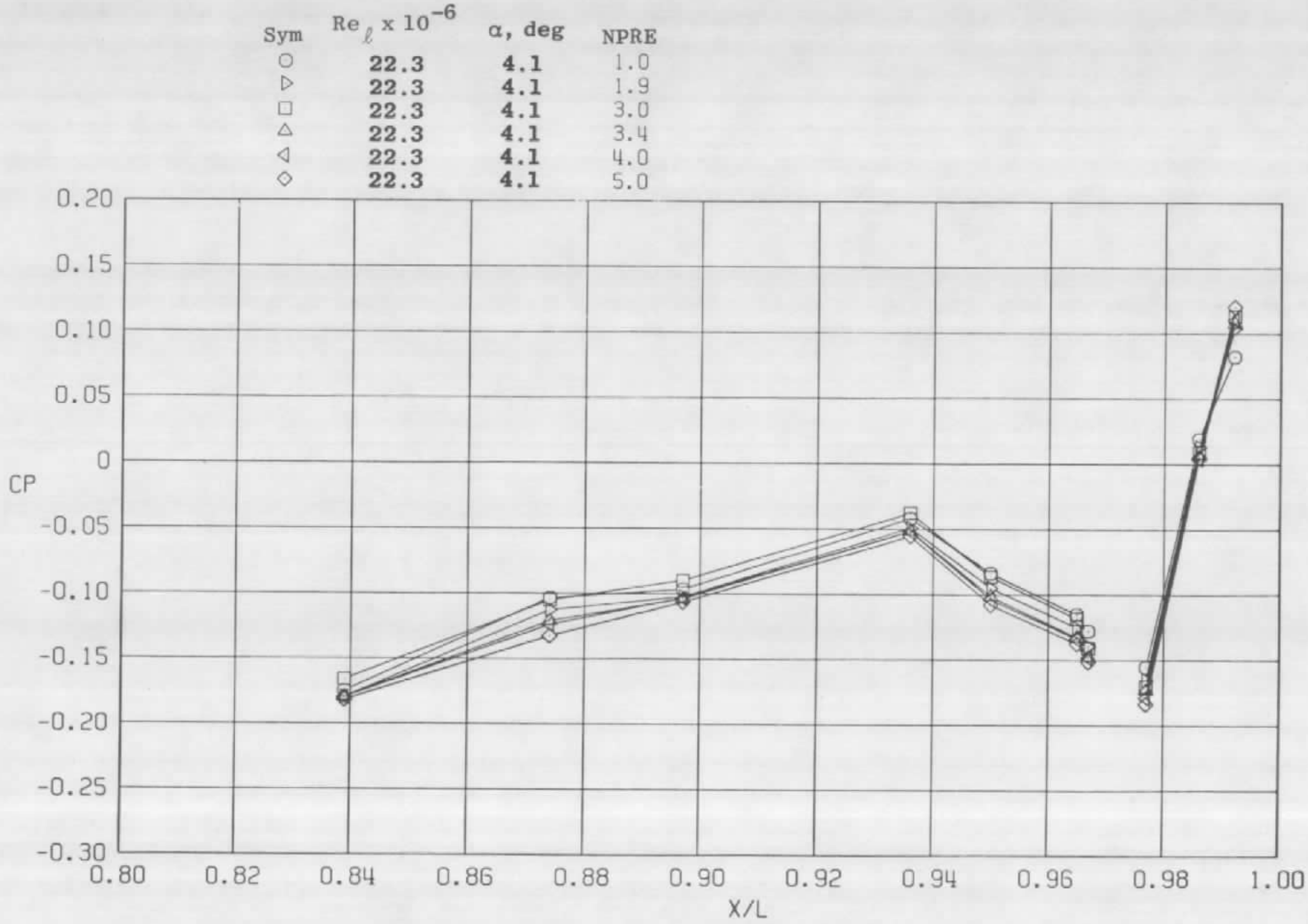

a. $\phi = 0$

Figure 14. Effective nozzle pressure ratio effects on surface pressure coefficients, A8 = 200 in.^{2}, M = 0.6 (SS).

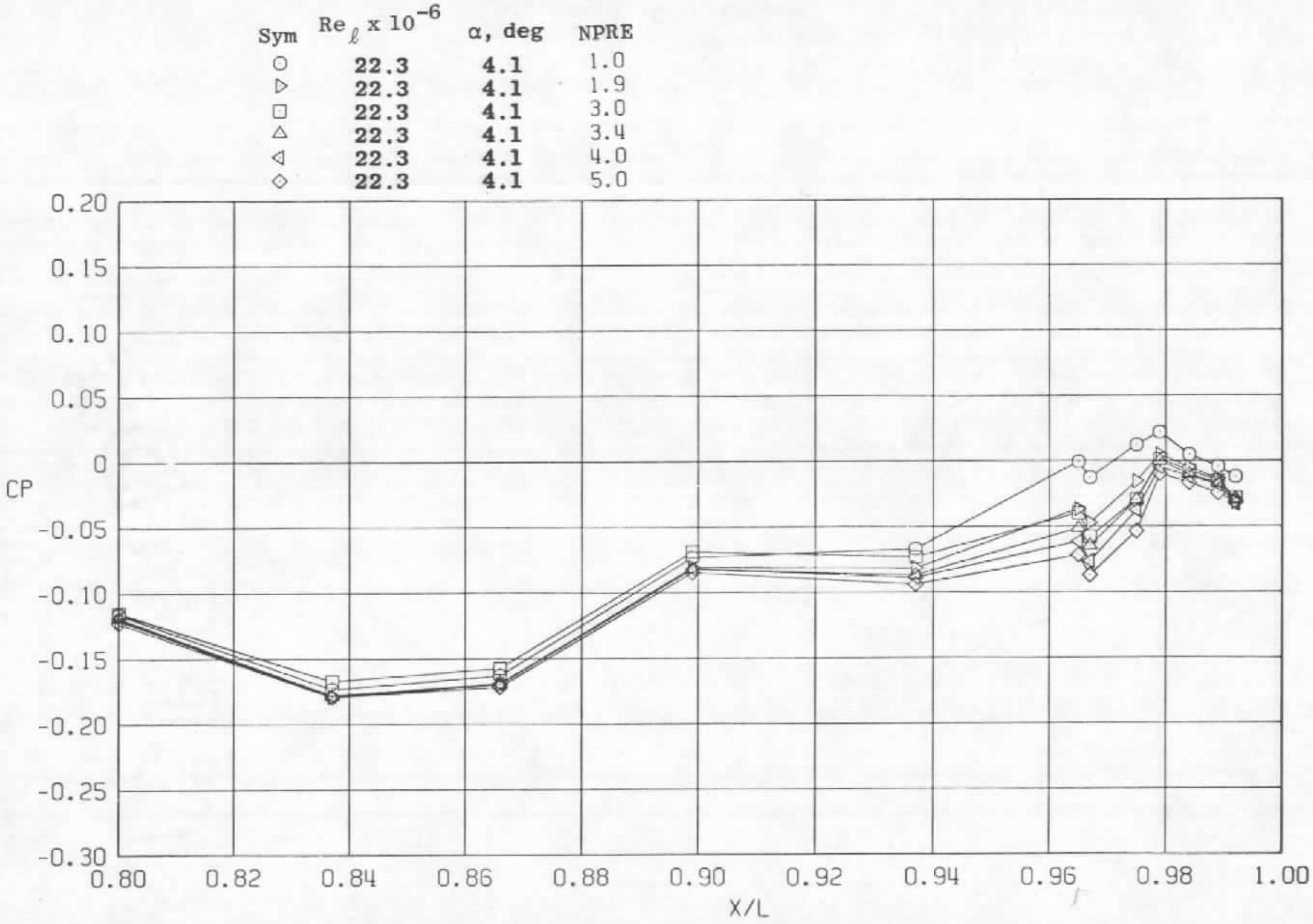

b. ϕ = 45 deg
Figure 14. Continued.

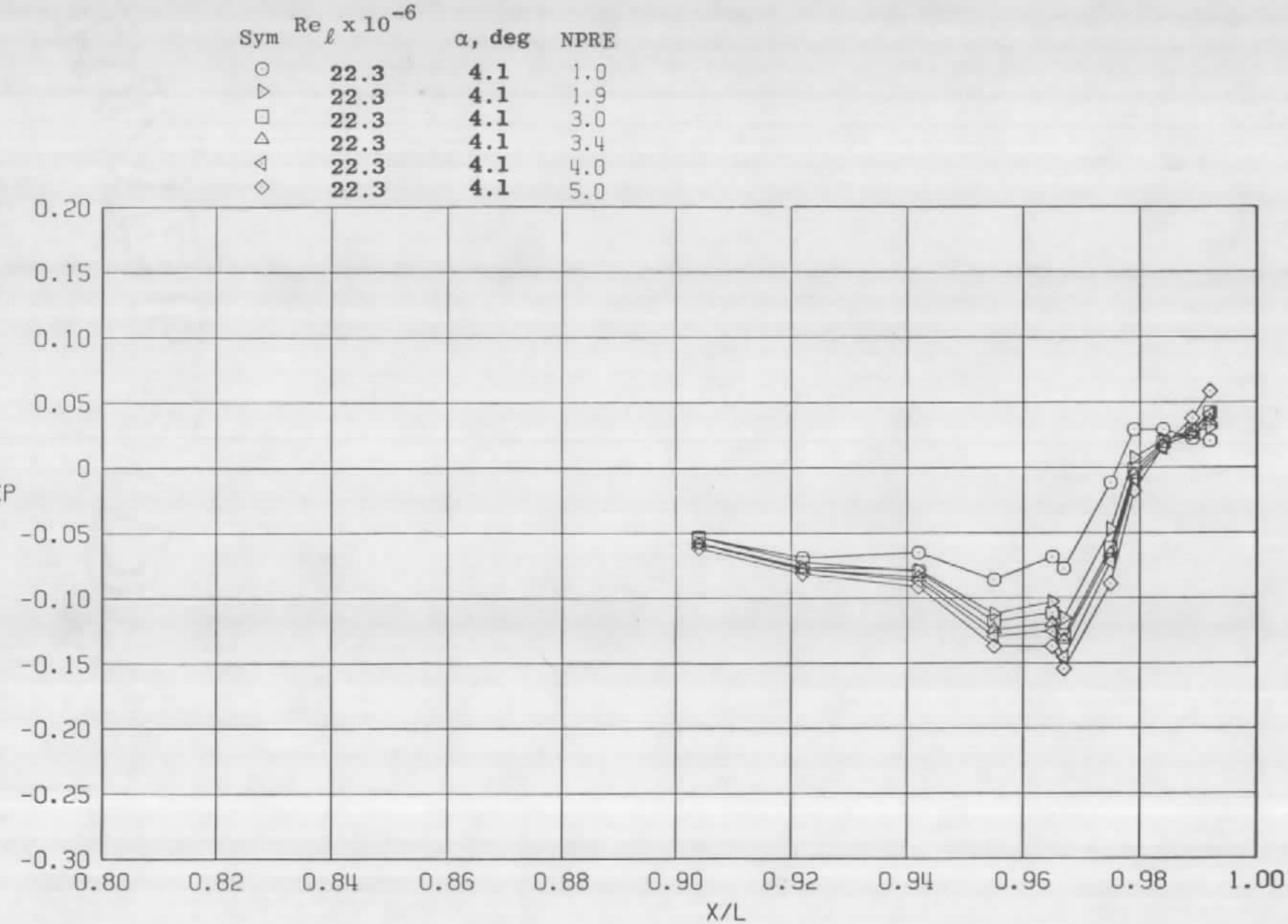

c. ϕ = 135 deg
Figure 14. Continued.

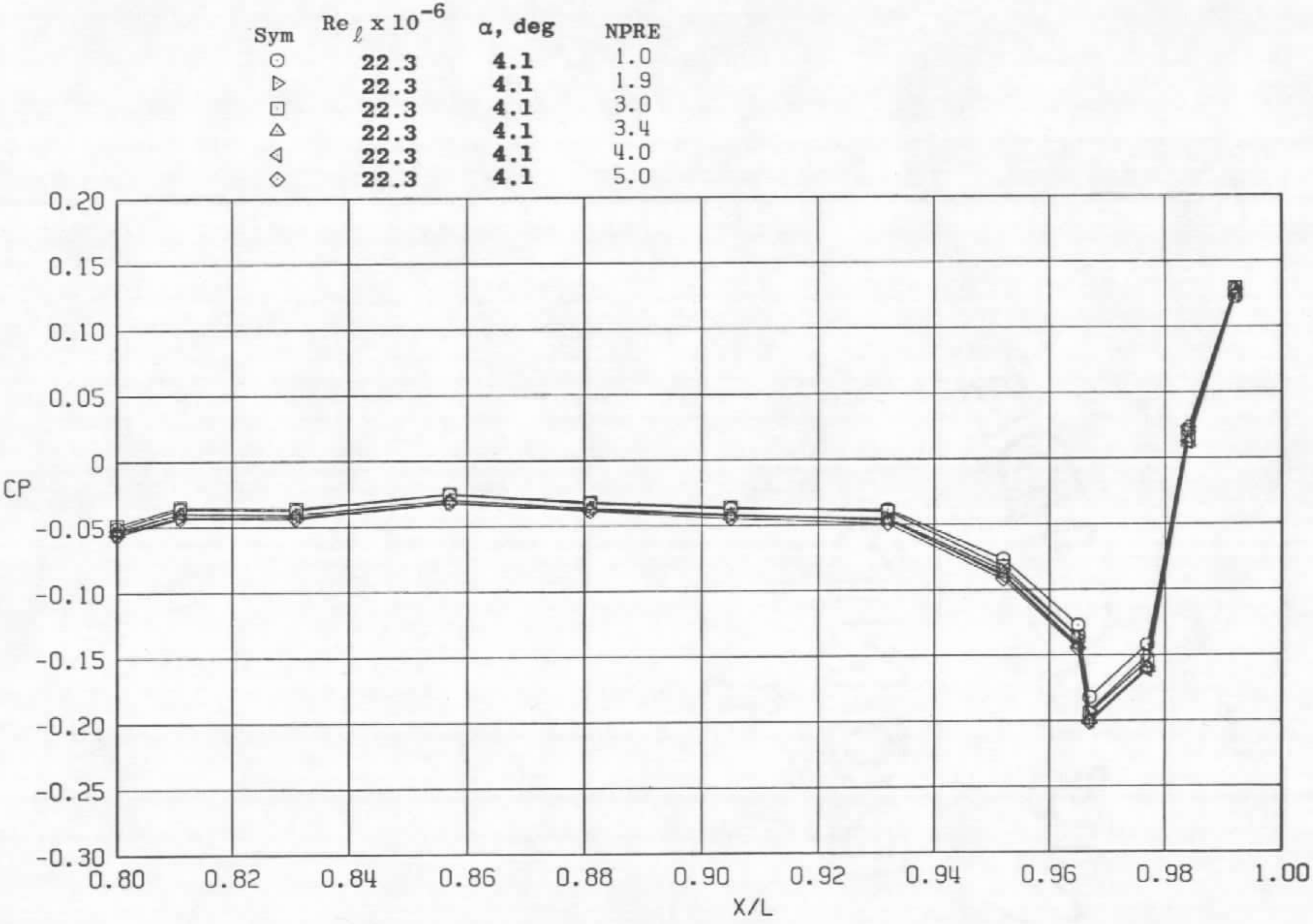

d. ϕ = 180 deg

Figure 14. Continued.

e. ϕ = 225 deg
Figure 14. Continued.

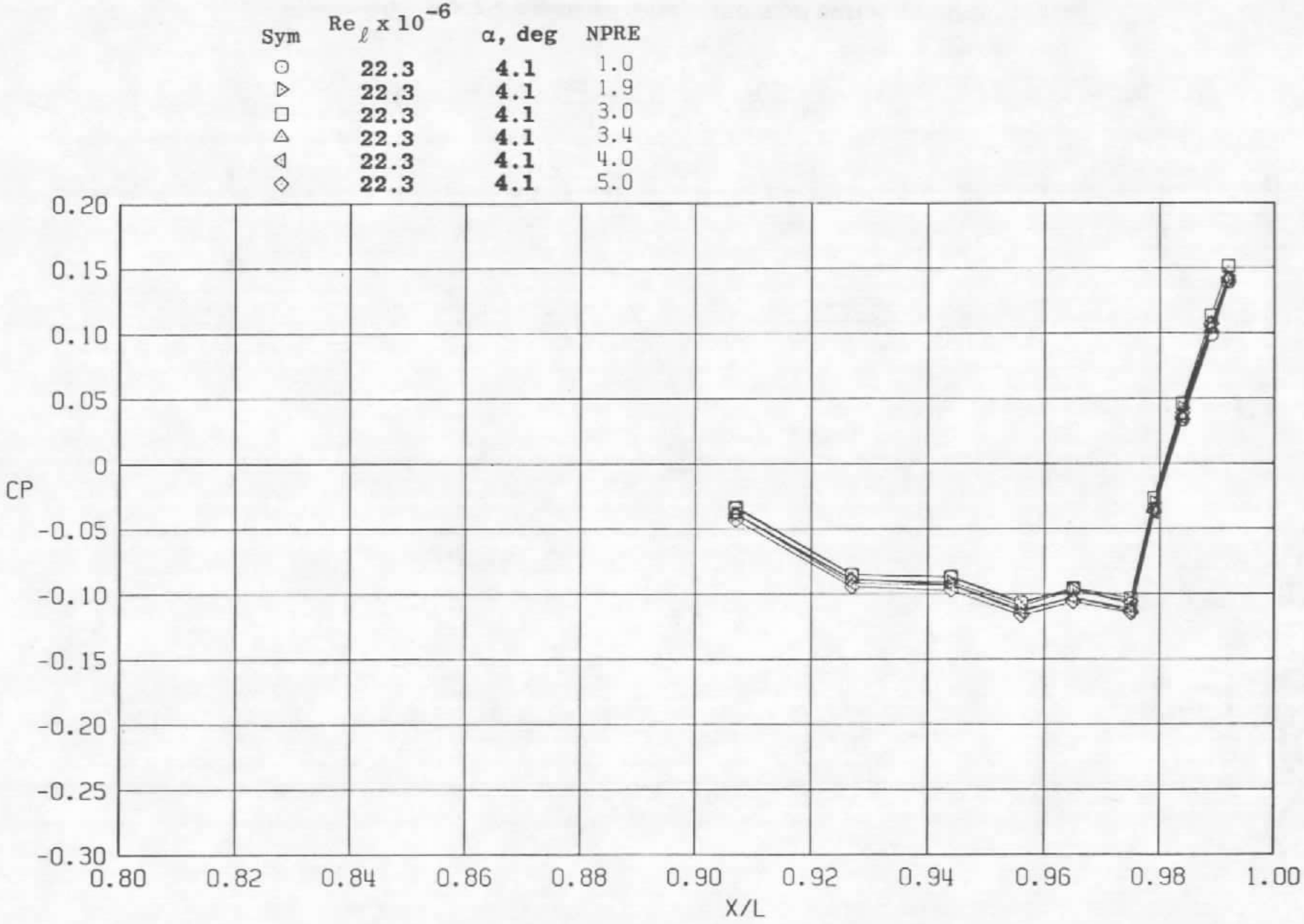

f. ϕ = 315 deg
Figure 14. Concluded.

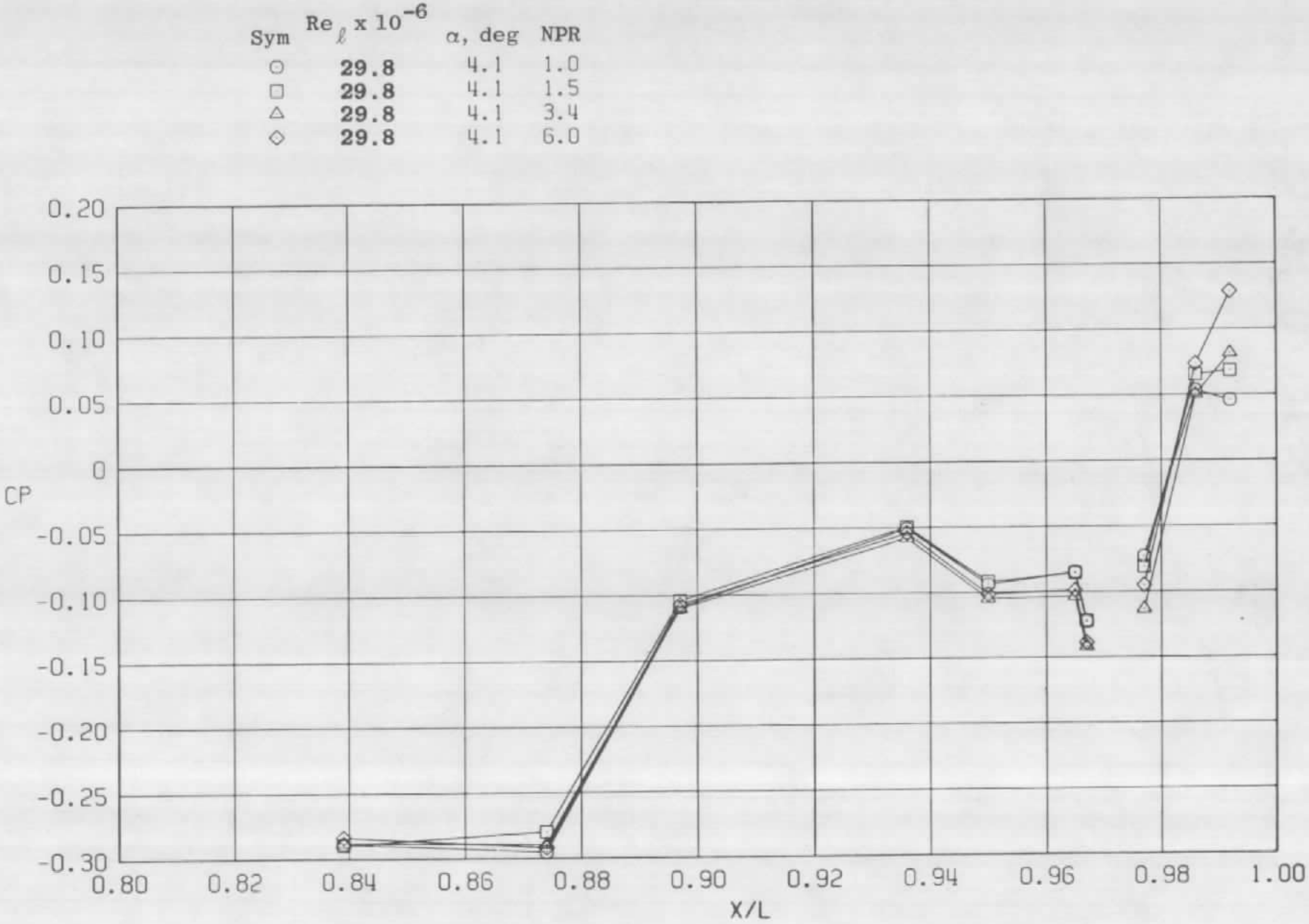

a. $\phi = 0$

Figure 15. Nozzle pressure ratio effects on surface pressure coefficients, A8 = 200 in.², M = 0.9 (WT).

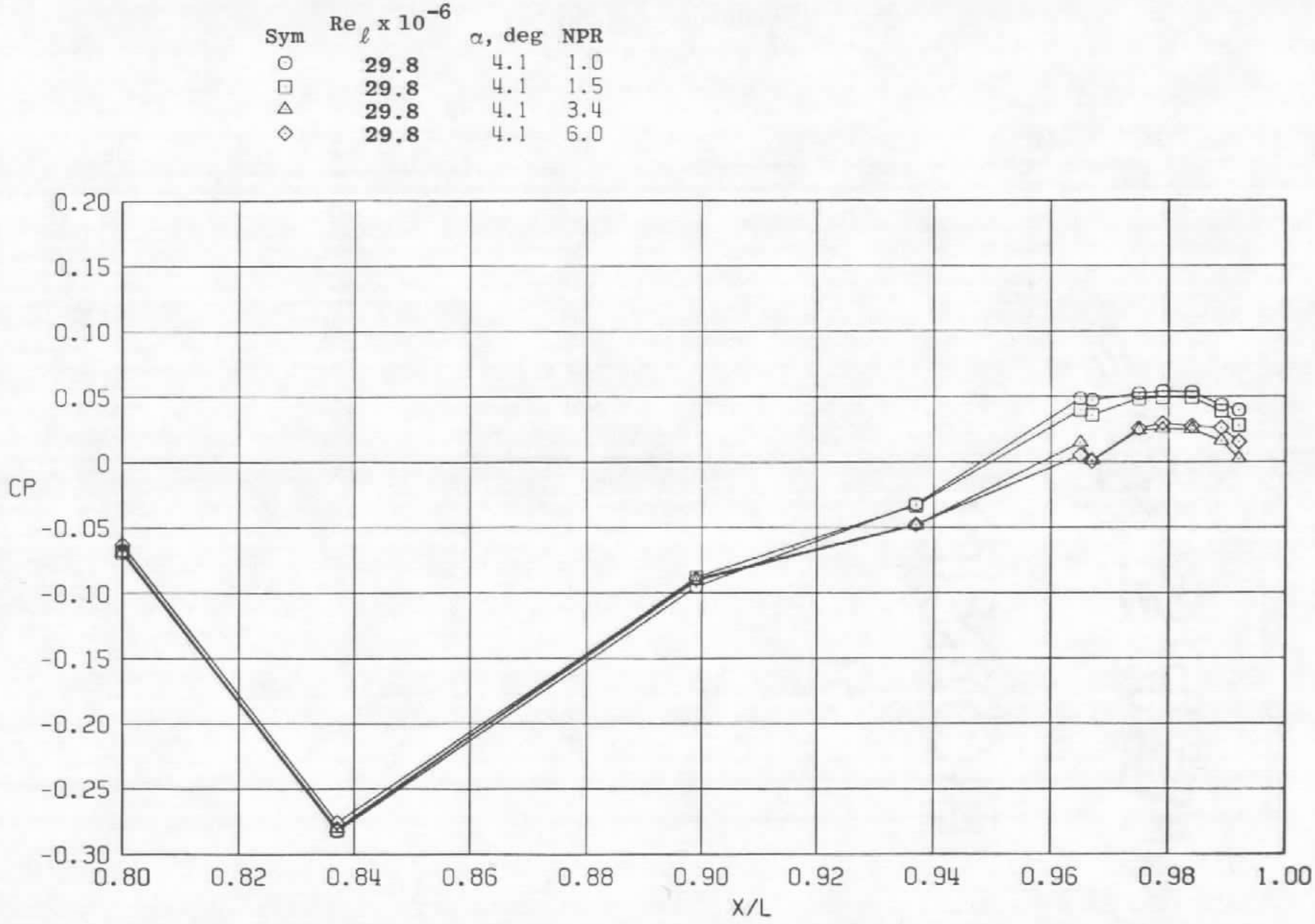

b. ϕ = 45 deg
Figure 15. Continued.

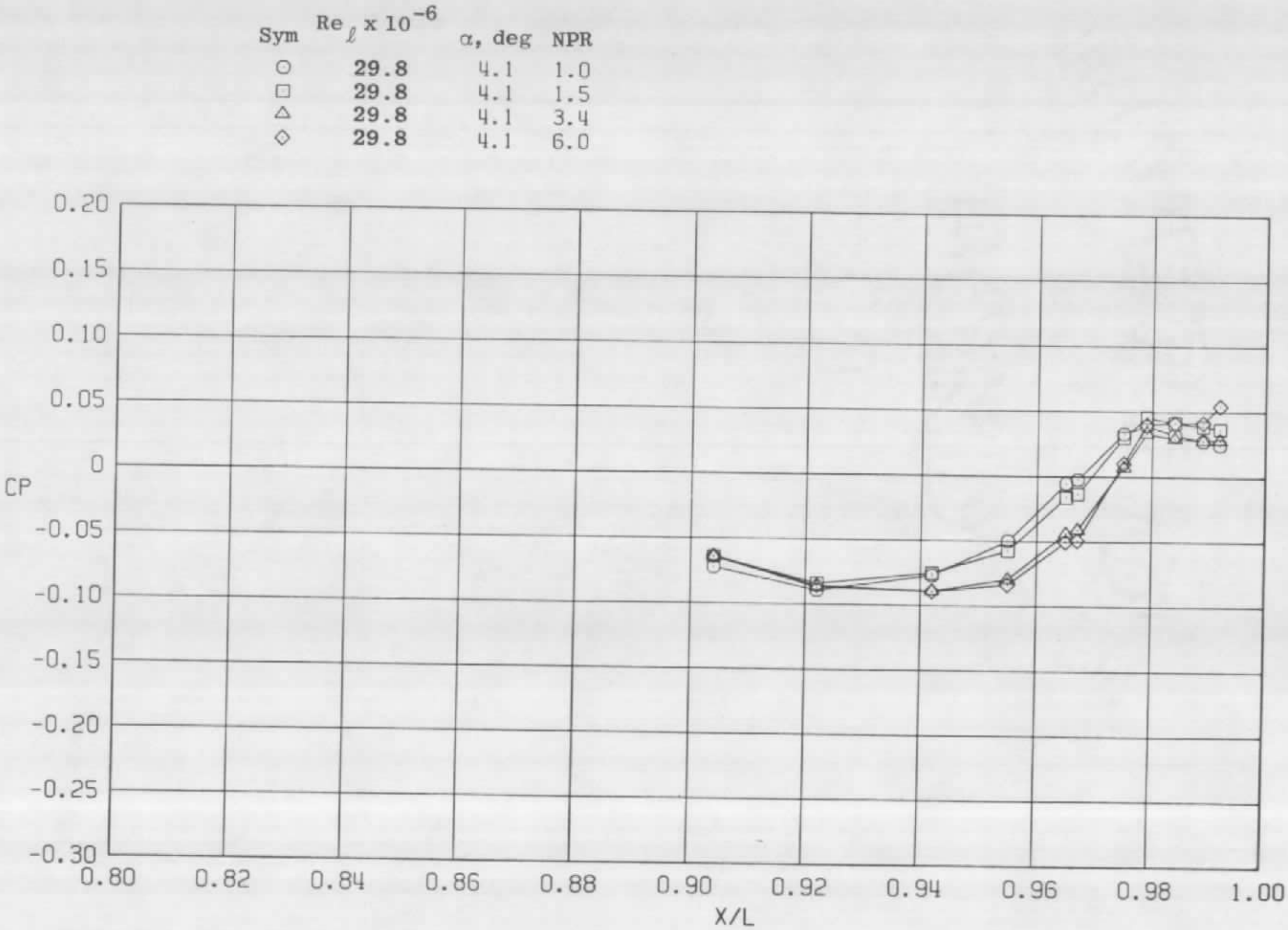

c. ϕ = 135 deg

Figure 15. Continued.

d. ϕ = 180 deg
Figure 15. Continued.

Sym	$Re_{\ell} \times 10^{-6}$	α, deg	NPR
○	29.8	4.1	1.0
□	29.8	4.1	1.5
△	29.8	4.1	3.4
◇	29.8	4.1	6.0

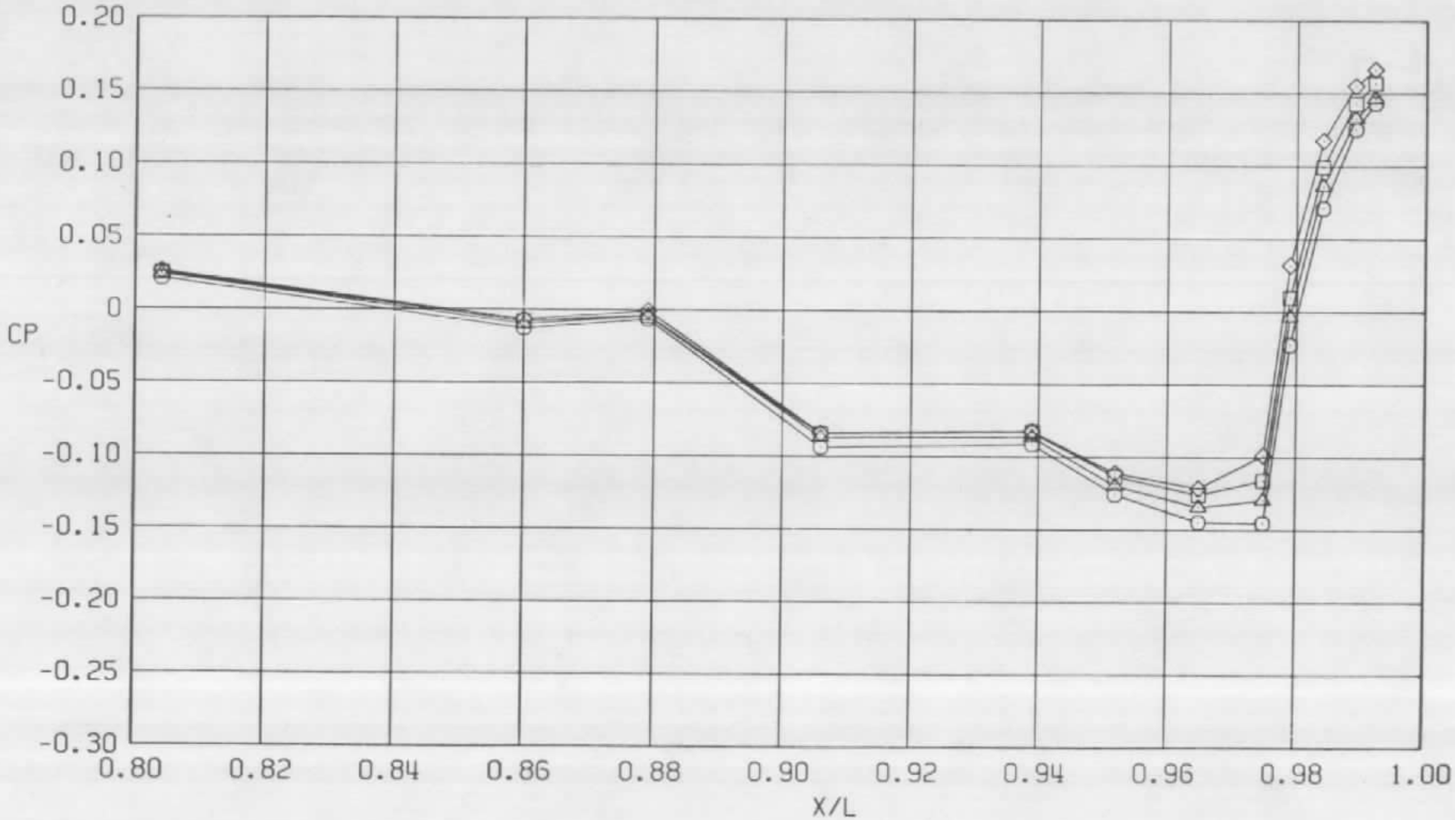

e. ϕ = 225 deg
Figure 15. Continued.

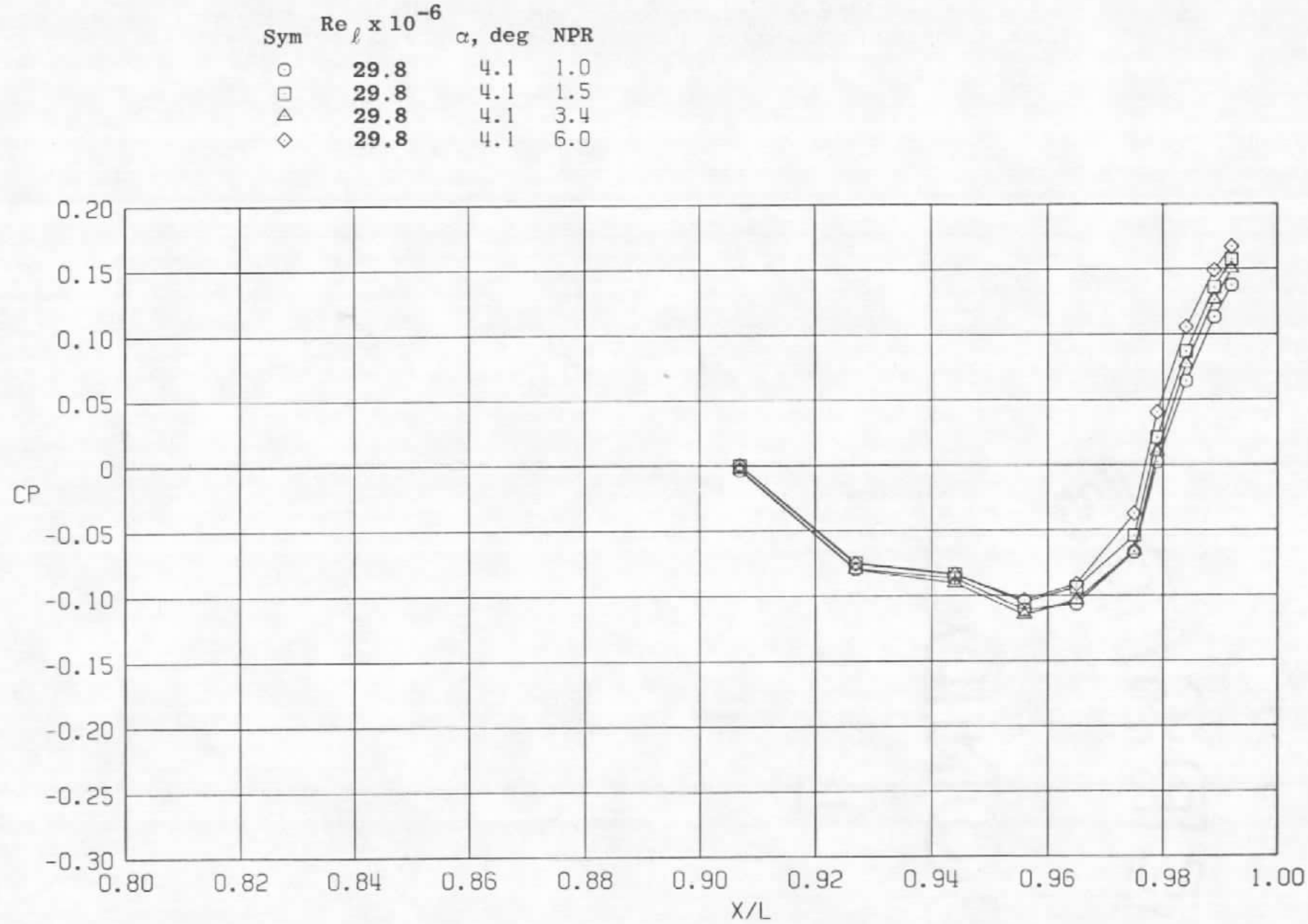

f. ϕ = 315 deg
Figure 15. Concluded.

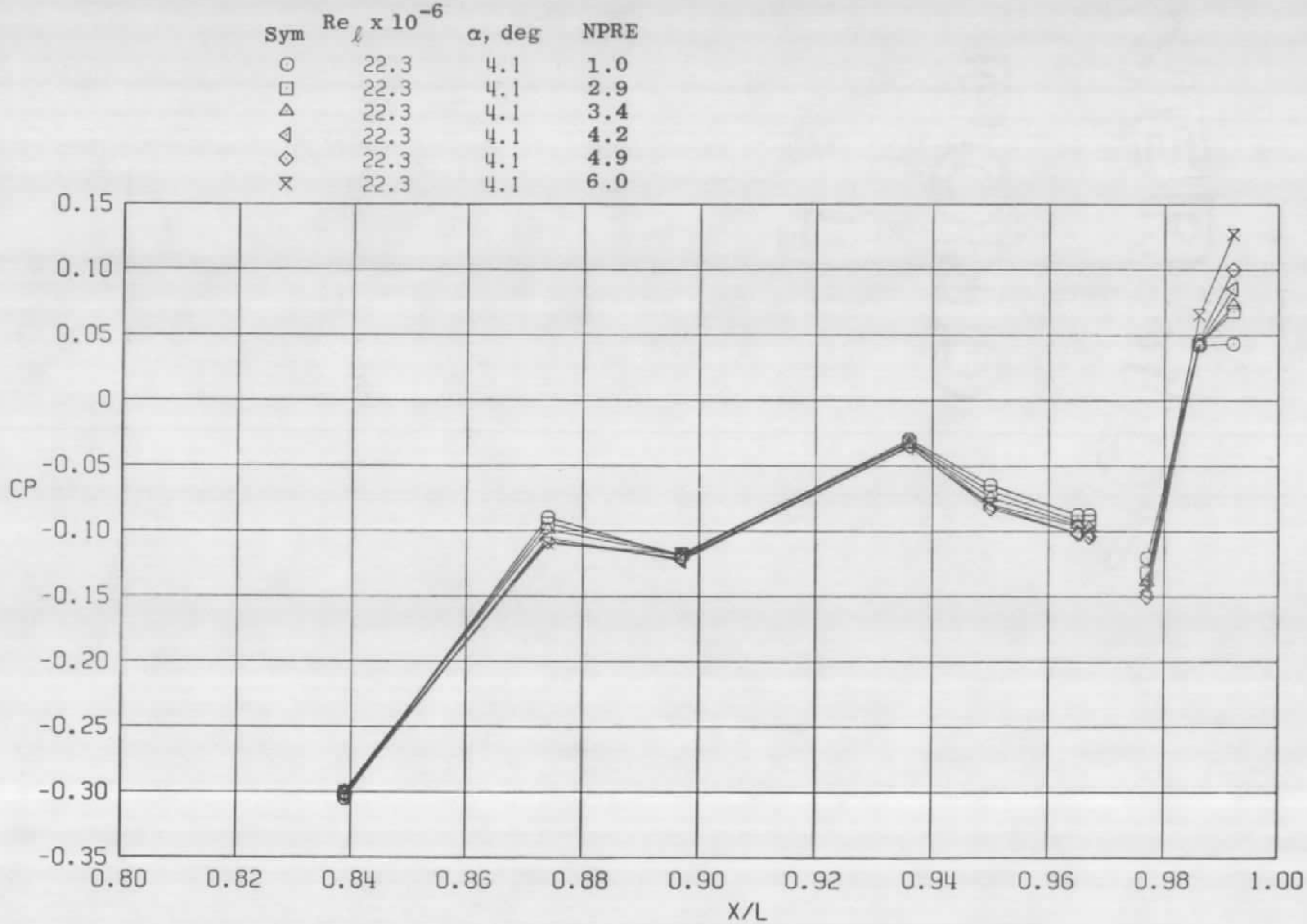

a. $\phi = 0$

Figure 16. Effective nozzle pressure ratio effects on surface pressure coefficients, A8 = 200 in.^{2}, M = 0.9 (SS).

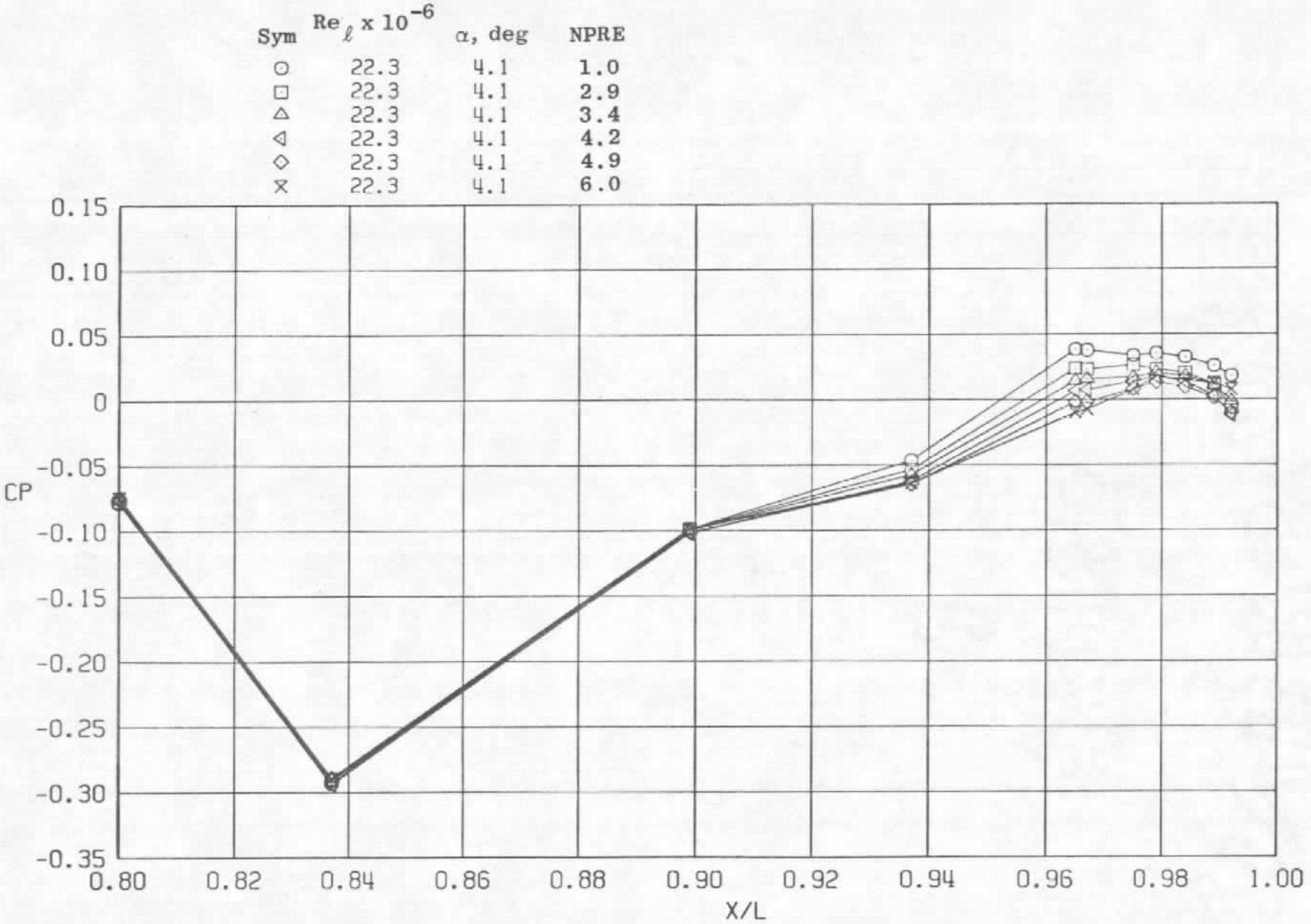

b. ϕ = 45 deg
Figure 16. Continued.

Sym	$Re_{\ell} \times 10^{-6}$	α, deg	NPRE
⊙	22.3	4.1	1.0
□	22.3	4.1	2.9
△	22.3	4.1	3.4
◁	22.3	4.1	4.2
◇	22.3	4.1	4.9
⌅	22.3	4.1	6.0

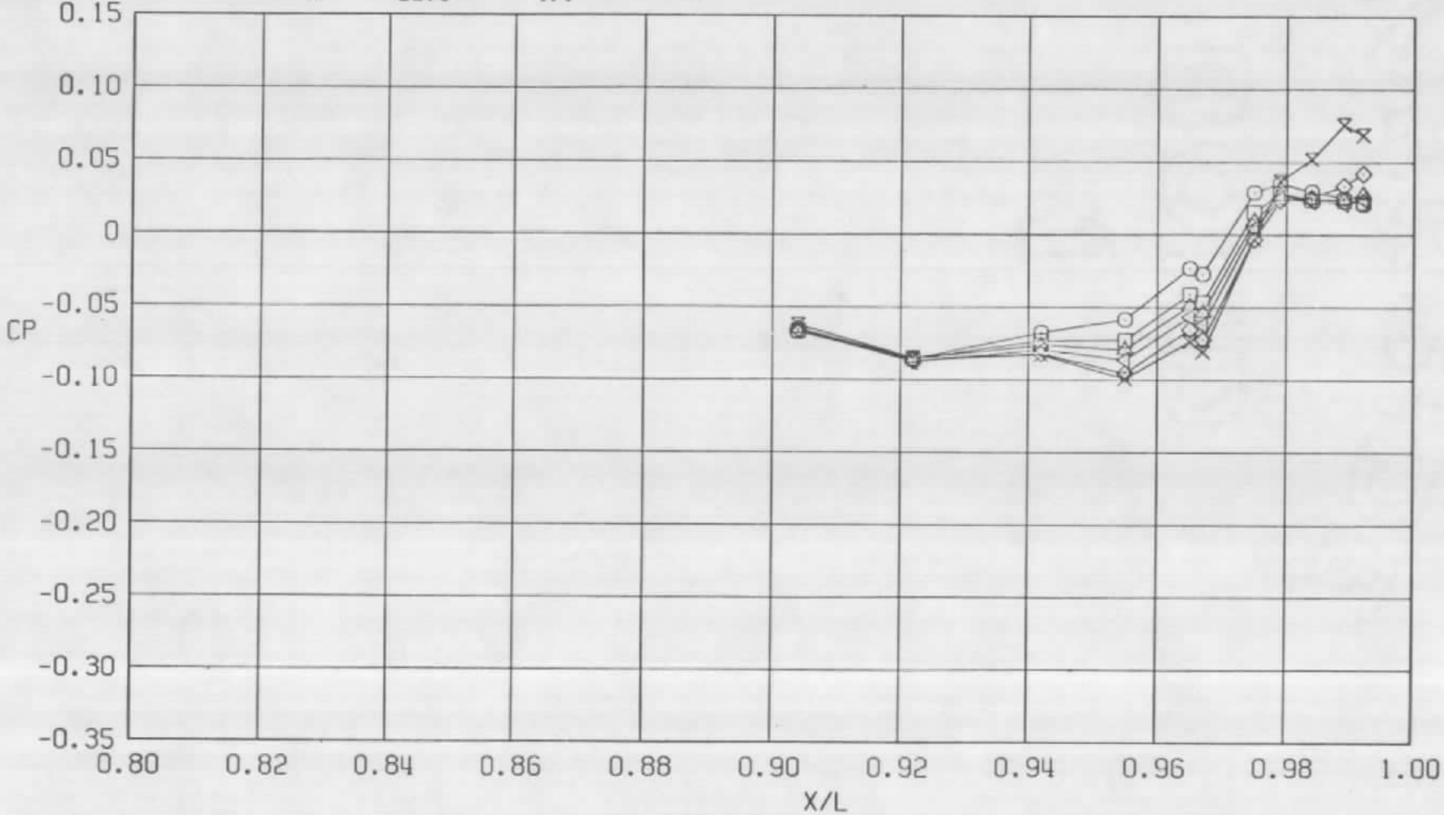

c. ϕ = 135 deg
Figure 16. Continued.

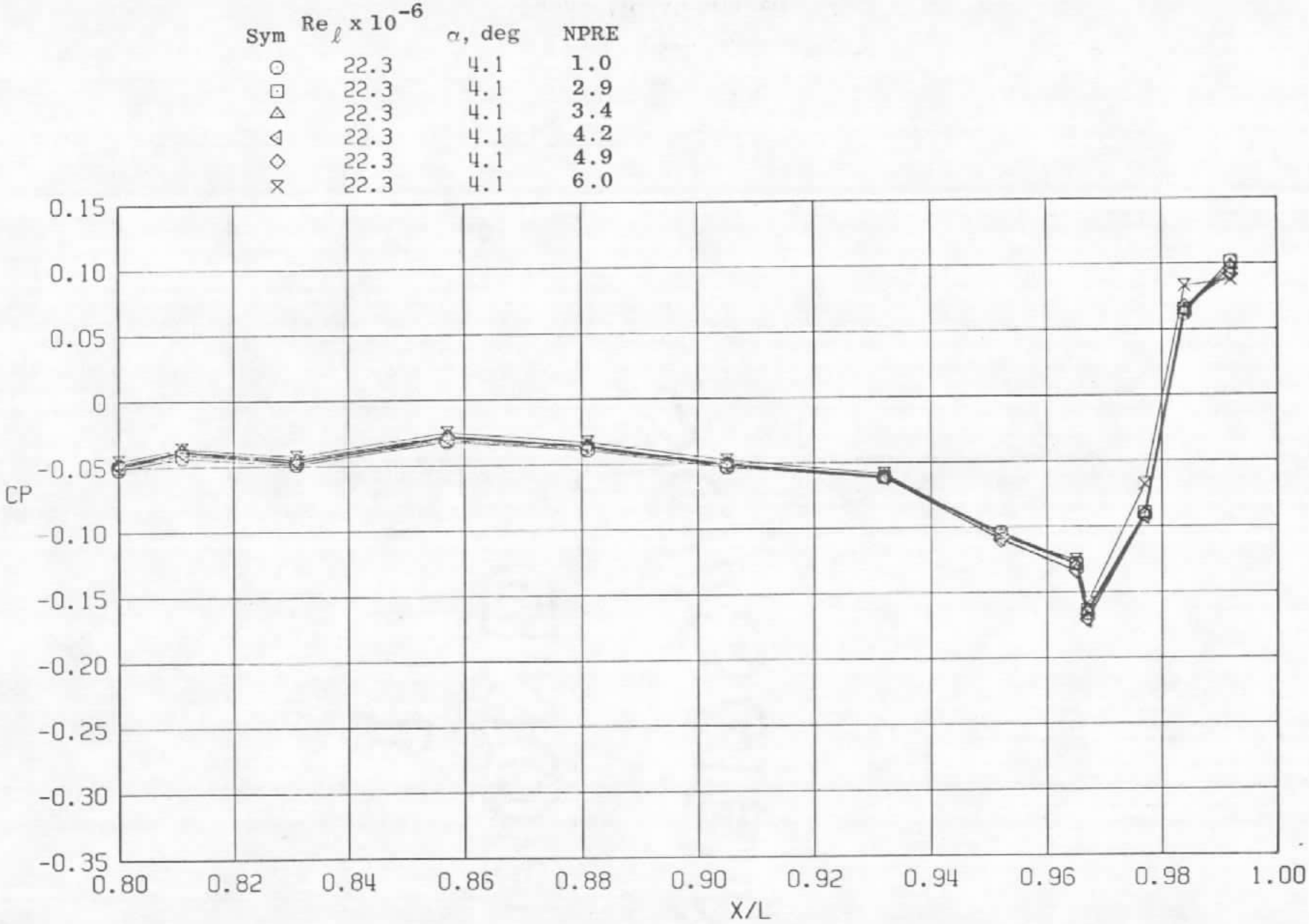

d. ϕ = 180 deg
Figure 16. Continued.

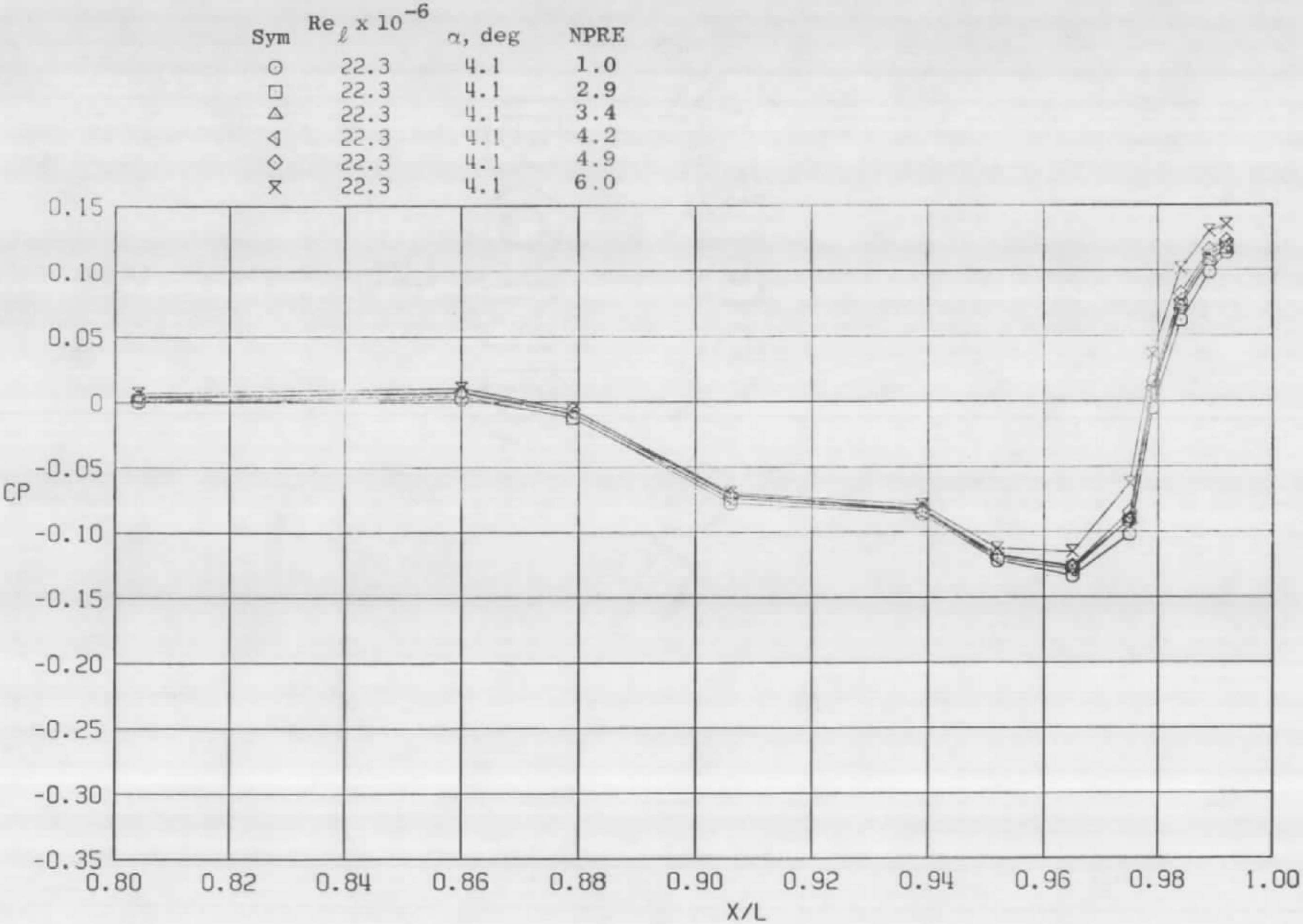

e. ϕ = 225 deg
Figure 16. Continued.

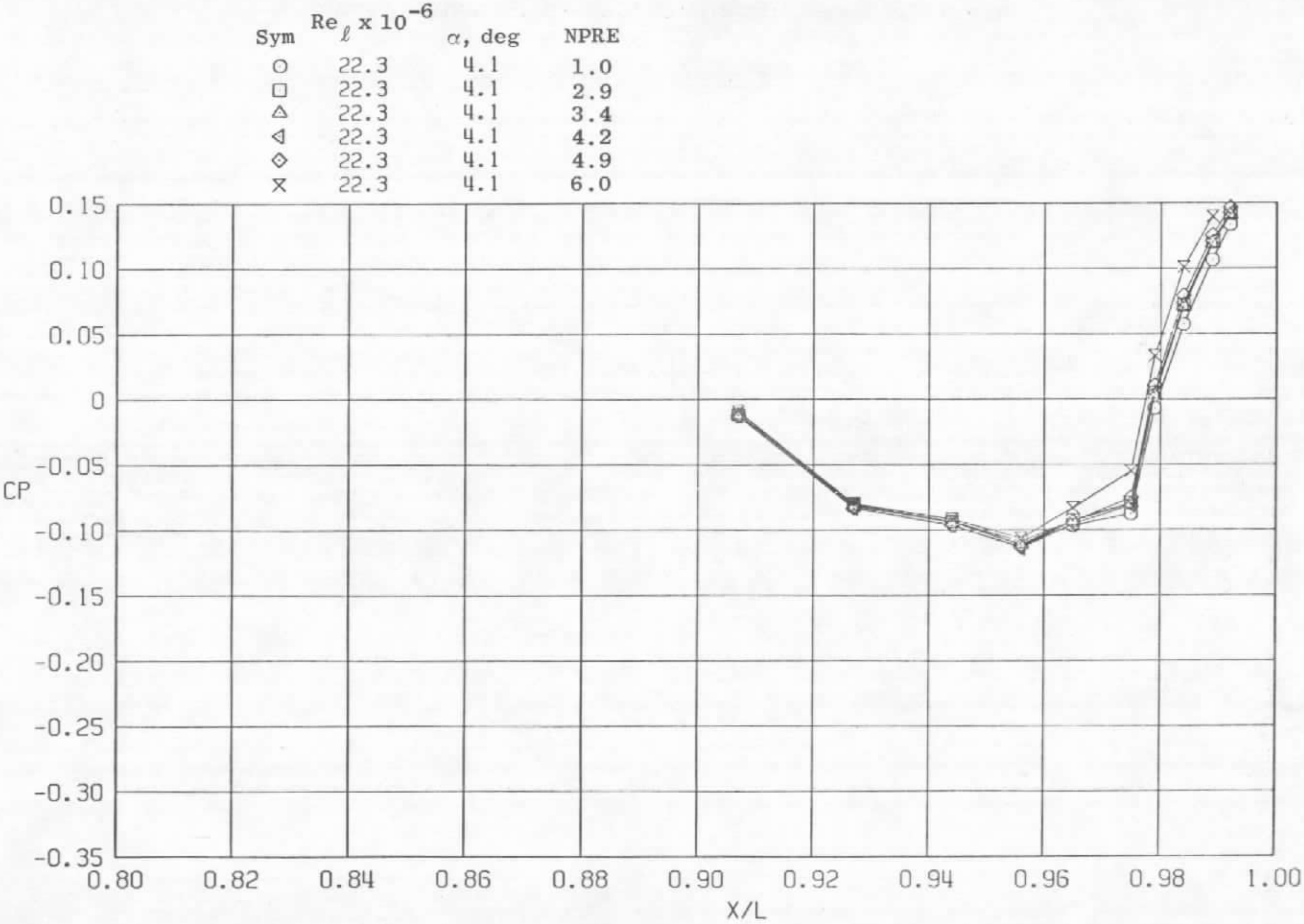

f. ϕ = 315 deg

Figure 16. Concluded.

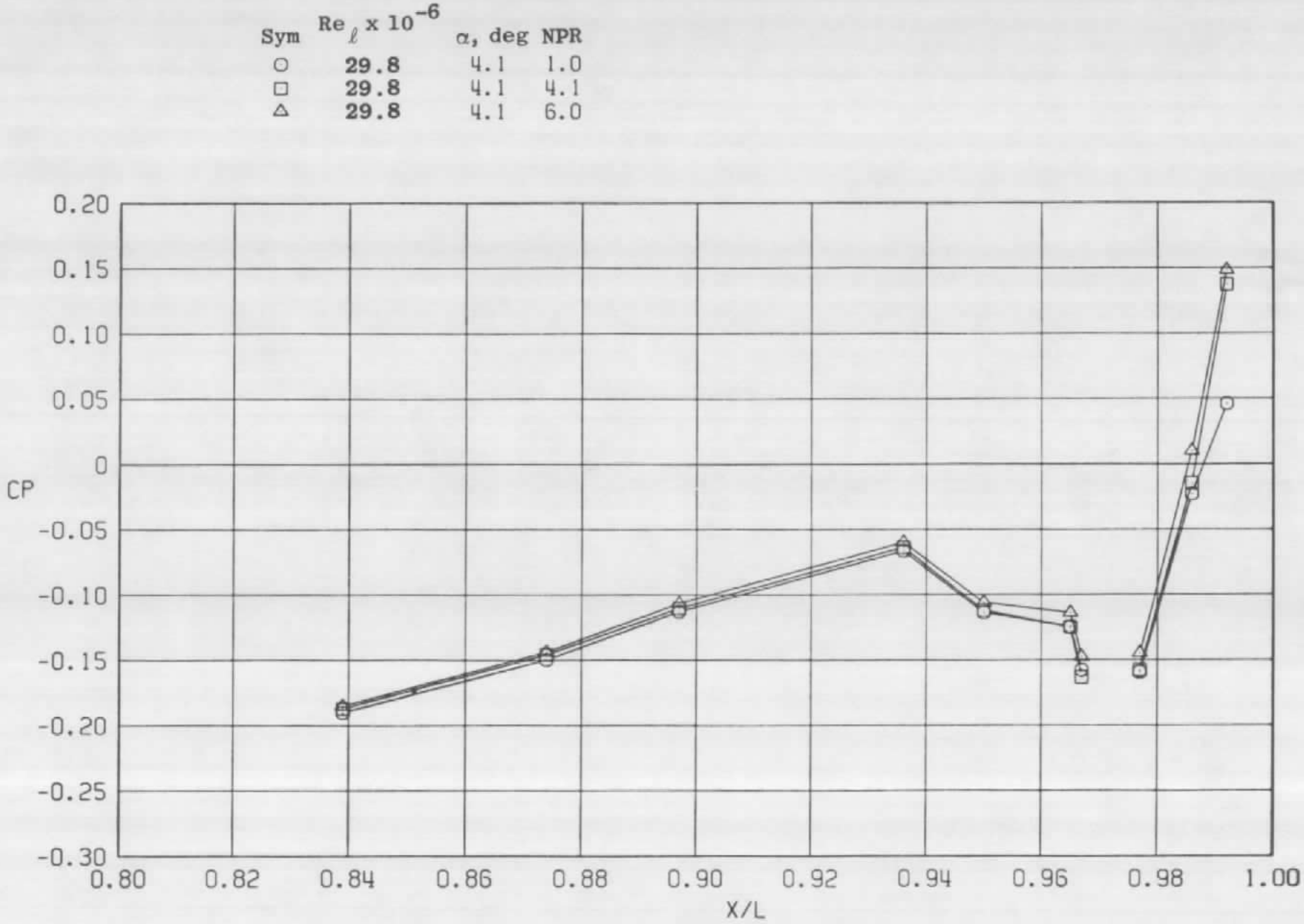

a. $\phi = 0$

Figure 17. Nozzle pressure ratio effects on surface pressure coefficients, A8 = 230 in.², M = 0.6 (WT).

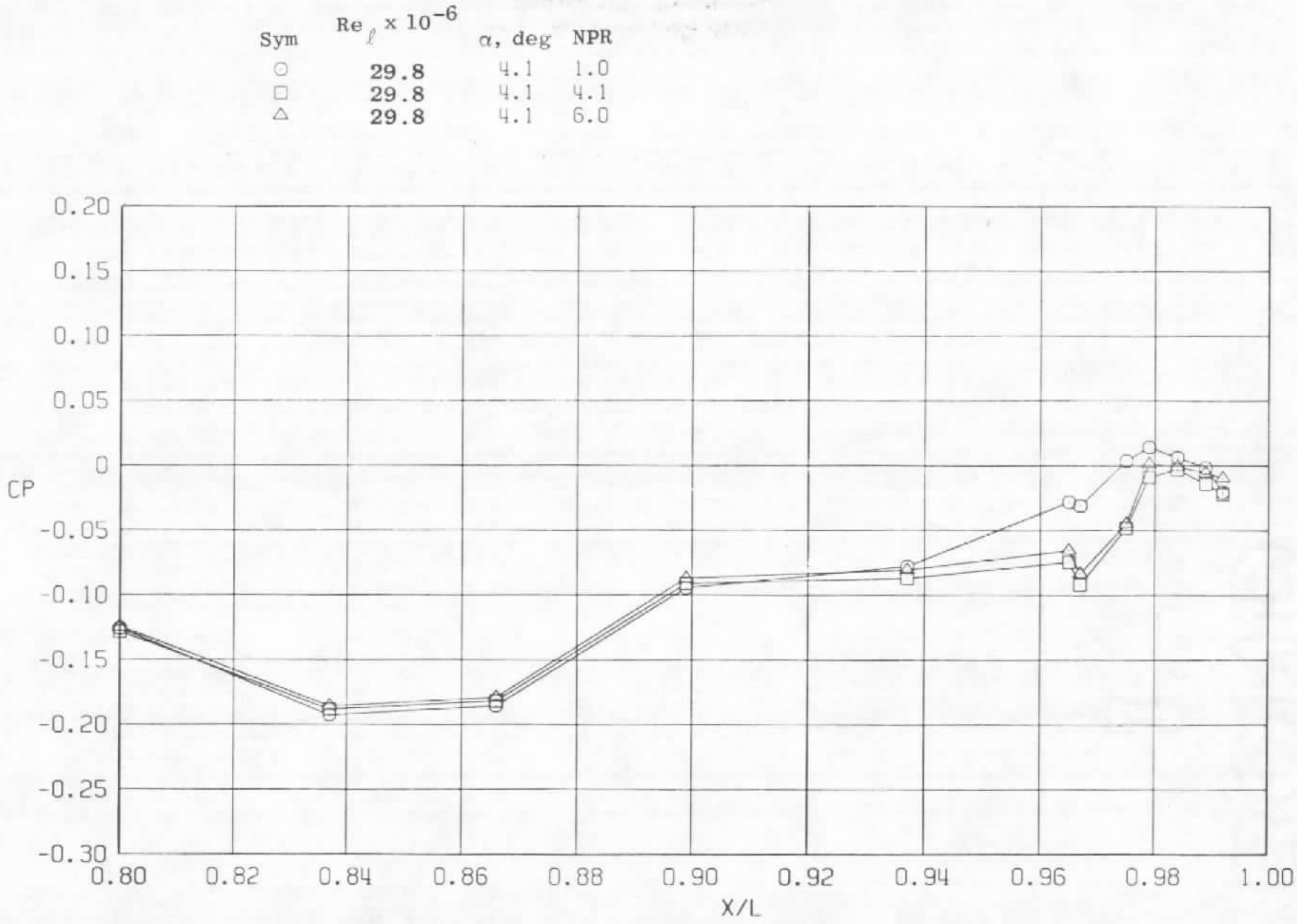

b. ϕ = 45 deg
Figure 17. Continued.

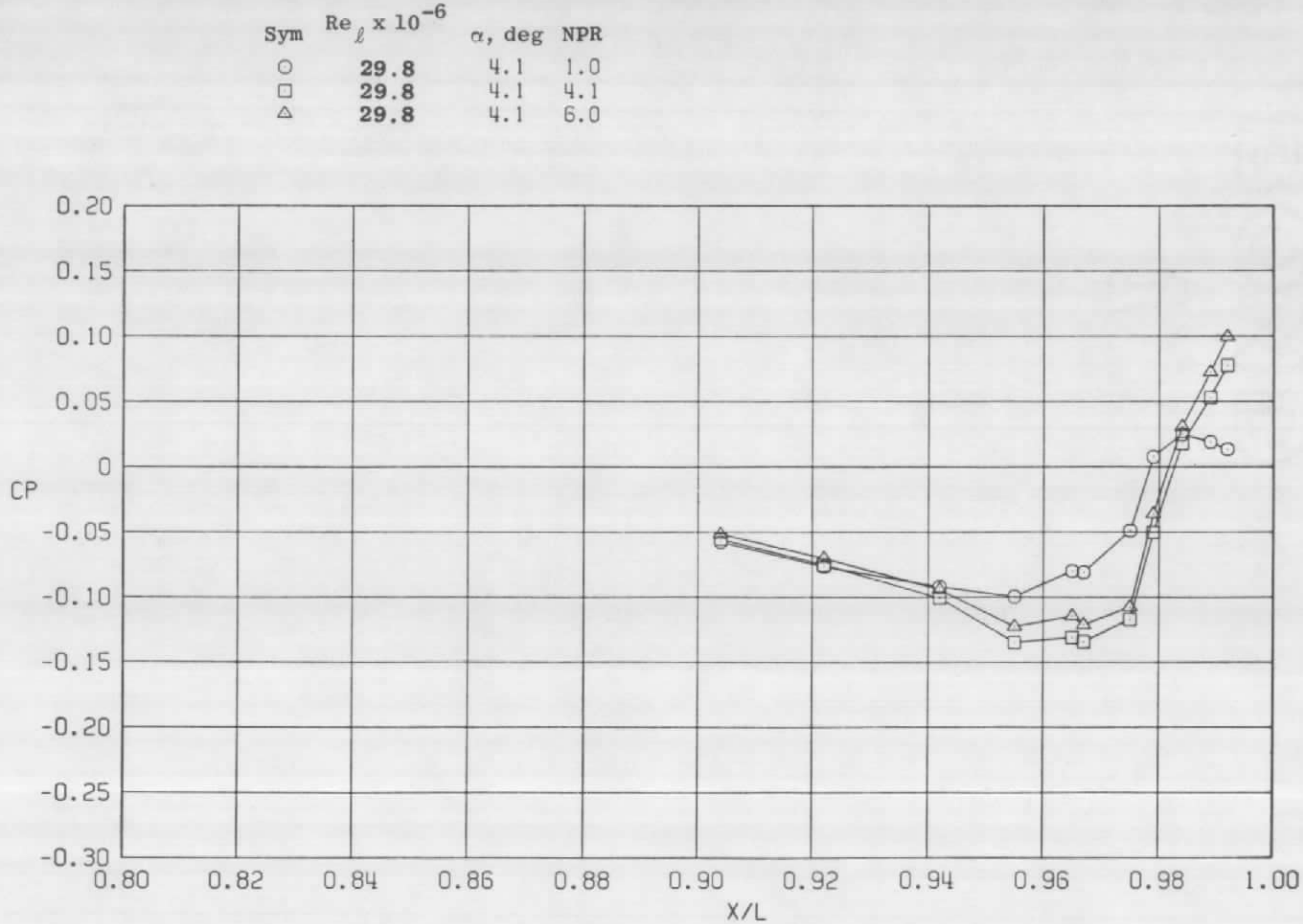

c. ϕ = 135 deg
Figure 17. Continued.

d. ϕ = 180 deg
Figure 17. Continued.

e. ϕ = 225 deg
Figure 17. Continued.

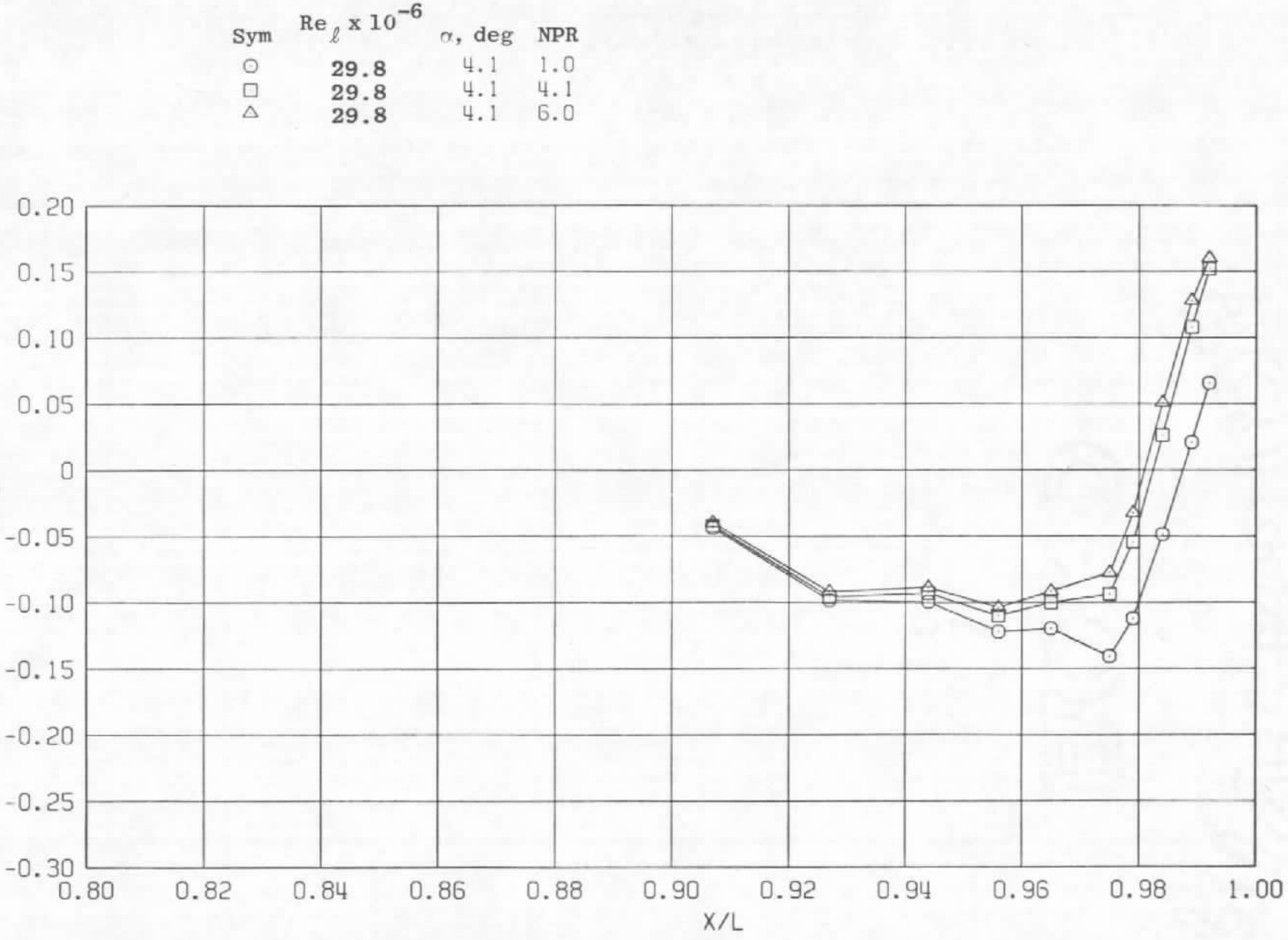

f. ϕ = 315 deg
Figure 17. Concluded.

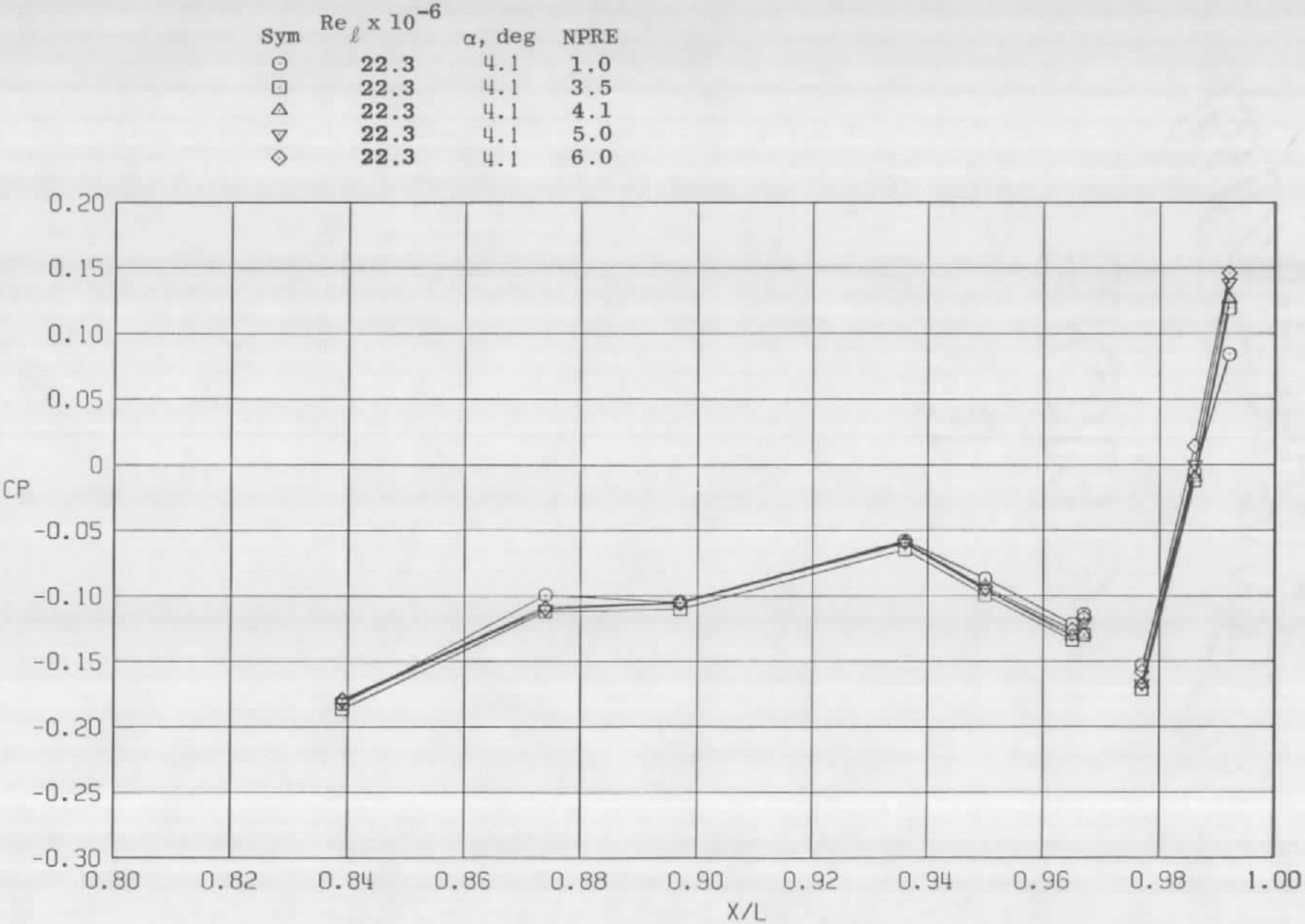

a. $\phi = 0$

Figure 18. Effective nozzle pressure ratio effects on surface pressure coefficients, A8 = 230 in.^{2}, M = 0.6 (SS).

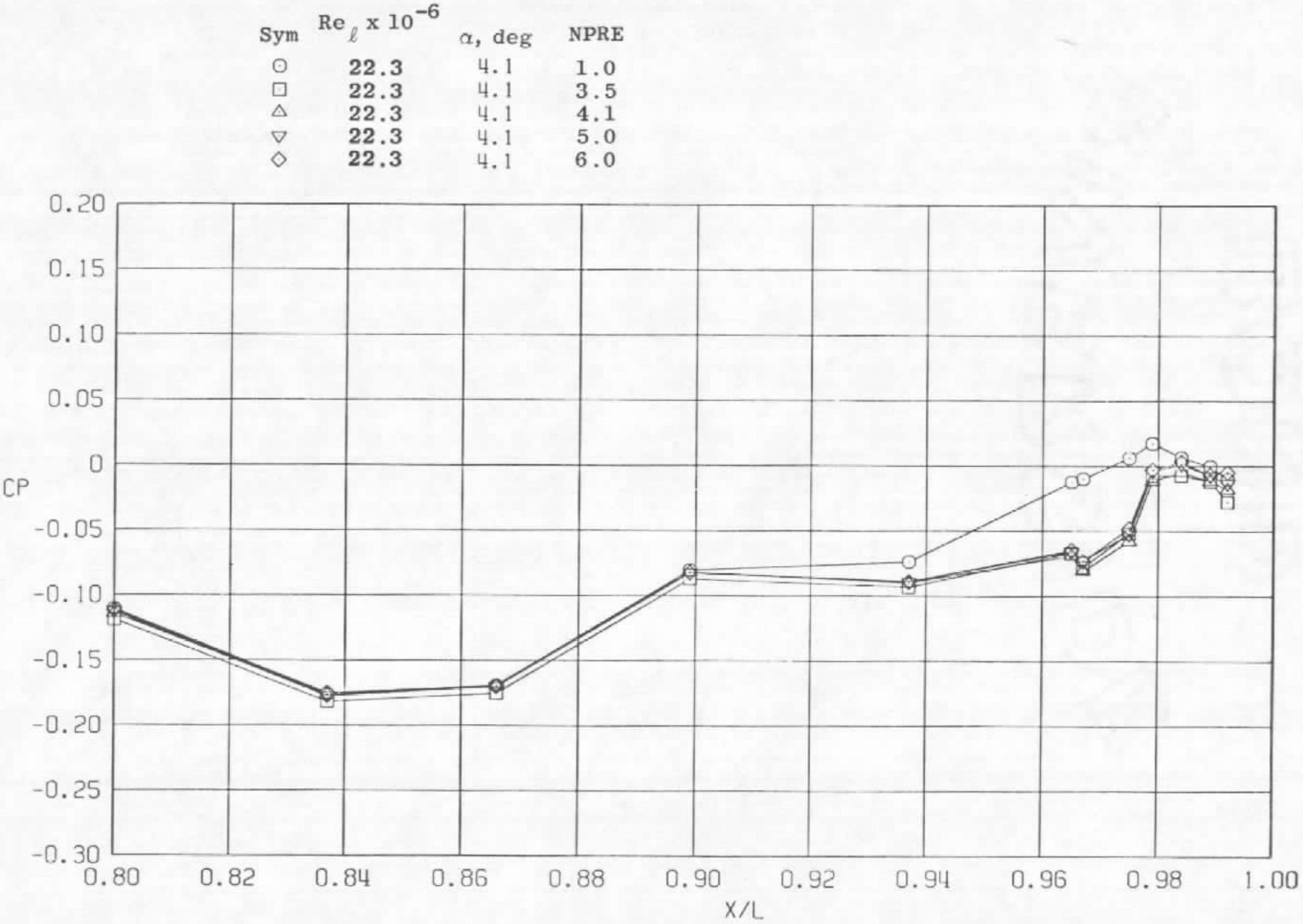

b. ϕ = 45 deg
Figure 18. Continued.

c. ϕ = 135 deg
Figure 18. Continued.

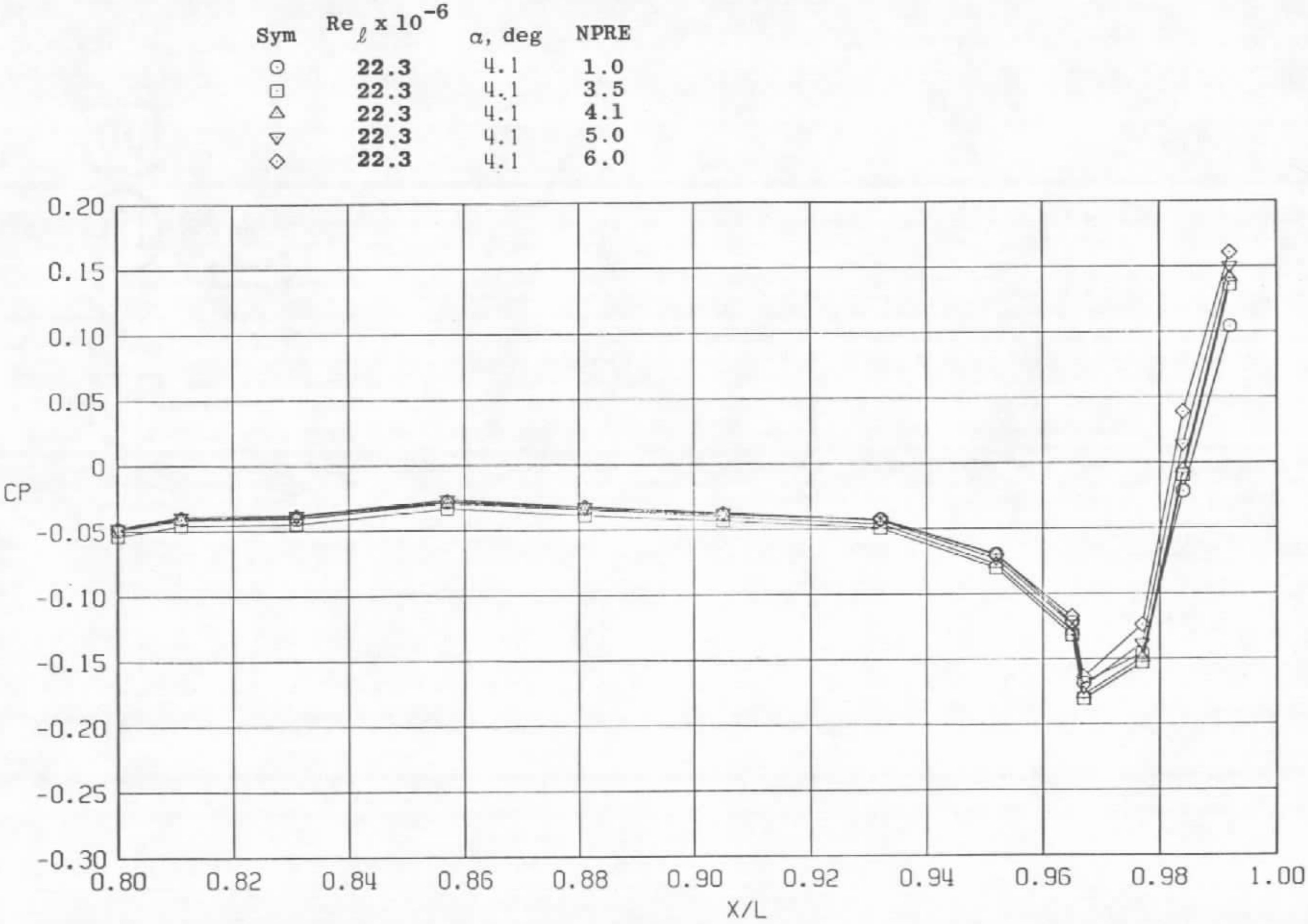

d. ϕ = 180 deg

Figure 18. Continued.

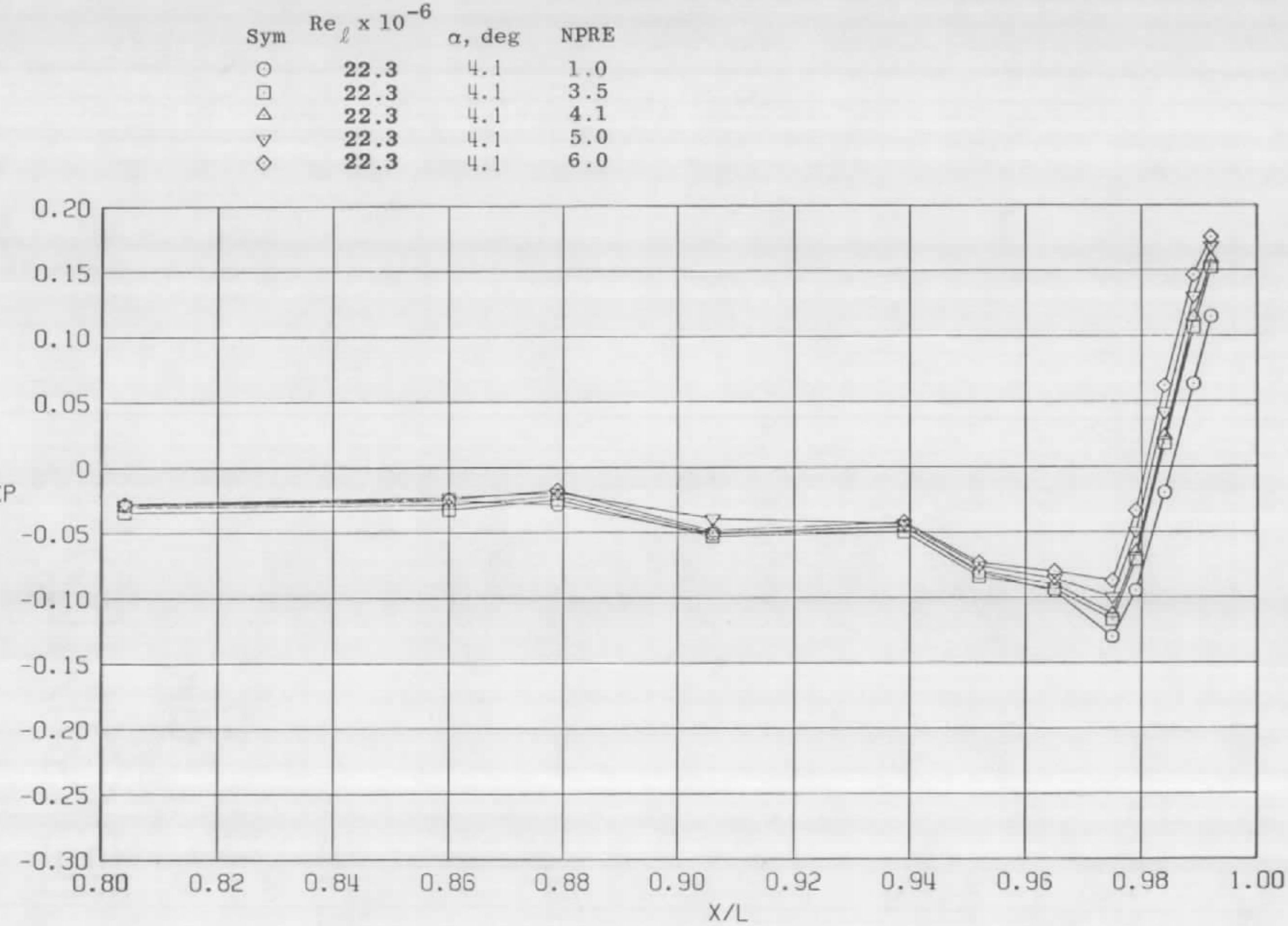

e. ϕ = 225 deg

Figure 18. Continued.

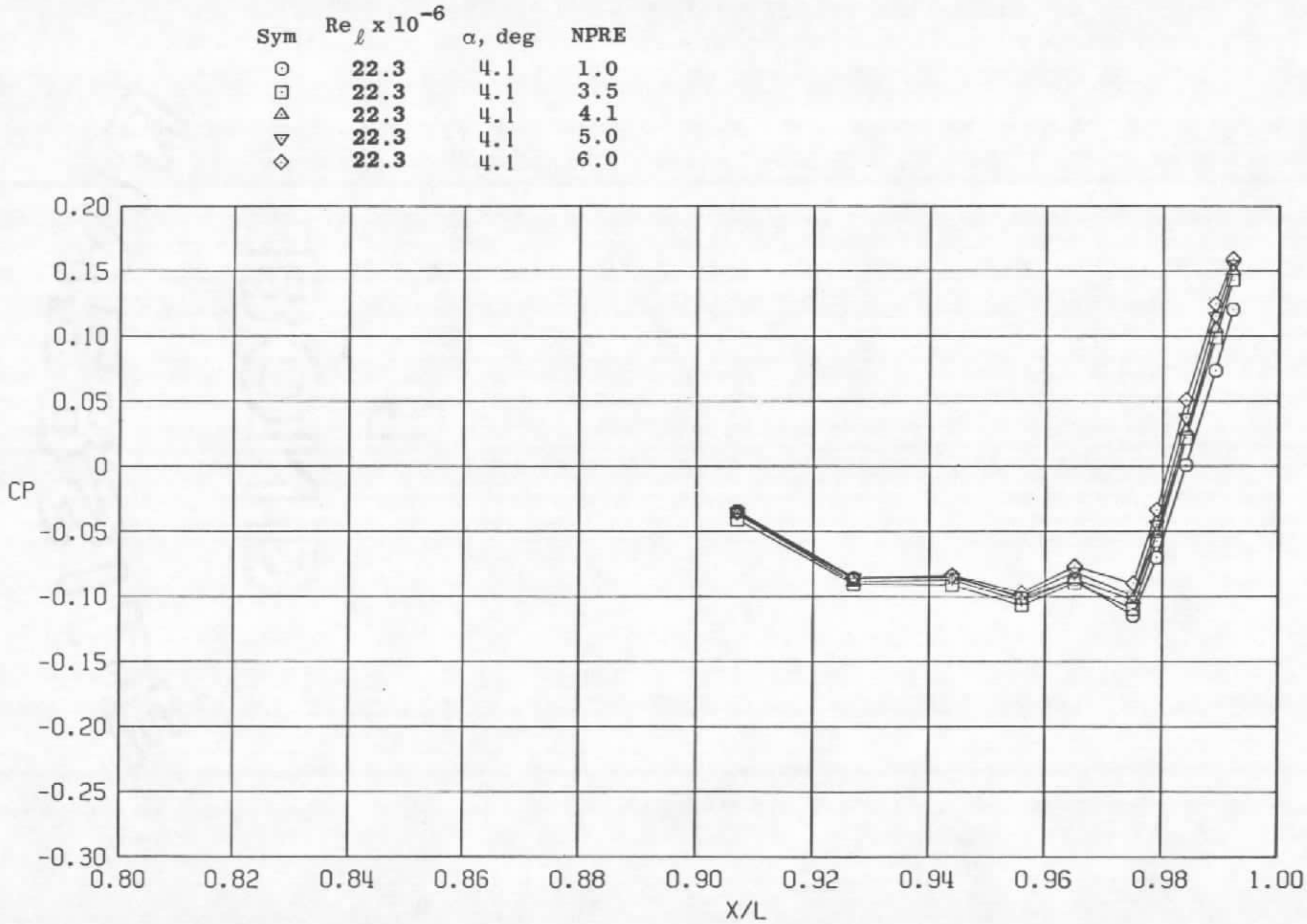

f. ϕ = 315 deg
Figure 18. Concluded.

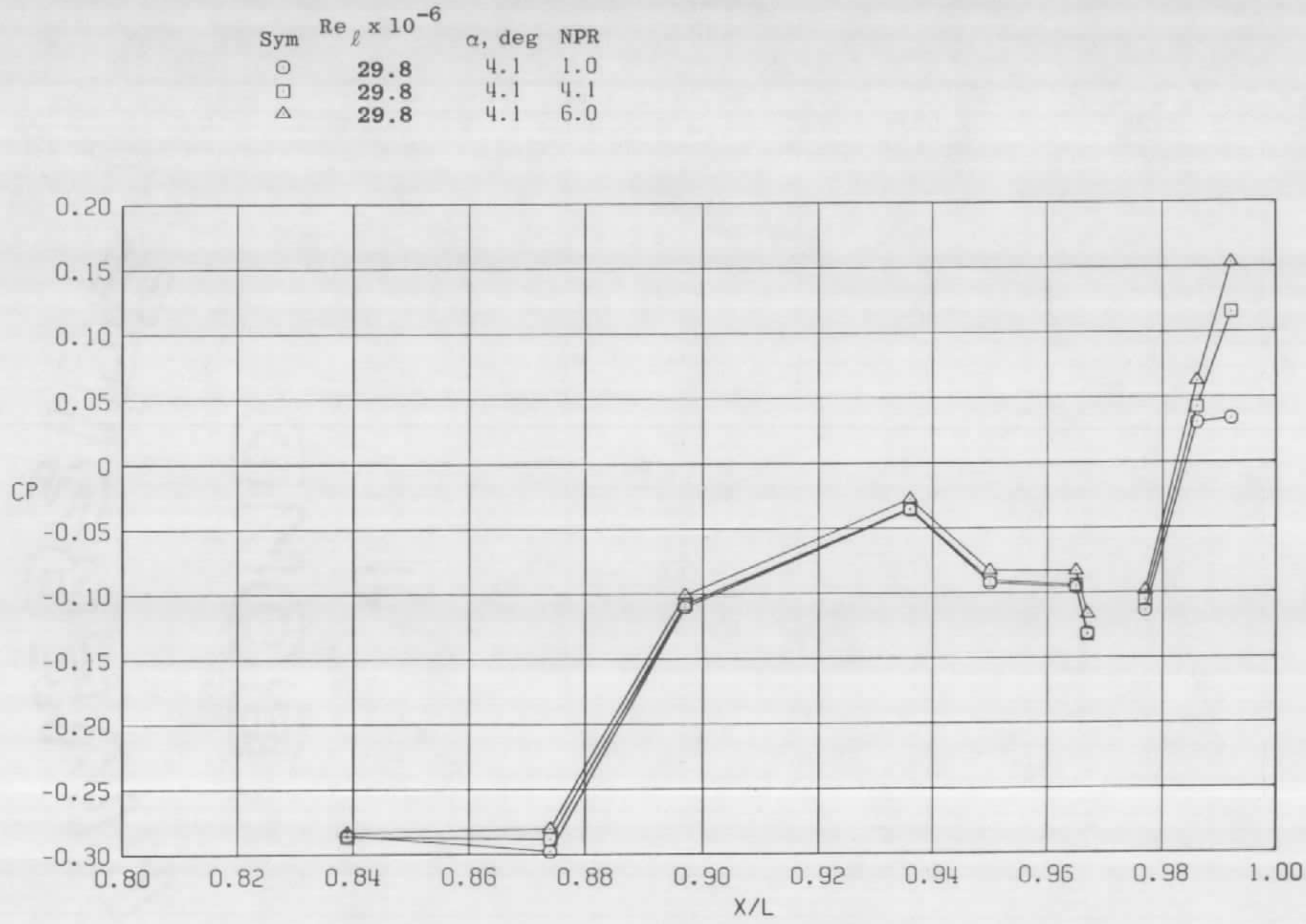

a. $\phi = 0$

Figure 19. Nozzle pressure ratio effects on surface pressure coefficients, A8 = 230 in.^{2}, M = 0.9 (WT).

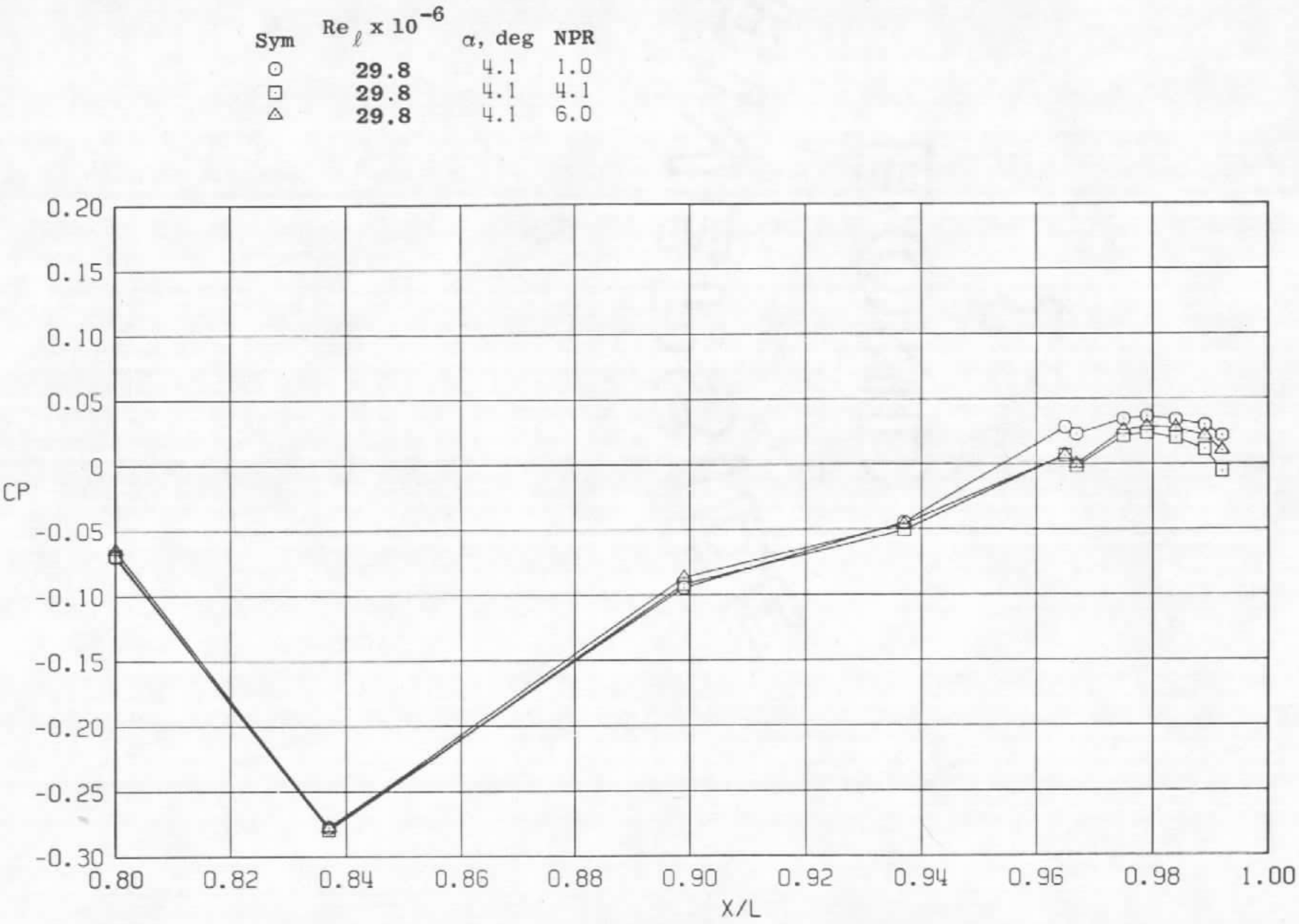

b. ϕ = 45 deg
Figure 19. Continued.

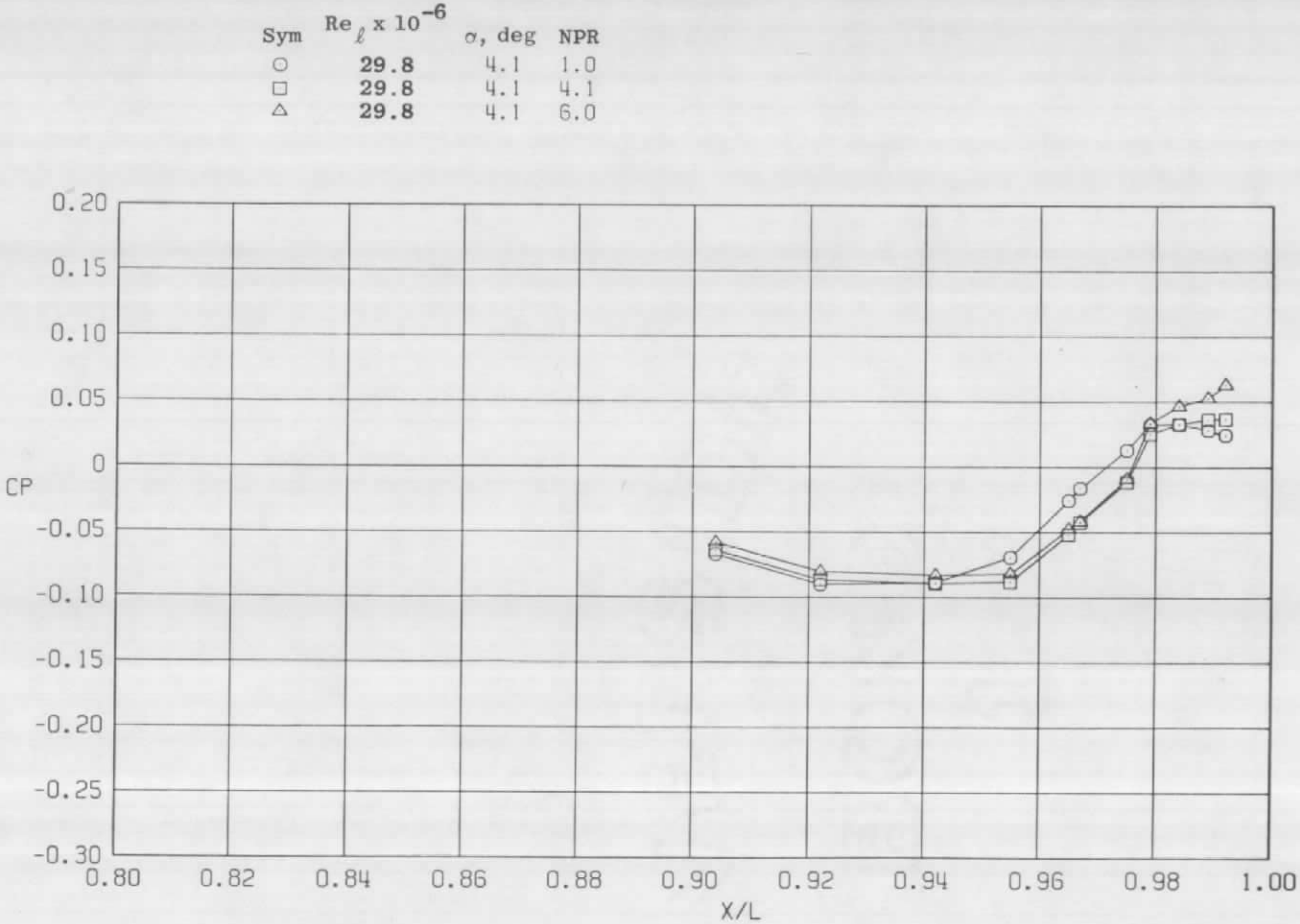

c. ϕ = 135 deg
Figure 19. Continued.

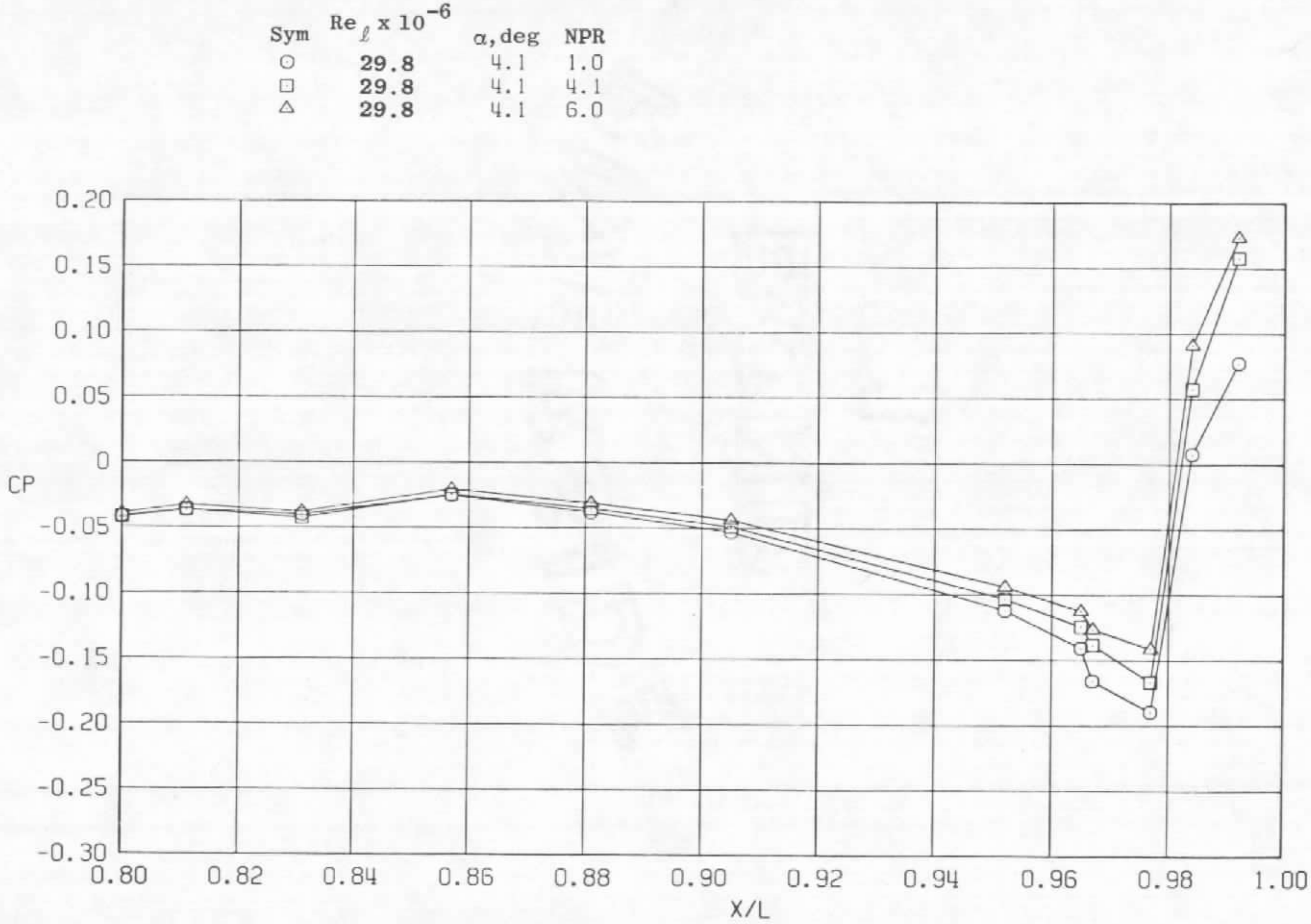

d. ϕ = 180 deg
Figure 19. Continued.

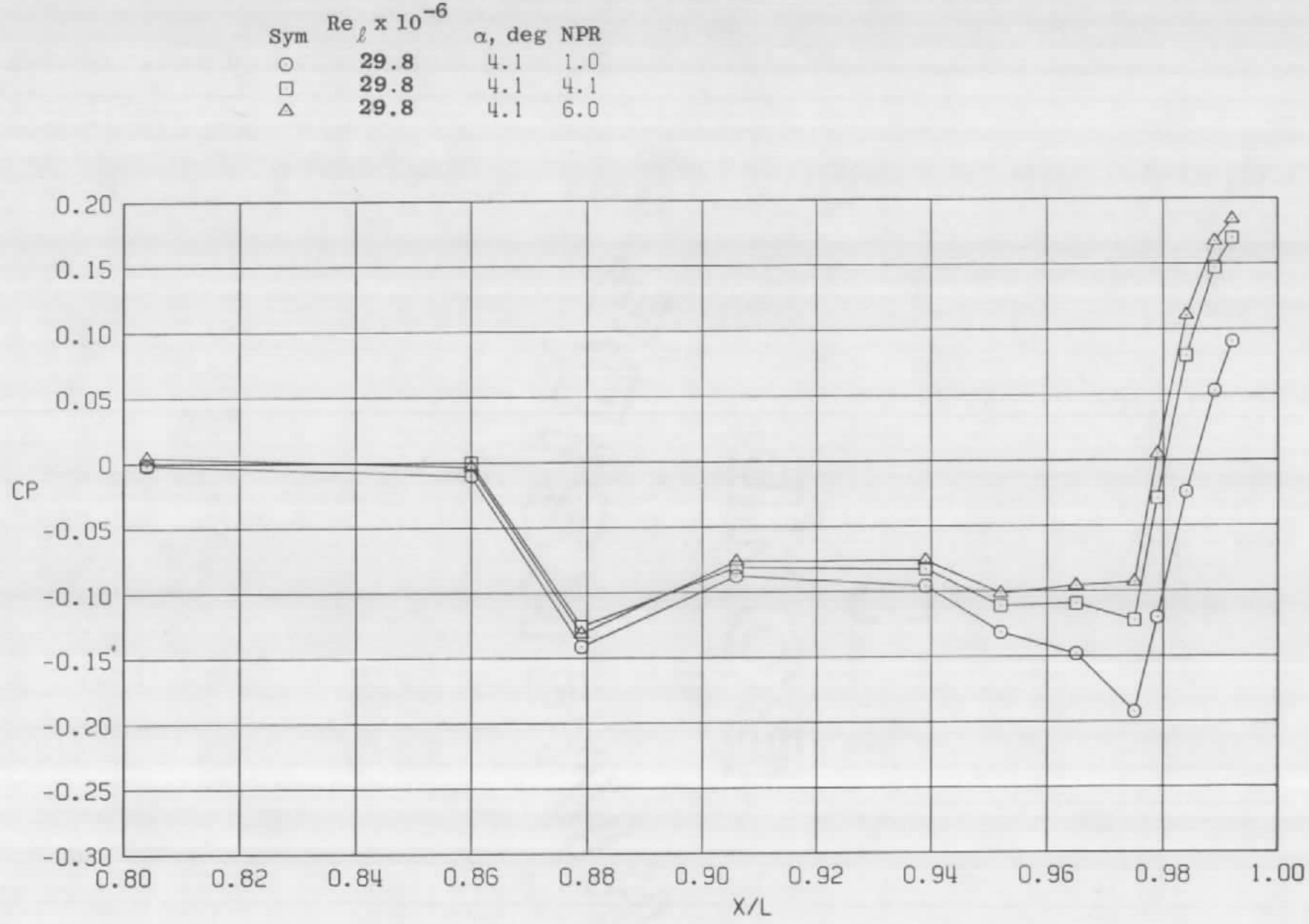

e. ϕ = 225 deg
Figure 19. Continued.

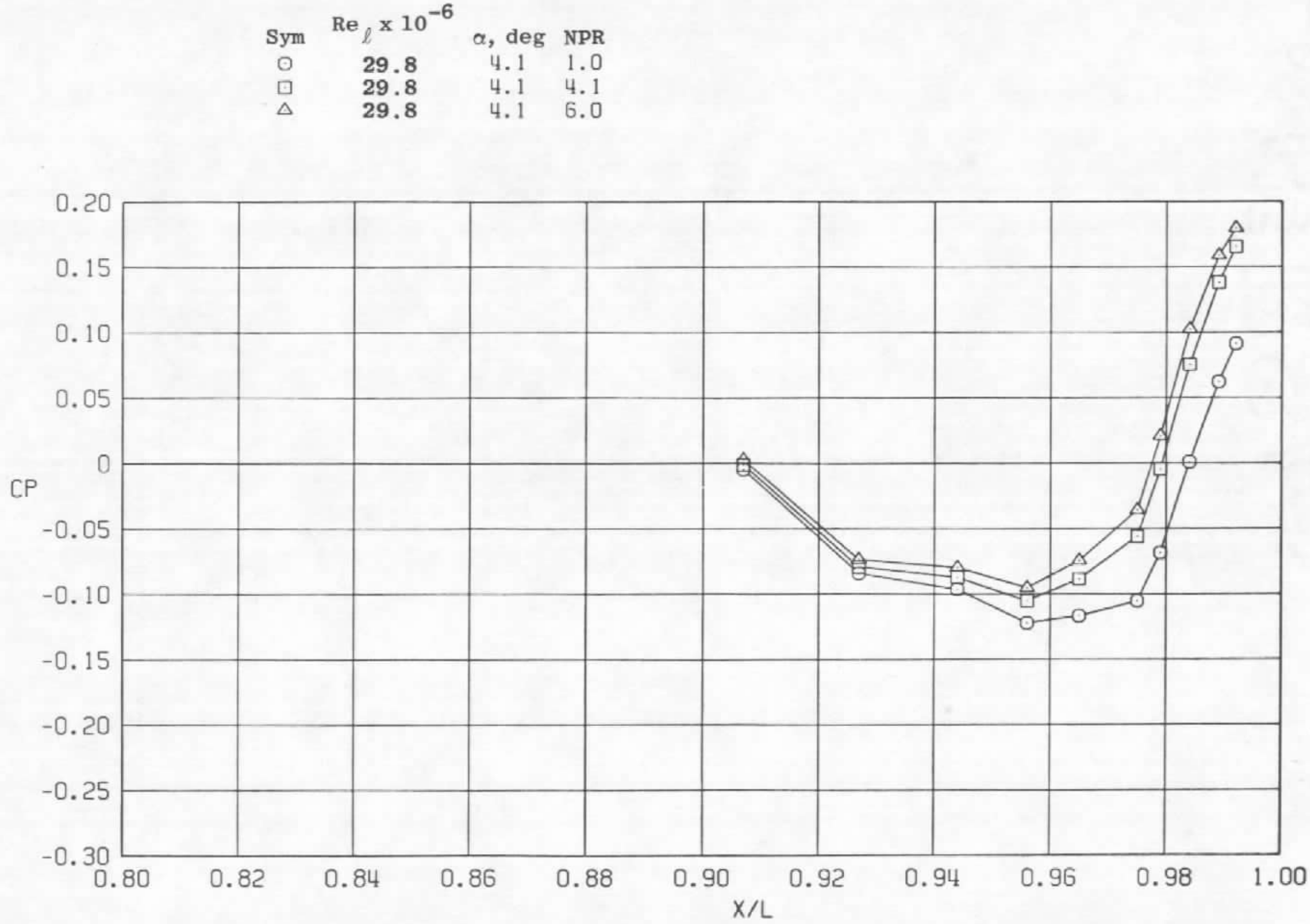

f. ϕ = 315 deg
Figure 19. Concluded.

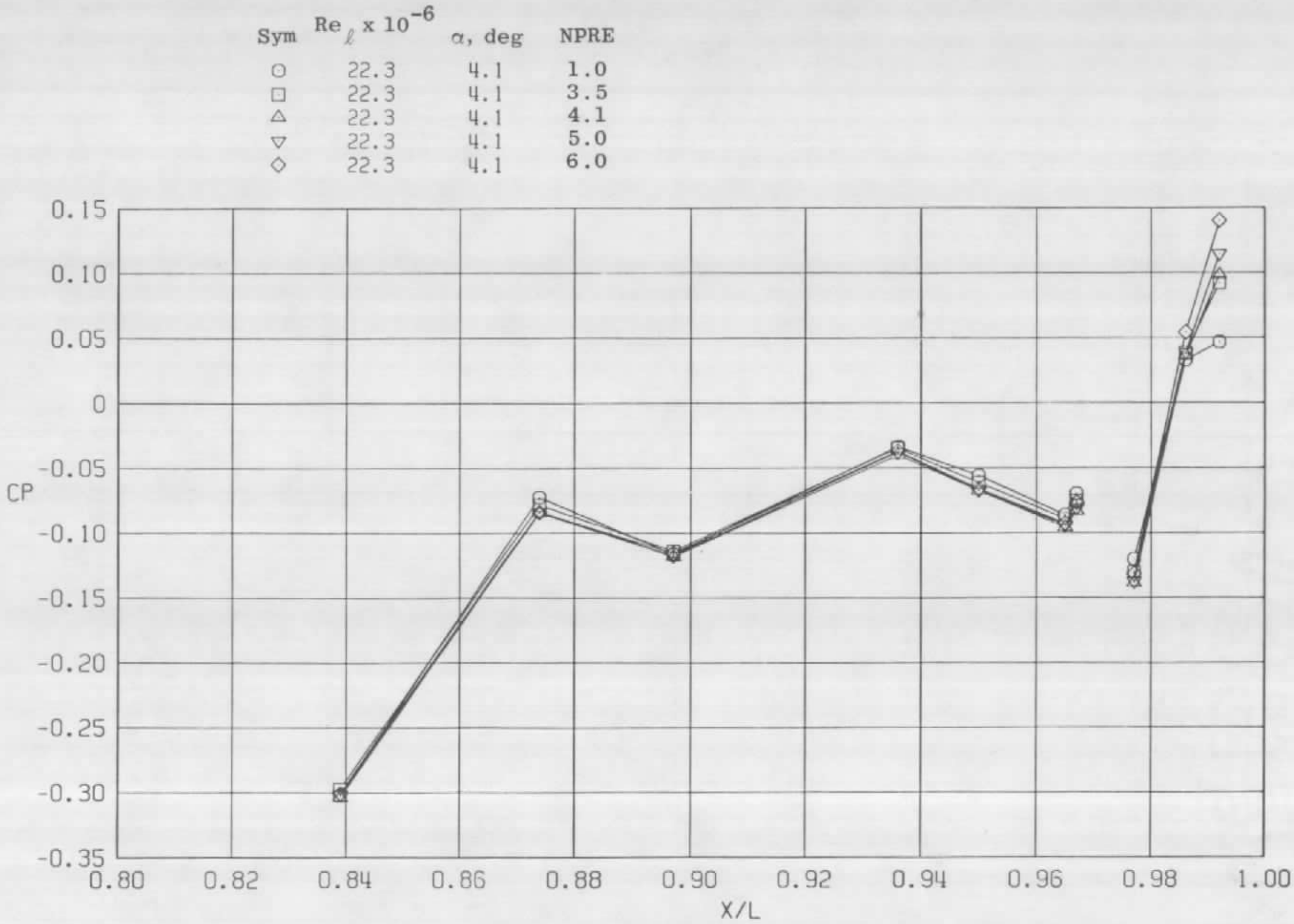

a. $\phi = 0$

Figure 20. Effective nozzle pressure ratio effects on surface pressure coefficients, A8 = 230 in.^{2}, M = 0.9 (SS).

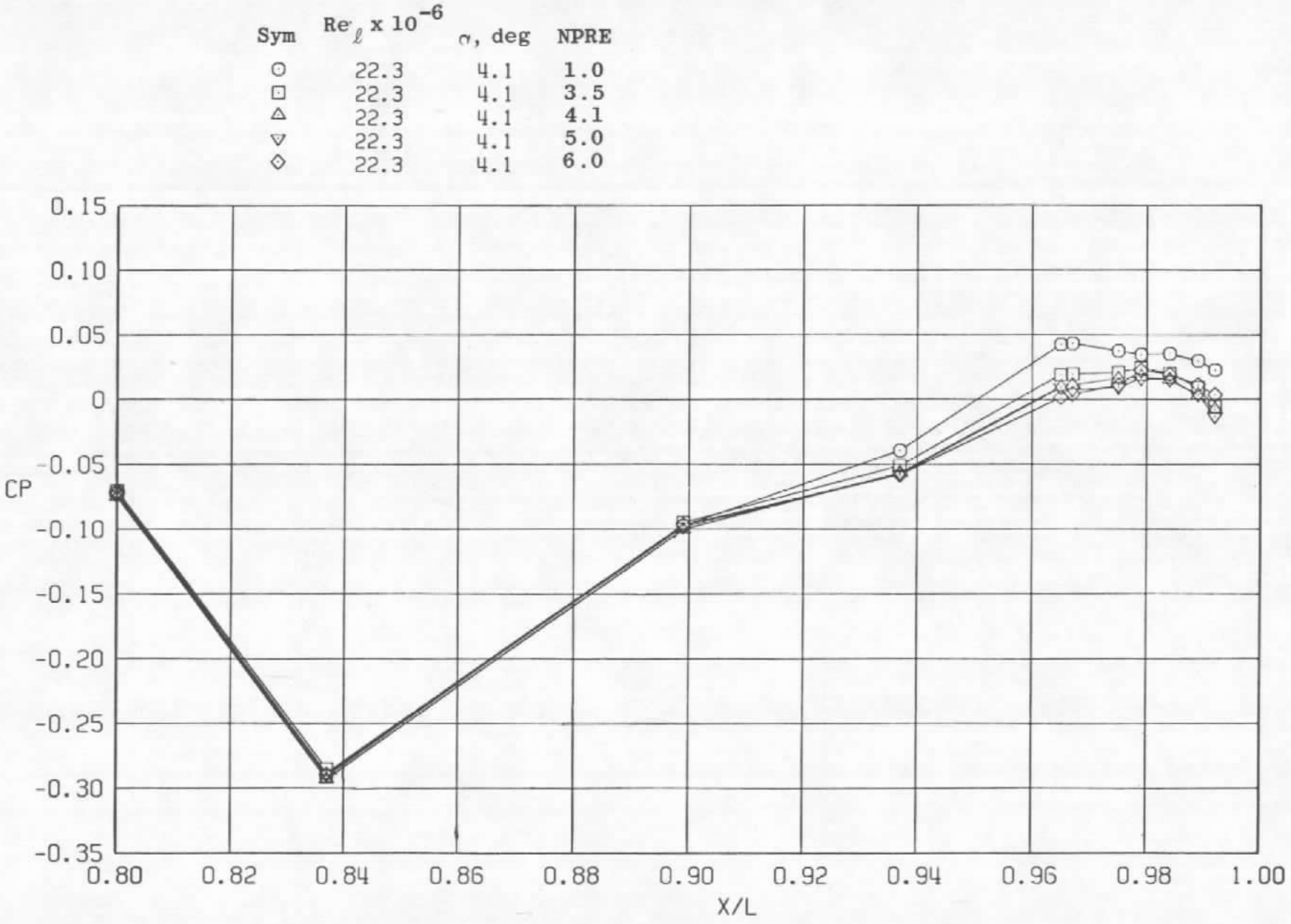

b. ϕ = 45 deg
Figure 20. Continued.

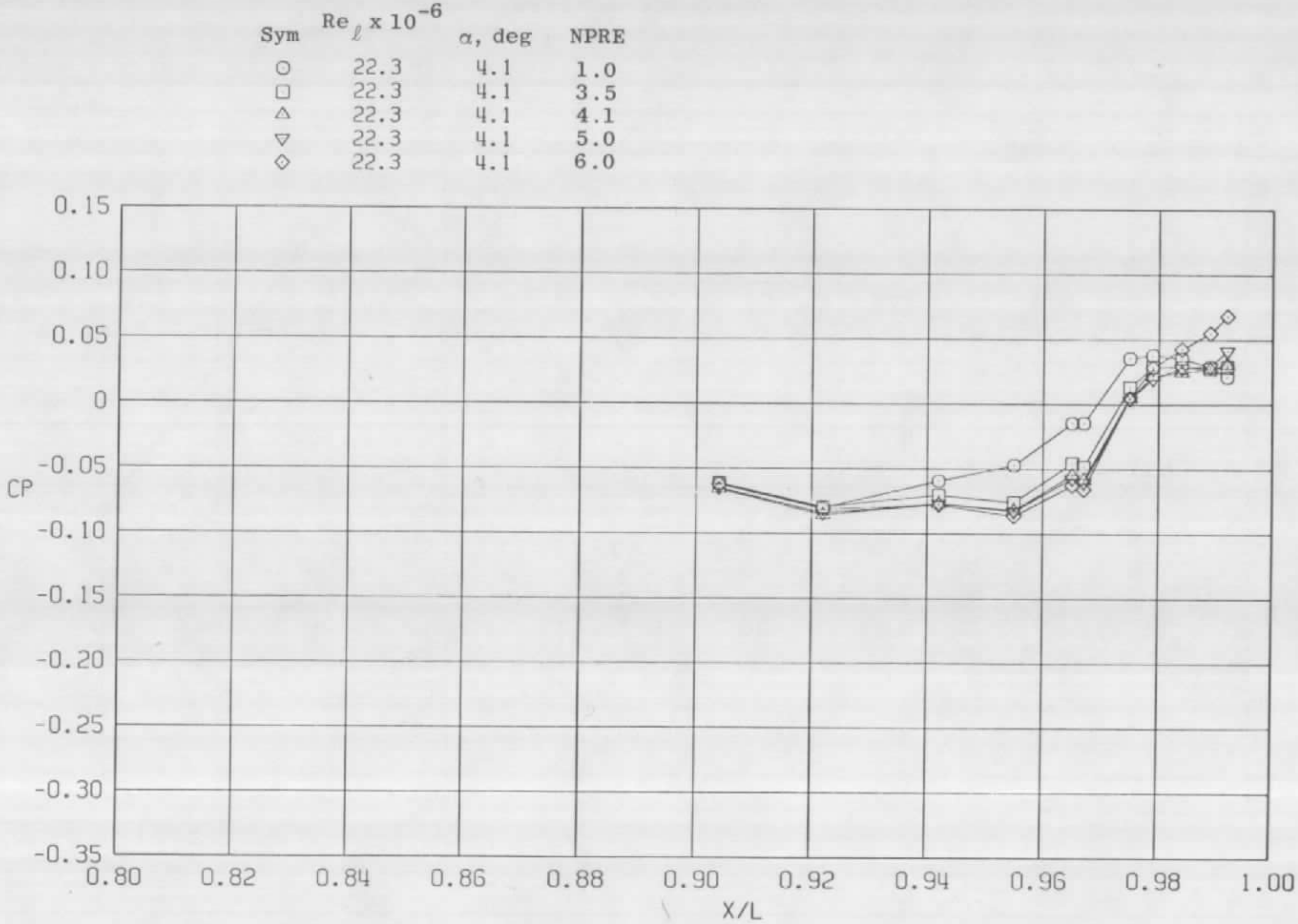

c. ϕ = 135 deg
Figure 20. Continued.

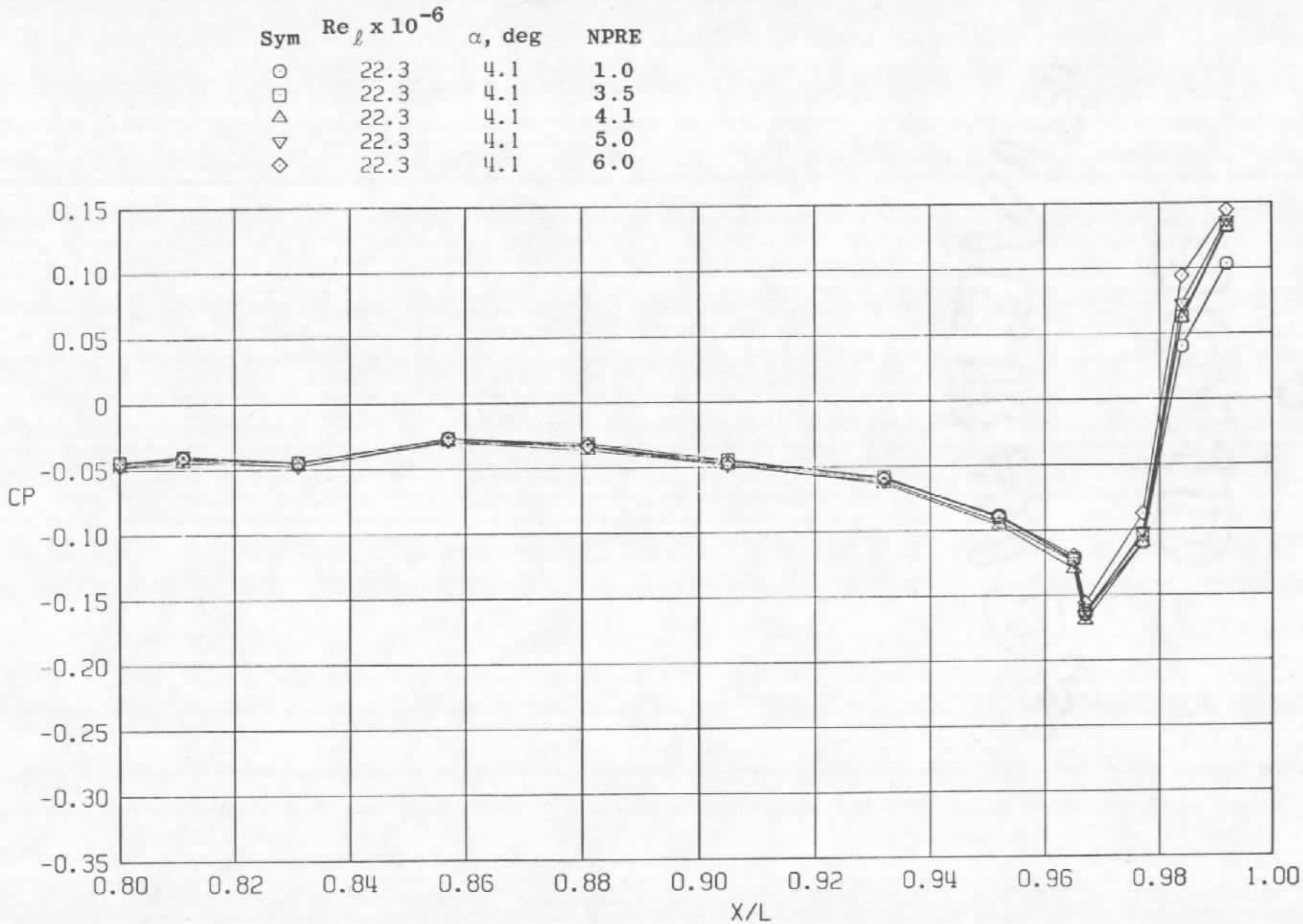

d. ϕ = 180 deg
Figure 20. Continued.

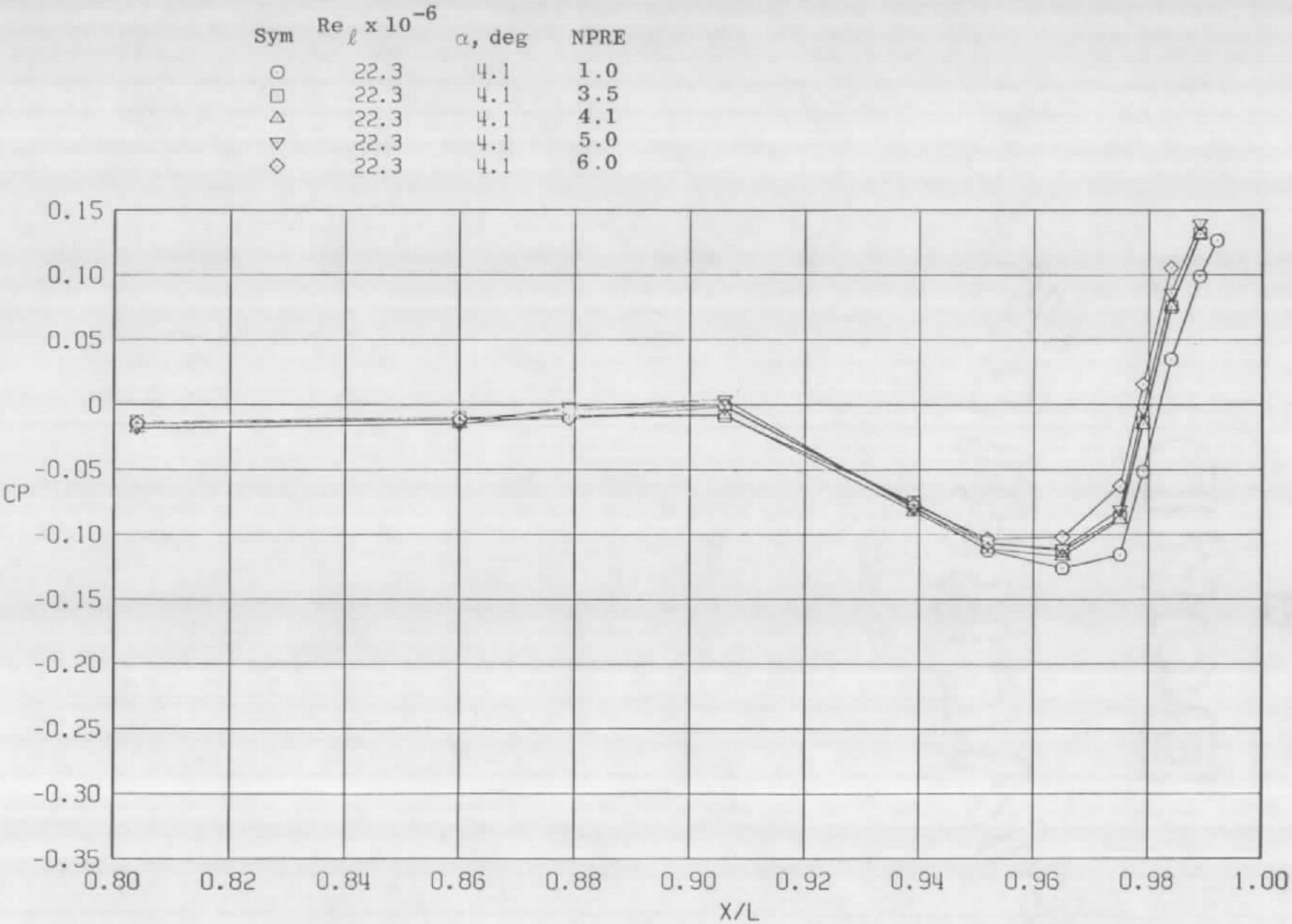

e. ϕ = 225 deg
Figure 20. Continued.

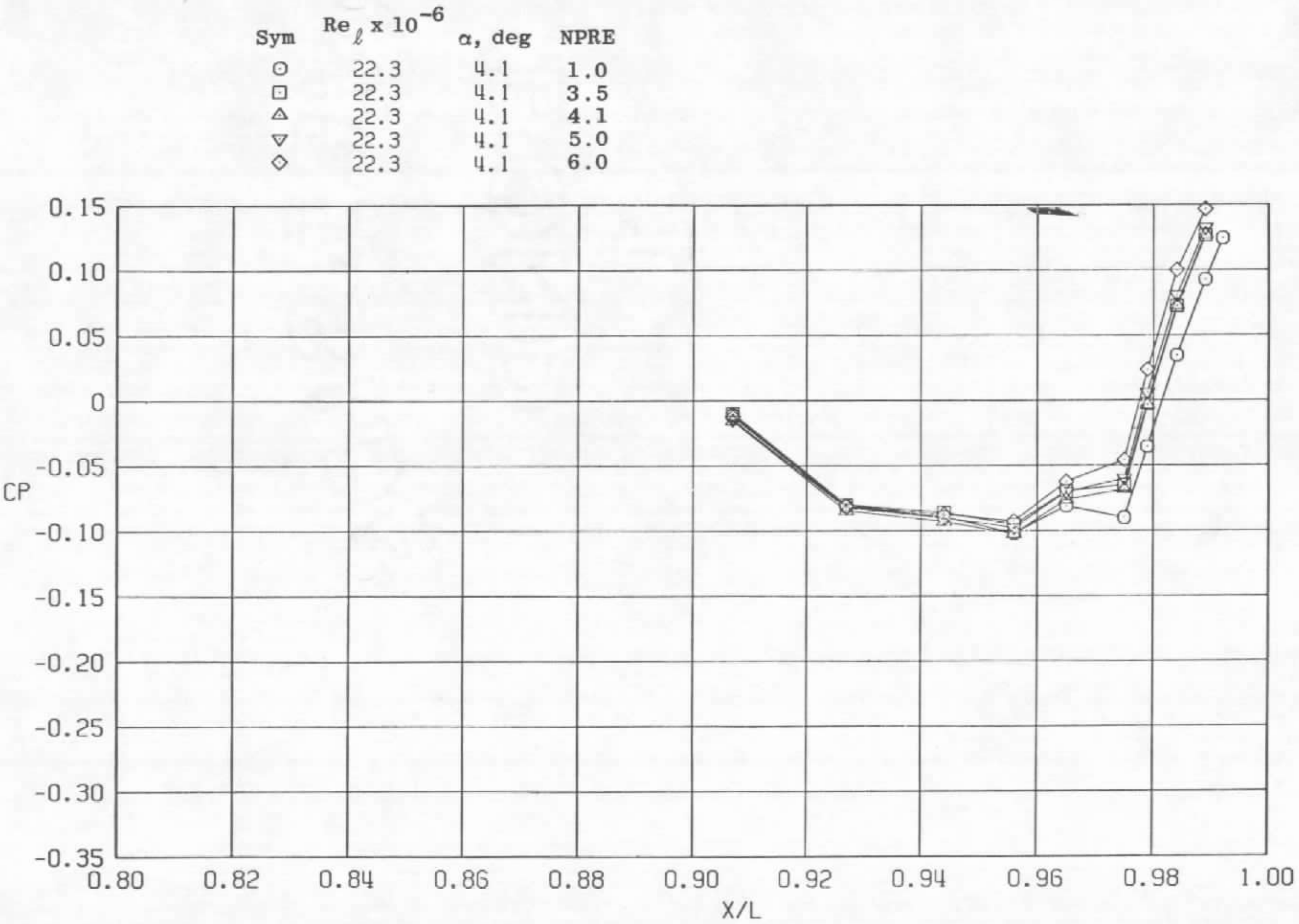

f. ϕ = 315 deg
Figure 20. Concluded.

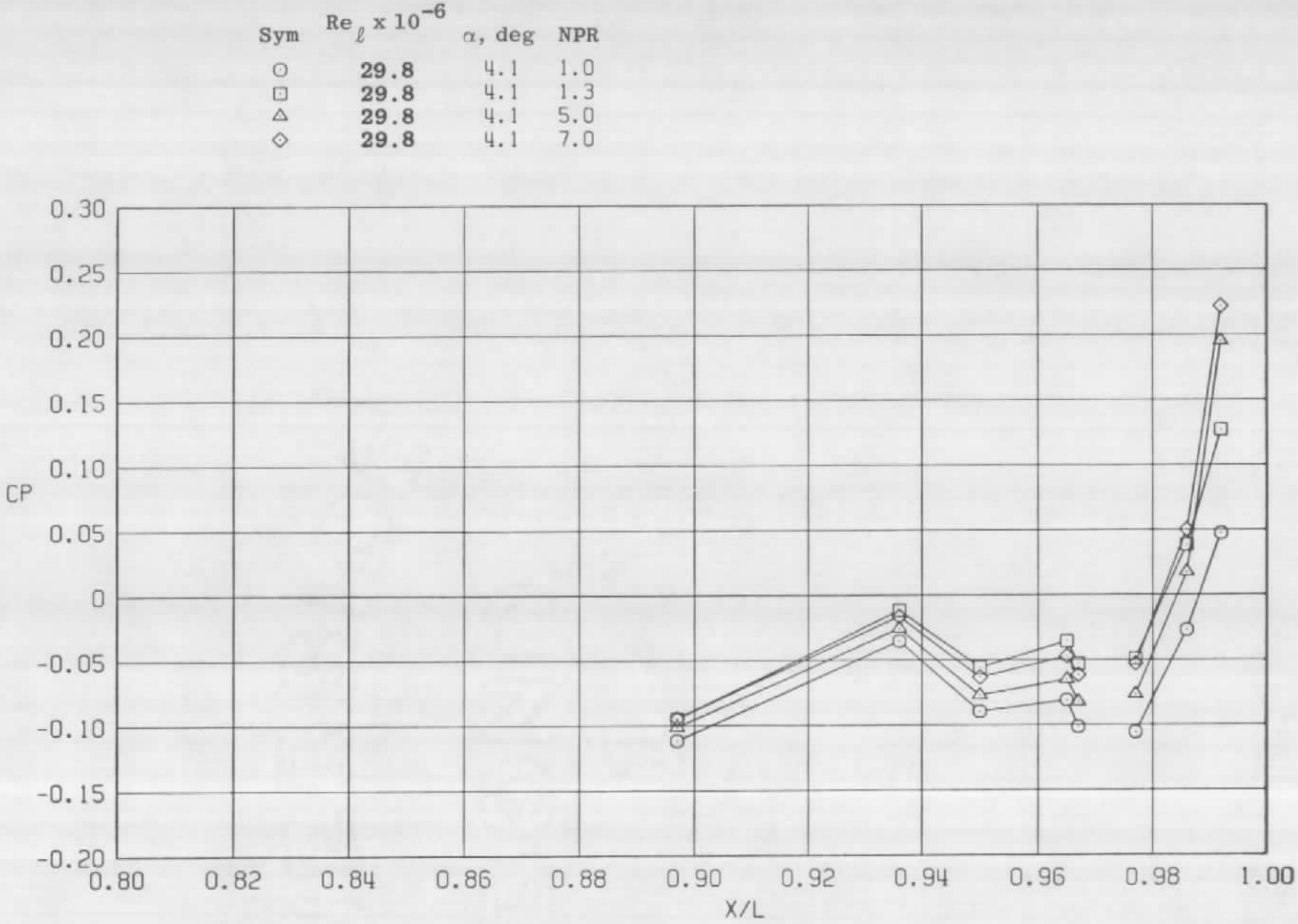

a. $\phi = 0$

Figure 21. Nozzle pressure ratio effects on surface pressure coefficients, A8 = 300 in.², M = 0.9 (WT).

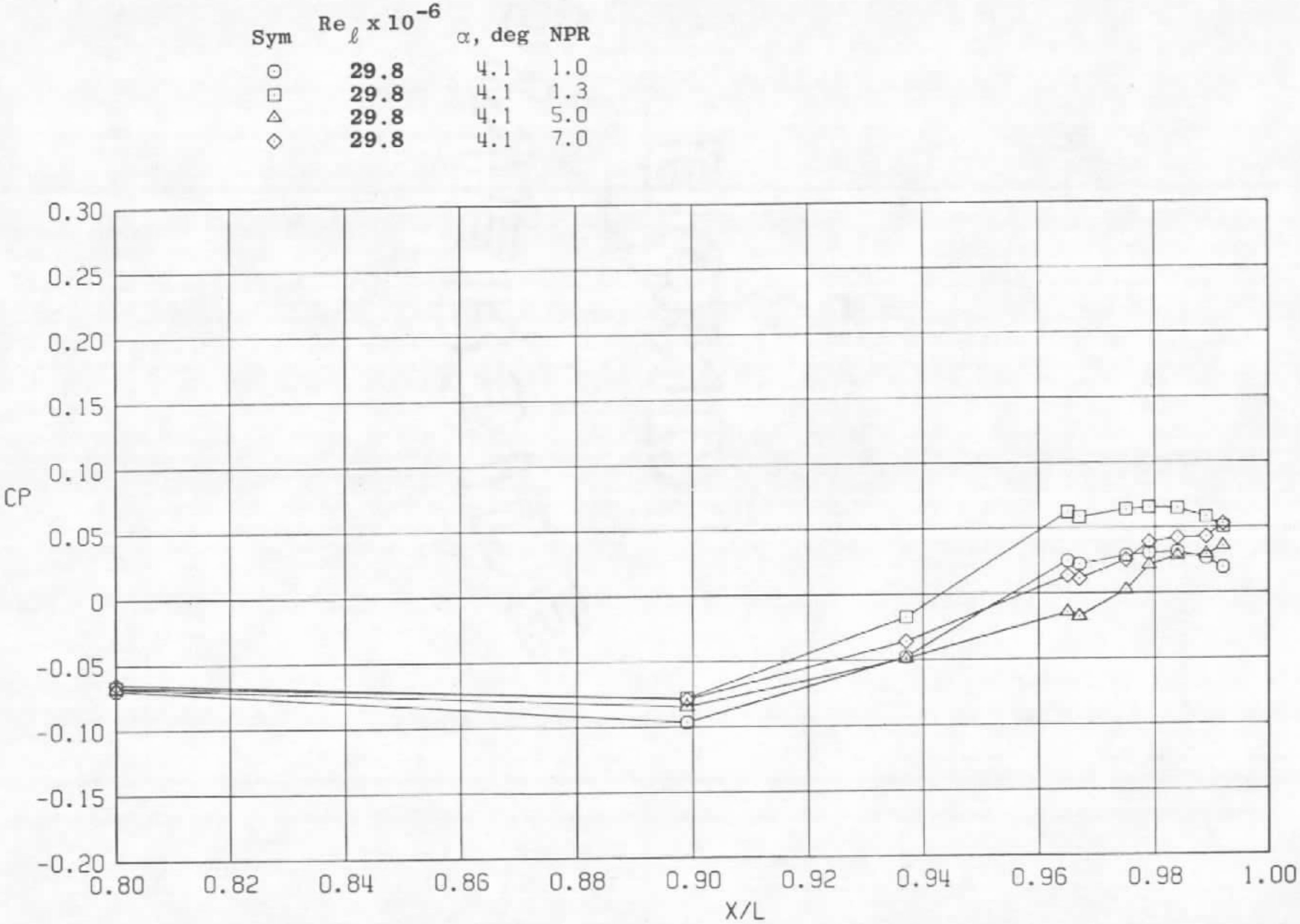

b. ϕ = 45 deg
Figure 21. Continued.

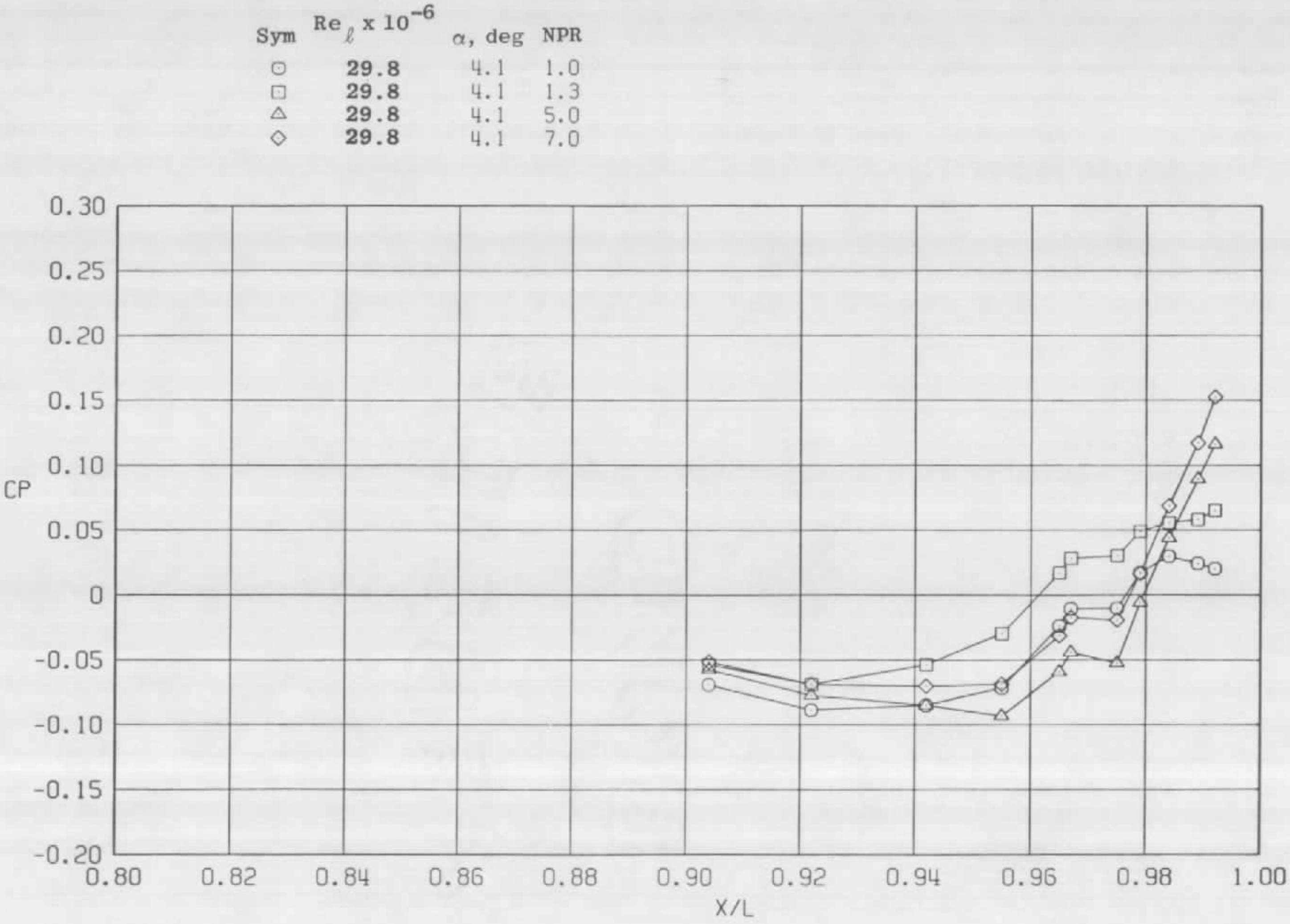

c. ϕ = 135 deg
Figure 21. Continued.

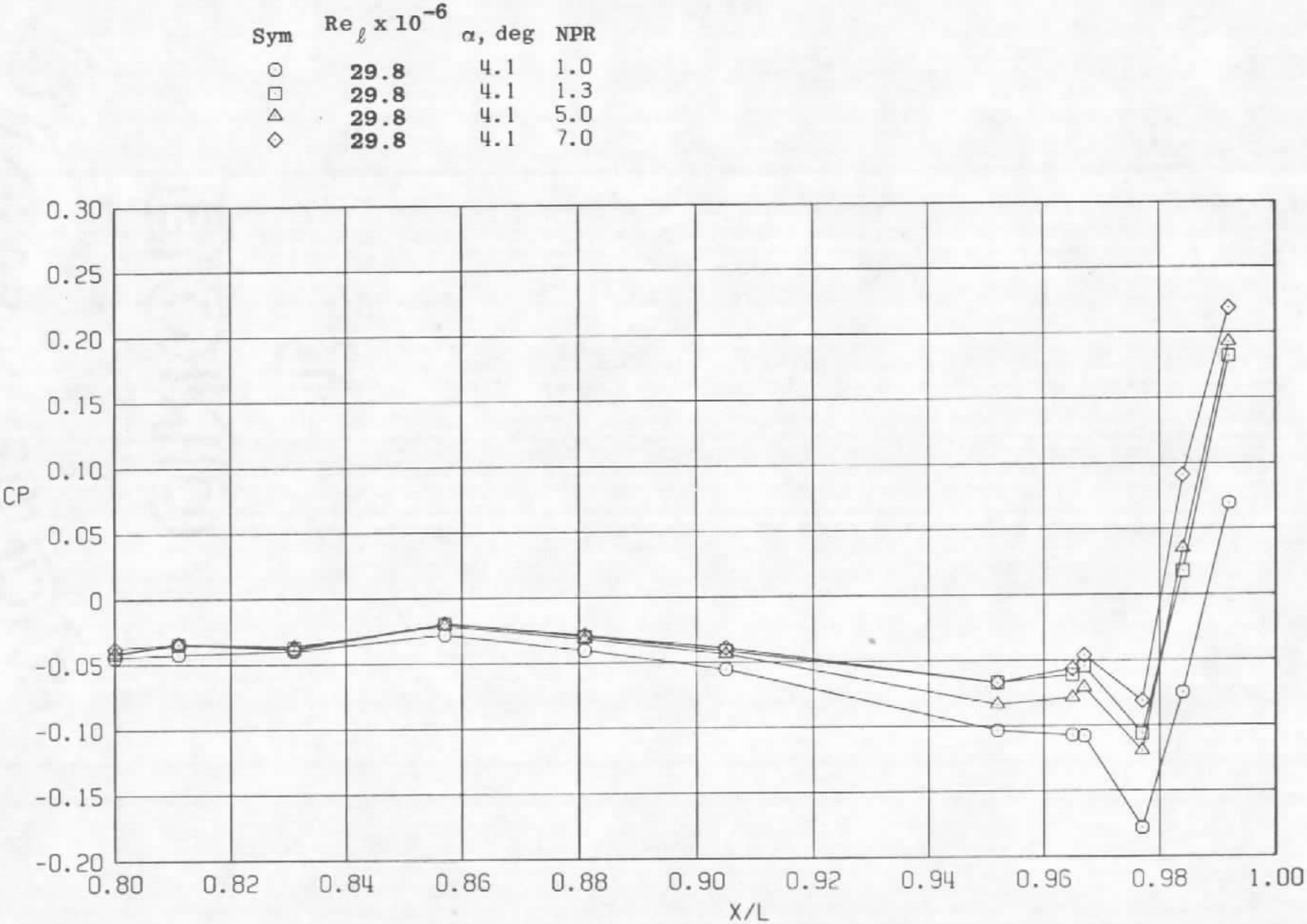

d. ϕ = 180 deg

Figure 21. Continued.

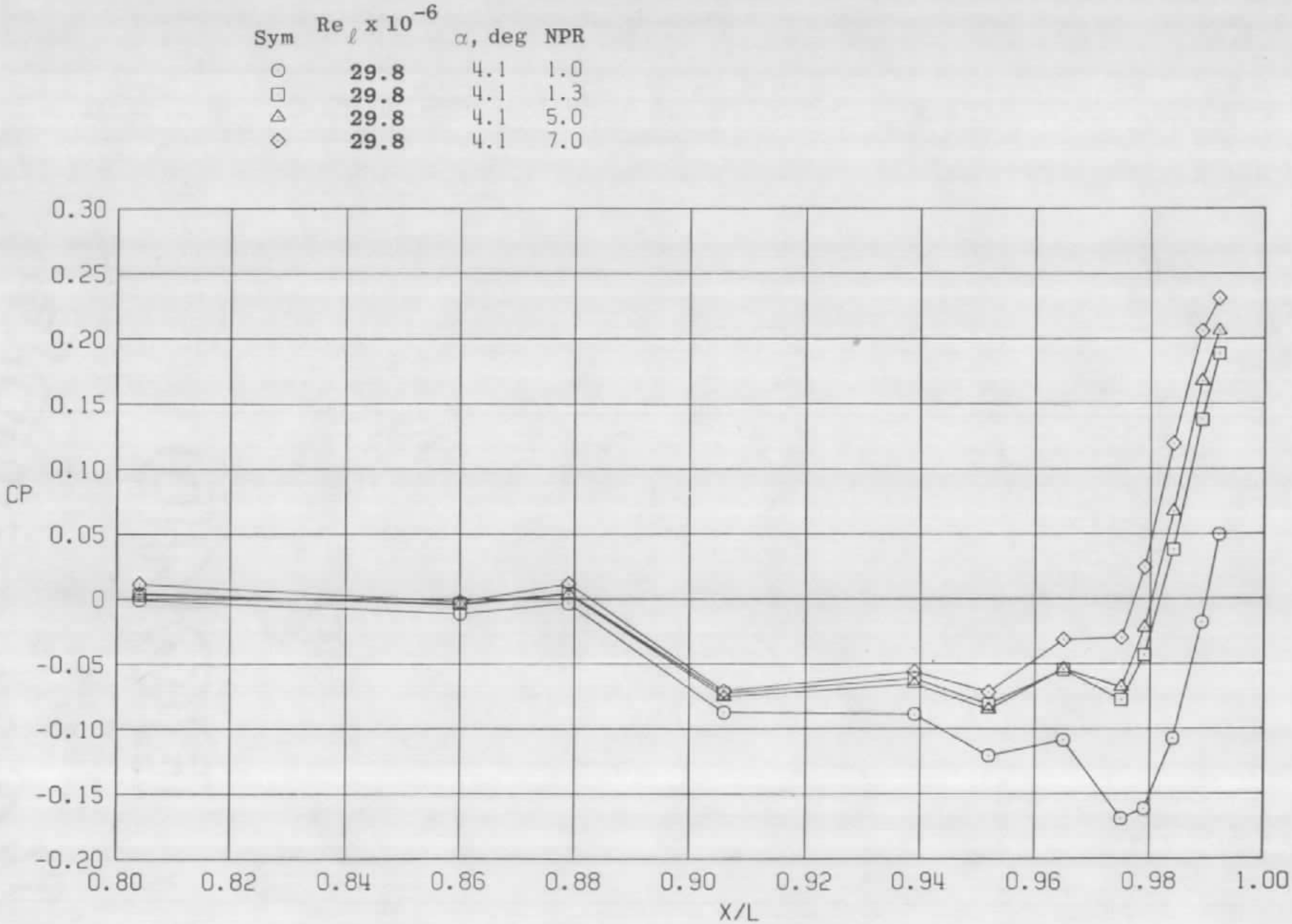

e. ϕ = 225 deg
Figure 21. Continued.

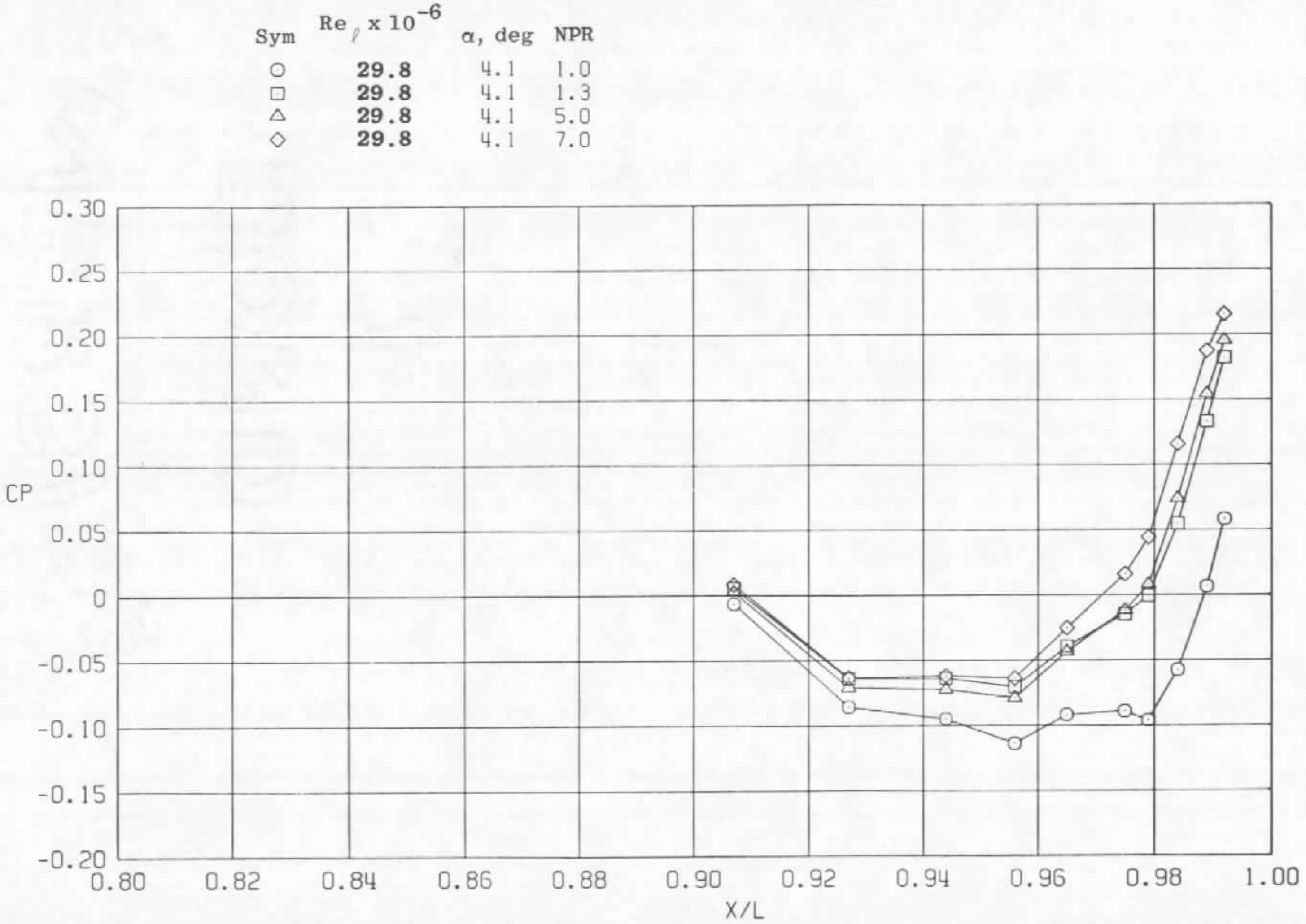

f. ϕ = 315 deg
Figure 21 Concluded.

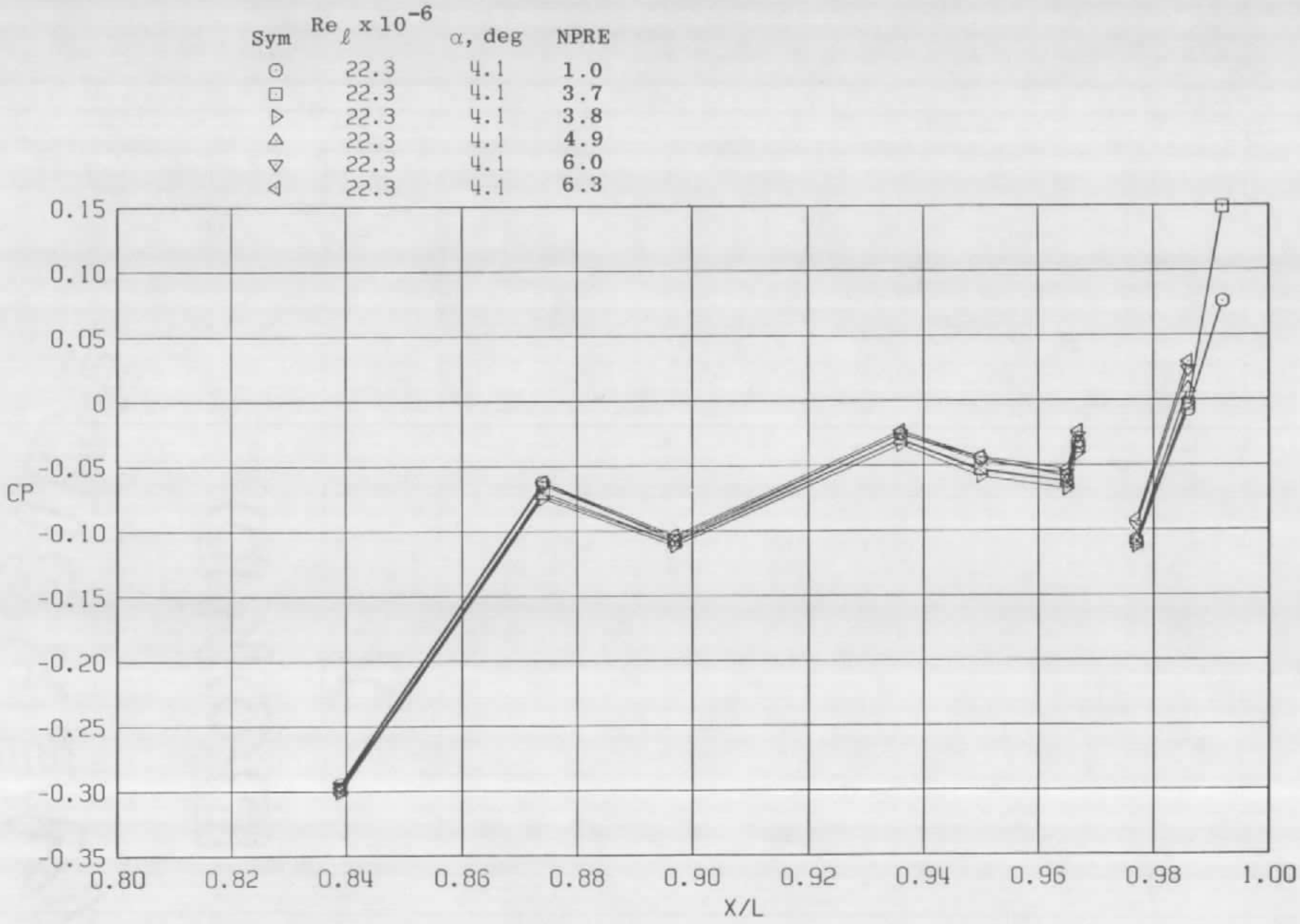

a. $\phi = 0$

Figure 22. Effective nozzle presssure ratio effects on surface pressure coefficients, A8 = 300 in.², M = 0.9 (SS).

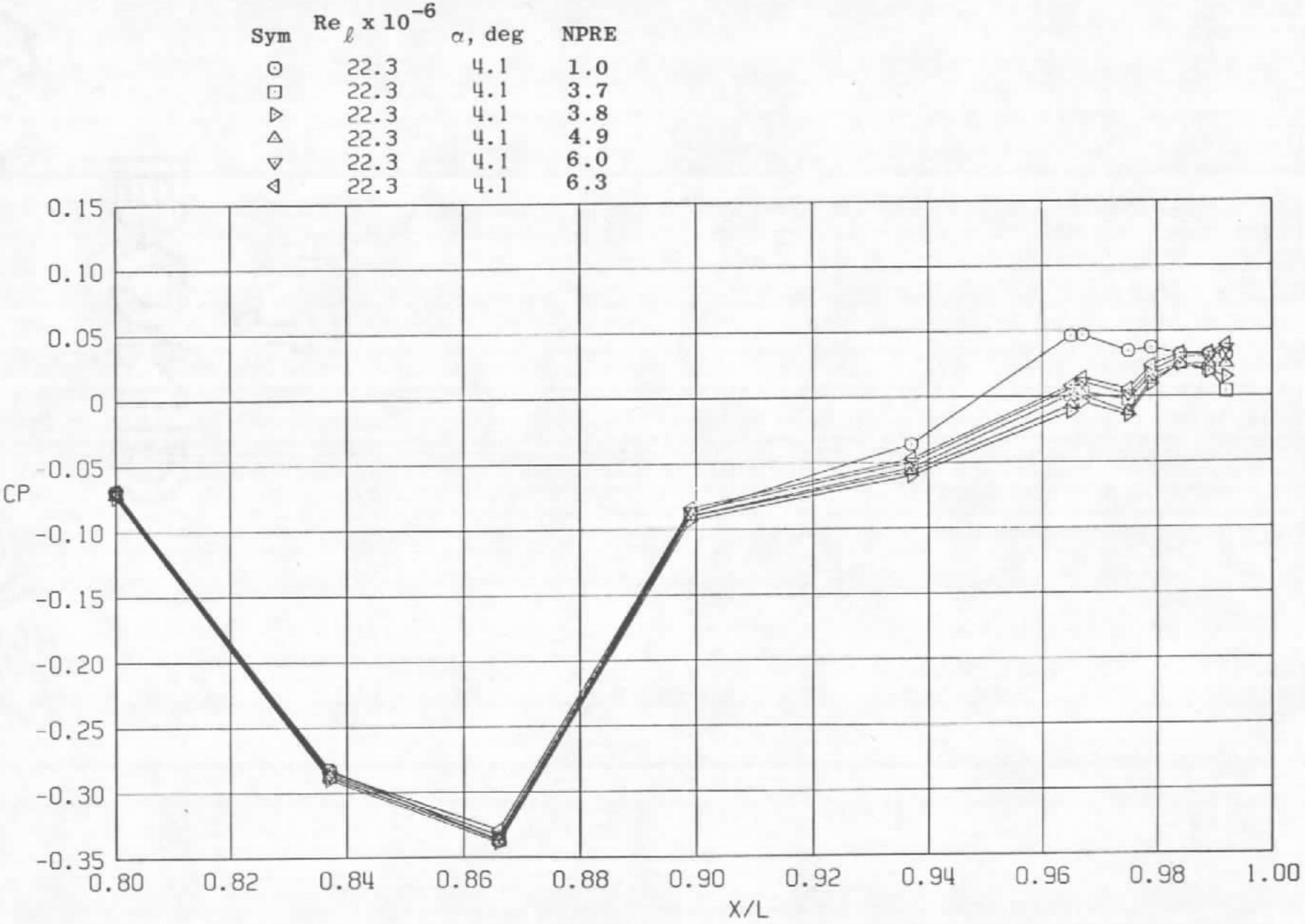

b. ϕ = 45 deg
Figure 22. Continued.

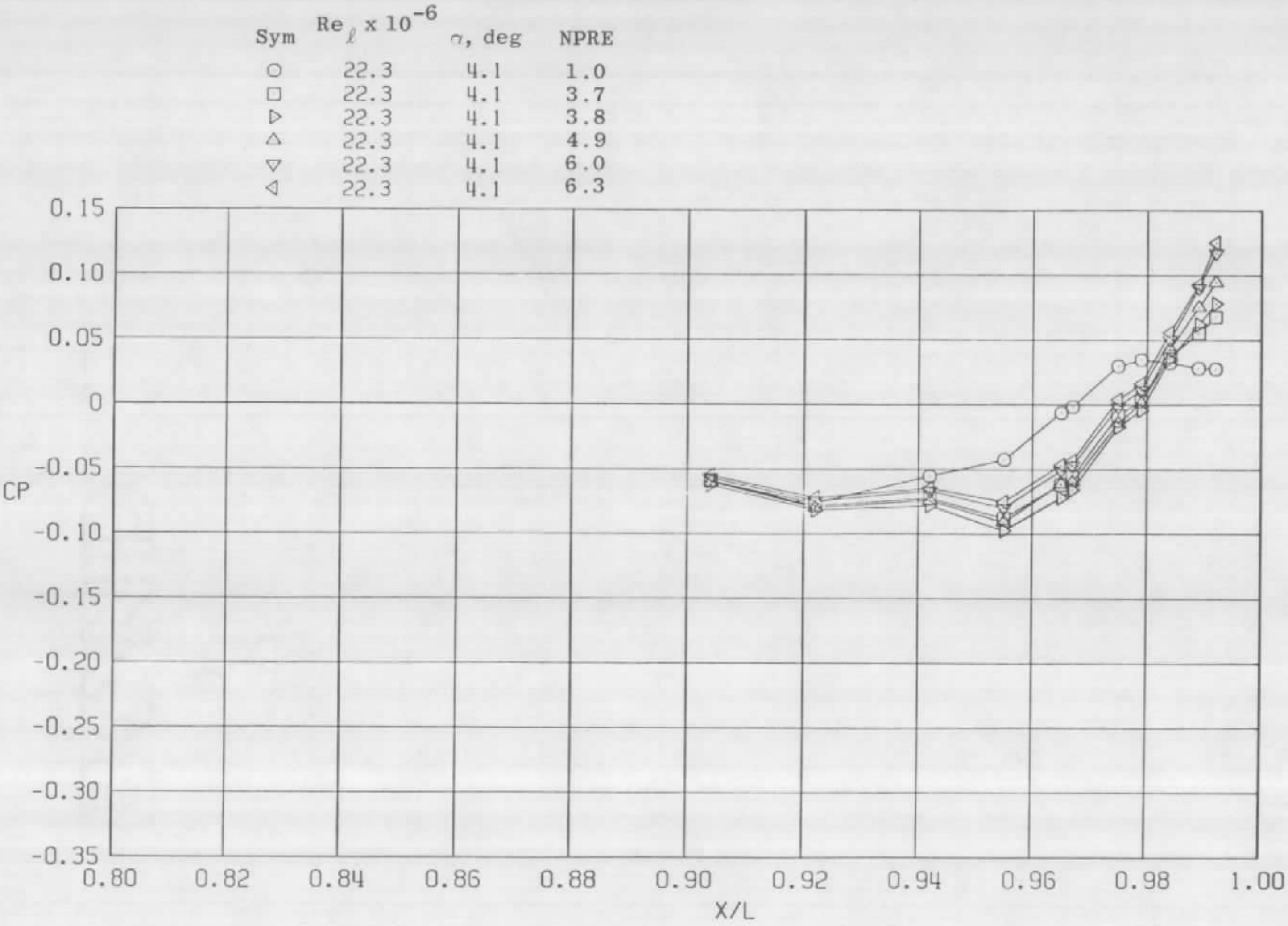

c. ϕ = 135 deg
Figure 22. Continued.

d. ϕ = 180 deg
Figure 22. Continued.

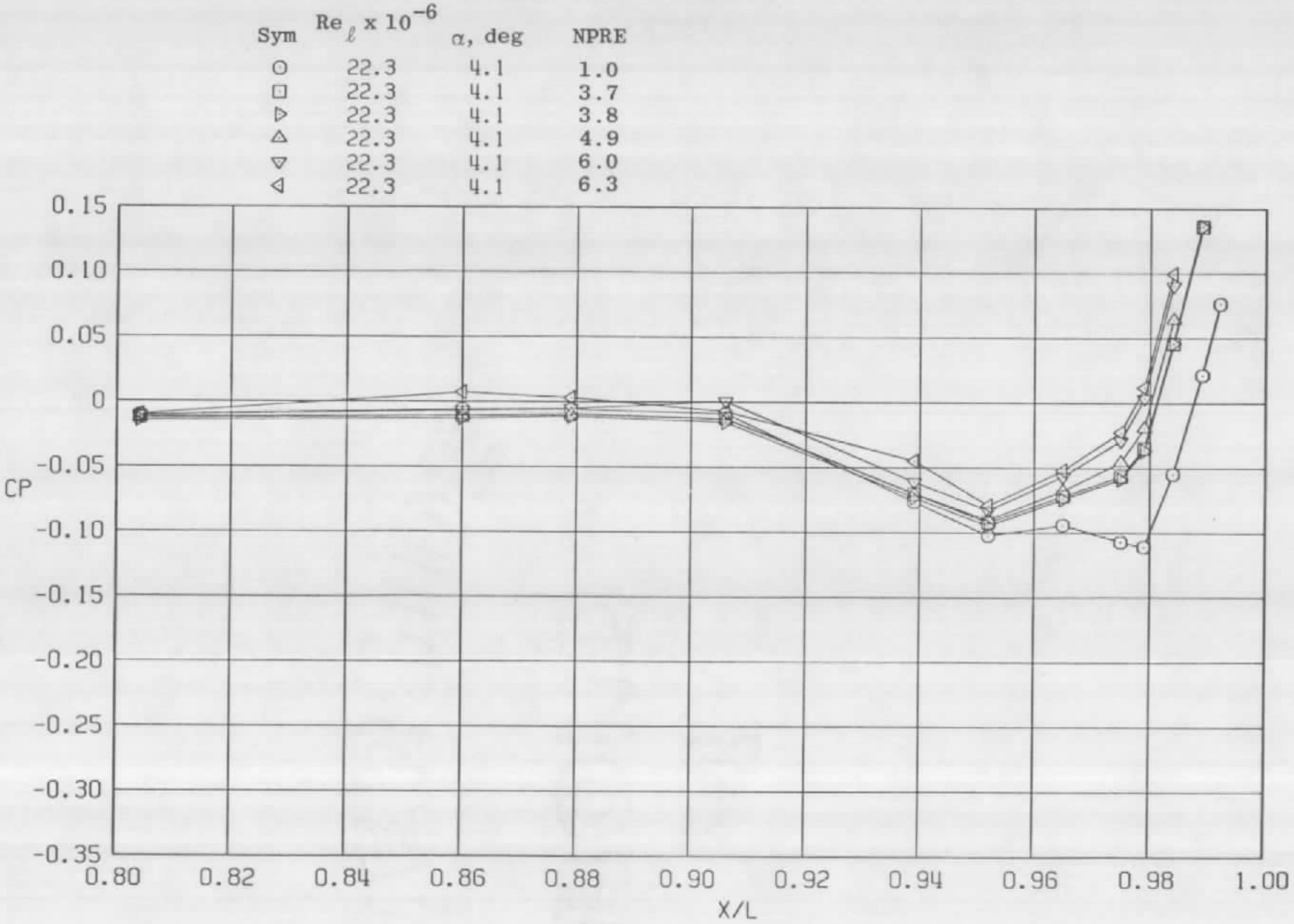

e. ϕ = 225 deg

Figure 22. Continued.

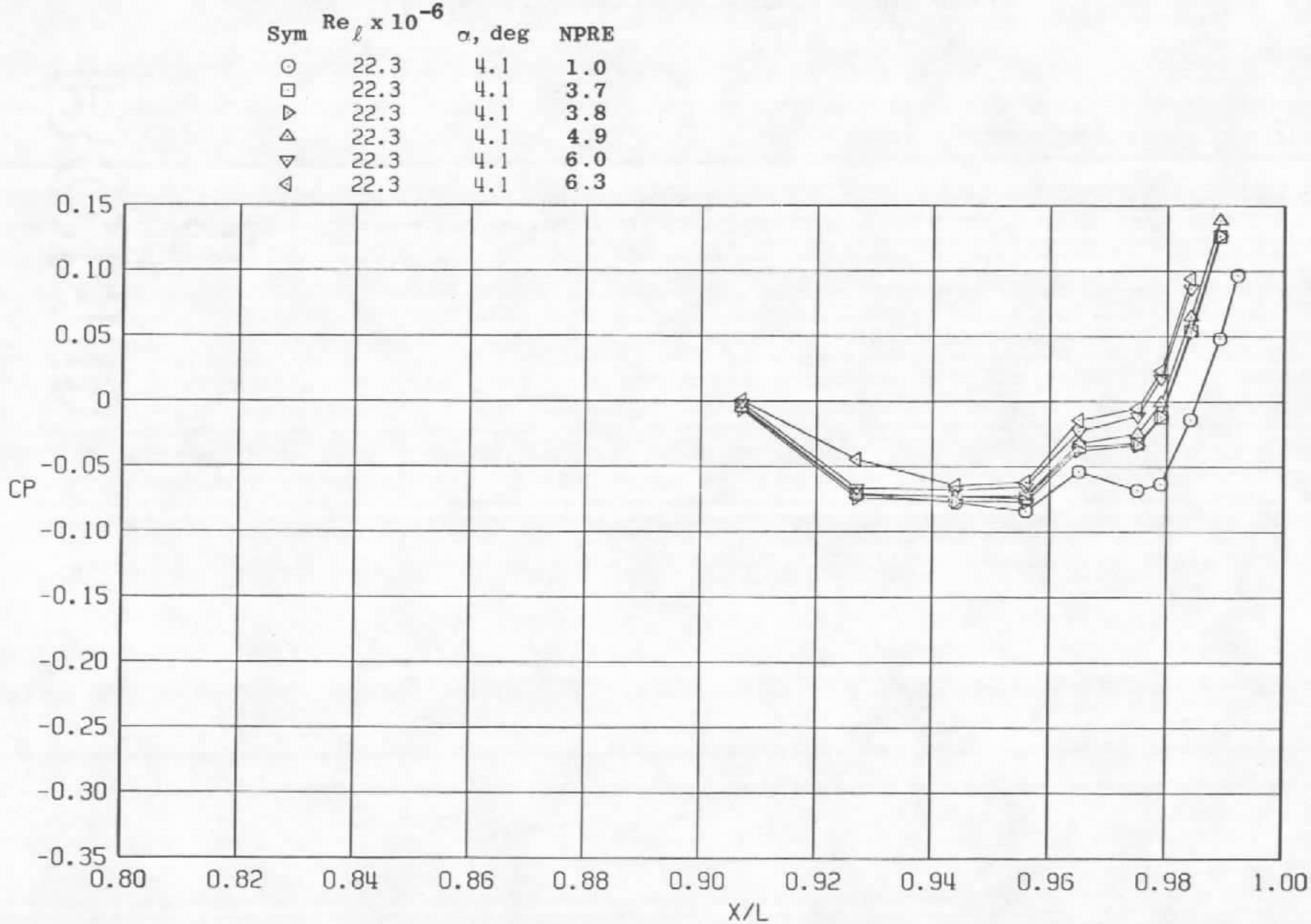

f. ϕ = 315 deg
Figure 22. Concluded.

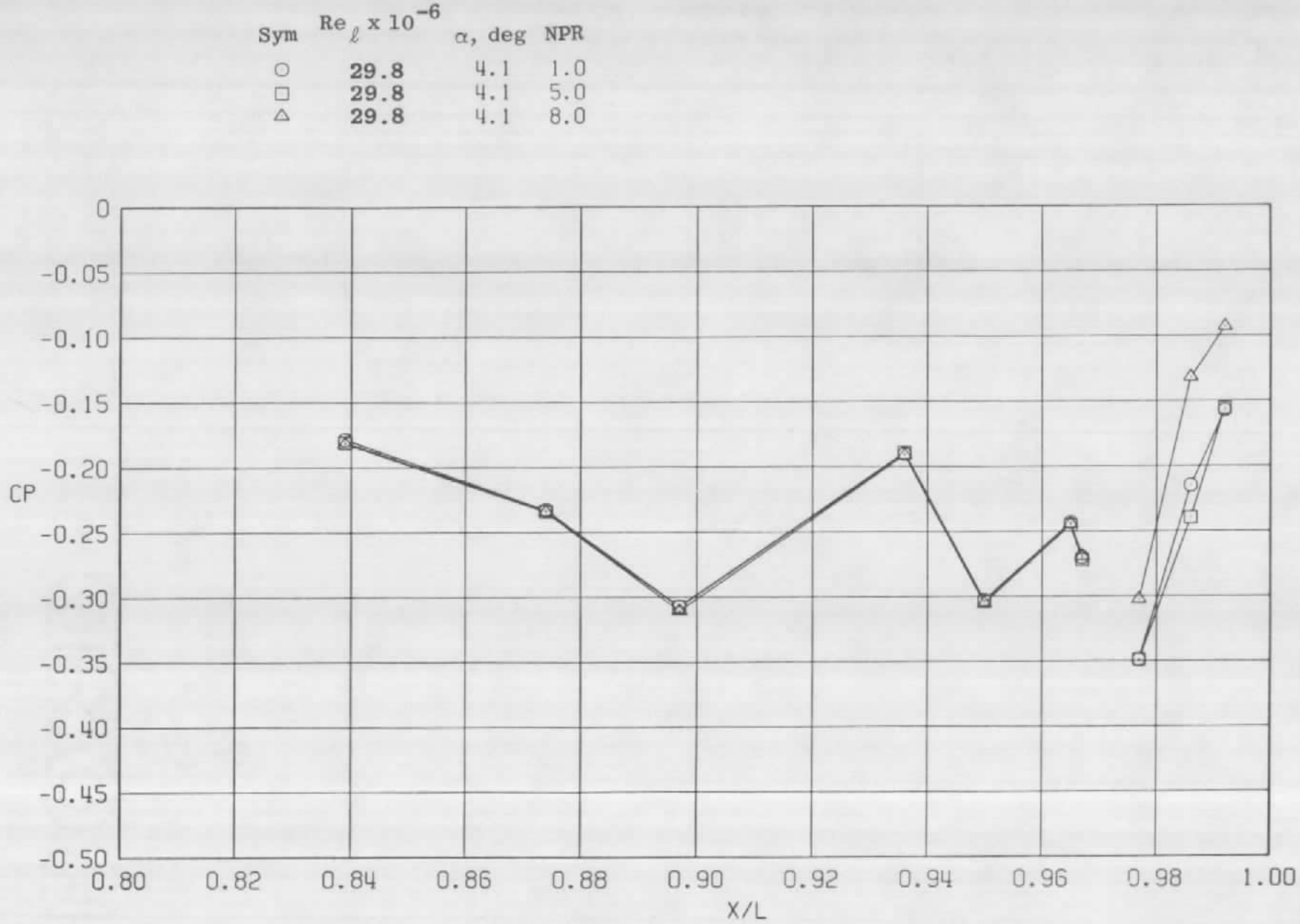

a. $\phi = 0$

Figure 23. Nozzle pressure ratio effects on surface pressure coefficients, A8 = 300 in.², M = 1.2 (WT).

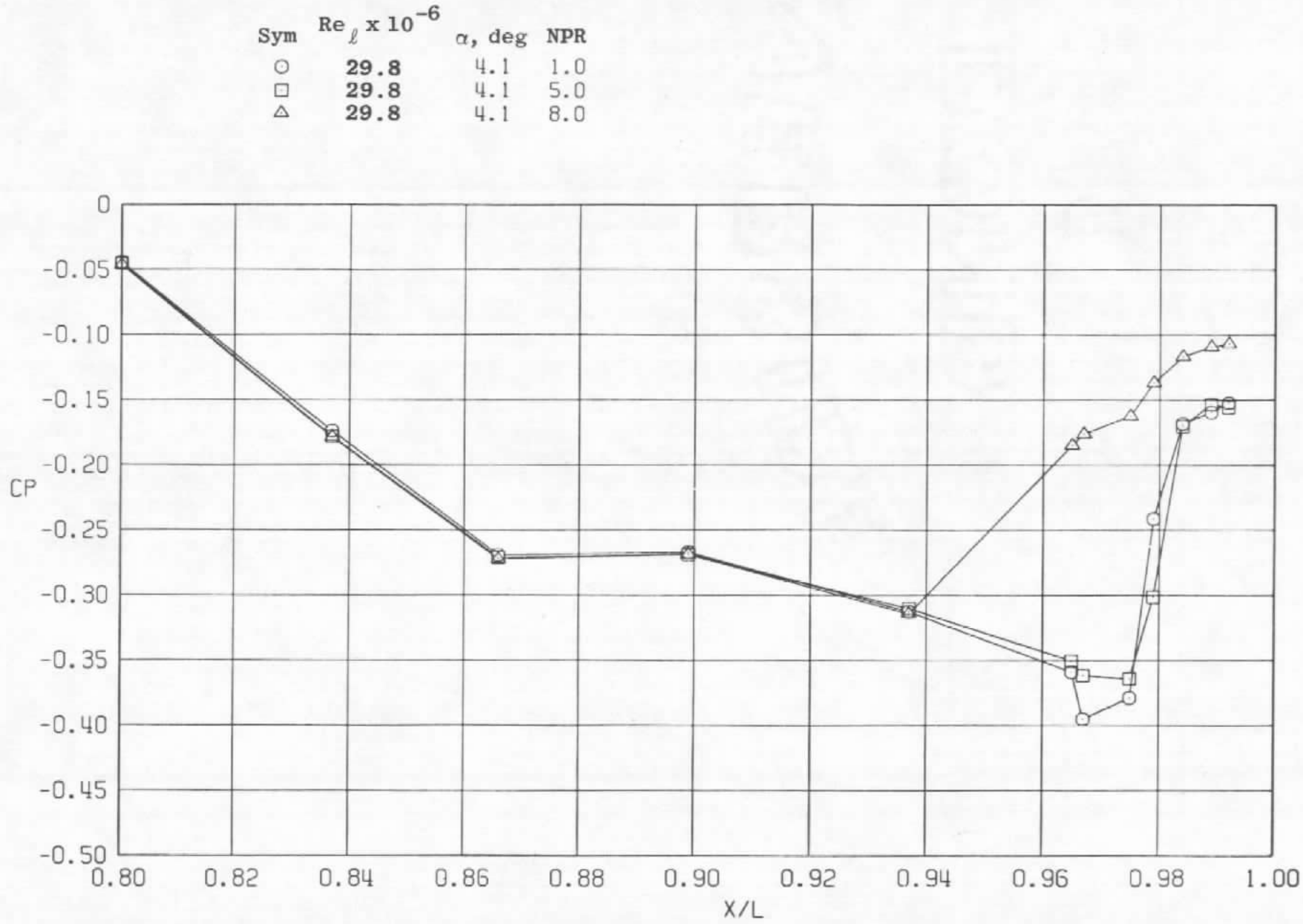

b. ϕ = 45 deg
Figure 23. Continued.

c. ϕ = 135 deg
Figure 23. Continued.

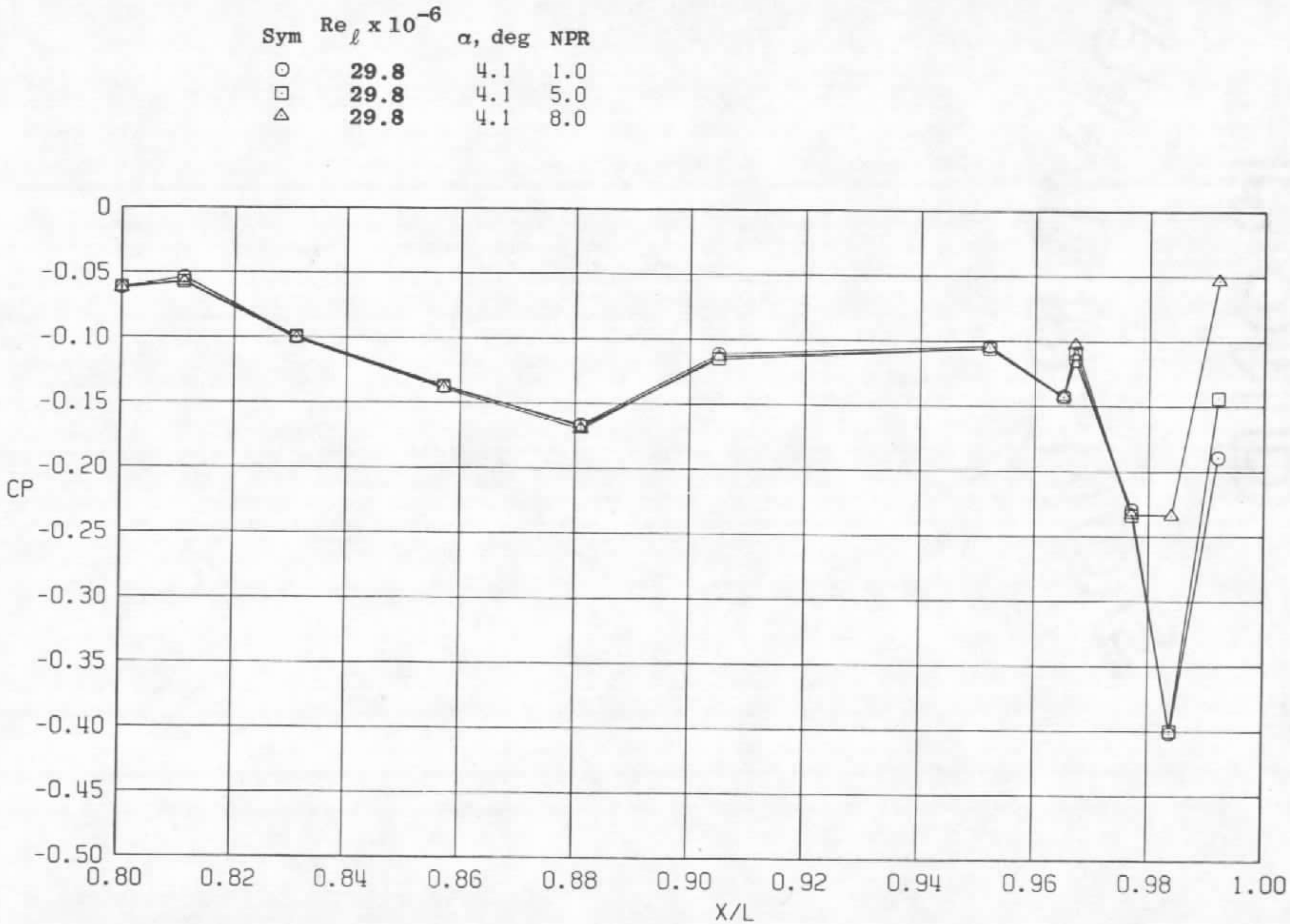

d. ϕ = 180 deg
Figure 23. Continued.

e. ϕ = 225 deg

Figure 23. Continued.

Sym	$Re_{\ell} \times 10^{-6}$	α, deg	NPR
○	29.8	4.1	1.0
□	29.8	4.1	5.0
△	29.8	4.1	8.0

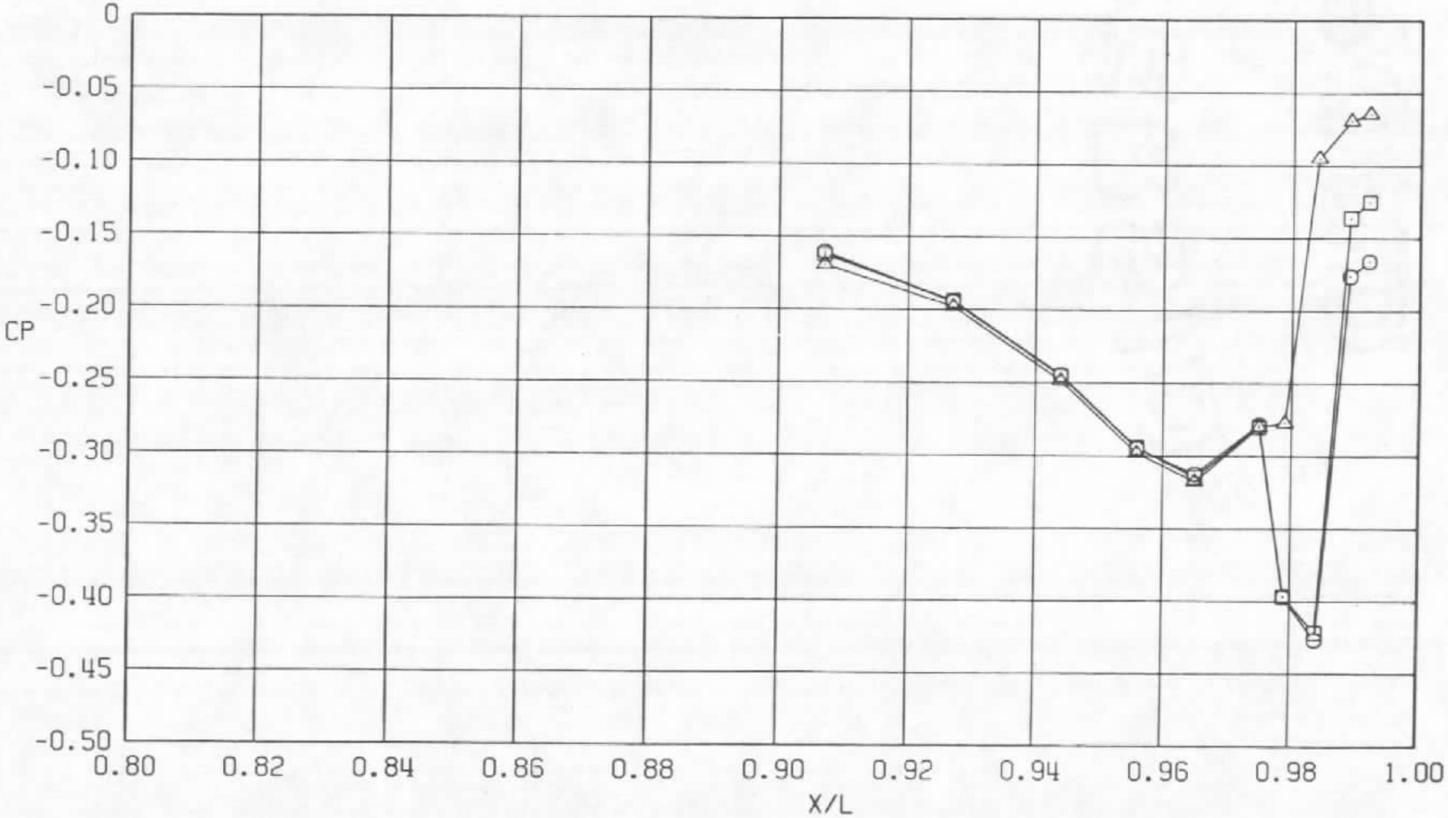

f. ϕ = 315 deg
Figure 23. Concluded.

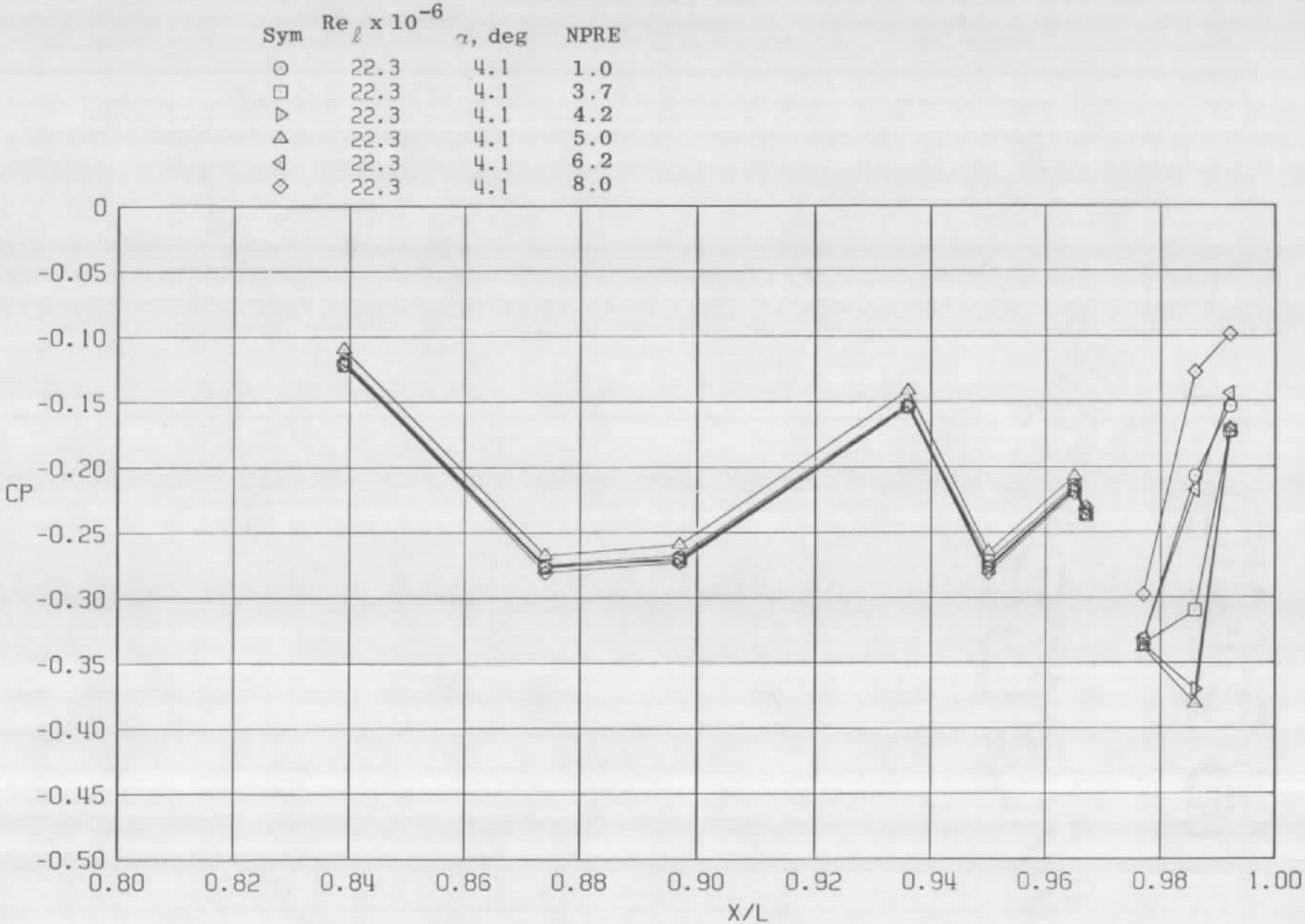

a. $\phi = 0$

Figure 24. Effective nozzle pressure ratio effects on surface pressure coefficients, A8 = 300 in.², M = 1.2 (SS).

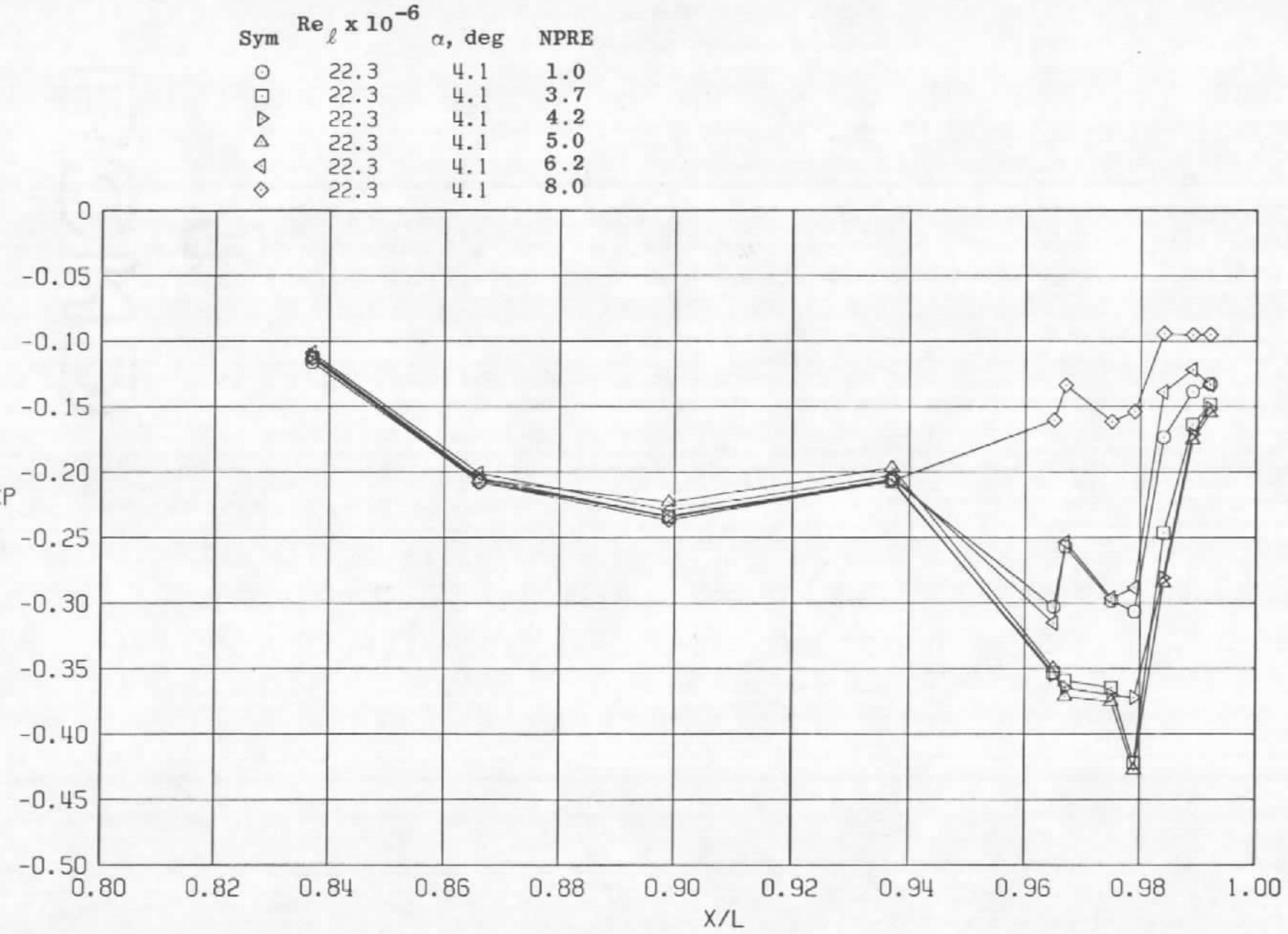

b. ϕ = 45 deg
Figure 24. Continued.

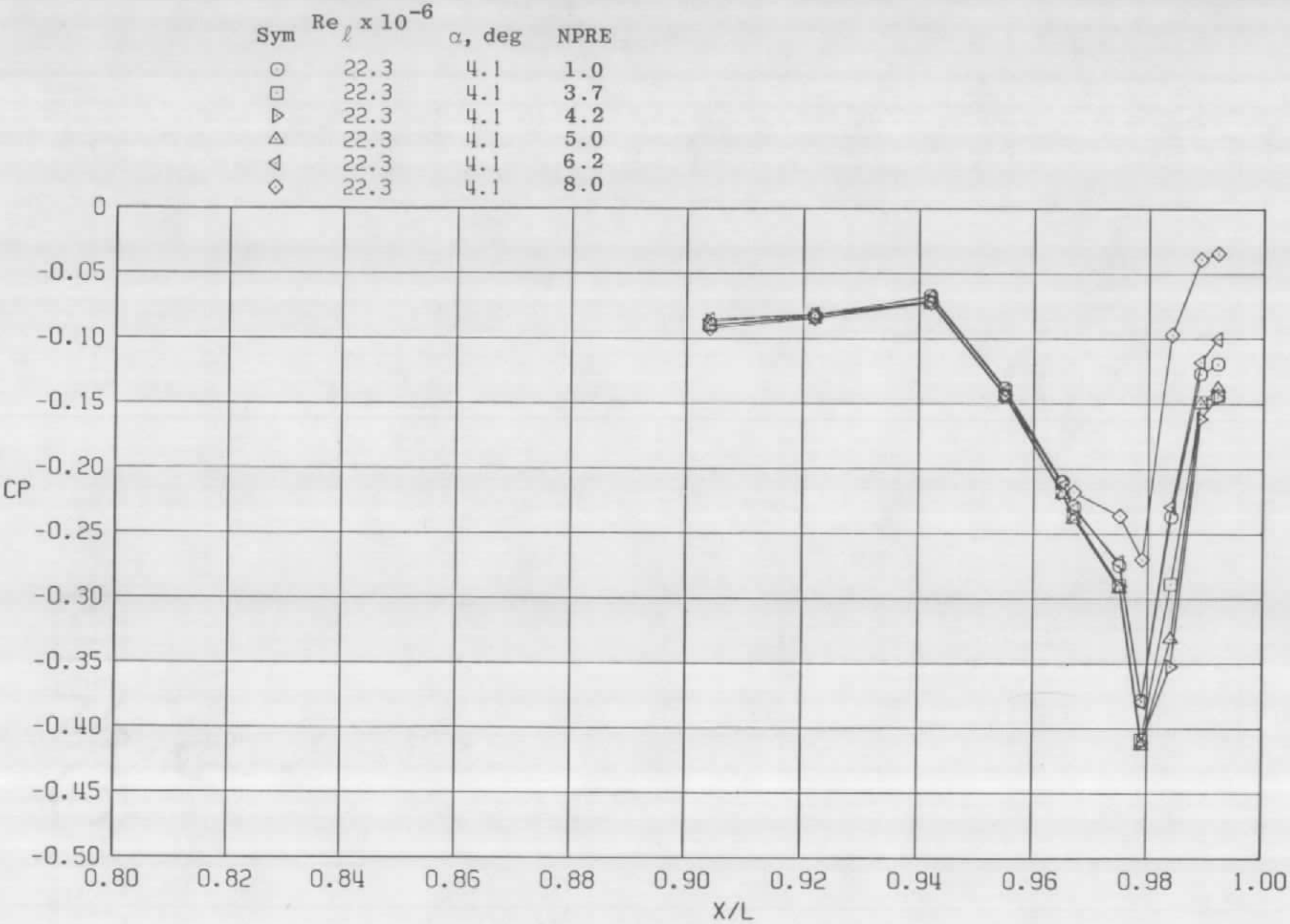

c. ϕ = 135 deg

Figure 24. Continued.

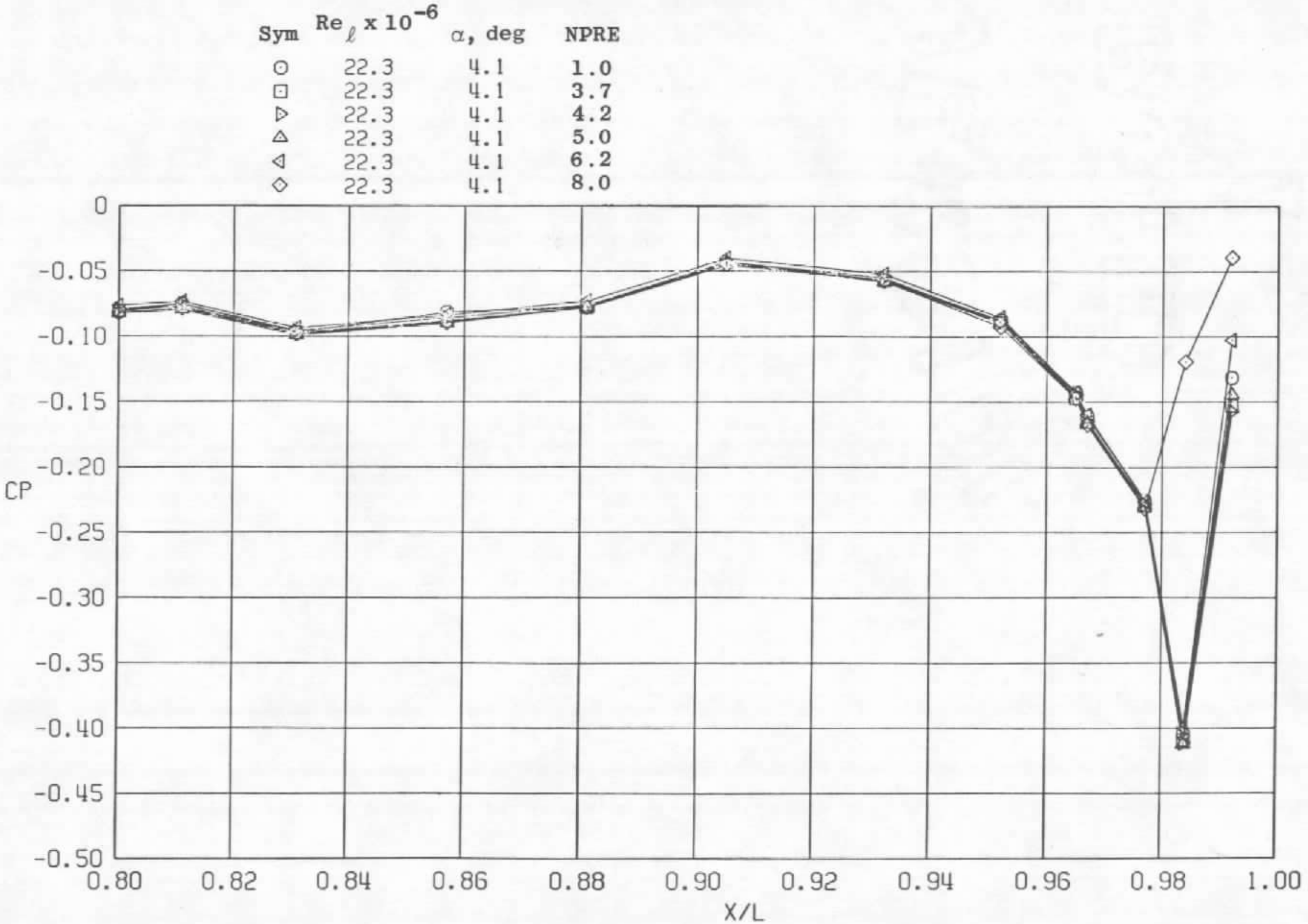

d. ϕ = 180 deg

Figure 24. Continued.

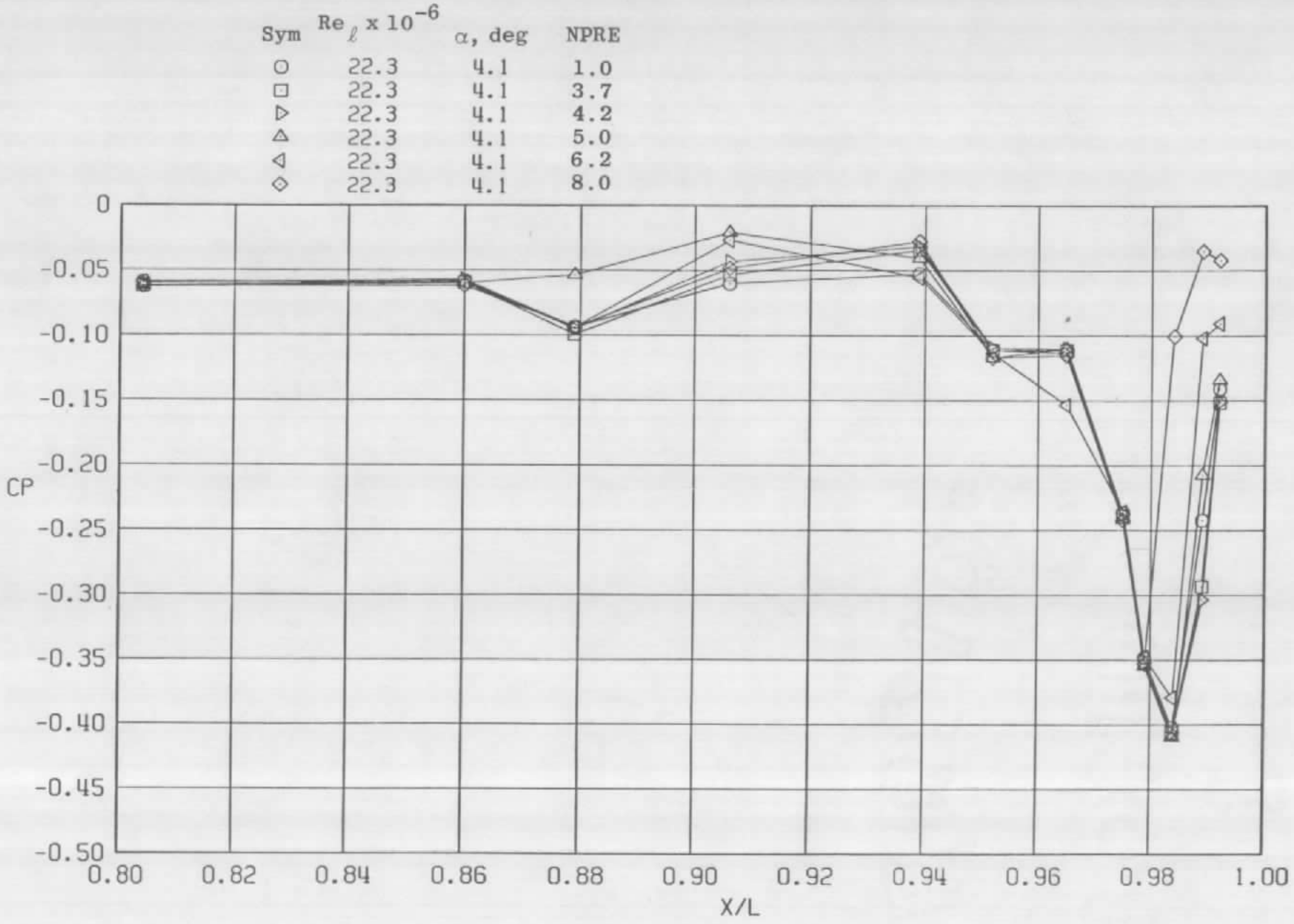

e. ϕ = 225 deg

Figure 24. Continued.

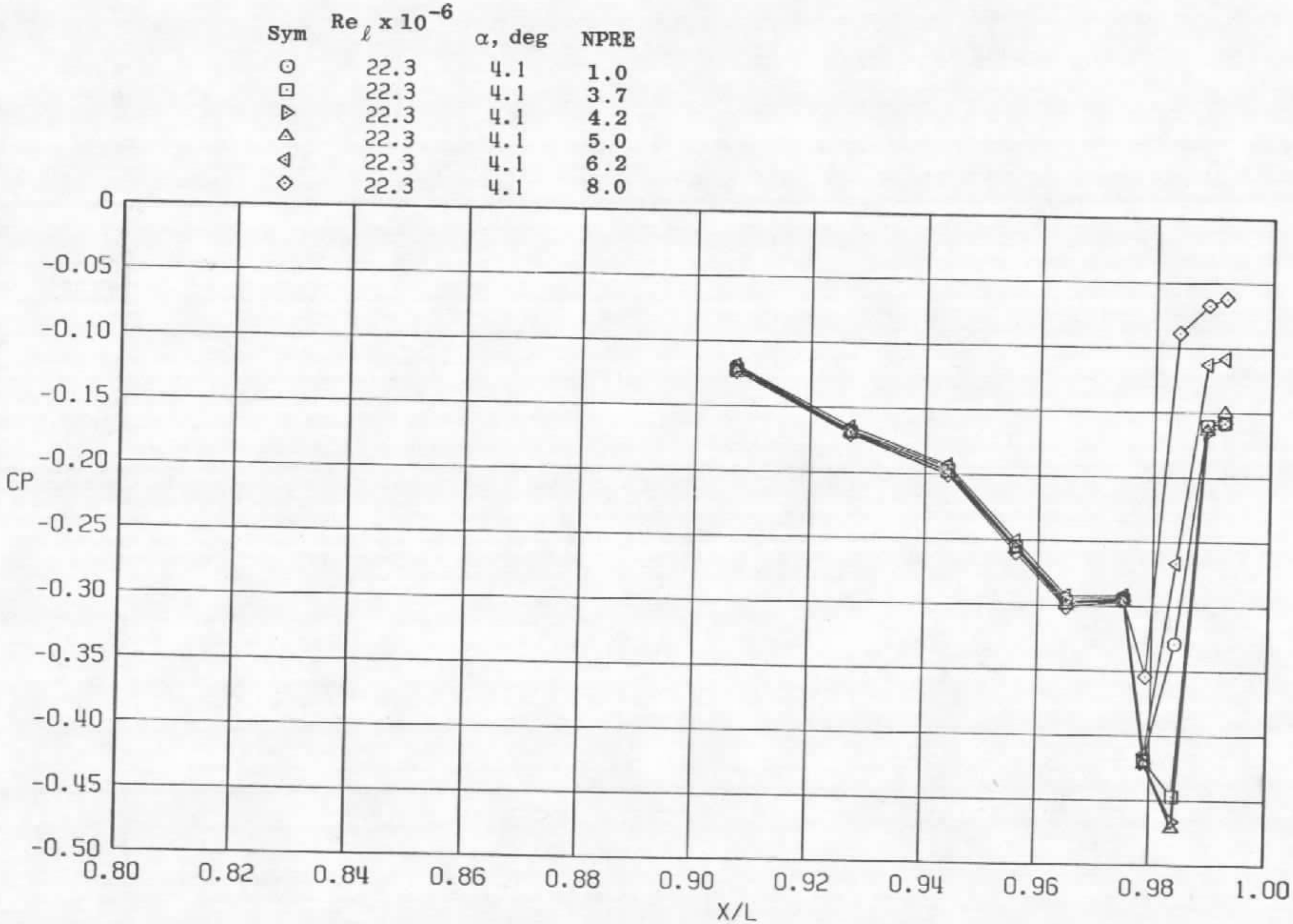

f. ϕ = 315 deg
Figure 24. Concluded.

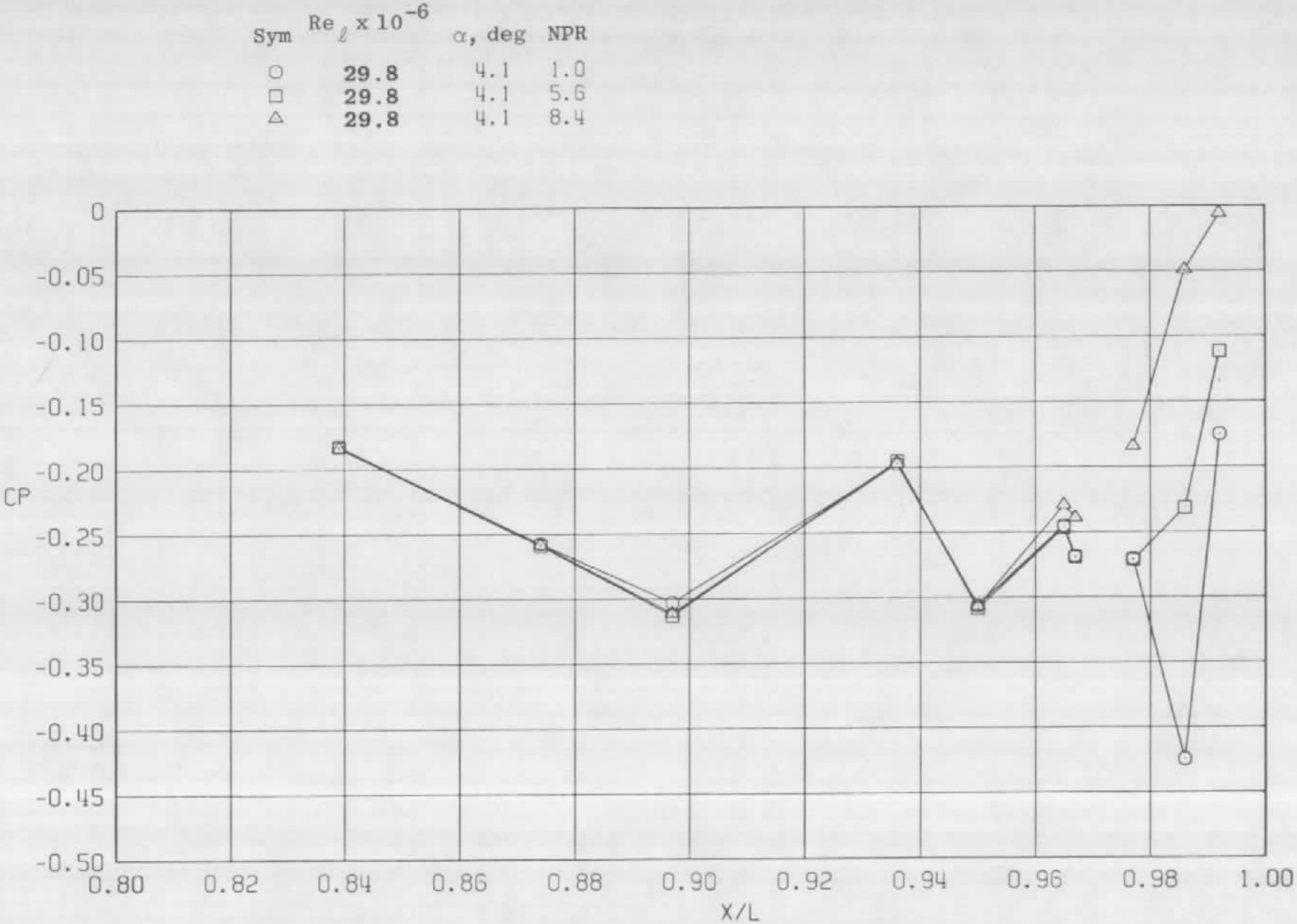

a. $\phi = 0$

Figure 25. Nozzle pressure ratio effects on surface pressure coefficients, A8 = 360 in.², M = 1.2 (WT).

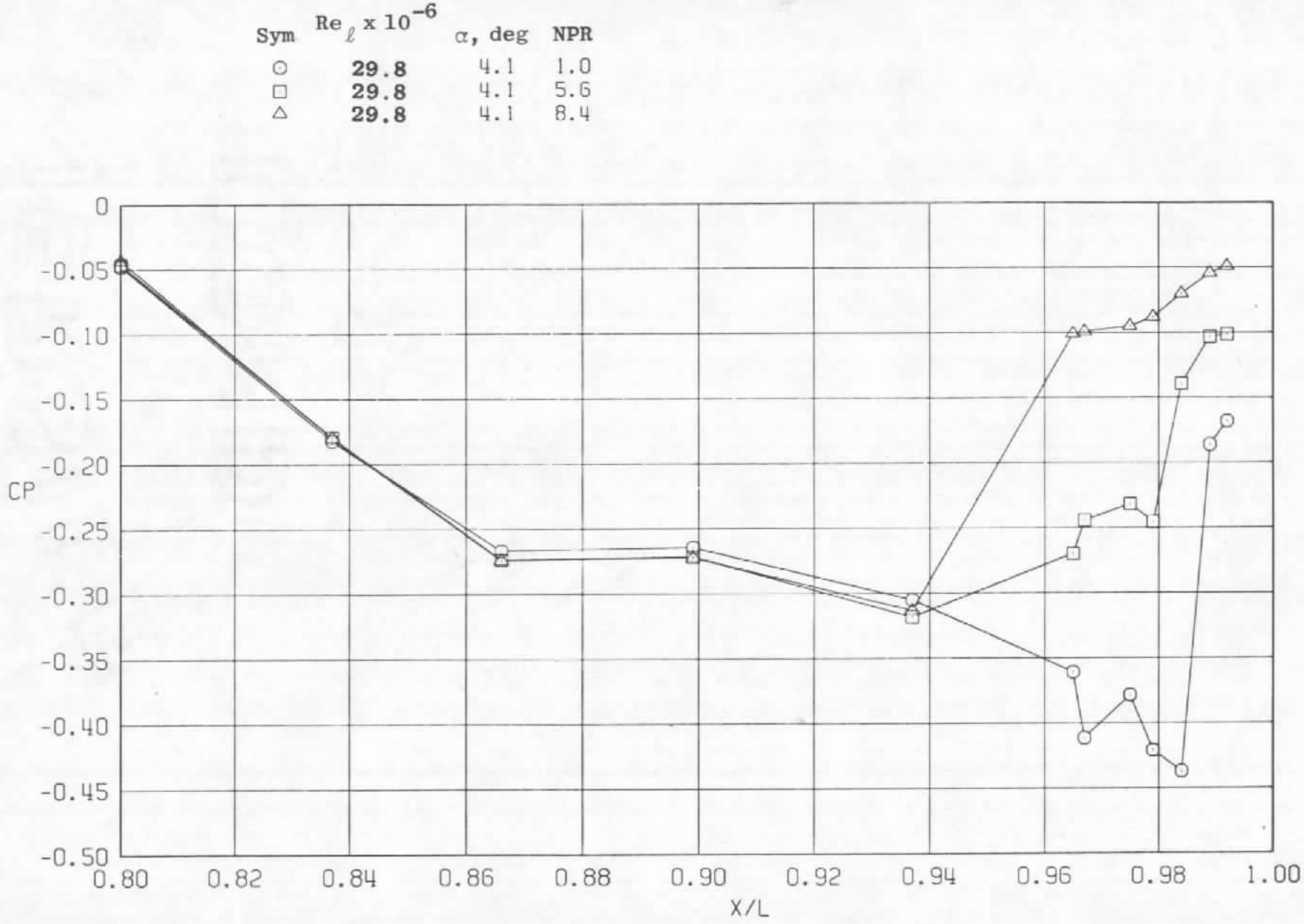

b. ϕ = 45 deg
Figure 25. Continued.

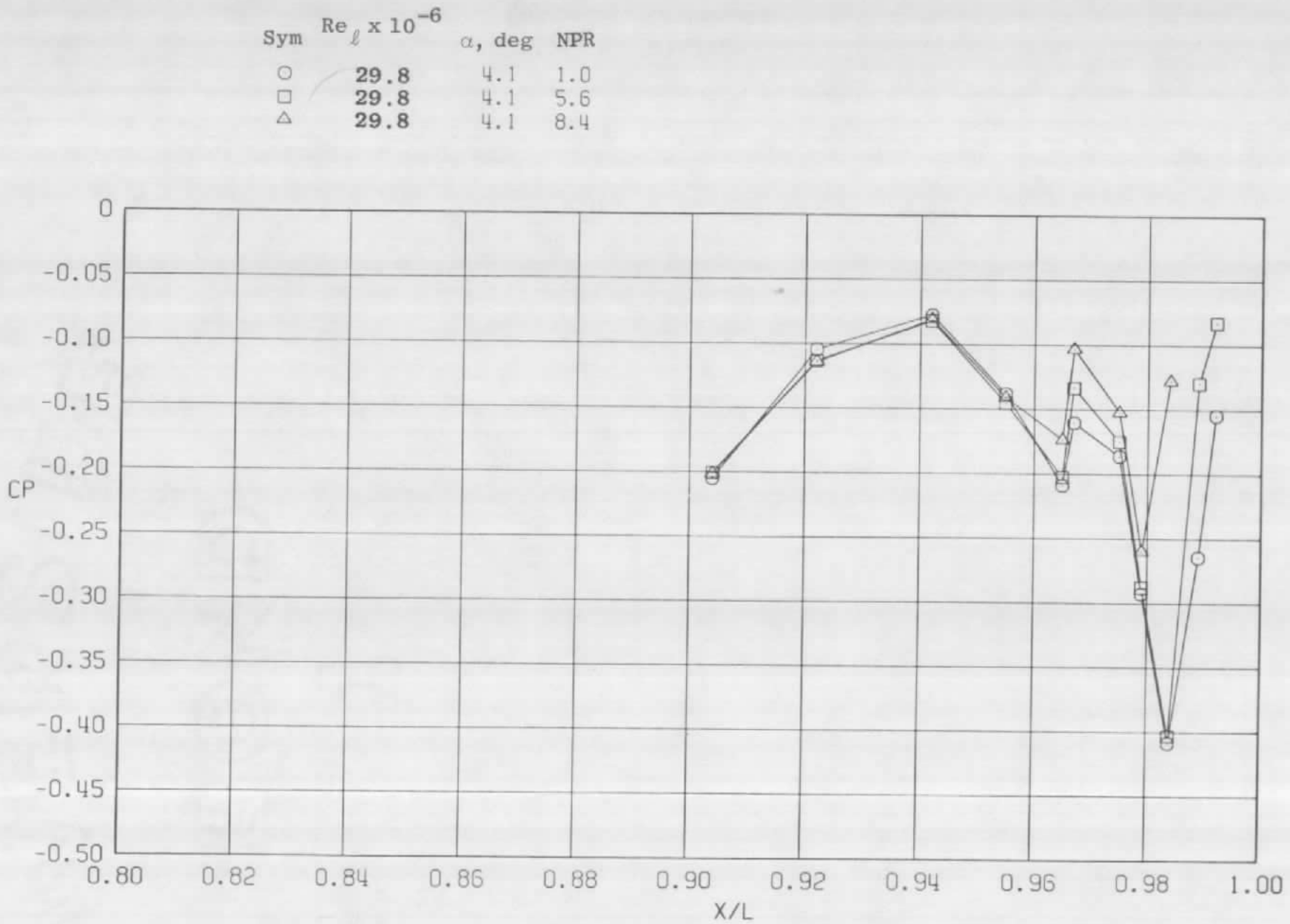

c. ϕ = 135 deg
Figure 25. Continued.

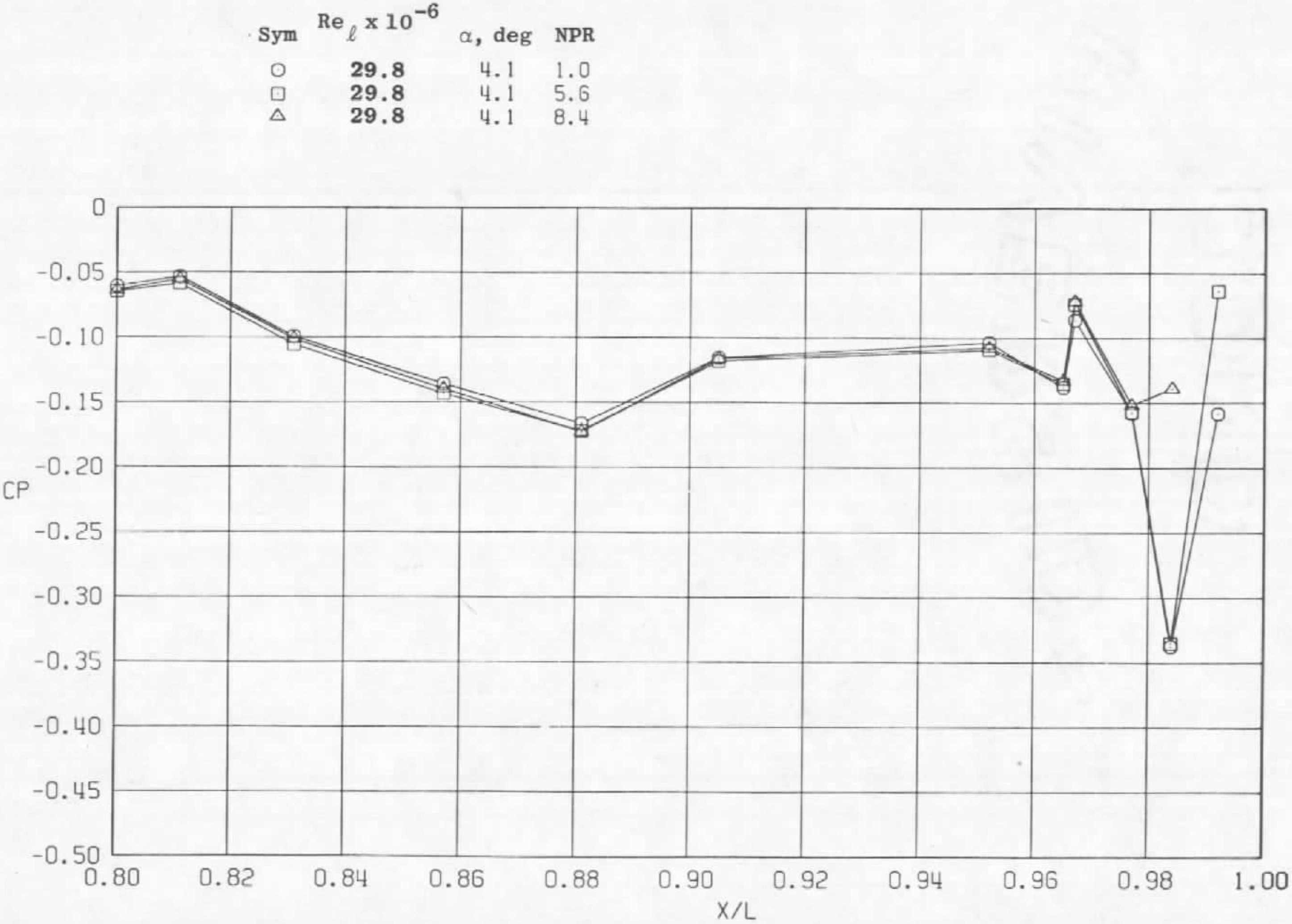

d. ϕ = 180 deg
Figure 25. Continued.

Sym	$Re_\ell \times 10^{-6}$	α, deg	NPR
○	29.8	4.1	1.0
□	29.8	4.1	5.6
△	29.8	4.1	8.4

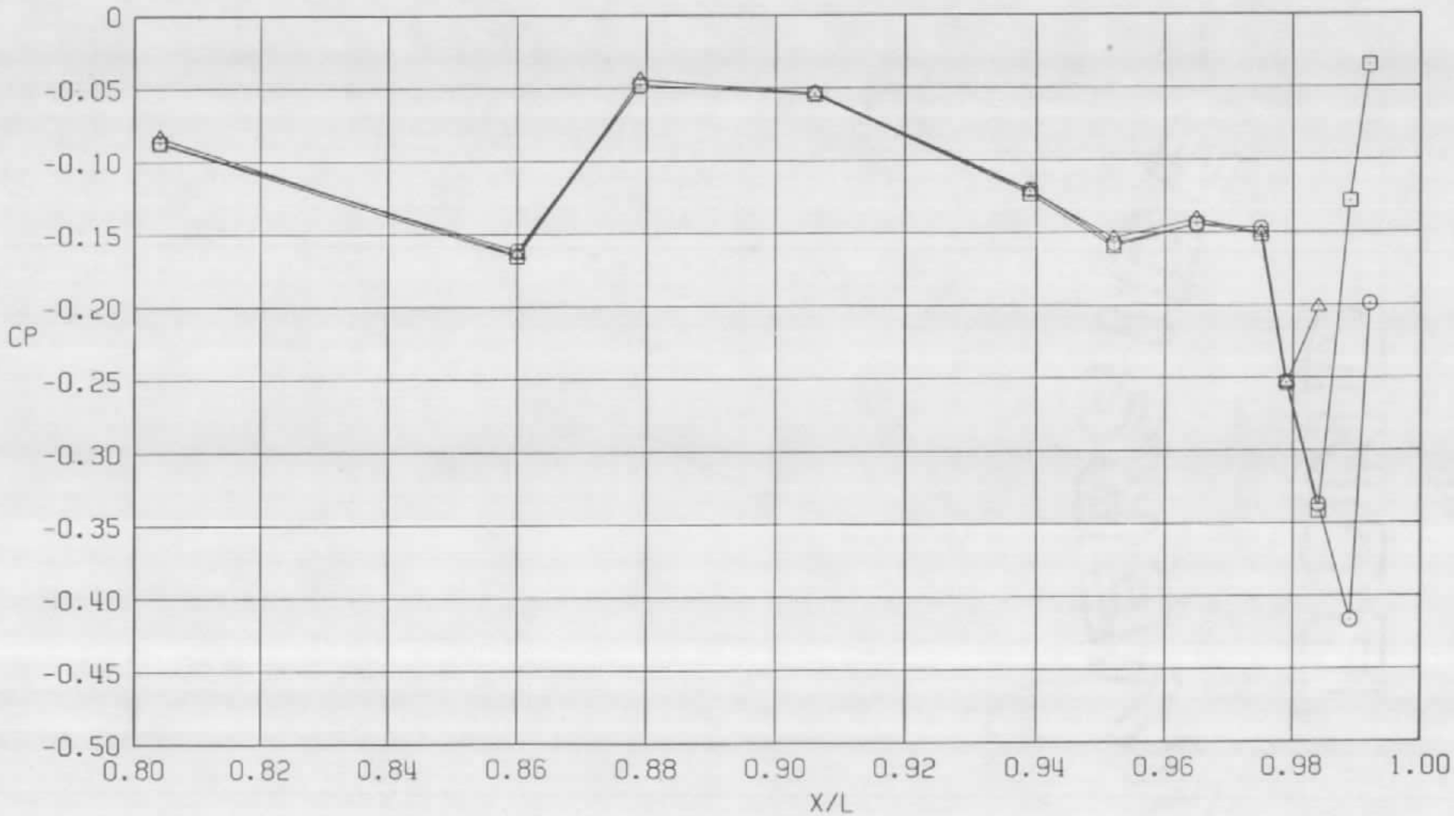

e. ϕ = 225 deg
Figure 25. Continued.

Sym	$Re_{\ell} \times 10^{-6}$	α, deg	NPR
○	29.8	4.1	1.0
□	29.8	4.1	5.6
△	29.8	4.1	8.4

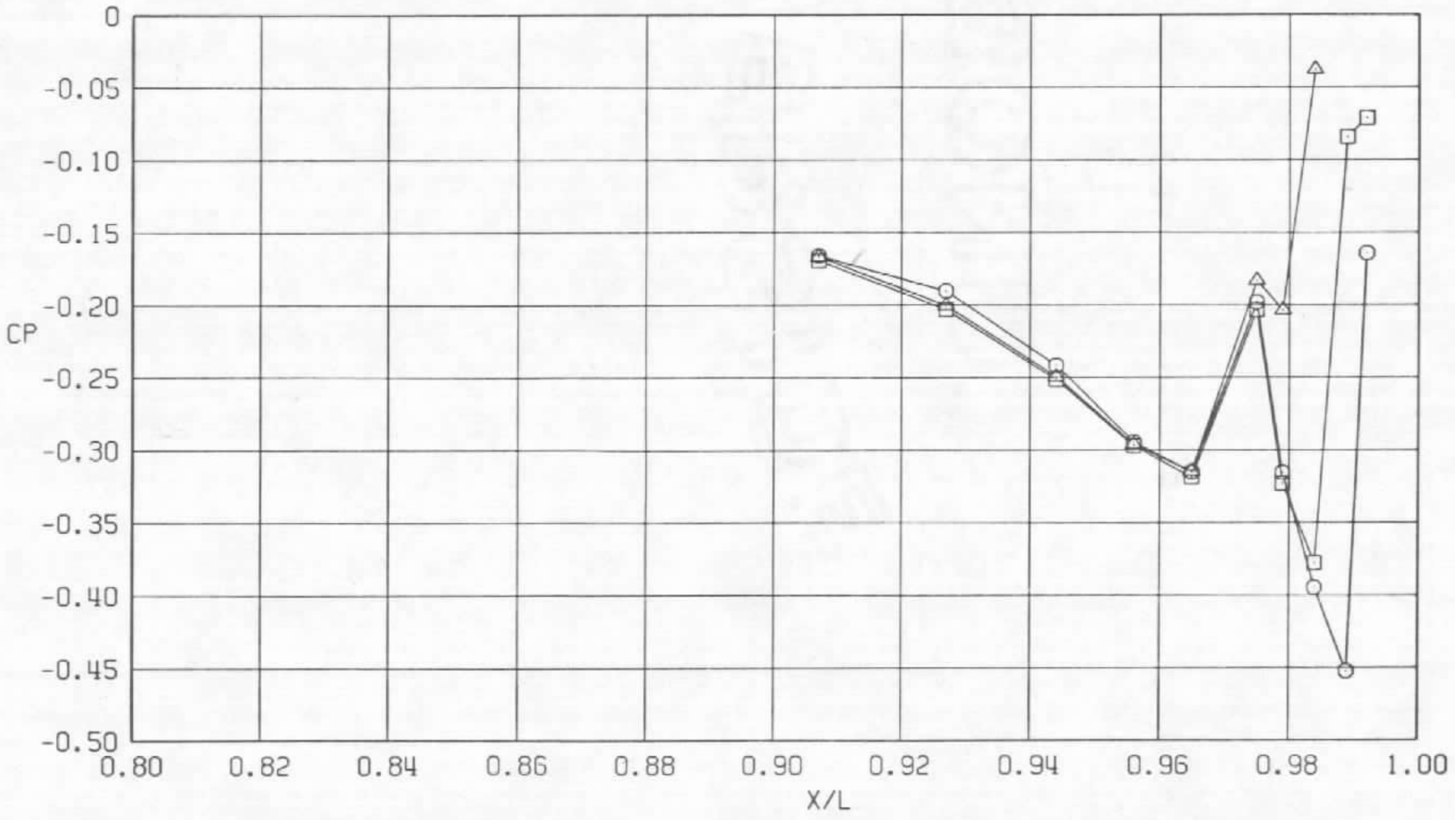

f. ϕ = 315 deg
Figure 25. Concluded.

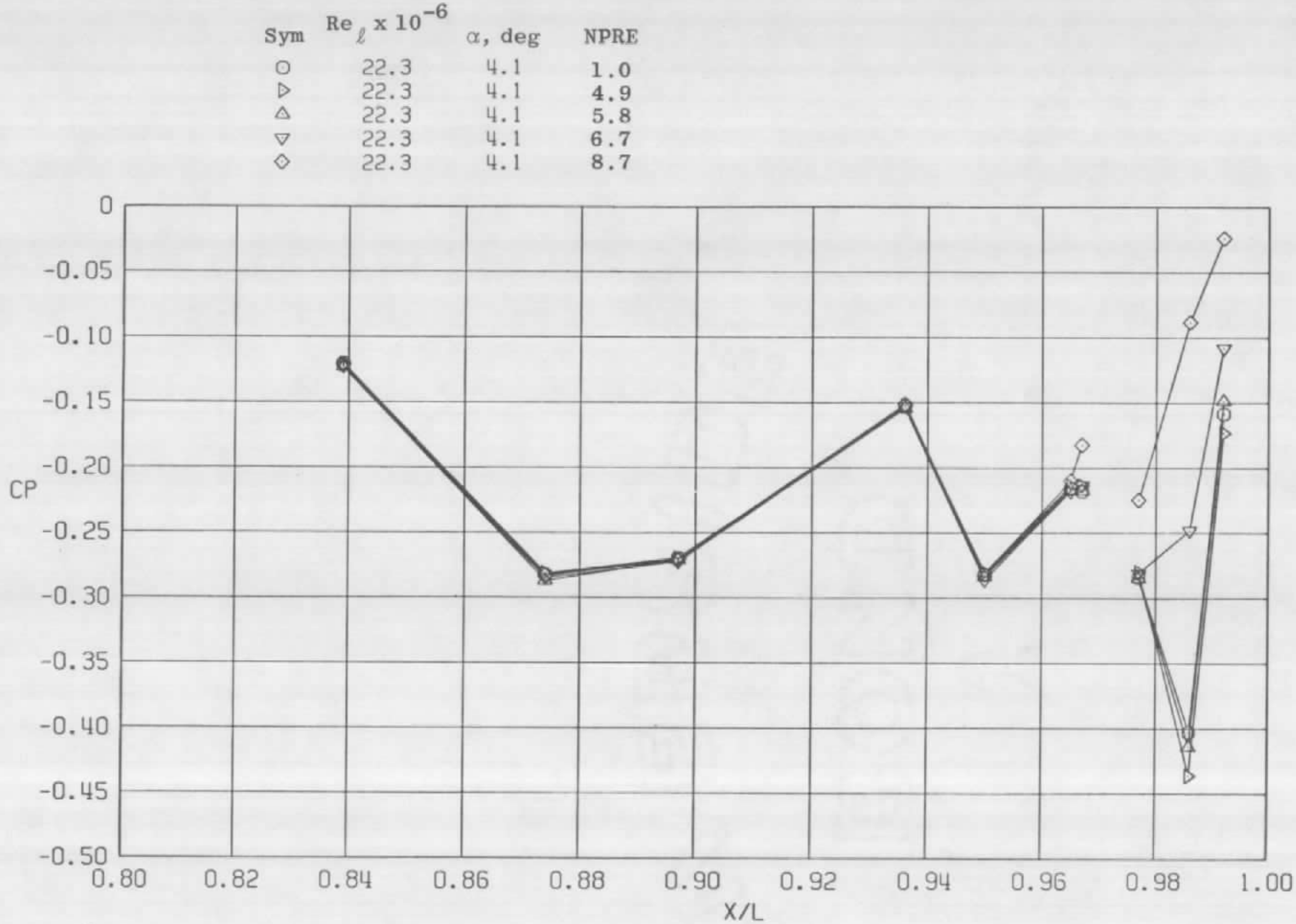

a. $\phi = 0$

Figure 26. Effective nozzle pressure ratio effects on surface pressure coefficients, A8 = 360 in.², M = 1.2 (SS).

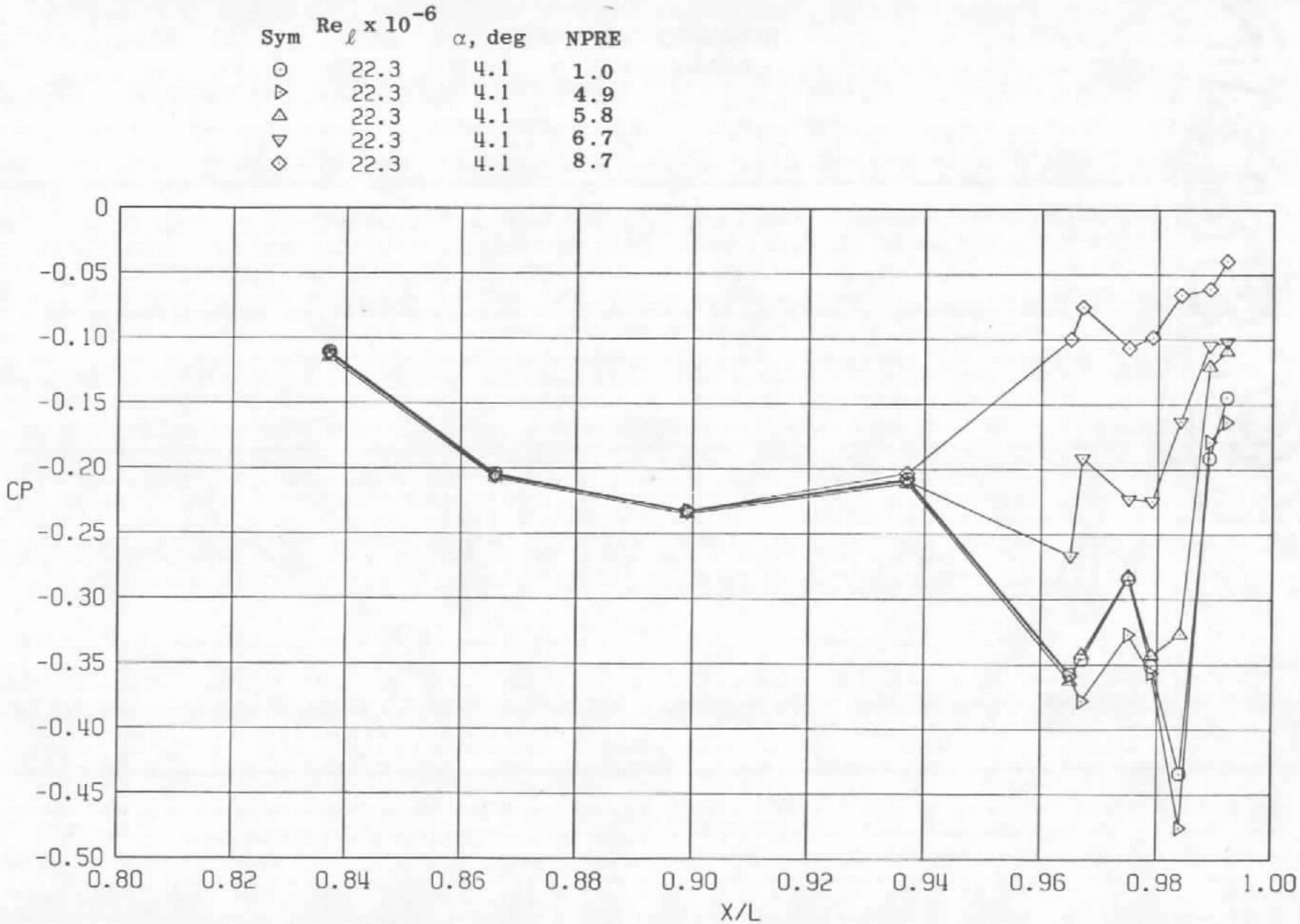

b. ϕ = 45 deg

Figure 26. Continued.

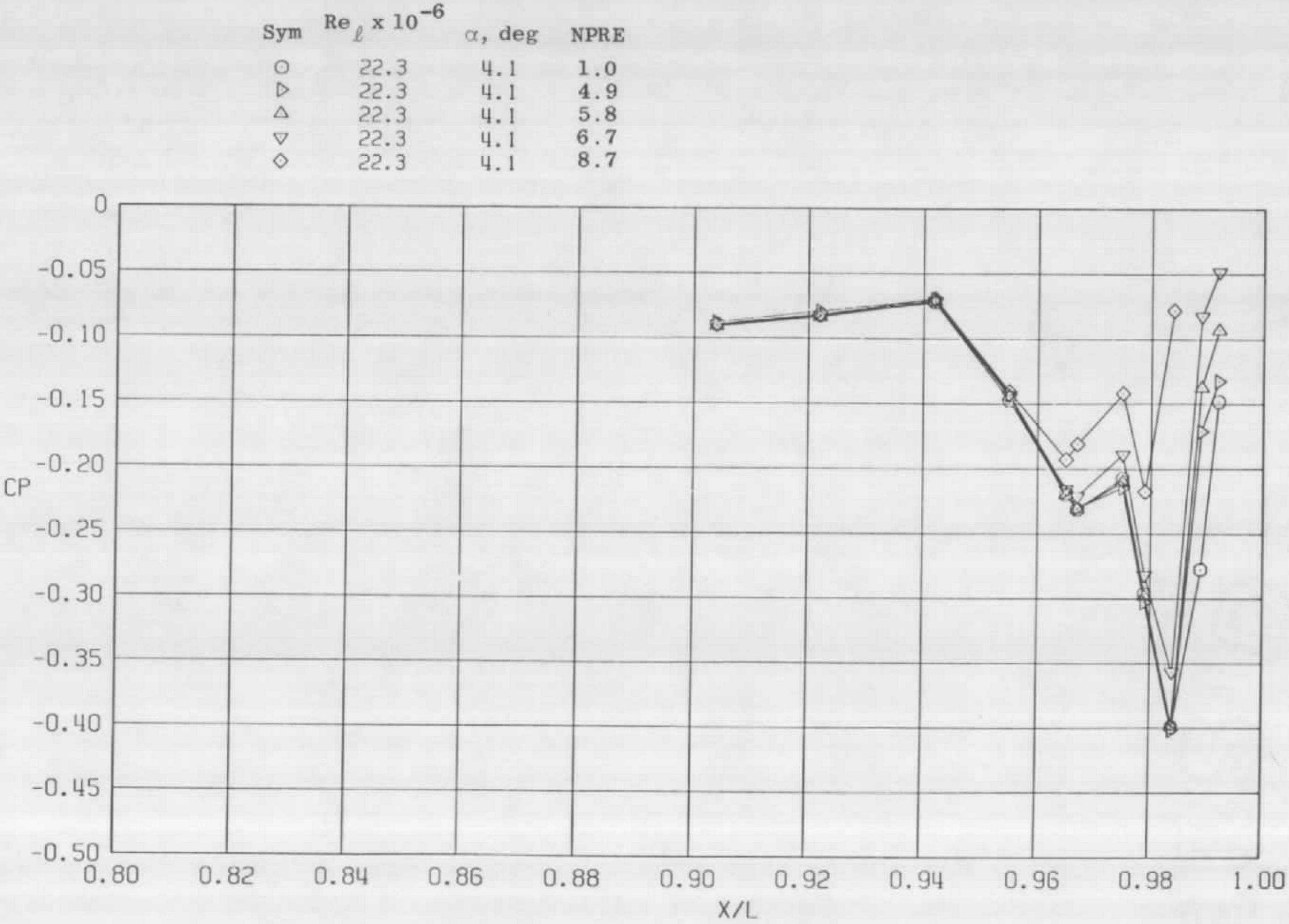

c. ϕ = 135 deg

Figure 26. Continued.

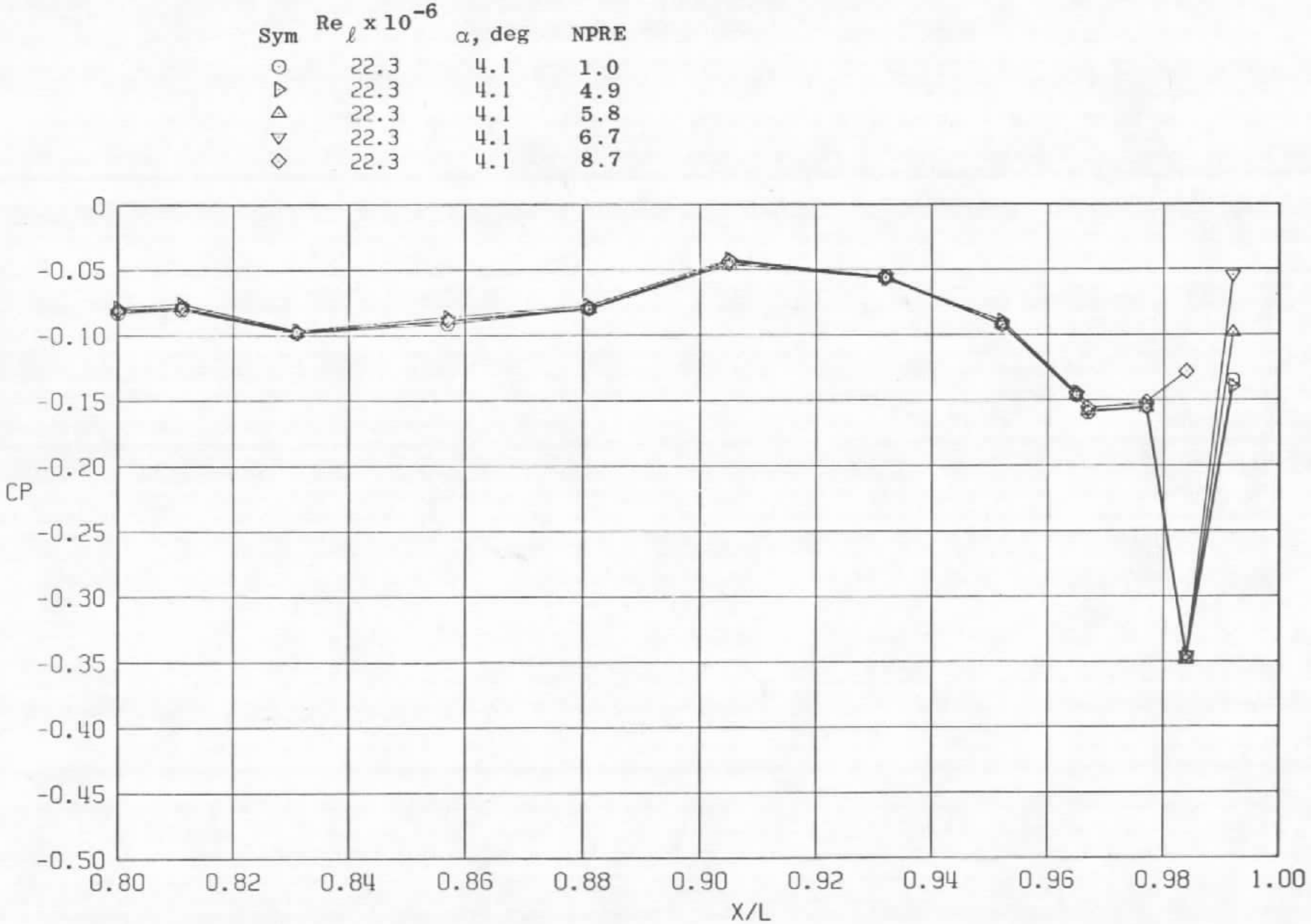

d. ϕ = 180 deg
Figure 26. Continued.

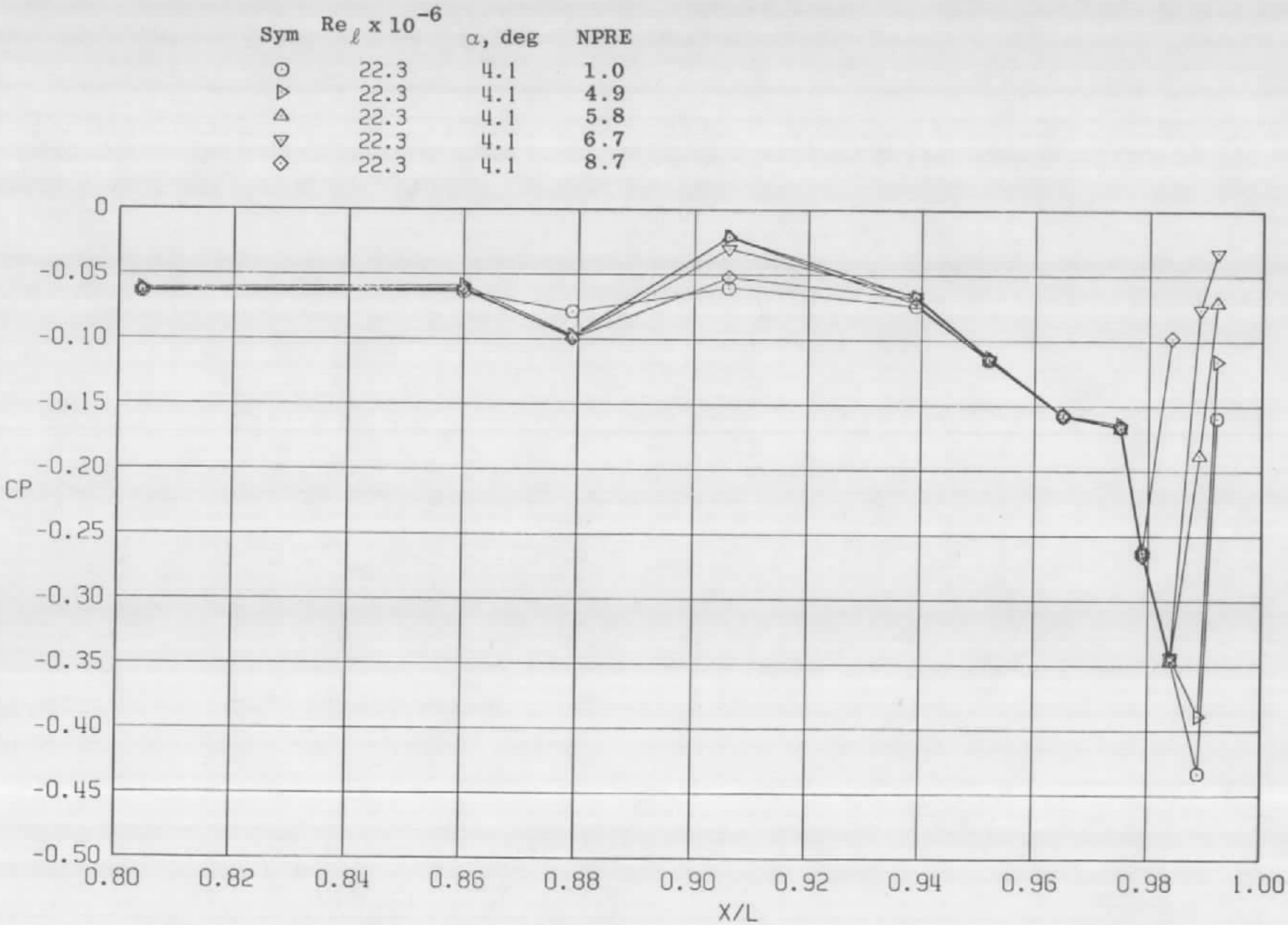

e. ϕ = 225 deg
Figure 26. Continued.

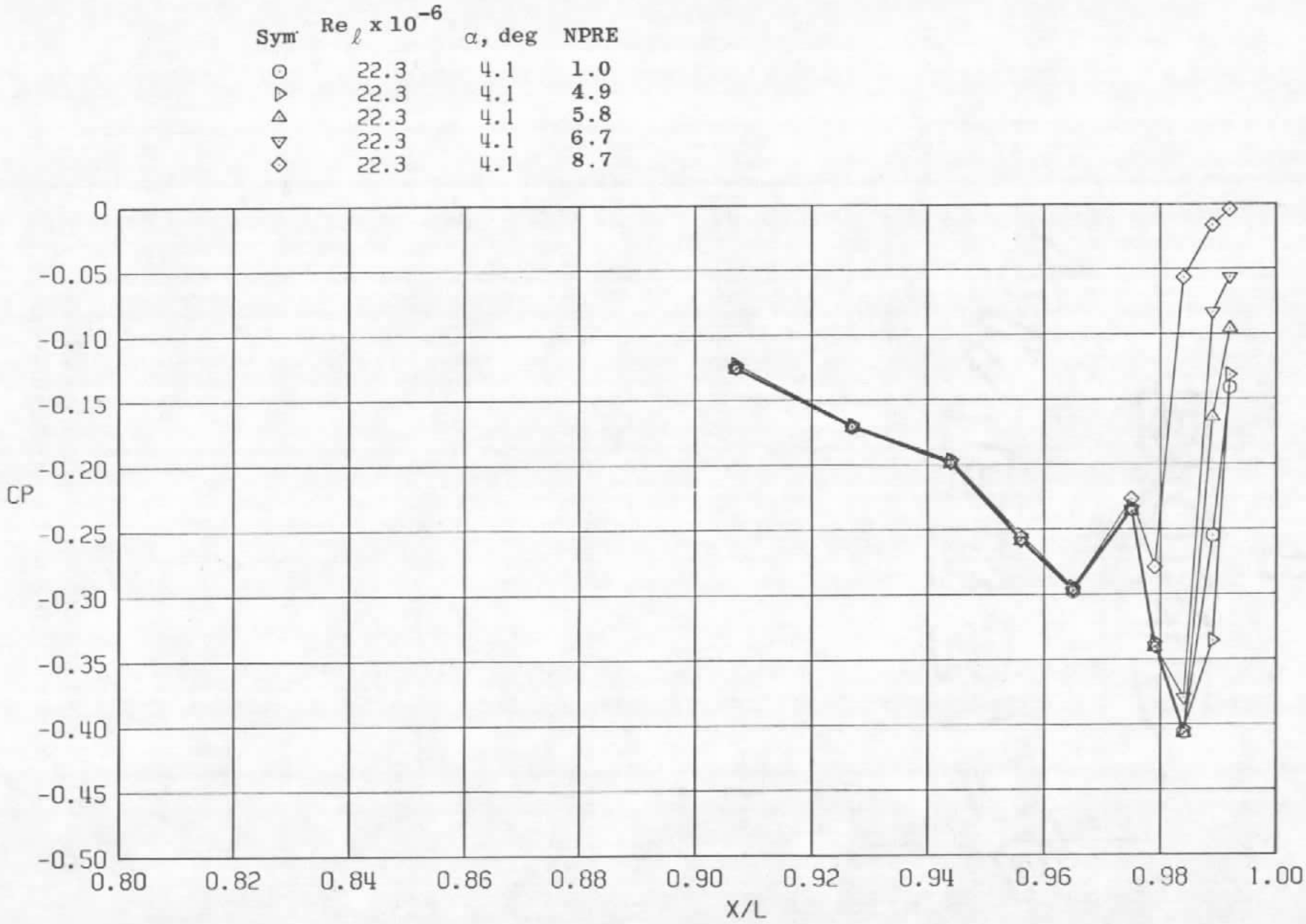

f. ϕ = 315 deg
Figure 26. Concluded.

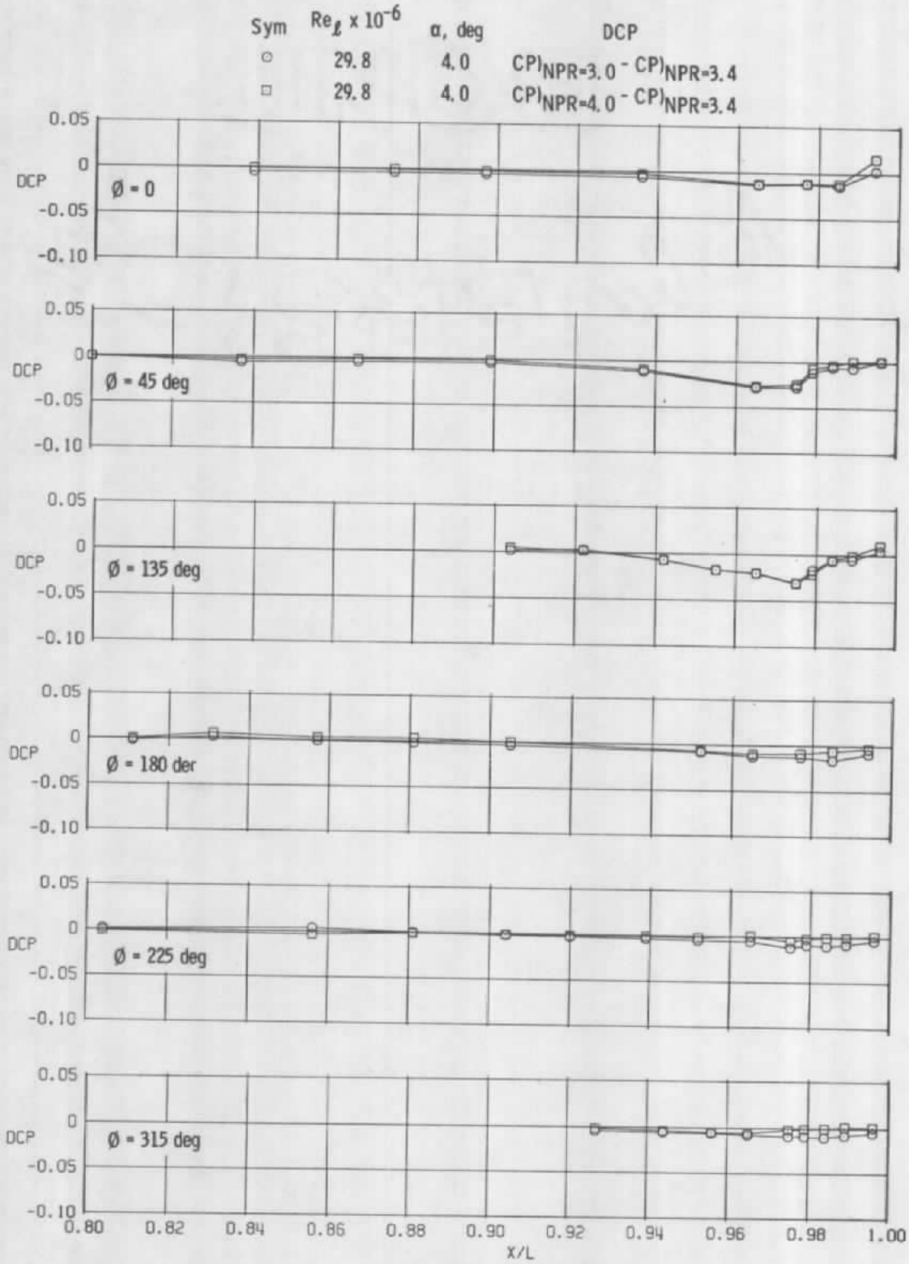

a. M = 0.6, A8 = 200 in.^{2}

Figure 27. Effect of incremental nozzle pressure ratio changes on surface pressure coefficients (WT).

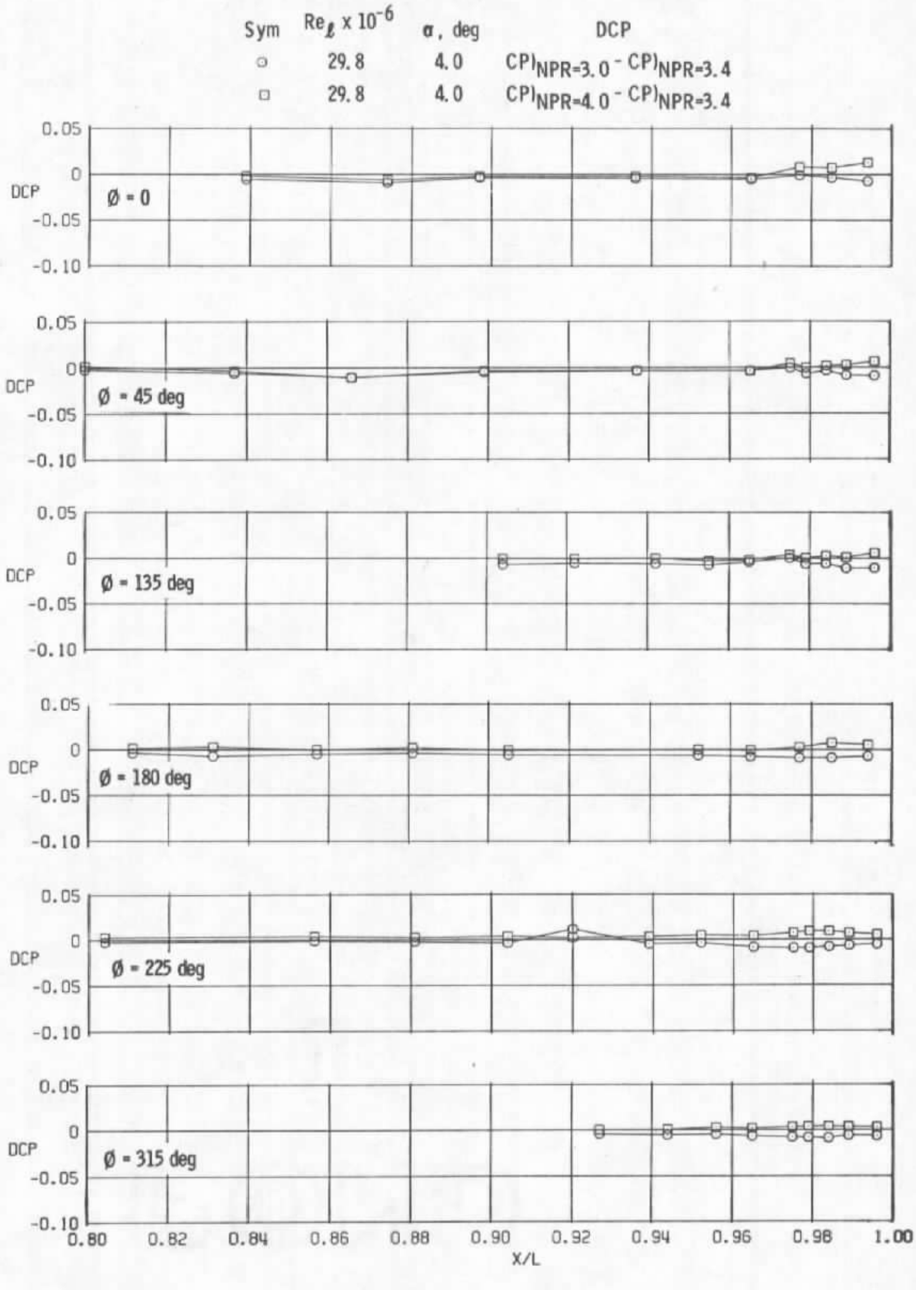

b. M = 0.9, A8 = 200 in.^{2}

Figure 27. Continued.

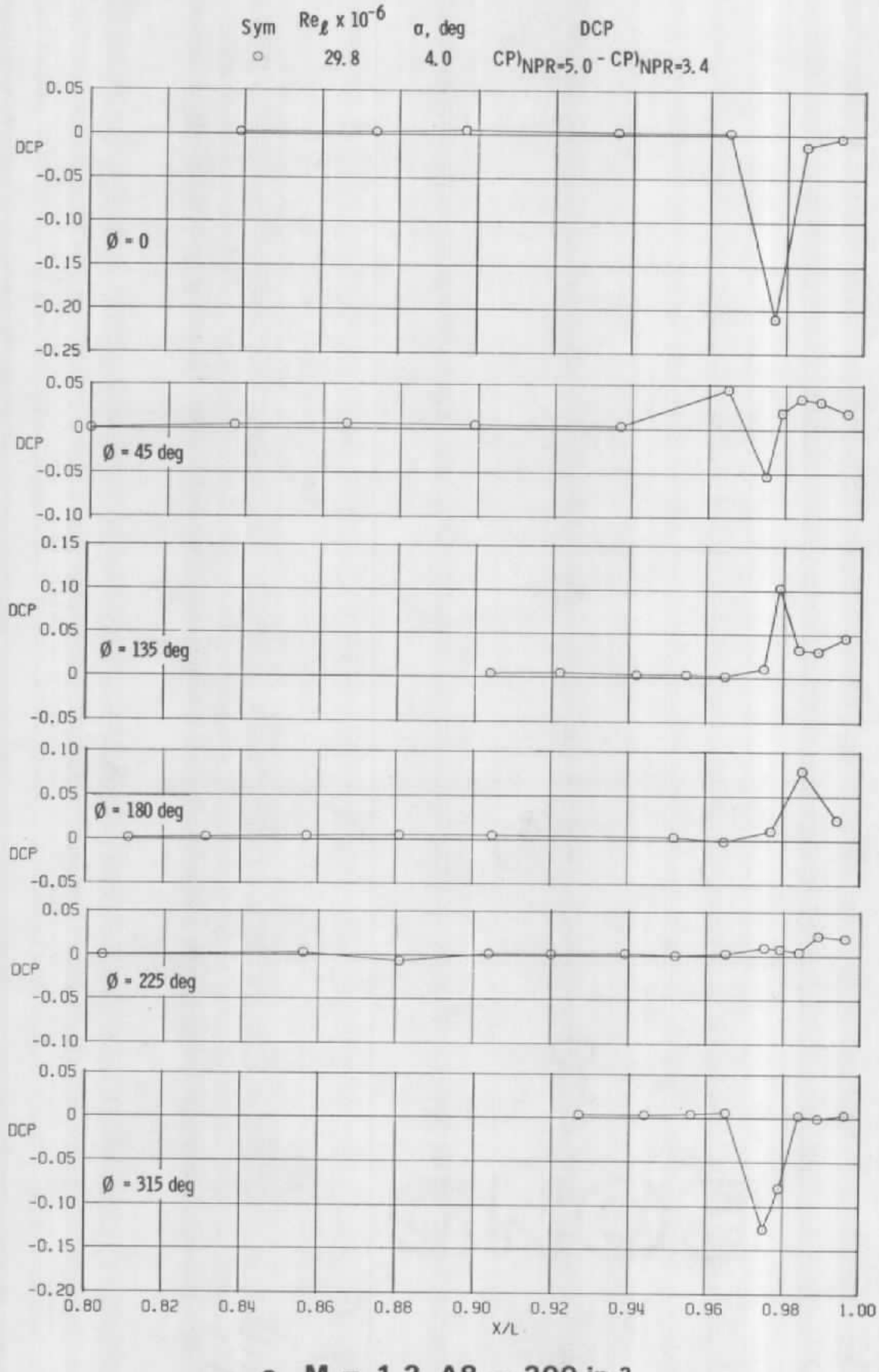

c. M = 1.2, A8 = 200 in.²
Figure 27. Continued.

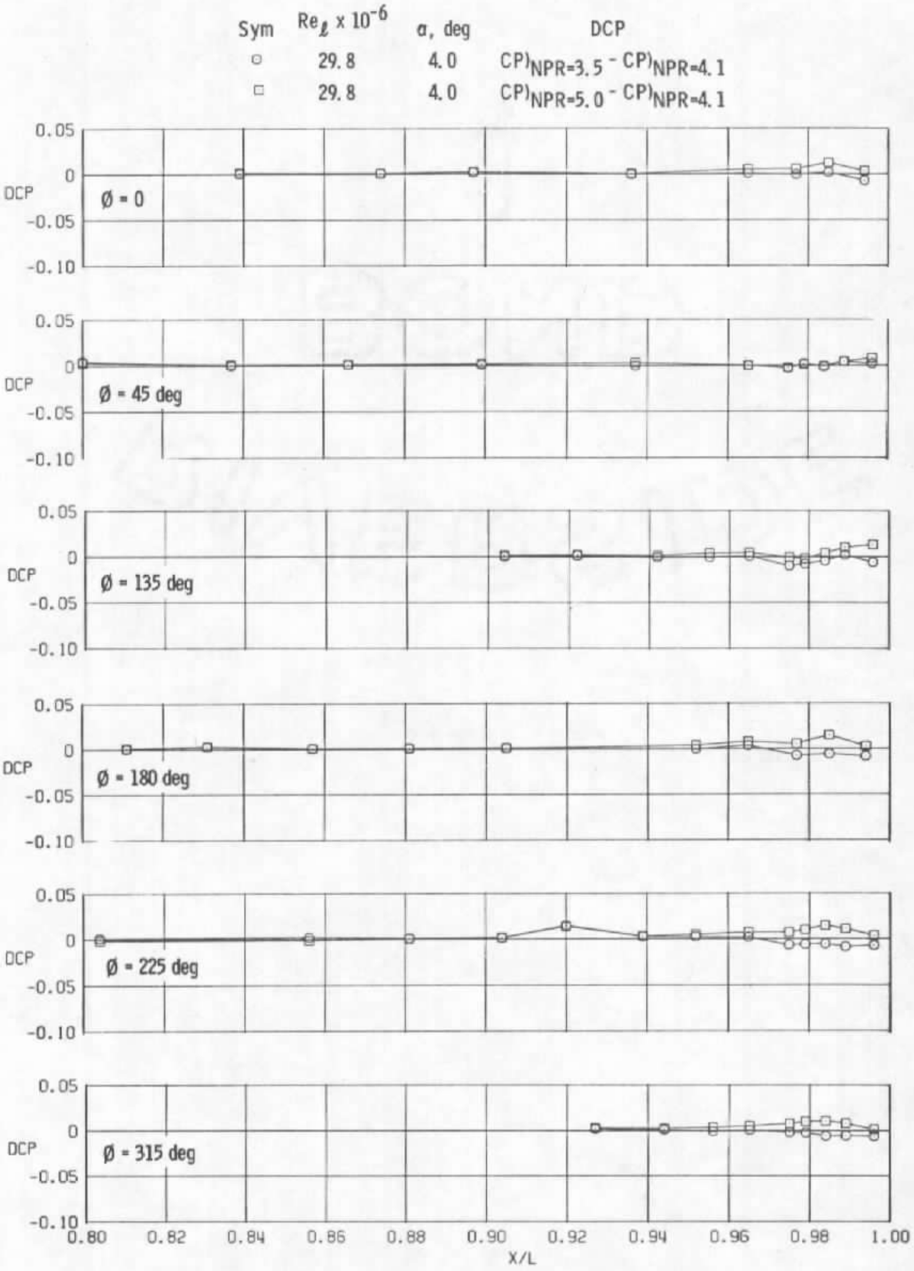

d. M = 0.6, A8 = 230 in.^{2}
Figure 27. Continued.

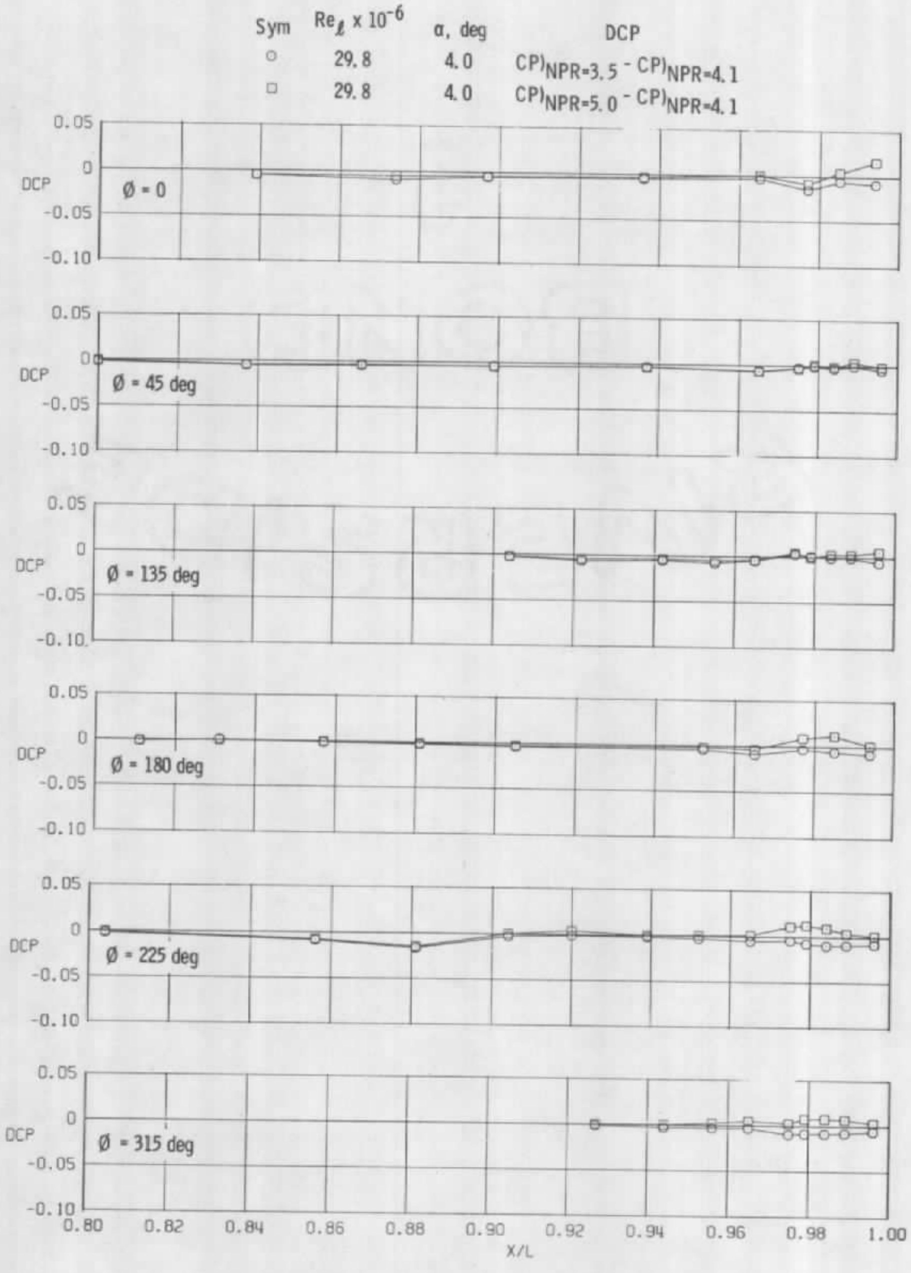

e. M = 0.9, A8 = 230 in.^{2}
Figure 27. Continued.

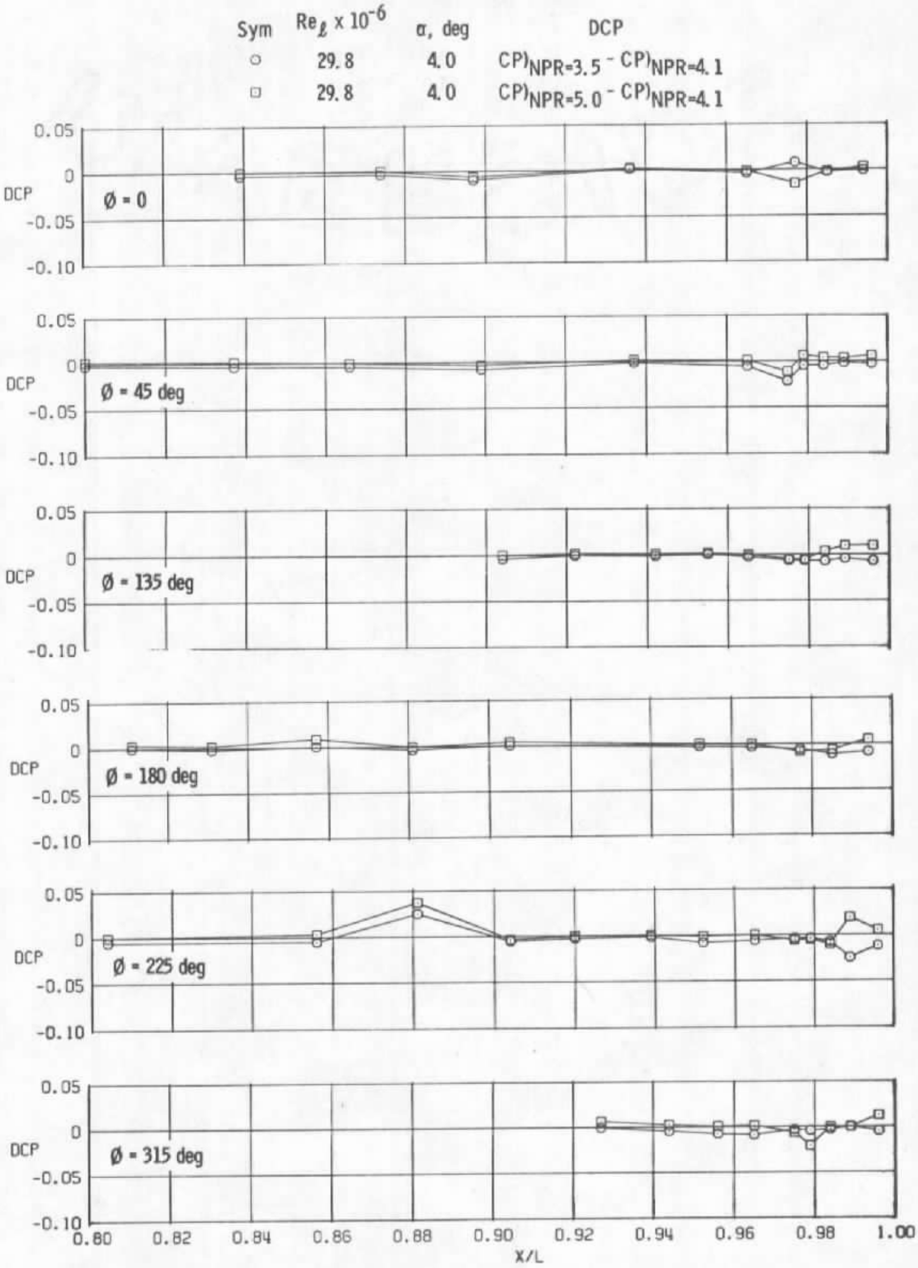

f. M = 1.2, A8 = 230 in.^{2}
Figure 27. Continued.

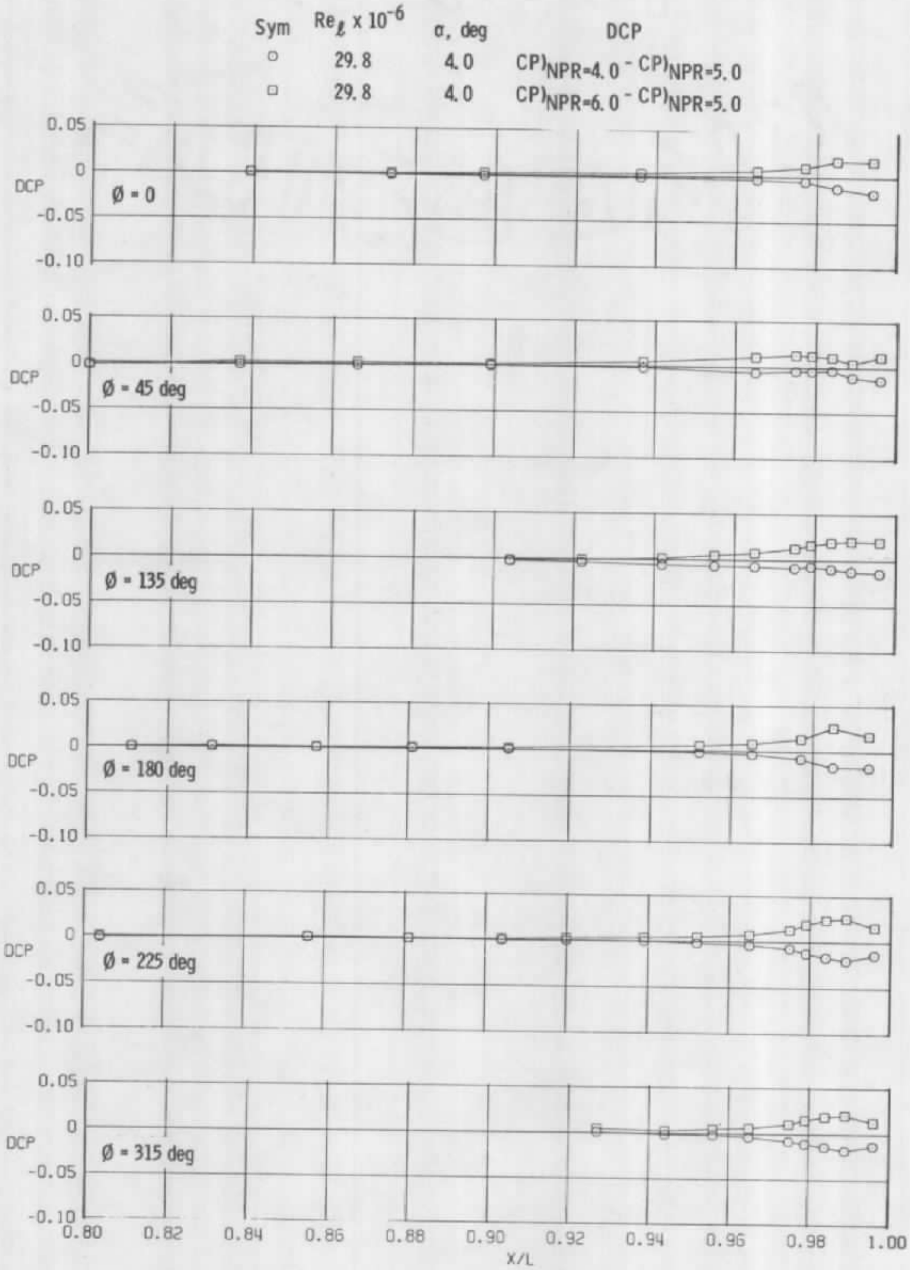

g. M = 0.6, A8 = 300 in.²
Figure 27. Continued.

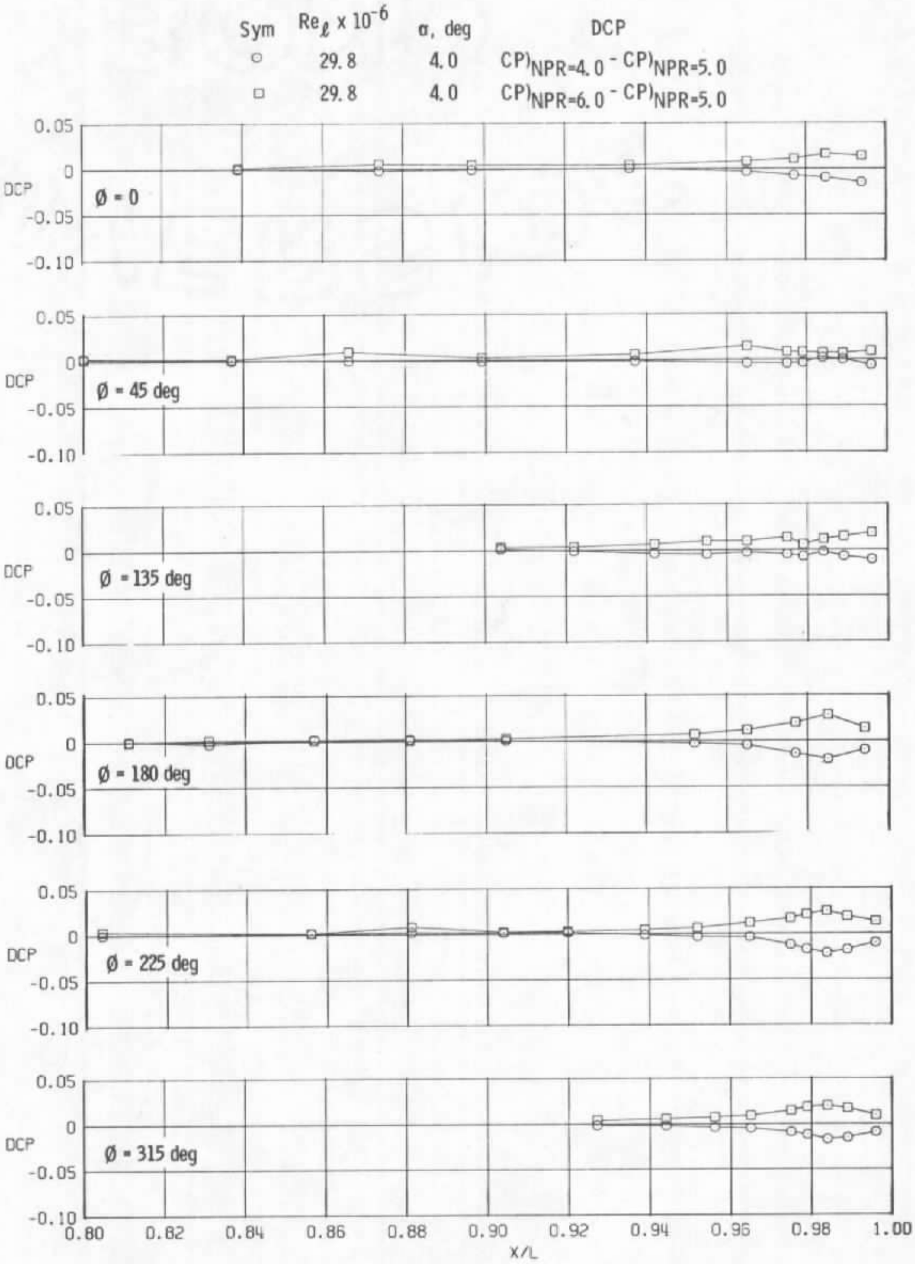

h. M = 0.9, A8 = 300 in.²
Figure 27. Continued.

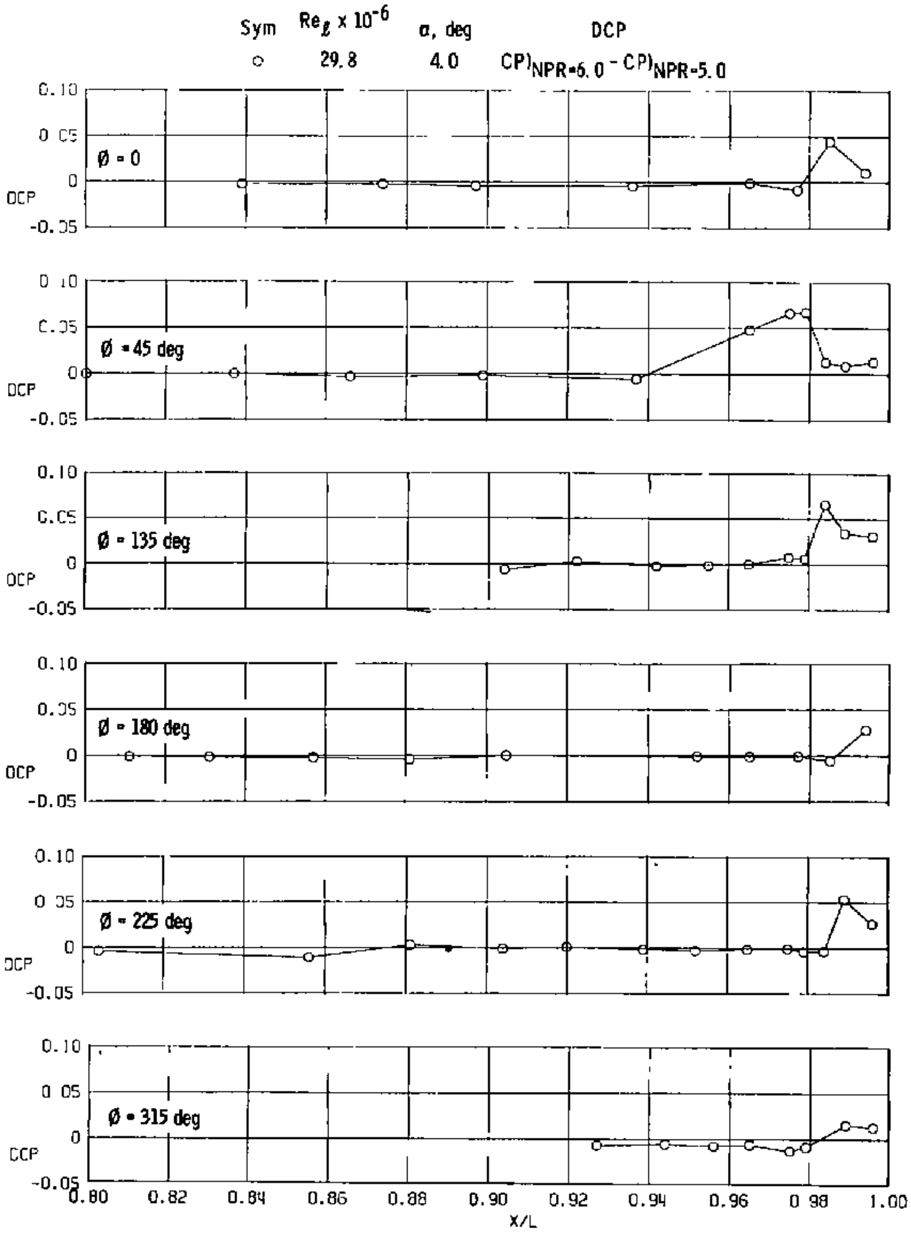

i. M = 1.2, A8 = 300 in.²
Figure 27. Continued.

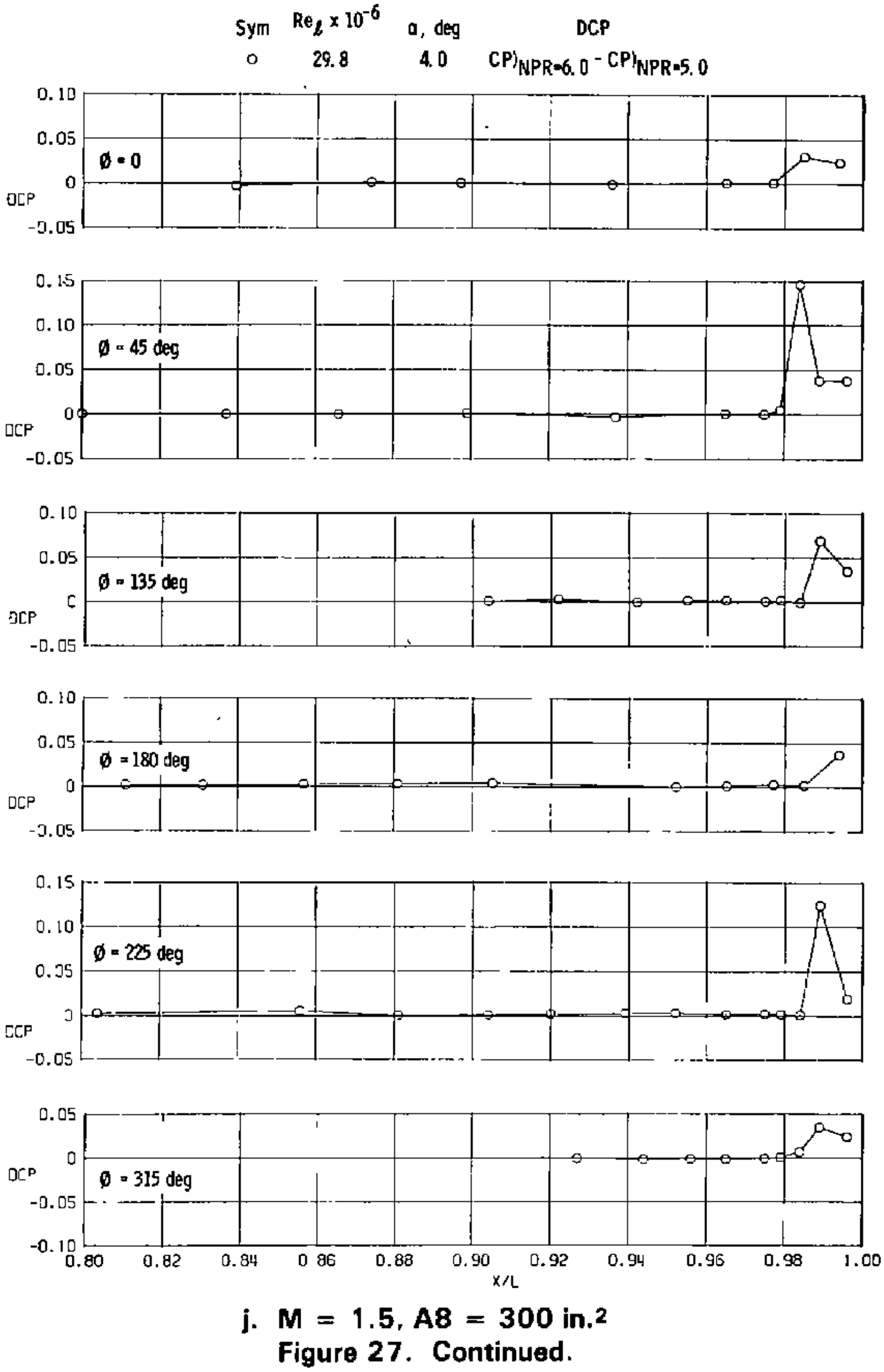

j. M = 1.5, A8 = 300 in.²
Figure 27. Continued.

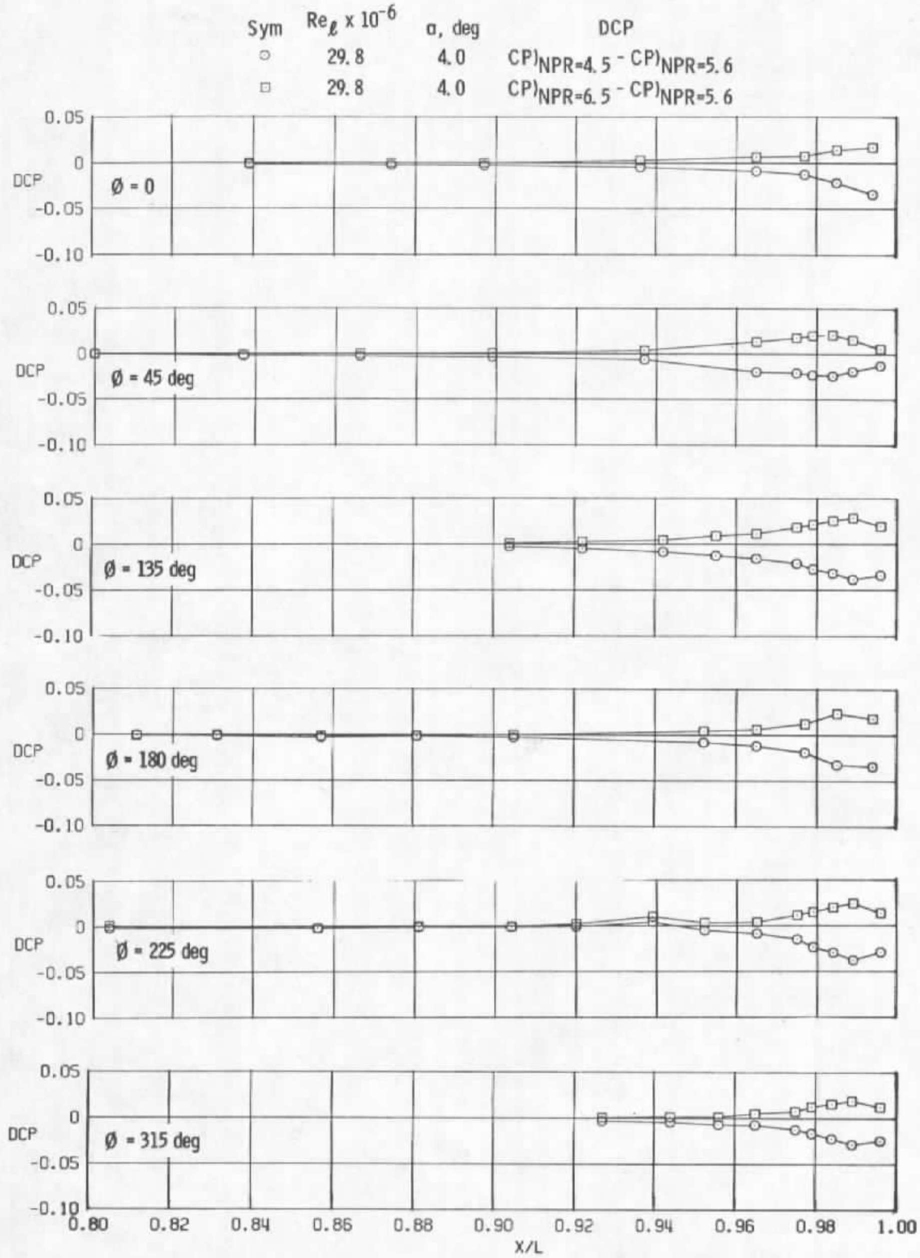

k. M = 0.6, A8 = 360 in.²
Figure 27. Continued.

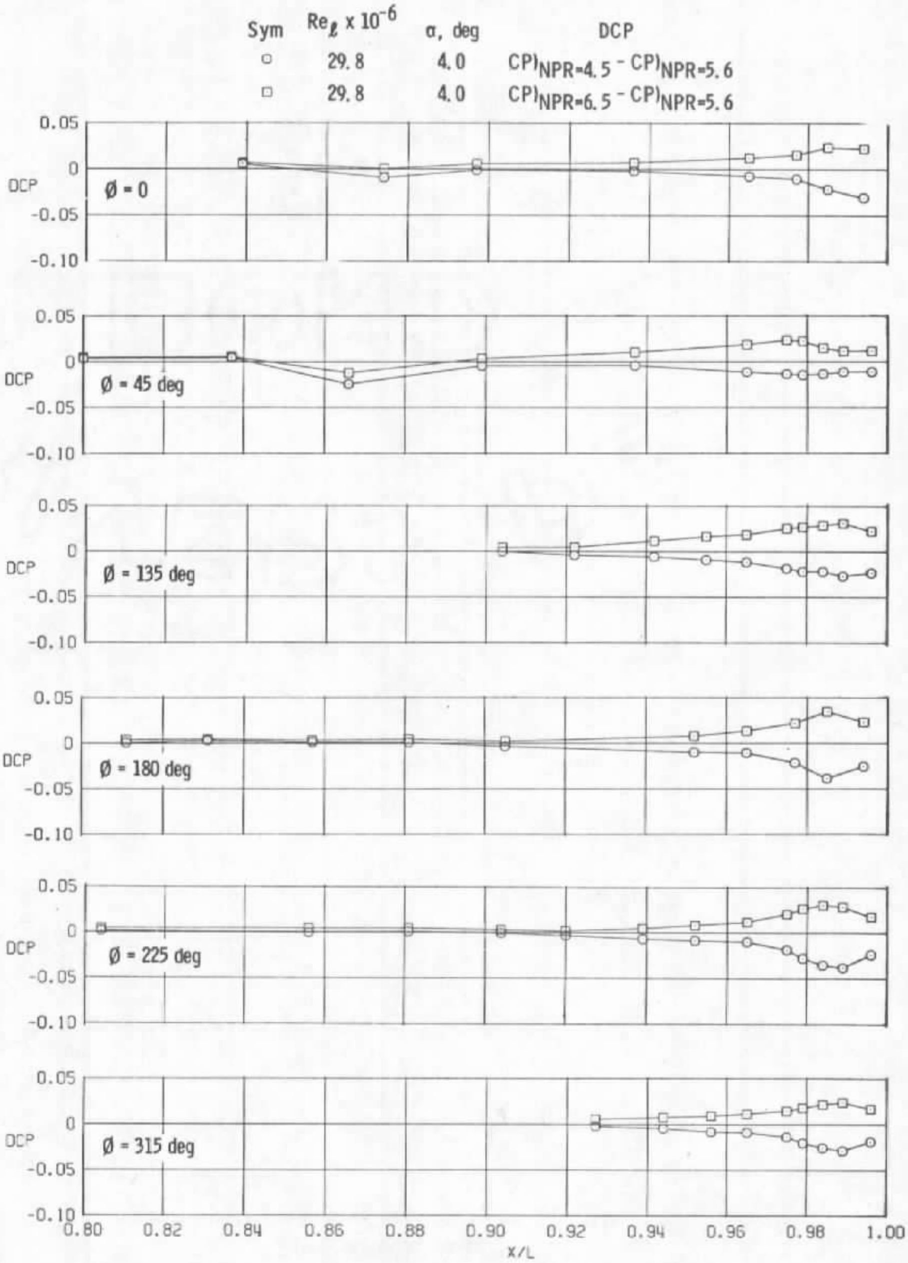

l. M = 0.9, A8 = 360 in.^{2}
Figure 27. Continued.

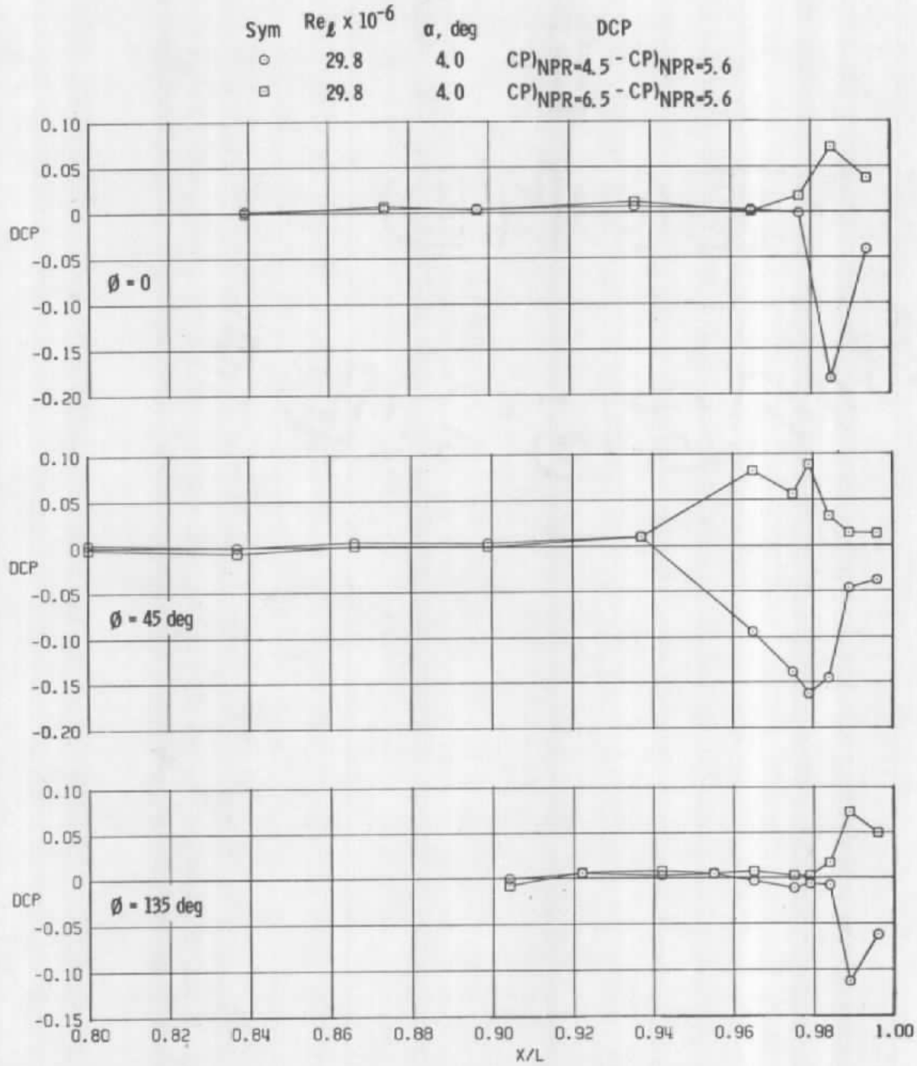

m. M = 1.2, A8 = 360 in.²
Figure 27. Continued.

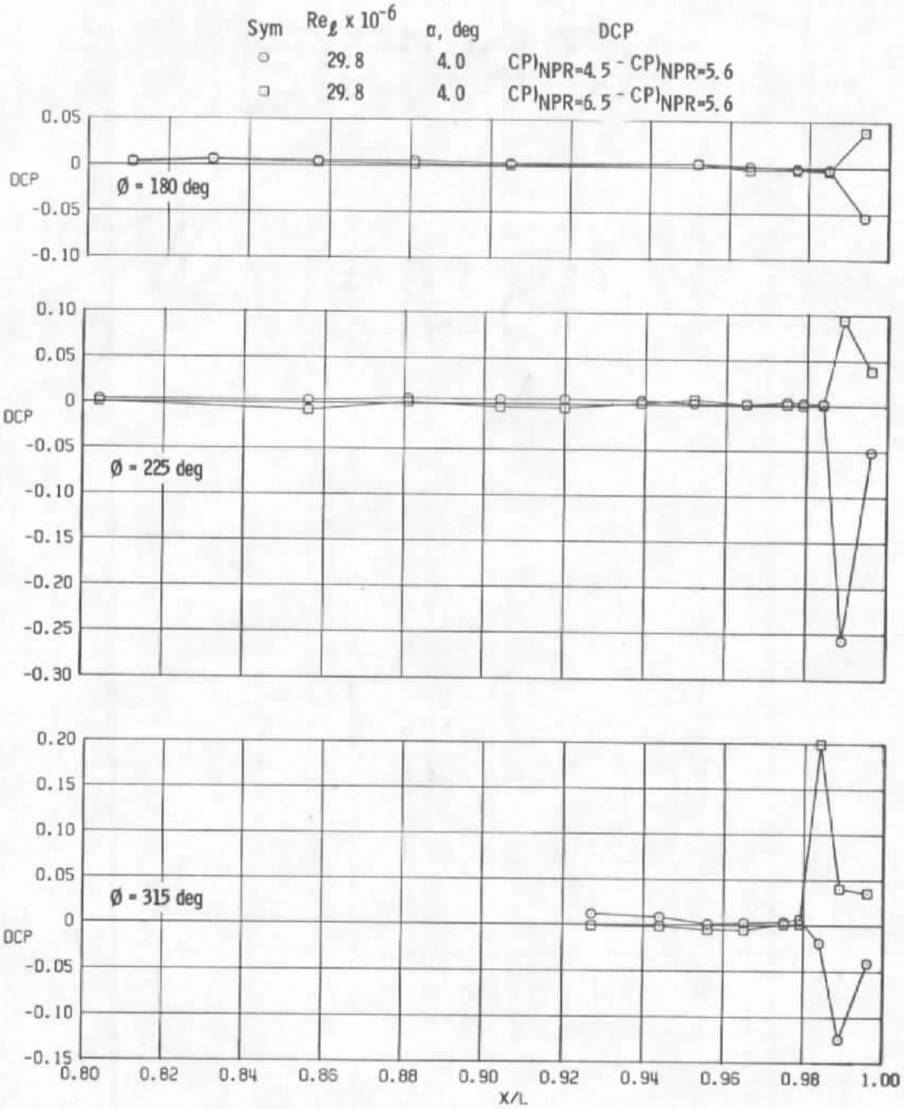

m. Concluded
Figure 27. Continued.

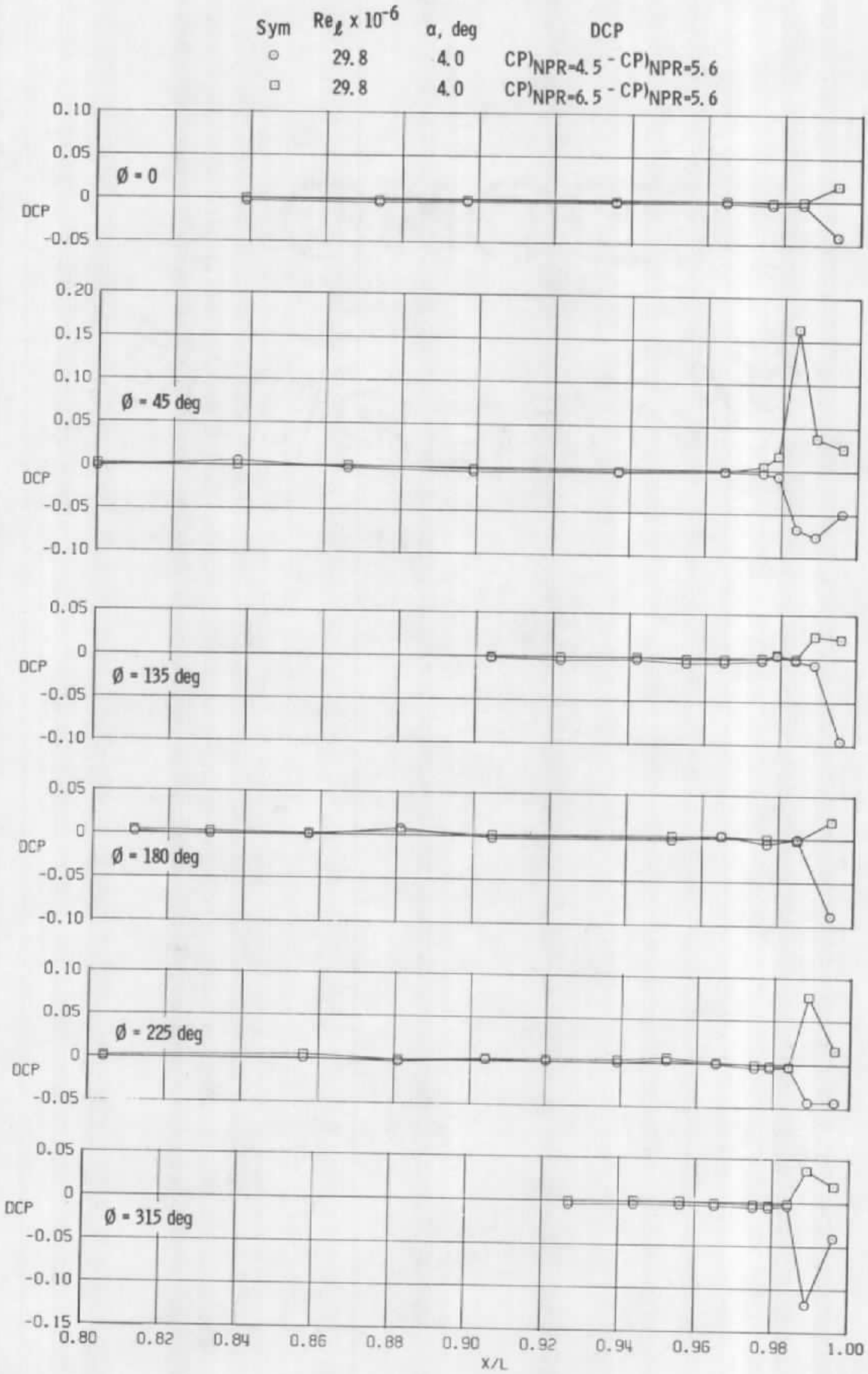

n. M = 1.5, A8 = 360 in.^{2}
Figure 27. Concluded.

a. $\phi = 0$

Figure 28. Model attitude effects on surface pressure coefficients, A8 = 200 in.², M = 0.6, NPR = 3.4 (WT).

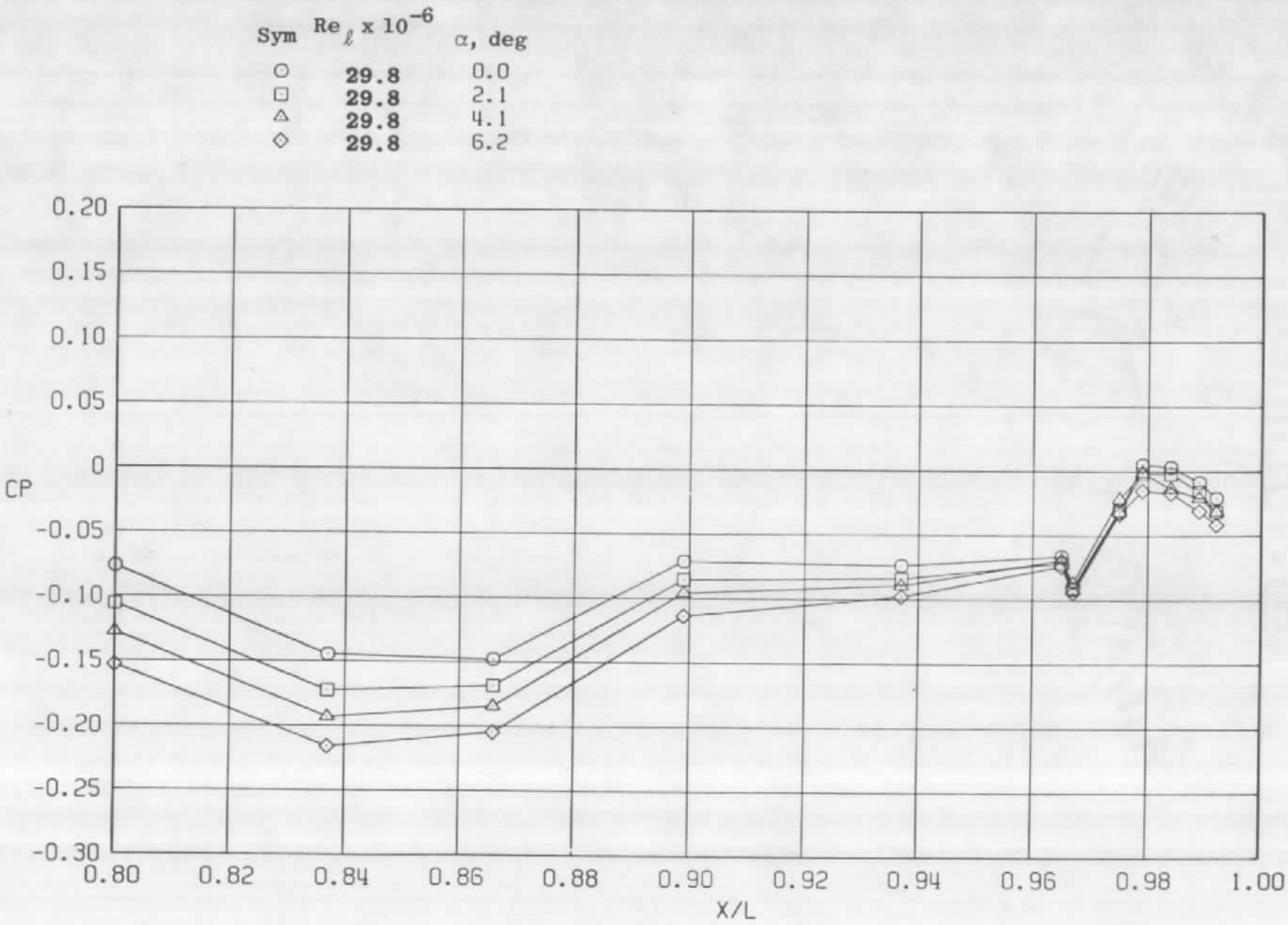

b. ϕ = 45 deg
Figure 28. Continued.

c. ϕ = 135 deg
Figure 28. Continued.

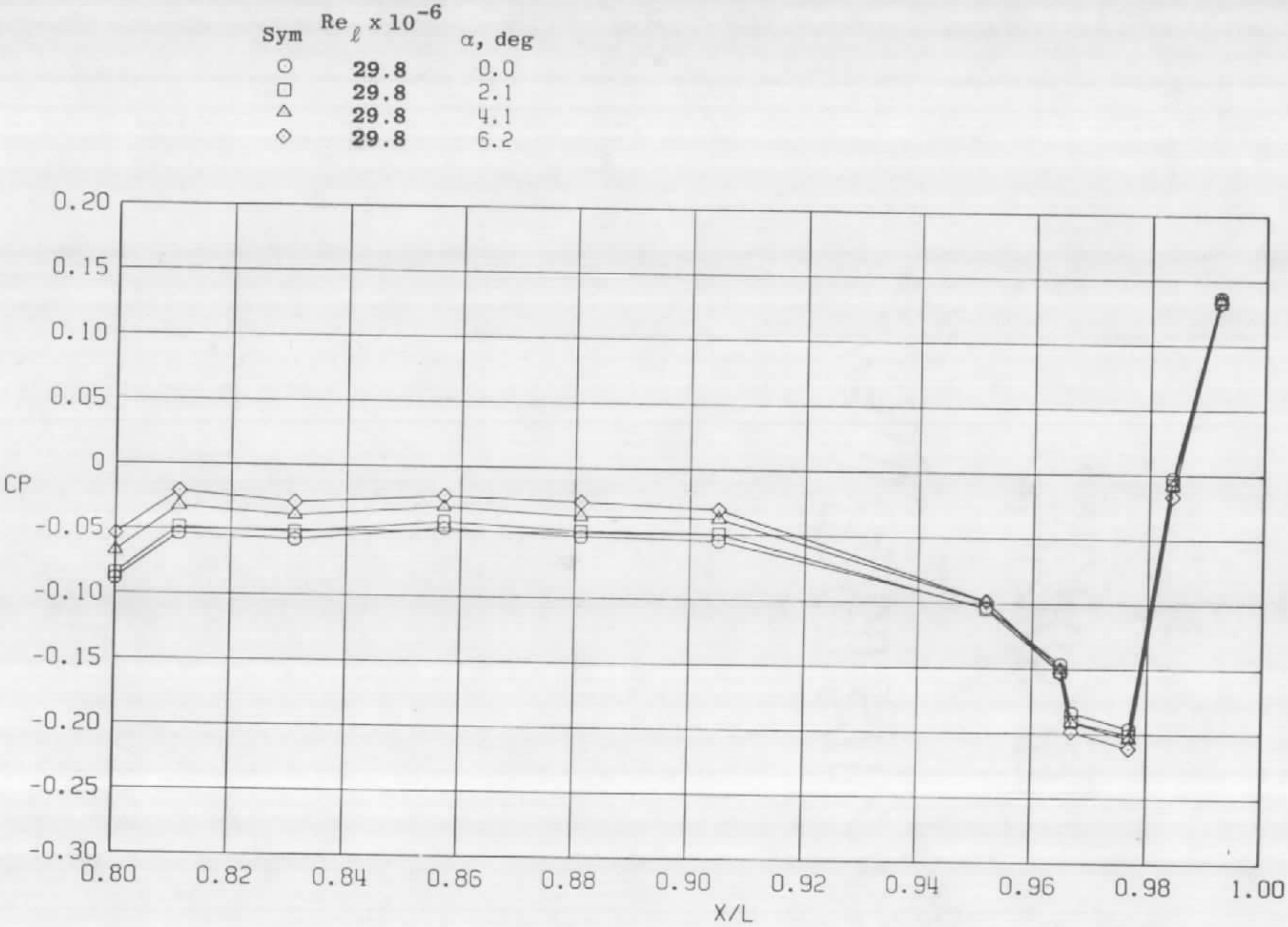

d. ϕ = 180 deg
Figure 28. Continued.

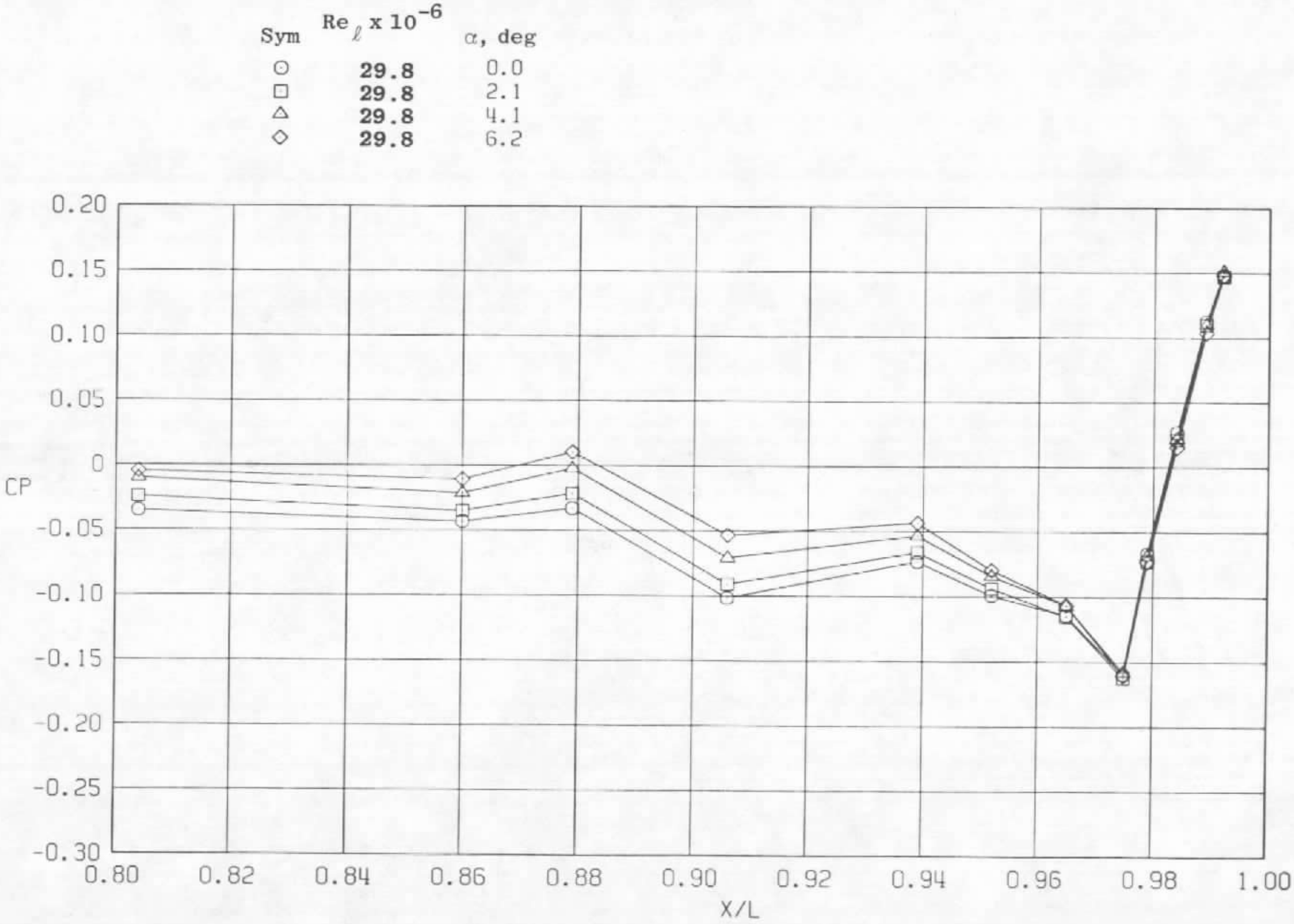

e. ϕ = 225 deg
Figure 28. Continued.

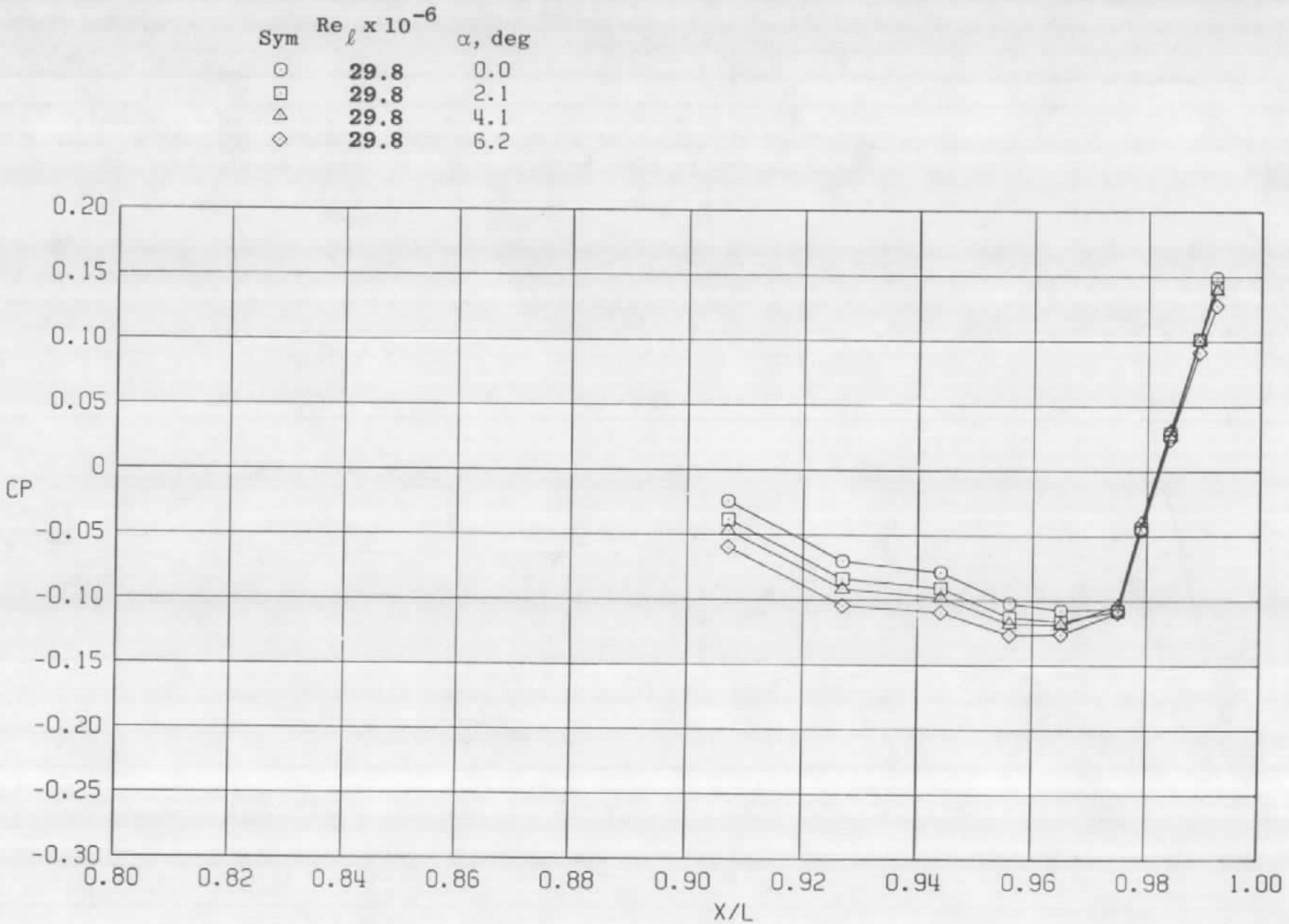

f. ϕ = 315 deg
Figure 28. Concluded.

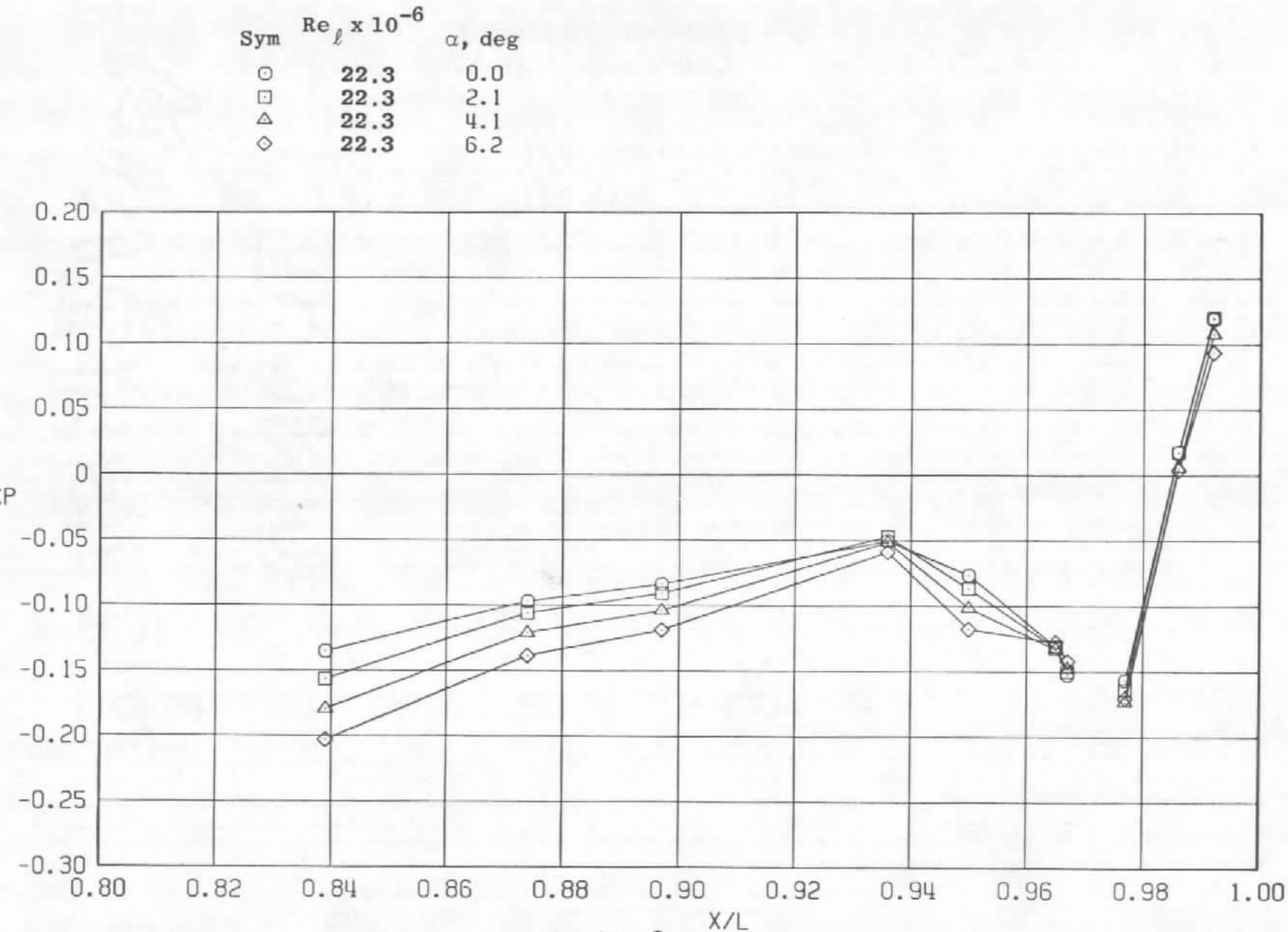

a. $\phi = 0$

Figure 29. Effect of model attitude on surface pressure coefficients, A8 = 200 in.^{2}, M = 0.6, NPRE = 3.4 (SS).

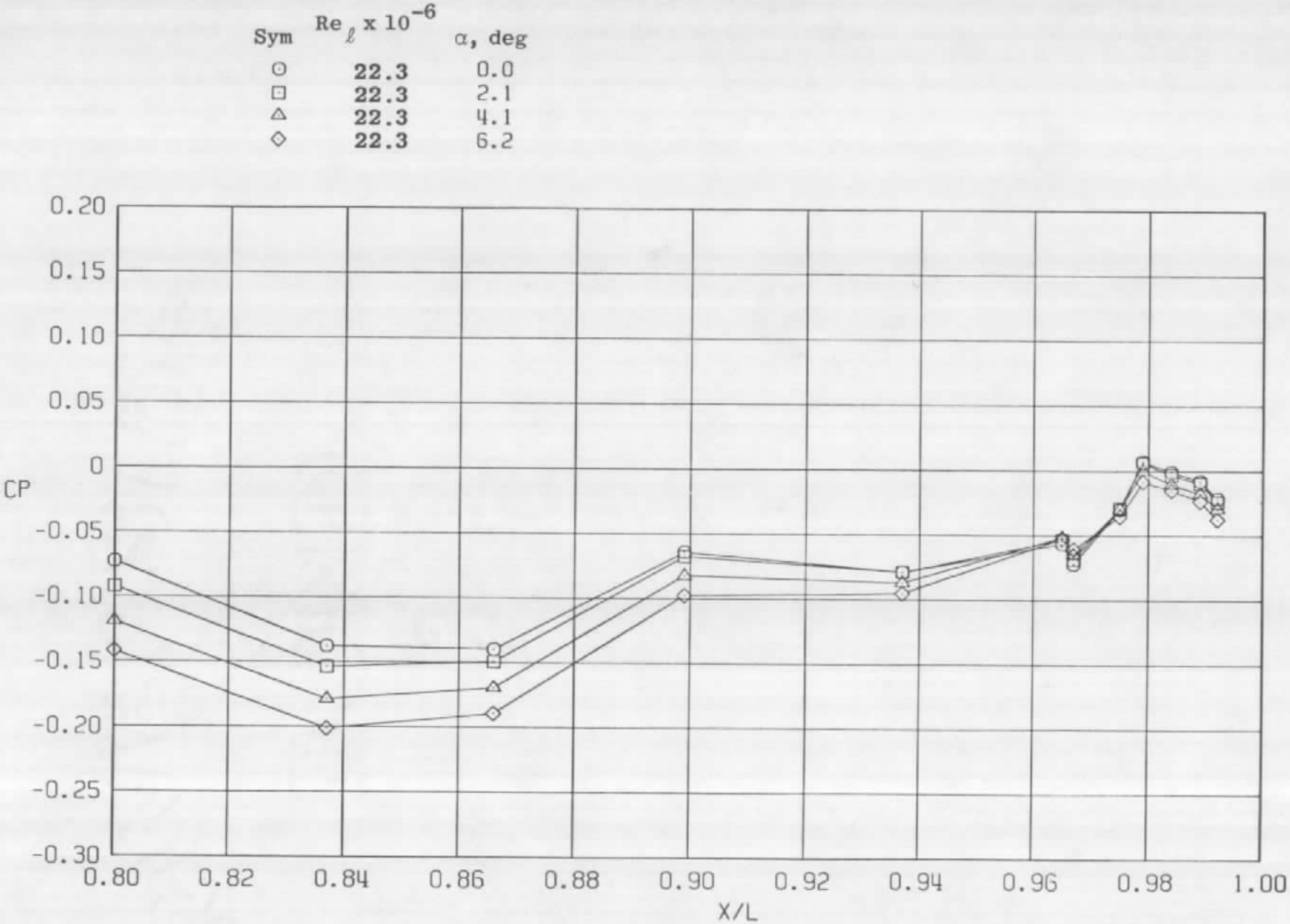

b. ϕ = 45 deg
Figure 29. Continued.

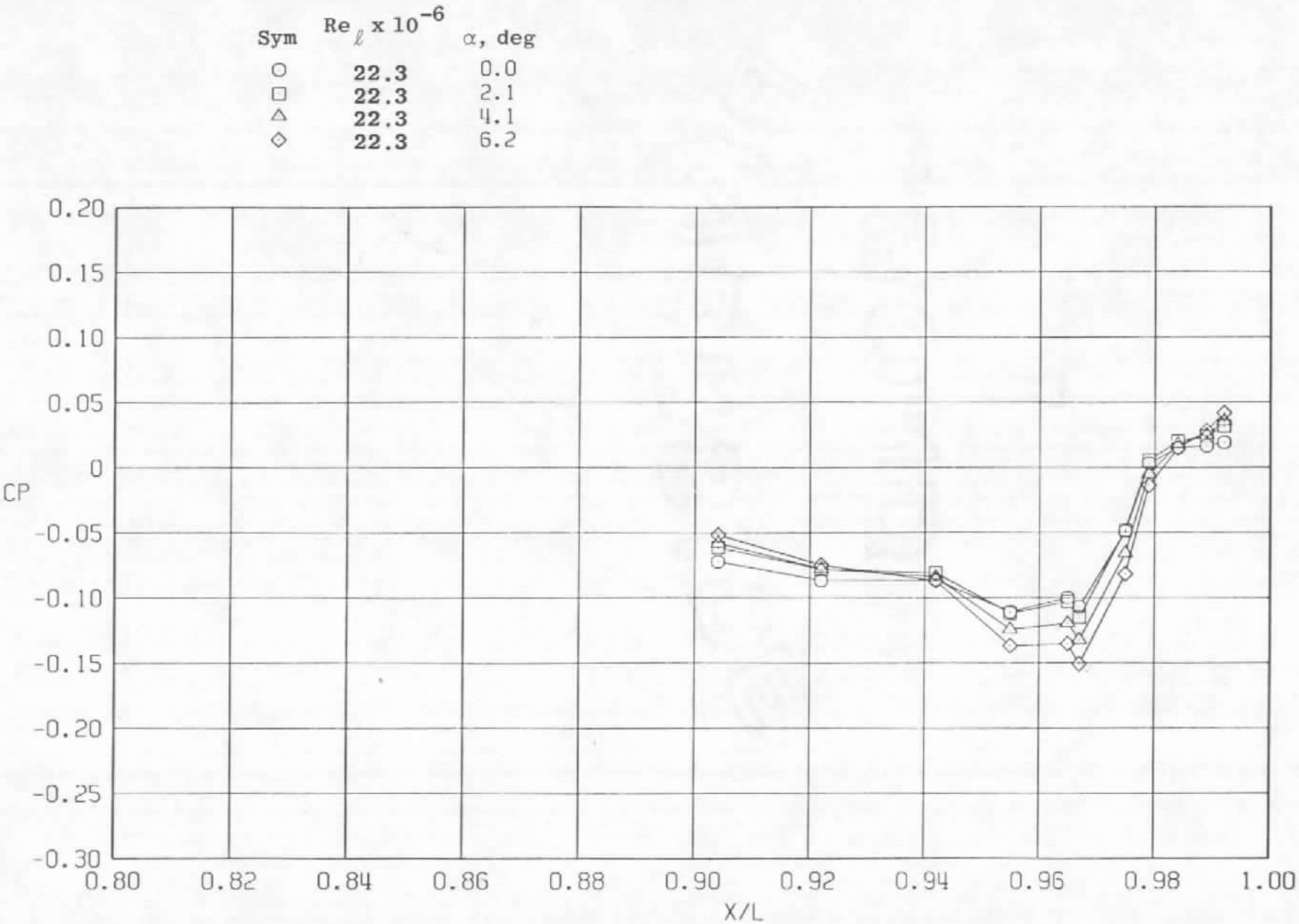

c. ϕ = 135 deg
Figure 29. Continued.

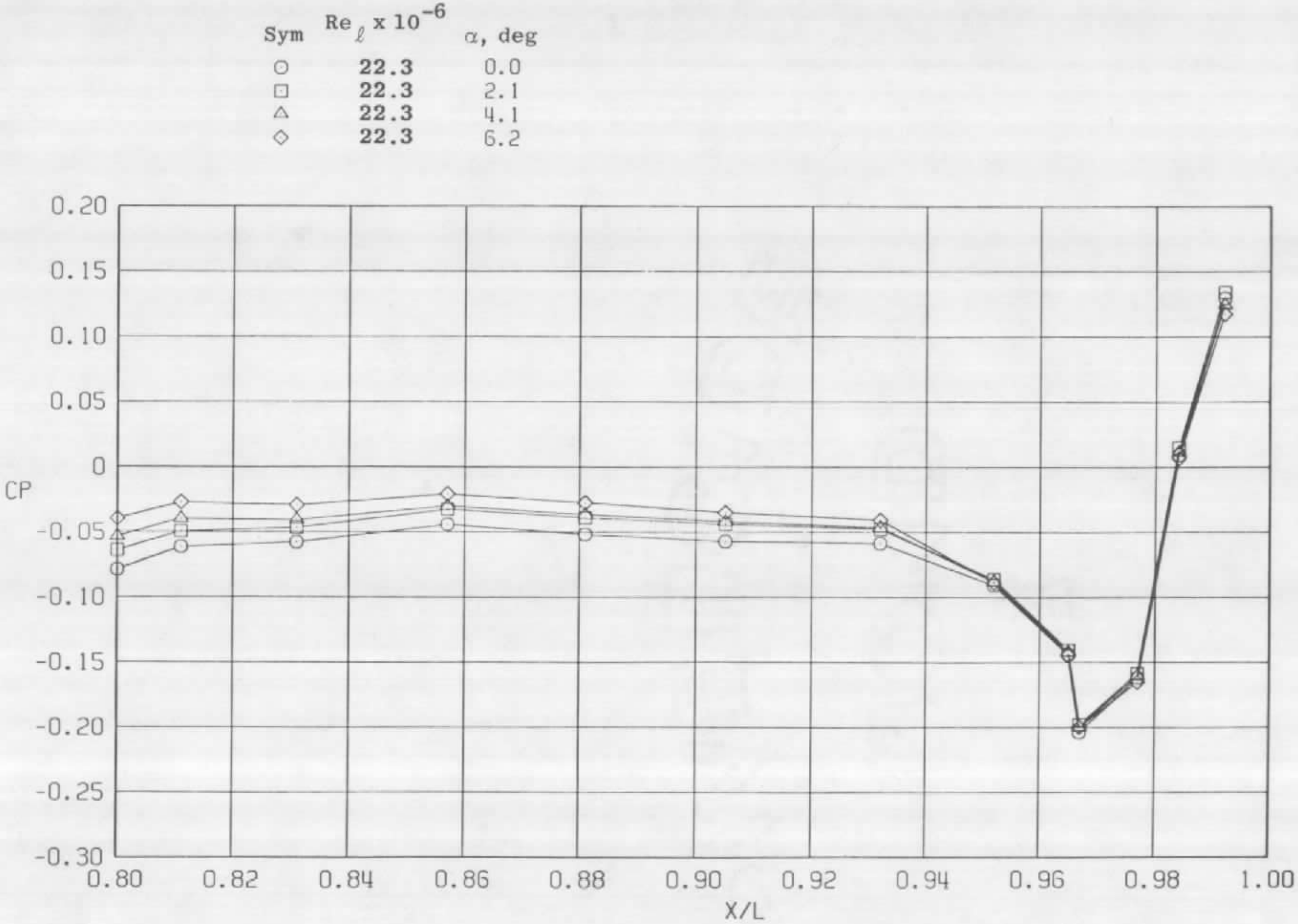

d. ϕ = 180 deg

Figure 29. Continued.

e. ϕ = 225 deg
Figure 29. Continued.

f. ϕ = 315 deg
Figure 29. Concluded.

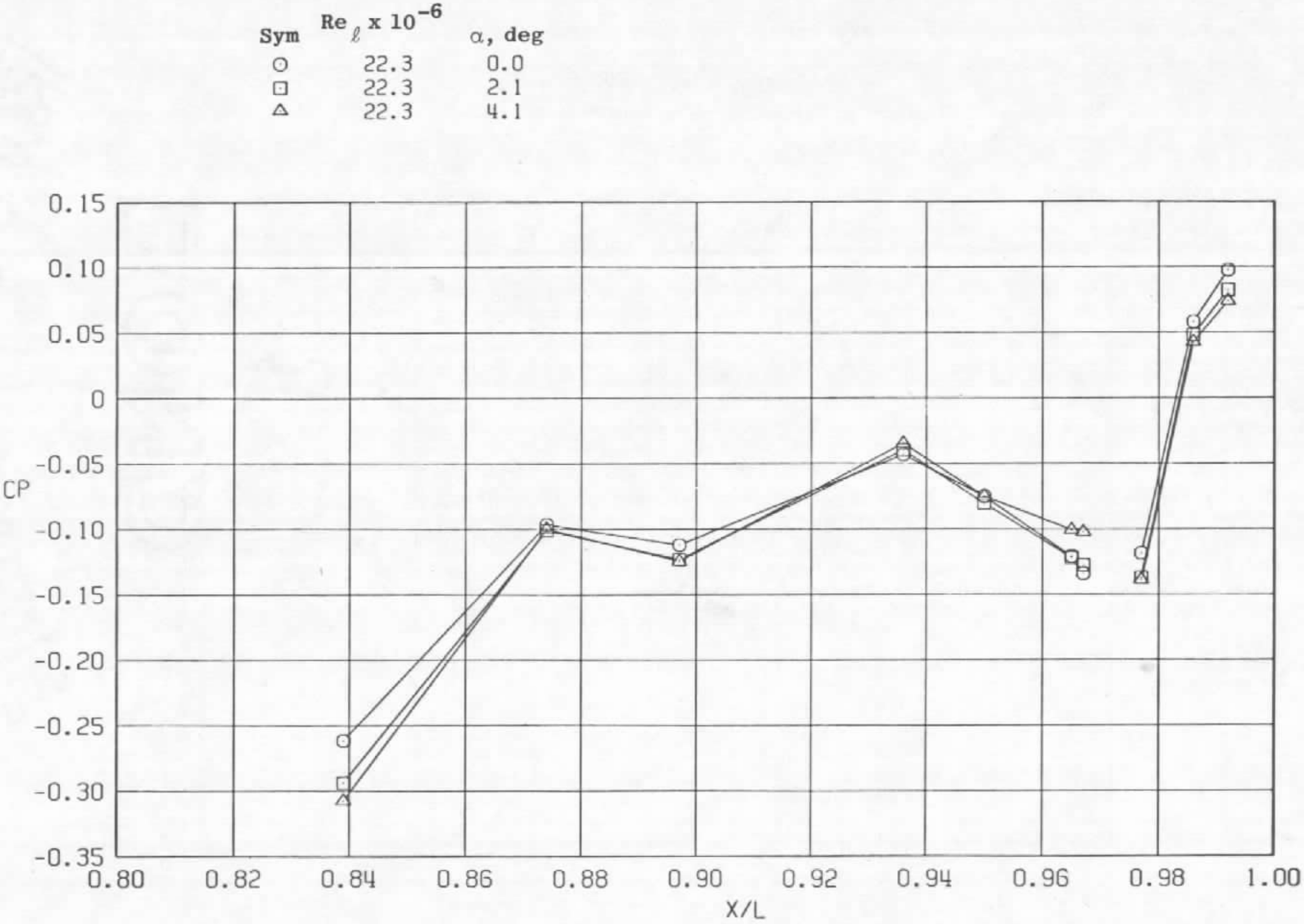

a. $\phi = 0$

Figure 30. Effect of model attitude on surface pressure coefficients, A8 = 200 in.², M = 0.9, NPRE = 3.4 (SS).

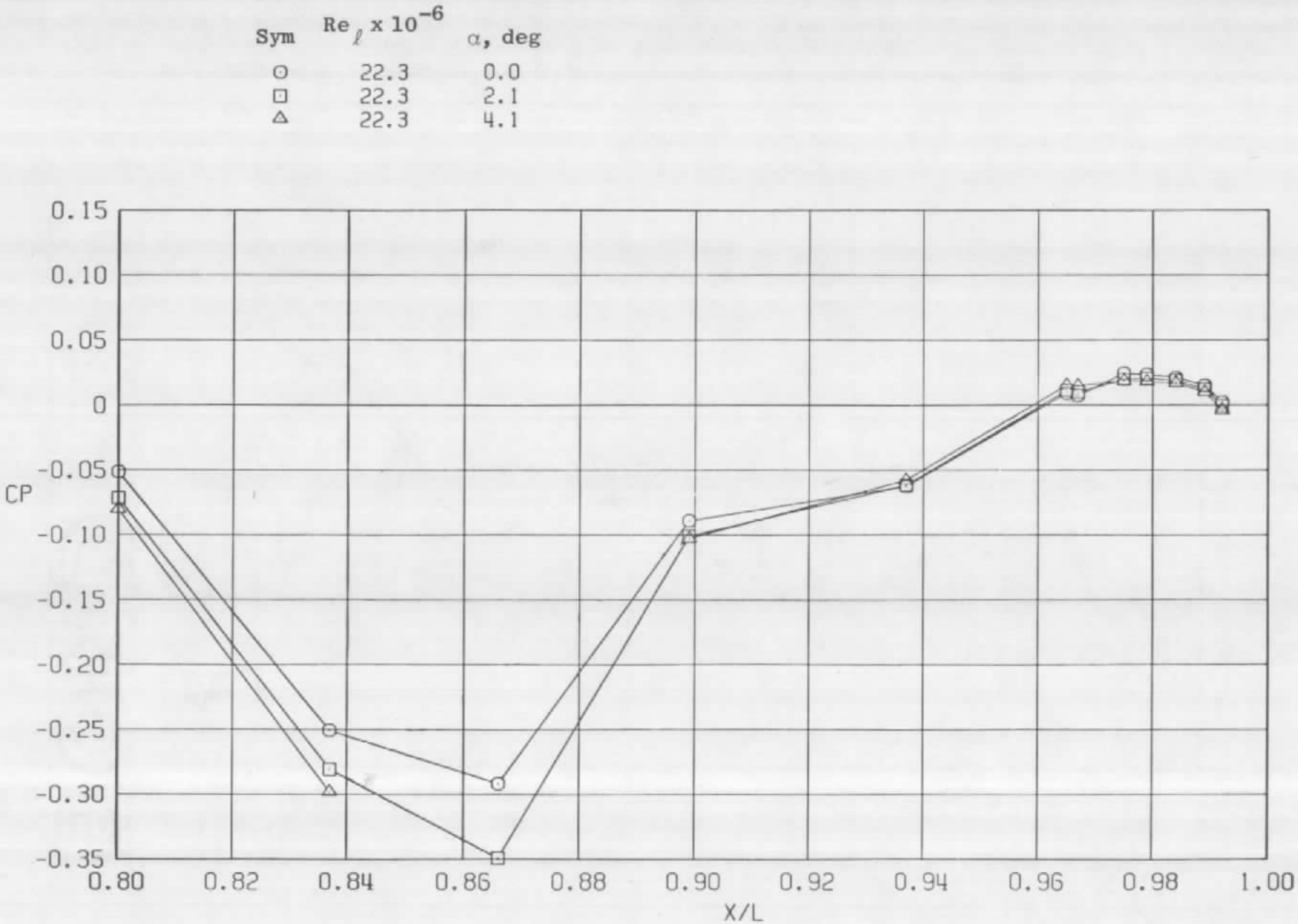

b. ϕ = 45 deg
Figure 30. Continued.

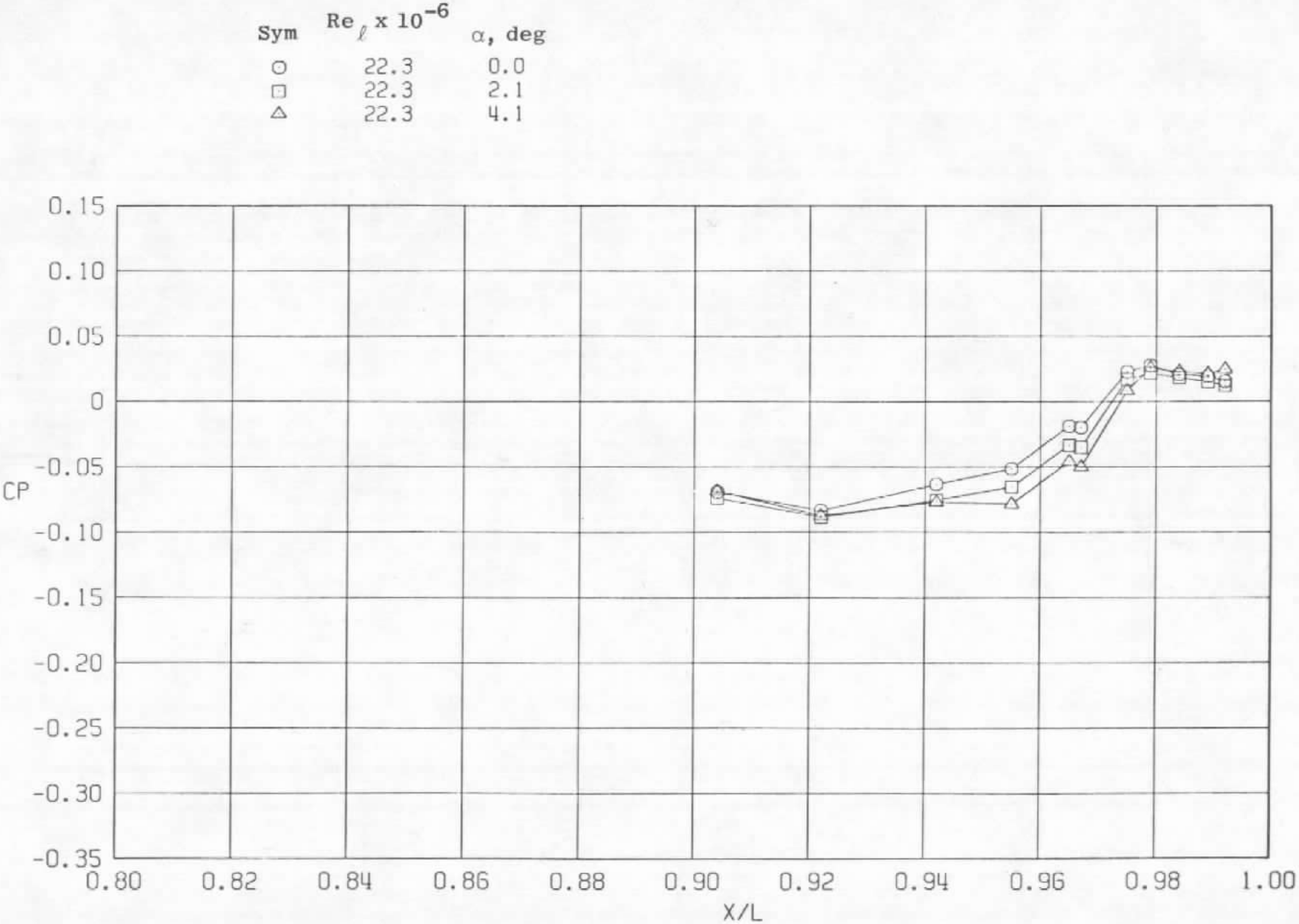

c. ϕ = 135 deg
Figure 30. Continued.

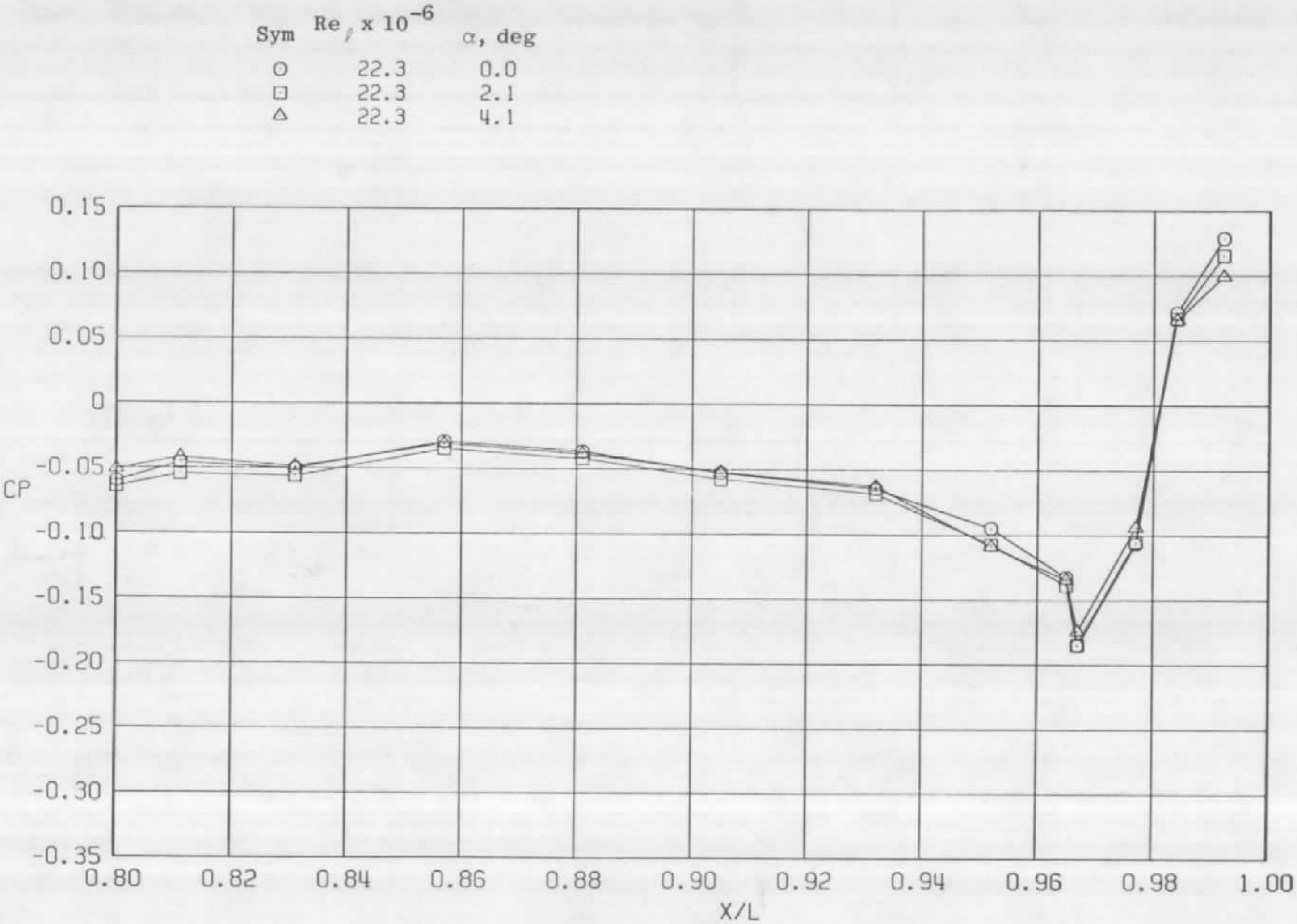

d. ϕ = 180 deg
Figure 30. Continued.

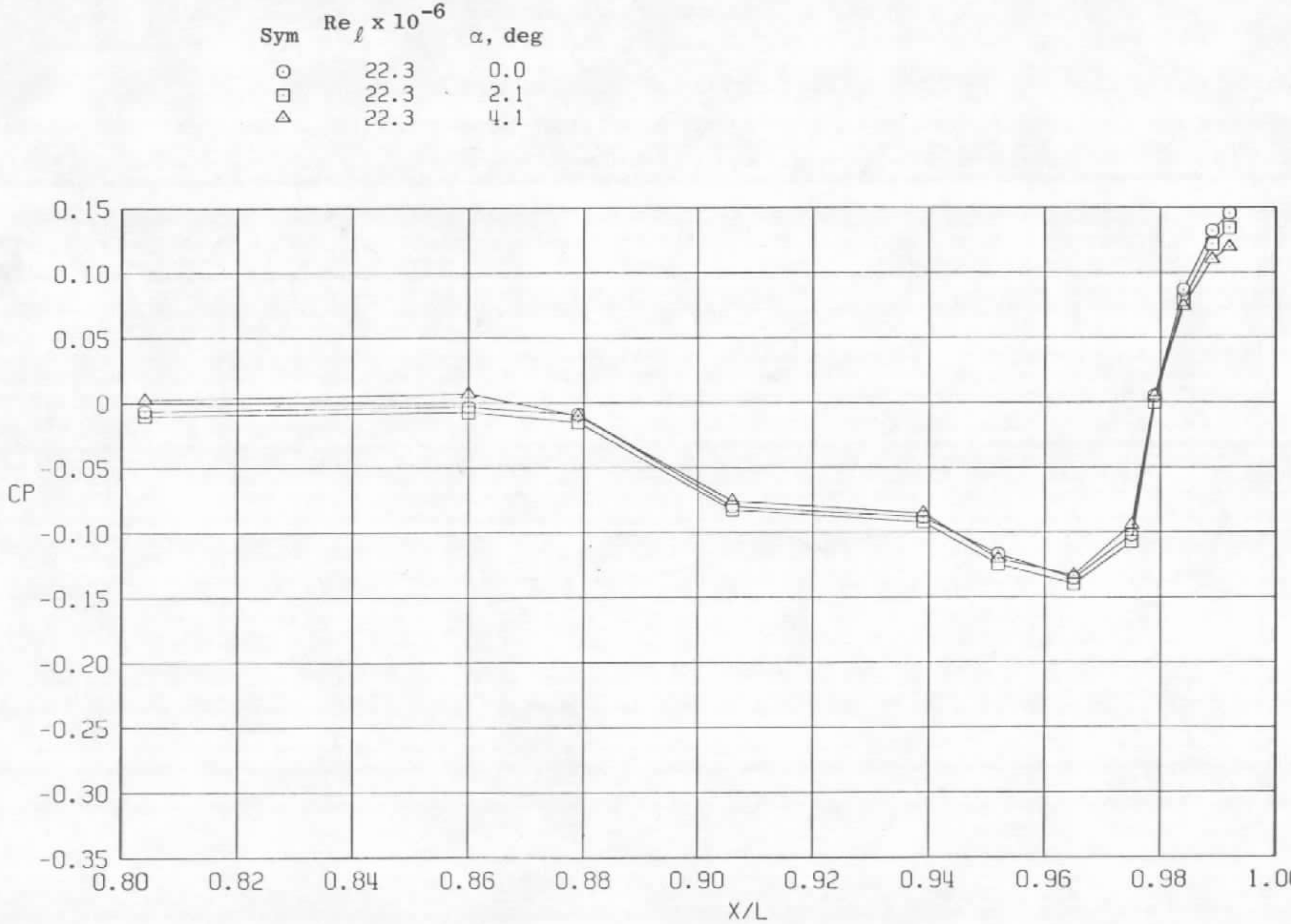

e. ϕ = 225 deg
Figure 30. Continued.

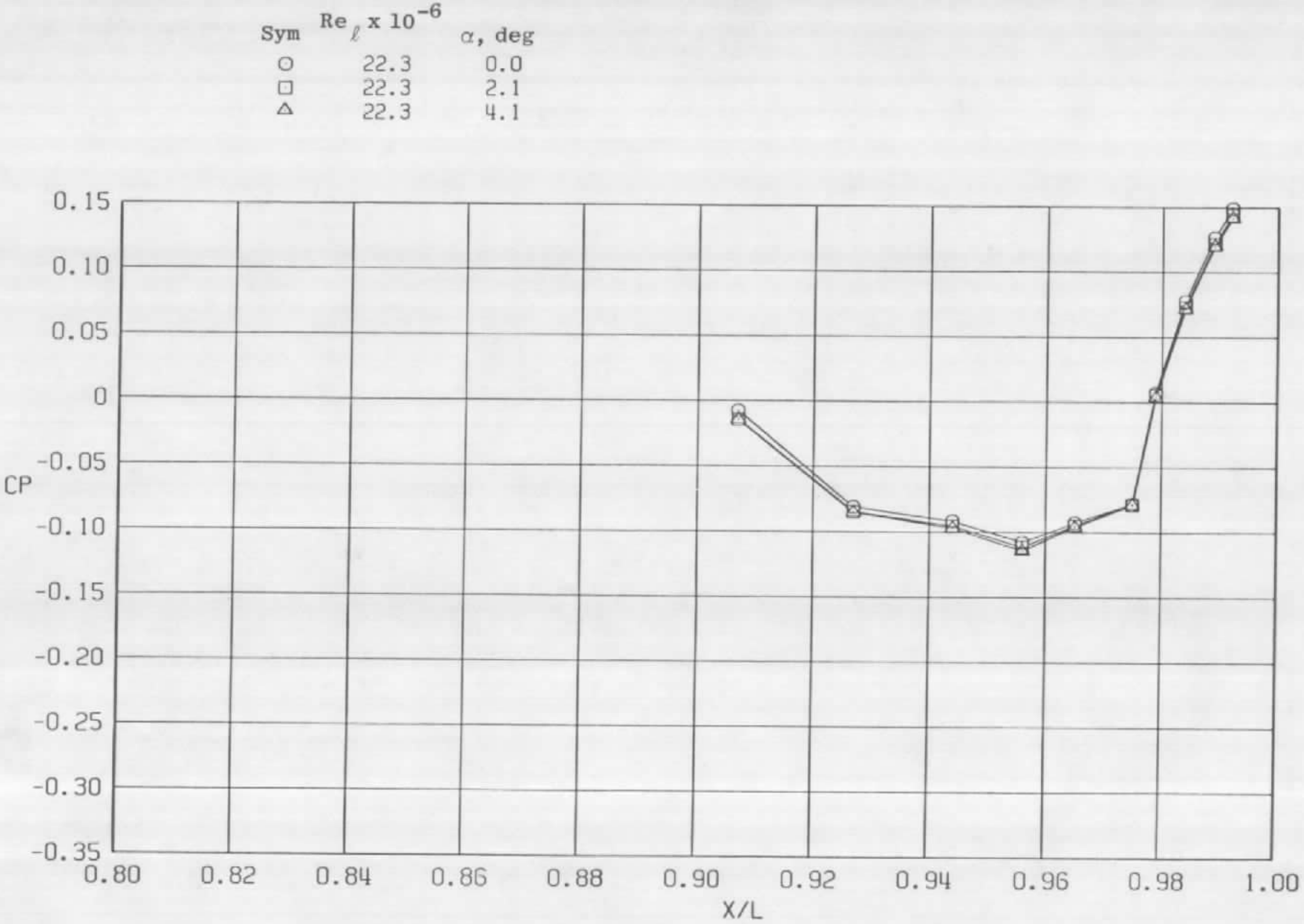

f. ϕ = 315 deg
Figure 30. Concluded.

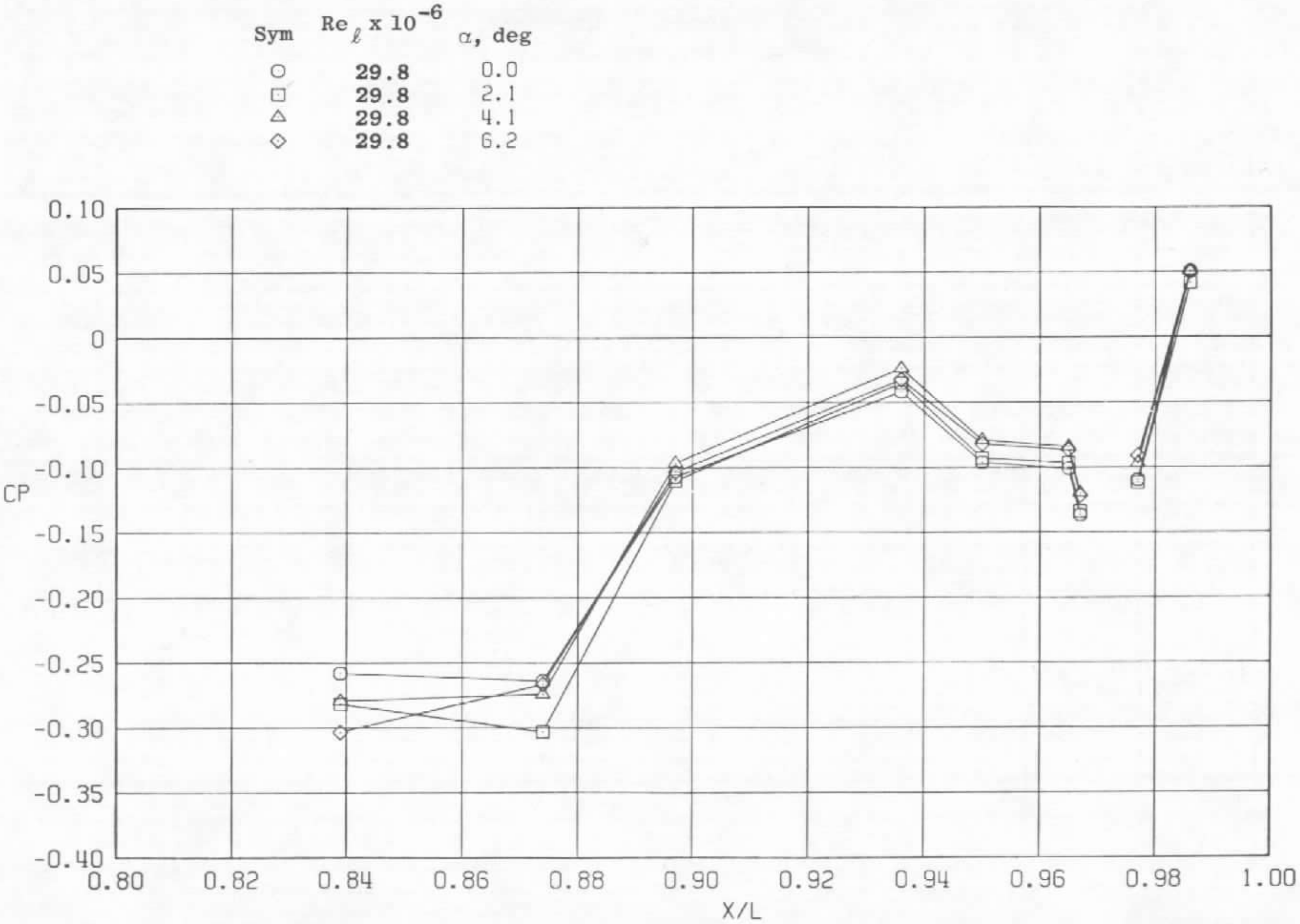

a. $\phi = 0$

Figure 31. Model attitude effects on surface pressure coefficients, A8 = 230 in.², M = 0.9, NPR = 4.1 (WT).

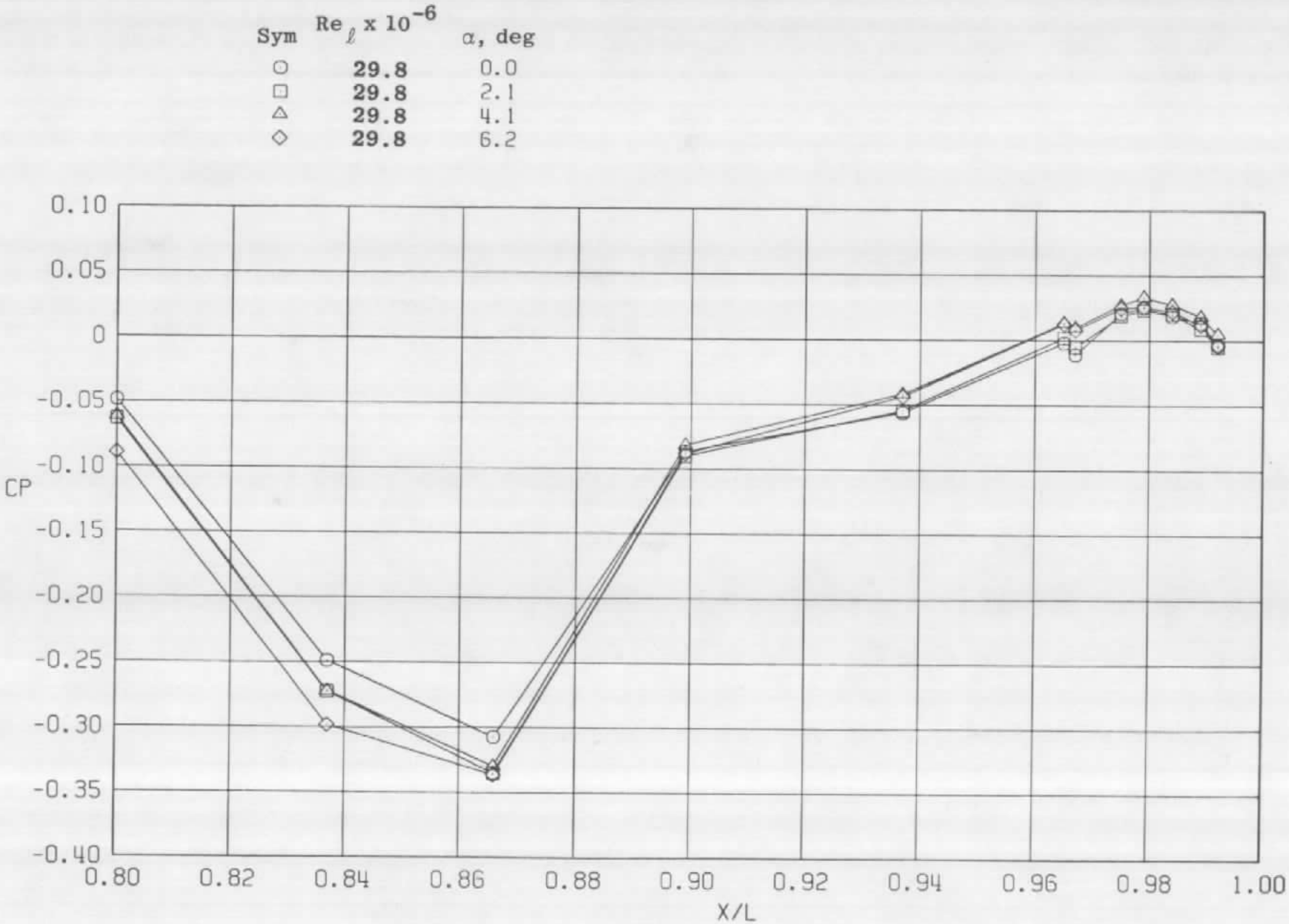

b. ϕ = 45 deg
Figure 31. Continued.

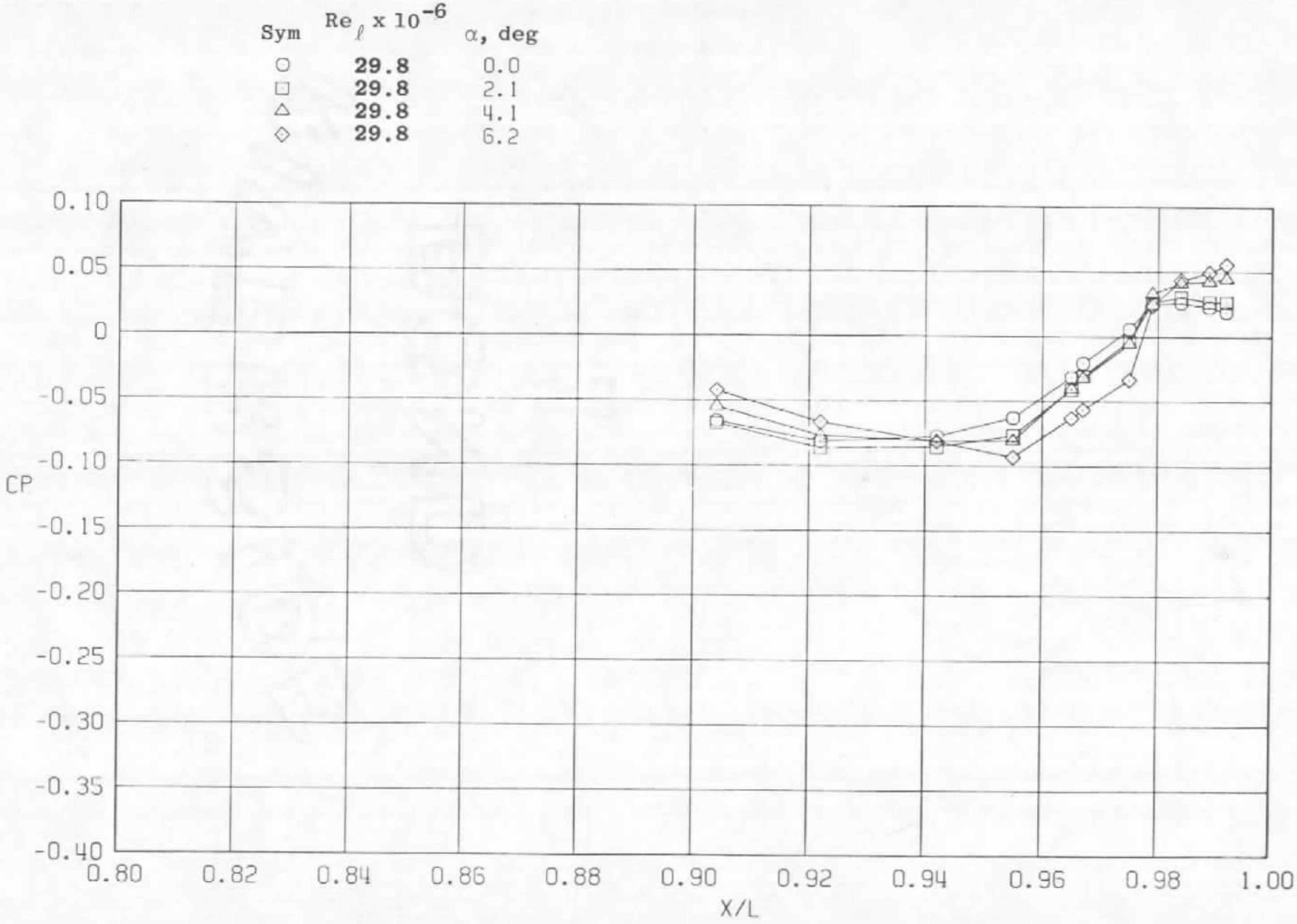

c. ϕ = 135 deg
Figure 31. Continued.

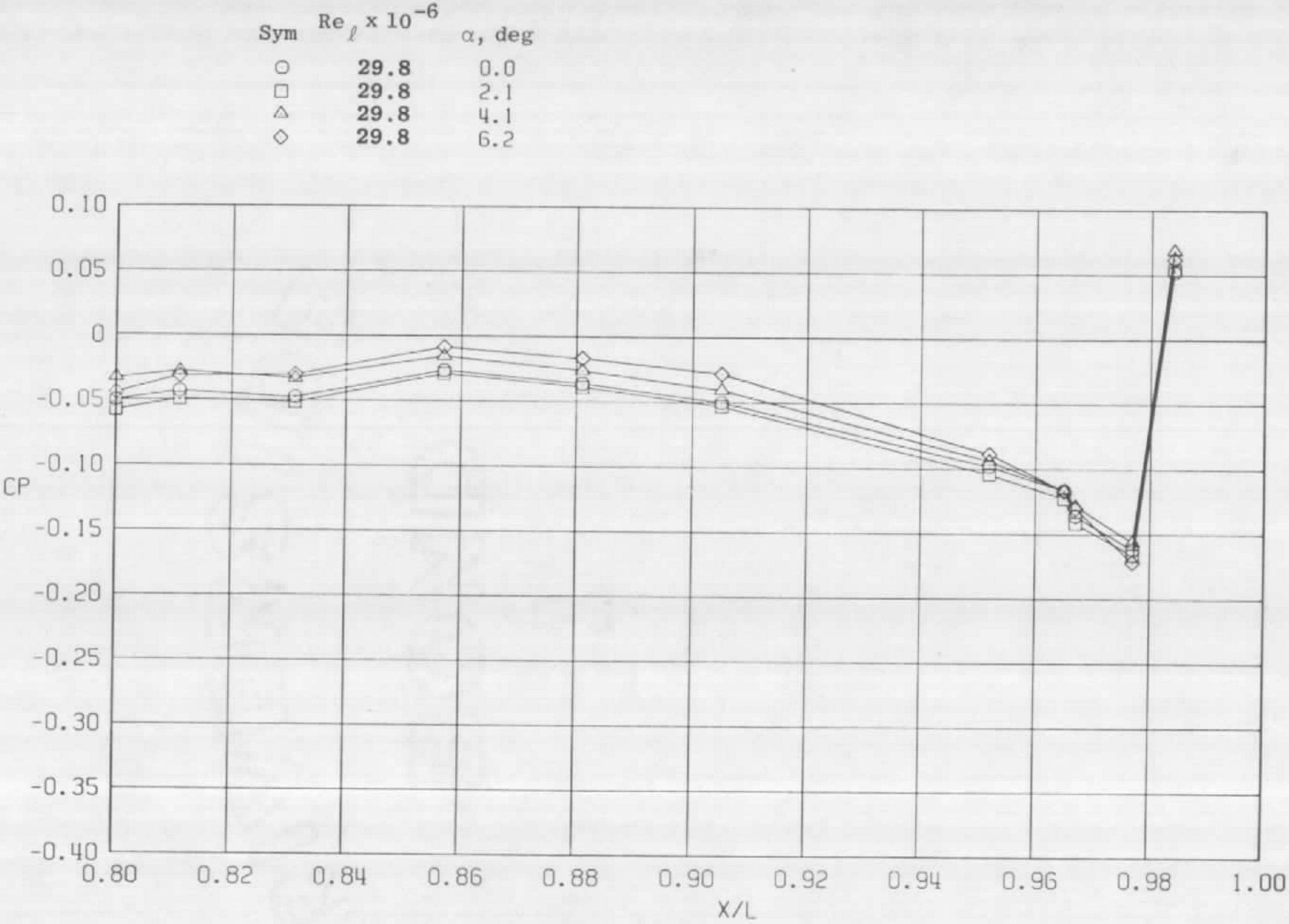

d. ϕ = 180 deg

Figure 31. Continued.

e. ϕ = 225 deg
Figure 31. Continued.

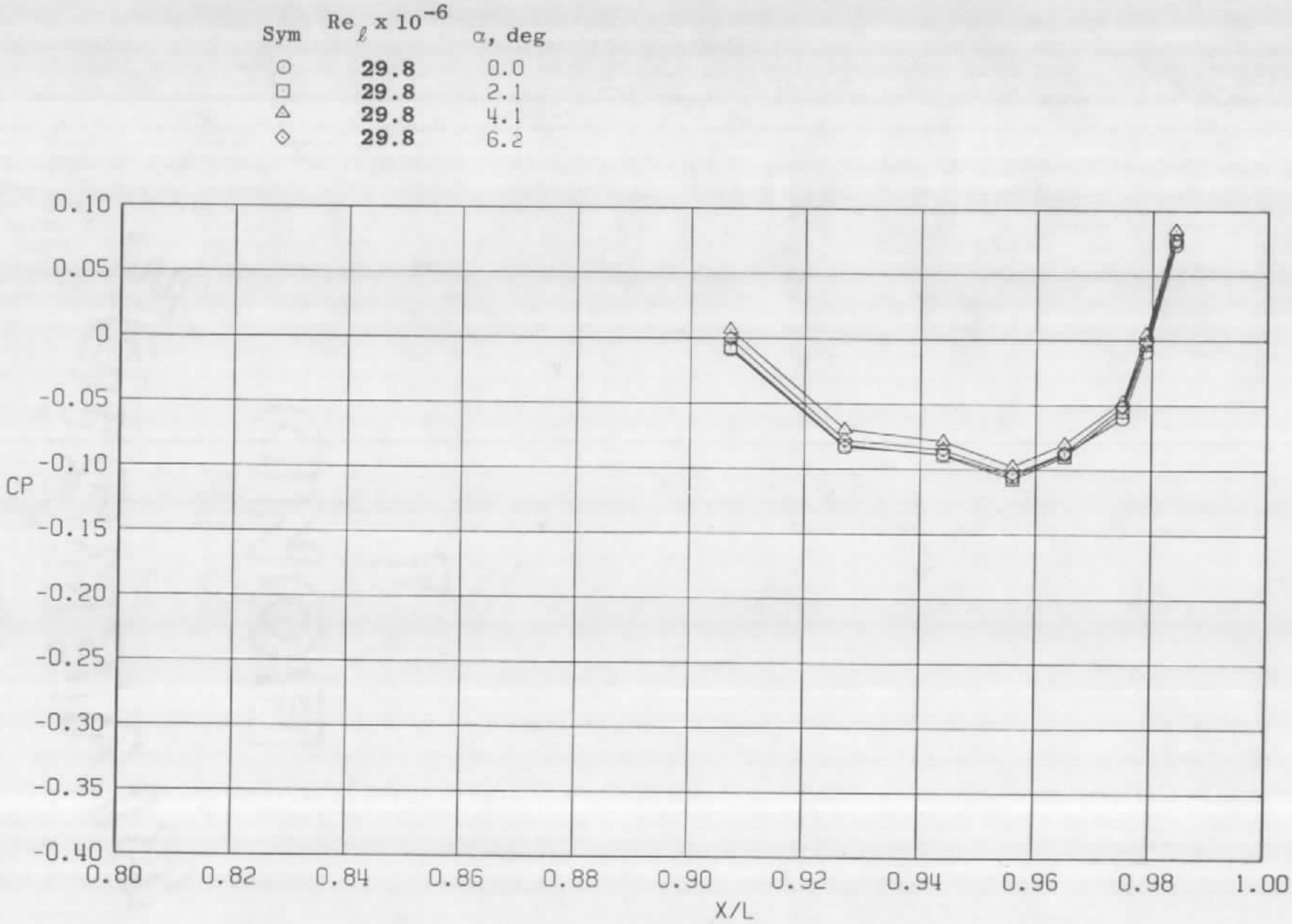

f. ϕ = 315 deg
Figure 31. Concluded.

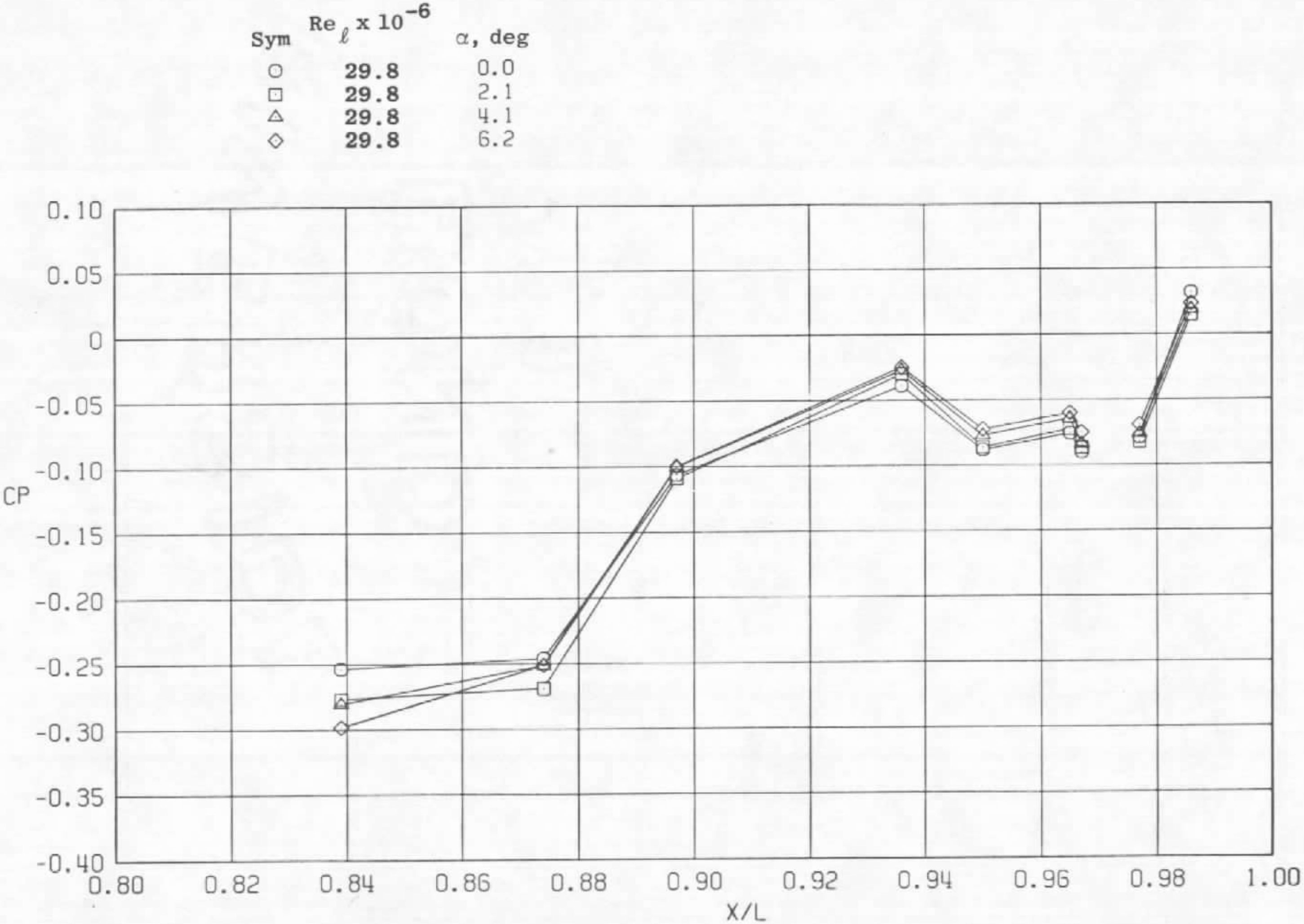

a. ϕ = 0

Figure 32. Model attitude effects on surface pressure coefficients, A8 = 300 in.², M = 0.9, NPR = 5.0 (WT).

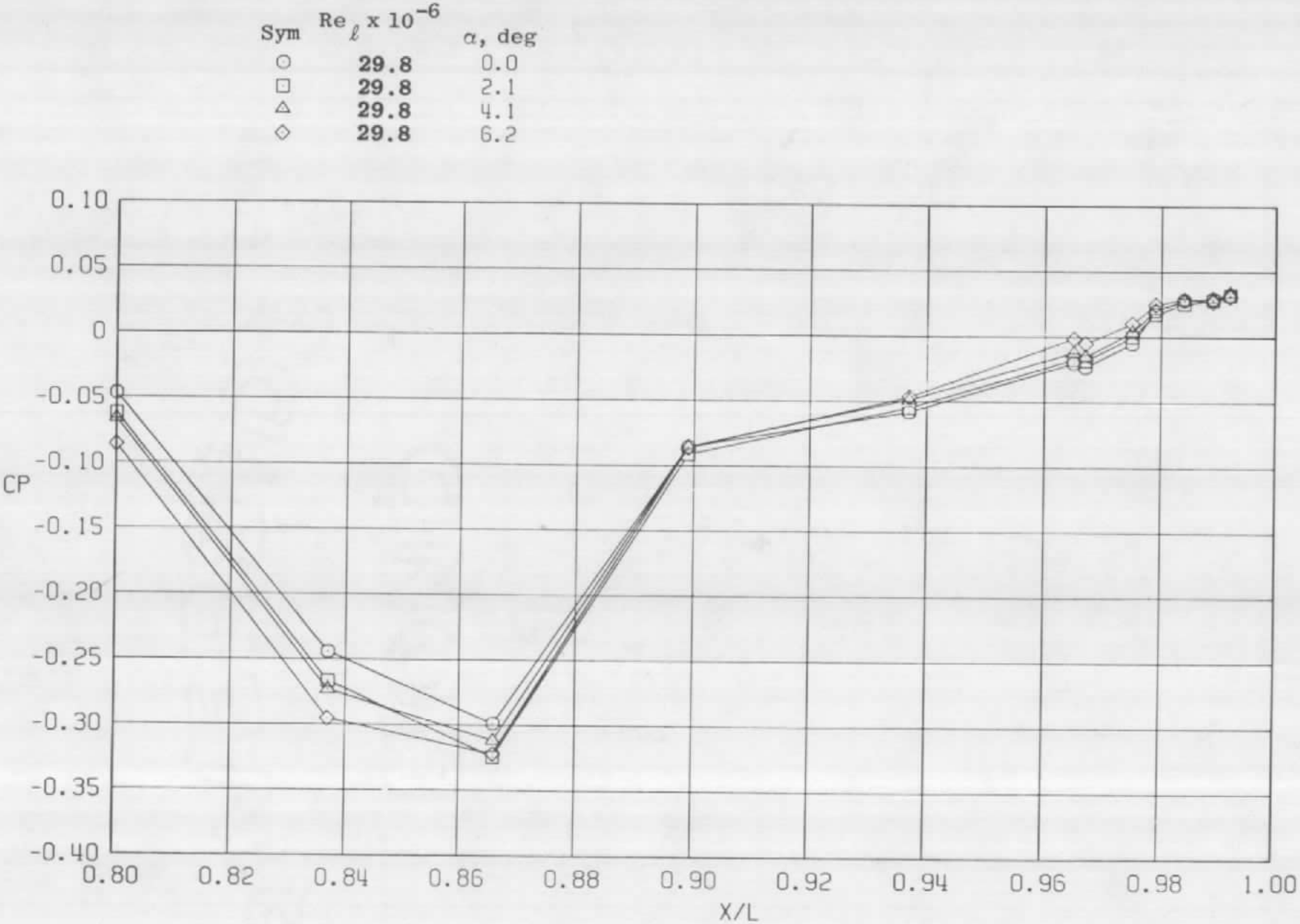

b. ϕ = 45 deg
Figure 32. Continued.

c. ϕ = 135 deg
Figure 32. Continued.

d. ϕ = 180 deg
Figure 32. Continued.

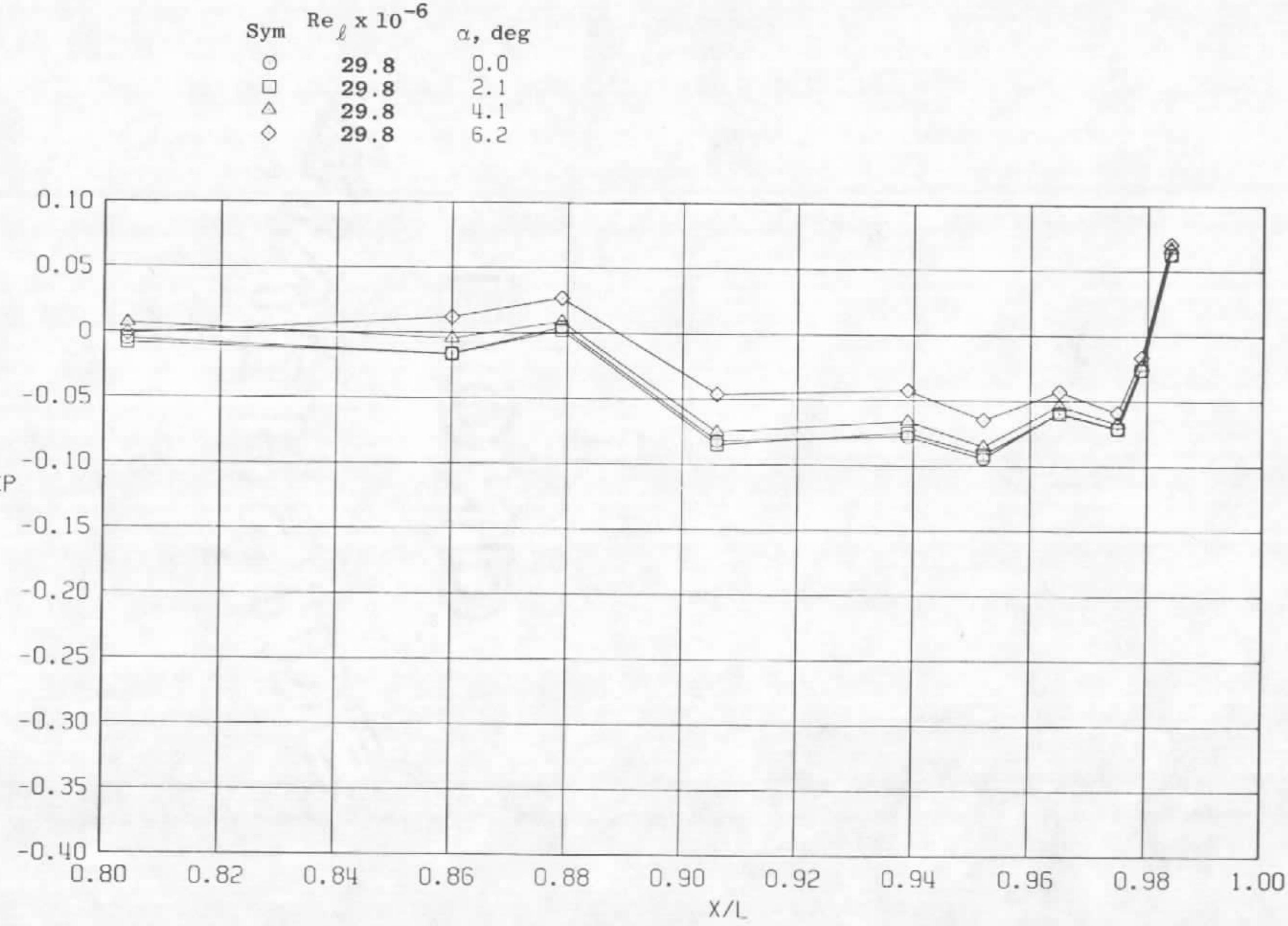

e. ϕ = 225 deg
Figure 32. Continued.

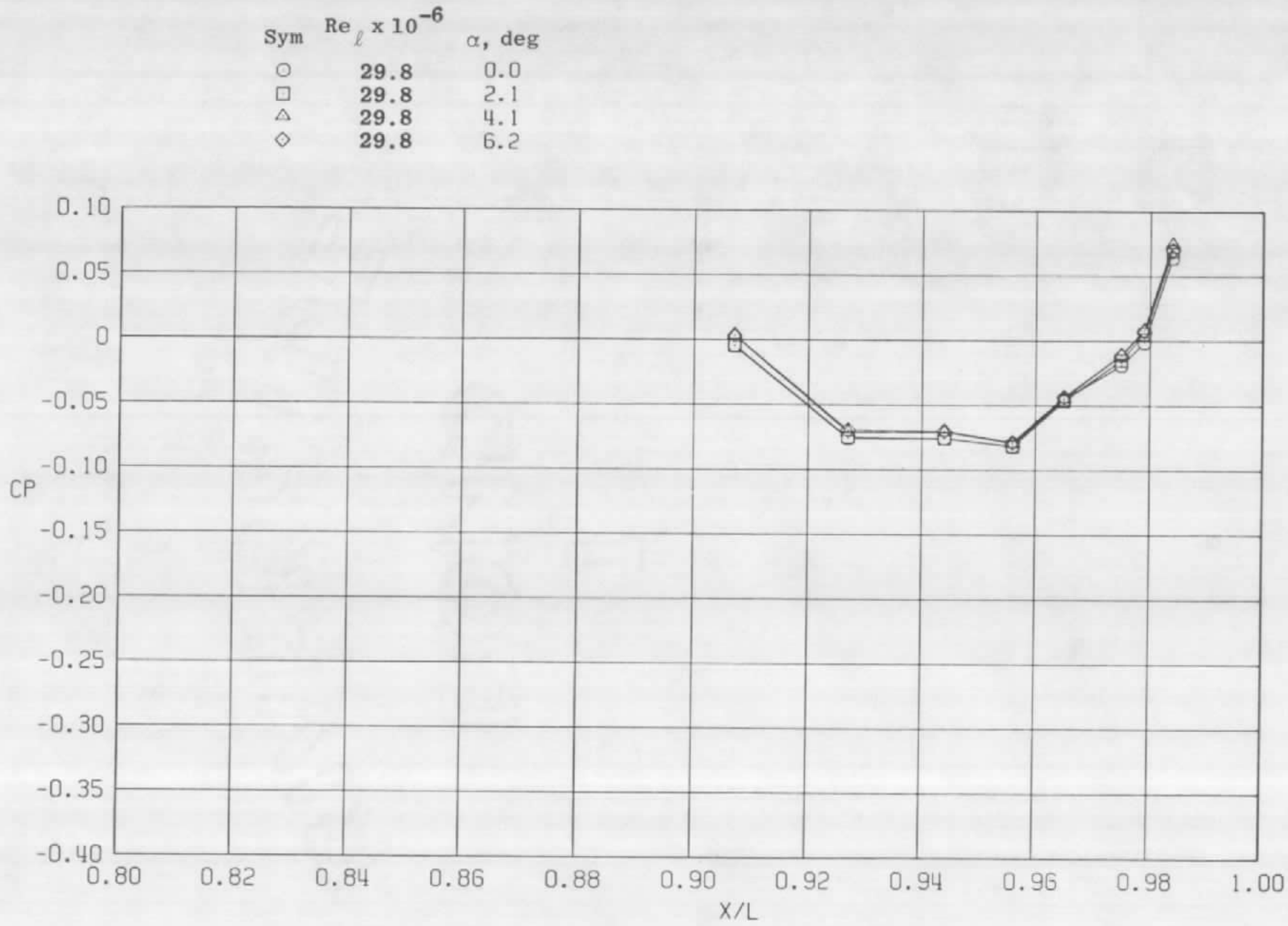

f. ϕ = 315 deg
Figure 32. Concluded.

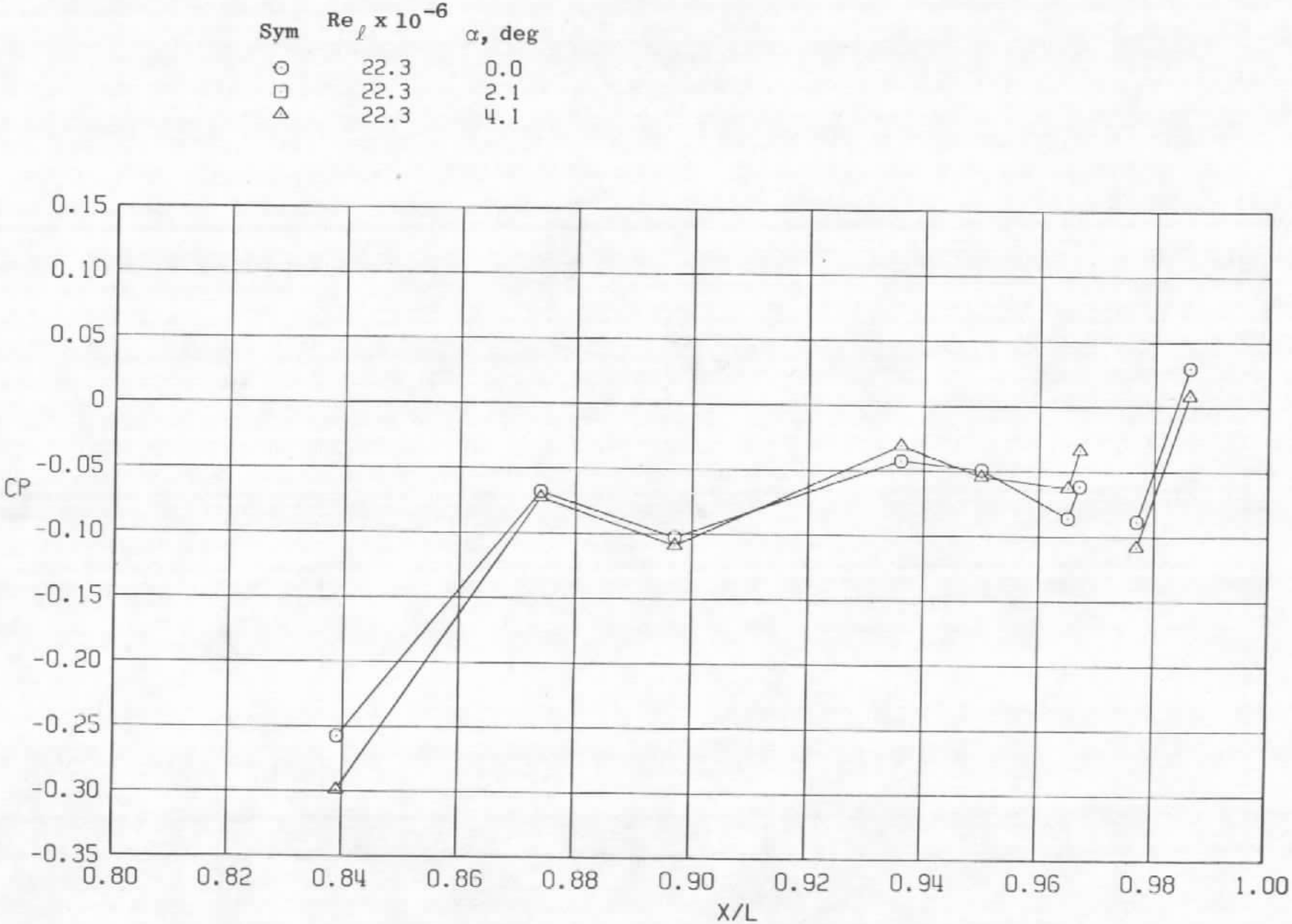

a. $\phi = 0$

Figure 33. Effect of model attitude on surface pressure coefficients A8 = 300 in.², M = 0.9, NPRE = 5.0 (SS).

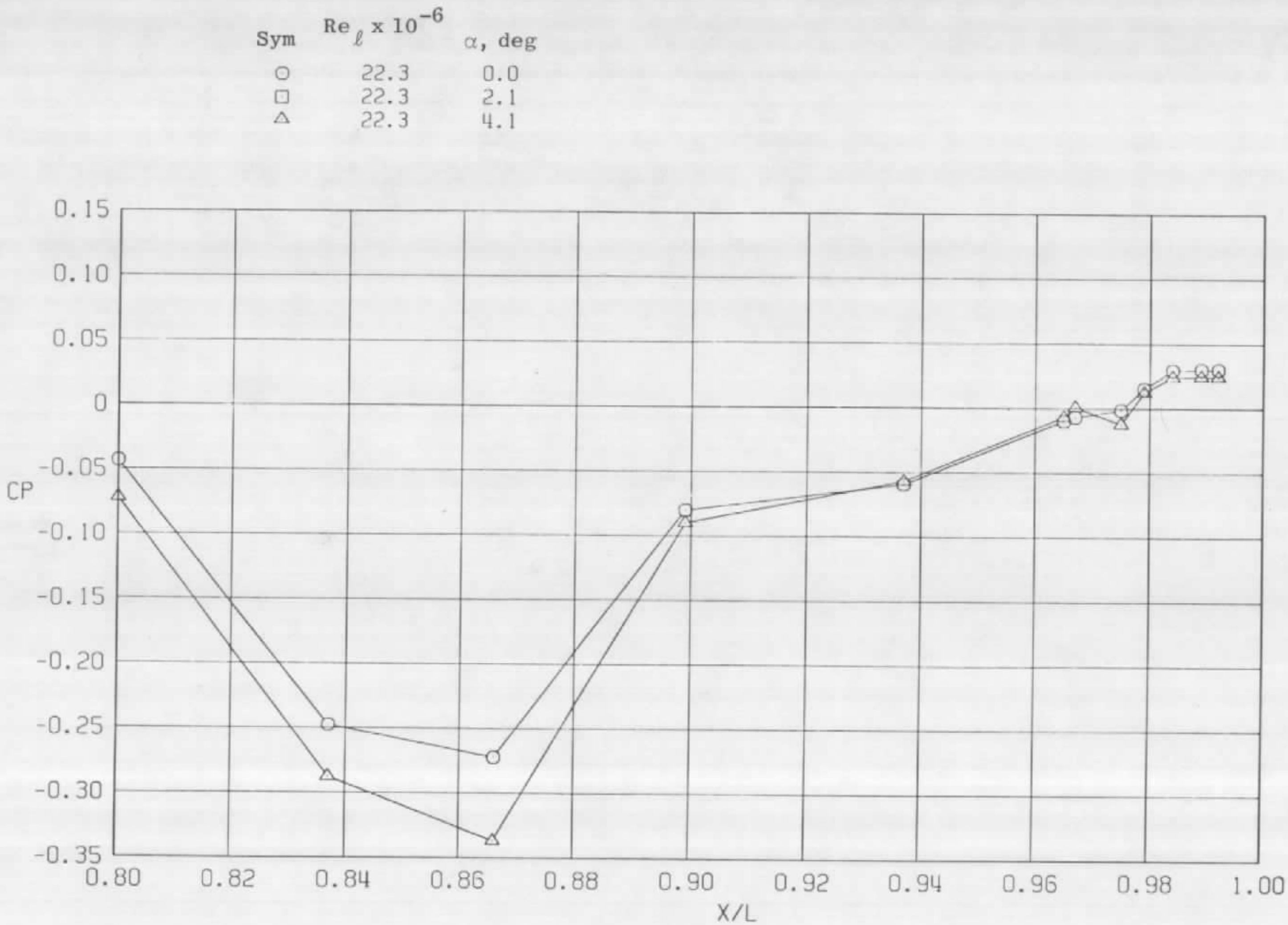

b. ϕ = 45 deg
Figure 33. Continued.

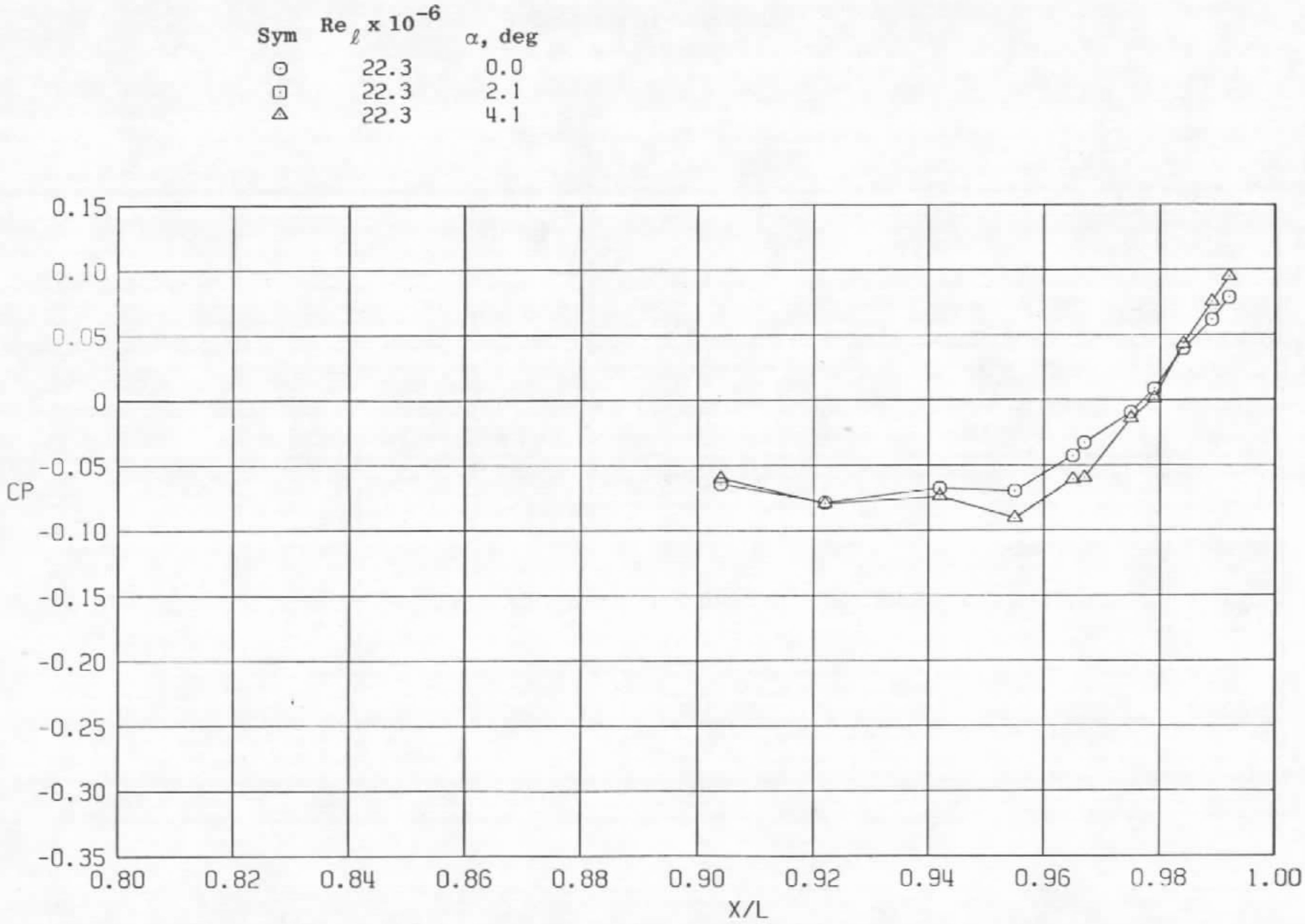

c. ϕ = 135 deg
Figure 33. Continued.

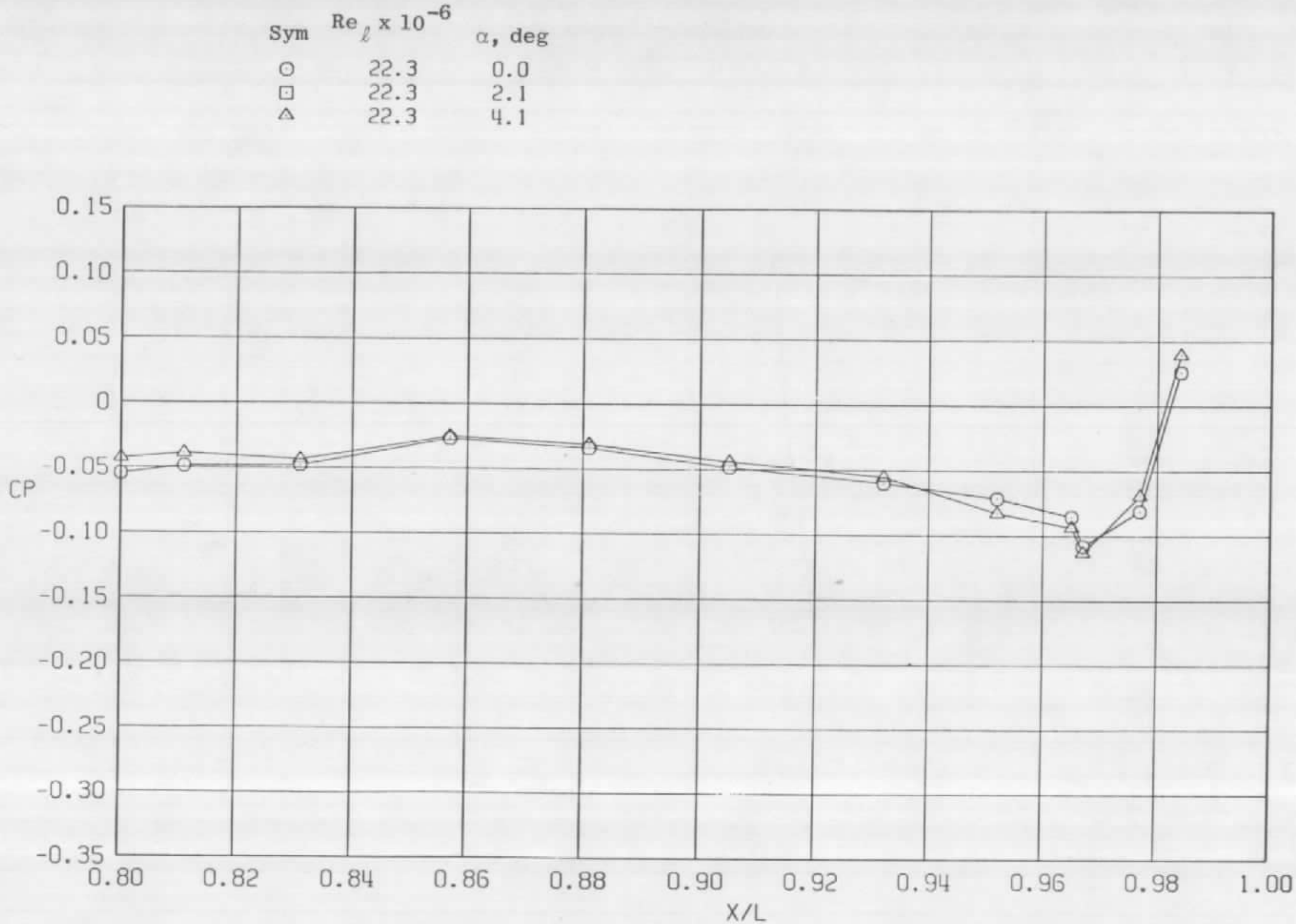

d. ϕ = 180 deg

Figure 33. Continued.

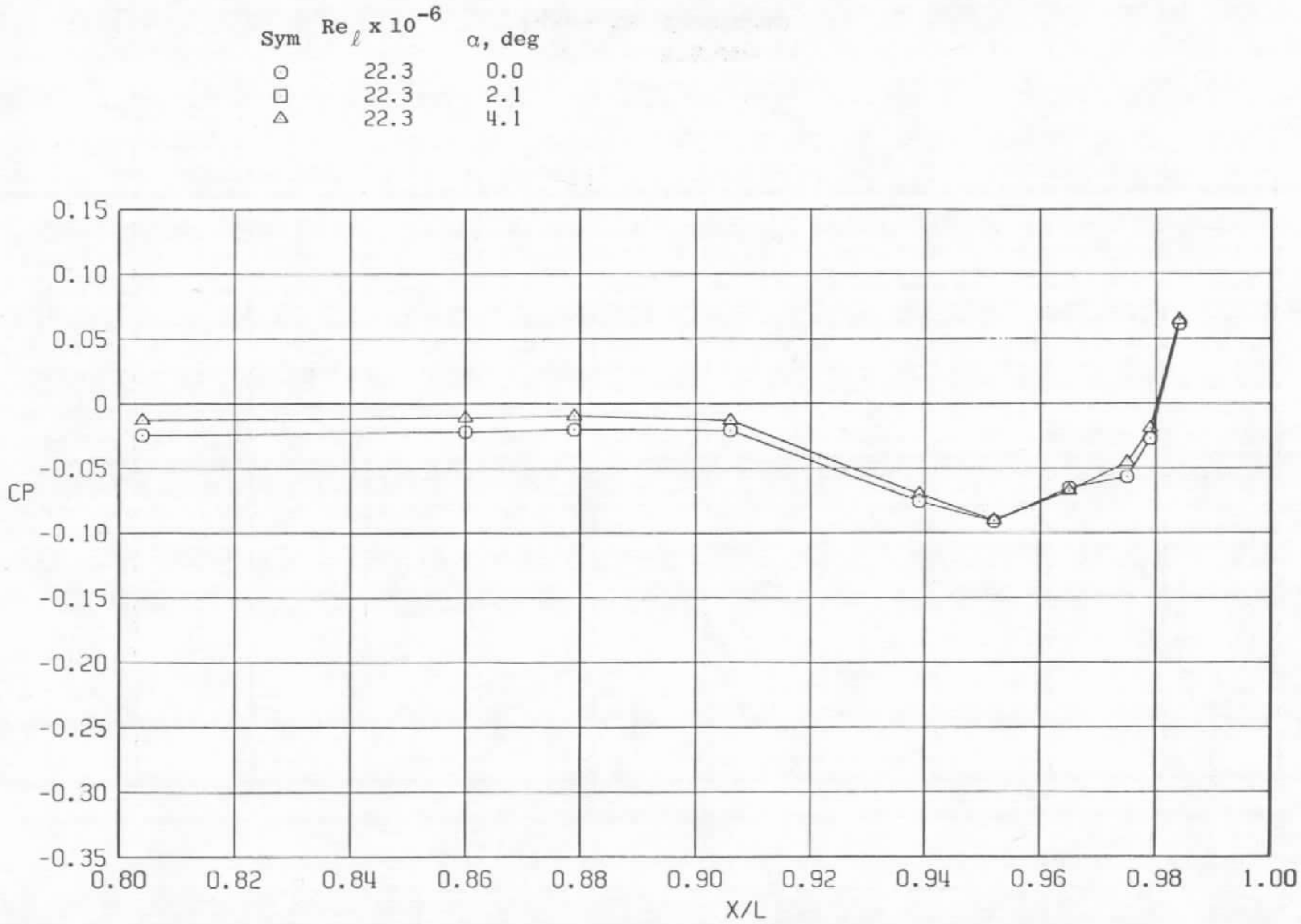

e. ϕ = 225 deg
Figure 33. Continued.

f. ϕ = 315 deg

Figure 33. Concluded.

a. $\phi = 0$

Figure 34. Model attitude effects on surface pressure coefficients, A8 = 300 in.², M = 1.2, NPR = 5.0 (WT).

b. ϕ = 45 deg
Figure 34. Continued.

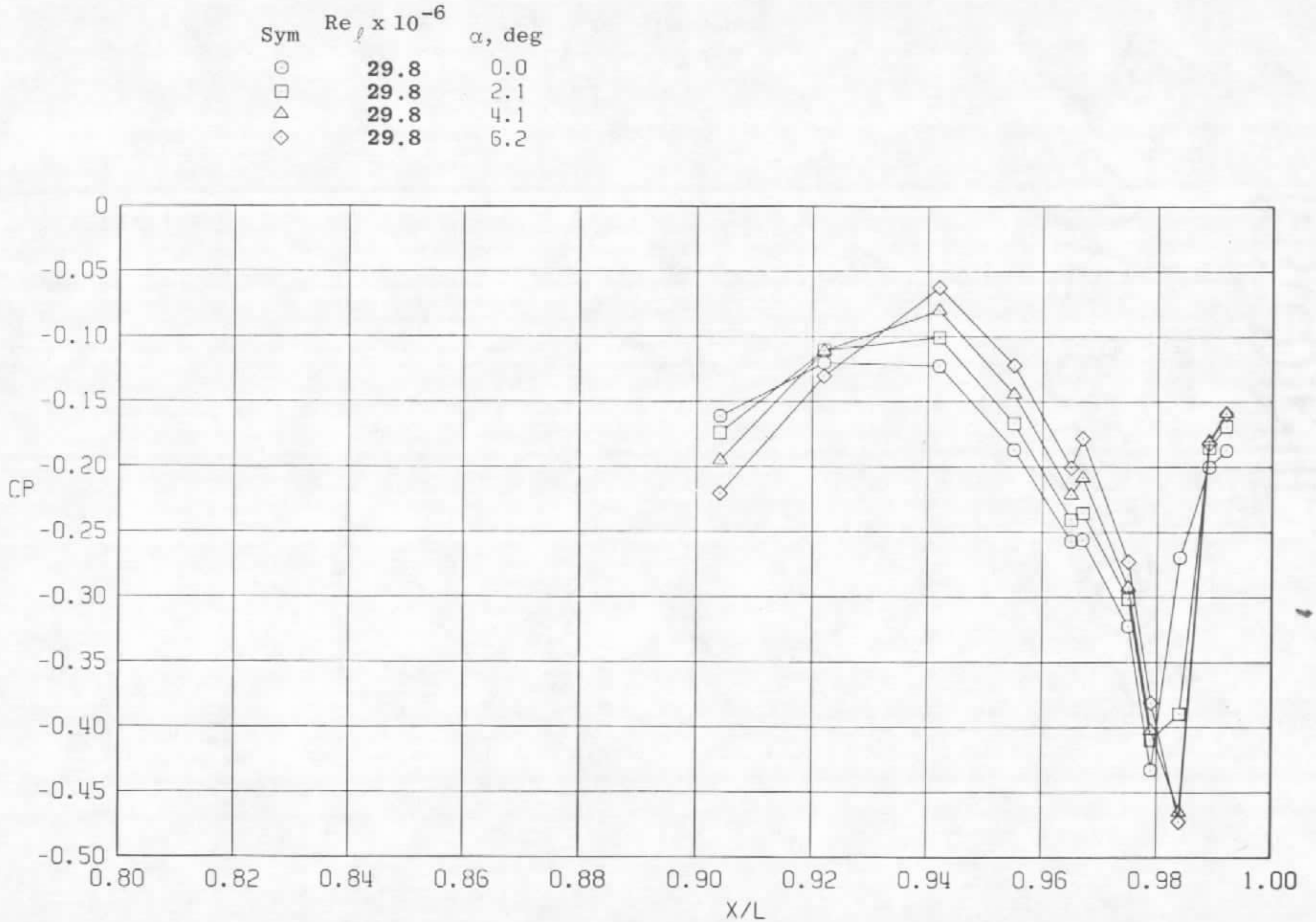

c. ϕ = 135 deg

Figure 34. Continued.

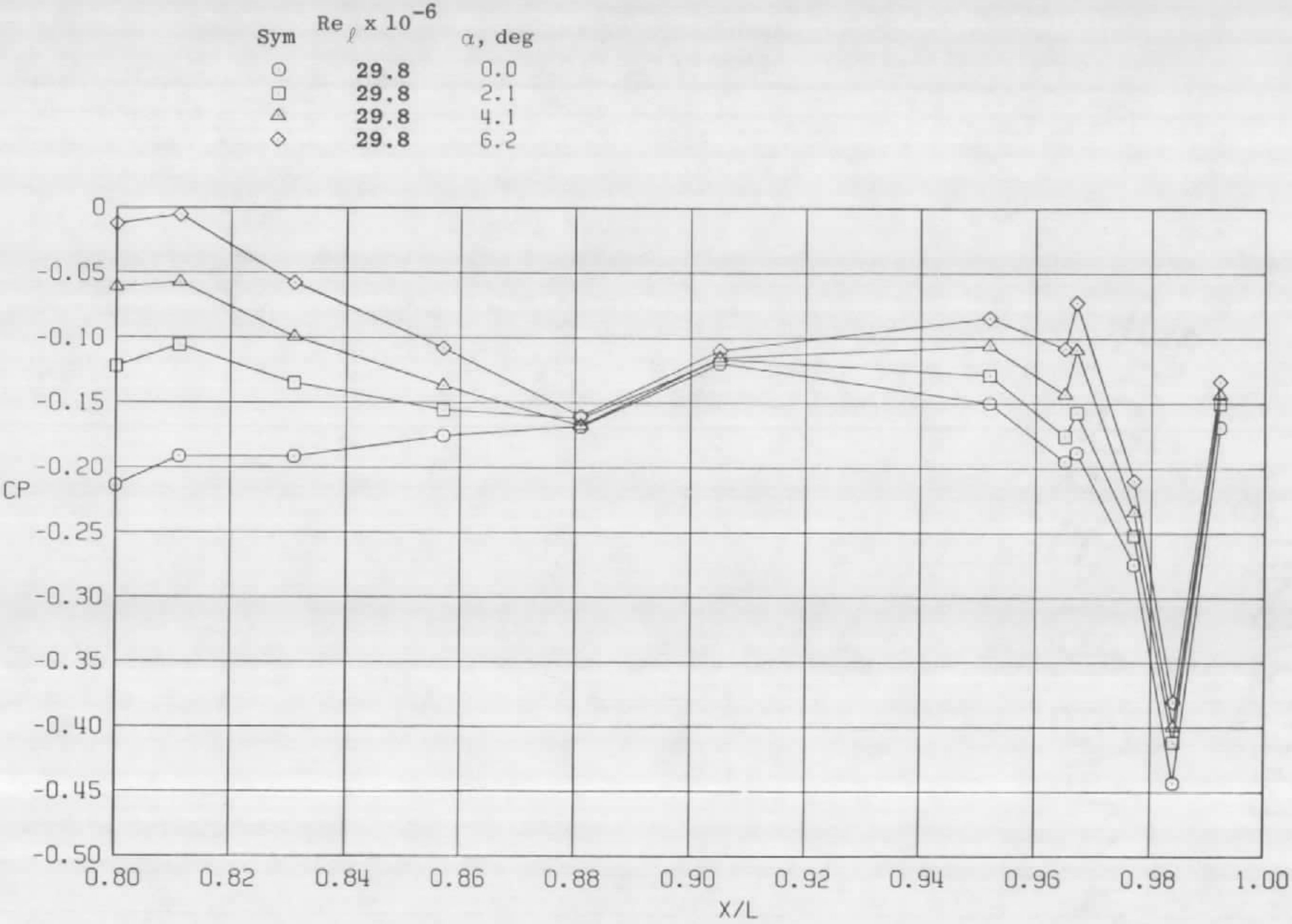

d. ϕ = 180 deg
Figure 34. Continued.

e. ϕ = 225 deg
Figure 34. Continued.

f. ϕ = 315 deg
Figure 34. Concluded.

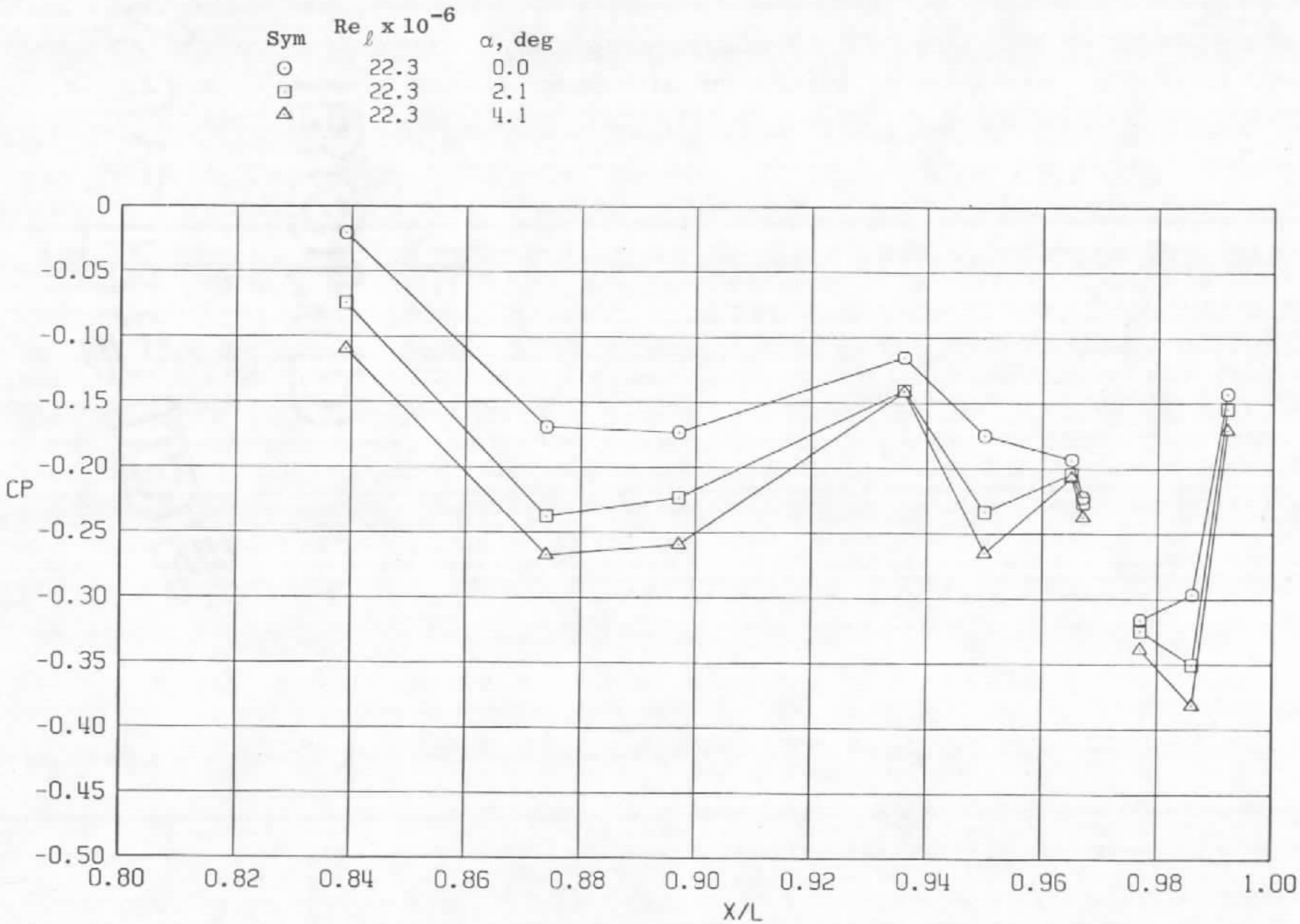

a. $\phi = 0$

Figure 35. Effect of model attitude on surface pressure coefficients, A8 = 300 in.², M = 1.2, NPRE = 5.0 (SS).

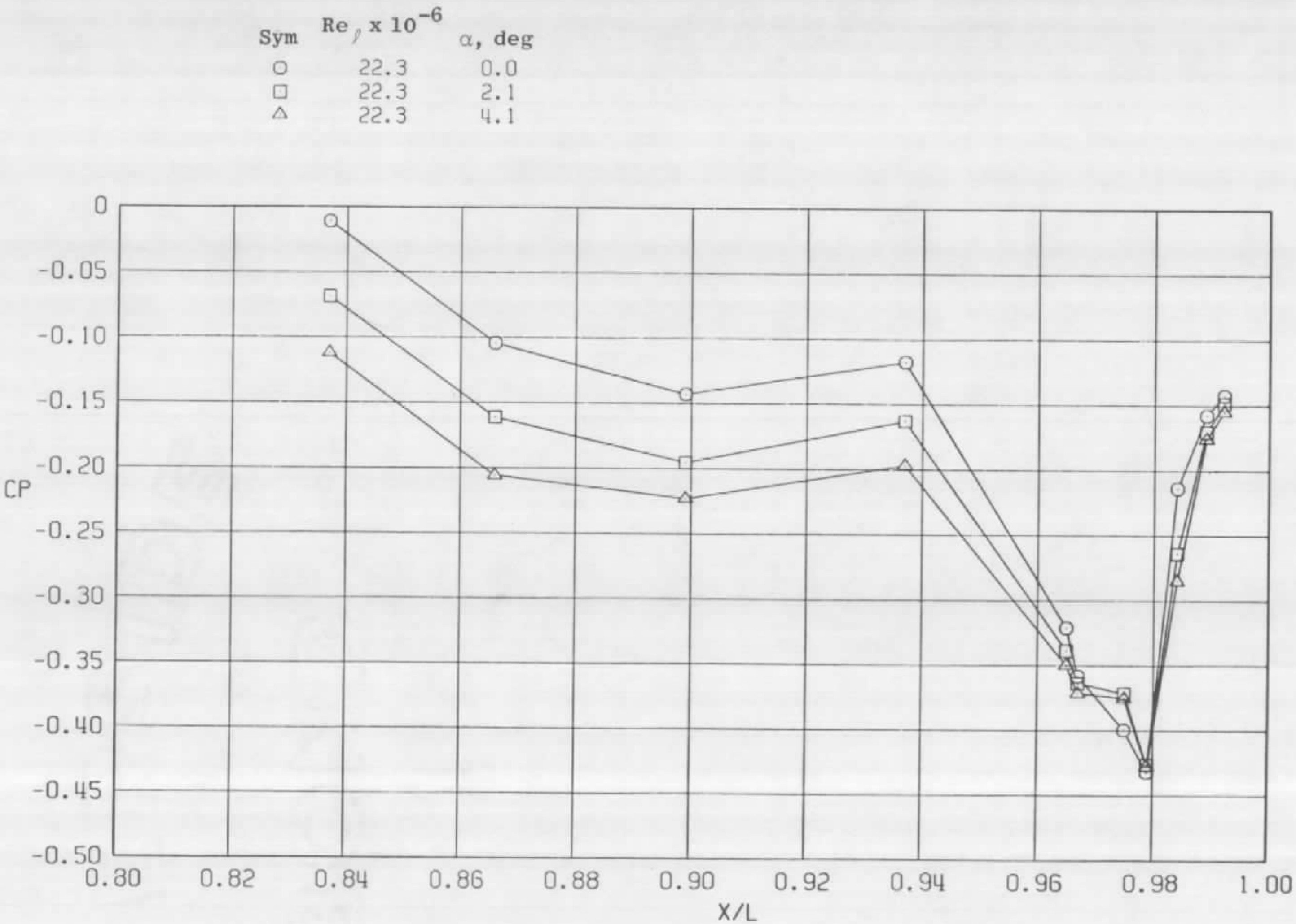

b. ϕ = 45 deg
Figure 35. Continued.

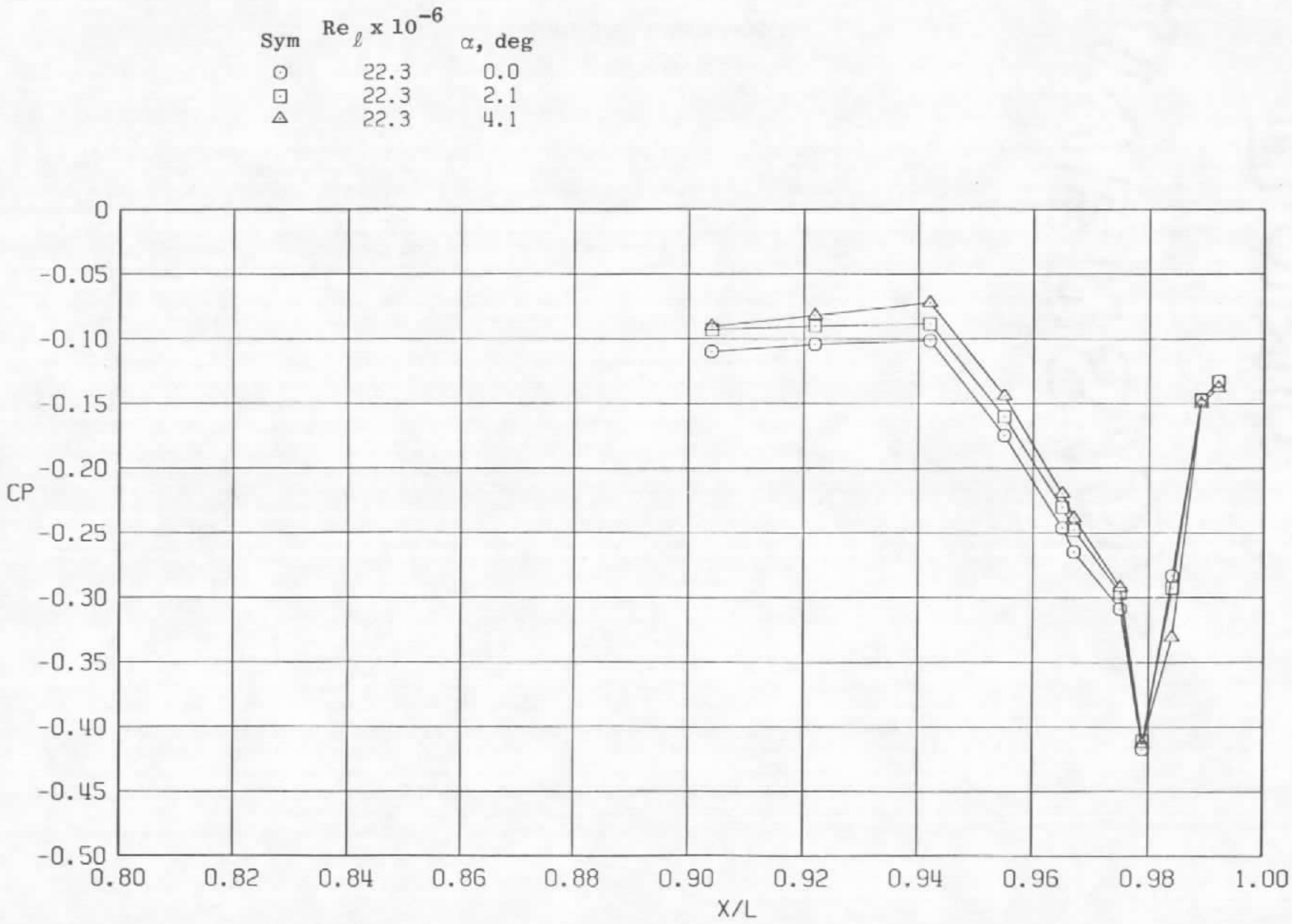

c. ϕ = 135 deg
Figure 35. Continued.

d. ϕ = 180 deg

Figure 35. Continued.

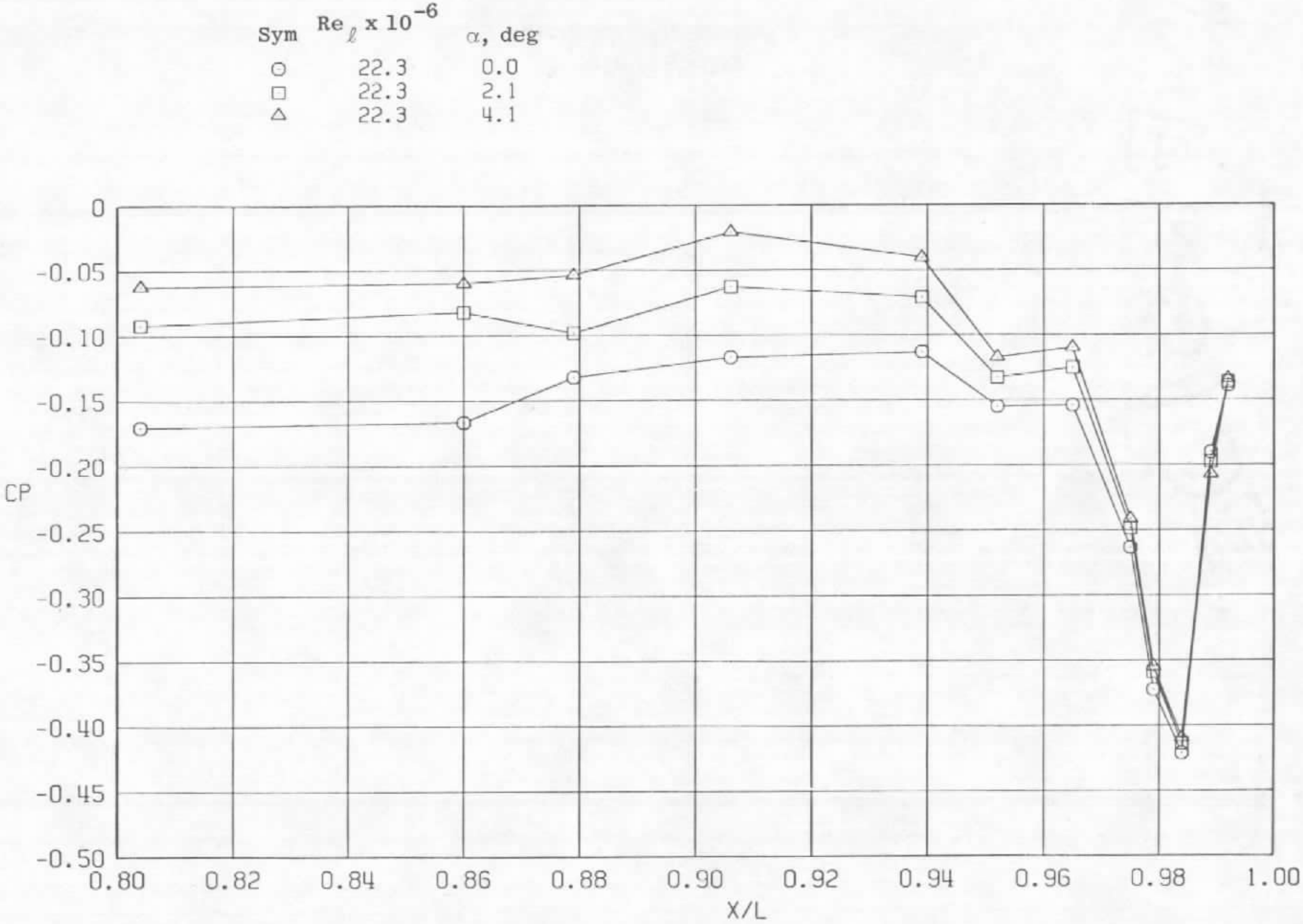

e. ϕ = 225 deg
Figure 35. Continued.

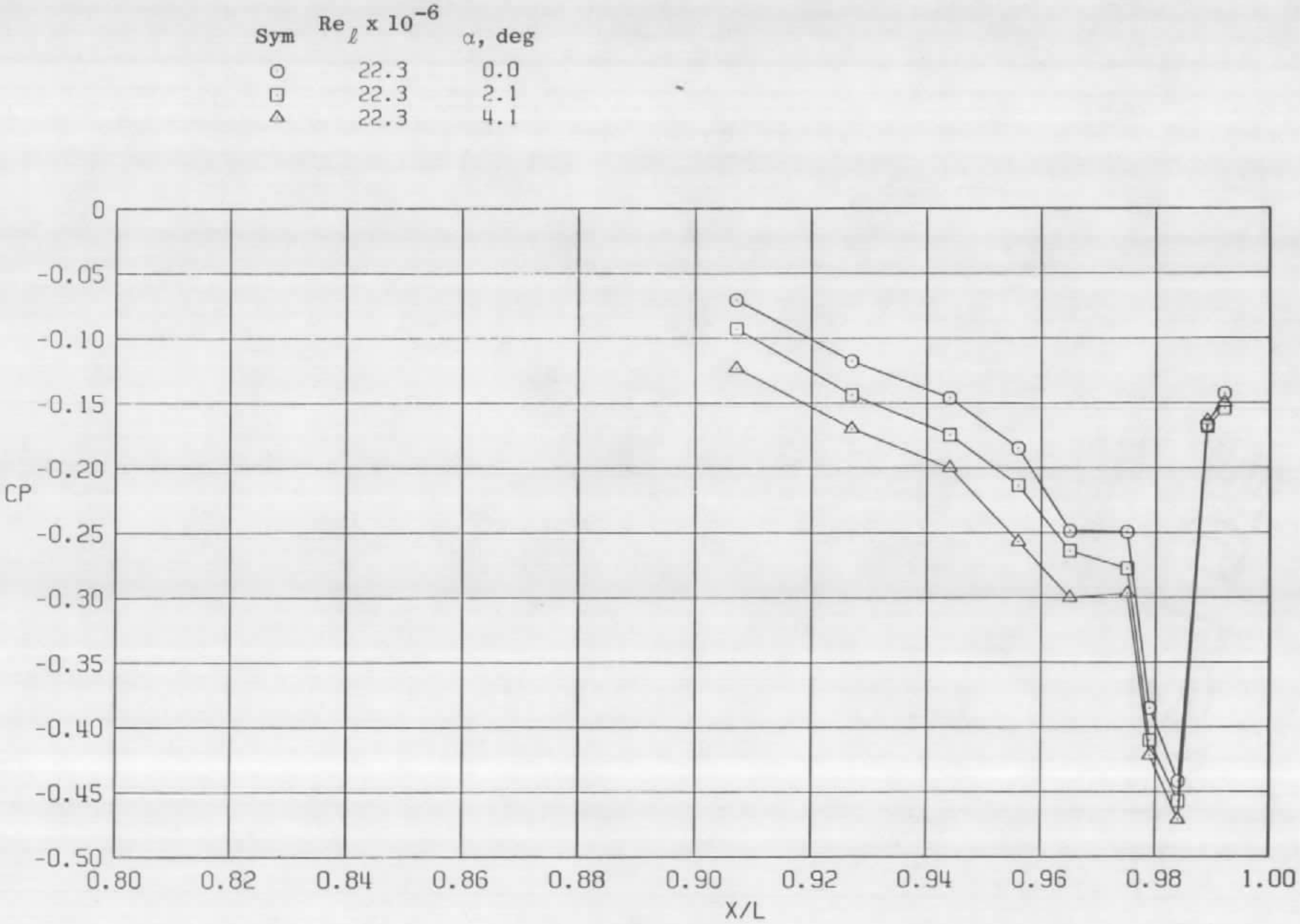

f. ϕ = 315 deg
Figure 35. Concluded.

a. $\phi = 0$

Figure 36. Model attitude effects on surface pressure coefficients, A8 = 360 in.², M = 1.2, NPR = 5.6 (WT).

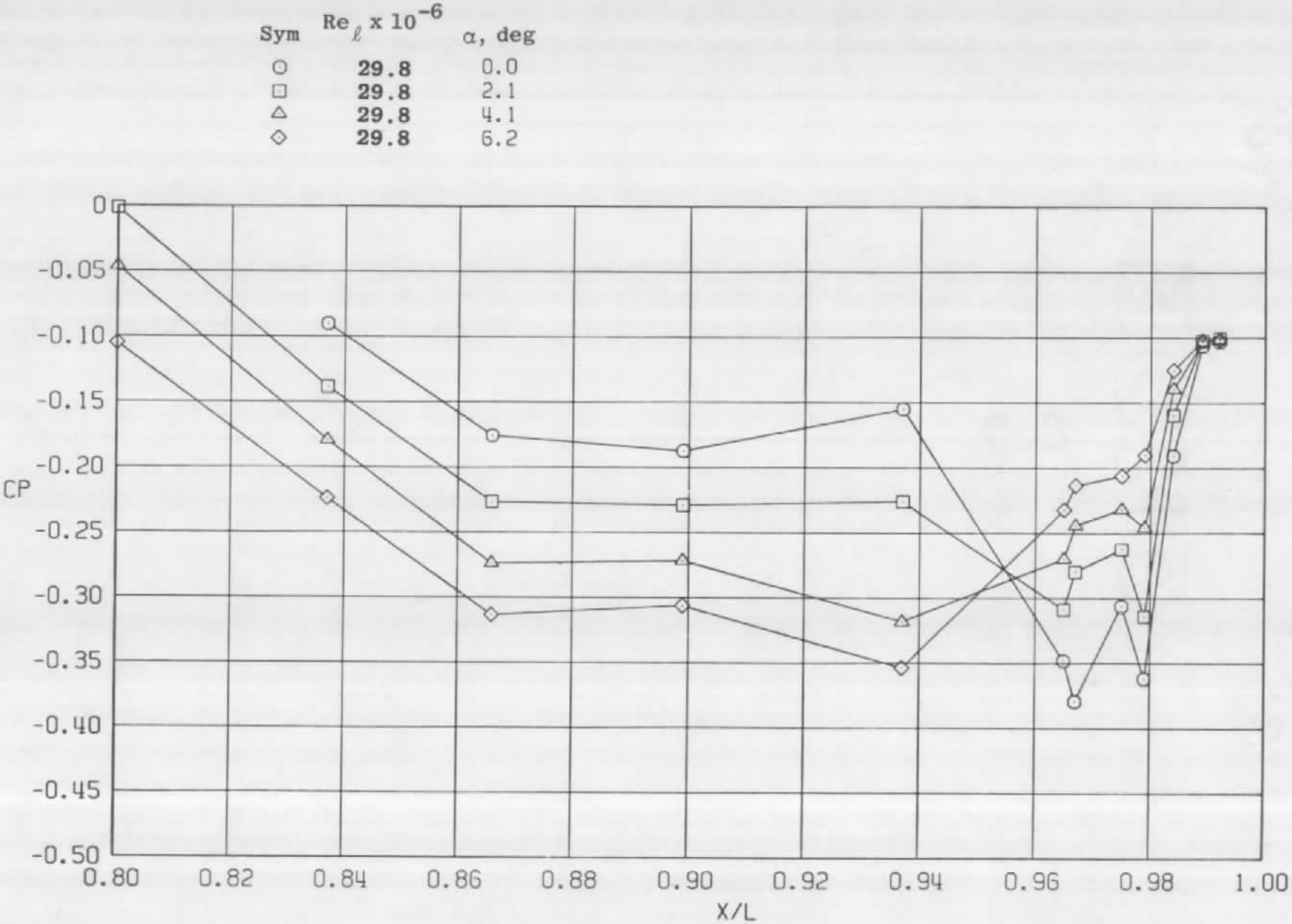

b. ϕ = 45 deg
Figure 36. Continued.

c. ϕ = 135 deg
Figure 36. Continued.

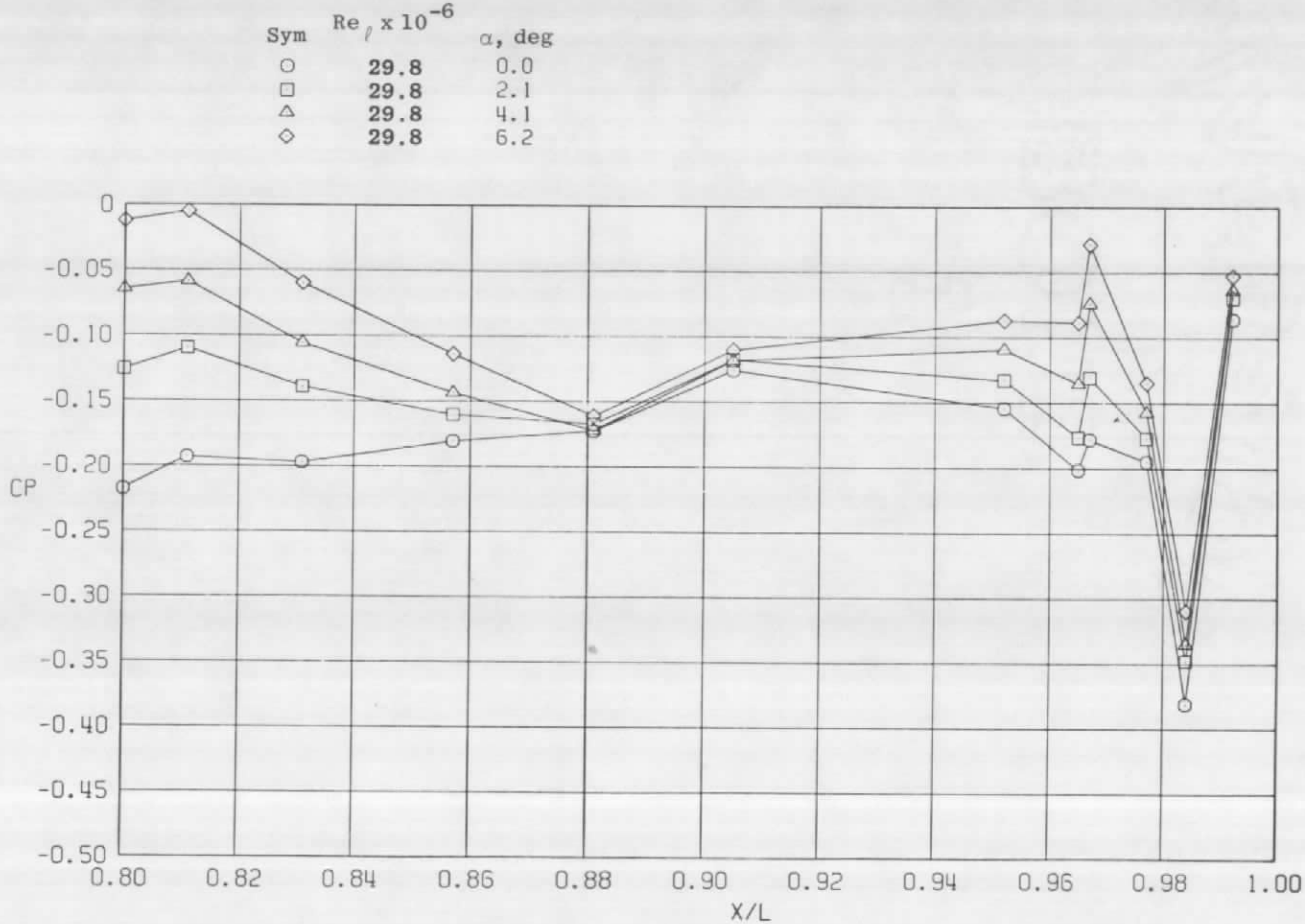

d. ϕ = 180 deg
Figure 36. Continued.

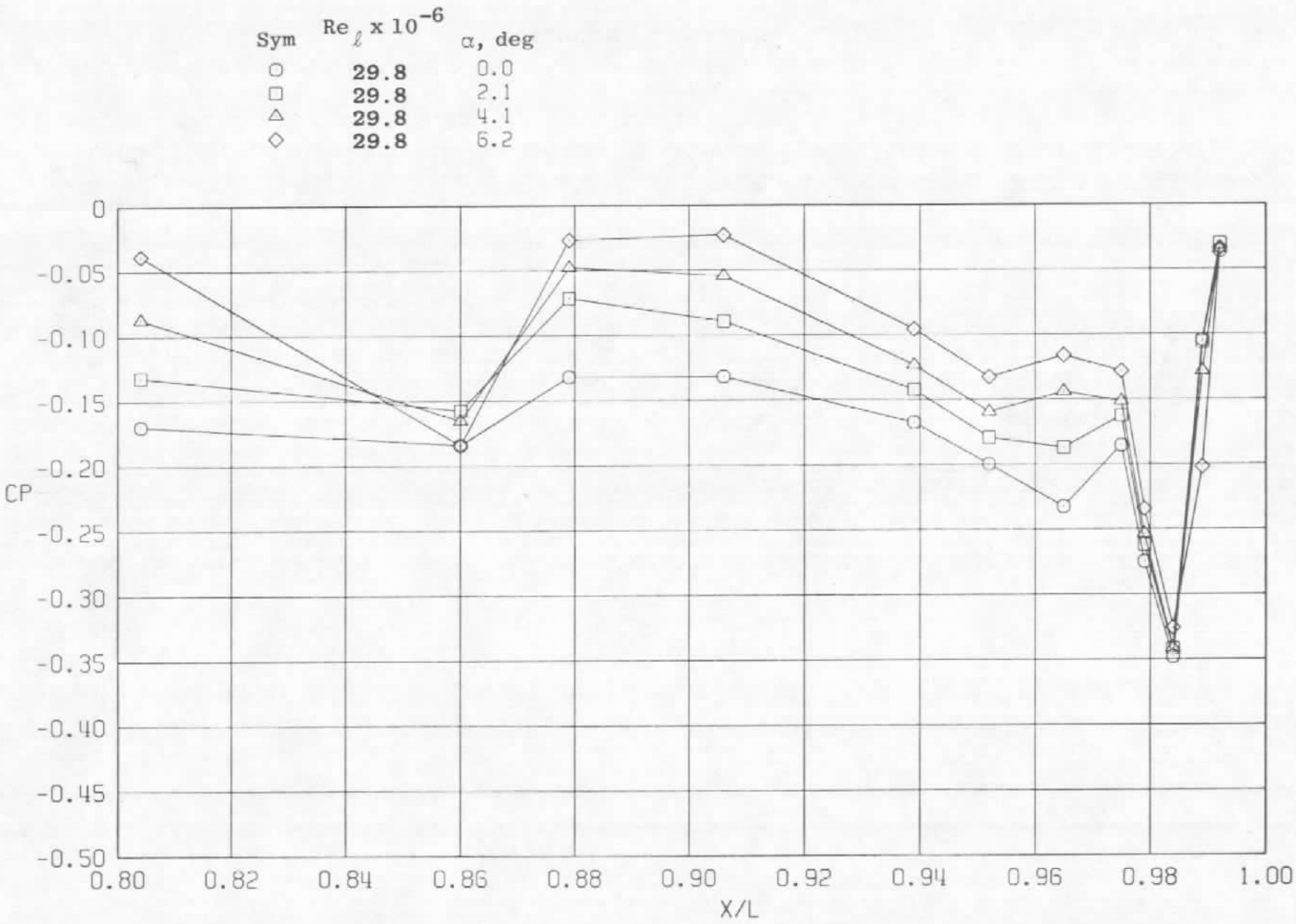

e. ϕ = 225 deg
Figure 36. Continued.

f. ϕ = 315 deg
Figure 36. Concluded.

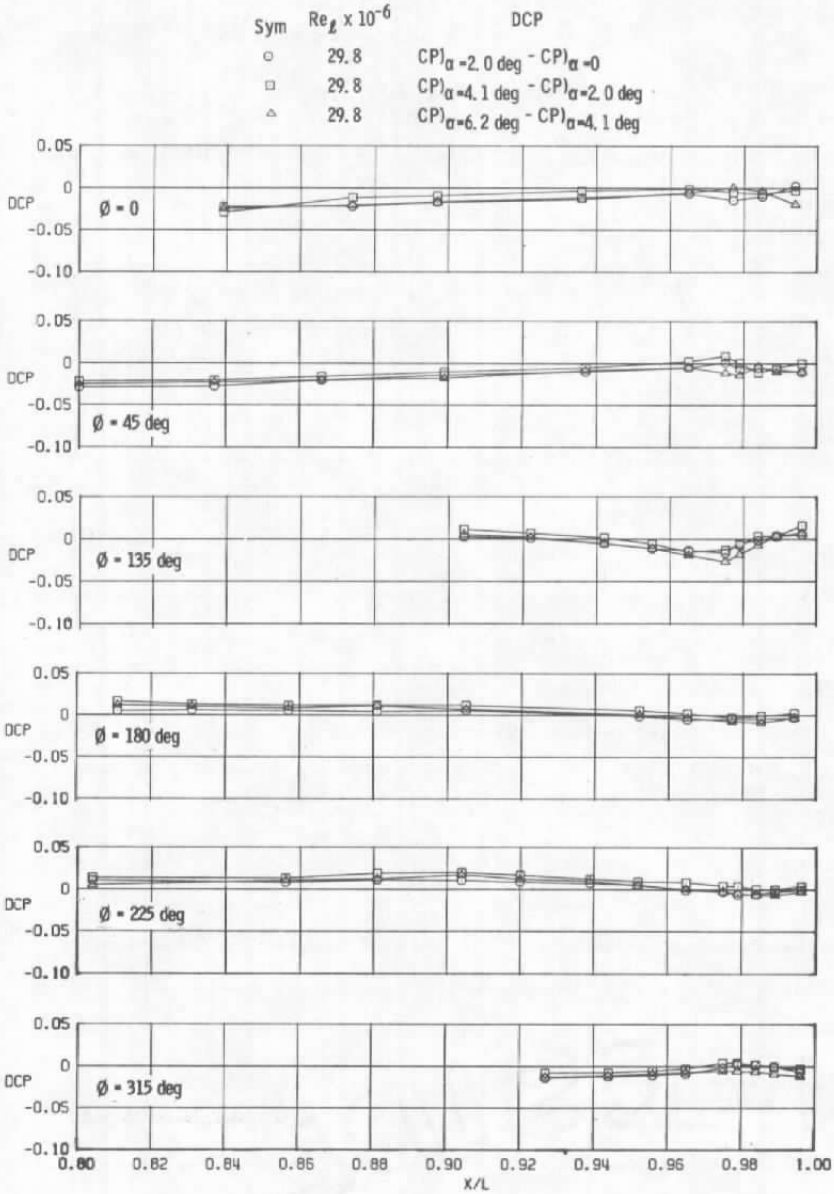

a. M = 0.6, A8 = 200 in.^{2}, NPR = 3.4 (WT)
Figure 37. Effect of incremental changes in model attitude on surface pressure coefficients.

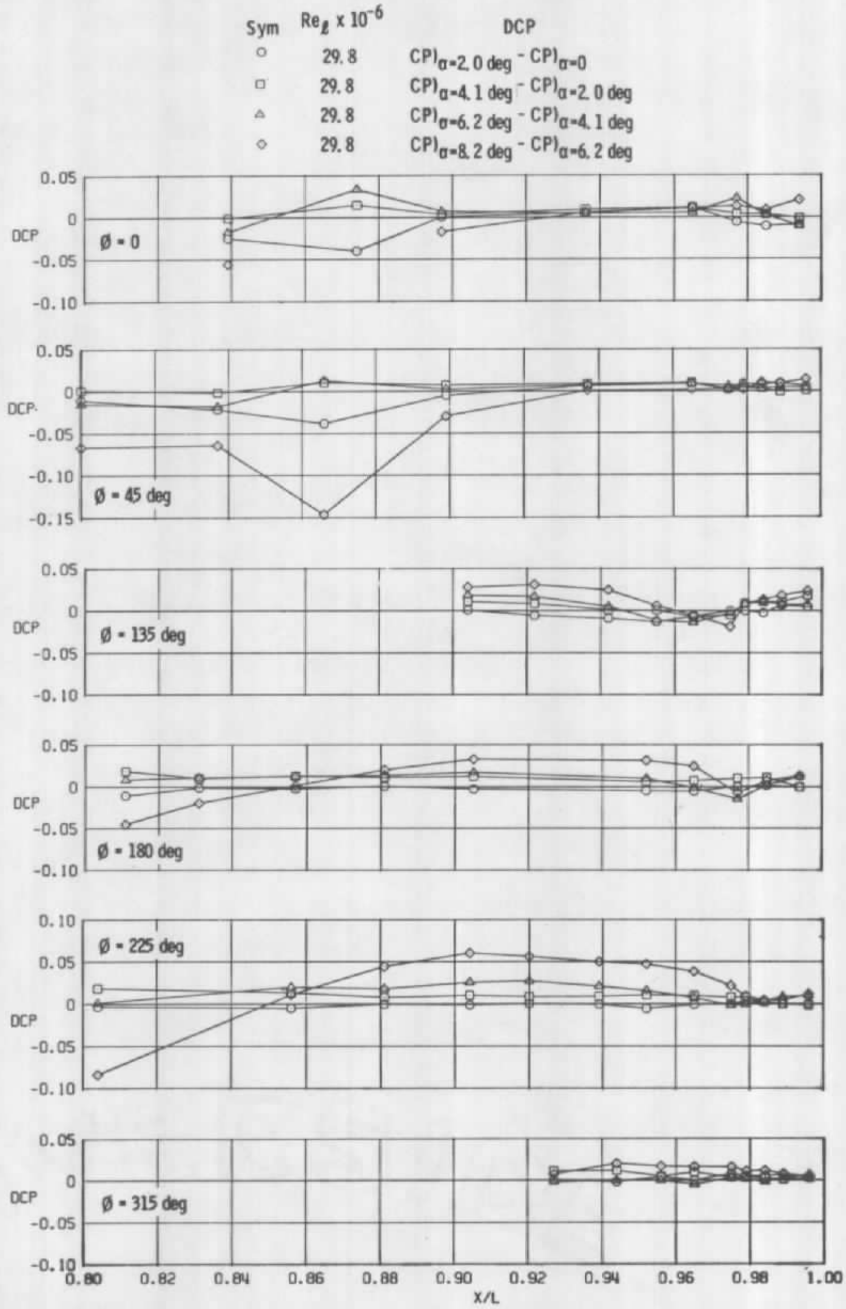

b. M = 0.9, A8 = 200 in.^{2}, NPR = 3.4 (WT)

Figure 37. Continued.

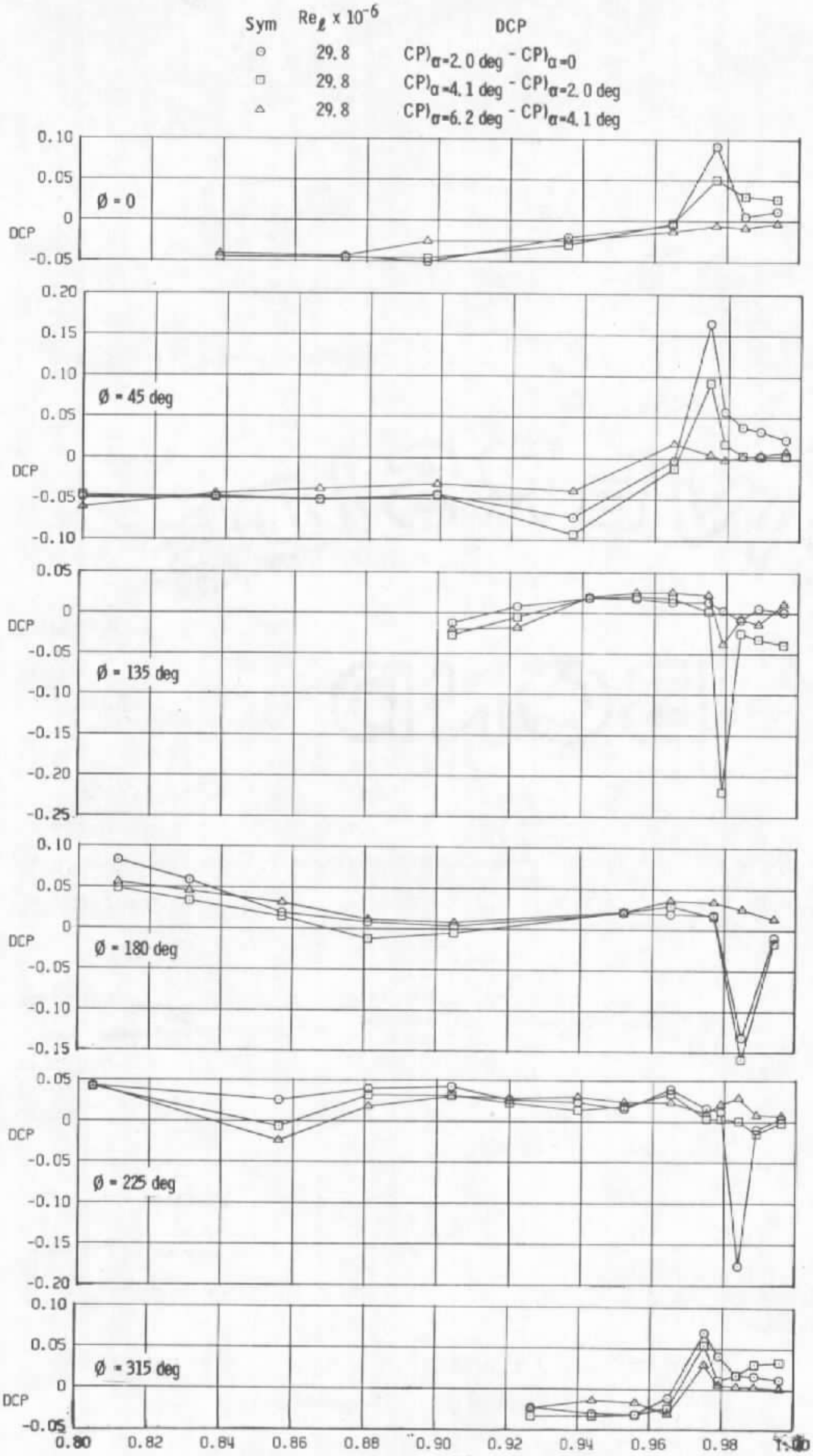

c. M = 1.2, A8 = 200 in.^{2}, NPR = 3.4 (WT)
Figure 37. Continued.

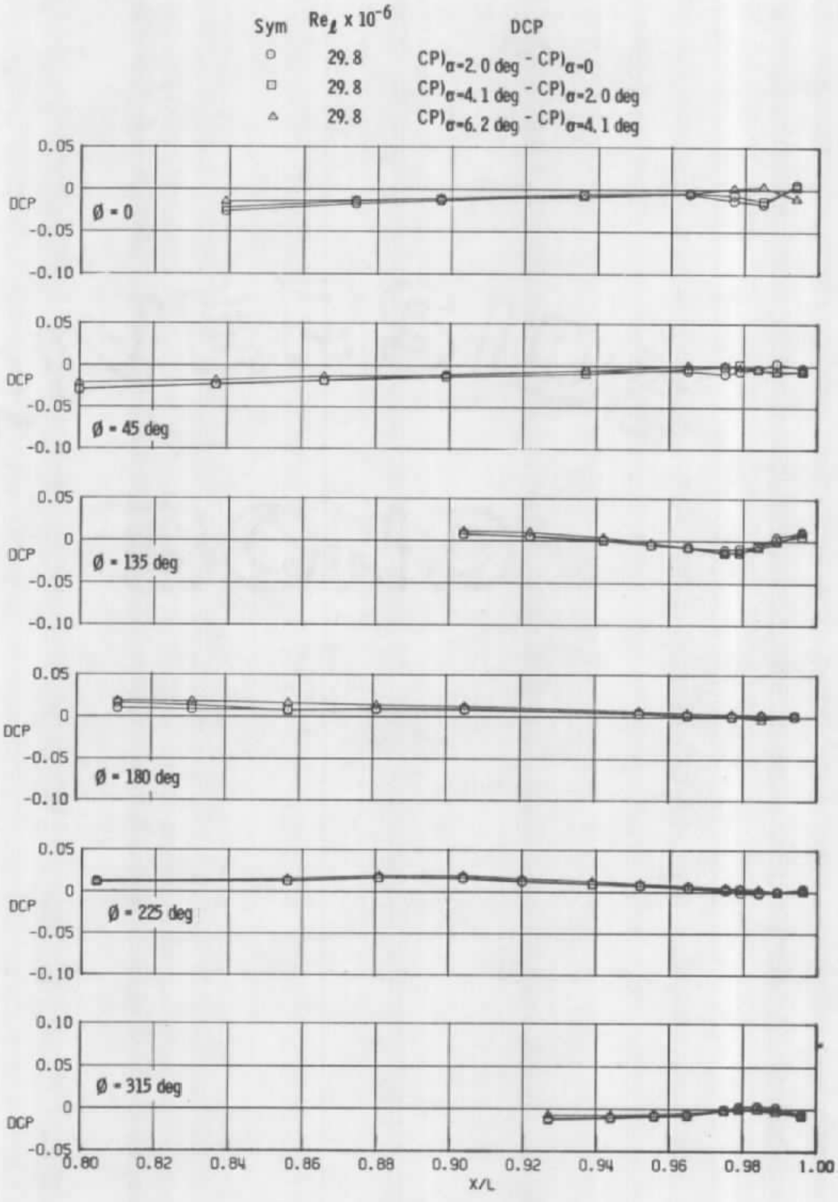

d. M = 0.6, A8 = 300 in.², NPR = 5.0 (WT)
Figure 37. Continued.

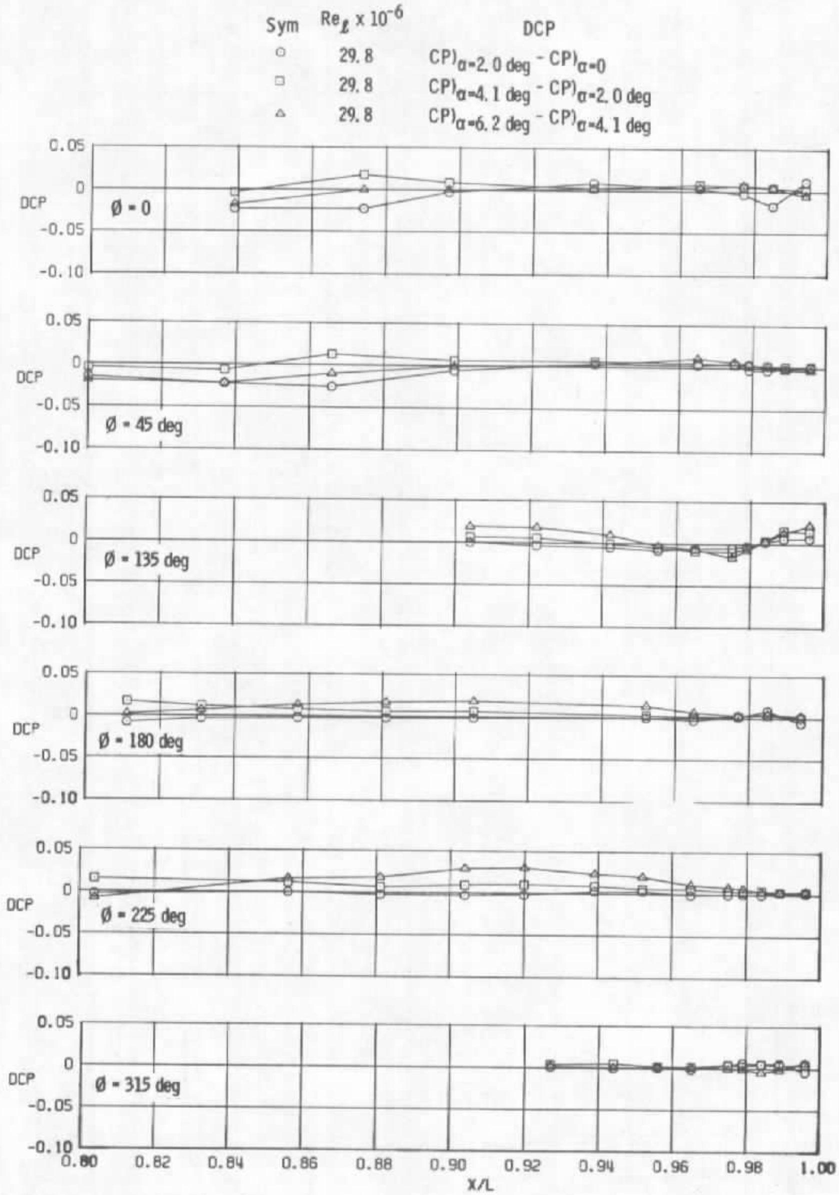

e. M = 0.9, A8 = 300 in.^{2}, NPR = 5.0 (WT)

Figure 37. Continued.

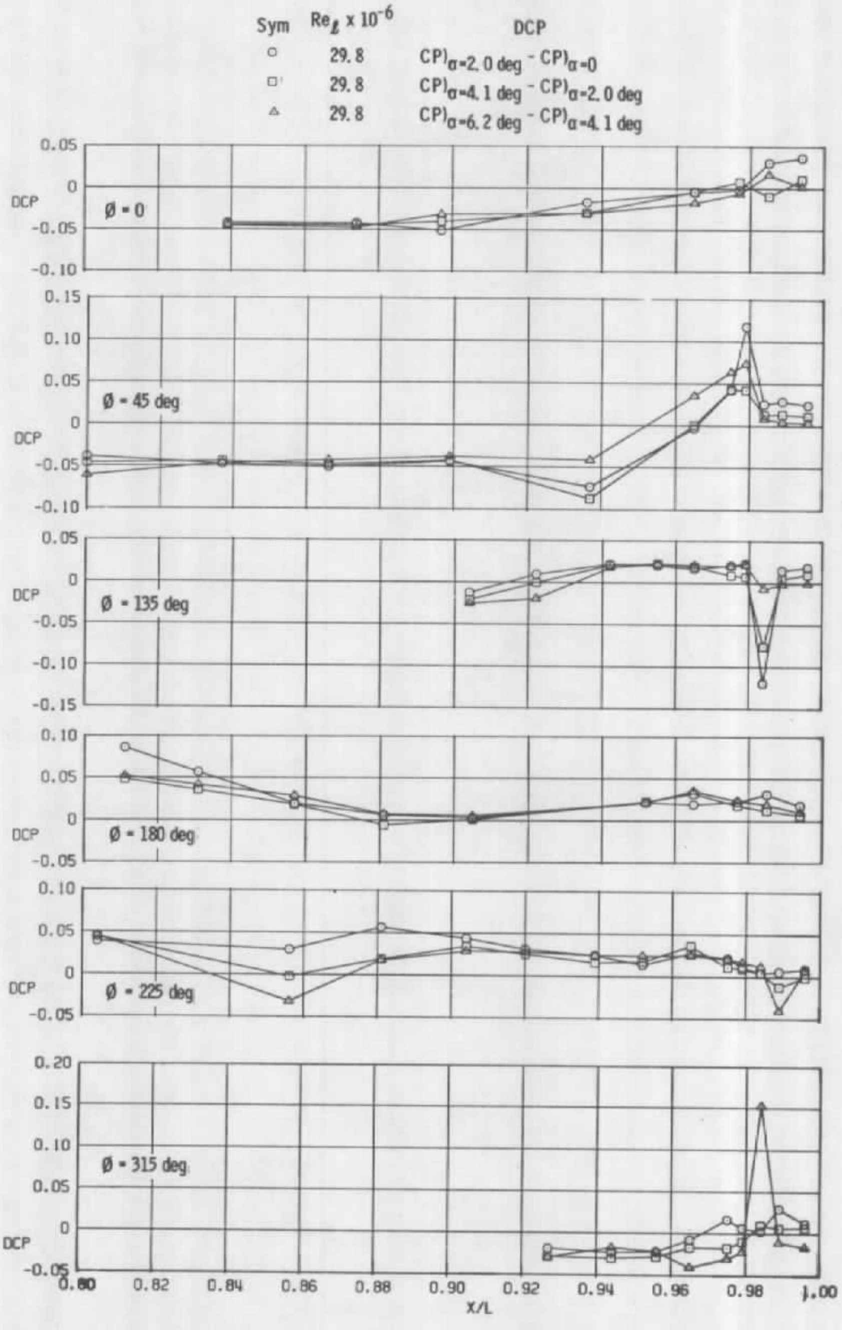

f. M = 1.2, A8 = 300 in.², NPR = 5.0 (WT)
Figure 37. Continued.

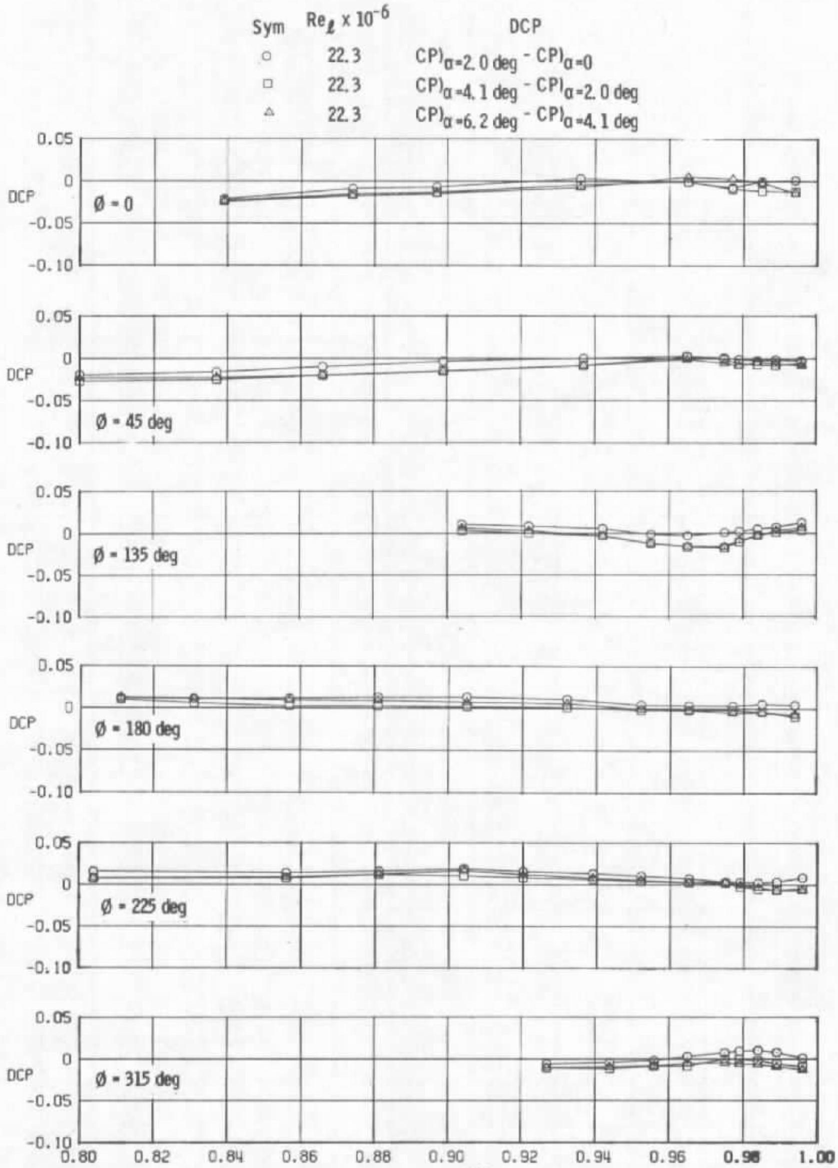

g. M = 0.6, A8 = 200 in.², NPRE = 3.4 (SS)
Figure 37. Continued.

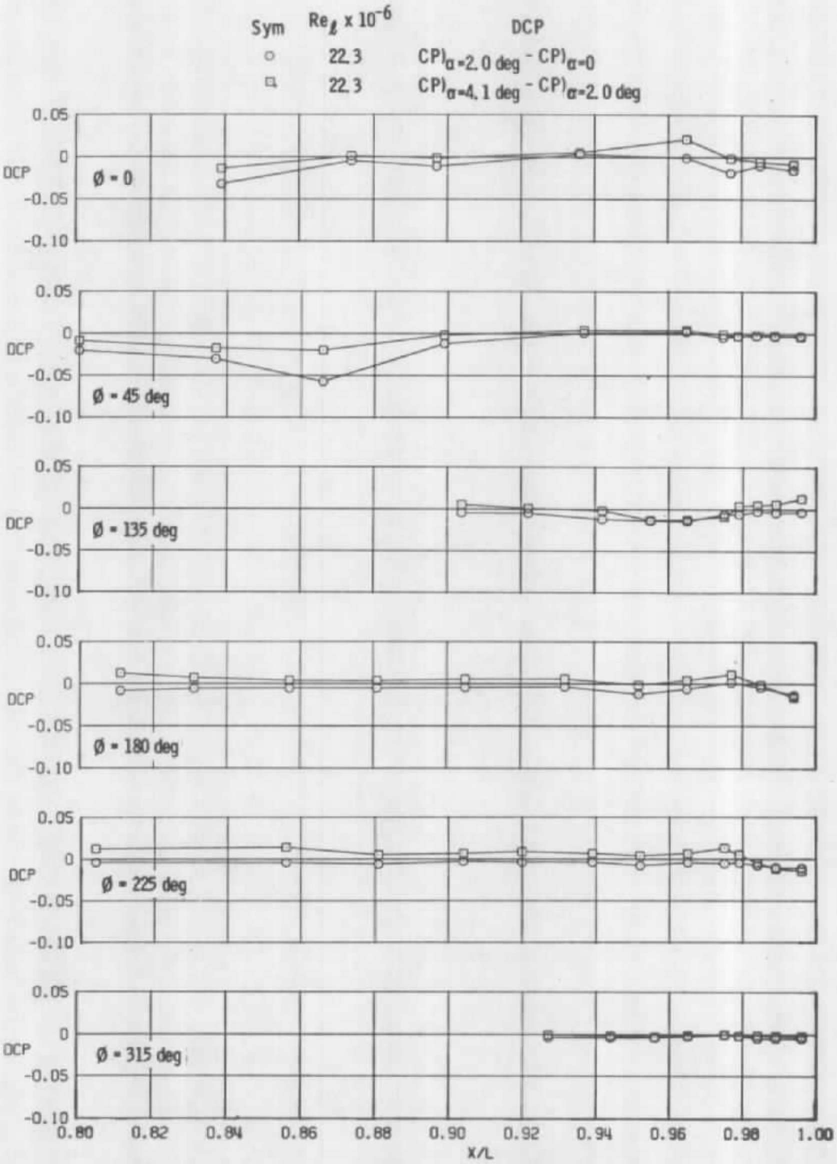

h. M = 0.9, A8 = 200 in.², NPRE = 3.4 (SS)

Figure 37. Continued.

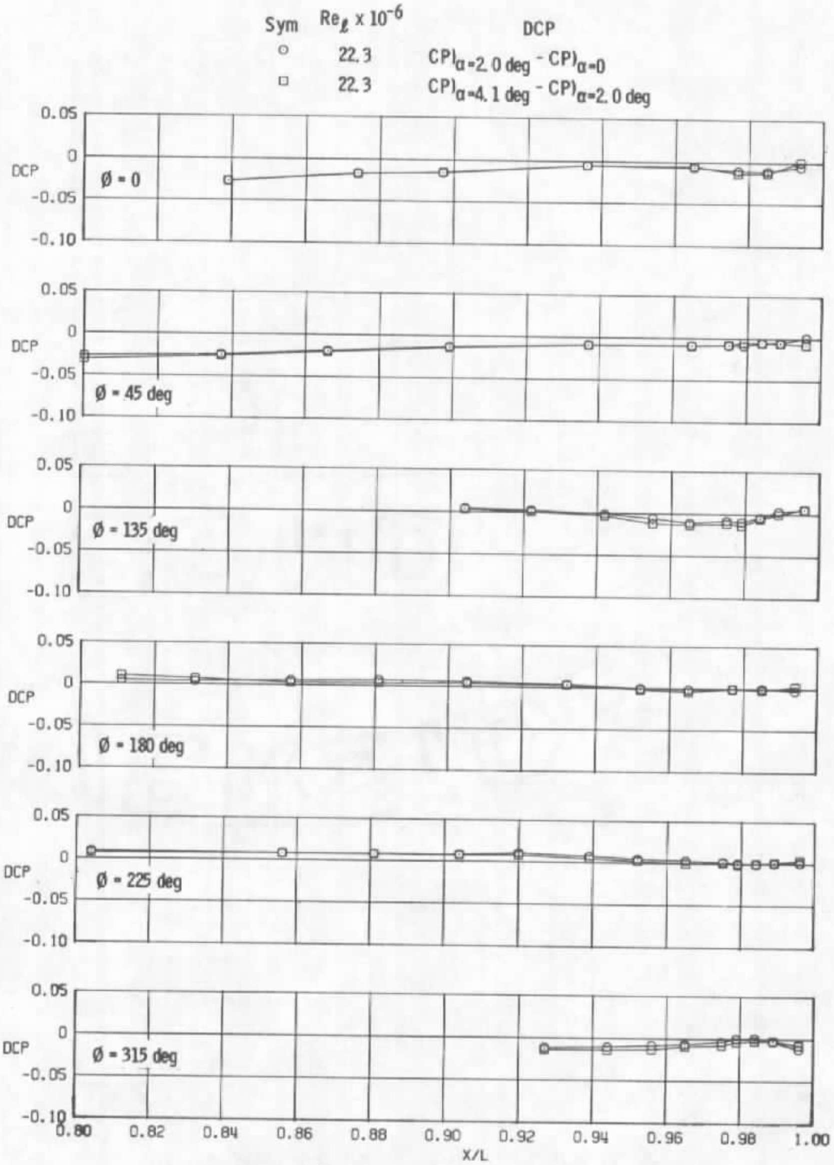

i. M = 0.6, A8 = 300 in.², NPRE = 5.0 (SS)
Figure 37. Continued.

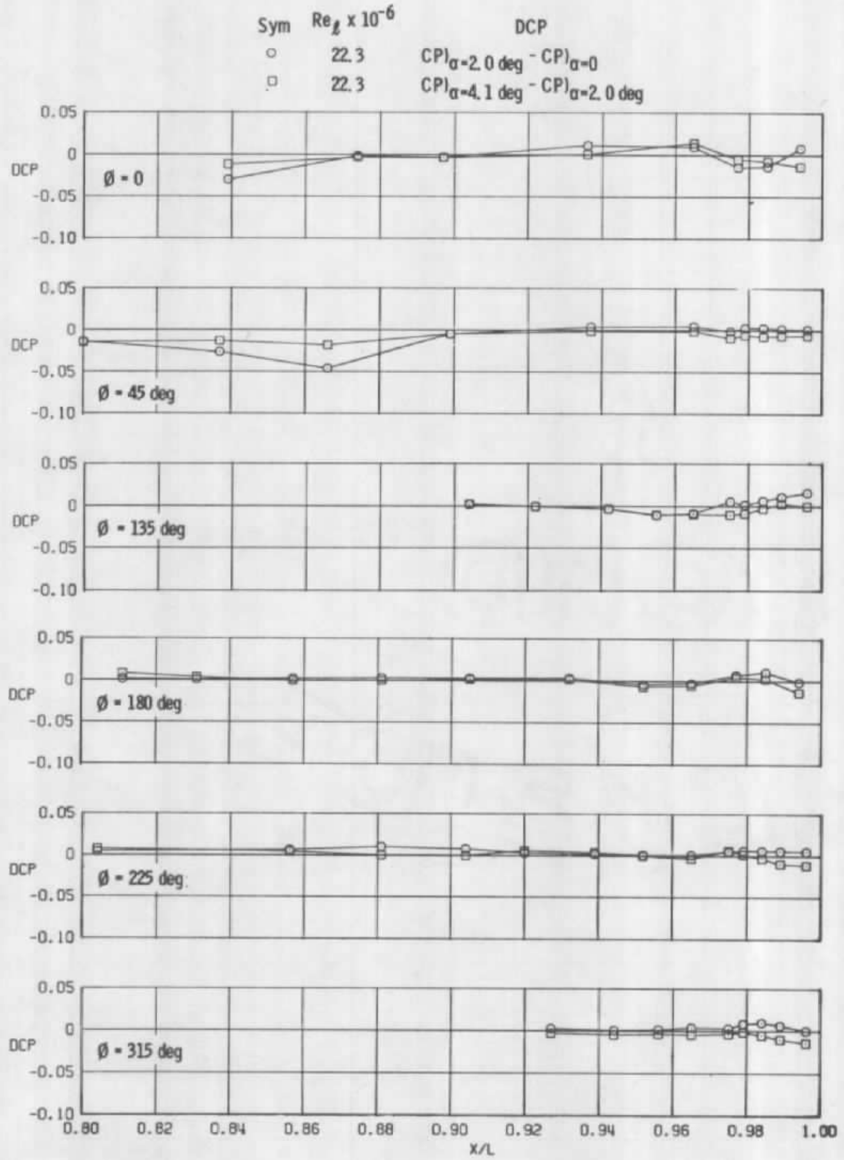

j. M = 0.9, A8 = 300 in.^{2}, NPRE = 5.0 (SS)
Figure 37. Continued.

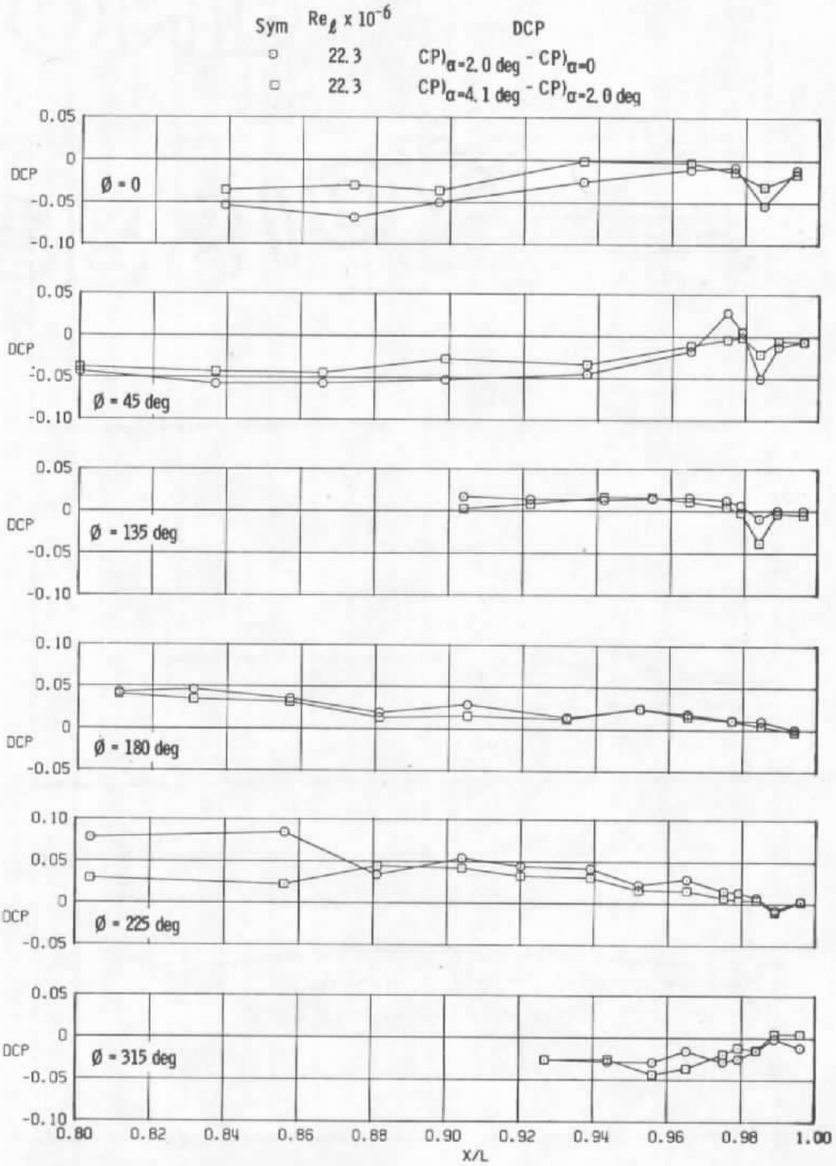

k. M = 1.2, A8 = 300 in.^{2}, NPRE = 5.0 (SS)

Figure 37. Concluded.

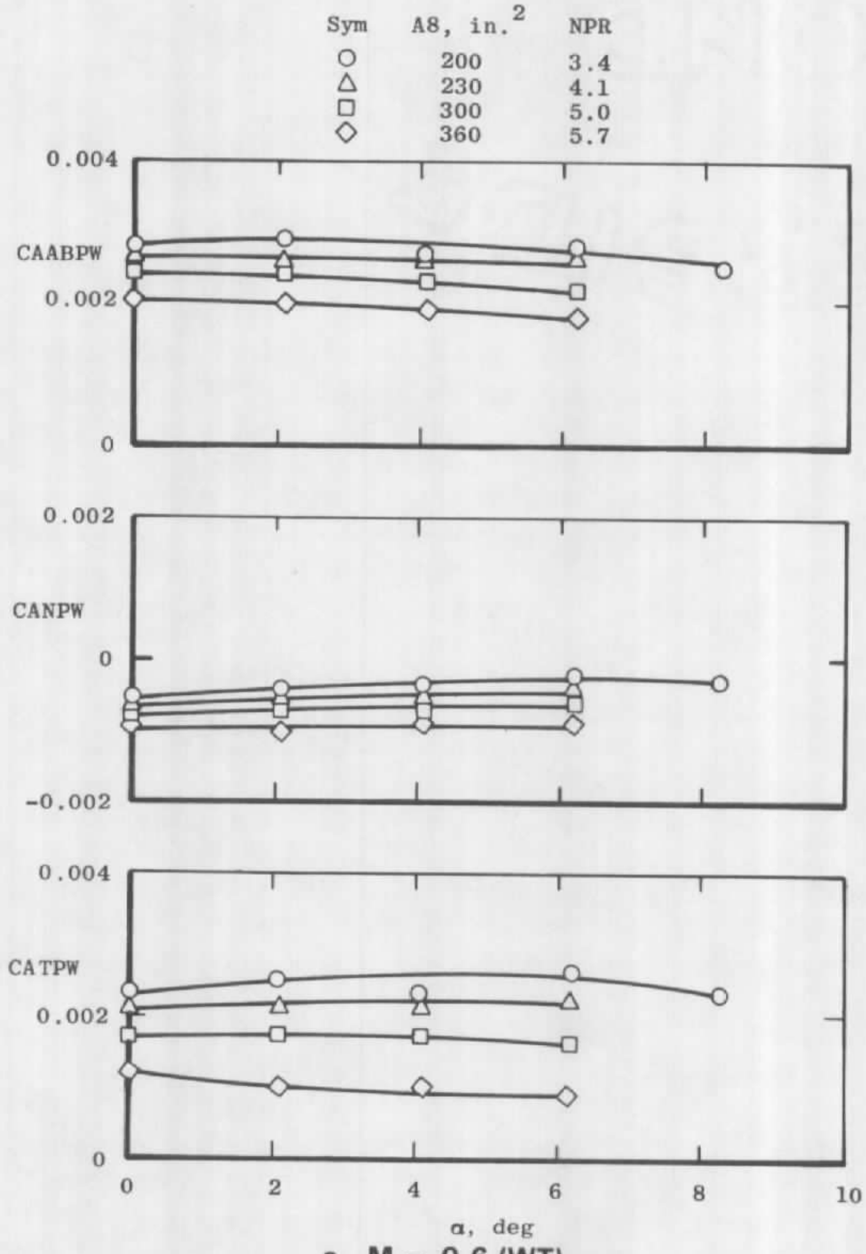

a. M = 0.6 (WT)

Figure 38. Effect of model attitude on axial force coefficients (WT).

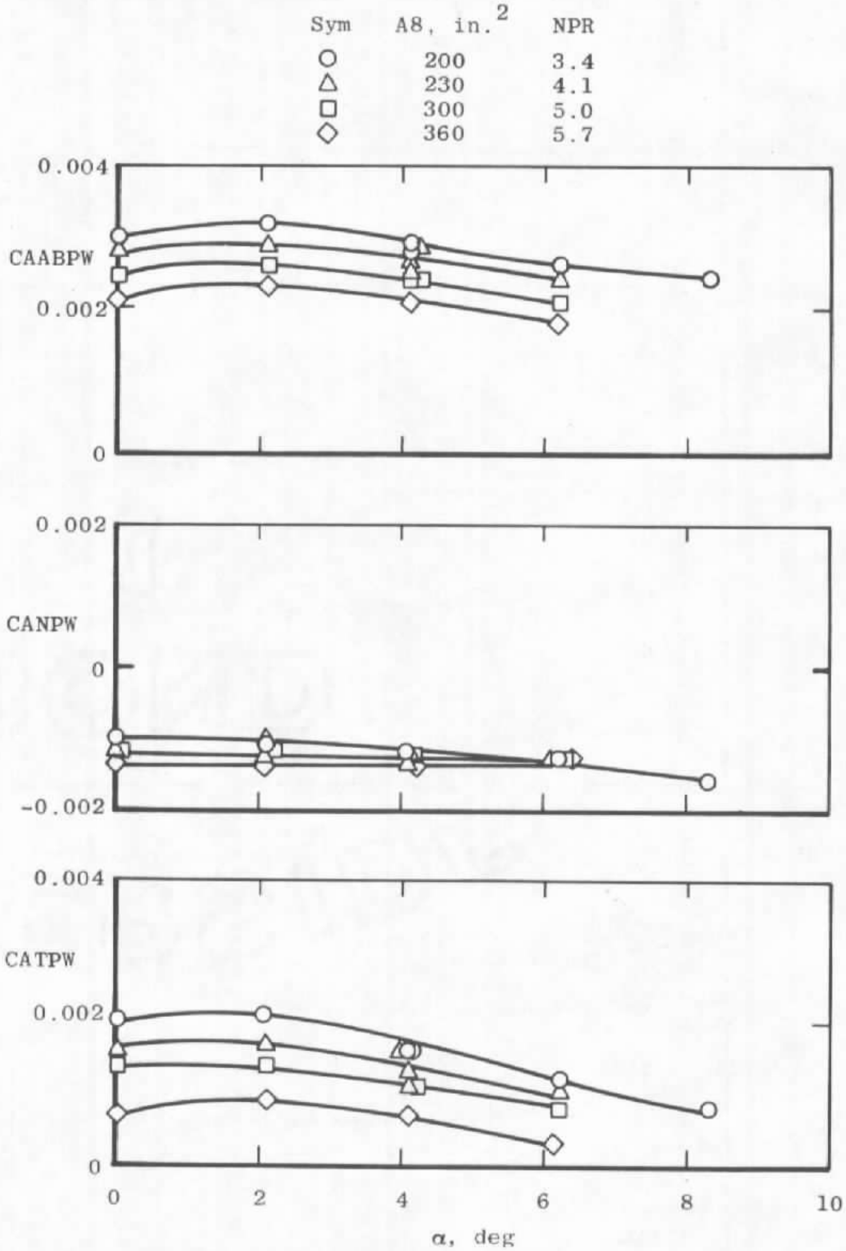

b. M = 0.9 (WT)
Figure 38. Continued.

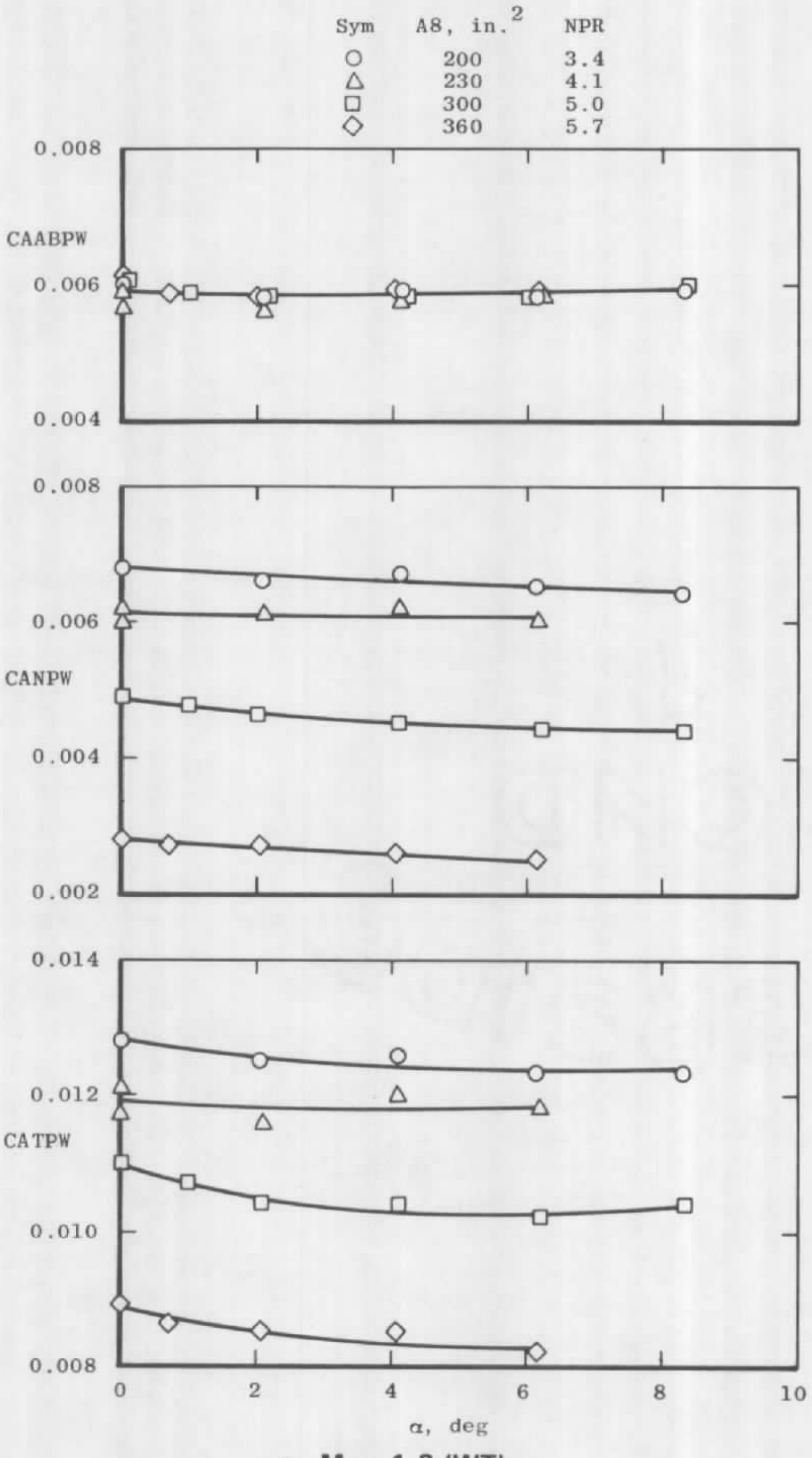

c. M = 1.2 (WT)
Figure 38. Continued.

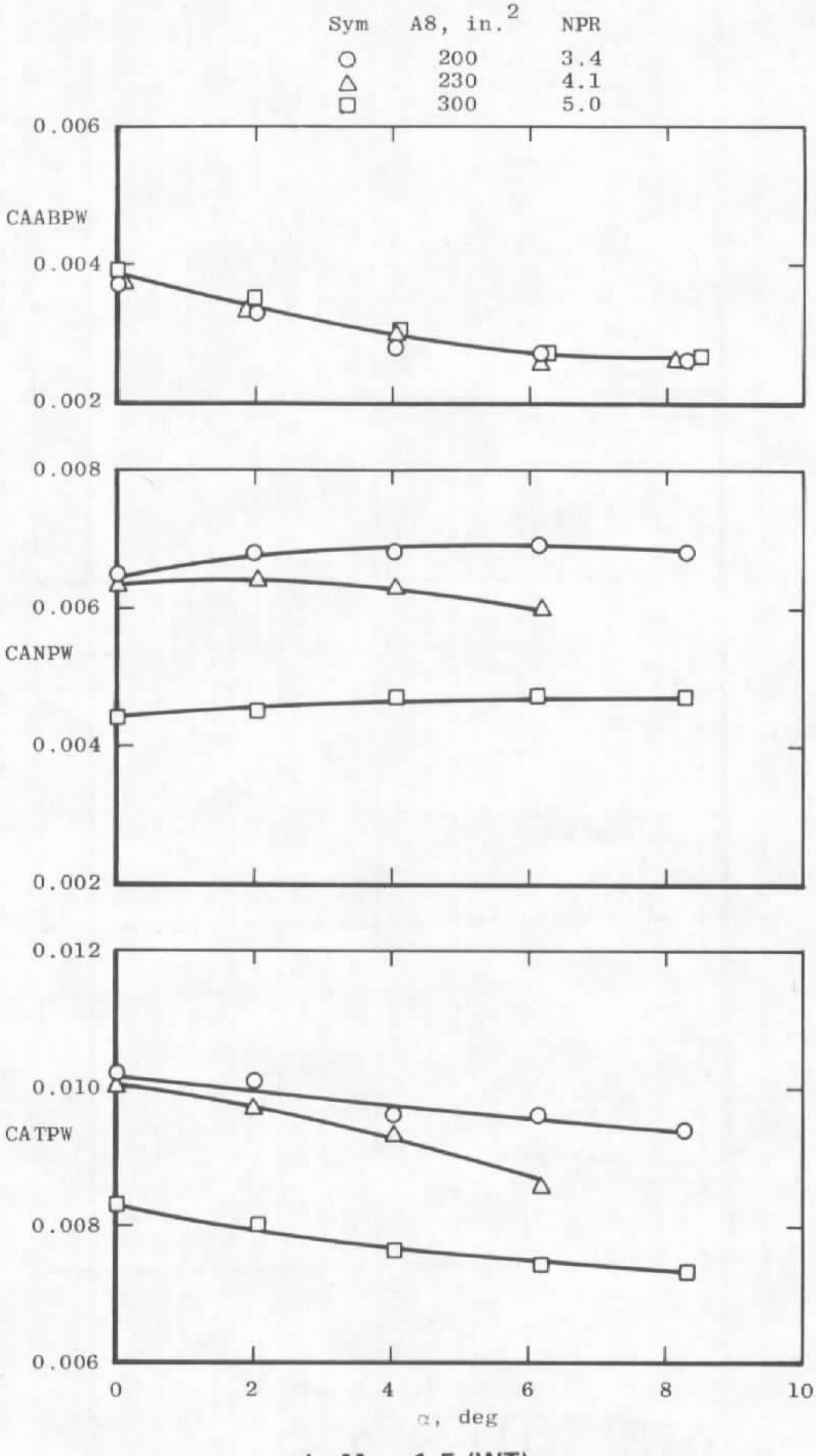

d. M = 1.5 (WT)
Figure 38. Continued.

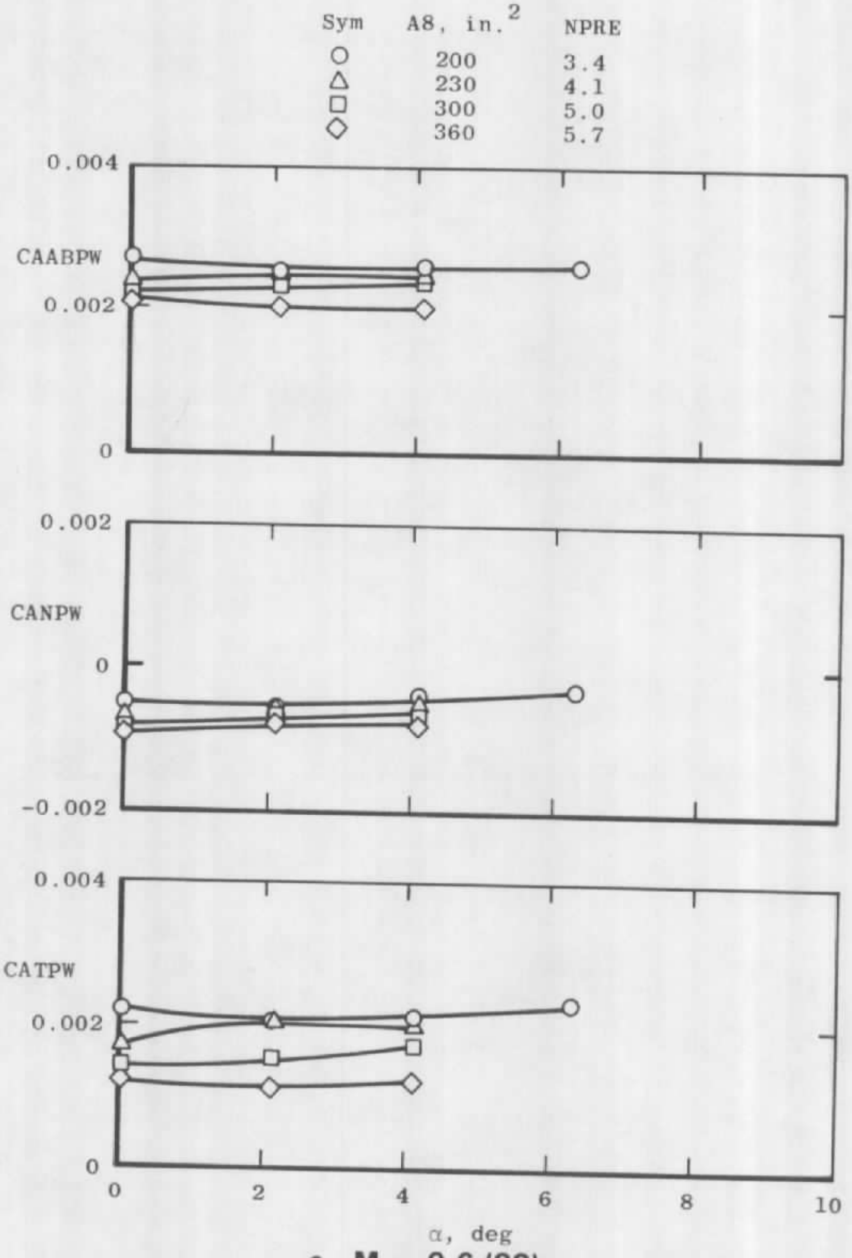

e. M = 0.6 (SS)

Figure 38. Continued.

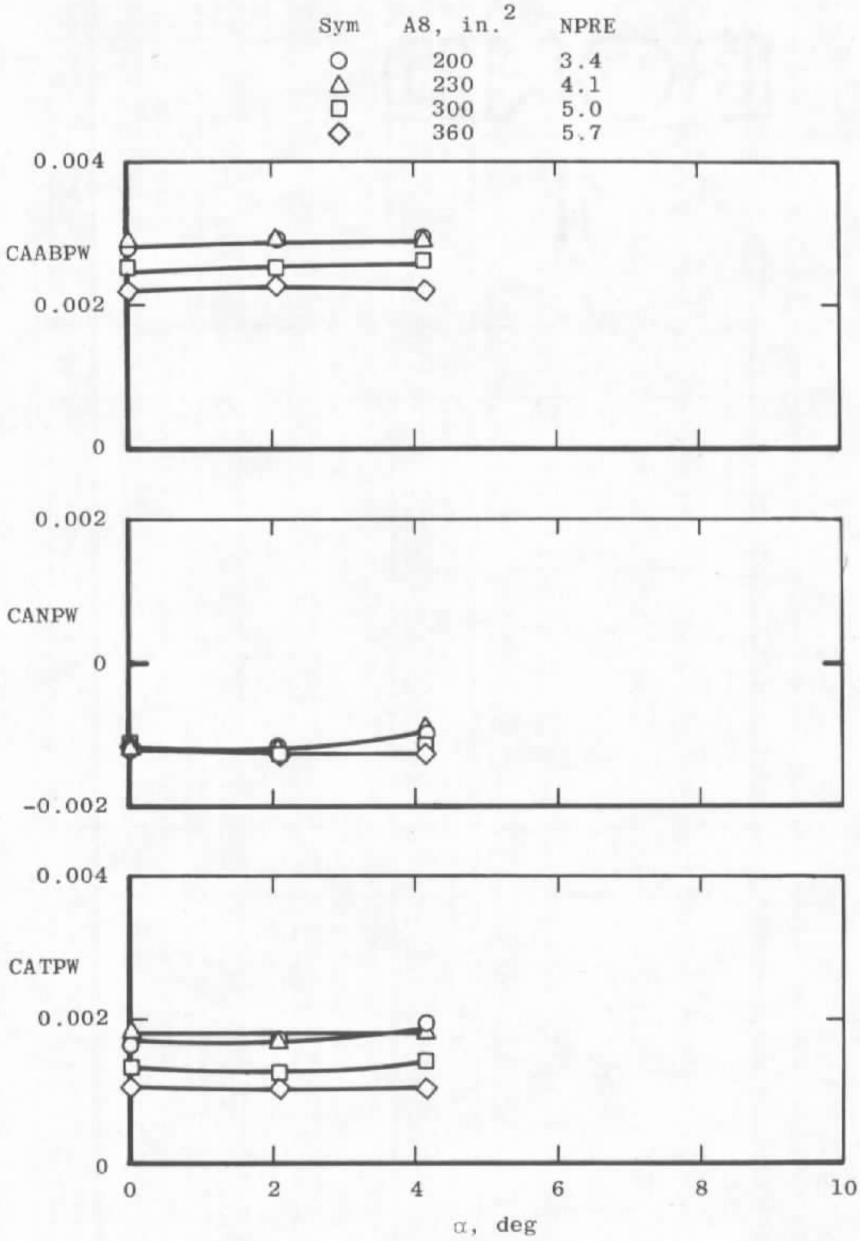

f. M = 0.9 (SS)
Figure 38. Continued.

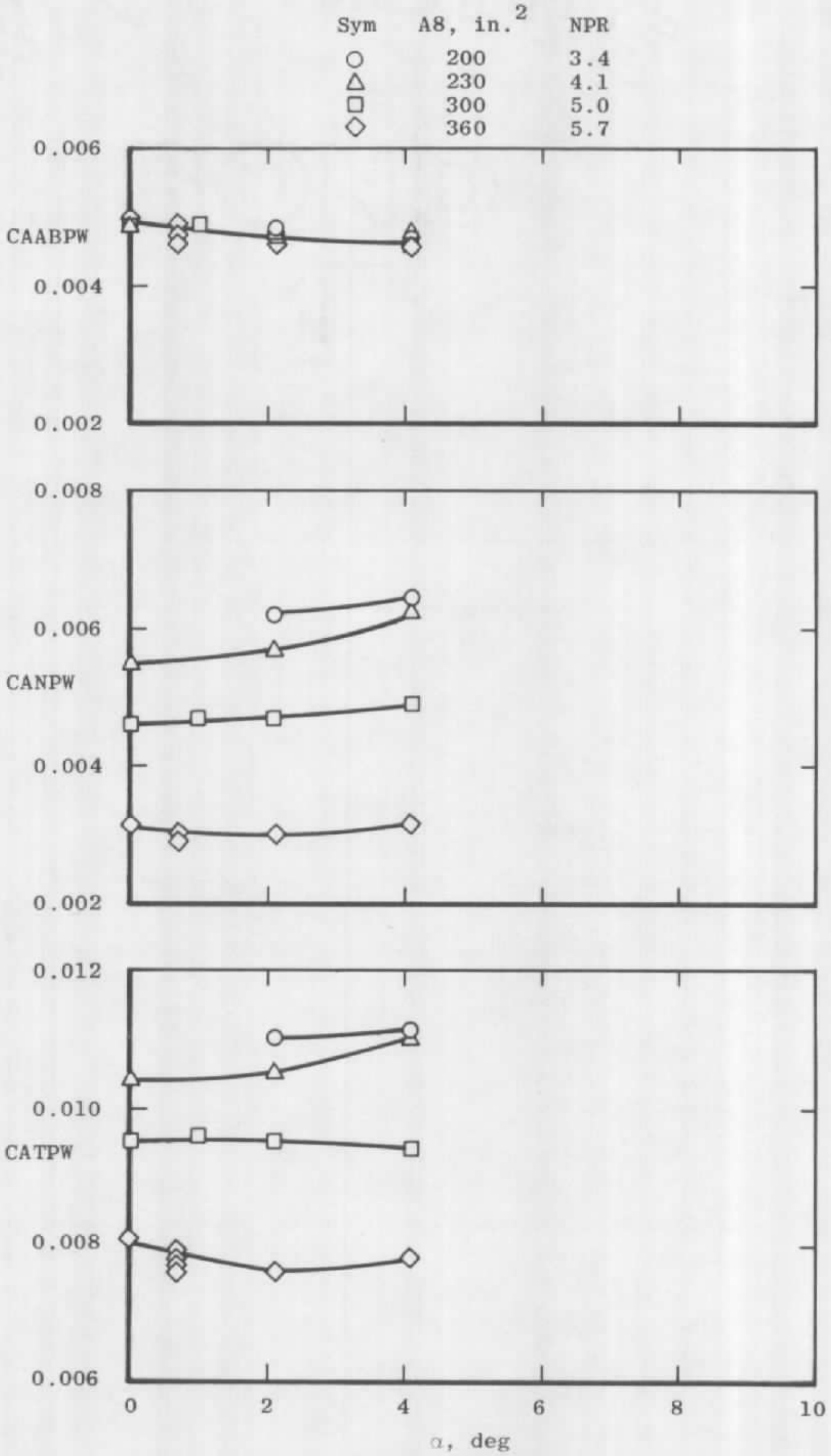

g. M = 1.2 (SS)

Figure 38. Concluded.

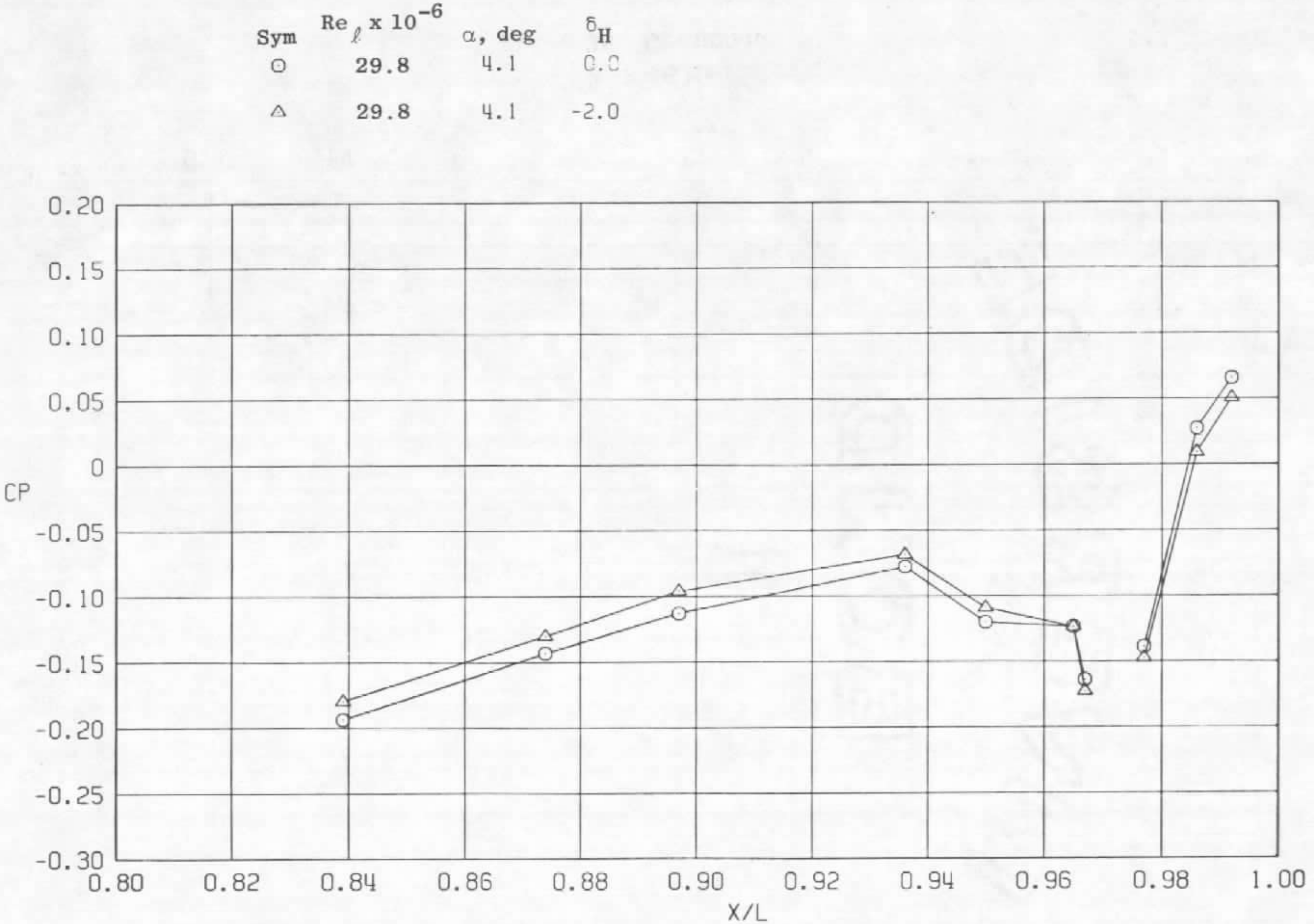

a. $\phi = 0$

Figure 39. Effect of horizontal tail deflections on surface pressure coefficients A8 = 200 in.², M = 0.6, NPR = 1.0 (WT).

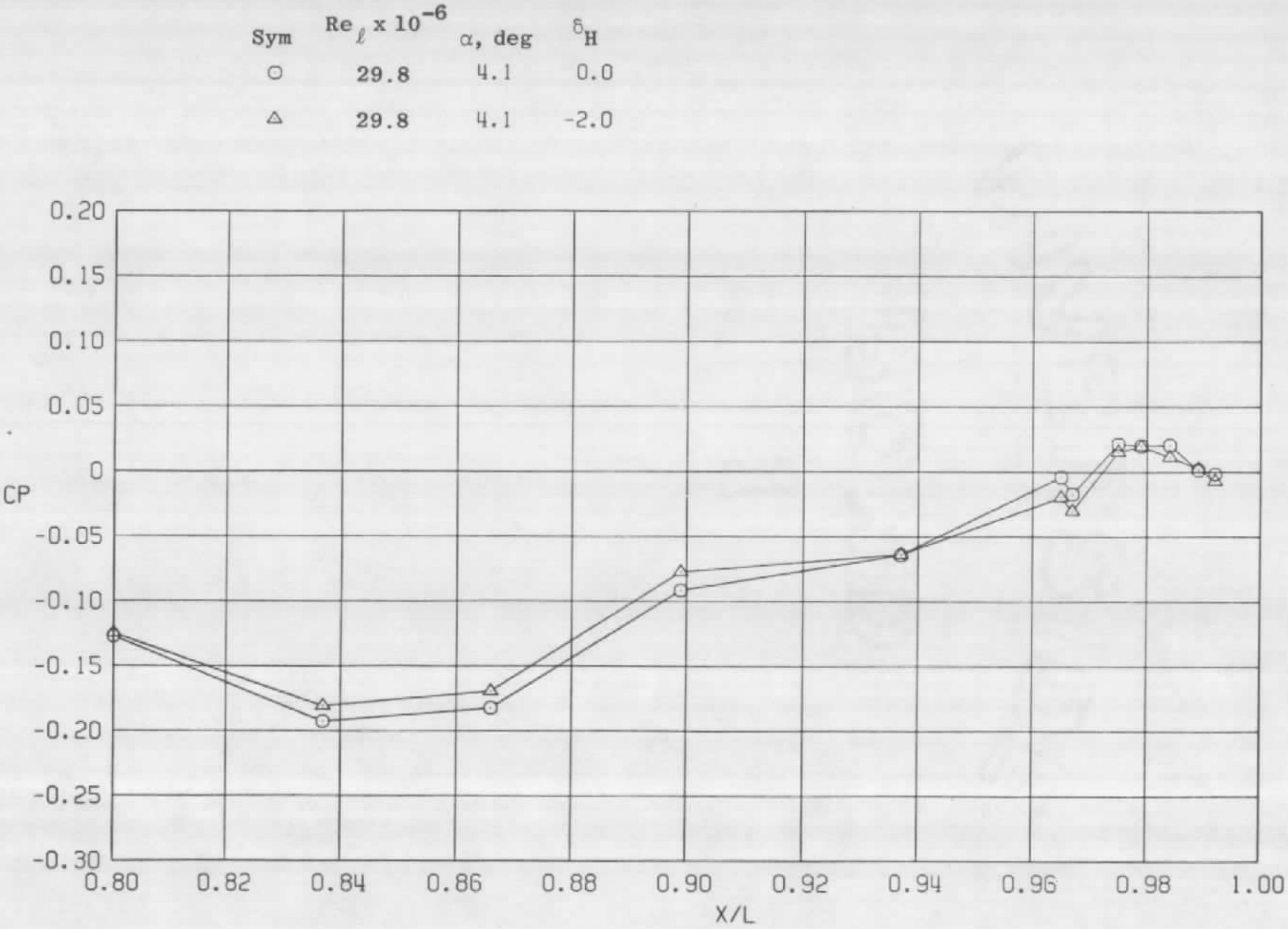

b. ϕ = 45 deg
Figure 39. Continued.

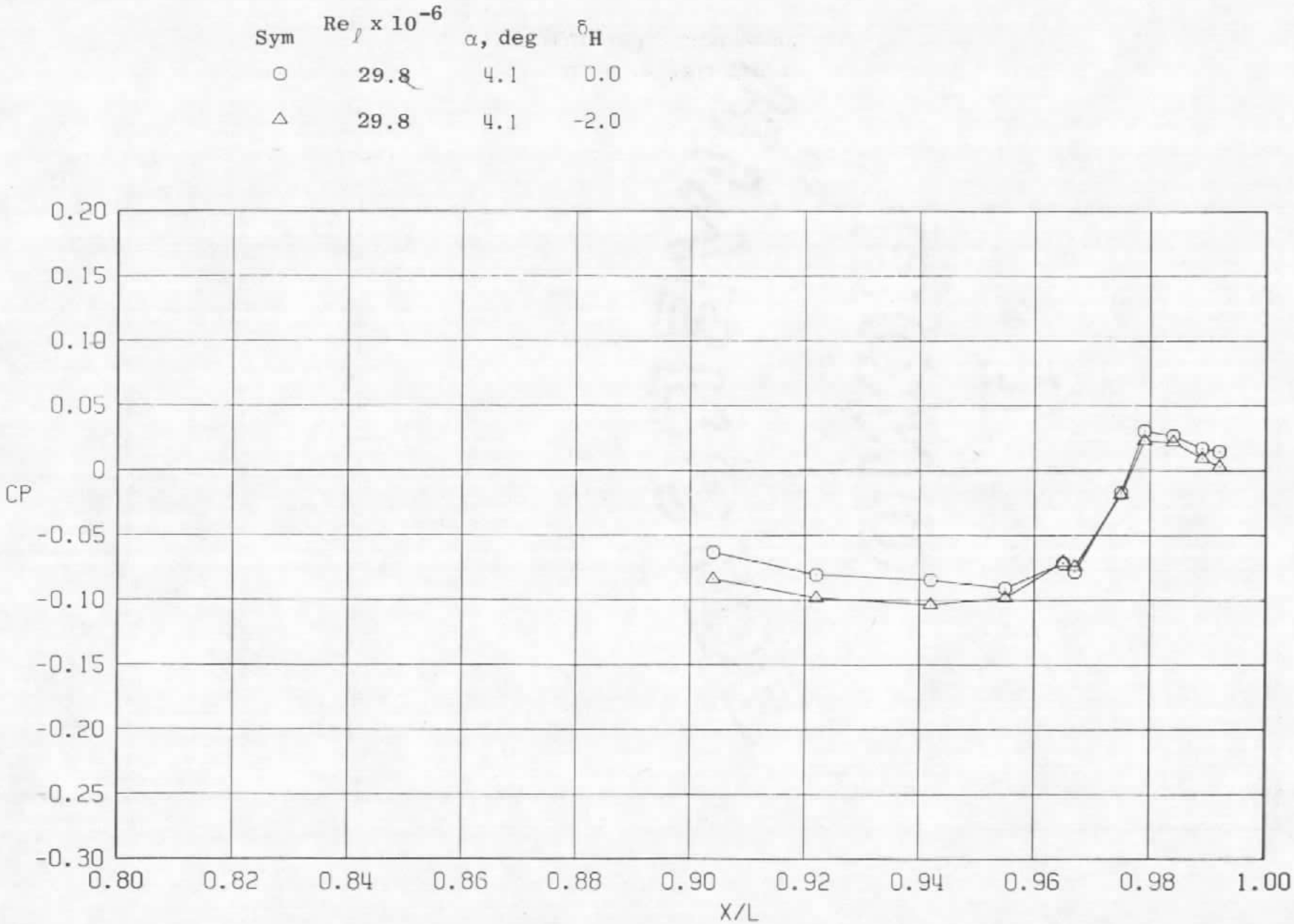

c. ϕ = 135 deg
Figure 39. Continued.

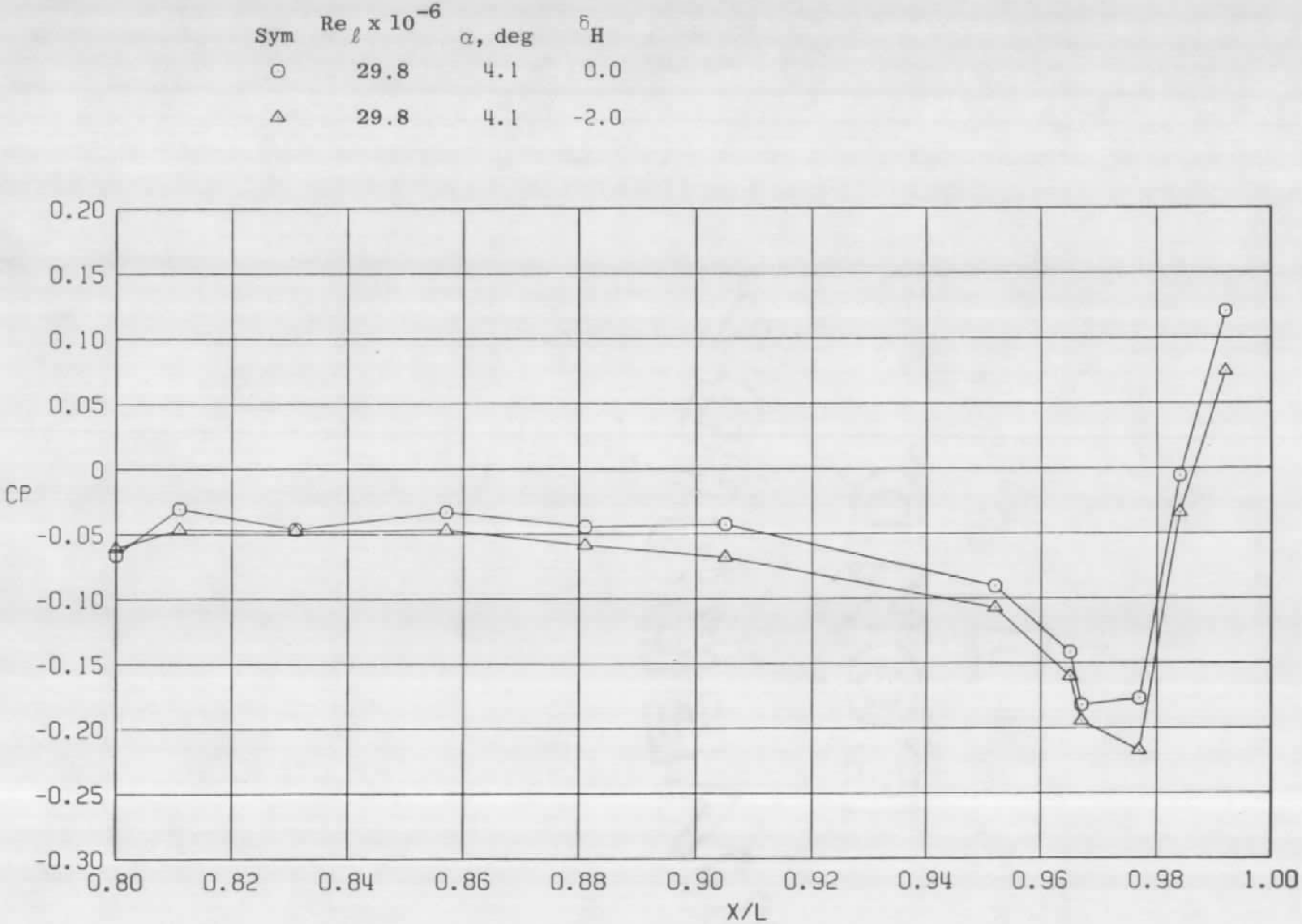

d. ϕ = 180 deg
Figure 39. Continued.

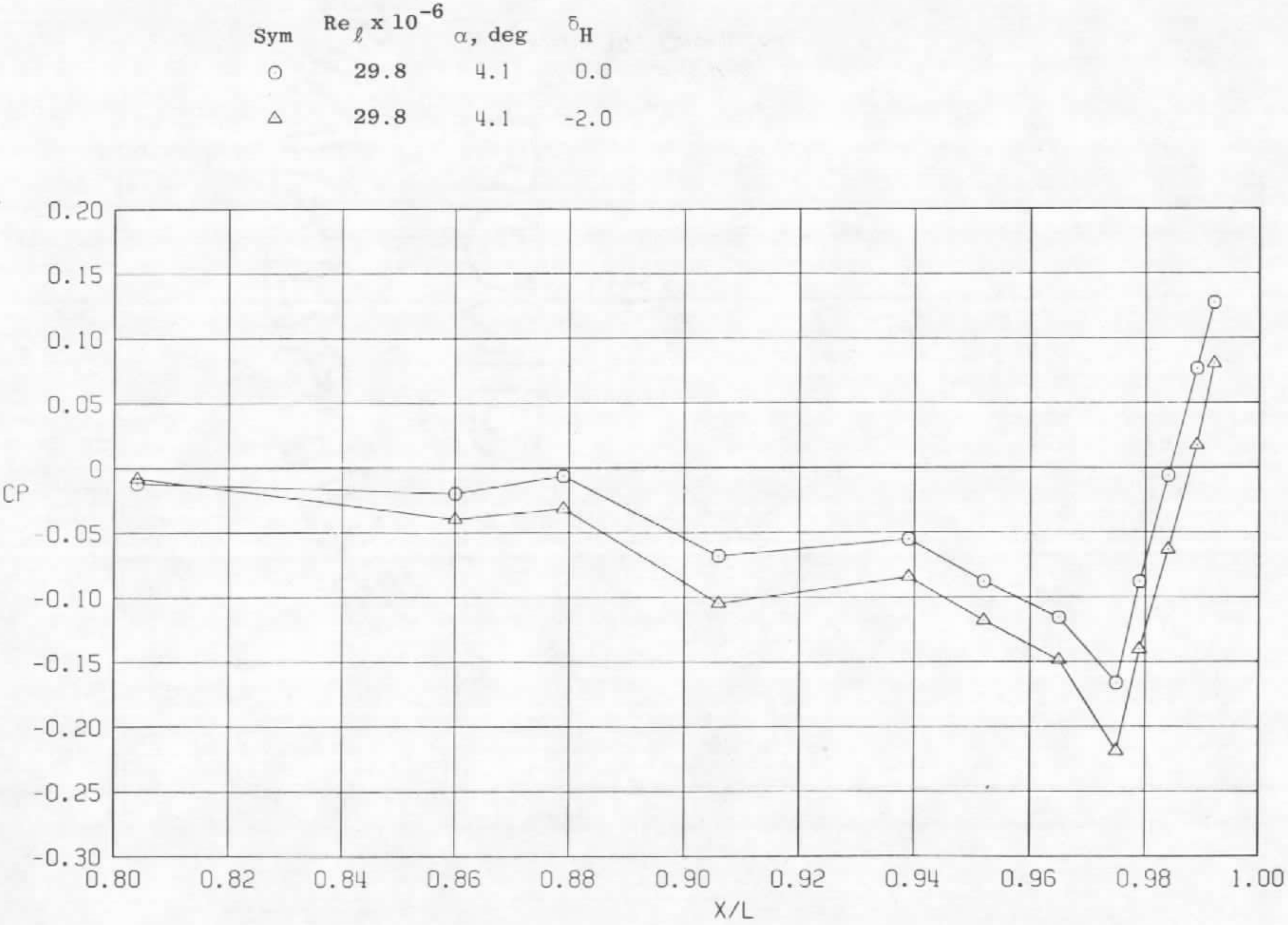

e. ϕ = 225 deg
Figure 39. Continued.

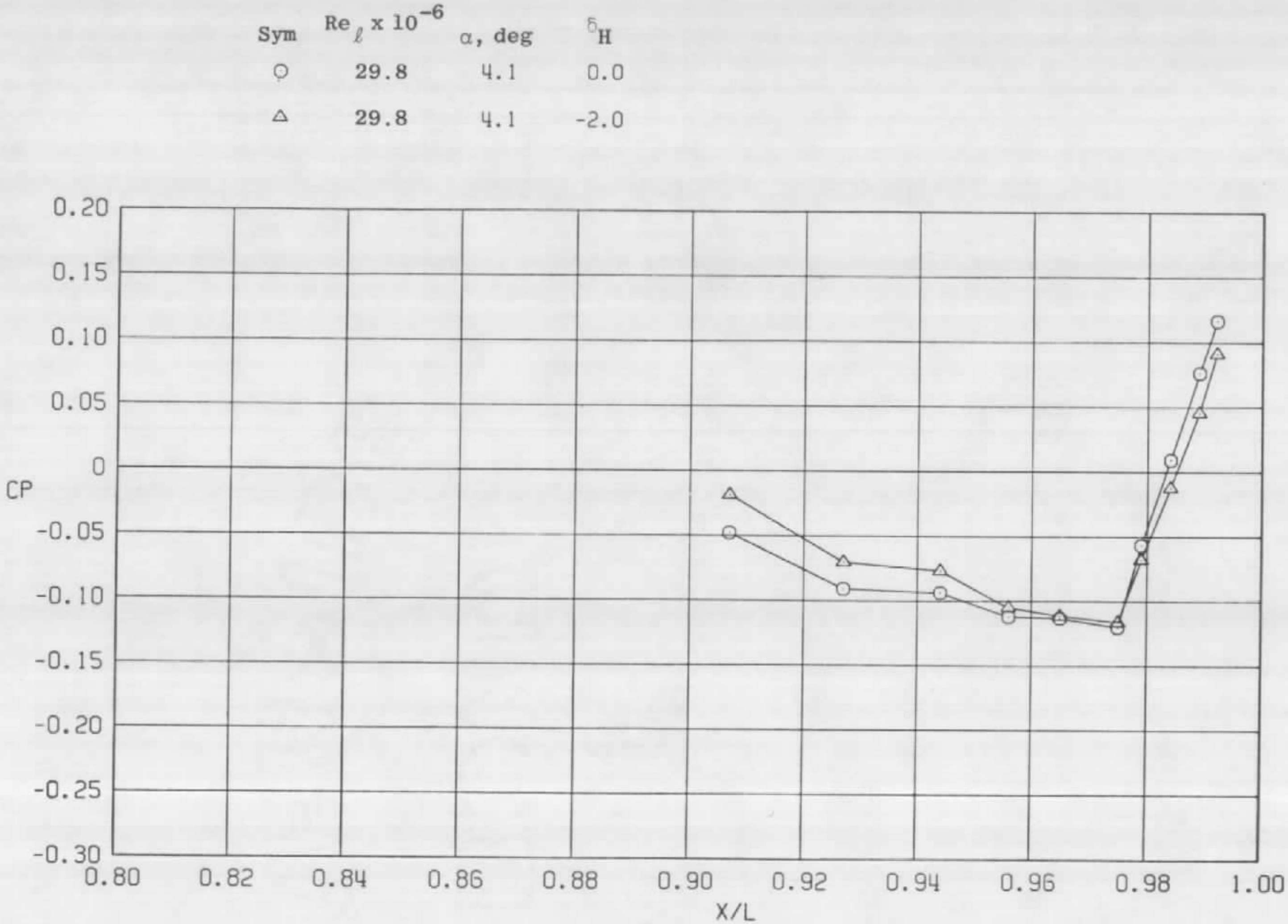

f. ϕ = 315 deg
Figure 39. Concluded.

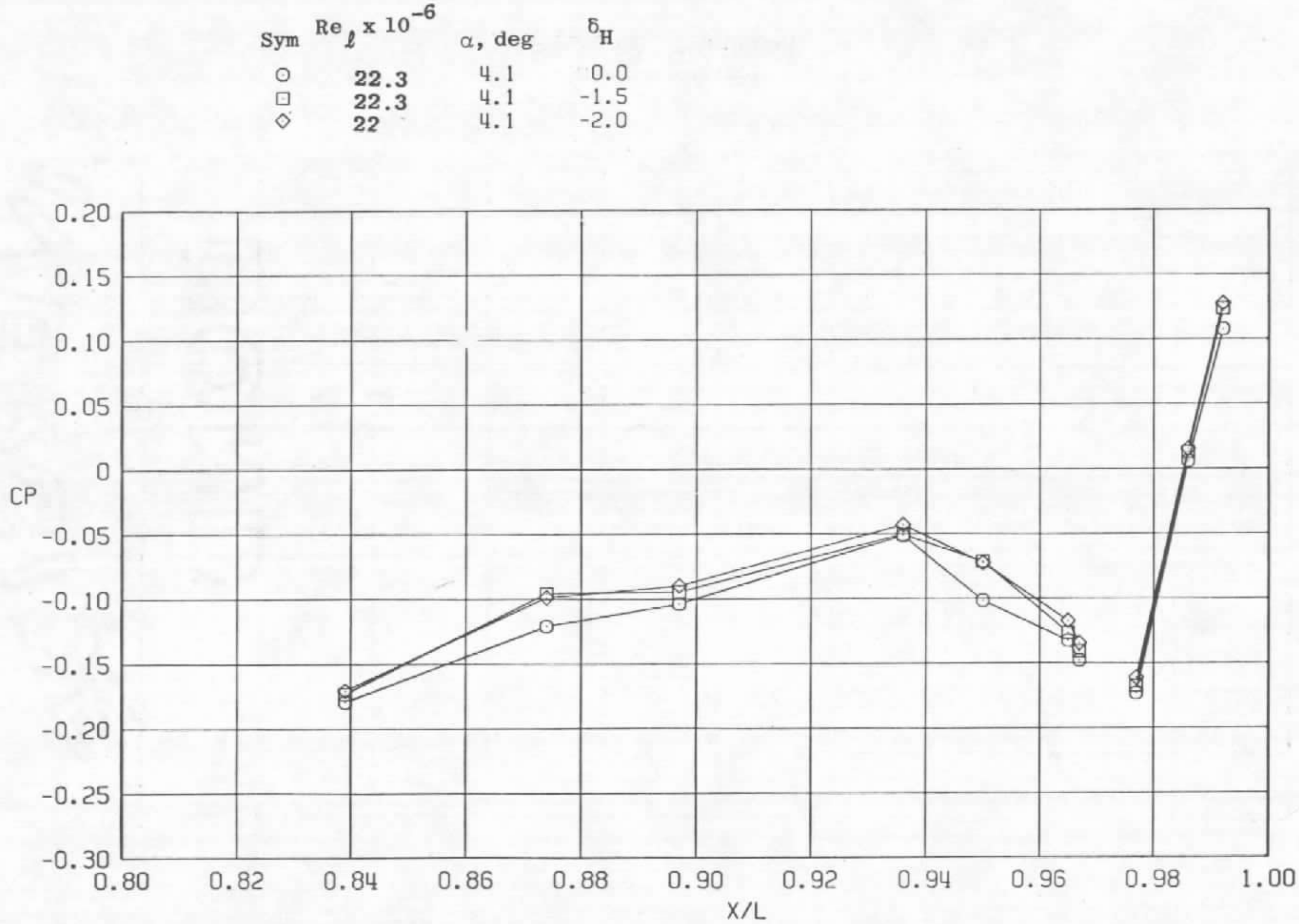

a. $\phi = 0$

Figure 40. Effect of horizontal tail deflection on surface pressure coefficients, A8 = 200 in.², M = 0.6, NPRE = 3.4 (SS).

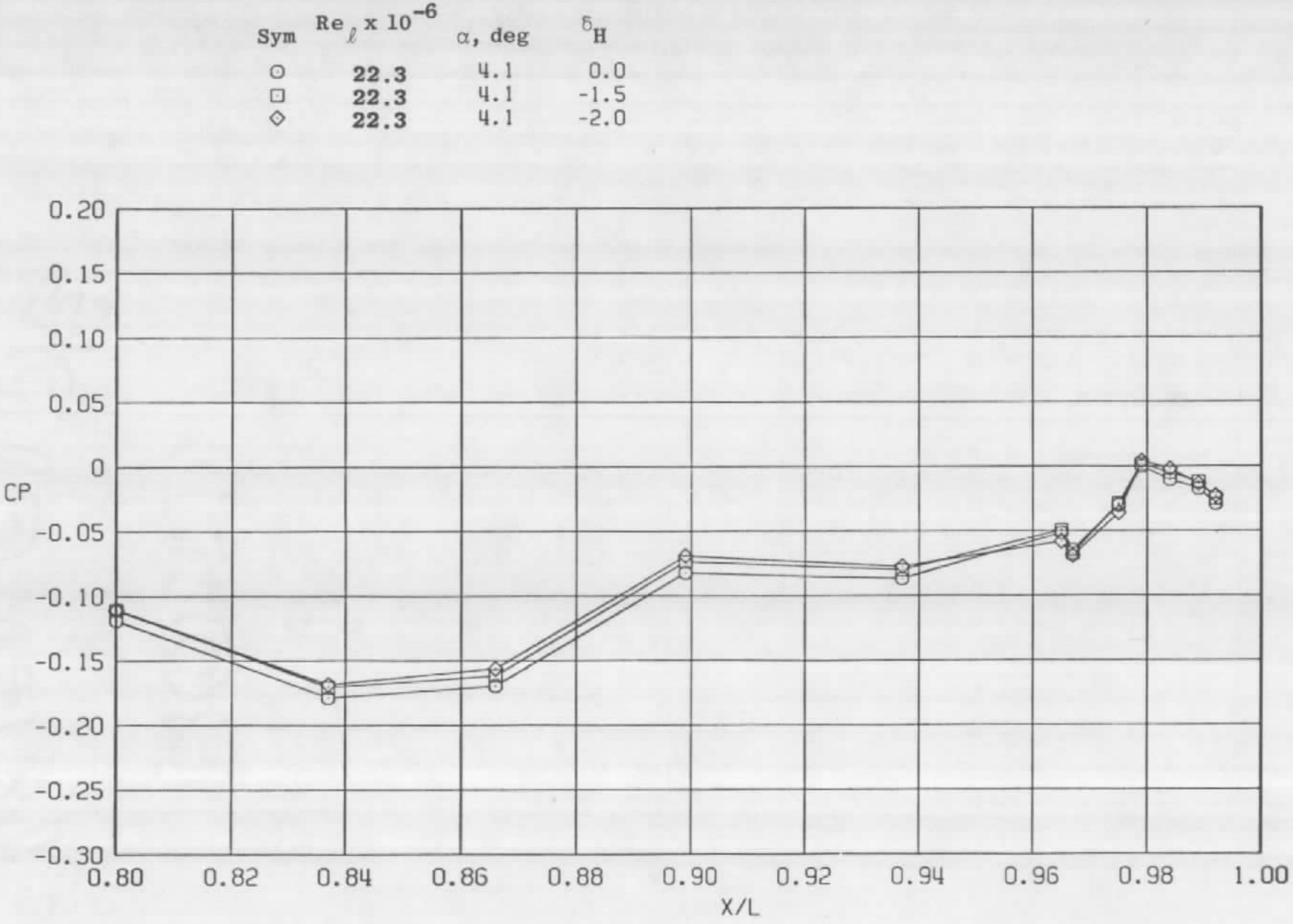

b. ϕ = 45 deg
Figure 40. Continued.

c. ϕ = 135 deg
Figure 40. Continued.

d. ϕ = 180 deg
Figure 40. Continued.

e. ϕ = 225 deg
Figure 40. Continued.

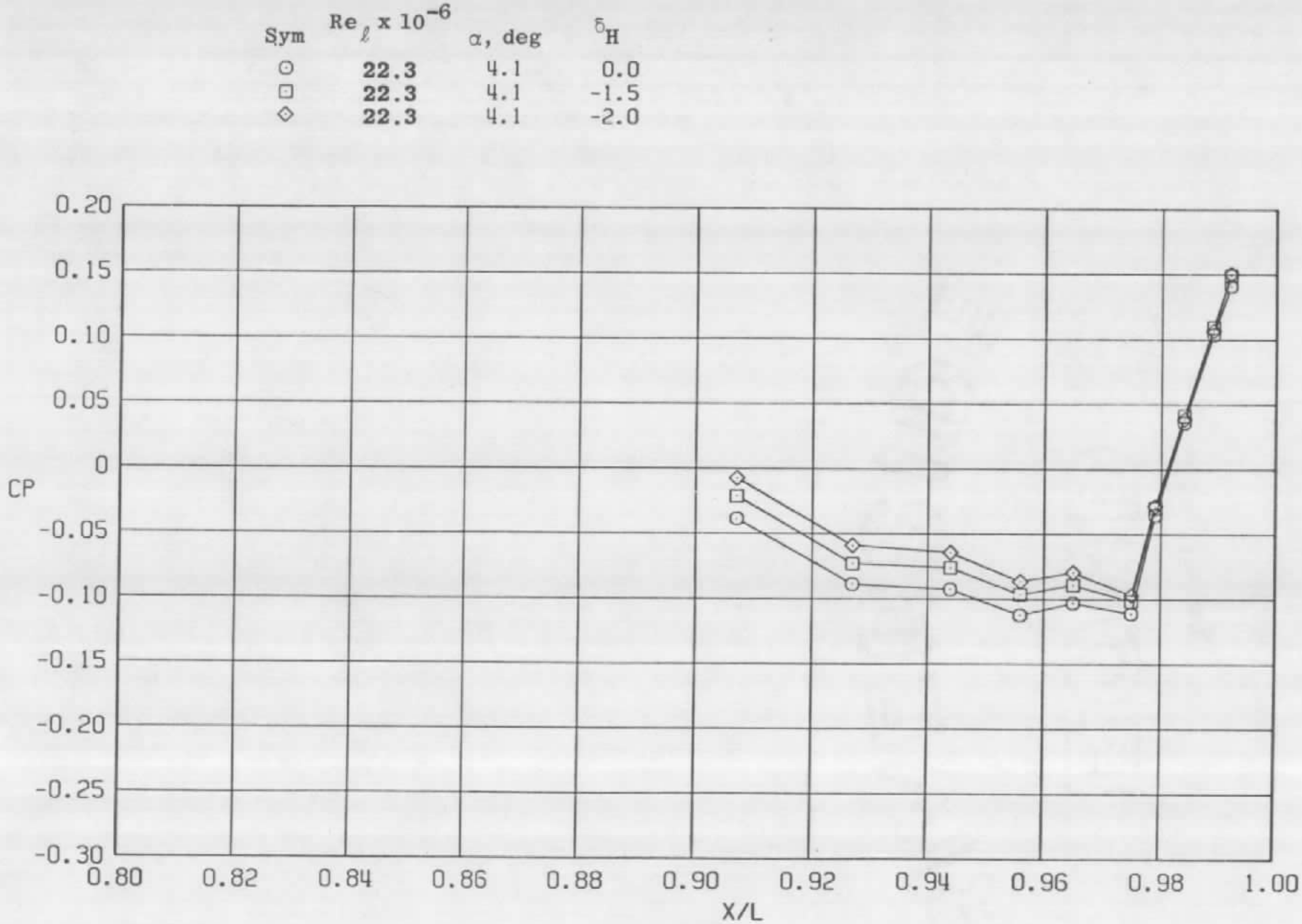

f. ϕ = 315 deg
Figure 40. Concluded.

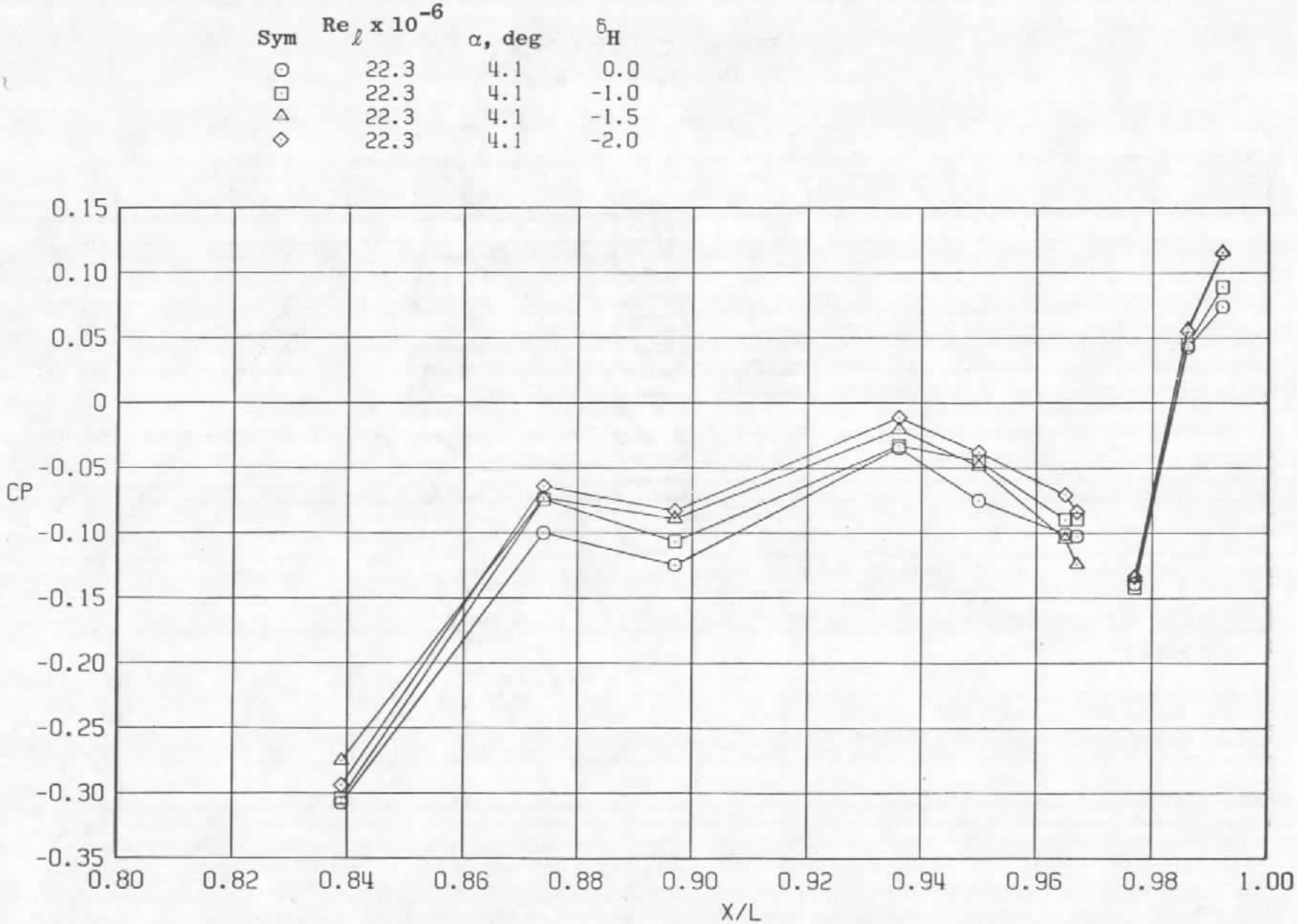

a. ϕ = 0

Figure 41. Effect of horizontal tail deflection on surface pressure coefficients, A8 = 200 in.^{2}, M = 0.9, NPRE = 3.4 (SS).

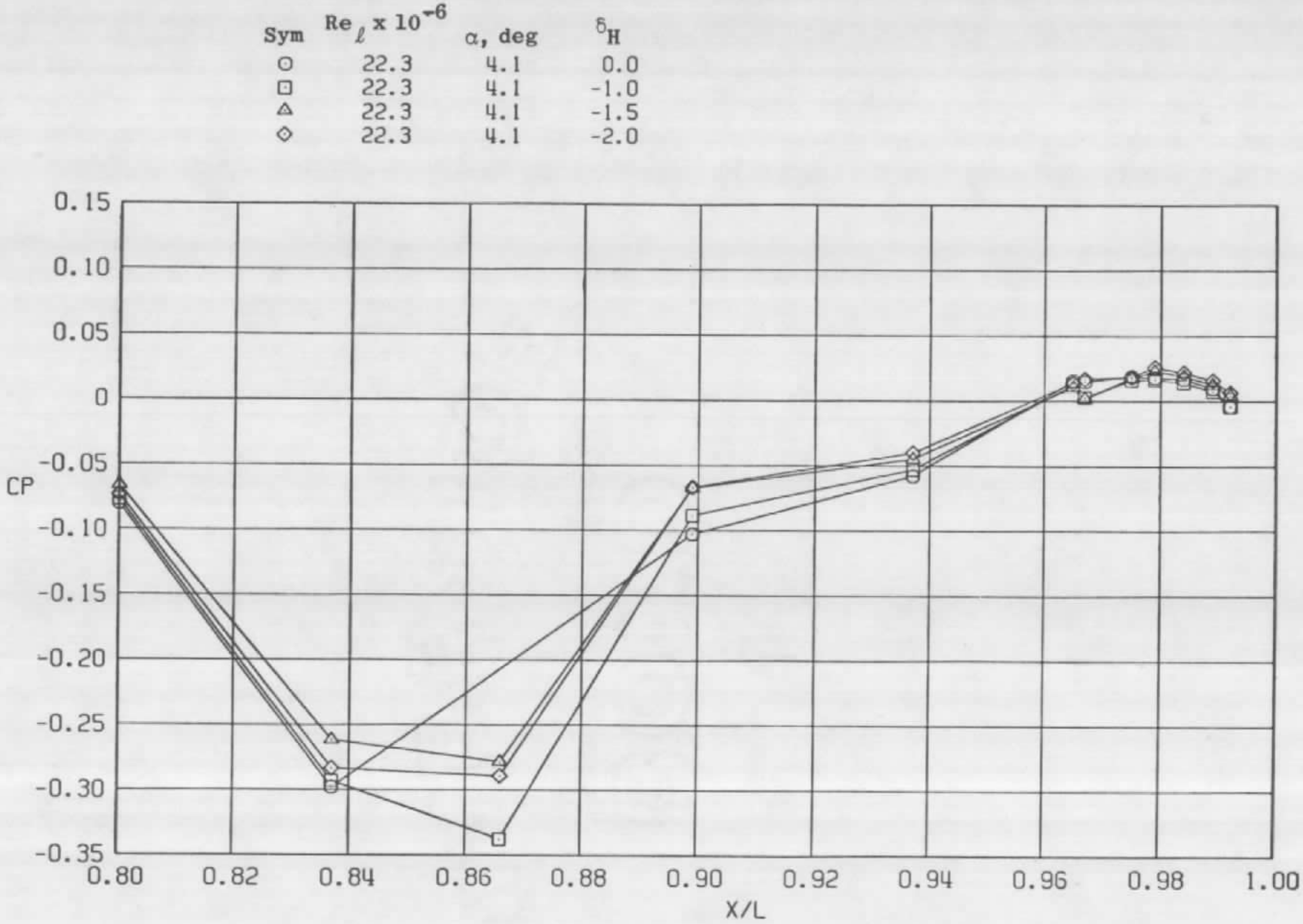

b. ϕ = 45 deg
Figure 41. Continued.

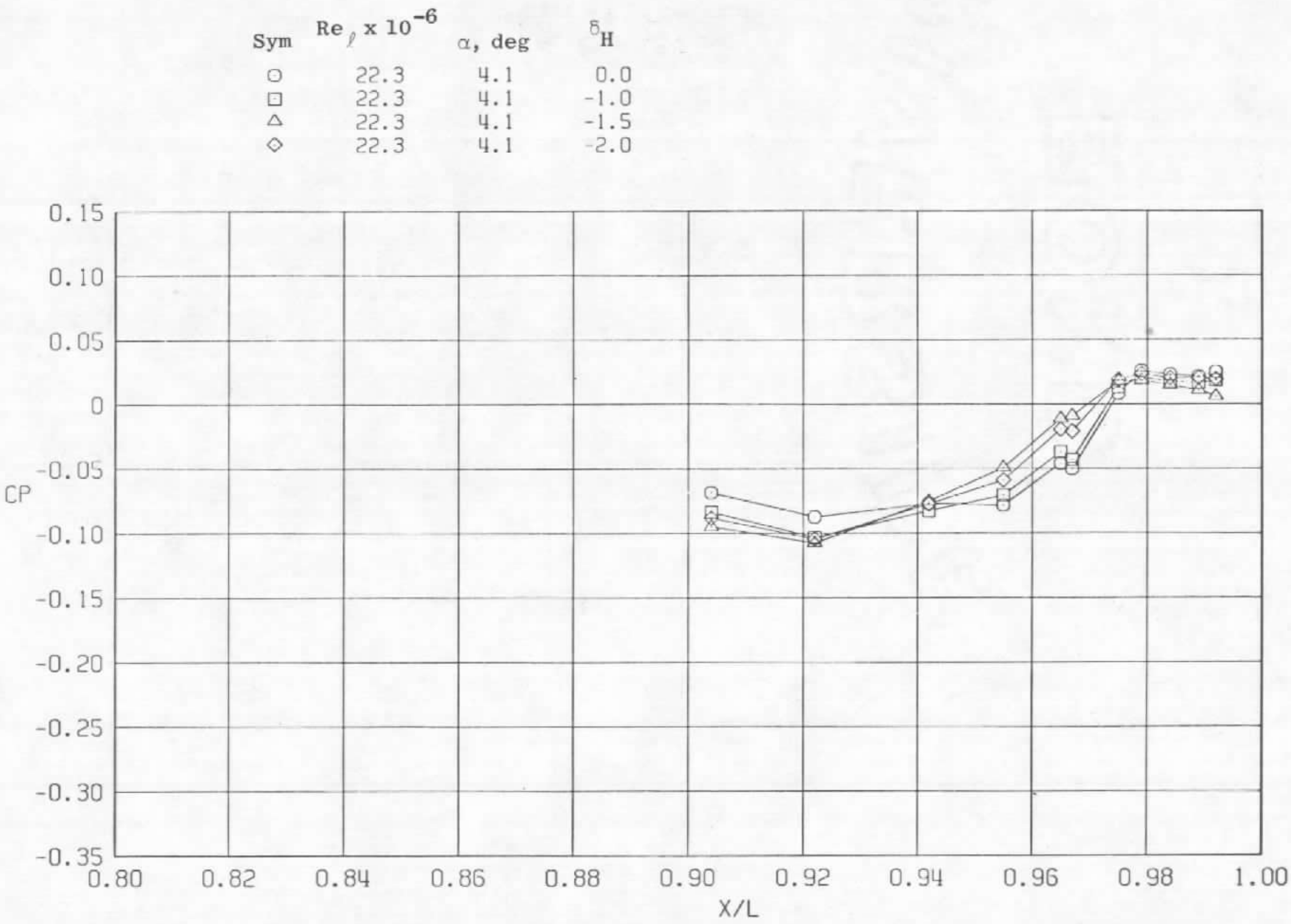

c. ϕ = 135 deg
Figure 41. Continued.

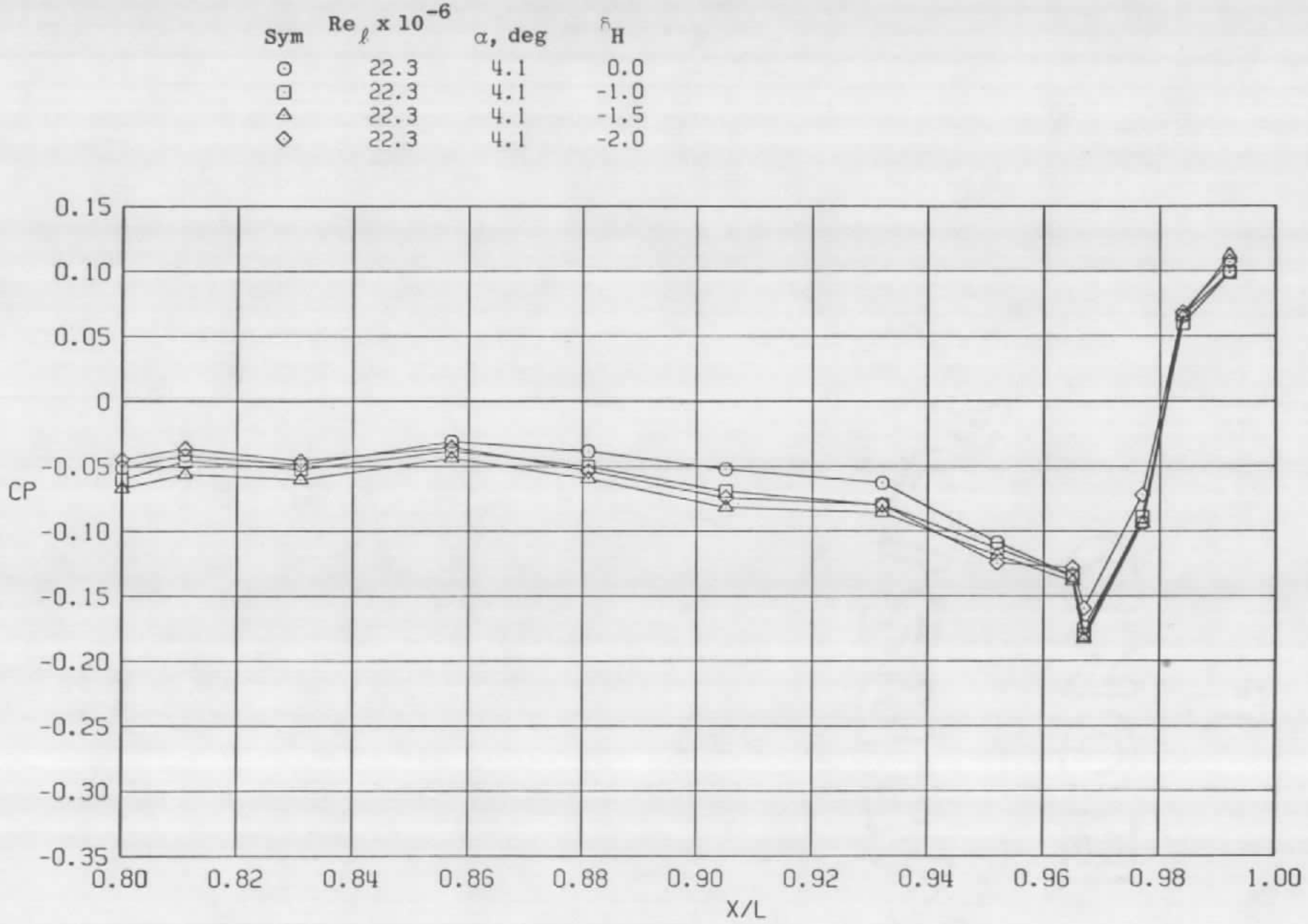

d. ϕ = 180 deg

Figure 41. Continued.

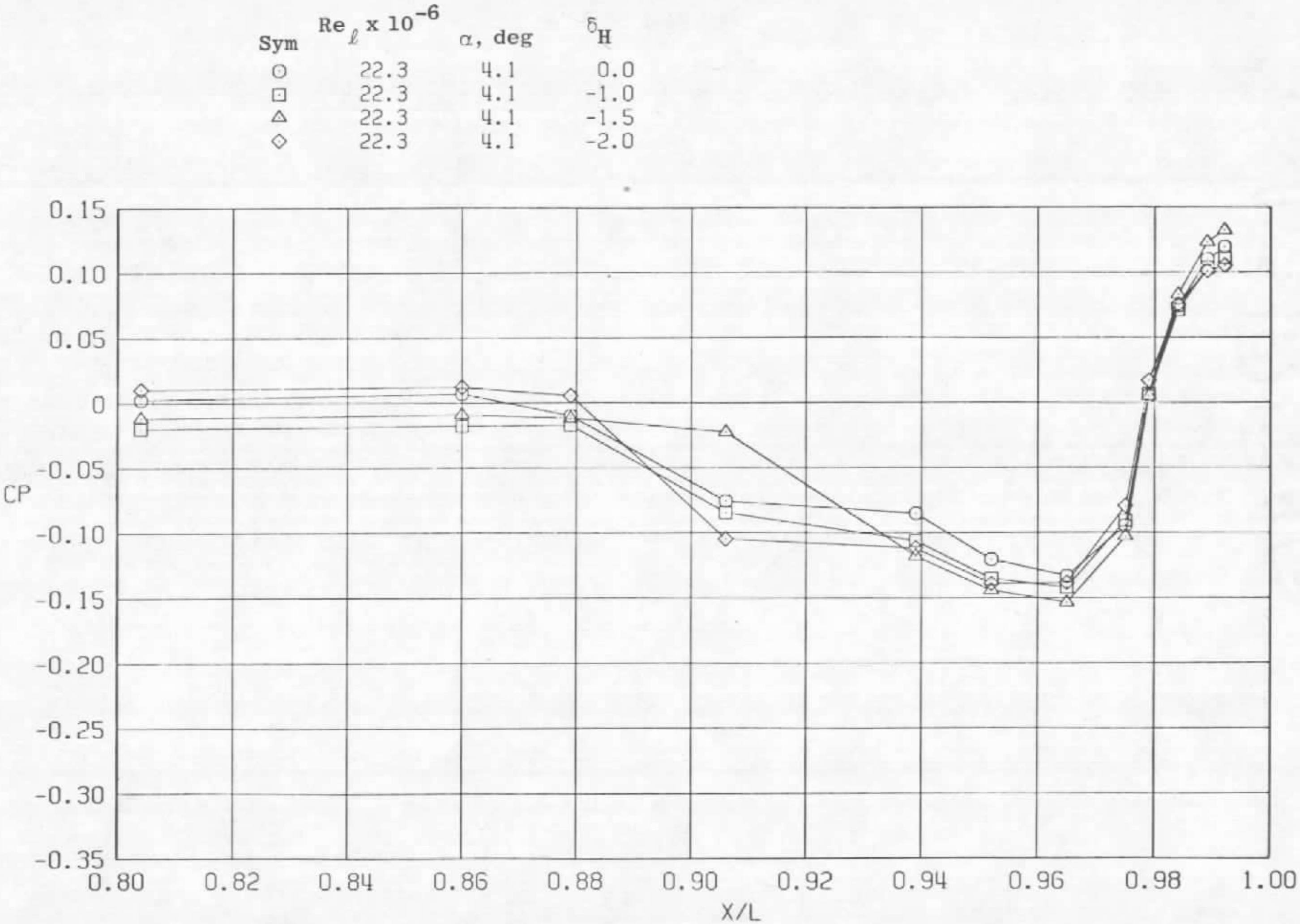

e. ϕ = 225 deg
Figure 41. Continued.

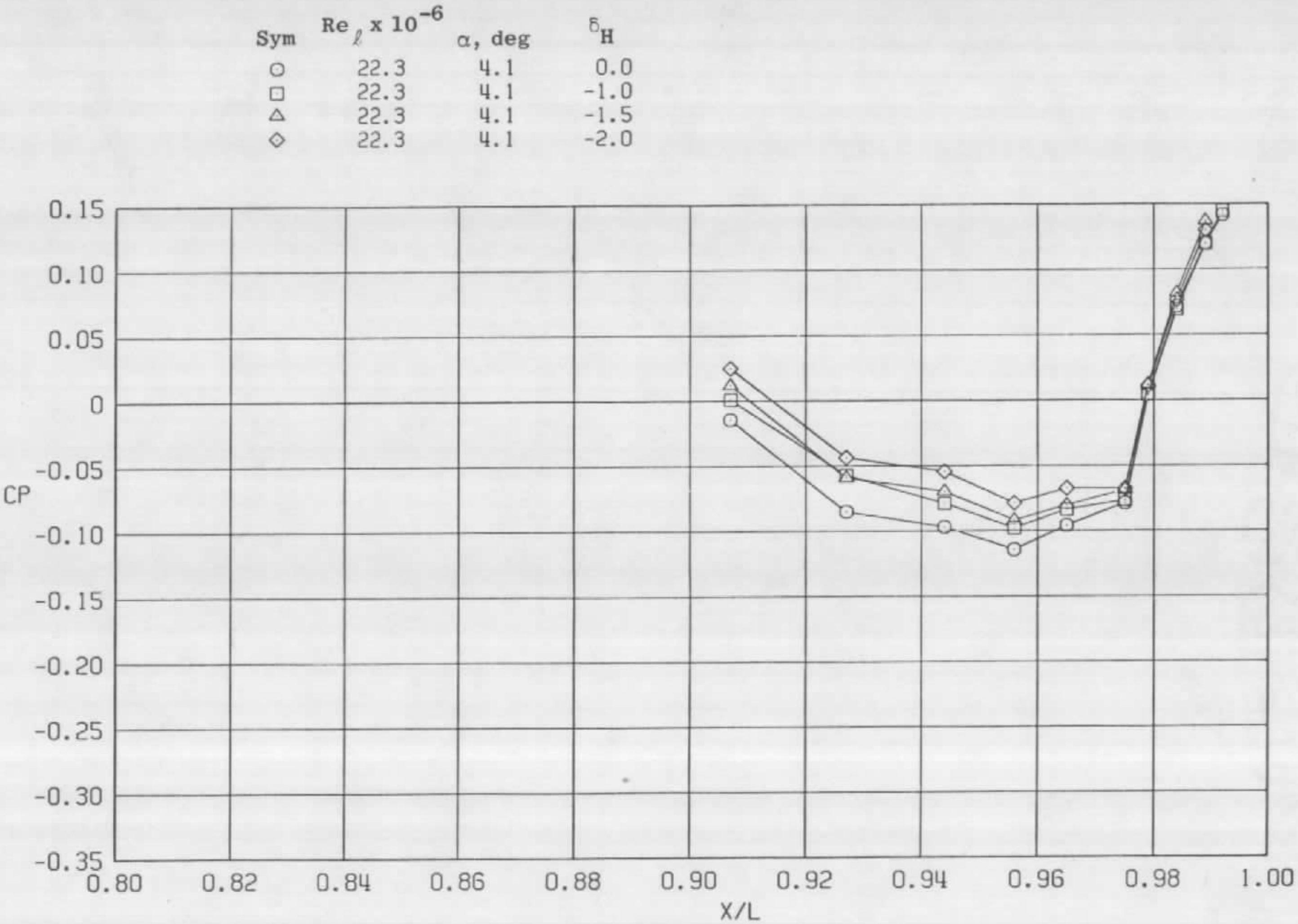

f. ϕ = 315 deg
Figure 41. Concluded.

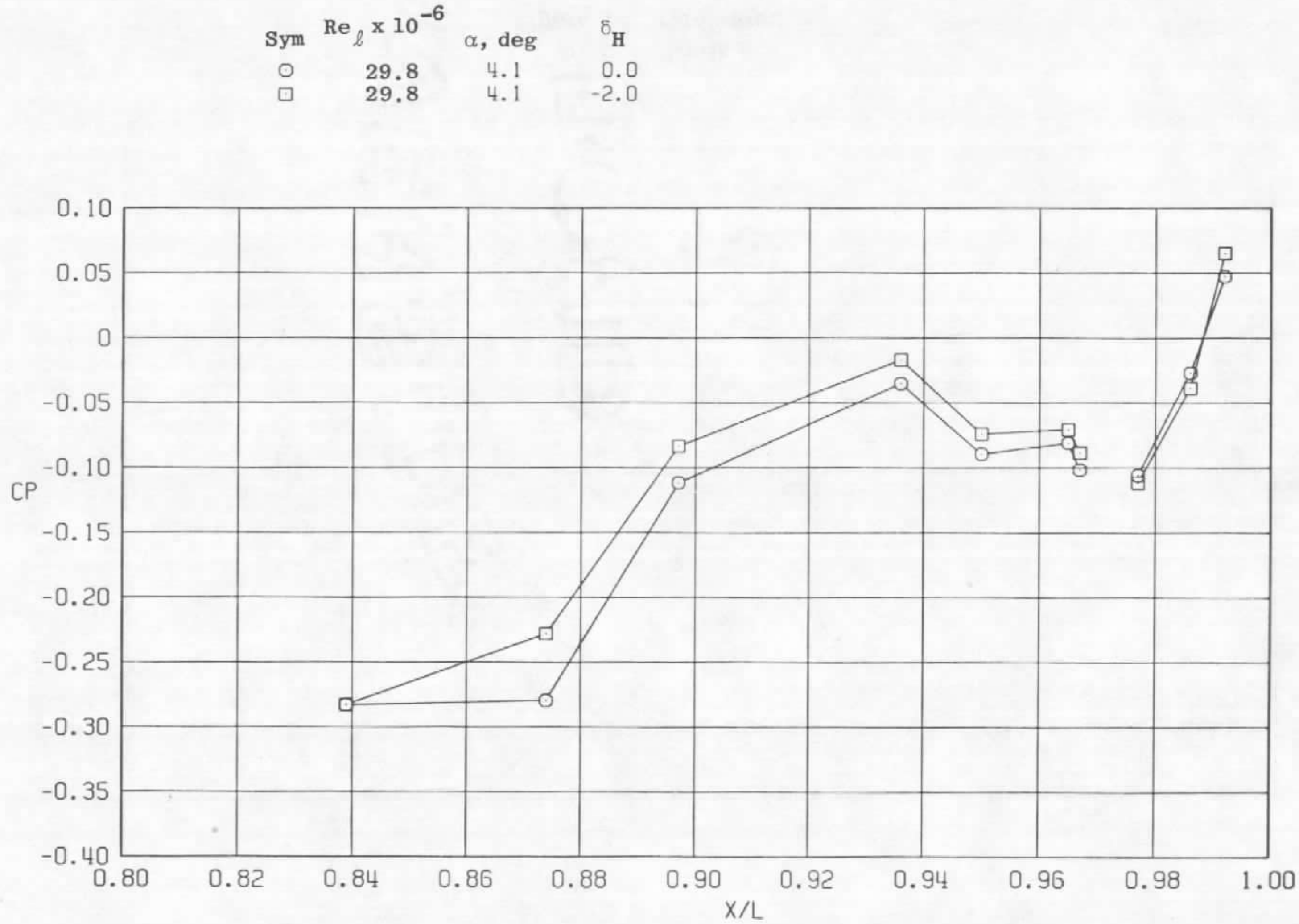

a. $\phi = 0$

Figure 42. Effect of horizontal tail deflections on surface pressure coefficients, A8 = 300 in.², M = 0.9, NPR = 1.0 (WT).

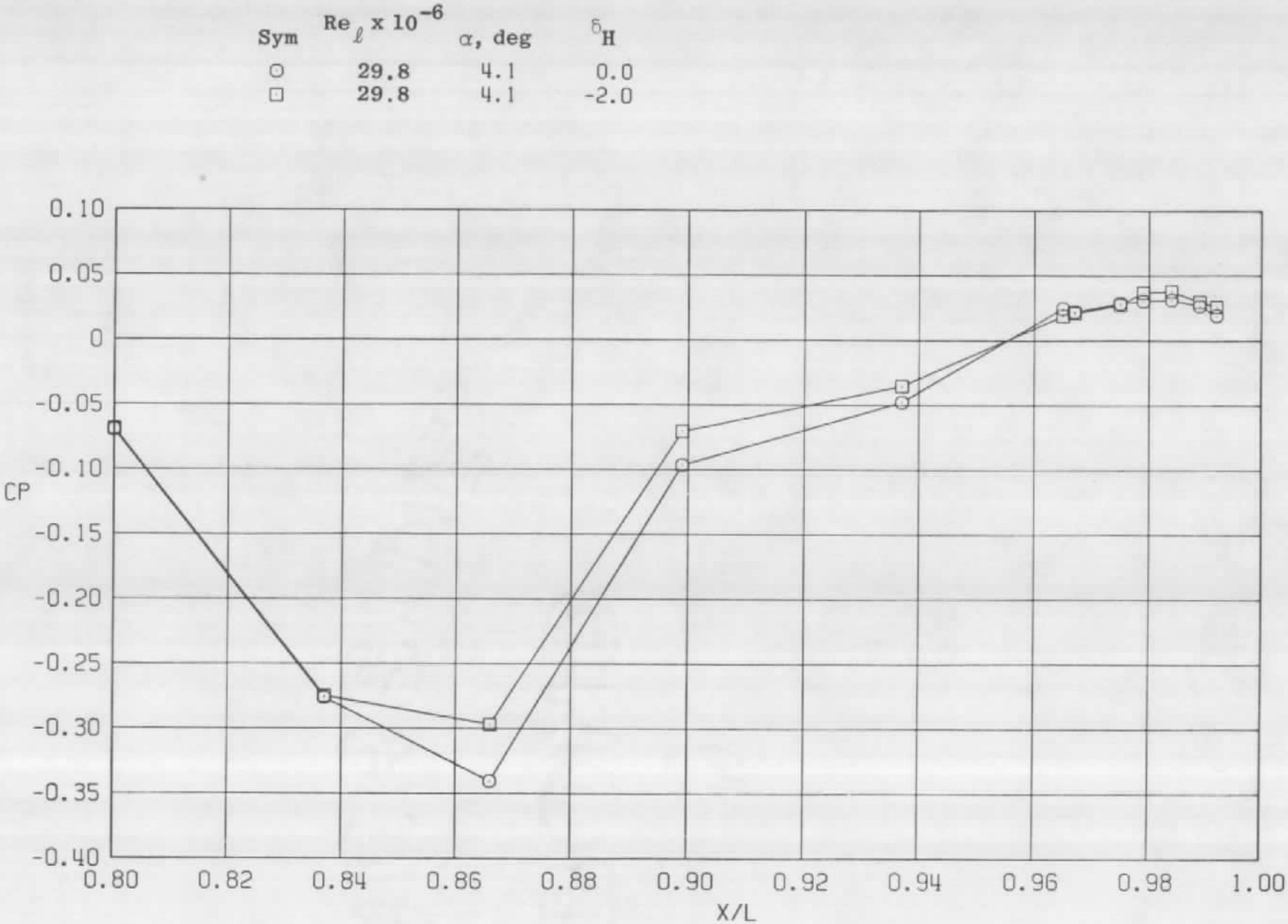

b. ϕ = 45 deg
Figure 42. Continued.

Sym	$Re_{\ell} \times 10^{-6}$	α, deg	δ_H
○	29.8	4.1	0.0
□	29.8	4.1	-2.0

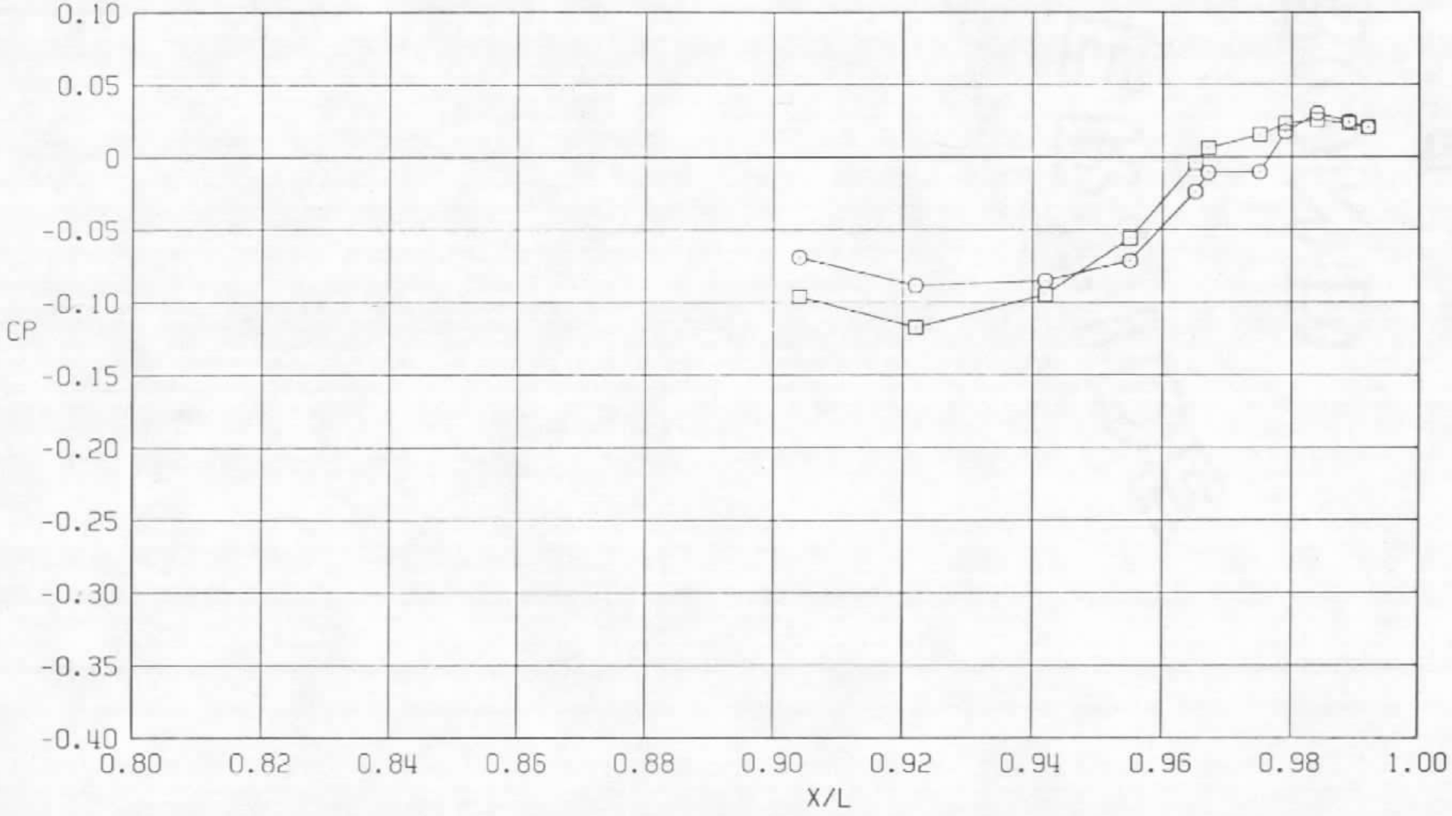

c. ϕ = 135 deg
Figure 42. Continued.

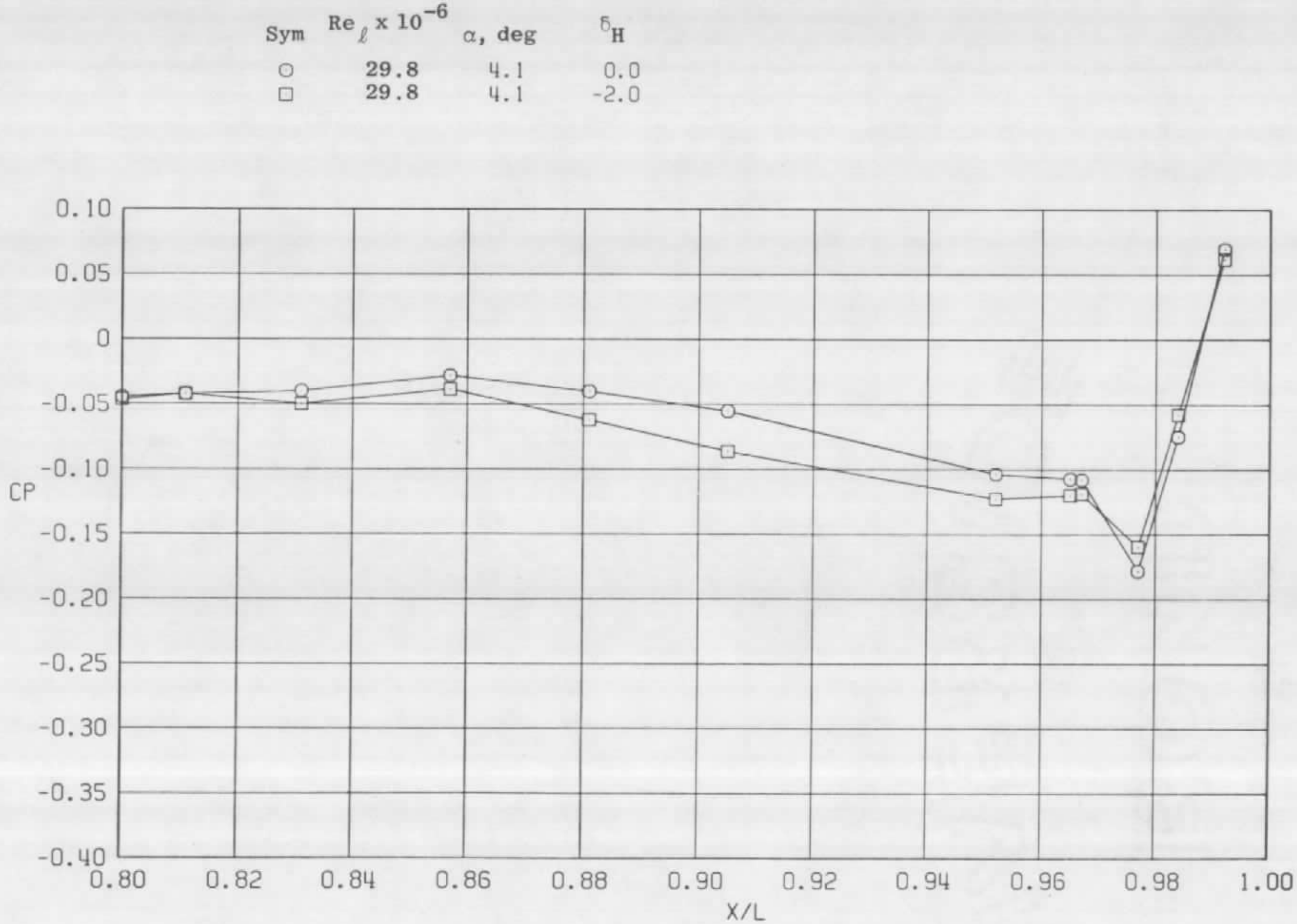

d. ϕ = 180 deg

Figure 42. Continued.

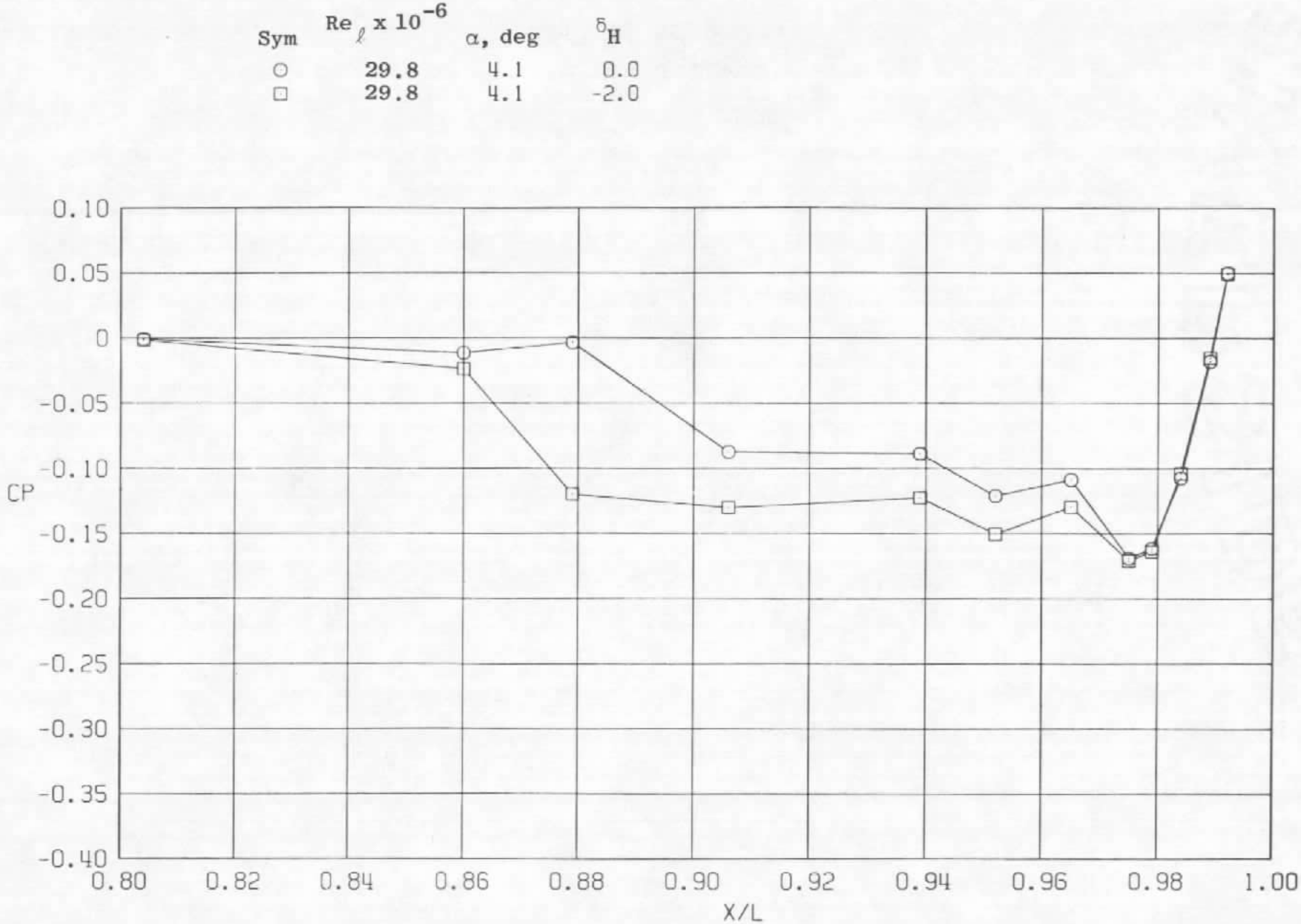

e. ϕ = 225 deg
Figure 42. Continued.

f. ϕ = 315 deg
Figure 42. Concluded.

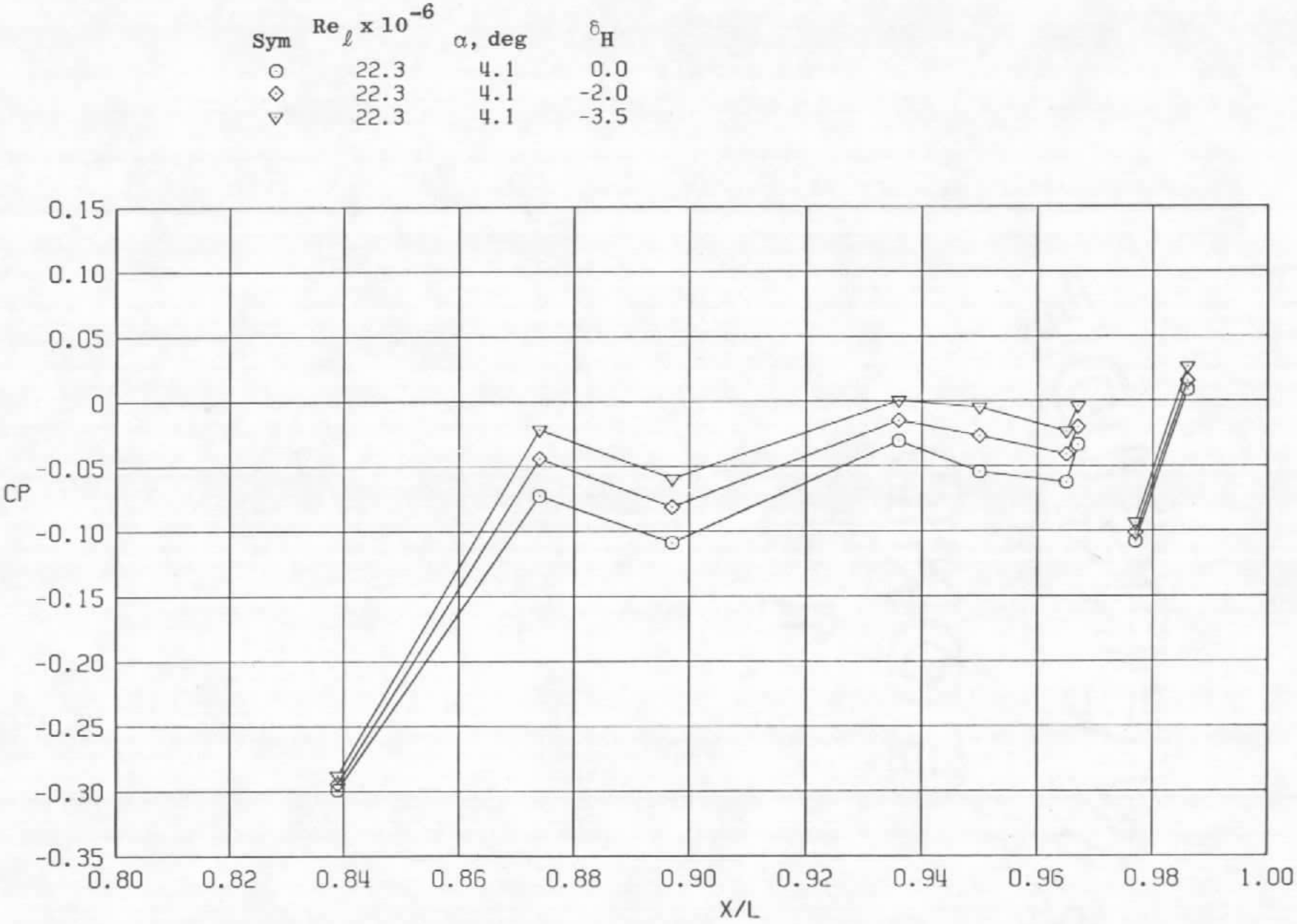

a. $\phi = 0$

Figure 43. Effect of horizontal tail deflection on surface pressure coefficients, A8 = 300 in.², M = 0.9, NPRE = 5.0 (SS).

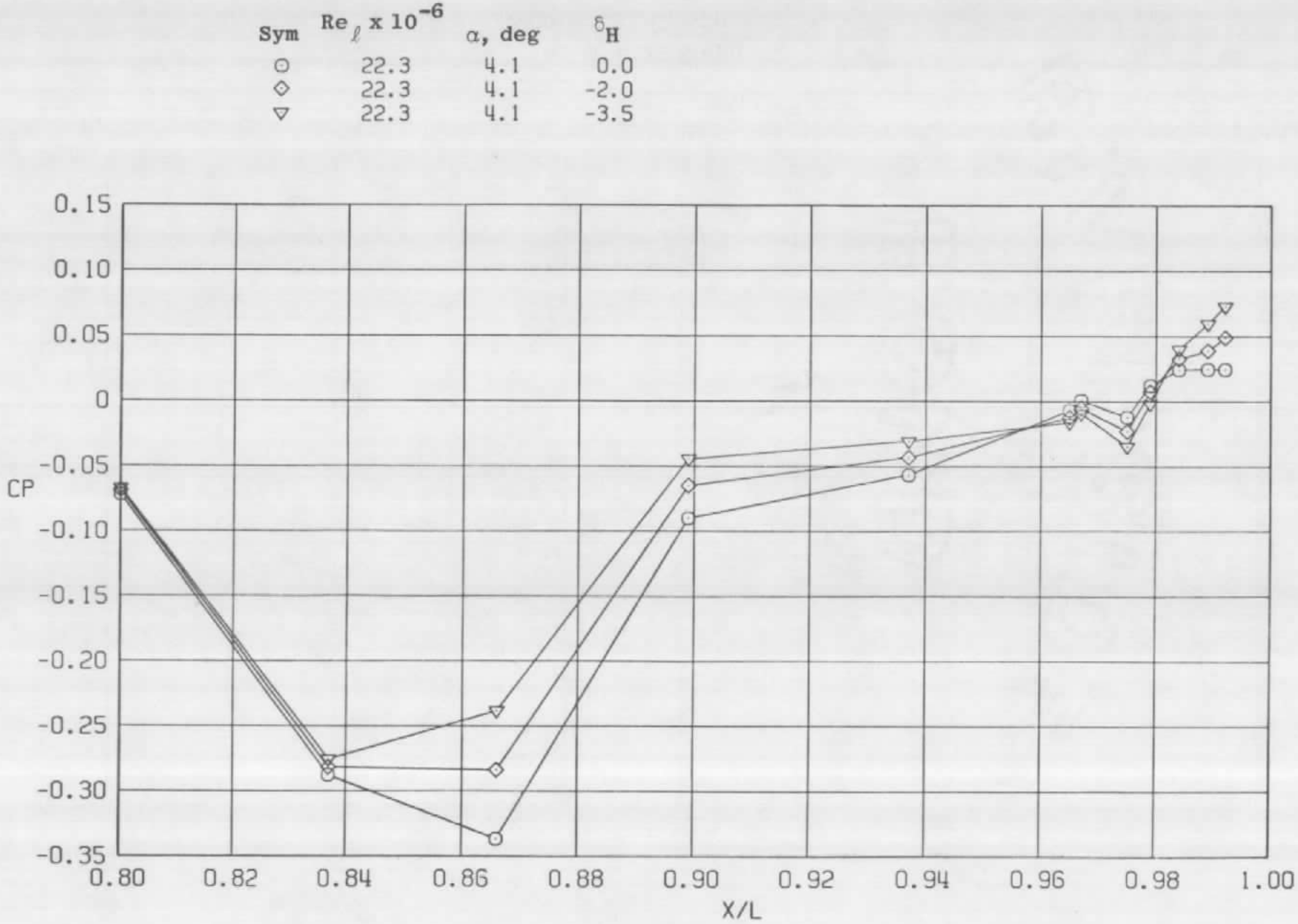

b. ϕ = 45 deg
Figure 43. Continued.

c. ϕ = 135 deg
Figure 43. Continued.

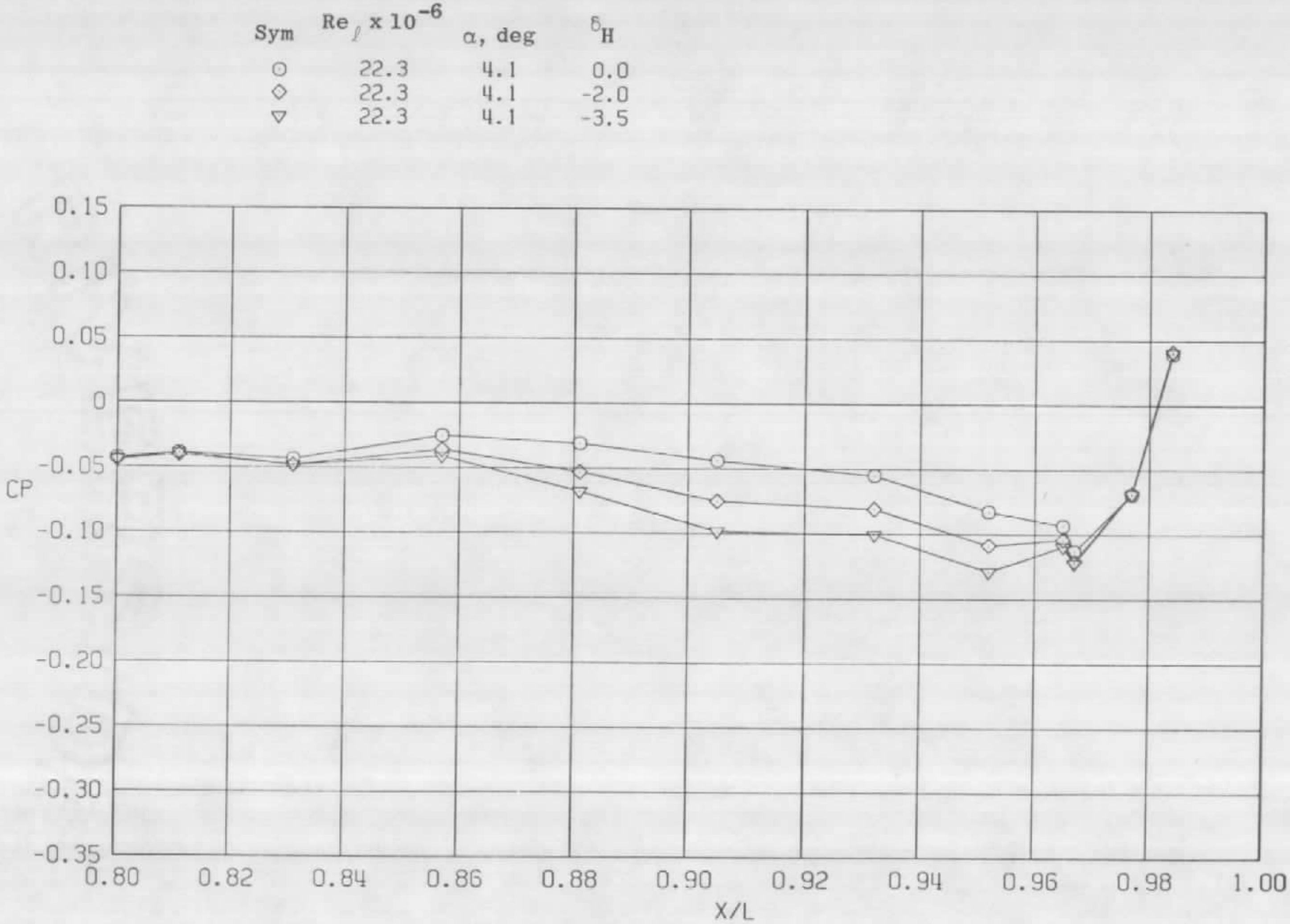

d. ϕ = 180 deg
Figure 43. Continued.

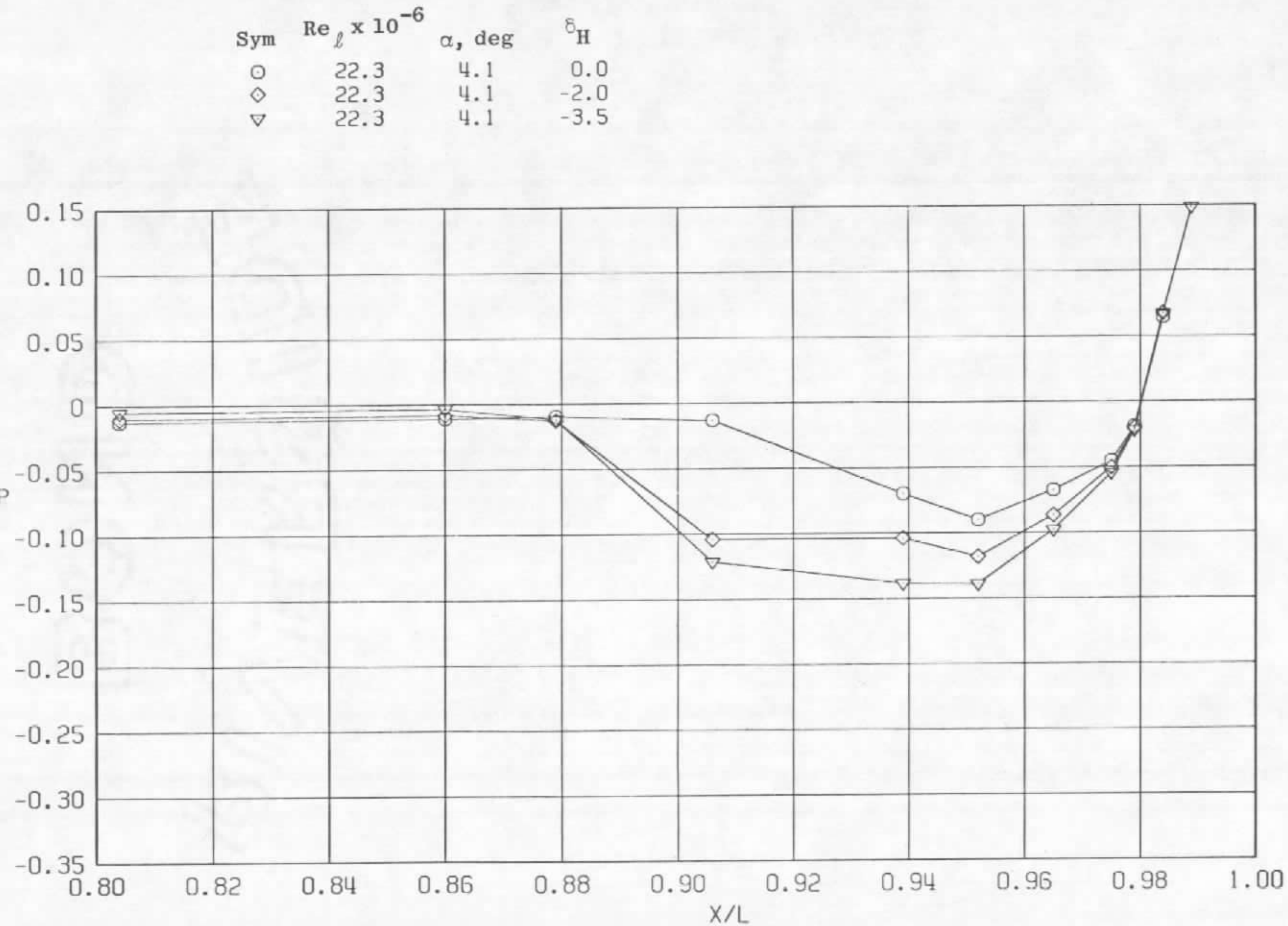

e. ϕ = 225 deg
Figure 43. Continued.

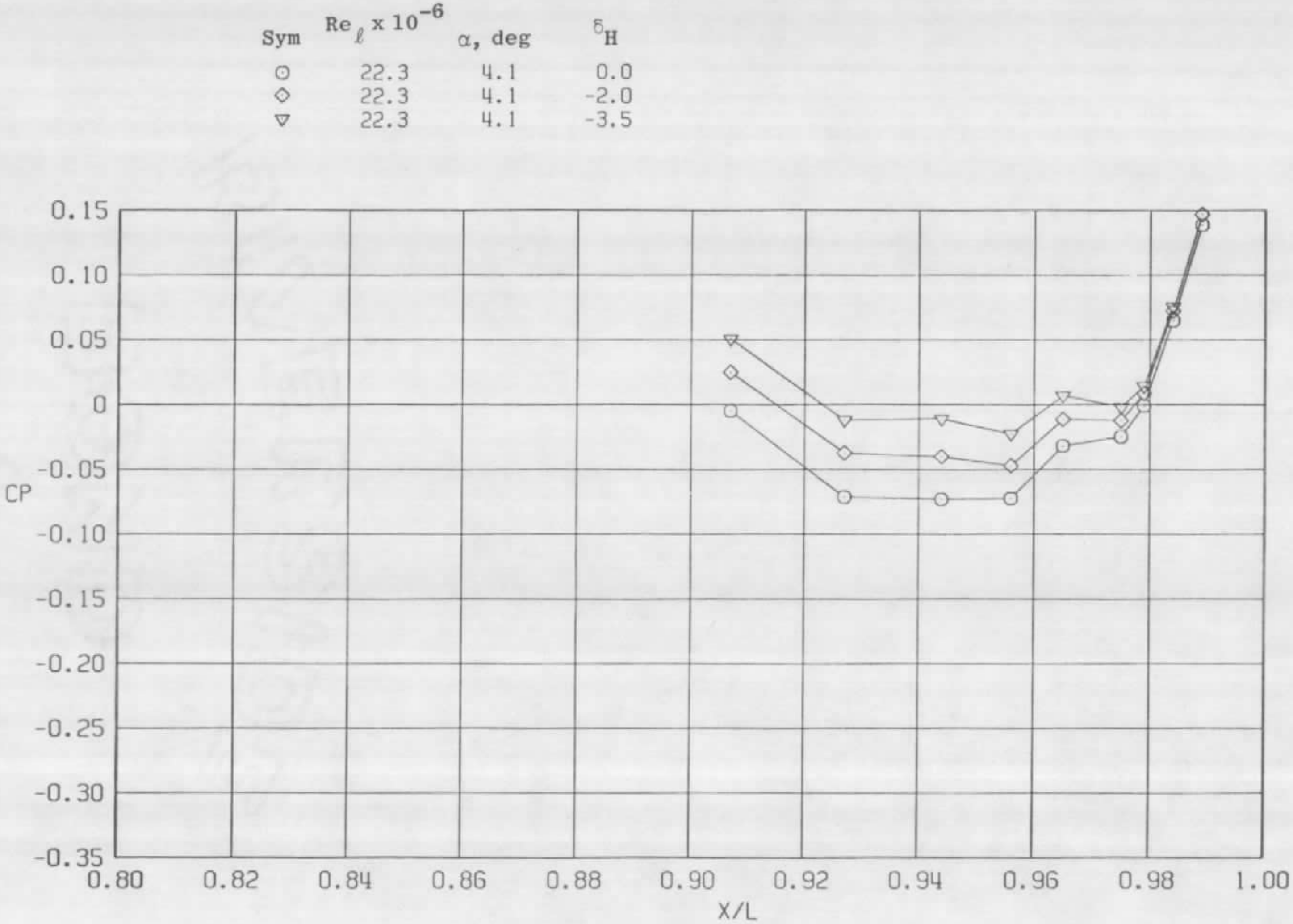

f. ϕ = 315 deg

Figure 43. Concluded.

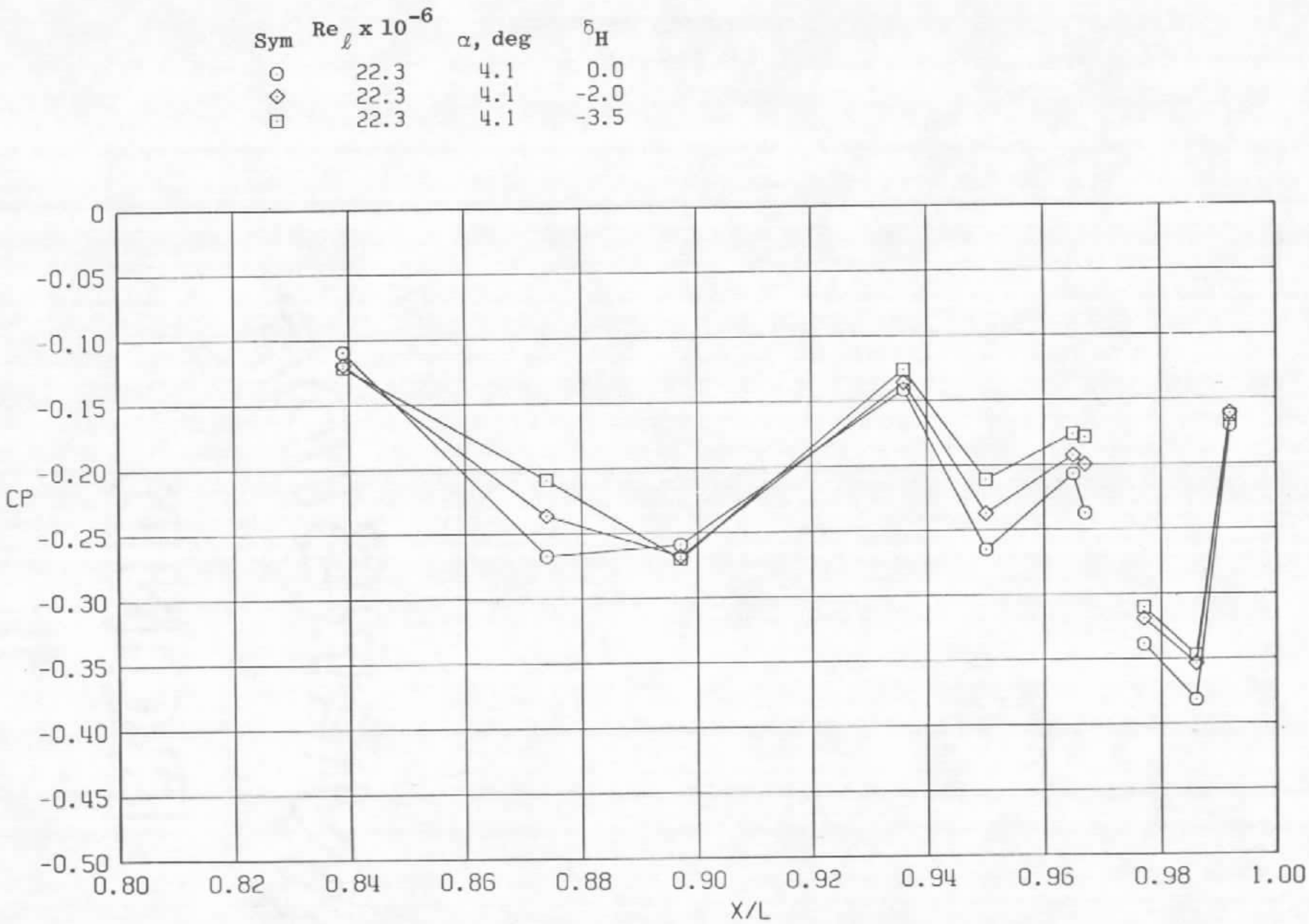

a. $\phi = 0$

Figure 44. Effect of horizontal tail deflection on surface pressure coefficients, A8 = 300 in.², M = 1.2, NPRE = 5.0 (SS).

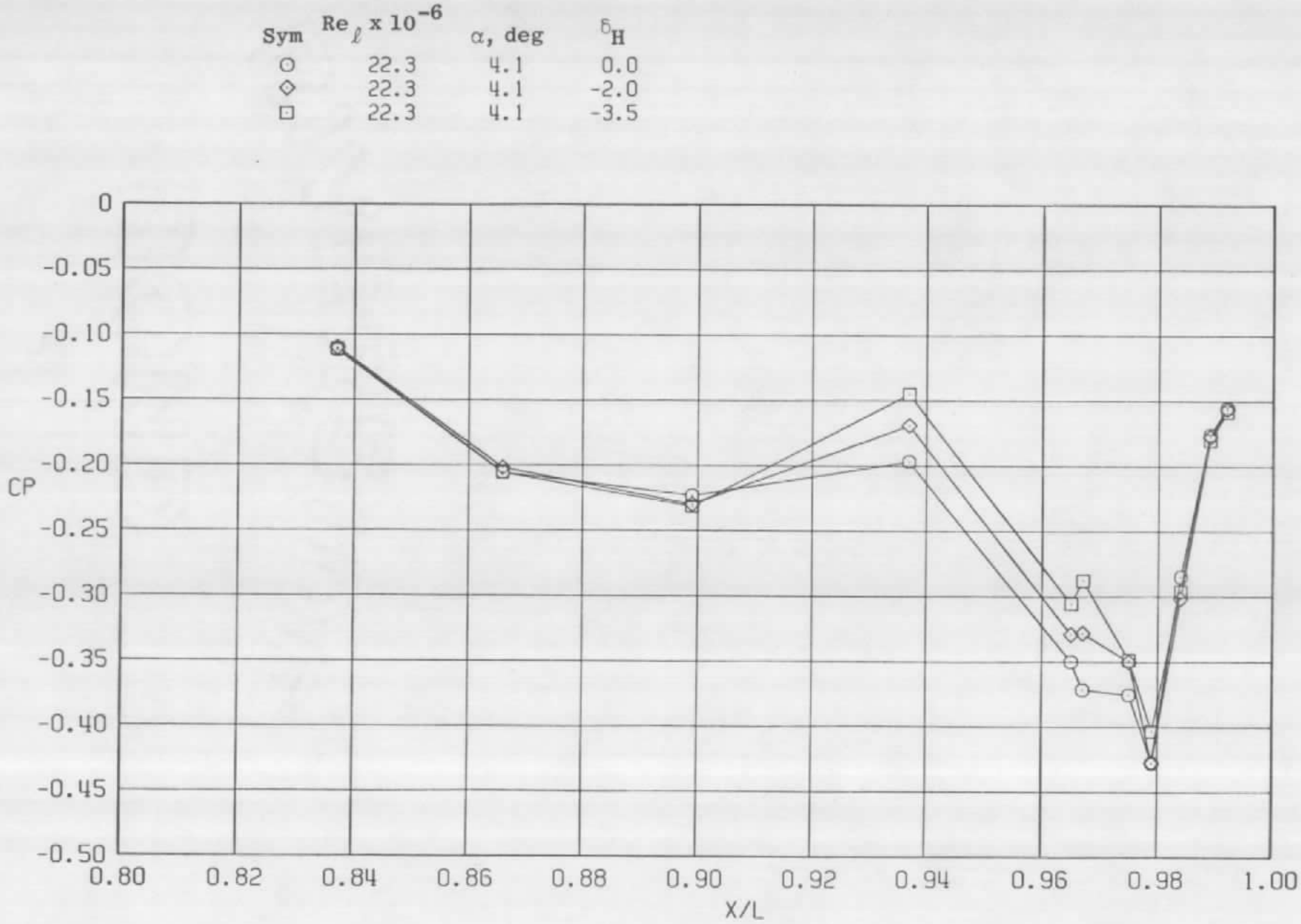

b. ϕ = 45 deg
Figure 44. Continued.

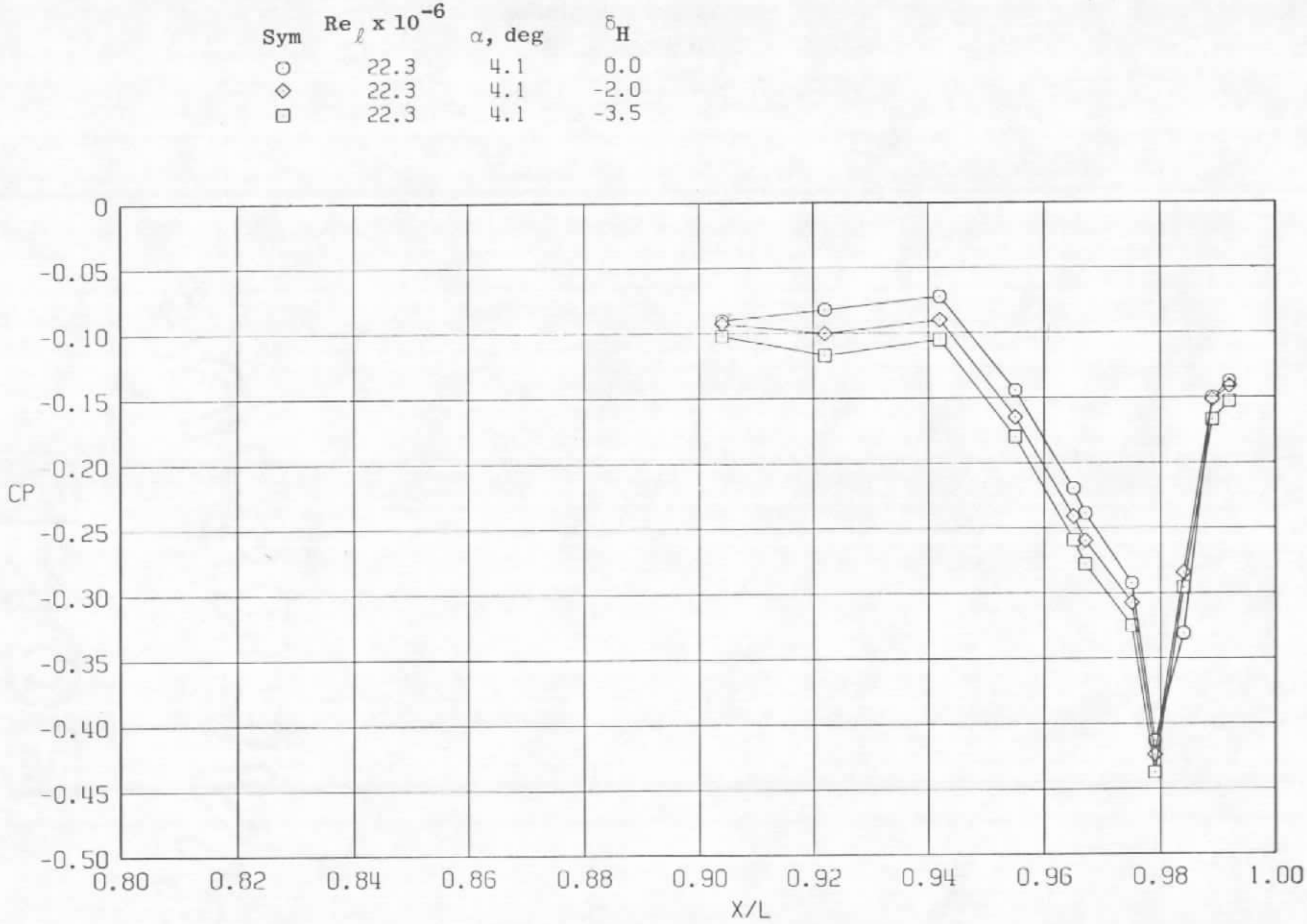

c. ϕ = 135 deg
Figure 44. Continued.

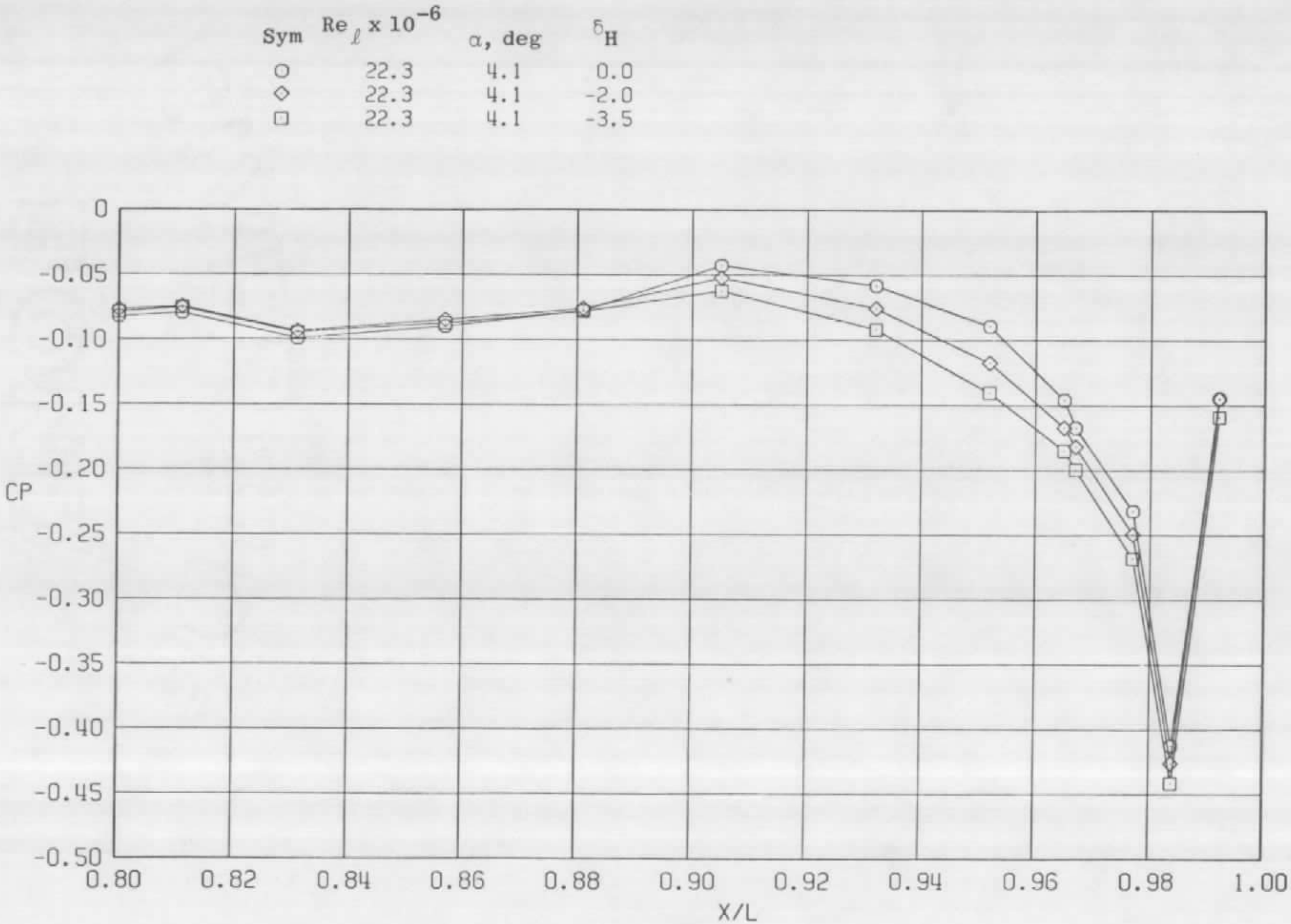

d. ϕ = 180 deg

Figure 44. Continued.

Sym	$Re_{\ell} \times 10^{-6}$	α, deg	δ_H
⊙	22.3	4.1	0.0
◇	22.3	4.1	-2.0
⊡	22.3	4.1	-3.5

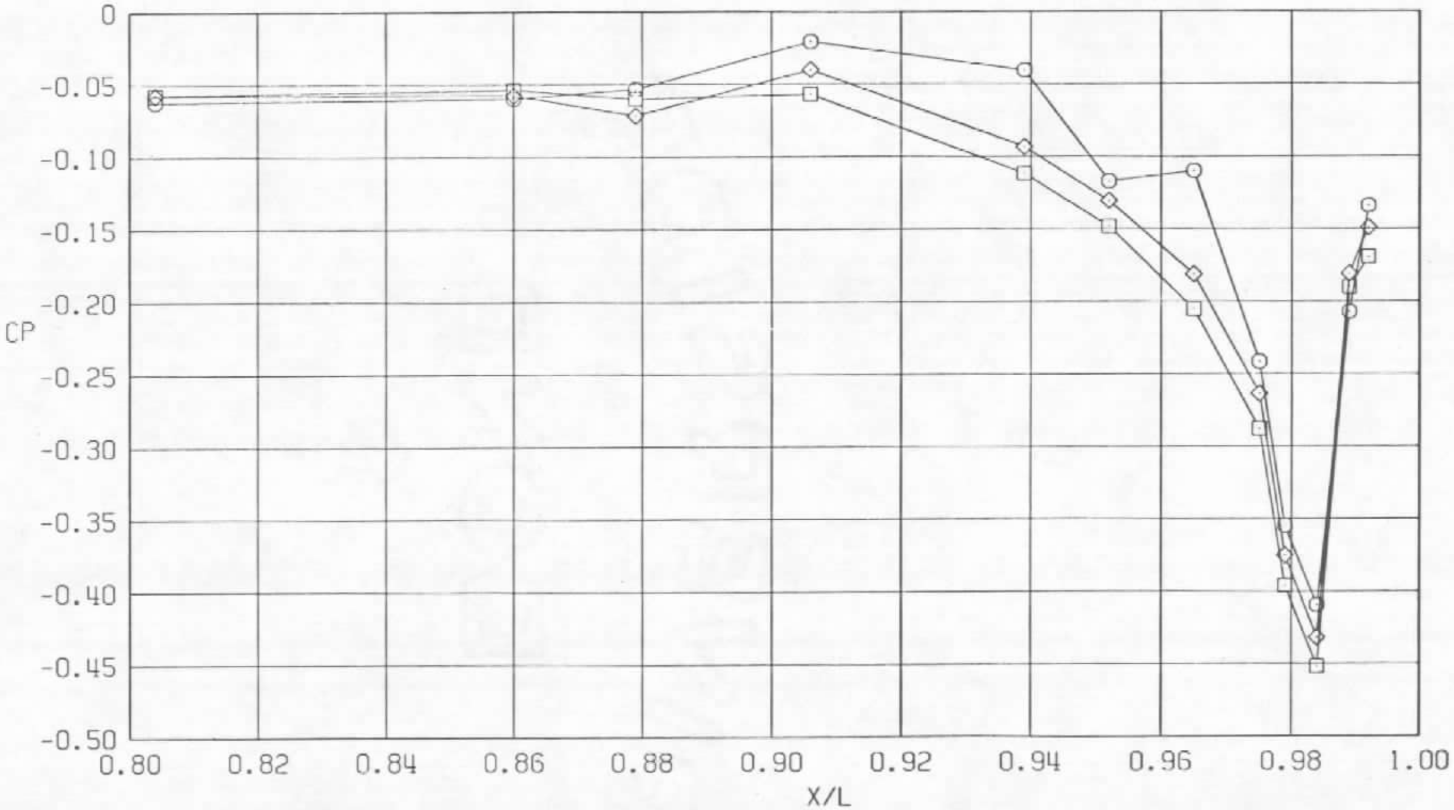

e. ϕ = 225 deg

Figure 44. Continued.

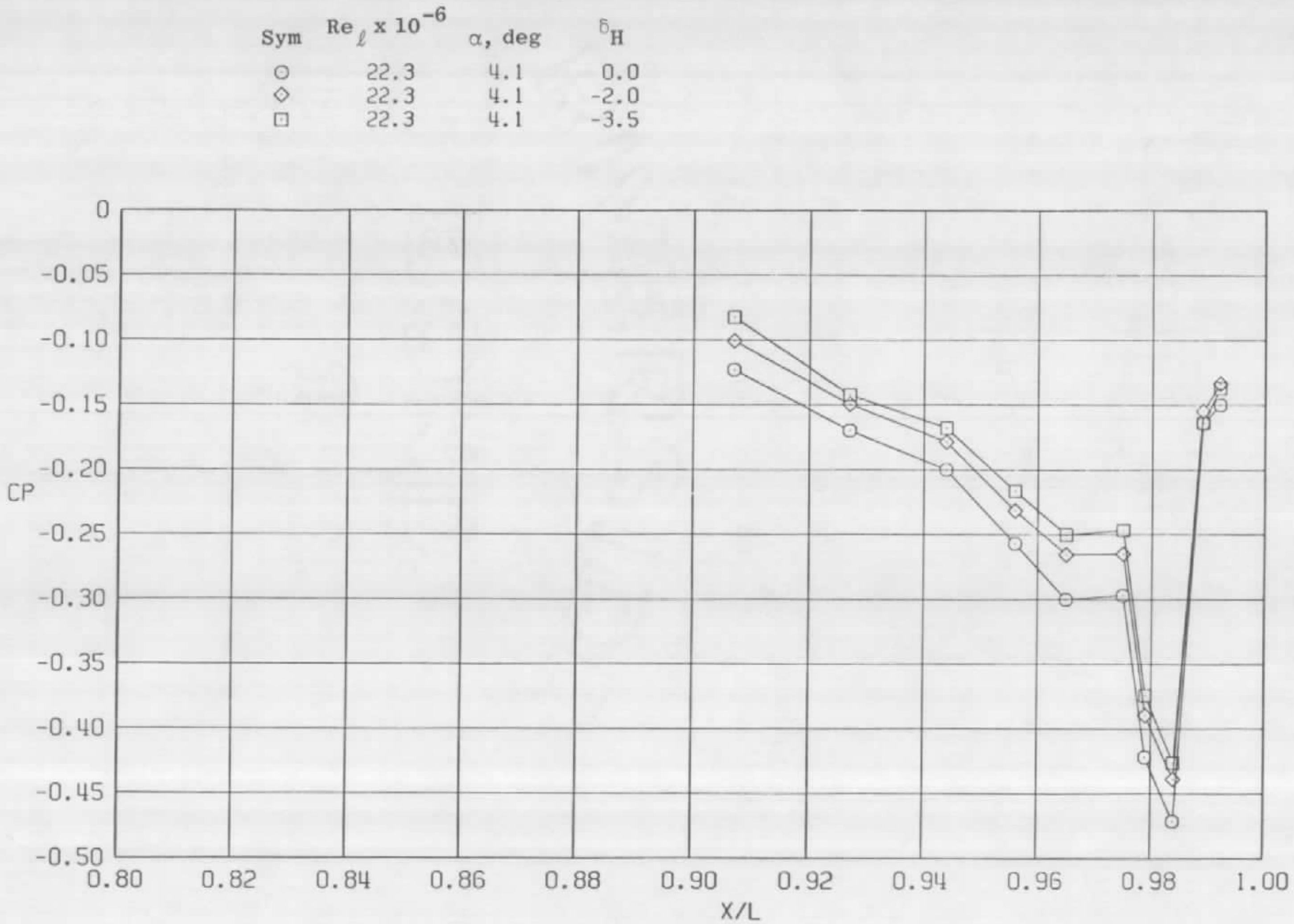

f. ϕ = 315 deg
Figure 44. Concluded.

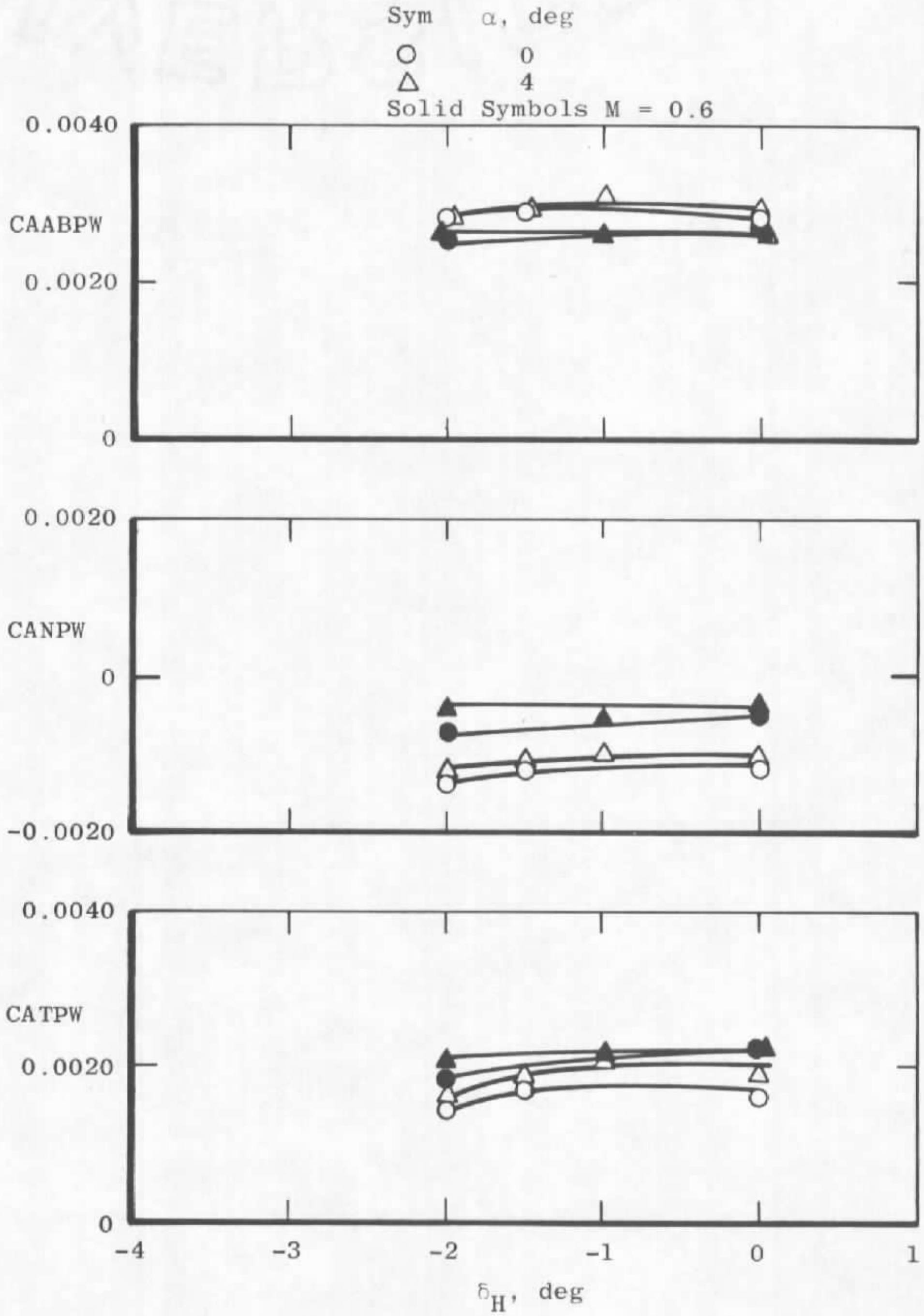

a. M = 0.9, A8 = 200 in.², NPRE = 3.4

Figure 45. Effect of horizontal tail deflections on axial force coefficients (SS).

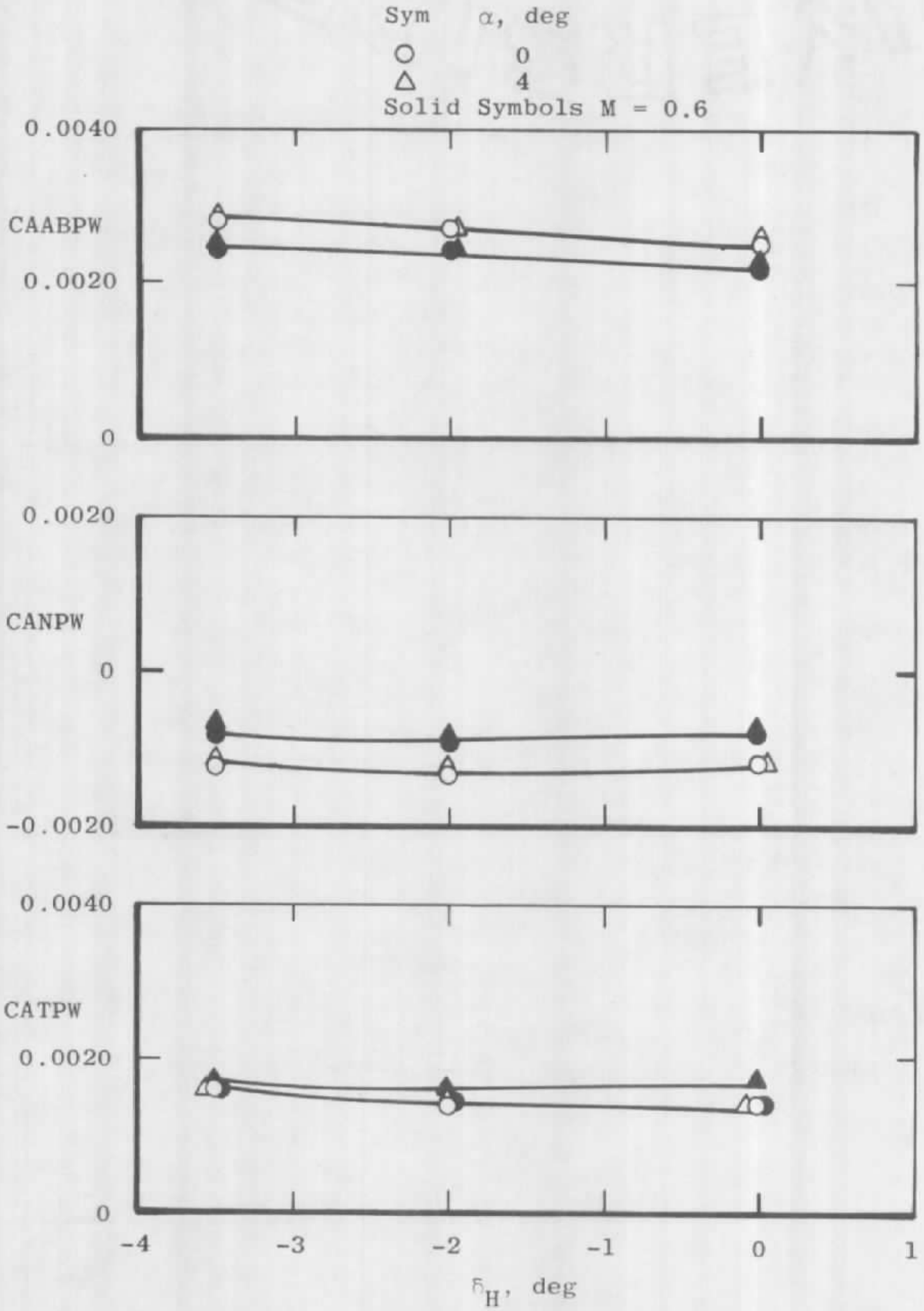

b. M = 0.9, A8 = 300 in.², NPRE = 5.0
Figure 45. Continued.

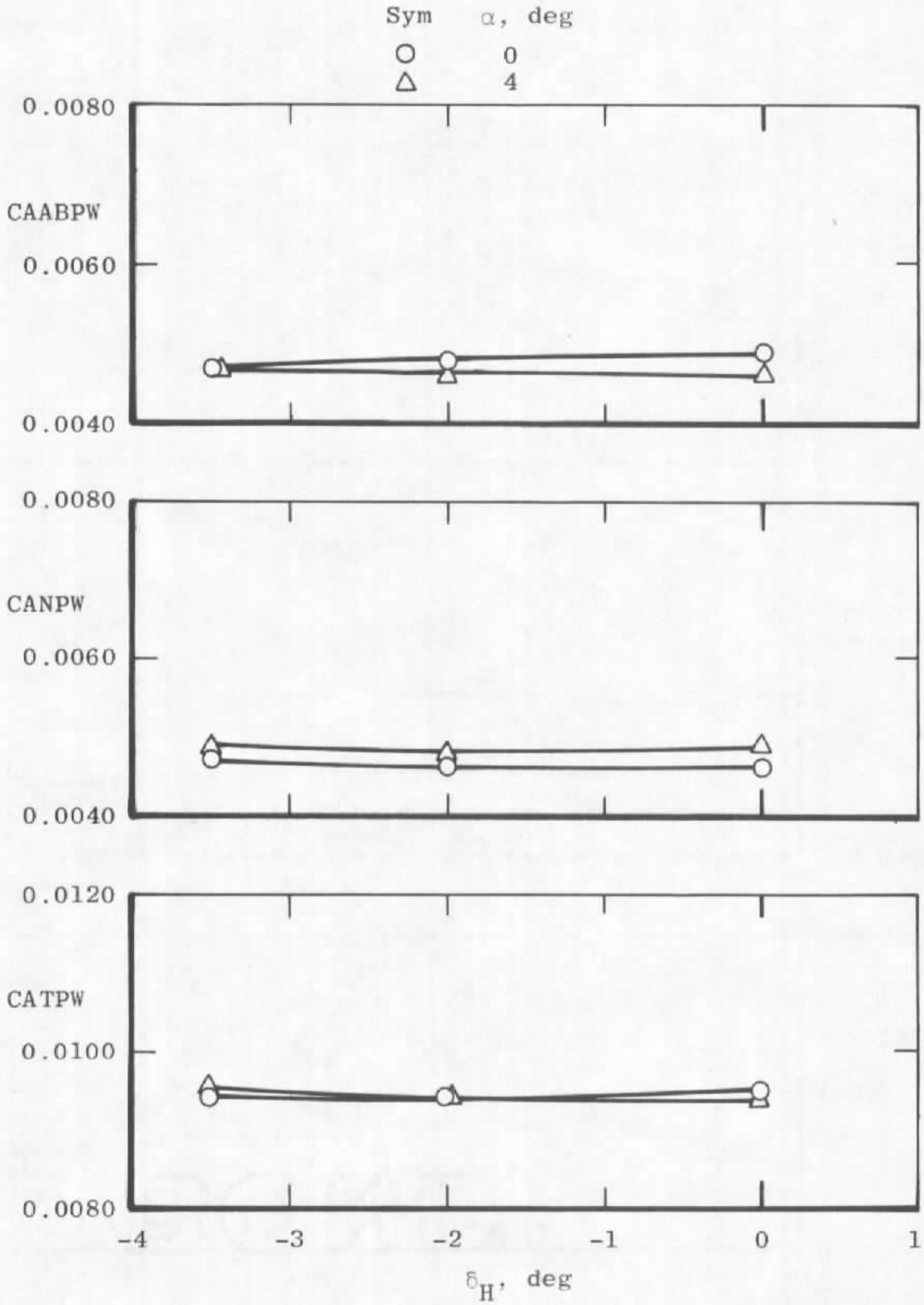

c. M = 1.2, A8 = 300 in.², NPRE = 5.0
Figure 45. Concluded.

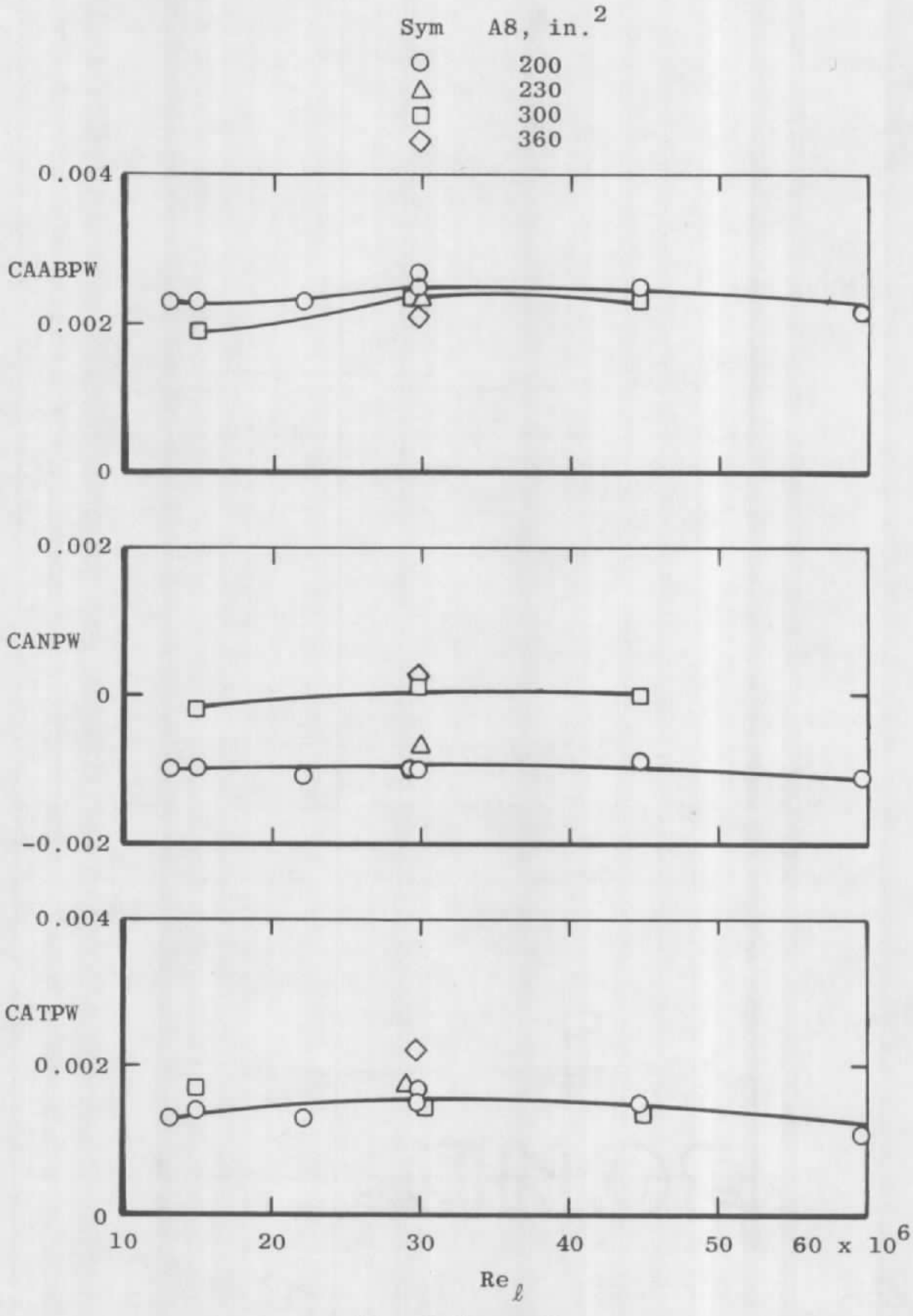

a. M = 0.6, α = 0

Figure 46. Reynolds number effects on axial force coefficients (LS).

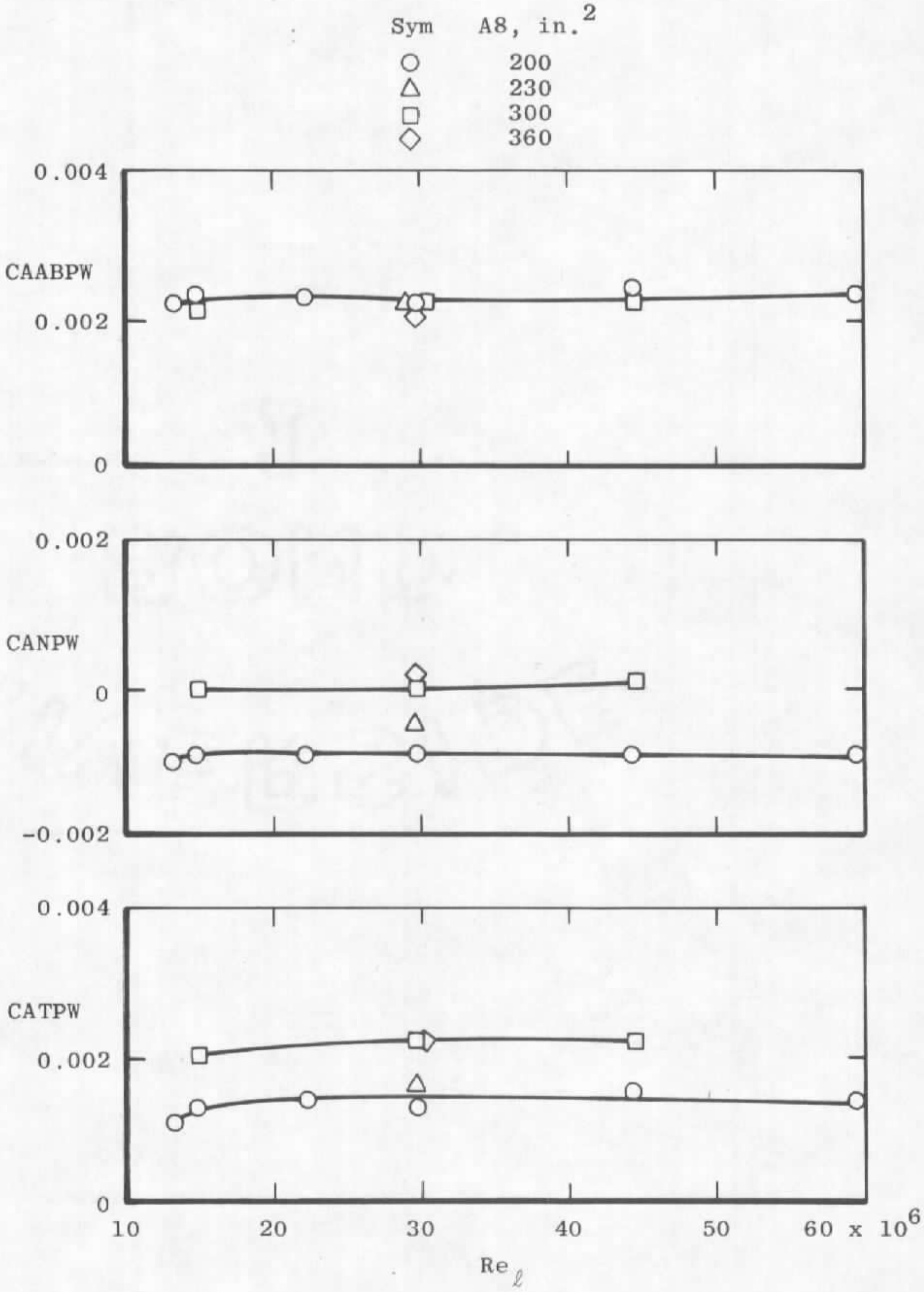

b. M = 0.6, α = 4.1 deg
Figure 46. Continued.

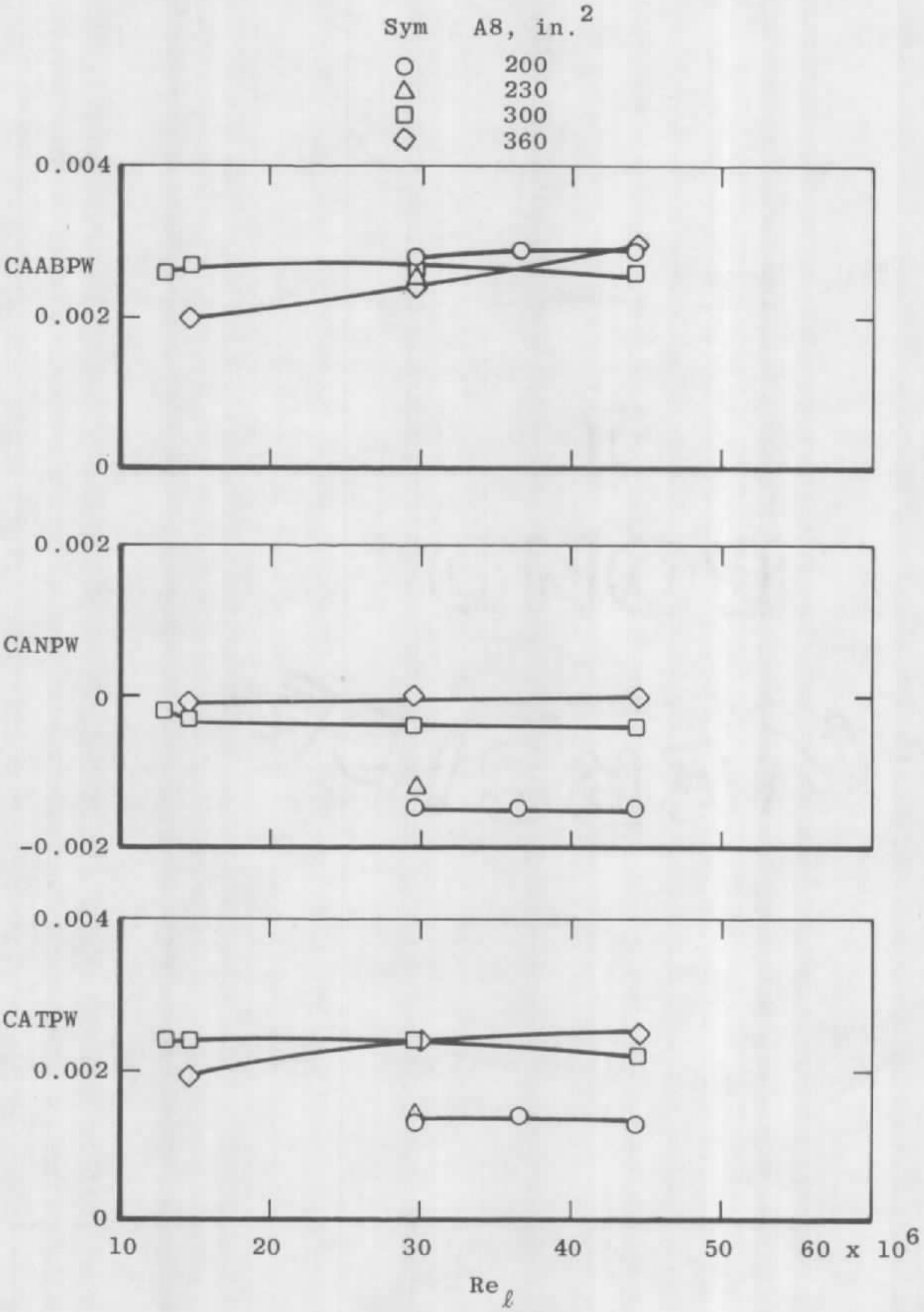

c. M = 0.9, α = 0
Figure 46. Continued.

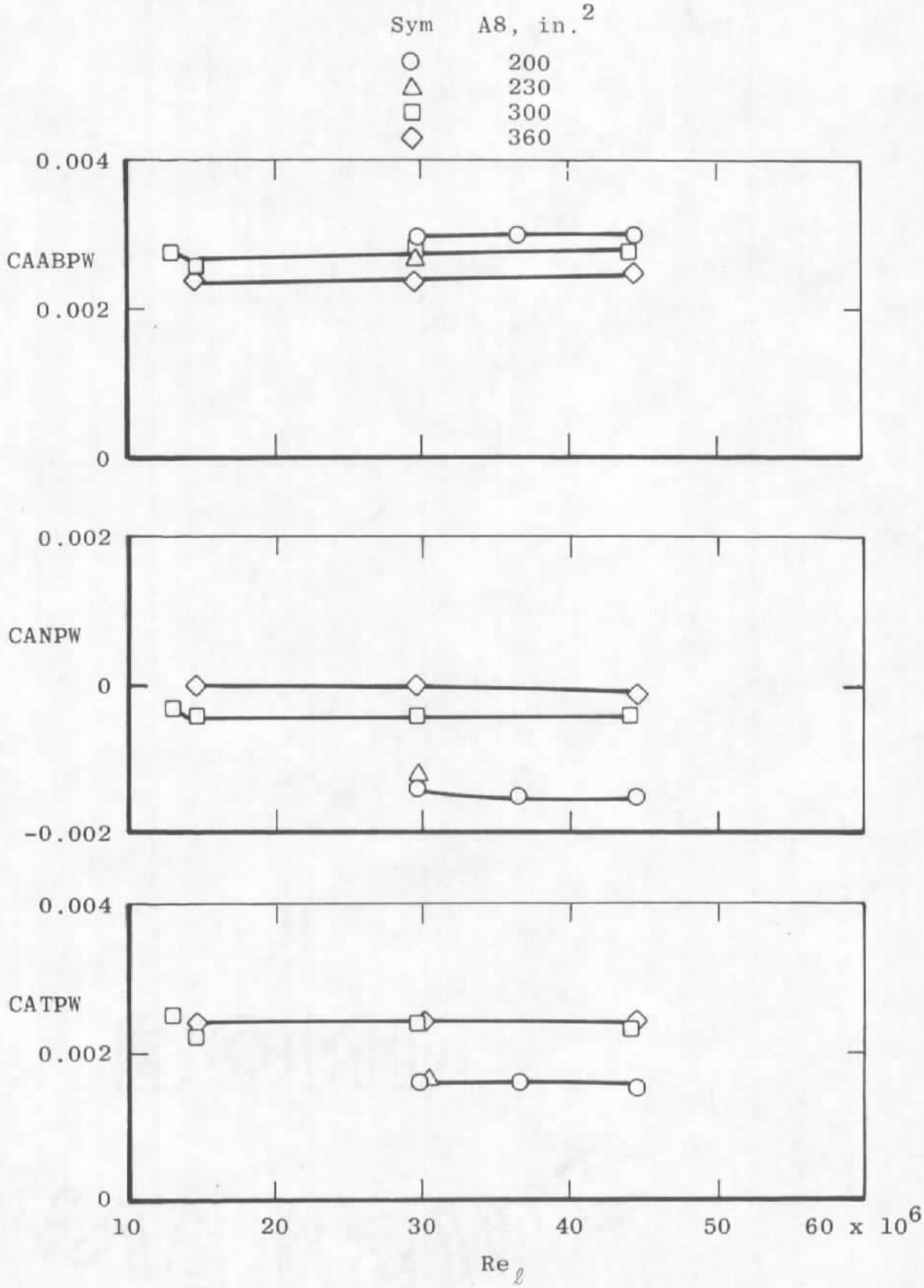

d. M = 0.9, α = 4 deg
Figure 46. Continued.

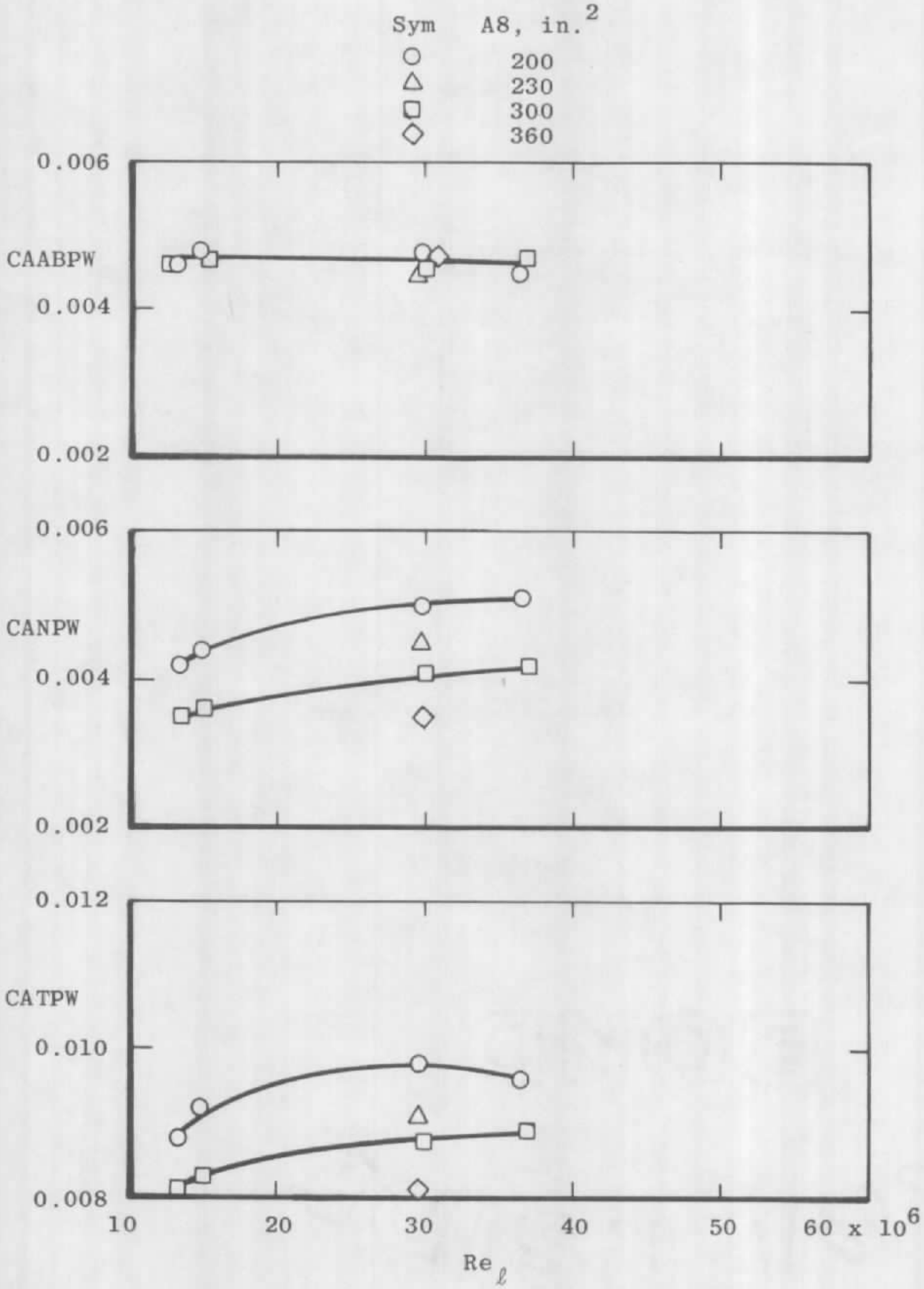

e. M = 1.2, α = 0
Figure 46. Continued.

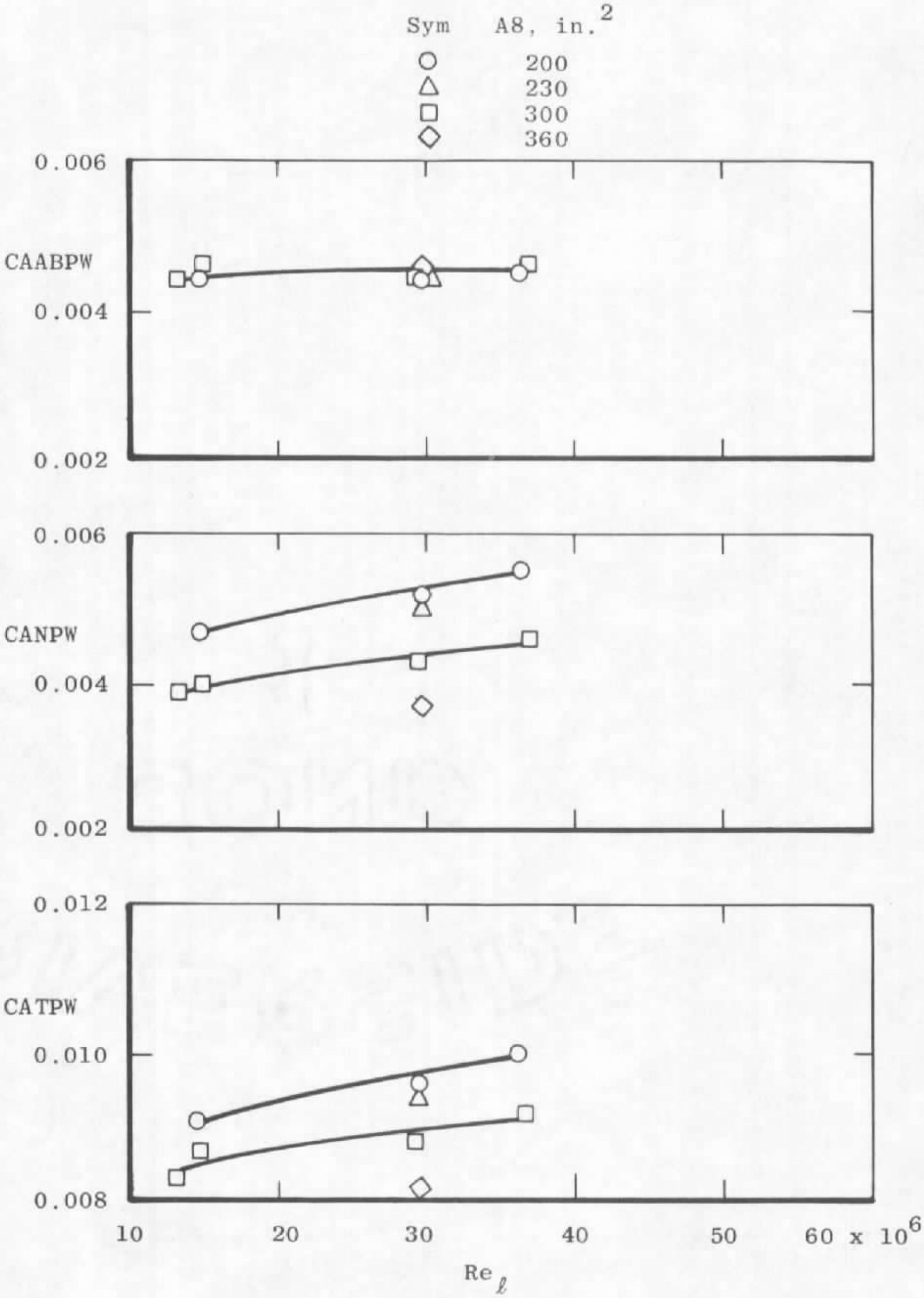

f. M = 1.2, α = 4.1 deg
Figure 46. Concluded.

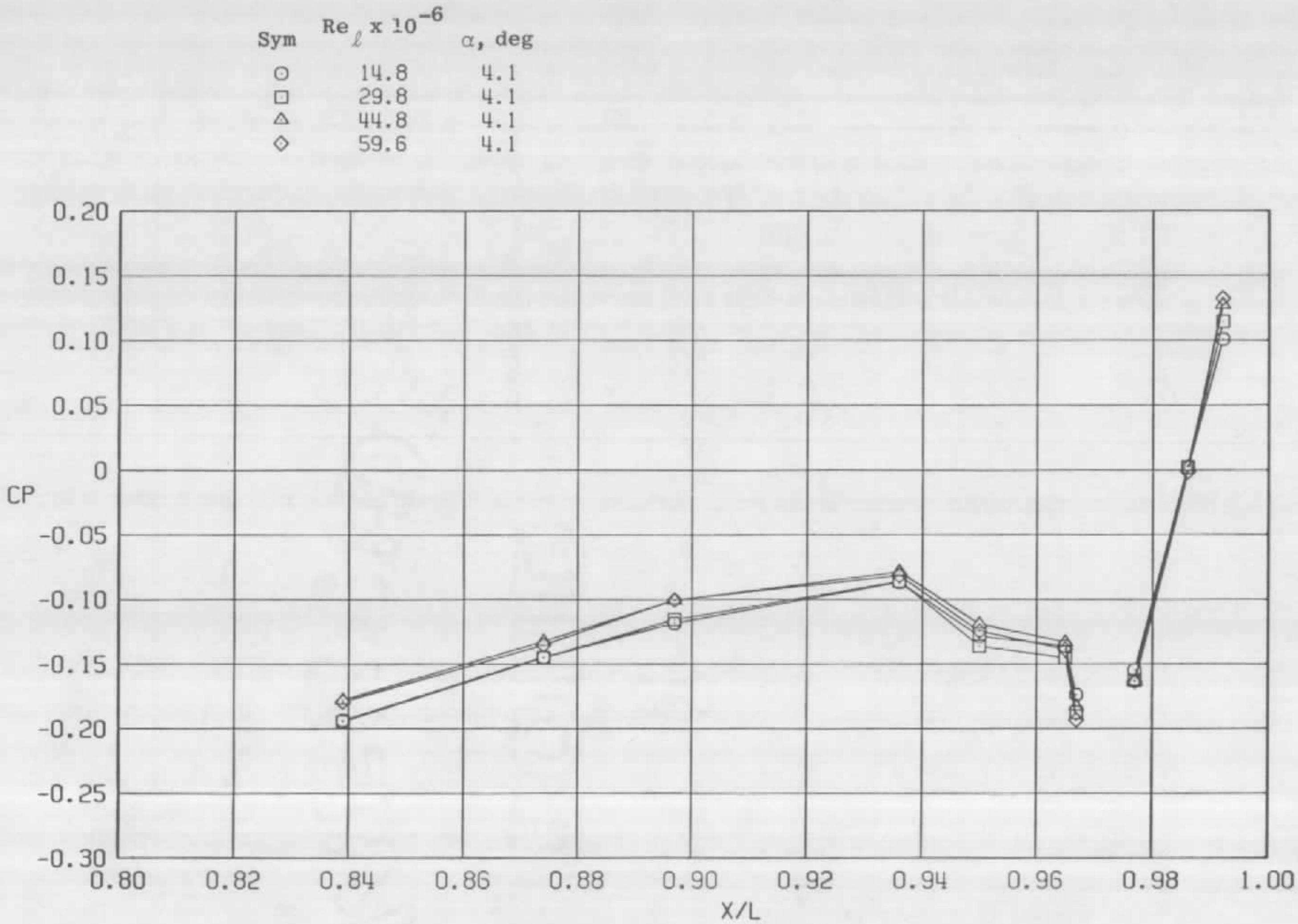

a. $\phi = 0$

Figure 47. Reynolds number effects on surface pressure coefficients $A8 = 200$ in.^{2}, $M = 0.6$, $NPR = 3.4$ (WT).

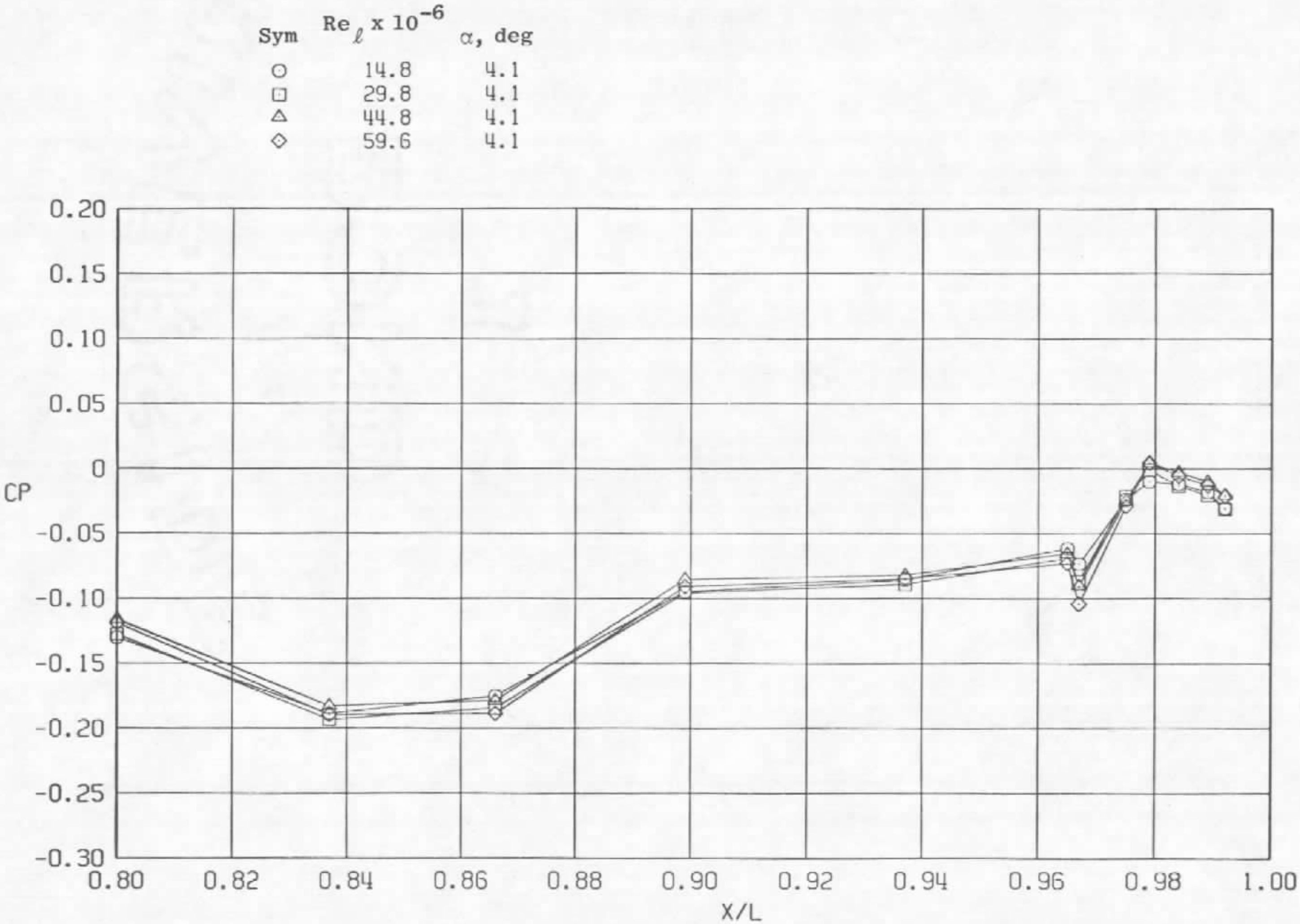

b. ϕ = 45 deg

Figure 47. Continued.

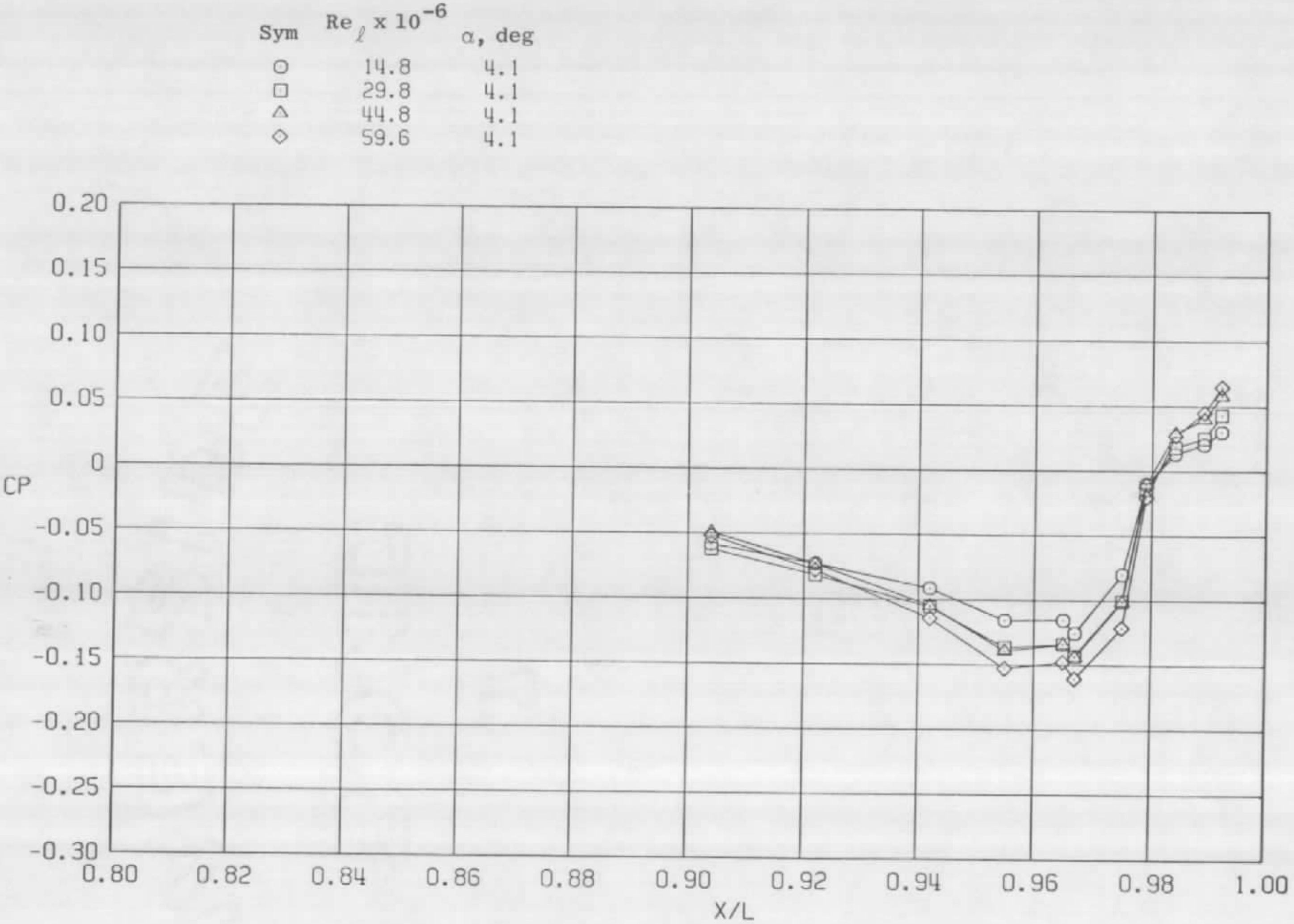

c. ϕ = 135 deg

Figure 47. Continued.

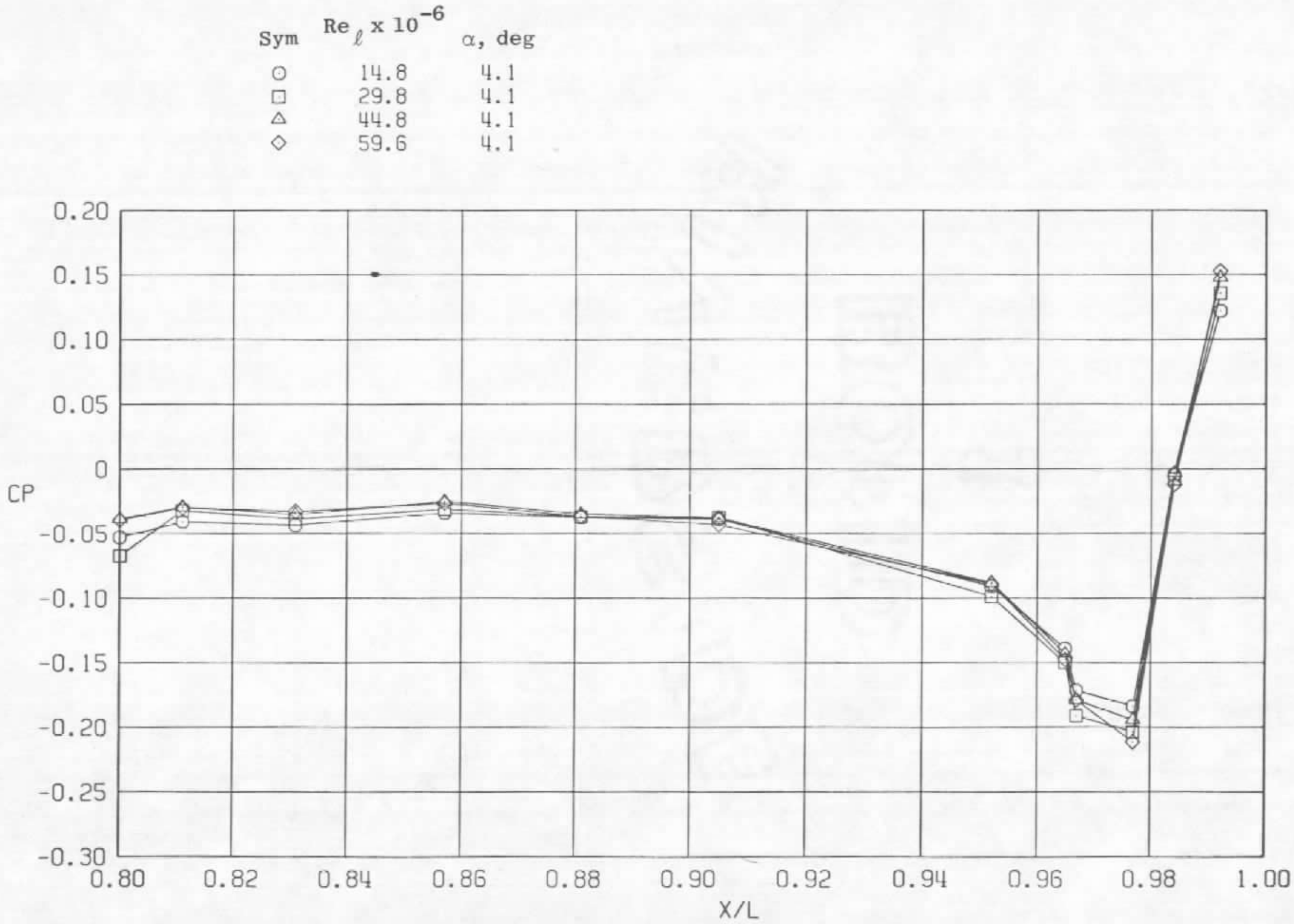

d. ϕ = 180 deg
Figure 47. Continued.

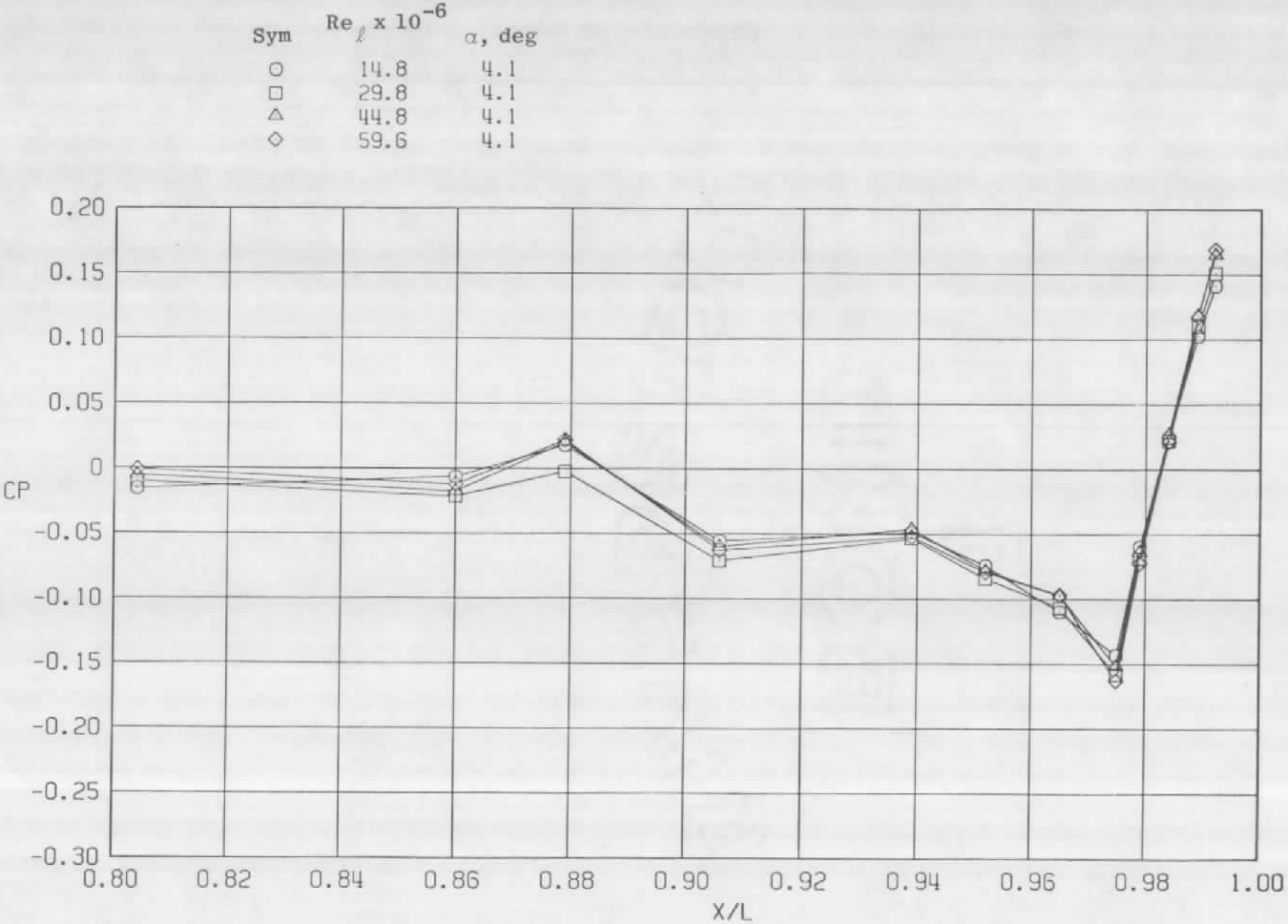

e. ϕ = 225 deg
Figure 47. Continued.

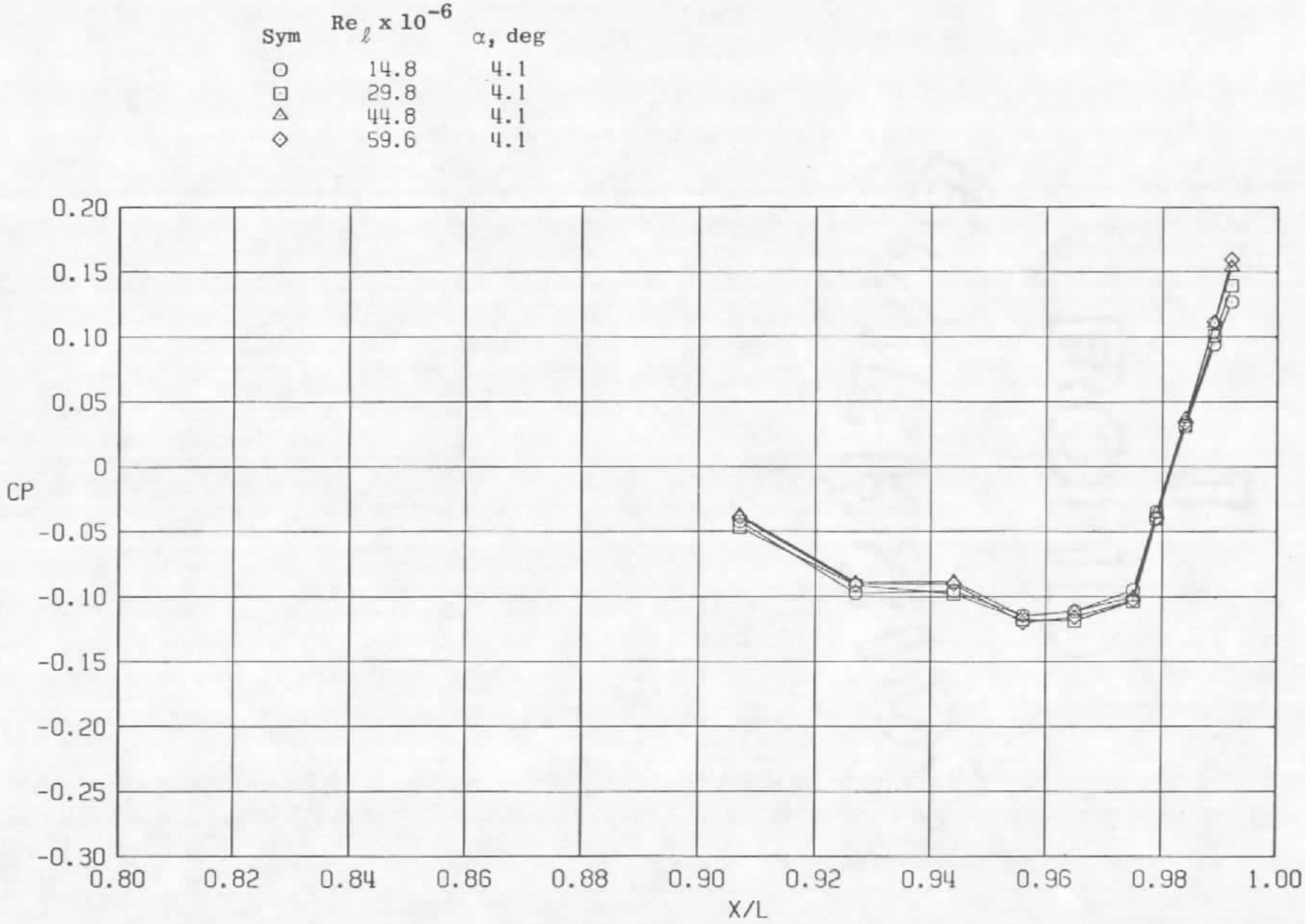

f. ϕ = 315 deg
Figure 47. Concluded.

a. $\phi = 0$

Figure 48. Reynolds number effects on surface pressure coefficients, A8 = 200 in.², M = 0.6 (LS).

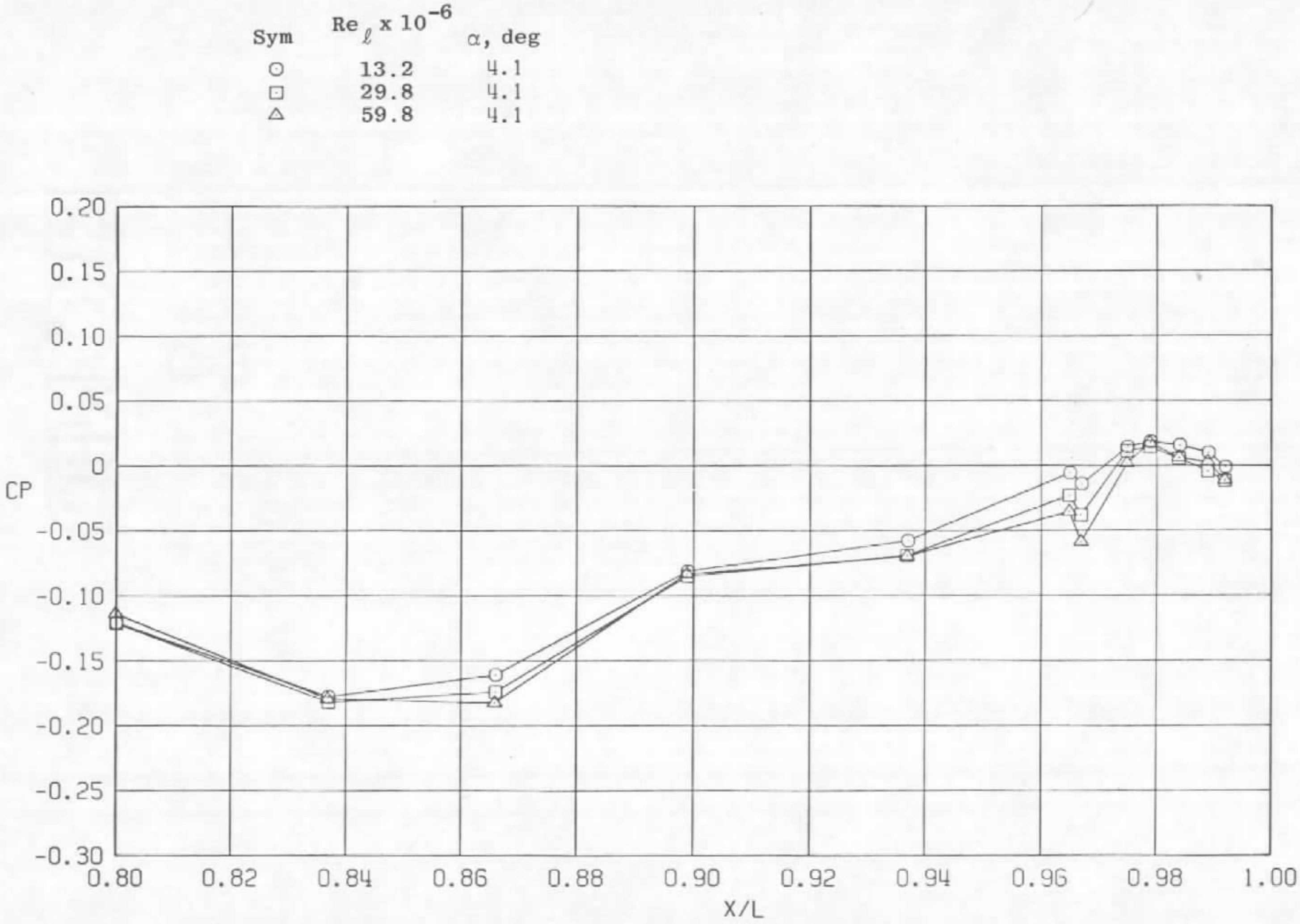

b. ϕ = 45 deg
Figure 48. Continued.

c. ϕ = 135 deg
Figure 48. Continued.

d. ϕ = 180 deg
Figure 48. Continued.

e. ϕ = 225 deg

Figure 48. Continued.

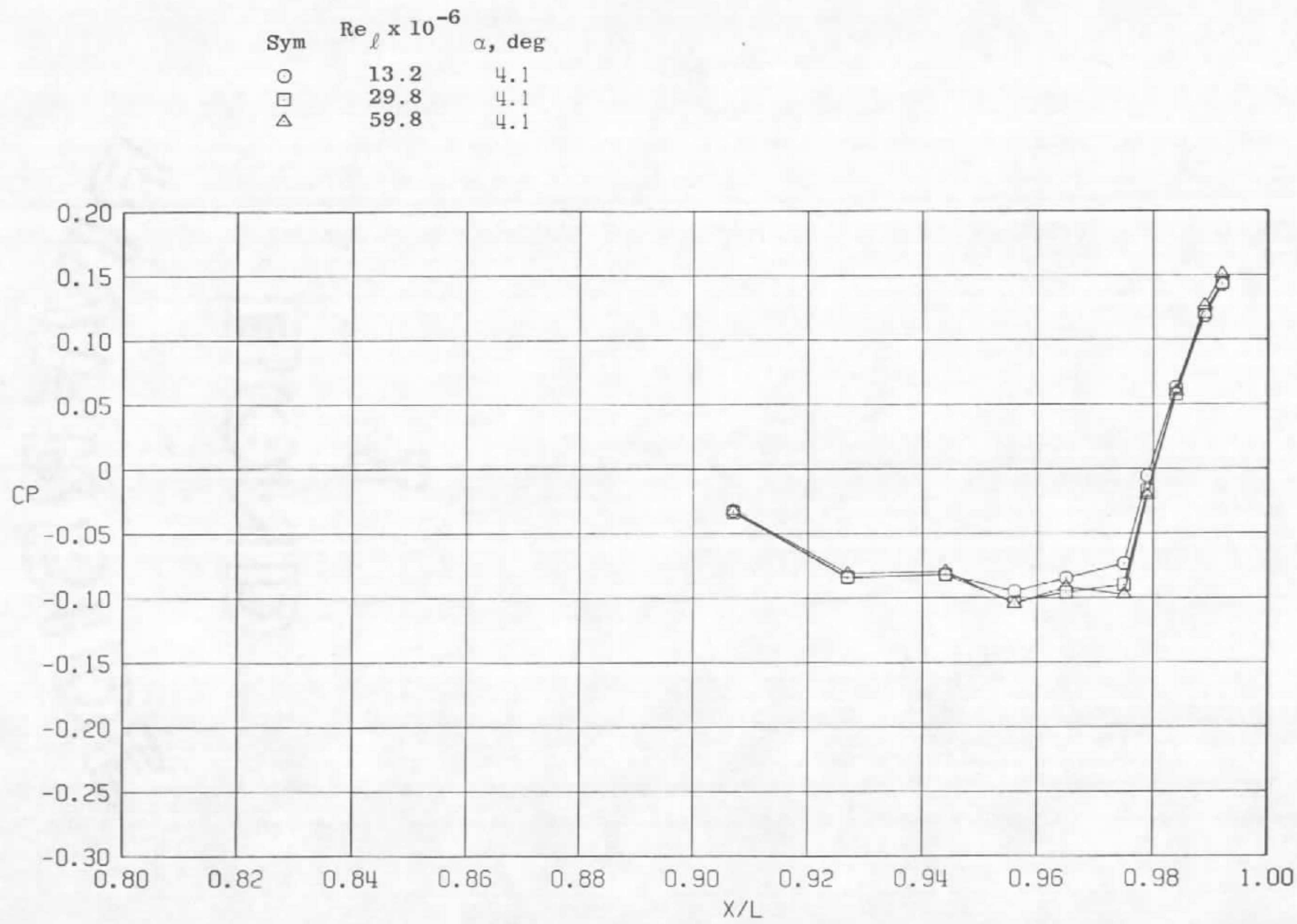

f. ϕ = 315 deg

Figure 48. Concluded.

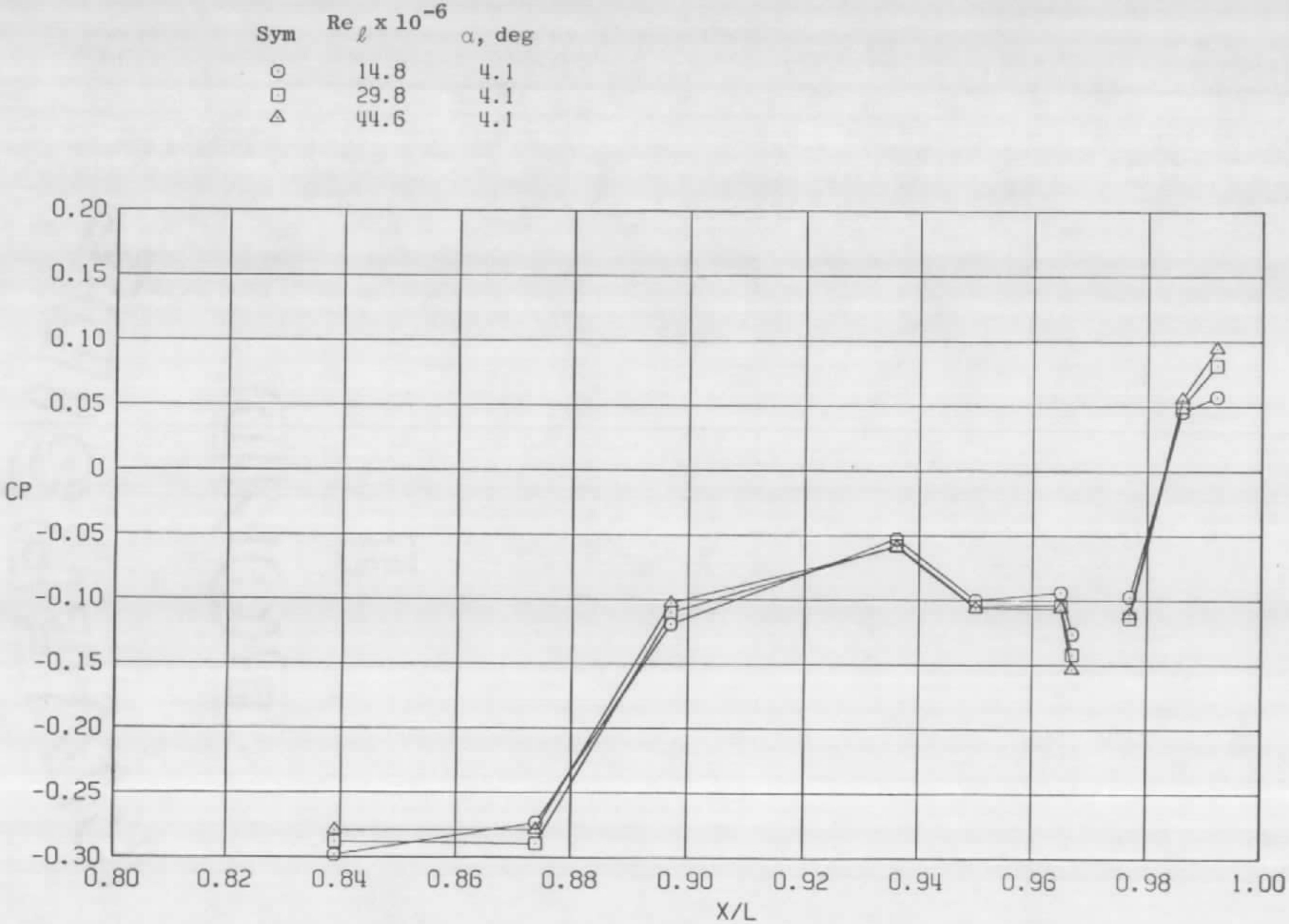

a. $\phi = 0$

Figure 49. Reynolds number effects on surface pressure coefficients, A8 = 200 in.^{2}, M = 0.9, NPR = 3.4 (WT).

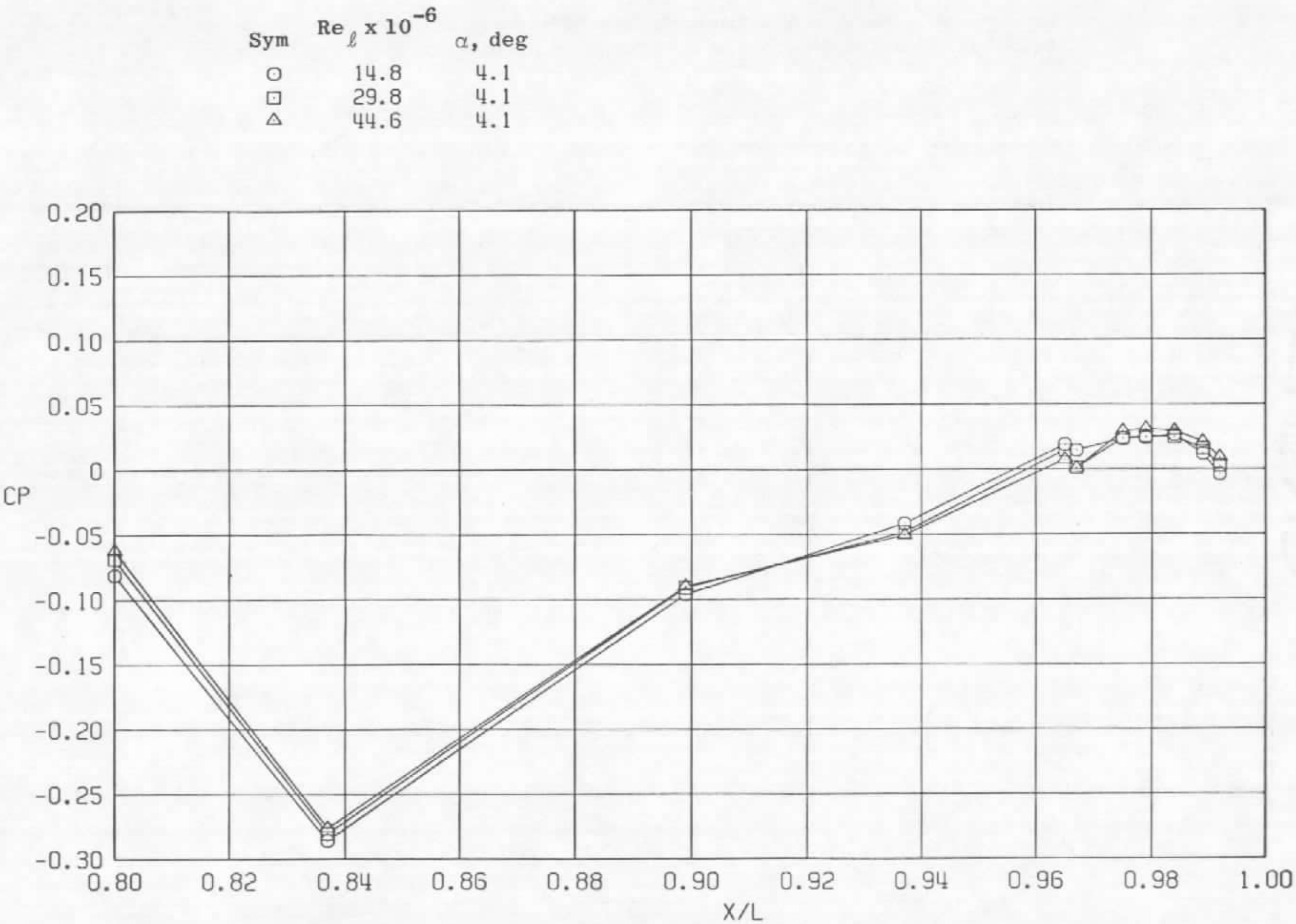

b. ϕ = 45 deg
Figure 49. Continued.

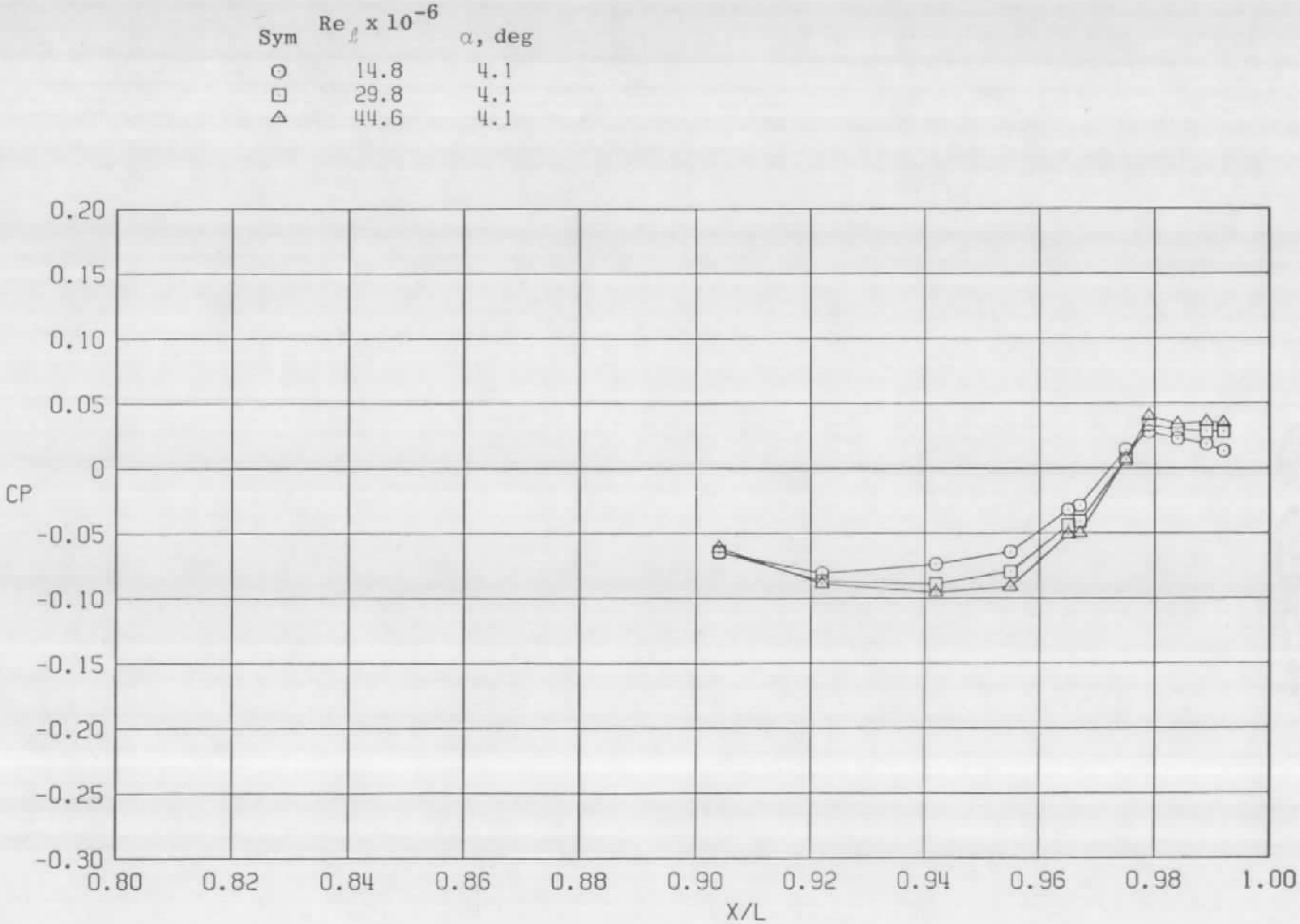

c. ϕ = 135 deg
Figure 49. Continued.

d. ϕ = 180 deg
Figure 49. Continued.

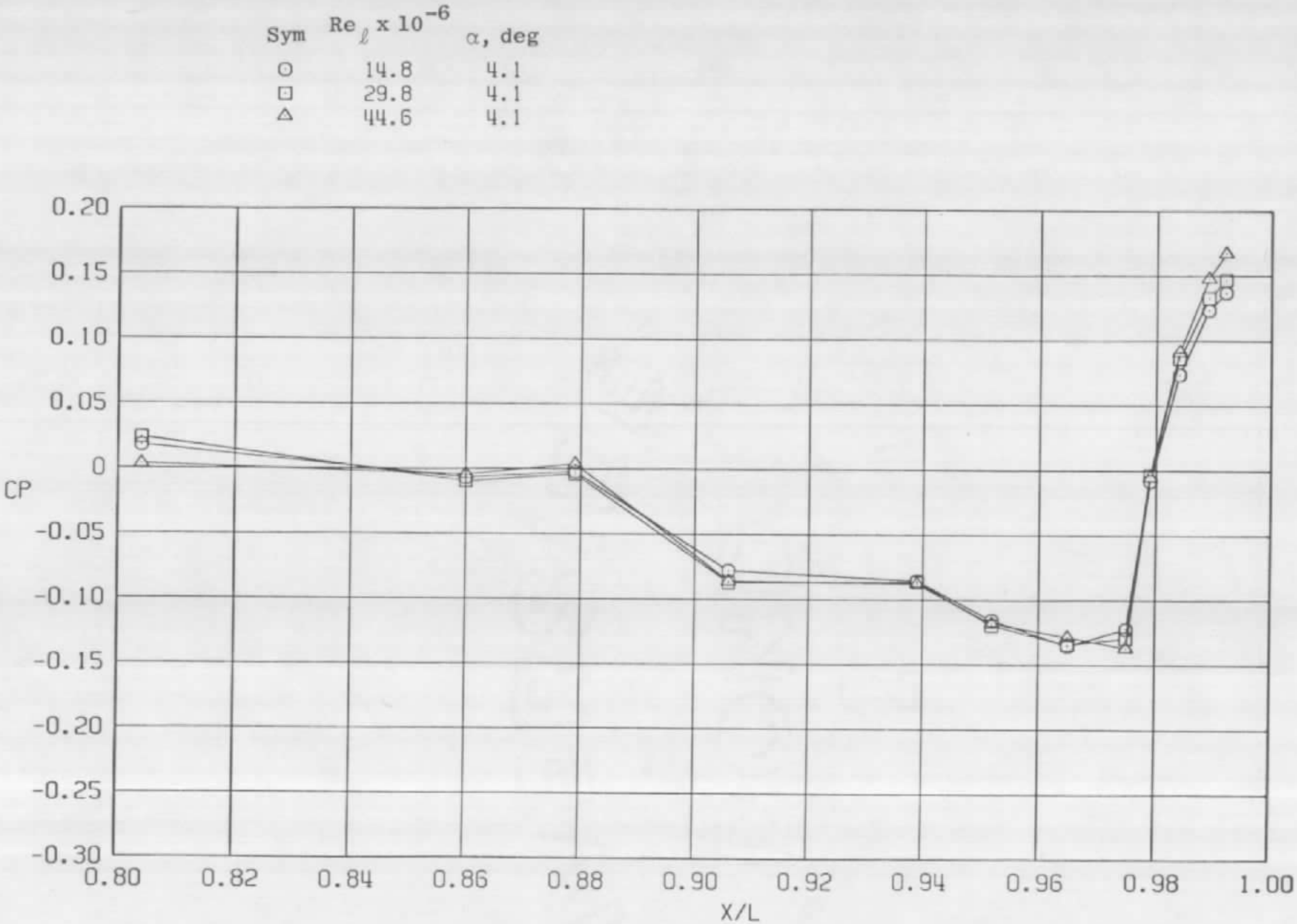

e. ϕ = 225 deg
Figure 49. Continued.

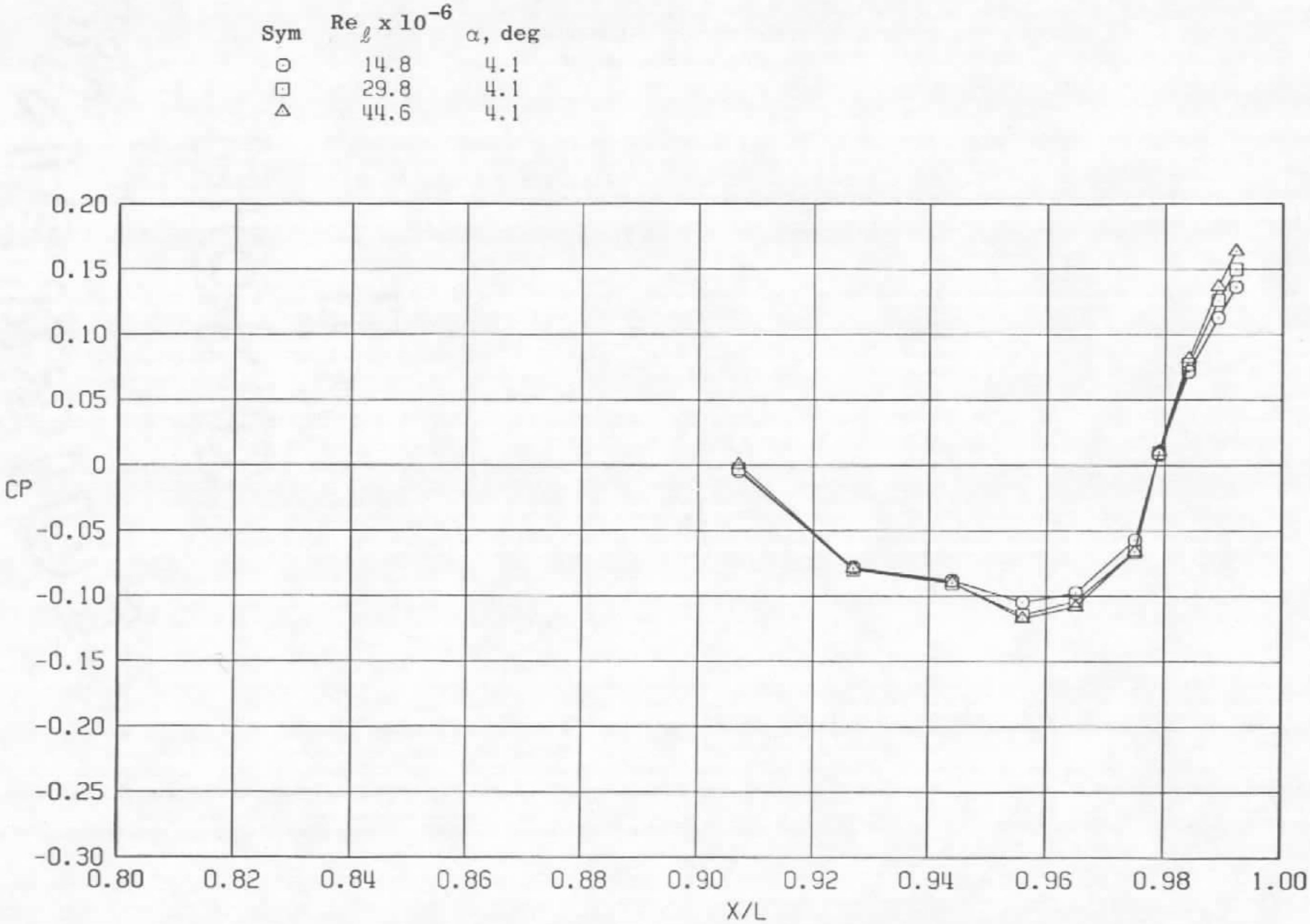

f. ϕ = 315 deg
Figure 49. Concluded.

a. $\phi = 0$

Figure 50. Reynolds number effects on surface pressure coefficients, A8 = 200 in.^{2}, M = 1.2, NPR = 3.4 (WT).

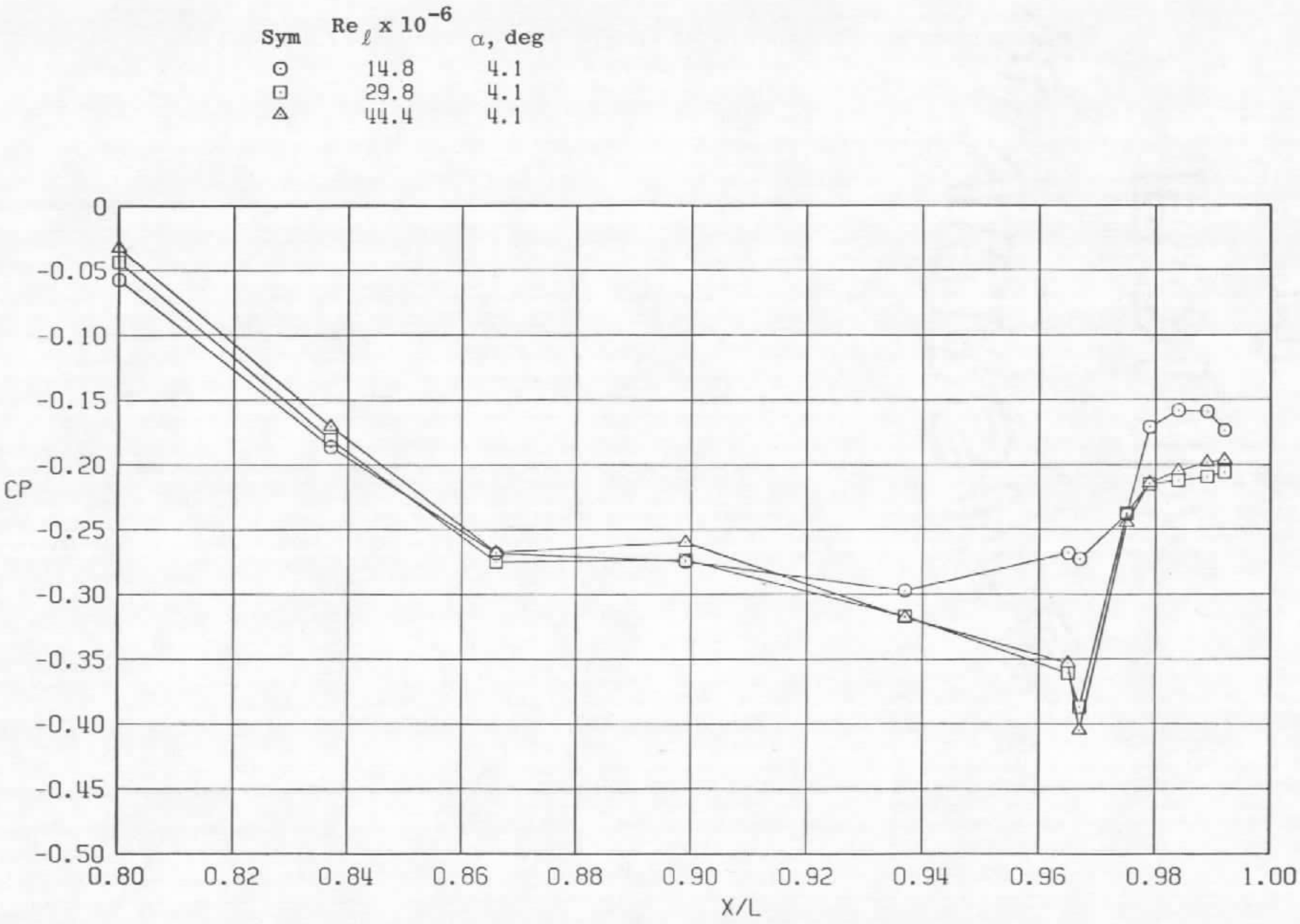

b. ϕ = 45 deg
Figure 50. Continued.

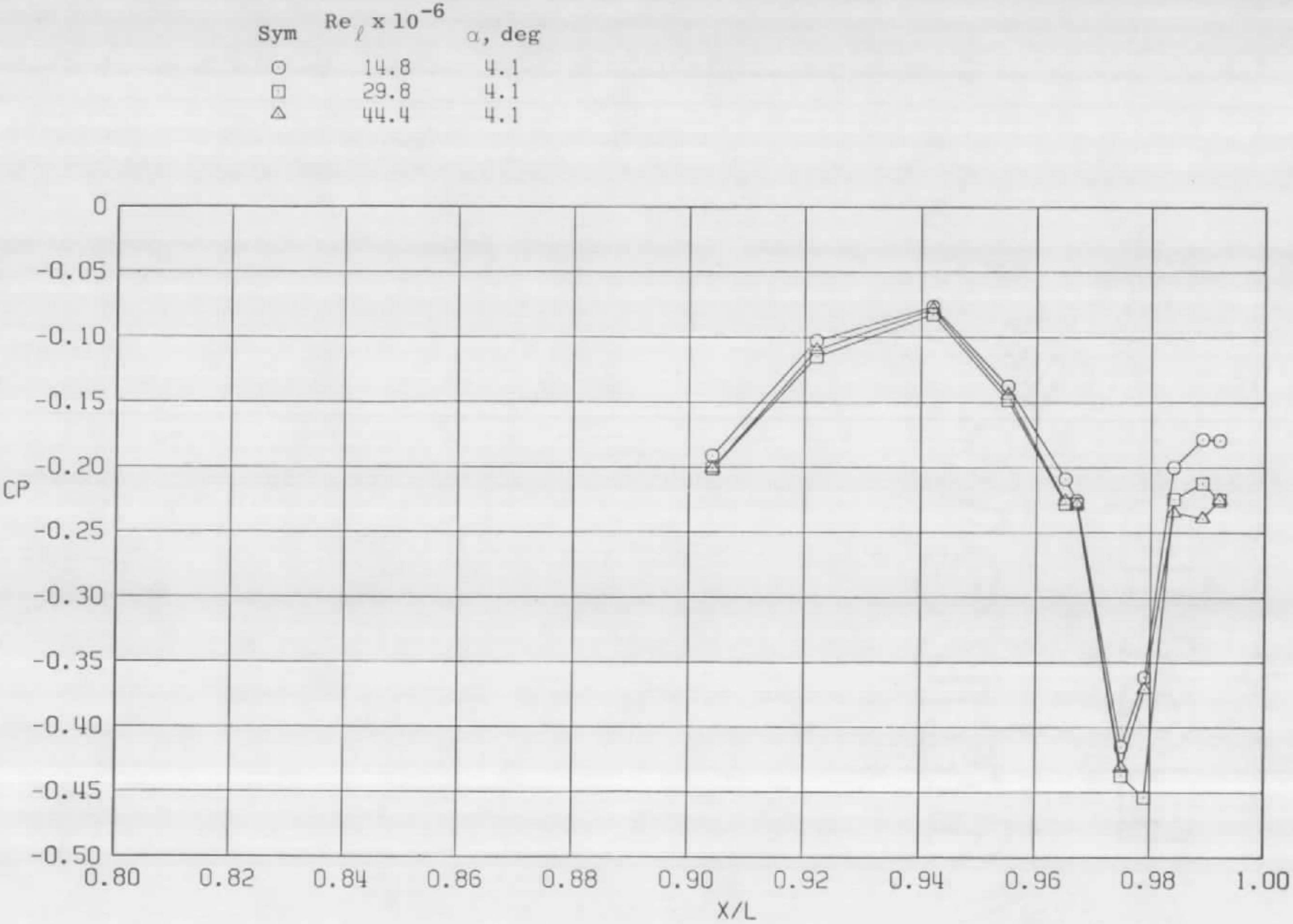

c. ϕ = 135 deg

Figure 50. Continued.

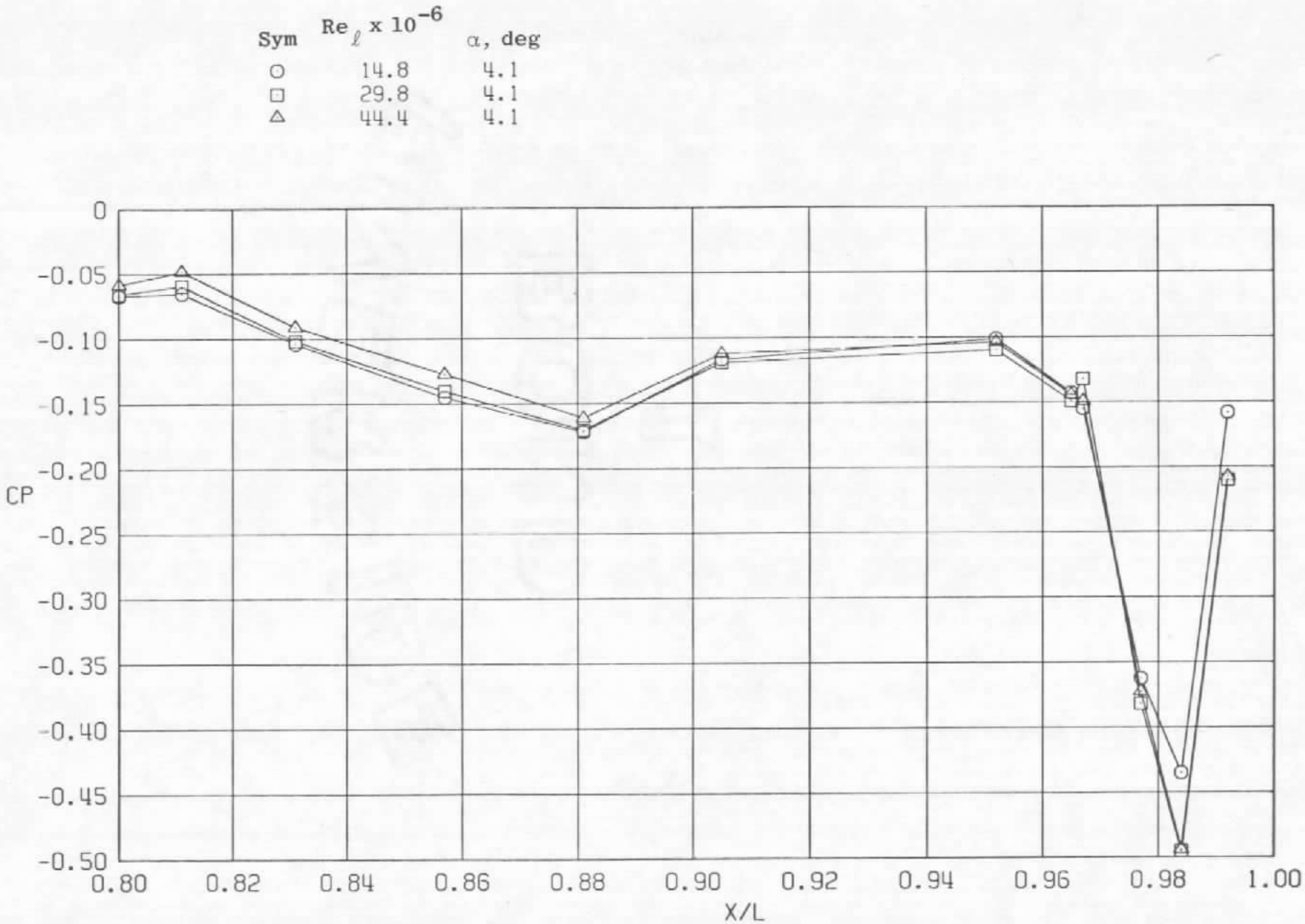

d. ϕ = 180 deg

Figure 50. Continued.

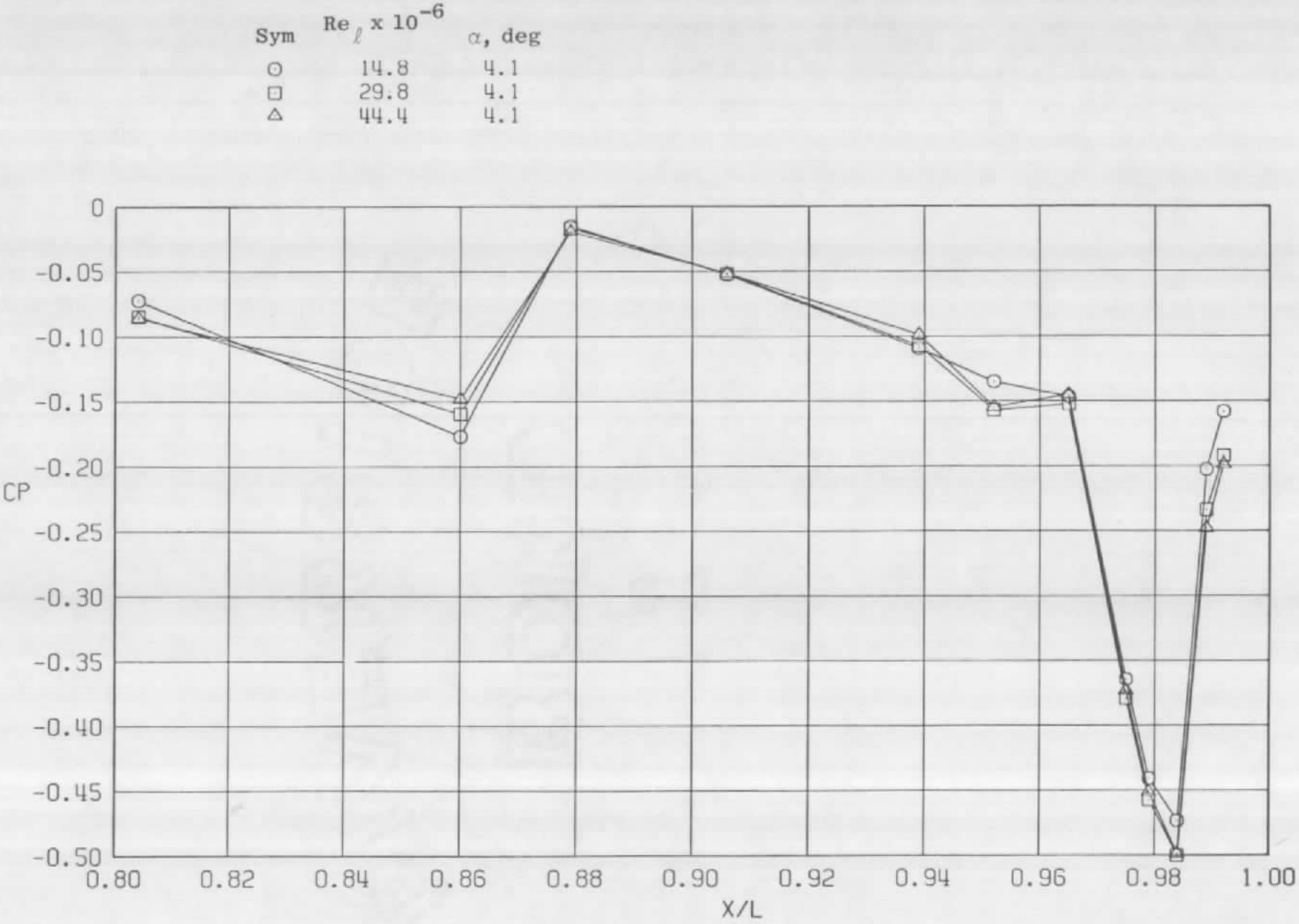

e. ϕ = 225 deg
Figure 50. Continued.

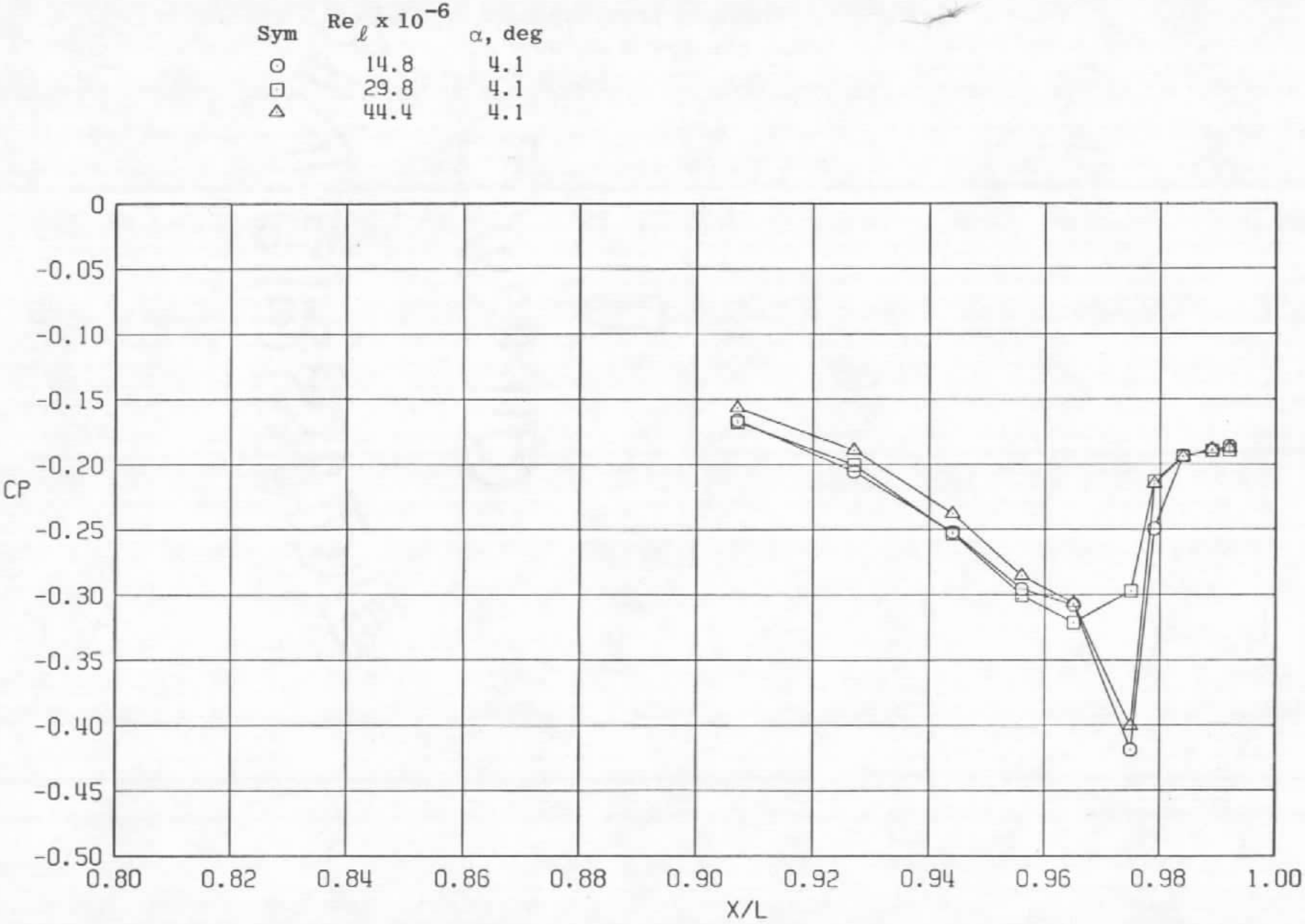

f. ϕ = 315 deg
Figure 50. Concluded

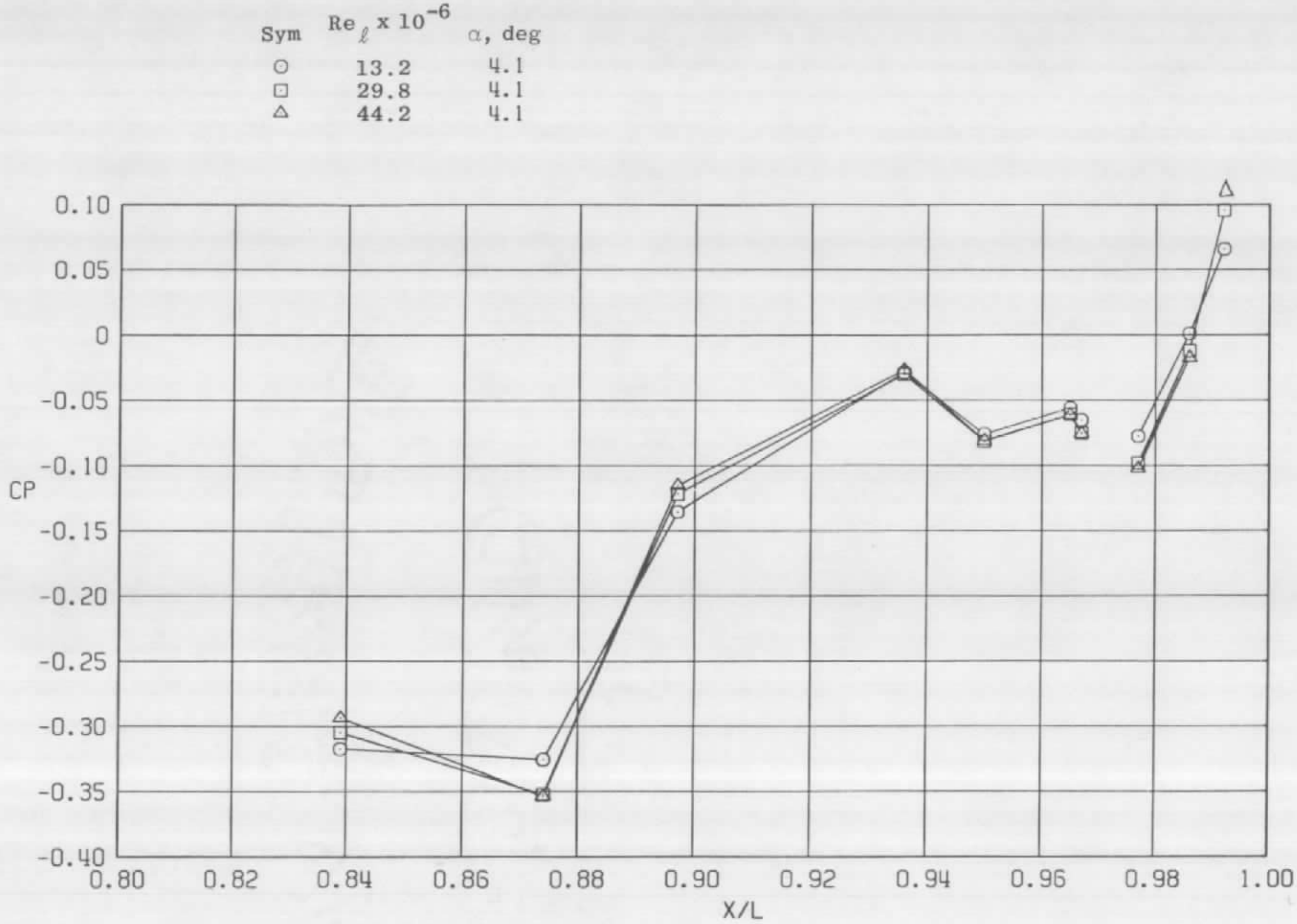

a. $\phi = 0$

Figure 51. Reynolds number effects on surface pressure coefficients, A8 = 300 in.², M = 0.9 (LS)

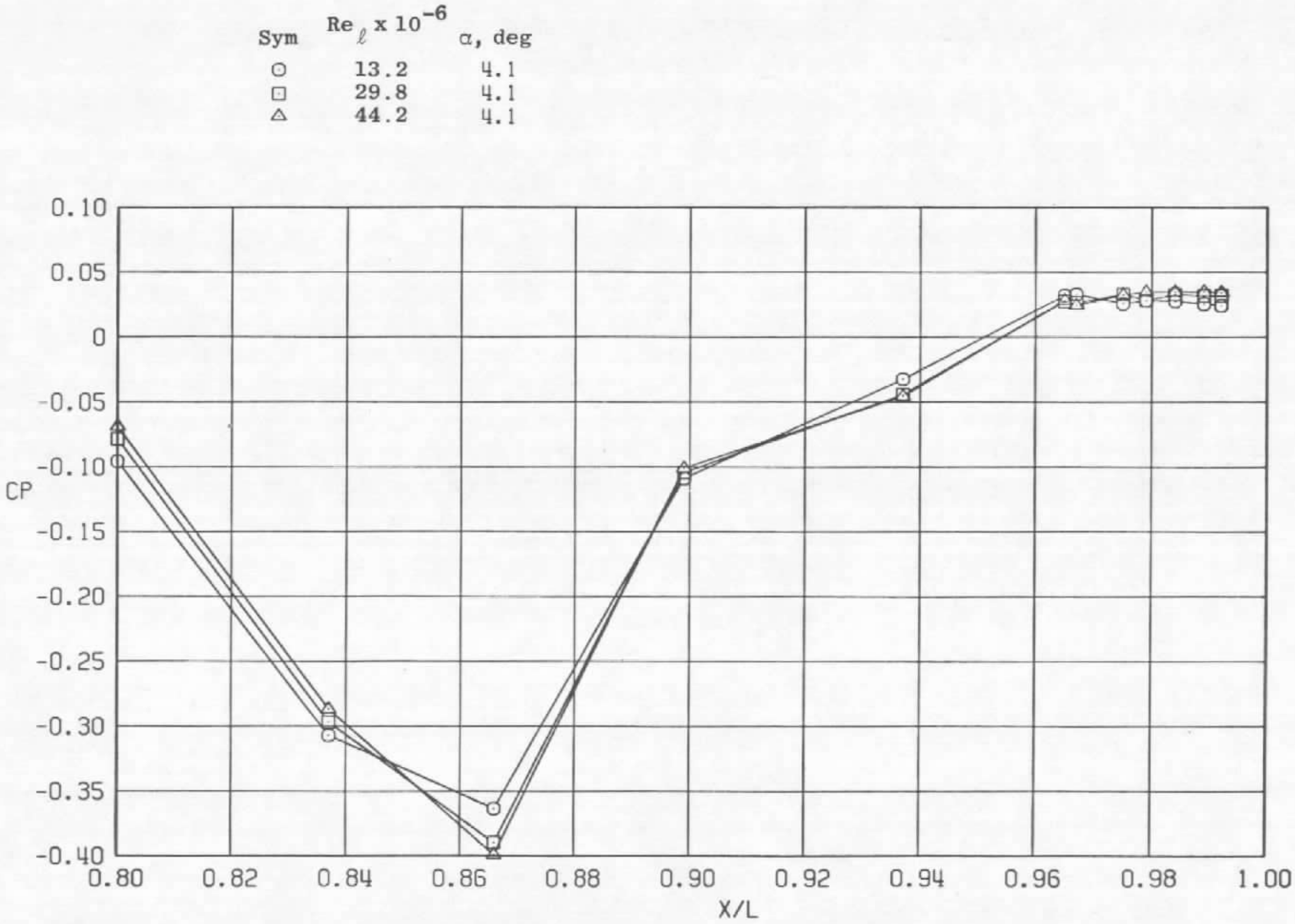

b. ϕ = 45 deg
Figure 51. Continued.

c. ϕ = 135 deg
Figure 51. Continued.

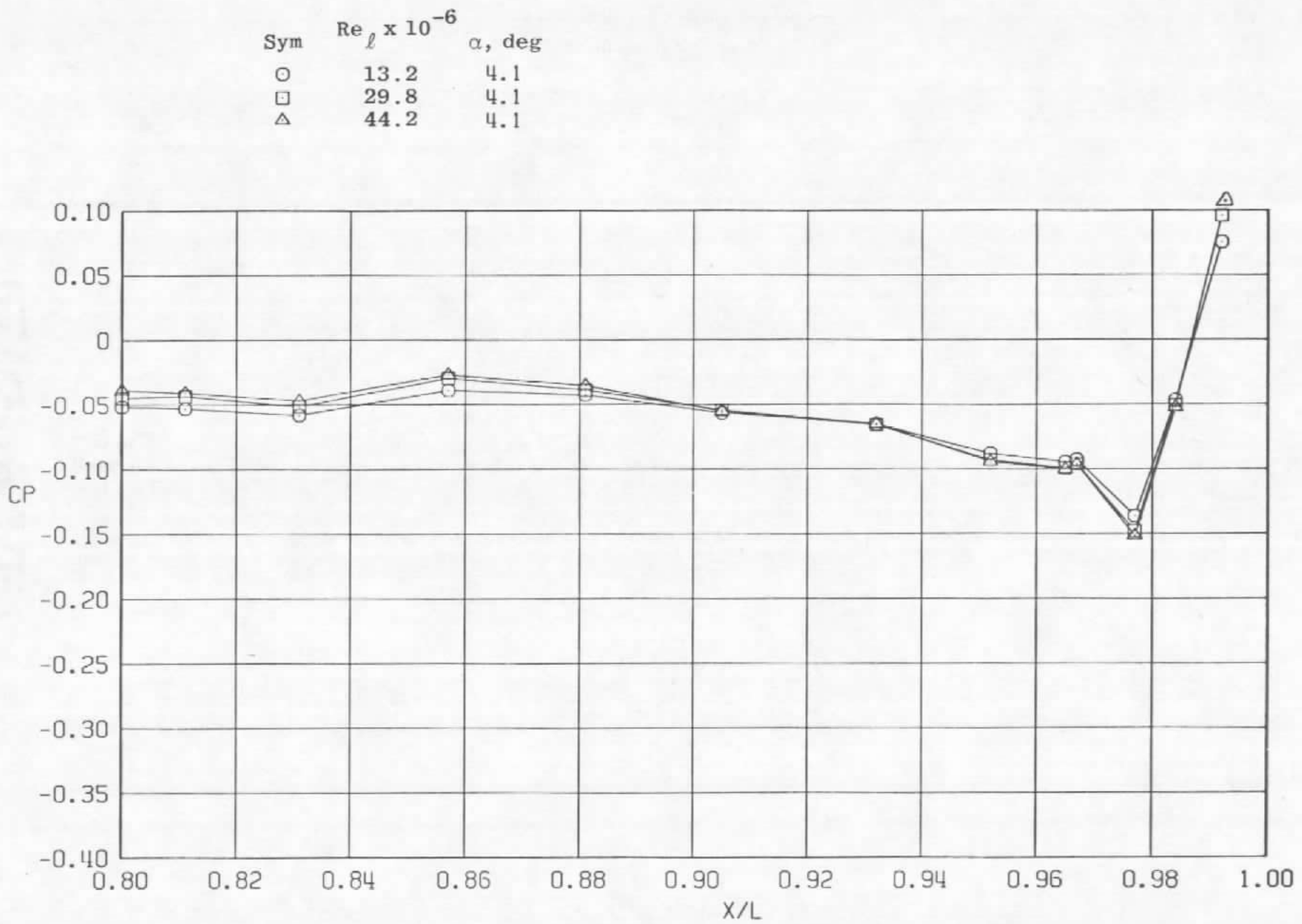

d. ϕ = 180 deg
Figure 51. Continued.

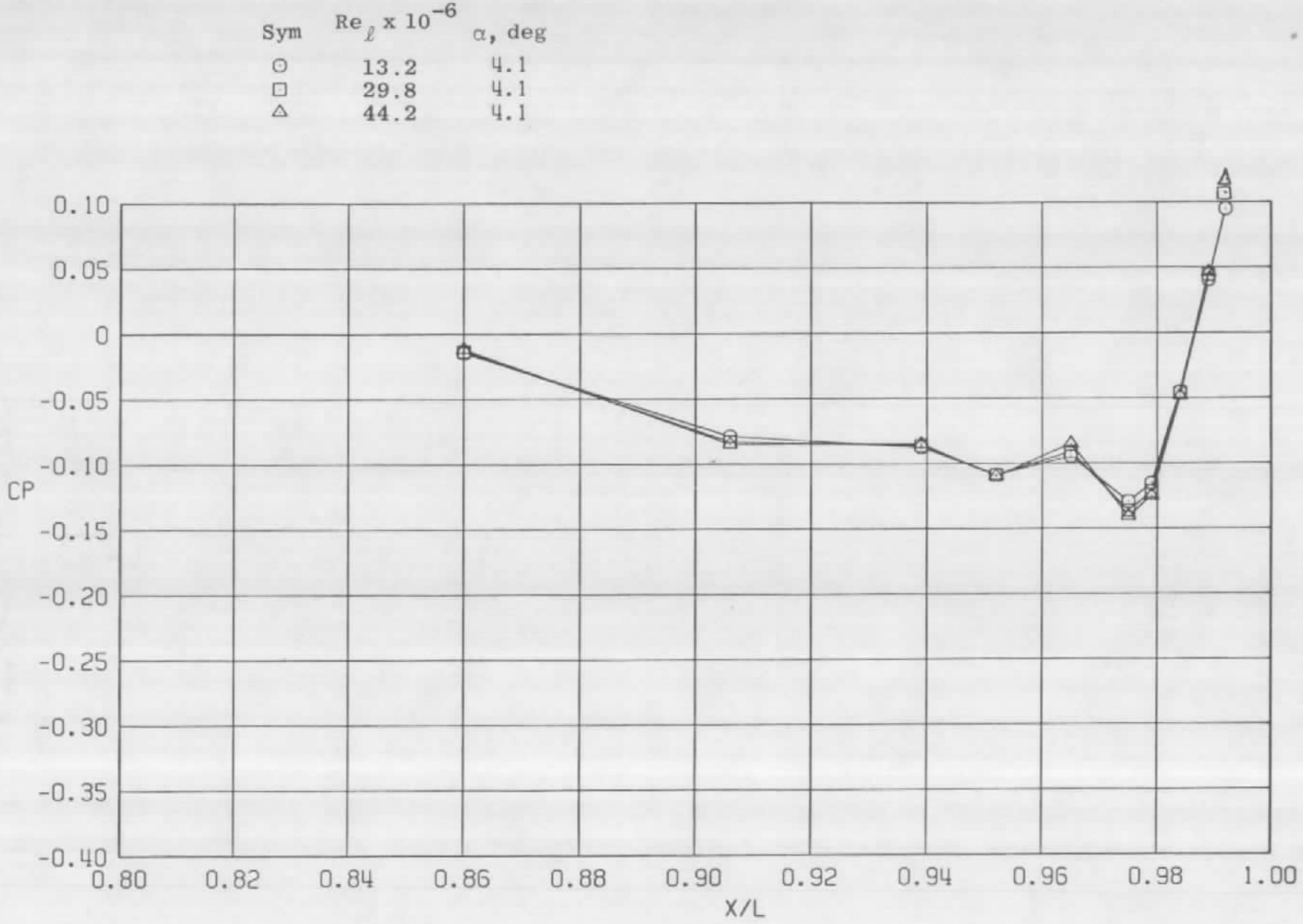

e. ϕ = 225 deg

Figure 51. Continued.

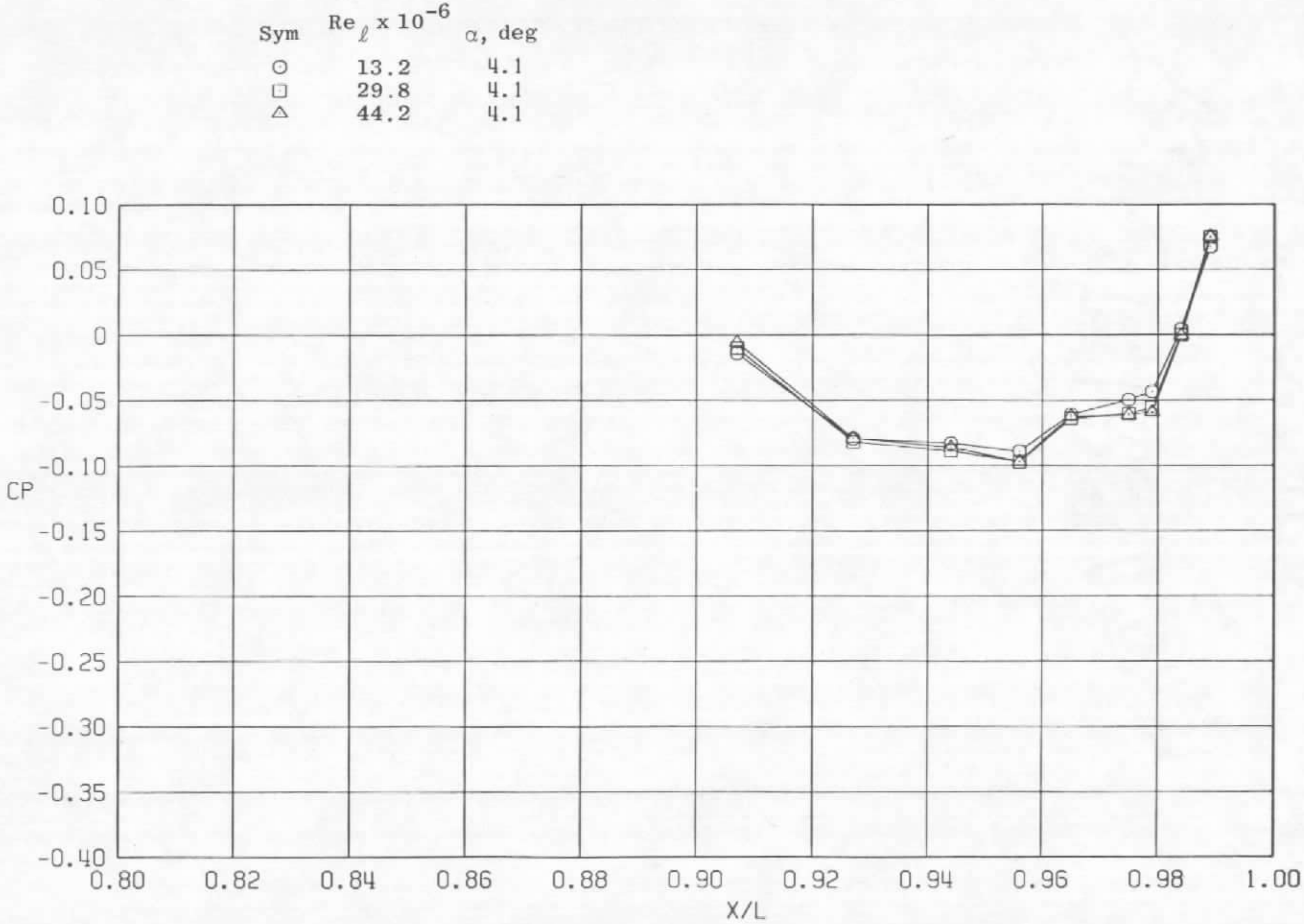

f. ϕ = 315 deg
Figure 51. Concluded.

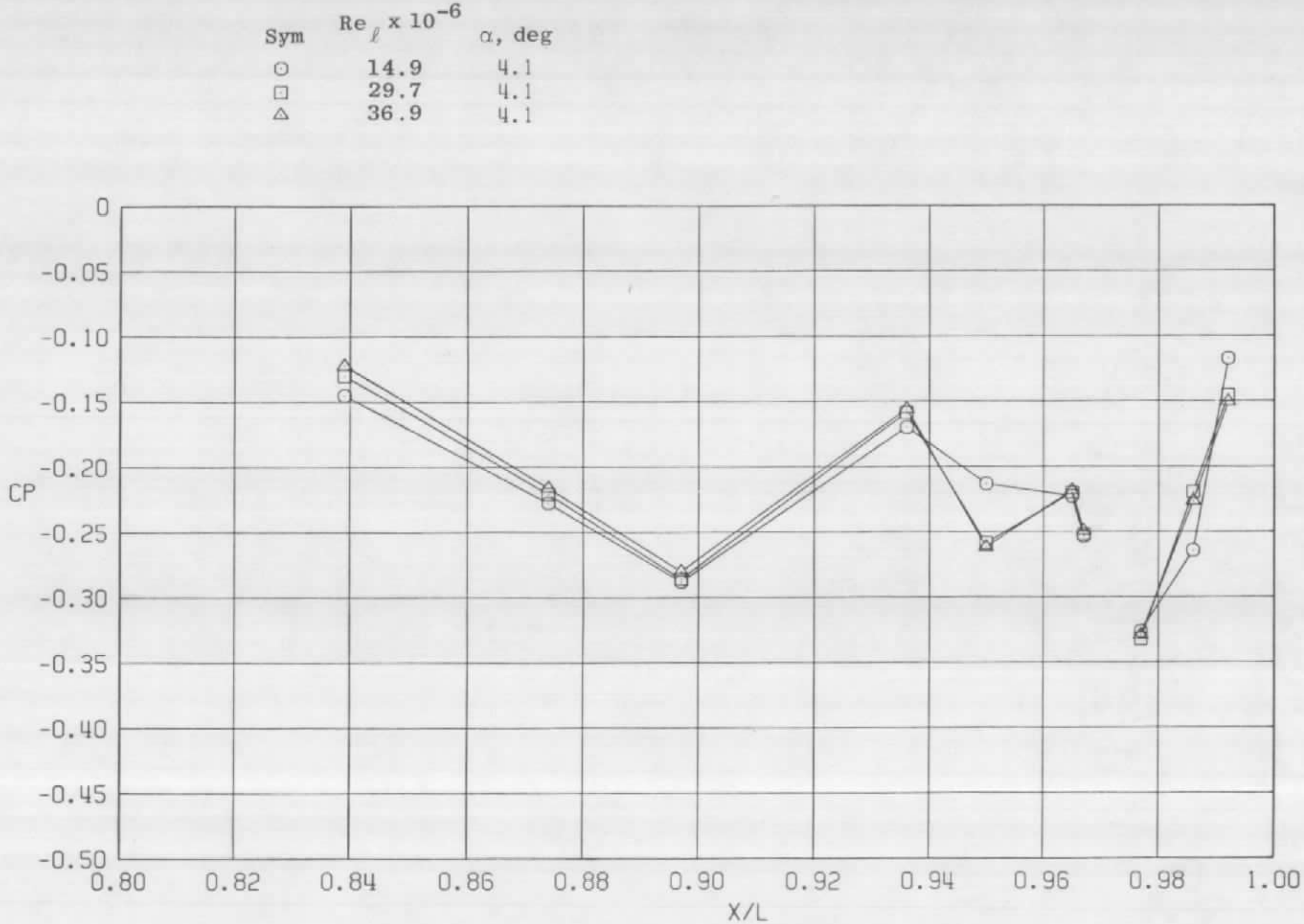

a. $\phi = 0$

Figure 52. Reynolds number effects on surface pressure coefficients, A8 = 300 in.^{2}, M = 1.2 (LS).

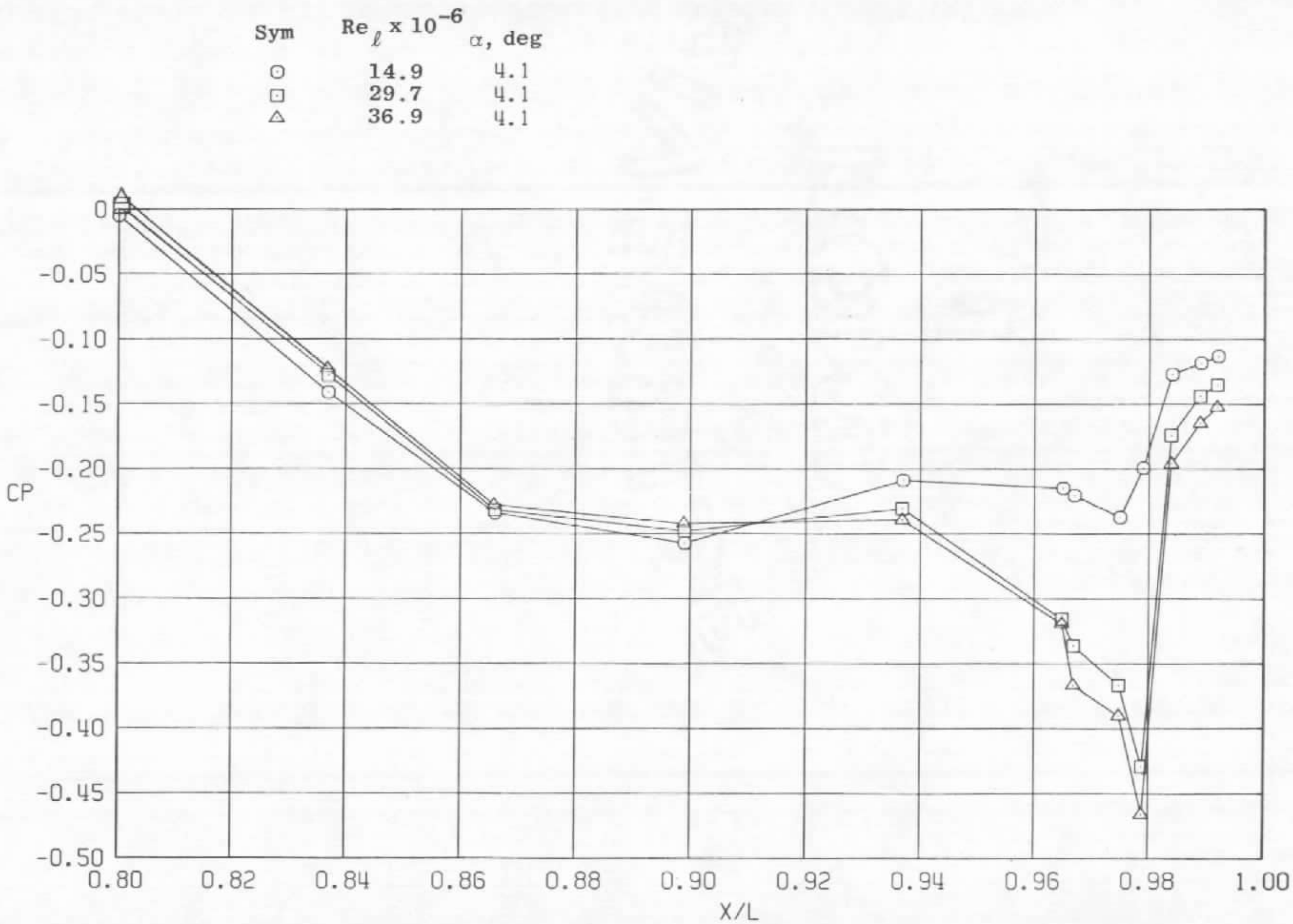

b. ϕ = 45 deg
Figure 52. Continued.

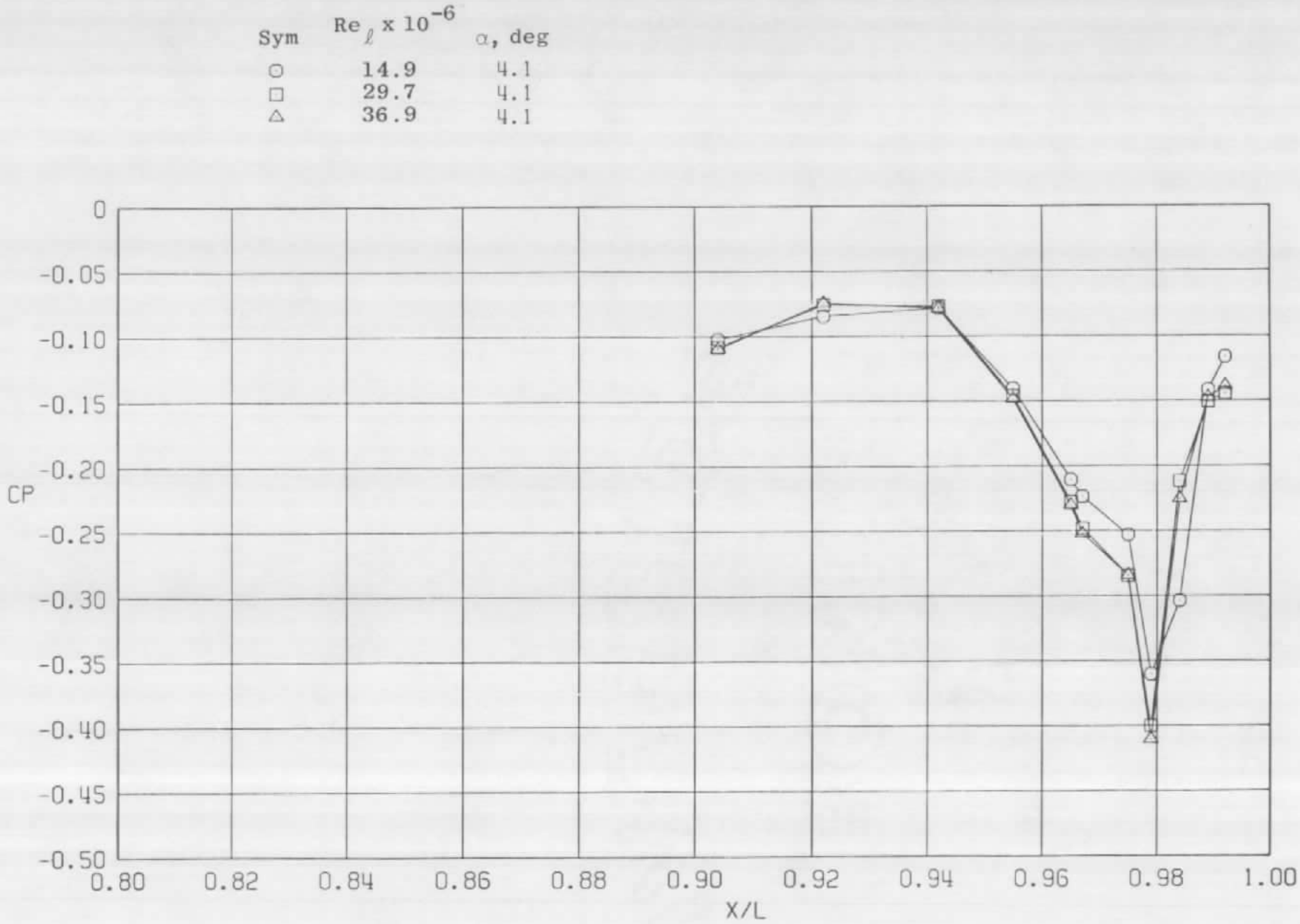

c. ϕ = 135 deg
Figure 52 Continued.

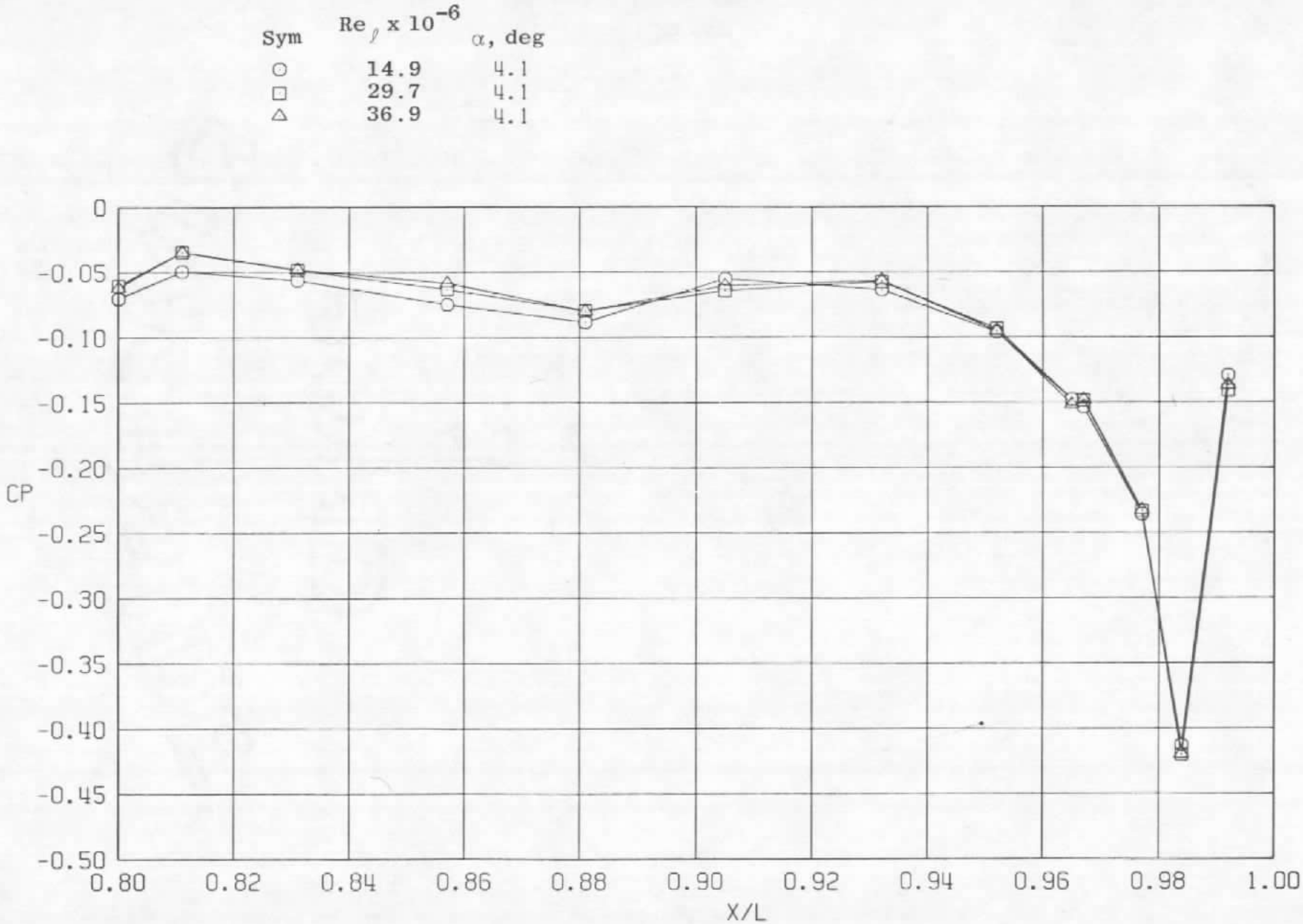

d. ϕ = 180 deg
Figure 52. Continued.

e. ϕ = 225 deg
Figure 52. Continued.

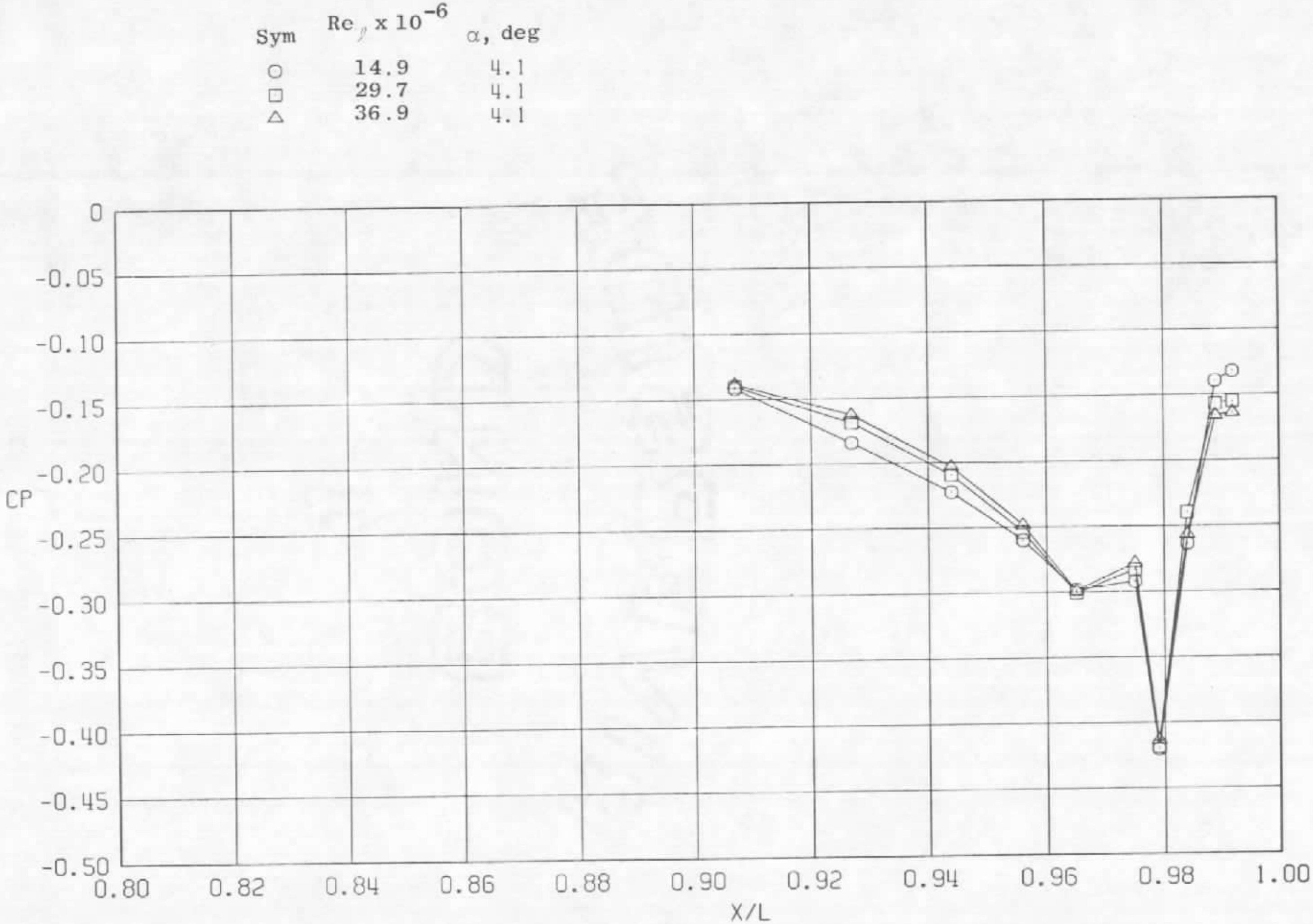

f. ϕ = 315 deg
Figure 52. Concluded.

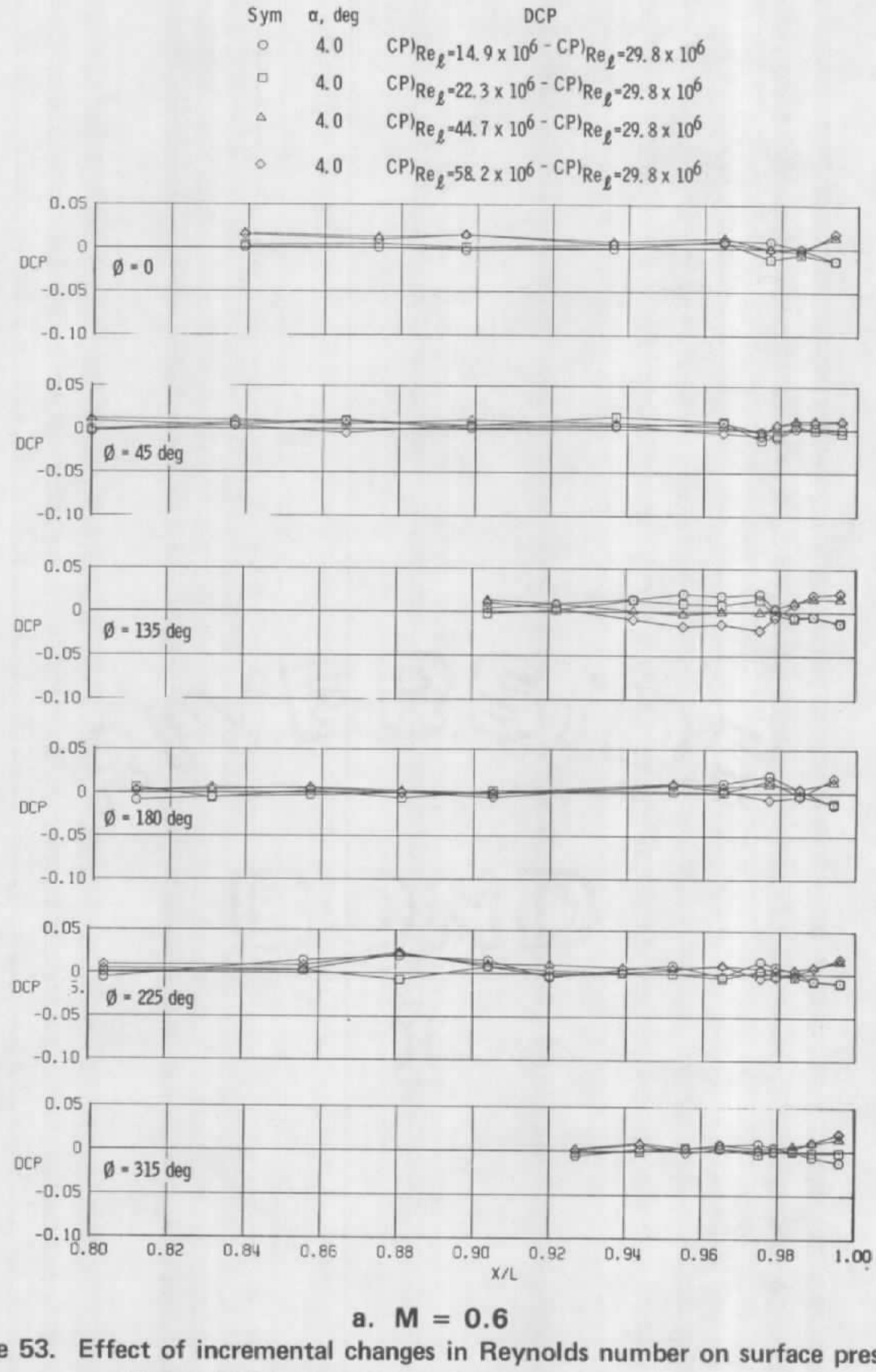

a. M = 0.6

Figure 53. Effect of incremental changes in Reynolds number on surface pressure coefficient (WT), A8 = 200 in.², NPR = 3.4.

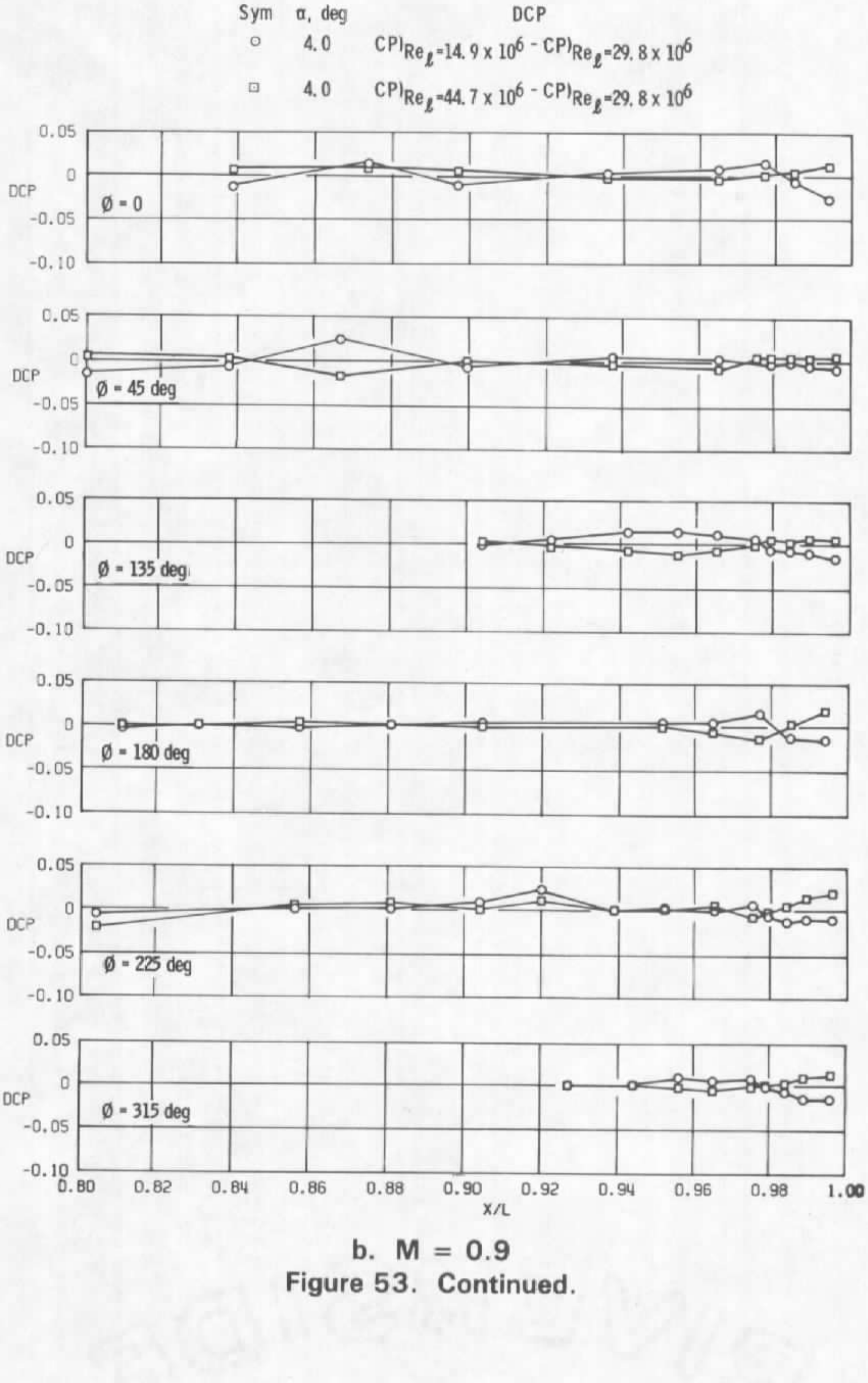

b. M = 0.9
Figure 53. Continued.

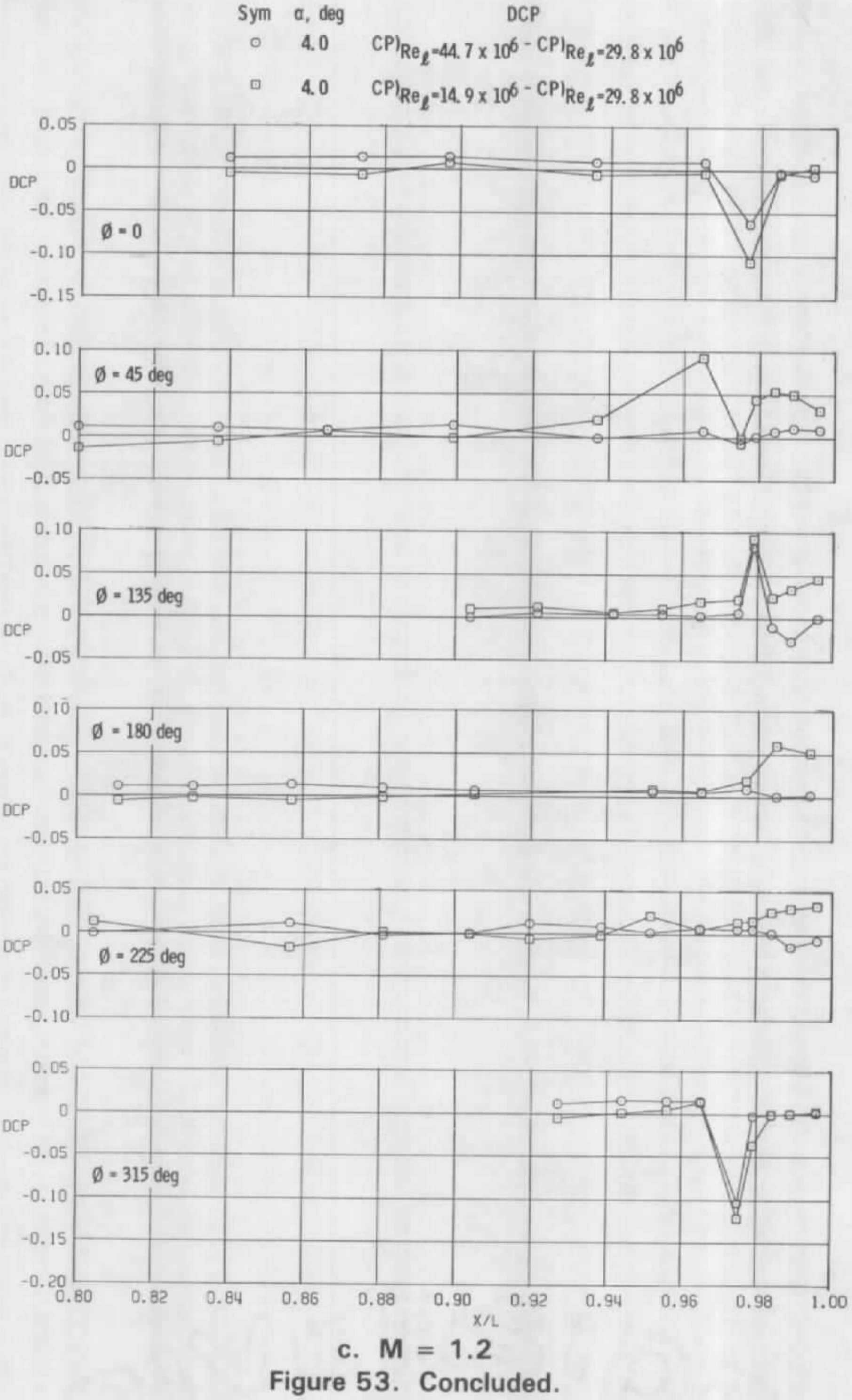

c. M = 1.2
Figure 53. Concluded.

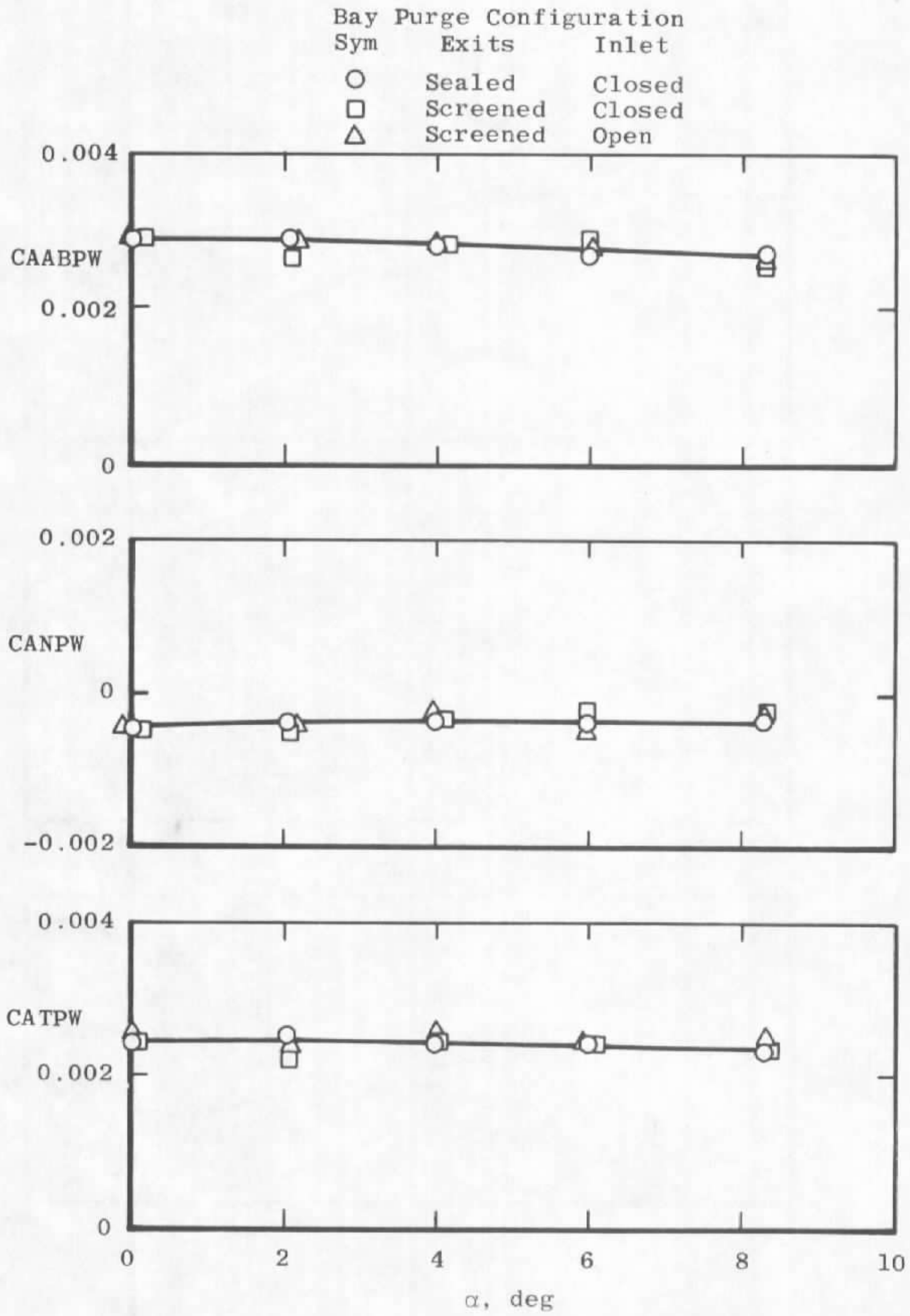

a. M = 0.6, NPR = 2.7

Figure 54. Bay purge effects on axial force coefficients, A8 = 200 in.^{2}, δ_H = −1.5 deg (WT).

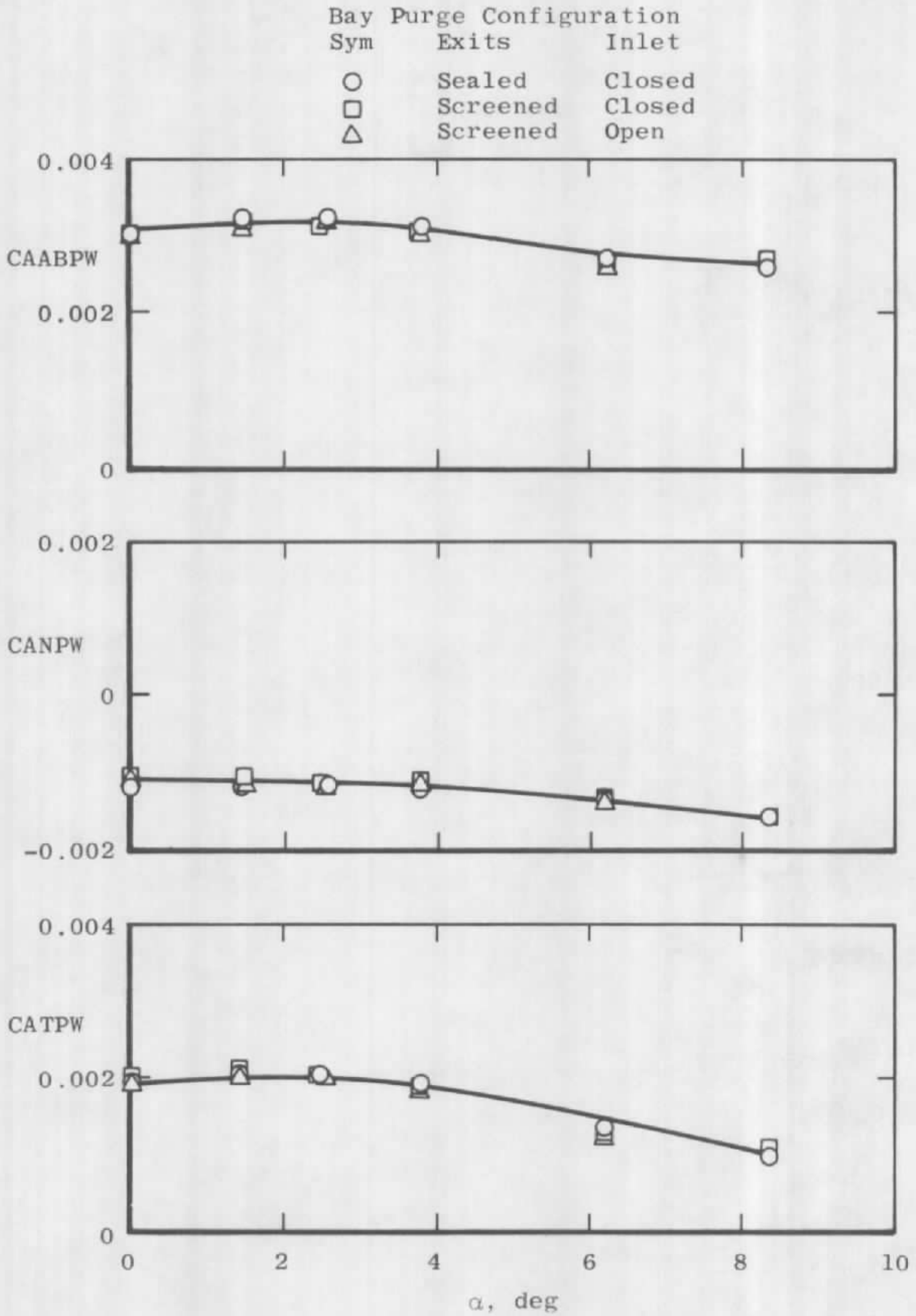

b. M = 0.9, NPR = 3.4
Figure 54. Continued

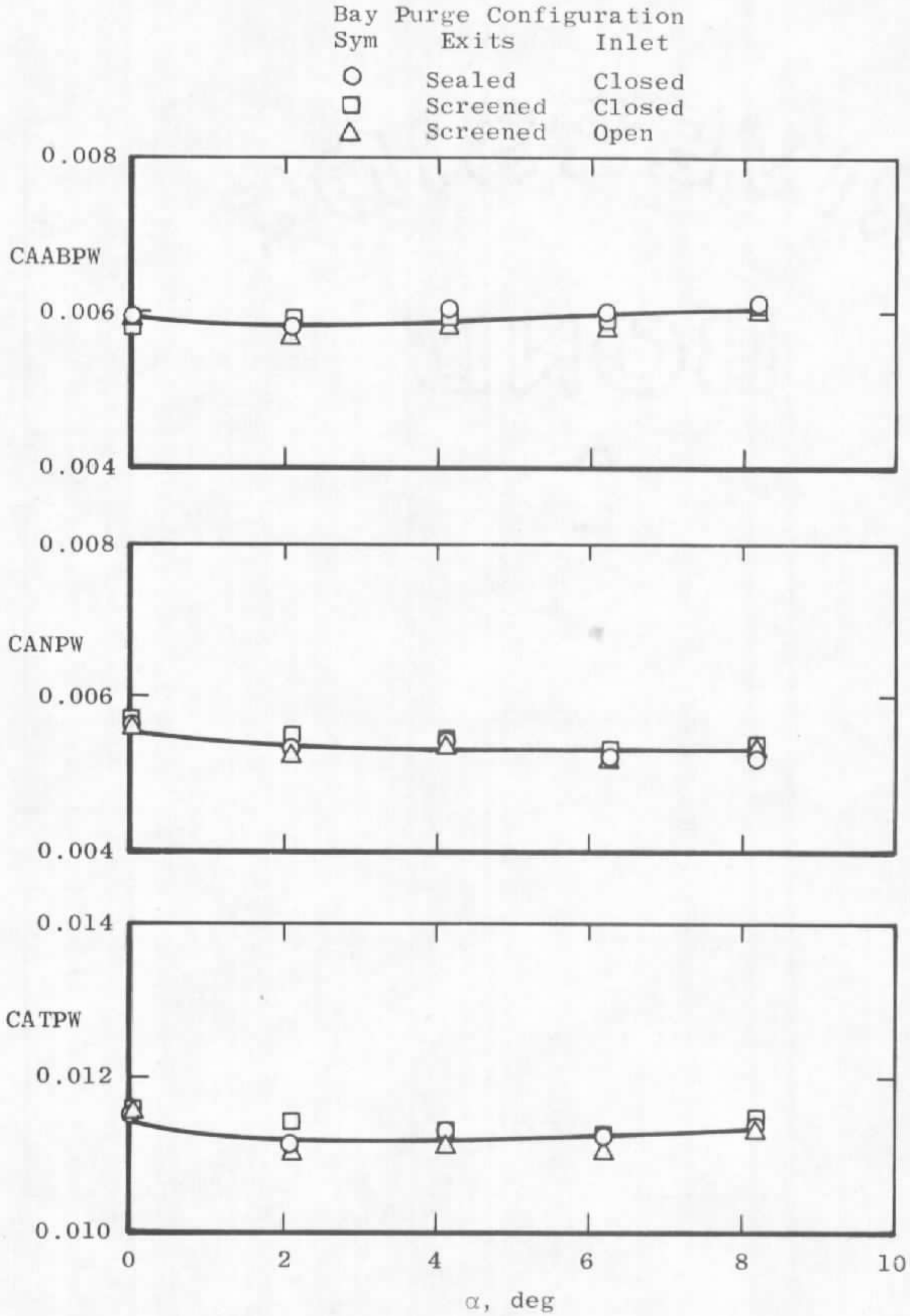

c. M = 1.2, NPR = 7.5
Figure 54. Concluded.

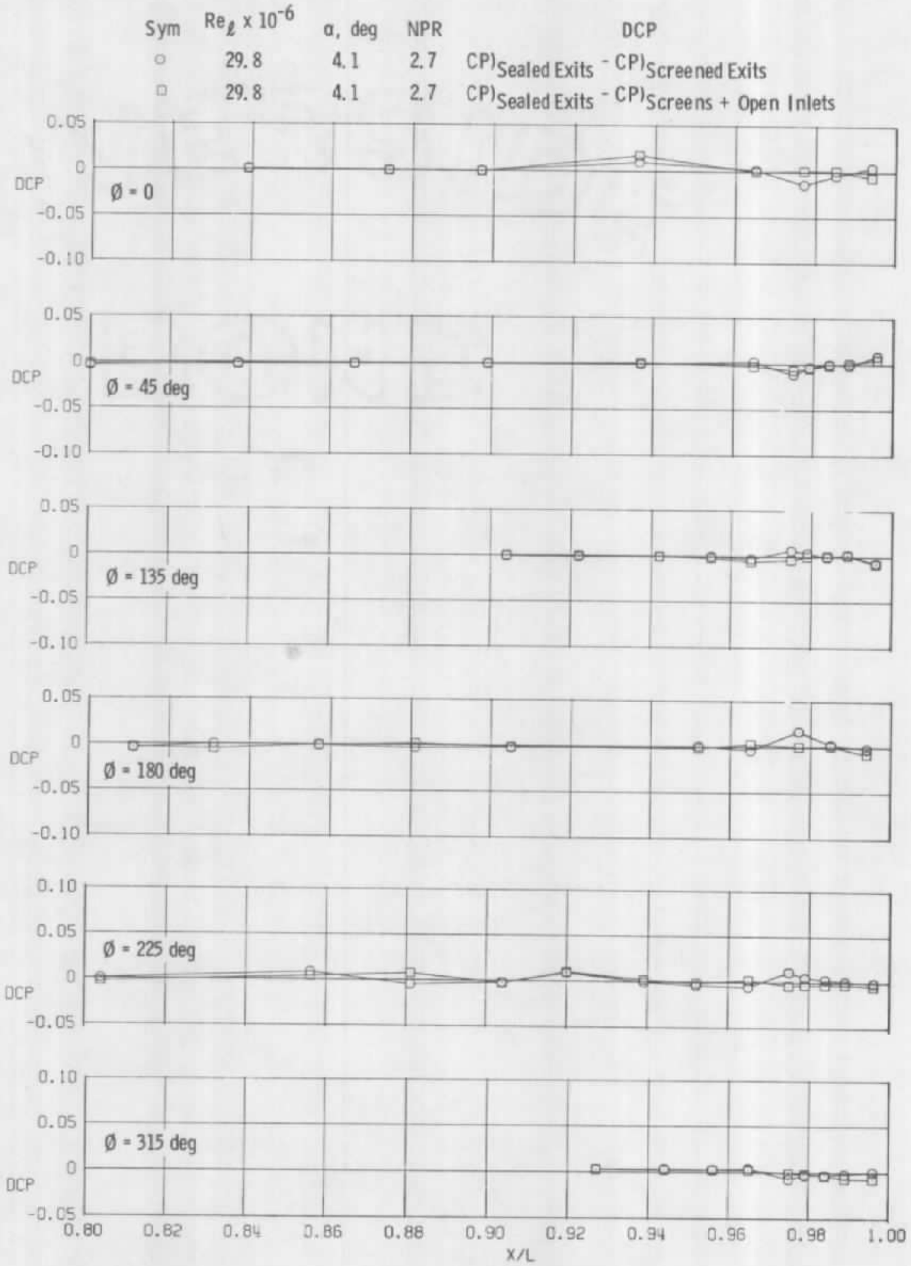

a. M = 0.6

Figure 55. Effect of incremental bay purge flow changes on surface pressure coefficients, A8 = 200 in.^{2}, δ_H = −1.5 deg (WT).

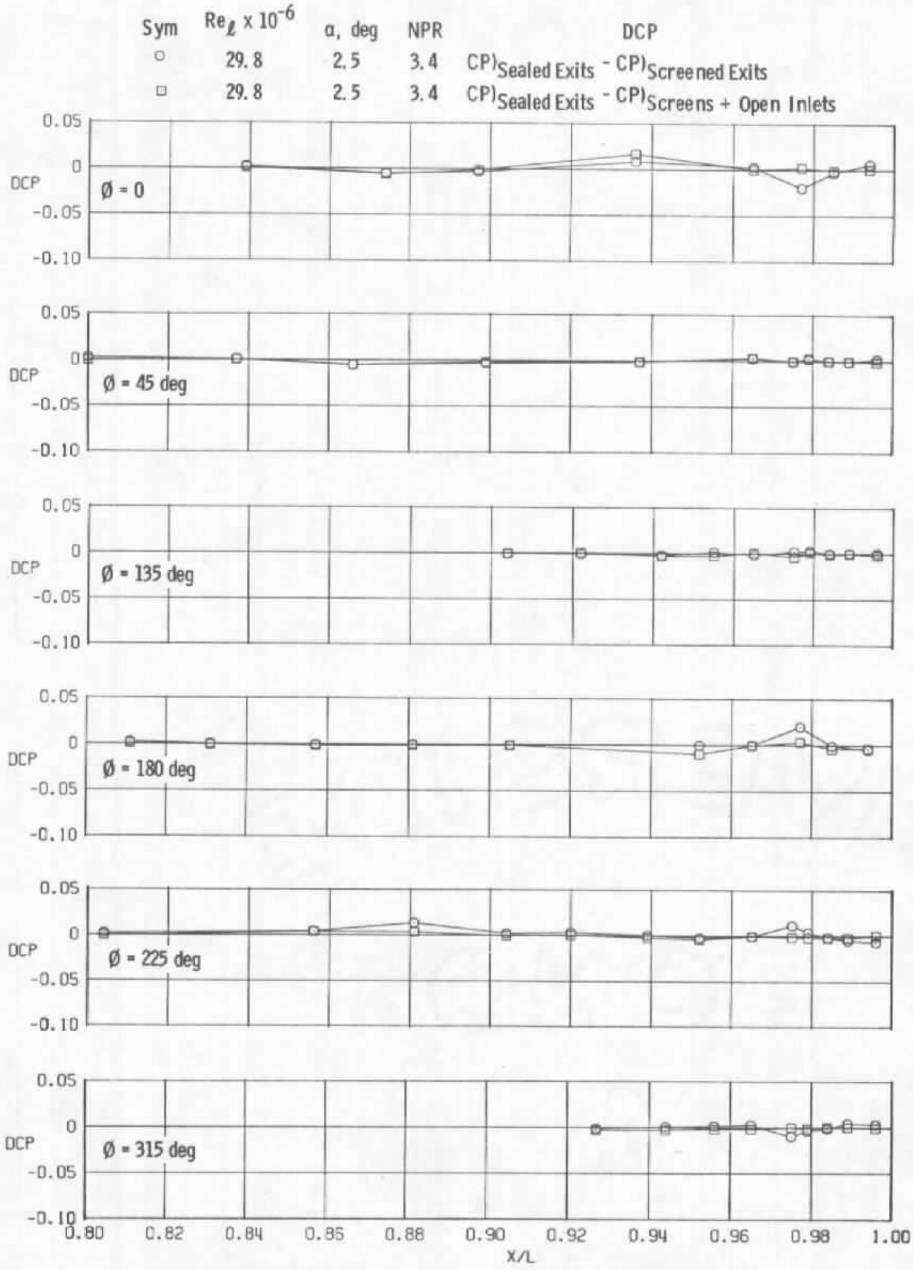

b. M = 0.9
Figure 55. Continued.

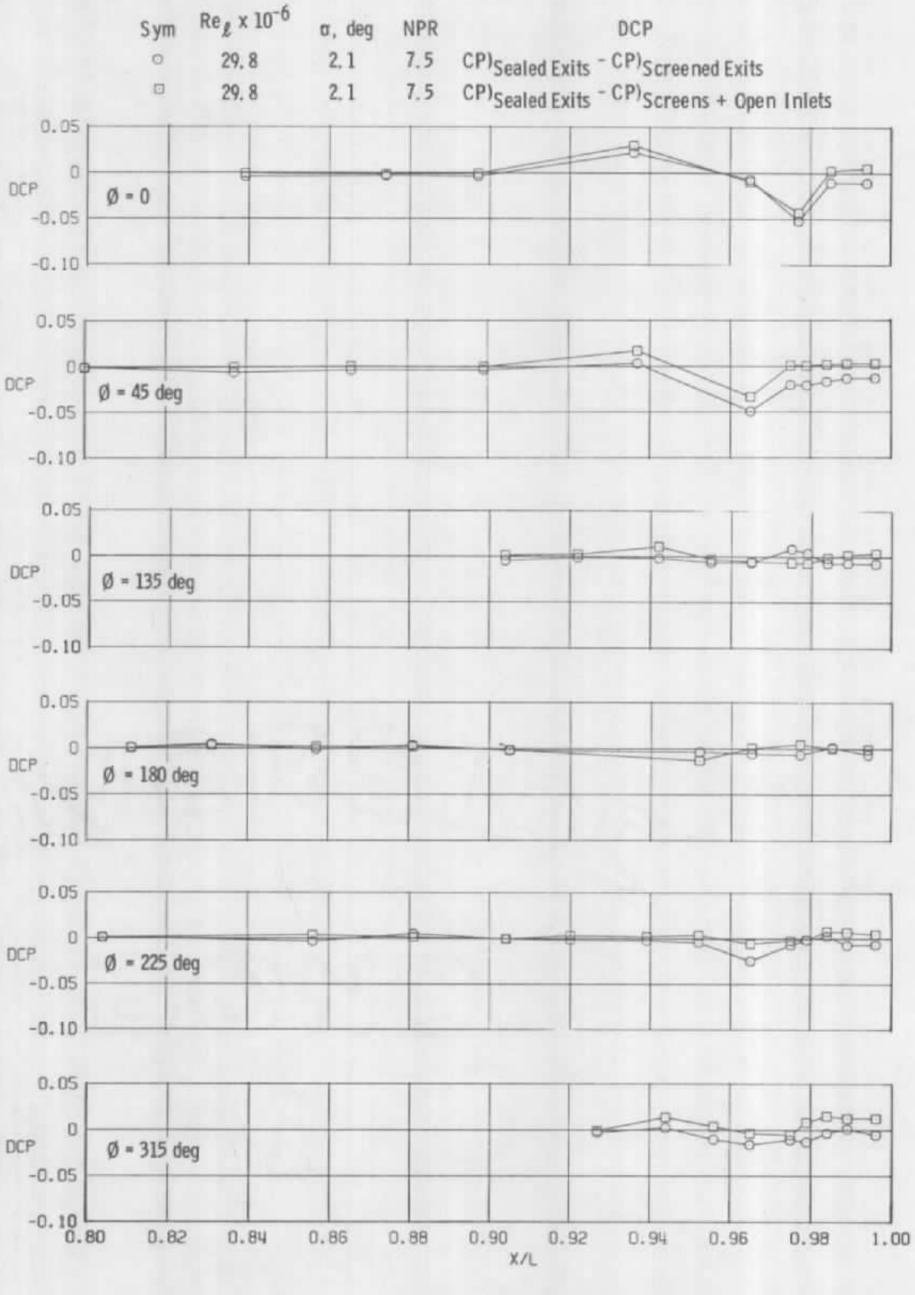

c. M = 1.2
Figure 55. Concluded.

NOMENCLATURE

Ai	Incremental areas used in pressure integration, in.^{2}
A8	Full-scale nozzle throat area, in.^{2} (see Fig. 4, Vol. I)
CAABPW	Afterbody integrated pressure axial force coefficient Σ(Cpi) (Ai)/S i = 221 to 442, and 522 to 603 (see Table 4, Vol. I)
CANPW	Nozzle integrated pressure axial force coefficient Σ(Cpi) (Ai)/S i = 102 to 220 (see Table 4, Vol. I)
CATPW	Total aft end (nozzle plus afterbody) integrated pressure axial force coefficient, CAABPW + CANPW
CPxx	Surface pressure coefficient, (Pi-P)/Q, along orifice ray at ϕ = xx
D	Sting diameter, in.
DCPxx	Pressure coefficient differences (WT-SS) on orifice ray at ϕ = xx
DE	Nozzle exit diameter, in. (see Fig. 4, Vol. I)
DS	Maximum sting diameter, (3.43 in.)
FS	Model fuselage station, in. (see Fig. 2, Vol. I)
L	Model length, 142.1 in.
ℓ	Body length, 126.6 in. (10.55 ft)
LS	Large-sting support system
M	Free-stream Mach number
NPR	Nozzle pressure ratio (model nozzle total pressure/free-stream static pressure)
NPRE	Equivalent nozzle pressure ratio (Ref. 1)
P	Free-stream static pressure, psfa
Pi	Model surface pressure, psfa (see Fig. 7 and Table 4, Vol. I)
PT	Free-stream total pressure, psfa

Q	Free-stream dynamic pressure, psfa
R	Nozzle and afterbody outer surface radius. in. (see Figs. 4b through 3 and Table 4, Vol. I)
Re	Free-stream unit Reynolds number, per foot
Re_ℓ	Characteristic Reynolds number based on body length
r	Nozzle internal surface radius, in. (see Figs. 4b through e)
S	Wing + fuselage planform area (2,020 in.^{2})
SS	Small-sting support system (annular jet test)
TS	Wind tunnel station, in.
UCPi	Uncertainty in surface pressure coefficient i
WT	Wingtip support system
X	Model axial station, in.
X_N	Nozzle axial station, in. (see Figs. 4b through e, Vol. I)
X_s	Distance between nozzle exit and beginning of sting taper, in. (see Table 1, Vol. I)
Y	Lateral location of pressure orifice (see Fig. 7, Vol. I)
Z	Vertical location of pressure orifice (see Fig. 7, Vol. I)
α	Model angle of attack, deg
δ_H	Horizontal tail deflection angle, deg (positive leading edge up)
ϕ	Angular location of pressure orifice, deg (see Fig. 7b, Vol. I)
Part Number	Data part number (a data subset containing variations of only one independent parameter)
Data Point	Data point number (a single record of all test parameters)